

UNIVERSIDAD DE CÓRDOBA

Programa de doctorado: *Electroquímica. Ciencia y Tecnología.*

Título de la tesis (español e inglés): *Caracterización estructural y funcional de la Interfase nano-bio en Sistemas de 2- y 3-Dimensiones.*

*Structural and functional characterization of the nano-bio Interface in 2- and 3-Dimensional systems.*

Director/Directores:

María Teresa Pineda Rodríguez

Rafael Madueño Jiménez

Autor de la tesis: Miriam Chávez Peraza

Fecha de depósito tesis en el Idep: octubre de 2022

TITULO: *Caracterización estructural y funcional de la Interfase nano-bio en Sistemas de 2- y 3-Dimensiones*

AUTOR: *Miriam Chávez Peraza*

---

© Edita: UCOPress. 2022  
Campus de Rabanales  
Ctra. Nacional IV, Km. 396 A  
14071 Córdoba

<https://www.uco.es/ucopress/index.php/es/>  
[ucopress@uco.es](mailto:ucopress@uco.es)

---

UNIVERSIDAD DE CÓRDOBA  
FACULTAD DE CIENCIAS  
DEPARTAMENTO DE QUÍMICA FÍSICA Y  
TERMODINÁMICA APLICADA



*CARACTERIZACIÓN ESTRUCTURAL Y FUNCIONAL DE  
LA INTERFASE NANO-BIO EN SISTEMAS DE 2- Y 3-  
DIMENSIONES*

*STRUCTURAL AND FUNCTIONAL CHARACTERIZATION  
OF THE NANO-BIO INTERFACE IN 2- AND 3-  
DIMENSIONAL SYSTEMS*

*Autora: Miriam Chávez Peraza*

*Directores: Teresa Pineda Rodríguez*

*Rafael Madueño Jiménez*

*Córdoba, 2022*

Trabajo presentado para optar al Grado de Doctor en Electroquímica. Ciencia y Tecnología

Fdo.: Miriam Chávez Peraza

Graduada en Química

Título de Tesis:

**Caracterización estructural y funcional de la Interfase nano-bio en Sistemas de 2- y 3-Dimensiones.**

**Structural and functional characterization of the nano-bio Interface in 2- and 3-Dimensional systems.**

Los directores del trabajo:

Fdo.: María Teresa Pineda Rodríguez

Catedrática de Universidad del  
Departamento de Química Física y  
Termodinámica Aplicada de la  
Universidad de Córdoba

Fdo. Rafael Madueño Jiménez

Profesor titular de Universidad del  
Departamento de Química Física y  
Termodinámica Aplicada de la  
Universidad de Córdoba





**TÍTULO DE LA TESIS:** Caracterización estructural y funcional de la Interfase nano-bio en sistemas de 2- y 3-Dimensiones.

**DOCTORANDO/A:** Miriam Chávez Peraza

INFORME RAZONADO DEL/DE LOS DIRECTOR/ES DE LA TESIS

D<sup>a</sup> María Teresa Pineda Rodríguez, Catedrática de Universidad, y D. Rafael Madueño Jiménez, Profesor Titular de Universidad, miembros del Departamento de Química Física y Termodinámica Aplicada (Área de Química Física) de la Universidad de Córdoba, informan que la Tesis Doctoral presentada por Dña. Miriam Chávez Peraza, se ha realizado bajo su supervisión.

El trabajo presentado se desarrolló dentro del Programa de Doctorado en “Electroquímica. Ciencia y Tecnología,” en el Departamento de Química Física y Termodinámica Aplicada (Área de Química Física) de la Universidad de Córdoba, durante el desarrollo de los proyectos RED2018-102412-T (Ministerio de Ciencia e Innovación, Red de Excelencia de Sensores y Biosensores Electroquímicos) y UCO-FEDER-2018: ref. 1265074-2B (Junta de Andalucía y Universidad de Córdoba, Plan Propio, Sub. 1.2.P.P. 2019). Durante el tiempo de realización del trabajo la doctoranda ha disfrutado de un contrato de Formación de Profesorado Universitario del Ministerio de Universidades (FPU 17/03873).

La presente memoria reúne, a juicio de los directores, los requisitos exigidos, y ha dado lugar a siete artículos publicados en revistas científicas en los que la doctoranda es primera autora, además de varias comunicaciones a congresos nacionales e internacionales. Por otro lado, los directores de la Tesis informan de la adecuada dedicación de la doctoranda, los conocimientos que ha adquirido en el campo objeto de su trabajo y su capacidad investigadora, incluyendo el diseño y realización de experimentos, la discusión de resultados y la extracción de conclusiones. Asimismo, informan de la realización de una estancia de tres meses la doctoranda en los laboratorios del Dipartimento di Scienze Chimiche de la Università degli Studi di Padova (Italia) y de la existencia de dos informes favorables de doctores extranjeros.

Por todo ello, se autoriza la presentación de la Tesis Doctoral.

Córdoba, 3 de octubre de 2022

Fdo. María Teresa Pineda Rodríguez

Fdo. Rafael Madueño Jiménez



Mediante la defensa de esta memoria se pretende optar a la mención de “Doctorado Internacional”, habida cuenta que el doctorando reúne los requisitos exigidos para tal mención:

1. Se cuenta con informes favorables de dos doctores expertos, con experiencia investigadora acreditada, pertenecientes a alguna institución de educación superior o instituto de investigación fuera de España.

2. En el Tribunal, que ha de evaluar la Tesis Doctoral, existe un miembro de una institución de educación superior o centro de investigación de un extranjero.

3. Parte de la redacción y defensa de esta Memoria se realizará en una de las lenguas habituales para la comunicación científica y distinta a cualquiera de las lenguas oficiales en España.

4. La doctoranda ha realizado una estancia de investigación de tres meses de duración en Dipartimento di Scienze Chimiche de la Università degli Studi di Padova (Italia). Esta estancia se ha realizado gracias a una ayuda para la movilidad a fin de obtener el Doctorado con Mención Internacional, concedida por la Universidad de Córdoba.





La investigación realizada en la presente Tesis Doctoral forma parte de la programación plurianual de actividades del Grupo de Investigación FQM-111 de la Universidad de Córdoba, para la cual ha recibido financiación a través de:

- El apoyo financiero del Ministerio de Ciencia e Innovación, proyecto RED2018-102412-T (Red de Excelencia de Sensores y Biosensores Electroquímicos).
- El apoyo financiero de la Junta de Andalucía y la Universidad de Córdoba en el marco de las ayudas "Plan Propio de Investigación de la Universidad de Córdoba" (UCO-FEDER-2018: ref. 1265074-2B, Plan Propio, Sub. 1.2.P.P. 2019)

Al mismo tiempo, el trabajo ha sido realizado durante el periodo de disfrute de un contrato de Formación de Profesorado Universitario del Ministerio de Universidades (FPU 17/03873).



# Índice





<b>Resumen / Summary</b> .....	1
<b>Hipótesis y objetivos</b> .....	11
<b>Capítulo 1. Introducción</b> .....	21
1.1. Nanociencia y Nanotecnología.....	23
1.1.1. Interacción de los NMs y recubrimientos moleculares con el entorno biológico.....	24
1.1.2. Estrategias <i>grafting to</i> y <i>grafting from</i> para la funcionalización de superficies.....	26
1.1.3. PEGilación.....	28
1.2. SAMs en sustratos planos.....	30
1.2.1. Formación de SAMs desde disolución.....	31
1.2.2. Organización de SAMs. Estructura, ensamblaje y defectos.....	32
1.2.3. SAMs de EGn.....	35
2.3.1. SAMs Cn-EGn.....	35
1.2.3.2. EGn-SAMs.....	37
1.3. NMs 3D: AuNPs.....	42
1.3.1. Estabilidad coloidal de AuNPs.....	44
1.3.1.1. Fenomenología de la doble capa eléctrica.....	44
1.3.1.2. Teoría DLVO.....	46
1.3.1.3. Influencia de las fuerzas estéricas en la estabilidad coloidal.....	48
1.3.2. EGn-SAMs en sistemas 3D.....	50
1.3.2.1. Recubrimiento superficial y diámetro hidrodinámico de EGn-AuNP.....	50
1.3.2.2. Respuesta frente a la temperatura y la concentración salina.....	52
1.4. Polimerización radical controlada.....	55
1.4.1. ATRP.....	57
1.4.2. eATRP.....	61
1.4.3. SI-eATRP.....	62
1.4.4. Formación de polímeros brush de EGn mediante SI-ATRP.....	64
1.5. Bibliografía.....	66
<b>Capítulo 2. Técnicas experimentales</b> .....	75
2.1. Experimentación electroquímica.....	77
2.1.1. Técnicas electroquímicas.....	77
2.1.1.1. Voltamperometría cíclica (CV).....	77
2.1.1.2. Espectroscopia de impedancia electroquímica (EIS).....	78
2.1.1.3. Cronoamperometría.....	79
2.1.1.4. Balanza electroquímica de cuarzo (EQCM).....	80

2.1.2. Celdas y electrodos.....	81
2.1.3. Instrumentación.....	83
2.1.3.1. CV, EIS y cronoamperometría.....	83
2.1.3.2 EQCM.....	84
2.3. Técnicas espectroscópicas.....	85
2.3.1. Espectroscopía UV-vis.....	86
2.3.2. Espectroscopía IRRAS.....	87
2.3.3. Espectroscopía XPS.....	90
2.4. Técnicas microscópicas.....	92
2.4.1. Microscopía TEM.....	93
2.4.2. Microscopía SEM.....	94
2.5. Técnicas de DLS y medidas de potencial $\zeta$ .....	95
2.6. Medidas de ángulo de contacto.....	97
2.7. Cromatografía de permeación en gel (GPC).....	98
2.8. Materiales y análisis de datos.....	100
2.9. Bibliografía.....	100
<b>Capítulo 3. Publicaciones.....</b>	<b>103</b>
3.1. Artículo 1.....	105
Caracterización de monocapas autoensambladas de O-(2-Mercaptoethyl)-O'-methyl-hexa(ethylene glycol) (EG7-SAM) en electrodos de oro.....	105
3.2. Artículo 2.....	131
Monocapas autoensambladas de O-(2-Mercaptoethyl)-O'-methyl-hexa(ethylene glycol) (EG7-SAM) en electrodos de oro. Efectos de la naturaleza de la disolución/electrolito en la formación y propiedades bloqueantes frente a la transferencia electrónica.....	131
3.3. Artículo 3.....	161
Evaluación mediante espectroscopía de impedancia electroquímica del efecto del potencial y la naturaleza del electrolito en la integridad de monocapas autoensambladas de O-(2-Mercaptoetil)-O'-metil-hexa(etilenglicol) (EG7-SAM).....	161
3.4. Artículo 4.....	183
Evaluación electroquímica de la densidad de empaquetamiento formadas mediante la aproximación grafting to de monocapas autoensambladas de polietilenglicol de diferente longitud de cadena en condiciones próximas al punto de nube.....	183
3.5. Artículo 5.....	209
Evaluación electroquímica de la densidad de empaquetamiento formadas mediante la aproximación grafting to de monocapas autoensambladas de polietilenglicol de diferente longitud de cadena en condiciones próximas al punto de nube.....	209
3.6. Artículo 6.....	243
Caracterización de autoensamblajes de Bis[2-(2-bromoisobutyryloxy) undecyl] disulphide (DTBU) en superficies de oro con potenciales usos en polimerizaciones tipo superficies inicializadas mediante transferencia atómica radicalaria (SI-ATRP).....	243
3.7. Artículo 7.....	271



Formación de películas poliméricas tipo brush de poli(etilenglicol) empleando ATRP por mediación electroquímica iniciada en superficie (SI-eATRP).....	271
<b>Capítulo 4. Conclusiones</b> .....	305
<b>Glosario de abreviaturas</b> .....	313
<b>Indicios de calidad</b> .....	319
<b>Otras aportaciones científicas</b> .....	323
<b>Publicaciones</b> .....	329



# **Resumen / Summary**



## Introducción

La Nanomedicina es una disciplina emergente en la que se combinan la Nanotecnología y la Biotecnología, lo que justifica que para su evolución sea necesario reunir investigaciones del campo médico, químico, farmacéutico y de ciencias e ingeniería de materiales [1]. De forma general, el término Nanomedicina hace referencia a la interacción a escala nanométrica que se produce en el interior de un sistema vivo entre un material y determinados órganos o células, sin afectar al resto de tejidos. En este contexto, es posible diseñar nanomateriales (NMs) tridimensionales (3D) y recubrimientos sobre sustratos macroscópicos (2D). Las superficies en 2D y 3D se funcionalizan con ligandos específicos que permiten tanto la internalización y liberación de moléculas portadoras en las células diana, como la mejora de los tiempos de circulación y por ende la prolongación de la vida útil del material, al conseguir mimetizarse con el entorno y evitar ser reconocido como un cuerpo extraño [2].

Muchos materiales que presentan recubrimientos de polímeros sintéticos y, en particular, los basados en polietilenglicol (EGn), han demostrado ser de gran aplicación en la distribución controlada de fármacos y la absorción celular. Por otro lado, los NMs y sustratos macroscópicos de oro son una de las superficies más estudiadas y que mayores ventajas presentan en aplicaciones biomédicas [3].

La modificación controlada de estas superficies inorgánicas con grupos funcionales específicos, frecuentemente de naturaleza orgánica, permite diseñar estructuras híbridas que presentan propiedades físicas y químicas únicas. Existen numerosas estrategias para modificar de manera controlada la superficie de los NMs y sustratos macroscópicos con los grupos funcionales deseados. Las monocapas autoensambladas (SAMs) son una opción atractiva para el diseño de la química superficial en una amplia gama de sustratos metálicos, que permite modificar de manera simple, flexible y exitosa, las propiedades intrínsecas de la superficie. Esta estrategia, enmarcada dentro de las aproximaciones *grafting to*, se basa en injertar moléculas, de tamaño y forma bien definidos, en la superficie de los sustratos mediante un grupo terminal [4]. Esta estrategia ha sido y es fundamental en la ciencia de superficies, sin embargo, presenta ciertas limitaciones relacionadas con el pequeño espesor de los recubrimientos que se obtienen. Estas limitaciones se pueden evitar mediante el diseño de películas orgánicas de mayor espesor, conocidas como recubrimientos compactos tipo *brush* [5]. Las metodologías más eficaces para alcanzar este tipo de películas son las *grafting from*, en la que las cadenas poliméricas se forman por adición sucesiva de monómeros a partir de un sustrato modificado con grupos funcionales iniciadores de la polimerización, obteniéndose películas poliméricas ancladas a la superficie de alta densidad

de empaquetamiento. Ambas estrategias, *grafting to* y *grafting from*, pueden emplearse para formar películas poliméricas tanto en NMs como en sustratos macroscópicos.

La investigación recogida en esta memoria aborda la preparación y caracterización de recubrimientos poliméricos de EGn sobre sustratos macroscópicos y nanopartículas de oro (AuNPs), empleando tanto la metodología *grafting to* de formación de SAMs como la polimerización radical controlada por transferencia atómica mediada electroquímicamente (eATRP), que es una de las estrategias *grafting from* más relevantes en la actualidad [6].

## Contenido

El trabajo comienza con el estudio de una molécula tiolada relativamente corta como es el EG7-SH, formando SAMs sobre sustratos de Au. Mediante las técnicas electroquímicas de voltamperometría cíclica (VC), espectroscopía de impedancia electroquímica (EIS) y curvas de capacidad se consigue una caracterización profunda de la película formada. El análisis estructural de la misma se complementa con las técnicas de caracterización superficial como son las espectroscopias fotoelectrónica de rayos X (XPS) e infrarroja de absorción-reflexión (IRRAS), la balanza electroquímica de cuarzo (EQCM) y las medidas de ángulo de contacto. La EG7-SAM se establece como sistema modelo sencillo en el que se fundamenten trabajos posteriores, empleando EGn-SH de mayor tamaño (n = 18, 45 y 136). Se estudian tanto los recubrimientos formados sobre sustratos macroscópicos de Au como en AuNPs. En este último caso, la estabilidad coloidal de las suspensiones EGn-AuNPs se evalúa en términos de temperatura, pH y concentración salina. Para ello, se emplean medidas de espectroscopia ultravioleta visible (UV-Vis), dispersión dinámica de luz (DLS) y medidas de potencial  $\zeta$ .

Por otro lado, se investiga la formación de películas compactas vía eATRP sobre superficies de Au en medio acuoso. En este punto, se evalúa, en primer lugar, el sistema de reacción multicomponente necesario para obtener recubrimientos de calidad. Una vez establecido, se profundiza en las condiciones experimentales que permiten formar estructuras tipo *brush* bien definidas. La caracterización de estas es análoga a la empleada para evaluar los recubrimientos obtenidos formando SAMs.

## Conclusión

En su conjunto, la investigación desarrollada en este trabajo contribuye a ampliar el conocimiento sobre recubrimientos moleculares basados en EGn en sustratos en 2D y 3D sobre sustratos de Au, obtenidos empleado diferentes aproximaciones experimentales. La caracterización profunda de las películas formadas permite afirmar que son potenciales

candidatas para diversas aplicaciones en el campo biomédico, pero también exhiben propiedades electroquímicas interesantes que las hacen atractivas en el diseño de sensores. Además, la caracterización químico-física de las películas basadas en EGN llena un hueco en el ámbito de conocimiento estructural y funcional de las películas moleculares.

## Bibliografía

- [1] B. Bhushan, V. Khanadeev, B. Khlebtsov, N. Khlebtsov, P. Gopinath, Impact of albumin based approaches in nanomedicine: Imaging, targeting and drug delivery, *Adv. Colloid. Interfac.* 246 (2017) 13-39.
- [2] J. Kreuter, T. Hekmatara, S. Dreis, T. Vogel, S. Gelperina, K. Langer, Covalent attachment of apolipoprotein A-I and apolipoprotein B-100 to albumin nanoparticles enables drug transport into the brain, *J. Control. Release* 118(1) (2007) 54-58.
- [3] Z.B. Li, X.F. Yu, P.K. Chu, Recent advances in cell-mediated nanomaterial delivery systems for photothermal therapy, *J. Mater. Chem. B* 6(9) (2018) 1296-1311.
- [4] F. Schreiber, Structure and growth of self-assembling monolayers, *Prog. Surf. Sci.* 65(5-8) (2000) 151-256.
- [5] J.O. Zoppe, N.C. Ataman, P. Mocny, J. Wang, J. Moraes, H.A. Klok, Surface-Initiated controlled radical polymerization: state-of-the-art, opportunities, and challenges in surface and interface engineering with polymer brushes, *Chem. Rev.* 117(3) (2017) 1105-1318.
- [6] R. Barbey, L. Lavanant, D. Paripovic, N. Schuwer, C. Sugnaux, S. Tugulu, H.A. Klok, Polymer brushes via Surface-Initiated controlled radical polymerization: synthesis, characterization, properties, and applications, *Chem. Rev.* 109(11) (2009) 5437-5527.





## Introduction

Nanomedicine is an emerging discipline that combines nanotechnology and biotechnology, so there is a need for expertise in the medical, chemical, pharmaceutical and materials science and engineering fields for its development [1]. Overall, Nanomedicine refers to the interaction at the nanometric scale that occurs within a living system between a material and certain organs or cells, without affecting the rest of the tissues. In this context, it is possible to design both three-dimensional (3D) NMs and macroscopic (2D) coatings. The 2- and 3-dimensional surfaces are functionalized with specific ligands that allow both the internalization and release of carrier molecules into target cells, as well as improving circulation times and thus extending the lifetime of the nanomaterial (NM) or surface coating by mimicking the environment and avoiding recognition as a foreign body [2].

Many materials are usually surrounded by synthetic polymeric coatings and, in particular, those based on polyethylene glycol (EGn), have proven to be of great application in controlled drug delivery and cellular uptake. Additionally, gold NMs and macroscopic substrates are one of the most studied and most advantageous surfaces for biomedical applications [3].

Controlled modification of these inorganic surfaces with specific functional groups, often organic in nature, allows the design of hybrid structures that exhibit specific physical and chemical properties. It is possible to control the surface modification of both NMs and macroscopic substrates through different strategies. Self-assembled monolayers (SAMs) are an attractive option for the design of surface chemistry on a wide range of metal substrates, allowing simple, flexible, and successful modification of intrinsic surface properties. This strategy, framed within the grafting to approaches, is based on grafting molecules, of well-defined size and shape, onto the surface of the substrates by means of a terminal group [4]. This strategy has been, as still is, fundamental in surface science. However, it has certain limitations related to the small thickness of the coatings obtained. These limitations can be avoided by designing thicker organic films, known as compact brush coatings [5]. The most effective methodologies to achieve this kind of films are known as grafting from, in which polymer chains are formed by successive addition of monomers from a substrate modified with polymerization-initiating functional groups, thus obtaining surface-anchored polymer films of high packing density. Both strategies, grafting to and grafting from, can be used to prepare polymer films on both NMs and macroscopic substrates.

This research focuses on the preparation and characterization of Egn polymeric coatings from both macroscopic substrates and gold nanoparticles (AuNPs), using either the grafting to methodology of SAMs formation, or the electrochemically-mediated atom

transfer controlled radical polymerisation (eATRP), one of the most relevant grafting from approaches at present [6].

## Content

This work with the study of a relatively short thiolated molecule, EG7-SH, that is employed to prepare SAMs on Au substrates. By means of the electrochemical techniques of cyclic voltammetry, impedance spectroscopy and capacitance curves, an in-depth characterization of the EG7-SAM is achieved. The structural analysis of the film is complemented with XPS, IRRAS, QCM and contact angle measurements. EG7-SAM is established as a simple model system on which the subsequent works using larger EGn-SH ( $n = 18, 45$  and  $136$ ), are based. Both coatings formed on macroscopic substrates and AuNPs are studied. In the latter, the colloidal stability of the obtained EGn-AuNPs suspensions is evaluated in terms of temperature, pH and salt concentration. For this purpose, UV-Vis, DLS and  $\zeta$  characterization techniques are used.

On the other hand, the formation of compact films via eATRP on Au surfaces in aqueous media is investigated. First, the multicomponent reaction system required to obtain quality coatings is evaluated. Once it is established, the experimental conditions to obtain well-defined brush-like structures are further investigated. The characterization of these is analogous to that used to evaluate the coatings obtained by preparing SAMs.

## Conclusion

As a whole, the research developed in this work contributes to extend the knowledge about EGn-based molecular coatings on 2- and 3-dimensional substrates on Au substrates, obtained using different experimental approaches. The in-depth characterization of the films formed allows to affirm that they are potential candidates for various applications in the biomedical field, but also exhibit interesting electrochemical features that make them attractive for sensor design. Furthermore, the chemical-physical characterization of EGn-based films fills a gap in the field of structural and functional knowledge of molecular films.

## Bibliography

- [1] B. Bhushan, V. Khanadeev, B. Khlebtsov, N. Khlebtsov, P. Gopinath, Impact of albumin based approaches in nanomedicine: Imaging, targeting and drug delivery, *Adv Colloid Interfac* 246 (2017) 13-39.
- [2] J. Kreuter, T. Hekmatara, S. Dreis, T. Vogel, S. Gelperina, K. Langer, Covalent attachment of apolipoprotein A-I and apolipoprotein B-100 to albumin nanoparticles enables drug transport into the brain, *J. Control. Release* 118(1) (2007) 54-58.

- [3] Z.B. Li, X.F. Yu, P.K. Chu, Recent advances in cell-mediated nanomaterial delivery systems for photothermal therapy, *J. Mater. Chem. B* 6(9) (2018) 1296-1311.
- [4] F. Schreiber, Structure and growth of self-assembling monolayers, *Prog. Surf. Sci.* 65(5-8) (2000) 151-256.
- [5] J.O. Zoppe, N.C. Ataman, P. Mocny, J. Wang, J. Moraes, H.A. Klok, Surface-Initiated controlled radical polymerization: state-of-the-art, opportunities, and challenges in surface and interface engineering with polymer brushes, *Chem. Rev.* 117(3) (2017) 1105-1318.
- [6] R. Barbey, L. Lavanant, D. Paripovic, N. Schuwer, C. Sugnaux, S. Tugulu, H.A. Klok, Polymer brushes via Surface-Initiated controlled radical polymerization: synthesis, characterization, properties, and applications, *Chem. Rev.* 109(11) (2009) 5437-5527.



# **Hipótesis y objetivos**



A continuación, se resumen las hipótesis planteadas en la investigación desarrollada durante esta Tesis Doctoral, así como los objetivos que se han pretendido alcanzar a partir de cada una de ellas. Además, se señala en qué artículo publicado se aborda cada uno de los puntos detallados.

## **Hipótesis 1**

La modificación de superficies mediante EGn ha demostrado ser una estrategia acertada para reducir la adsorción inespecífica de materiales de componentes del medio biológico sobre (nano)materiales de interés. Se ha descubierto que la densidad de empaquetamiento y el orden conformacional de estas moléculas en las películas son cruciales para conseguir una inhibición de calidad. Una de las metodologías más empleadas para obtener este tipo de recubrimientos es la formación de SAMs a partir de moléculas tioladas sobre sustratos metálicos. Esta estrategia, que destaca por su simplicidad experimental y con frecuencia da lugar a buenos resultados, se enmarca en las aproximaciones *grafting to*.

Las superficies modificadas usando moléculas de EGn que presentan estructuras relativamente cortas se emplean como sistemas modelo. Así, la SAM de O-(2-Mercaptoetil)-O'-metil-hexa(etilenglicol) (EG7-SAM) formada sobre sustratos cristalinos de oro de diferente naturaleza es un sistema muy interesante mediante el que es posible evaluar los efectos que tienen diferentes parámetros en la organización estructural de los recubrimientos moleculares de EGn.

El autoensamblaje de moléculas de EG7-SH sobre sustratos de oro produce SAMs cuya estructura debería depender principalmente de los disolventes empleados en su formación. La composición atómica del esqueleto de las moléculas de EG7 hace que aparezcan interacciones específicas con las moléculas de disolvente, además de las típicas interacciones de van der Waals que se producen en películas basadas en alcanotioles.

## **Objetivo 1**

Se ha pretendido evaluar el efecto del tiempo de adsorción y la naturaleza del disolvente en la formación de EG7-SAM sobre sustratos de oro poli- y mono-orientados. Las propiedades finales de las EG7-SAMs formadas se estudian examinando el proceso de desorción reductiva (RD), así como el comportamiento de bloqueo electrónico e iónico de estas capas mediante el uso de VC y EIS. Se obtiene información adicional de la estructura, composición y organización mediante espectroscopias IRRAS y XPS y medidas del ángulo de contacto.

Los estudios sobre EG7-SAMs se han publicado en los artículos:

- *“Characterization of a self-assembled monolayer of O-(2-Mercaptoethyl)-O'-methyl-hexa(ethylene glycol) (EG7-SAM) on gold electrodes”*
- *“Self-assembled monolayers of O-(2-Mercaptoethyl)-O'-methyl-hexa(ethylene glycol) (EG7-SAM) on gold electrodes. Effects of the nature of solution/electrolyte on formation and electron transfer blocking characteristics.”*

## **Hipótesis 2**

La técnica EIS es una herramienta excelente que permite obtener información sobre la interfase de las superficies modificadas, aportando información complementaria a la obtenida mediante experimentos de VC. Basadas en pequeñas perturbaciones de potencial, las medidas EIS se pueden llevar a cabo en disoluciones que contienen sondas redox, a fin de evaluar el efecto bloqueante que ejercen las películas ancladas al electrodo, o bien, en disoluciones que únicamente contienen especies no electroactivas, obteniéndose información sobre la permeabilidad iónica. Así, mediante EIS se pueden determinar fácilmente tanto los parámetros cinéticos del proceso de transferencia electrónica como la presencia de poros o defectos en la película que recubre el electrodo. En base a esto, las propiedades de aislamiento iónico de SAMs de alcanotioles han sido extensamente evaluadas, encontrándose que cuando las películas están bien empaquetadas inhiben completamente la penetración iónica en un rango de frecuencias de entre 1 y 1000 Hz, presentando el comportamiento típico de un condensador ideal. Variando el potencial al que se realizan estas medidas, se encuentra un valor crítico que separa las regiones en las que la SAM se comporta como un aislante iónico y aquellas en las que comienza a permitirse la entrada de iones.

## **Objetivo 2**

El las SAMs de alcanotioles siempre aparece un potencial límite a partir del cual se permite claramente la permeabilidad iónica. La escasez bibliográfica de este tipo de estudios sobre EGN-SAMs invita a profundizar en el comportamiento electroquímico de estos recubrimientos frente a perturbaciones de frecuencia en ausencia de sondas redox en disolución. En concreto, se ha planteado estudio exhaustivo de la EG7-SAM formada desde diferentes medios utilizando EIS en ausencia de pares redox en disoluciones acuosas ácidas, alcalinas y neutras con objeto de analizar sus propiedades conductoras iónicas. Además, se pretende estudiar los efectos de la temperatura sobre las propiedades de las SAMs en un electrolito neutro. Con este trabajo se pretende ahondar en las propiedades de la EG7-SAM



desde la óptica de técnicas EIS, a fin de que los resultados obtenidos sirvan como modelo y/o punto de partida para caracterizar EGn-SAMs de diferentes longitudes de cadena.

En el artículo:

- *“Effects of the potential and the electrolyte nature in the integrity of the O-(2-Mercaptoethyl)-O'-methyl-hexa(ethylene glycol) self-assembled monolayer by electrochemical impedance spectroscopy”*

se investiga en profundidad la EG7-SAM formada sobre sustratos de oro mediante EIS.

### Hipótesis 3

En uso de moléculas de EGn de mayor tamaño puede dar lugar a películas en superficie que presenten, en función de su densidad de empaquetamiento, conformaciones compactas o *brush*, o poco pobladas o *mushroom*. De forma análoga a lo que sucede en películas formadas a partir de cadenas de EGn de pequeño tamaño, la densidad del empaquetamiento determina las propiedades finales y, por ende, las potenciales aplicaciones de este tipo de recubrimientos. Por otro lado, las condiciones de formación de la SAM (disolvente, temperatura o tiempo de inmersión, entre otros) son las principales responsables del ordenamiento alcanzado.

La mayoría de los trabajos recogidos en la literatura sobre EGn-SAMs emplean medidas de elipsometría, resonancia del plasmón superficial o microbalanza de cristal de cuarzo para determinar el recubrimiento molecular.

### Objetivo 3

Mediante el análisis de la RD, observada mediante la técnica de CV, es posible evaluar la densidad de empaquetamiento de EGn-SAMs formadas a partir de EGn-SH de diferente longitud (EGn, n = 18, 45 y 136). Empleando condiciones de formación bien establecidas en bibliografía, se obtiene un exceso de densidad de carga que es necesario investigar. En concreto, se plantea la posibilidad de la existencia de reacciones paralelas a la RD relacionadas con el disolvente retenido en las EGn-SAMs. Por otro lado, se recurre a la estrategia del punto de turbidez o punto de nube, mediante la que se consigue preparar películas disminuyendo el contenido de agua dentro de las cadenas. Se espera que los perfiles de RD se vean afectados en función de la estrategia de formación de la SAM, afectando claramente a los valores de densidad de empaquetamiento.

Por otro lado, las propiedades de las películas formadas se investigan en profundidad empleando estrategias electroquímicas, como la curvas de capacidad y medidas de CV y EIS

en presencia del par redox  $\text{Fe}(\text{CN})_6^{3-/4-}$ . Los resultados obtenidos se complementan con medidas de XPS y ángulo de contacto.

La caracterización de EGN-SAMs formadas a partir de EGN de elevado peso molecular se recoge en el artículo:

- *“Electrochemical evaluation of the grafting density of self-assembled monolayers of polyethylene glycol of different chain lengths formed by the grafting to approach under conditions close to the cloud point”.*

## Hipótesis 4

Evaluada las propiedades de las EGN-SAMs en sustratos macroscópicos, es interesante proceder al estudio de estas sobre estructuras tridimensionales, como son las AuNPs. En la actualidad, las películas poliméricas ancladas a AuNPs les otorgan interesantes propiedades que son necesarias para su aplicación en sistemas *in vivo* como, por ejemplo, la biocompatibilidad y la posibilidad de camuflarse con el medio, a fin de no ser detectadas como cuerpos extraños y, por tanto, mantener un tiempo de circulación suficiente para desempeñar las funciones con las que se han diseñado.

La caracterización de estos NMs híbridos se lleva a cabo mediante espectroscopía UV-vis, DLS y medidas de potencial  $\zeta$ . Estas técnicas permiten además evaluar el efecto de la fuerza iónica y la temperatura en la estabilidad coloidal, observándose cambios en la banda de plasmon superficial localizado (LSPR) del espectro, así como en el tamaño hidrodinámico registrado mediante DLS.

## Objetivo 4

En este trabajo persigue formar recubrimientos de EGN de diferente longitud de cadena ( $n = 7, 18, 45$  y  $136$ ) en la superficie de AuNPs en condiciones que permitan alcanzar las máximas densidades de empaquetamiento. Estas EGN-AuNPs dan lugar a suspensiones coloidales más estables con respecto a las AuNPs prístinas, recubiertas por aniones citrato, en disoluciones acuosas y en un amplio intervalo de temperaturas, y además forman suspensiones estables en soluciones de altas concentraciones de NaCl. Para mostrar la respuesta frente a cambios en la temperatura de estas EGN-AuNPs, se realizan experimentos de valoración con la temperatura en presencia de cantidades crecientes de sales. Las concentraciones de NaCl se eligen comprobando la estabilidad de las EGN-AuNPs a temperatura ambiente y seleccionando las concentraciones más altas que permiten formar suspensiones estables. El análisis de los experimentos de valoración de la temperatura monitorizados por espectroscopia UV-vis y DLS permite establecer la existencia de

transiciones de EGN-AuNPs individuales a ensambladas, la reversibilidad de las transiciones de temperatura y el comportamiento histórico de estos sistemas.

La síntesis y caracterización de NMs híbridos EGN-AuNPs se presenta en el artículo:

- *“Distinct thermoresponsive behaviour of oligo- and poly-ethylene glycol protected gold nanoparticles in concentrated salt solutions.”*

## Hipótesis 5

A pesar de sus numerosas ventajas, la estrategia de formación de SAMs también presenta ciertas limitaciones, especialmente al tratar de injertar, cadenas largas en superficie. En estos casos, con frecuencia, se obtienen empaquetamientos de baja densidad a consecuencia del impedimento estérico que las propias moléculas ancladas a la superficie ejercen. Para evitar esto, las estrategias *grafting from*, basadas en un crecimiento controlado de cadenas poliméricas usando monómeros a partir de sitios de iniciación previamente injertados en la superficie, son una alternativa interesante. La metodología de polimerización por transferencia atómica radicalica (ATRP) es una de las técnicas *grafting from* más extendida en la actualidad. La variante de esta que permite el crecimiento de películas poliméricas en superficies mediante control electroquímico se denomina *Surface-Initiated electrochemical ATRP* (SI-eATRP). Esta estrategia precisa contar con una superficie que contenga moléculas de iniciador ancladas. Una de las moléculas más usadas, (bis[2-(2-bromoisobutirilo) undecil] disulfuro) (DTBU), es un iniciador típicamente usado en polimerizaciones SI-ATRP; en concreto, permite funcionalizar superficies metálicas mediante la formación de SAMs. Determinar las características de la superficie que actúa como estructura de iniciación de la polimerización es fundamental para conseguir el crecimiento eficiente de polímeros que presenten las propiedades deseadas.

## Objetivo 5

Se plantea el diseño y estudio de monocapas que contienen el iniciador DTBU sobre electrodos policristalinos de oro. Así, es posible explorar el efecto de bloqueo de la barrera física que ejerce la SAM frente a diferentes sondas redox, lo cual es fundamental si se pretende usar esta estructura como superficie de partida para formar películas poliméricas mediante SI-eATRP. El DTBU forma una monocapa compacta que bloquea completamente la transferencia electrónica del par redox que actúa como catalizador en la reacción de polimerización. En base a esto, se preparan y caracterizan SAMs de DTBU y 6-mercaptopurina (6MP), para comprobar si el tiol facilita el intercambio de electrones, empleando diferentes proporciones de DTBU:6MP. La caracterización se consigue

estudiando los espectros IRRAS, las propiedades electroquímicas y el ángulo de contacto en la superficie modificada.

La preparación y caracterización de SAMs mixtas DTBU:6MP sobre superficies macroscópicas de Au como potenciales candidatos para su uso para la obtención de polímeros en superficie mediante la estrategia SI-eATRP se recoge en el artículo:

- *“Characterization of self-assembled Bis[2-(2-bromoisobutyryloxy) undecyl] disulphide (DTBU) on gold surfaces suitable for use in surface-initiated atom transfer radical polymerization (SI-ATRP).”*

## Hipótesis 6

La polimerización SI-eATRP es una novedosa y prometedora metodología que permite crecer, de manera controlada, películas poliméricas a partir de una amplia variedad de sustratos, incluyendo superficies metálicas. Más específicamente, la variante SI-eATRP en medio acuoso es atractiva al permitir trabajar con monómeros solubles en agua, que son los más demandados a la hora de diseñar estructuras que pretenden aplicarse en sistemas biológicos. Este es el caso de películas basadas en EGN, que pueden construirse a partir de monómeros comerciales que presentan diferente longitud de cadena, eligiendo para este fin un sistema catalítico basado en un complejo de cobre con ligandos amino tetradentados. Además, se trata de una estrategia que ha demostrado ser de utilidad para obtener películas homogéneas y compactas de calidad, que posibilita la construcción de copolímeros variando las proporciones de monómeros y también la introducción de diversos grupos funcionales, siendo esto de especial interés en los recubrimientos basados en EGN dadas sus potenciales aplicaciones en Nanomedicina.

## Objetivo 6

Las ventajas que presenta el enfoque de polimerización SI-eATRP motiva la formación y caracterización de películas tipo *brush* compactas de EGN a partir de monómeros oligo(etilenglicol)metracrilato sobre electrodos de oro. Se diseñan a partir de sustratos sobre los que previamente se injerta una SAM que contiene moléculas adecuadas para la iniciación de la reacción ATRP. Se evalúan diferentes parámetros como son el potencial aplicado usado en la reacción, la naturaleza de la superficie iniciadora y la duración del proceso de polimerización, a fin de optimizar el mecanismo para obtener recubrimientos poliméricos de mayor calidad.

Las técnicas electroquímicas son fundamentales a fin de lograr este objetivo. Así, la formación de las películas poliméricas se lleva a cabo mediante cronoamperometría, usando

un sistema de tres electrodos en un potenciostato convencional, y también adaptando el sistema a una celda de un sistema EQCM. Una vez formadas, se estudian mediante VC y EIS, obteniéndose información sobre su bloqueo electrónico e iónico. La conformación estructural, composición y organización se evalúan, además, mediante técnicas espectroscópicas IRRAS y XPS, medidas de ángulo de contacto y microscopías electrónicas de barrido (SEM) de fuerzas atómicas (AFM). En el trabajo:

- *“Efficient formation poly(ethylene glycol) polymer brushes on gold electrodes via surface initiated electrochemical mediated ATRP (SI-eATRP)”*

se describe la formación y caracterización de películas poliméricas compactas basadas en EG sobre sustratos de oro en medio acuoso, usando la estrategia *grafting from* SI-eATRP.



# **Capítulo 1. Introducción**





## 1.1. Nanociencia y Nanotecnología.

El avance en la Nanociencia y la Nanotecnología es un reto fundamental en la Química del siglo XXI. Sin embargo, el origen de estos conceptos es anterior, ya que la idea de “nanotecnología” aparece en 1959 de la mano de Richard Feynman, quien sugirió la posibilidad de usar “máquinas” para construir “máquinas” más pequeñas, hasta alcanzar la escala molecular. Años después en 1974, el científico japonés Norio Taniguchi usó el término nanotecnología definiéndolo como que consistía en “separar, consolidar y deformar materiales átomo por átomo, o molécula por molécula”. En la actualidad, ambos conceptos se explican de forma conjunta, entendiéndose la nanociencia como el estudio de estructuras y moléculas en la escala nanométrica (1-100 nm), y la nanotecnología, la aplicación práctica de esta ciencia para el desarrollo de dispositivos [7].

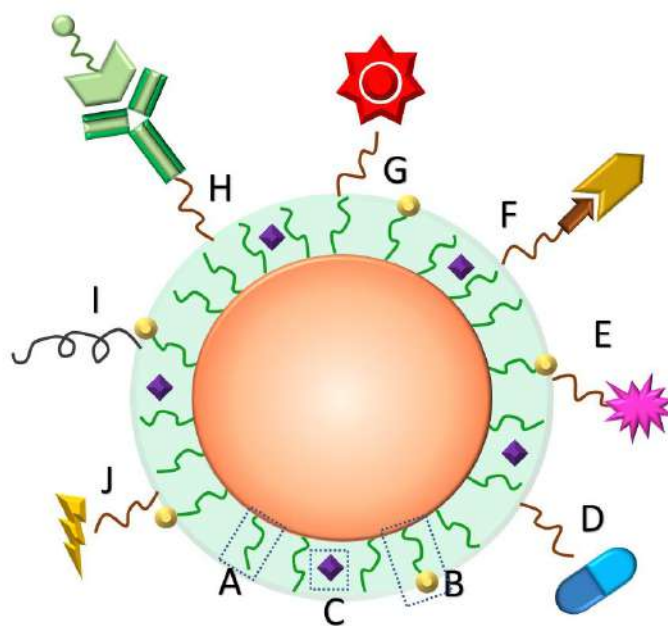
Desde su aparición, y con más fuerza aún durante las últimas dos décadas, numerosas investigaciones se están centrando en el diseño, síntesis y caracterización tanto de NMs como de recubrimientos moleculares en sustratos macroscópicos, dado el potencial y las prometedoras aplicaciones que presentan. Estas nanoestructuras son ya fundamentales en los avances que se están consiguiendo en diversos campos, desde la industria de materiales hasta el ámbito biomédico. En particular, el ensamblaje de recubrimientos moleculares para obtener dispositivos funcionales suele denominarse Nanotecnología Molecular [8]. La fabricación de estos materiales nanoestructurados se ha visto impulsada por el desarrollo de métodos sintéticos y avances en química supramolecular, que han permitido integrar estos ensamblajes en NMs y biomoléculas [9-11]. En combinación con los avances en ciencia de superficie, ha sido posible diseñar ensamblajes moleculares 2D de manera sencilla y reproducible, que han permitido introducir amplia variedad de grupos funcionales sobre sustratos conductores, semiconductores y aislantes.

Las películas 2D en escala nanométrica se clasifican, de forma general en SAMs, películas Langmuir-Blodgett (LBFs, *Langmuir-Blodgett Films*) y ensamblajes supramoleculares 2D [12]. Estas tres metodologías permiten diseñar recubrimientos superficiales de forma eficaz. Además, son capaces de interactuar con otros monómeros aislados para formar materiales funcionales [13, 14]. Así, uno de los objetivos principales de la funcionalización de superficies es el diseño de los conocidos como “materiales inteligentes”, caracterizados por responder de manera eficaz e inmediata frente al entorno externo en el que se encuentran. Dichas estructuras se emplearían de forma eficaz tanto en ciencia de materiales como en biomedicina, para la fabricación de nanodispositivos 2D, como (bio)sensores y sistemas con aplicaciones electrónicas, mejorando su rendimiento e

introduciendo nuevas características [15, 16]. Los materiales inteligentes pueden presentar naturaleza orgánica, inorgánica o híbrida. El extraordinario potencial de estos NMs se debe principalmente a la comentada funcionalización superficial, que proporciona una mejora significativa de sus propiedades y/o introduce otras nuevas.

### 1.1.1. Interacción de los NMs y recubrimientos moleculares con el entorno biológico.

Gran parte de las investigaciones en NMs y recubrimientos a escala nanométrica se relacionan con el campo de la Medicina. Aplicaciones como las técnicas de bio-imagen, manipulación celular o detección de metabolitos son sólo algunos ejemplos. El amplio abanico de utilidades que presentan los nanosistemas ha motivado la aparición de una nueva disciplina, la Nanomedicina, campo emergente y en continua evolución durante los últimos años [17] (Esquema 1).



**Esquema 1.** Nanopartícula multifuncional para aplicaciones biomédicas. El núcleo puede recubrirse por una capa molecular que aporta estabilidad (A) y/o funcionalidad (B), además de permitir el transporte de agentes de interés (C) para su distribución controlada. En función de su diseño, pueden interactuar con fármacos (D) o radioisótopos (E), actuar como diana de recepción específica (F), marcador fluorescente (G) o agente de contraste en imagen por resonancia magnética nuclear (IRMN) (J), además de participar en procesos más complejos, actuando simultáneamente como receptor específico y ligando (H) o simplemente variar la distribución de las diferentes moléculas de su entorno actuando como conectores o espaciadores (I).

Una de las mayores limitaciones de la Nanomedicina radica en el actual desconocimiento de la interfase que se genera cuando los NMs y recubrimientos

moleculares 2D entran en contacto con el medio biológico. Por tanto, es importante abordar el diseño de materiales que sean compatibles con el entorno biológico, a través de procedimientos avanzados de síntesis, tanto de nanopartículas (NP) metálicas como de capas moleculares soportadas en sustratos macroscópicos, que se alimentan de los conceptos de síntesis en química orgánica. Tras su preparación, resulta imprescindible estudiar su comportamiento en el medio biológico. En la literatura, esta región con propiedades particulares y poco conocidas generada por la interacción entre los NMs y el entorno biológico se conoce como interfase *nano-bio* [18].

En la descripción de la interfase *nano-bio* se consideran tres componentes dinámicos e interrelacionados, como son: la superficie del NM, que viene determinada por su composición físico-química; la interfase sólido/líquido, y los cambios que experimentan los NMs y recubrimientos moleculares al interactuar con los componentes del medio que los rodea; y la zona de contacto con el material biológico, que puede motivar la aparición de reacciones selectivas, dependientes de la temperatura o el pH, entre otros. Estas interacciones se producen tanto en ensayos *in vivo* o como *in vitro*. Así, cuando las nanoestructuras diseñadas entran en contacto con medios biológicos que contienen proteínas y otras macromoléculas complejas, estas últimas se adsorben alrededor de los NMs formando una “nube” de componentes biológicos que se conoce como *corona* de proteínas [19]. Las proteínas que interactúan con los NMs pueden alterar las propiedades superficiales de los primeros, así como las funciones con las que han sido diseñados. Este fenómeno, observado a escala macroscópica, se manifiesta en el deterioro superficial de implantes, catéteres y otros dispositivos médicos. Así, la adsorción inespecífica de material biológico y la formación de la *corona* de proteínas son fenómenos problemáticos e indeseados y, por tanto, resulta fundamental desarrollar estrategias para evitarlos o eliminarlos.

Sin embargo, esta tarea no es sencilla: en primer lugar, se encuentra que las propiedades de la *corona* de proteínas son imposibles de predecir. Por un lado, su integridad se debe a un balance entre diversos tipos de interacciones débiles y por otro, su composición viene determinada por los distintos entornos biológicos con los que interactúan los NMs y los recubrimientos moleculares [20]. Investigaciones recientes permiten concluir que incluso proteínas del mismo tipo presentan diferentes fuerzas de unión a la superficie de los NMs, que dependen de la química superficial, tamaño y forma de los últimos [21, 22]. La prevalencia de diferentes fuerzas de unión determina cómo ocurren los procesos de adsorción e intercambio de proteínas en la *corona*, determinando su composición. La existencia de la *corona* de proteínas fue ignorada durante años en las investigaciones en el campo biomédico, de manera que su estudio aún se encuentra en los estadios iniciales. Las

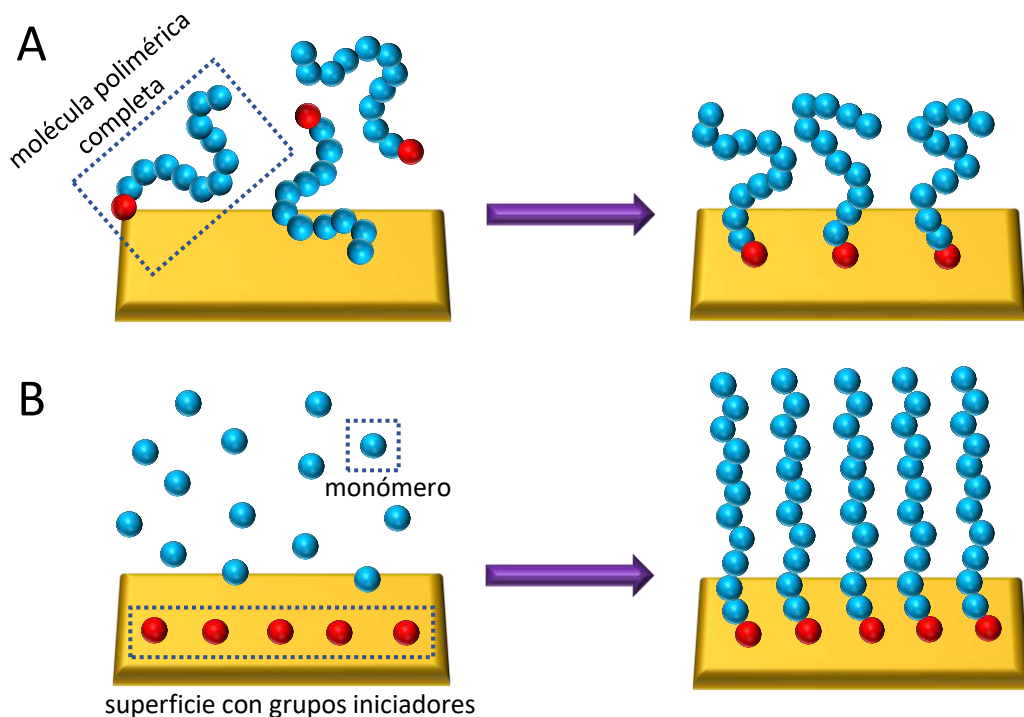
primeras investigaciones han abordado el comportamiento de los bioconjugados en entornos *in vitro*, sin embargo, ya hay resultados que indican que las *coronas* de proteínas formadas *in vitro* o *in vivo* difieren en el tipo y la abundancia de proteínas. En los entornos *in vivo*, los recubrimientos superficiales y NMs pueden interactuar con miles de tipos diferentes de macromoléculas biológicas, pero dado que presentan un área superficial finita, sólo una fracción de estas podrán adsorberse. Así, es de esperar que cada NM como entidad individual, presente una *corona* única, que determina sus propiedades [23].

### 1.1.2. Estrategias *grafting to* y *grafting from* para la funcionalización de superficies.

La elección adecuada de los ligandos para funcionalizar los NMs es clave en el avance de la Nanomedicina. Es necesario emplear compuestos específicos para diseñar recubrimientos que permitan transportar sustancias de interés, que se liberarían en las células diana, sin que afecten al resto de los componentes del organismo y que, al mismo tiempo, mantengan la integridad del NM. Las principales limitaciones que se encuentran en los sistemas nanoportadores y recubrimientos moleculares que interactúan con el entorno biológico son el alto coste de su producción, la toxicidad, la inmunogenicidad (debido a su origen extraño al sistema vivo) y la baja solubilidad en condiciones fisiológicas [24]. Por el contrario, como aspectos potenciales, destacan la protección que ejercen frente a la degradación de las moléculas transportadas y el aumento de la absorción, que facilita la internalización en las células y la distribución de medicación. Los NMs y recubrimientos moleculares construidos a base de polímeros sintéticos clásicos como son el ácido poliláctico-co-glicólico (PLGA), el EGN y la policaprolactona (PLC), que se han usado tanto para distribución controlada de fármacos como para absorción celular, despiertan gran interés. La combinación de este tipo de recubrimientos con NMs inorgánicos como las AuNPs de diferente forma y tamaño, por ejemplo, nano-esferas, -cápsulas, -cilindros y -prismas para formar estructuras híbridas, es una de las estrategias más estudiadas en la actualidad [3].

Existen numerosas estrategias para conseguir la modificación controlada de la superficie de los NMs y sustratos macroscópicos con grupos funcionales específicos. Las SAMs son una opción atractiva para el diseño de la química superficial en una amplia gama de sustratos metálicos, que permite modificar de manera simple, flexible y exitosa las propiedades intrínsecas de la superficie. El autoensamblado se define como la formación espontánea de estructuras ordenadas a partir de unidades de construcción prediseñadas, que involucra múltiples escalas de energía y grados de libertad [4]. Se trata de una aproximación *grafting to*, en la que moléculas, de tamaño y forma definidos, se injertan en

la superficie mediante un grupo terminal (Esquema 2A). Esta estrategia ha sido fundamental en el avance de la ciencia de superficies, permitiendo diseñar recubrimientos con aplicaciones en múltiples áreas, como la electrónica molecular, la electroquímica, el diseño de sistemas no incrustantes o el mojado (hidrofilicidad e hidrofobicidad) de superficies. No obstante, las SAMs presentan ciertas limitaciones relacionadas con sus propiedades mecánicas y estabilidad química, debido a los pequeños espesores de los recubrimientos a los que dan lugar. Para evitar estas limitaciones es posible recurrir al diseño de películas orgánicas de mayor espesor, conocidas como recubrimientos compactos tipo *brush* [5]. Sin embargo, al tratar de injertar cadenas poliméricas de gran tamaño en una superficie también se presentan ciertos impedimentos relacionados con la estructura molecular que no garantizan que se adopte una conformación tipo *brush*. La funcionalización de una superficie para garantizar un recubrimiento basado en este tipo de polímeros se puede conseguir partiendo de una SAM y combinando técnicas de polimerización controlada. Esta metodología se clasifica como *bottom-up*, y en la que las cadenas poliméricas se forman a partir de un sustrato modificado con grupos funcionales que permiten iniciar una reacción controlada de polimerización, lo que da lugar a un recubrimiento de polímeros anclados a la superficie de elevada densidad de empaquetamiento (Esquema 2B).



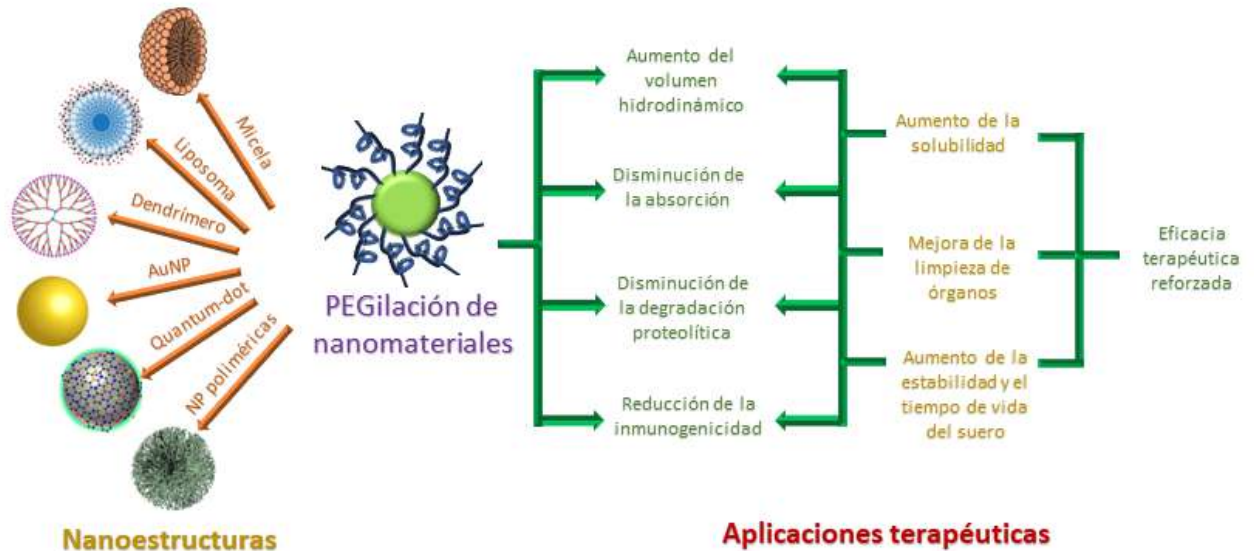
**Esquema 2.** Preparación de polímeros *brush* mediante las estrategias (A) *grafting to* y (B) *grafting from*.

La elección del mecanismo de polimerización está relacionada con la naturaleza del grupo terminal, iniciador de la reacción, que puede ser, entre otros, un radical libre, un sitio iónico, una polimerización por apertura de anillo (metátesis) o una desactivación reversible de radicales. La formación del recubrimiento superficial se produce mediante el anclaje de monómeros (estrategia *grafting from*), lo que permite un mayor control sobre las propiedades de la película formada [6]. Así, mientras que con la estrategia *grafting to* los espesores de las películas poliméricas están limitados por el tamaño molecular de los polímeros precursores, con las estrategias *grafting from* desaparece esta restricción. Dentro de esta familia de metodologías, una de las más atractivas es la polimerización controlada iniciada en superficie (SI-CRP, *Surface Initiated-Controlled Radical Polymerization*). Se trata de una aproximación versátil y tolerante hacia una gran variedad de grupos funcionales, lo que permite un control preciso sobre la composición, espesor y arquitectura de la película polimérica. Dentro de las técnicas SI-CRP, se enmarca la SI-ATRP, que ha ido evolucionado llamativamente en las dos últimas décadas hasta convertirse en una de las estrategias más eficaces para obtener polímeros *brush* [25]. Sin embargo, se trata de una estrategia más compleja que el autoensamblaje, que requiere de gran control sobre todas las etapas de la reacción para obtener recubrimientos con las propiedades deseadas.

### 1.1.3. PEGilación.

Los NMs y las superficies macroscópicas funcionalizadas interactúan de manera inevitable con el entorno biológico cuando se introducen en el mismo, inhibiendo con frecuencia las funciones para las que se habían diseñado. A fin de mantener estas propiedades, existen estrategias de funcionalización que evitan la detección por el entorno, impidiendo que sean identificadas como cuerpos extraños y eliminadas por el sistema inmune [2]. Los recubrimientos de polímeros biocompatibles han demostrado ser eficaces para este fin, destacando especialmente el uso de EGN, capaz de reducir la absorción de NPs por células de cultivos *in vitro* y por fluidos con componentes más complejos en sistemas *in vivo*, incrementándose los tiempos de circulación [26]. La versatilidad y eficacia de la funcionalización de todo tipo de sistemas con moléculas basadas en unidades EG ha hecho que esta metodología adquiriera un nombre propio: *PEGilación*, que se basa en unir covalentemente moléculas de EGN a las estructuras. El interés en la química de los EGN se inicia a finales de los 70, cuando se demuestra que las propiedades inmunológicas y la estabilidad de las proteínas albúmina y catalasa al recubrirlas con moléculas EGN [27, 28]. Estudios más recientes, utilizando espectrometría de masas o electroforesis en gel, han demostrado la reducción de la tendencia que presentan las proteínas y otros elementos biológicos a adsorberse sobre superficies con recubrimientos de EGN [29]. El proceso de

PEGilación ha sido eficazmente extendido a liposomas, péptidos, carbohidratos, enzimas, anticuerpos, micelas, partículas orgánicas pequeñas y NPs de diferente naturaleza [30-33] (Esquema 3).



**Esquema 3.** Nanoestructuras de diferente naturaleza que pueden conjugarse con EGN y representación de las principales ventajas de las terapias con materiales PEGilados.

La mayoría estudios que involucran la PEGilación tienen como objetivo aumentar la vida media en circulación de la estructura conjugada sin afectar a su actividad. Los distintos avances en las estrategias y la diversidad de la naturaleza de las cadenas basadas en EGN disponibles actualmente han contribuido al aumento de la demanda de este tipo de estructuras por parte de la industria farmacéutica. Así, la PEGilación mejora la eficacia terapéutica de los fármacos si se comparan con los productos sin modificar, aportando las ventajas que se presentan en el Esquema 3. El aumento del tiempo de vida del conjugado es la principal mejora que introduce la PEGilación de las superficies, ya que se consigue que el conjugado sea más hidrofílico y presente menor tasa de filtración glomerular [34]. Factores como la protección frente a las células reticuloendoteliales y las enzimas proteolíticas, y la disminución de la formación de anticuerpos neutralizantes contra las proteínas al enmascarar sitios antigénicos mediante un escudo hidrofílico, son algunas de las características clave con las que las moléculas de EGN contribuyen a mejorar el perfil farmacocinético de los conjugados [35].

Muchas cuestiones relacionadas con el comportamiento de los recubrimientos moleculares de EGN no han sido aún determinadas con claridad y su evaluación sigue despertando interés. Sin embargo, desde los primeros estudios, parece haber unanimidad en que la densidad del recubrimiento polimérico y el peso molecular de las cadenas

empleadas definen en gran medida la adsorción de proteínas, tanto en NP como en sustratos macroscópicos. Así, recubrimientos más densos y películas de mayor espesor serían favorables, mientras que la presencia de huecos podría facilitar la penetración de las proteínas, alcanzando la superficie reactiva subyacente [36]. Por tanto, con objeto de conseguir capas basadas en EGn que inhiban la adsorción inespecífica de proteínas, debe prestarse especial atención tanto a las moléculas elegidas como a la metodología de PEGilación. En sustratos planos se ha demostrado la posibilidad de diseñar recubrimientos de EGn que, en determinadas configuraciones, inhiben completamente la adsorción de proteínas [37, 38].

Otra de las propiedades superficiales de los materiales que se ve fuertemente influenciada por la PEGilación es la carga superficial. Aunque se empleen moléculas de EGn que, teóricamente, no presentan carga, en ocasiones se detecta cierta carga superficial. Esto puede deberse tanto al uso de sitios cargados como puntos de anclaje de las moléculas de EGn como a la quelación de cationes presentes en el medio [39]. Ambos fenómenos pueden afectar a la estabilidad coloidal en el caso de recubrimientos EGn en NPs, ya que disminuyen notablemente la carga superficial, lo que se traduce en menor repulsión electrostática que es lo que mantiene la estabilidad e integridad de las partículas como unidades discretas. Con la PEGilación, también se evita la pérdida de la desestabilización coloidal en base a repulsiones estéricas, que consiguen evitar la agregación incluso en elevadas concentraciones iónicas [40]. Esto es sumamente interesante, dado que el aumento de la estabilidad coloidal se ha relacionado con una disminución en la captación de los sistemas conjugados por células *in vitro* [41].

Con esto, no es de extrañar el esfuerzo que se está dedicando a profundizar en la química de los EGn, investigándose tanto cuestiones fundamentales como aplicaciones, ya que la PEGilación ha demostrado ser uno de los enfoques más prometedores para la mejora de la eficacia de NMs y recubrimientos superficiales en entornos biológicos.

## 1.2. SAMs en sustratos planos.

Las SAMs se definen como un conjunto de moléculas orgánicas que adquieren una conformación energéticamente estable en la interfase sólido-líquido sobre una superficie sólida, cuyo origen está en la quimisorción entre el grupo de cabeza de las moléculas y el sustrato, dando lugar a estructuras cristalinas o semicristalinas. Además del grupo de cabeza, la naturaleza del grupo terminal, localizado en el extremo opuesto de la cadena molecular, es fundamental ya que define la funcionalidad química del fragmento expuesto a la interfase. La presencia de una monocapa adsorbida en un sustrato disminuye la energía libre entre este y el entorno debido a que la película orgánica formada actúa como una

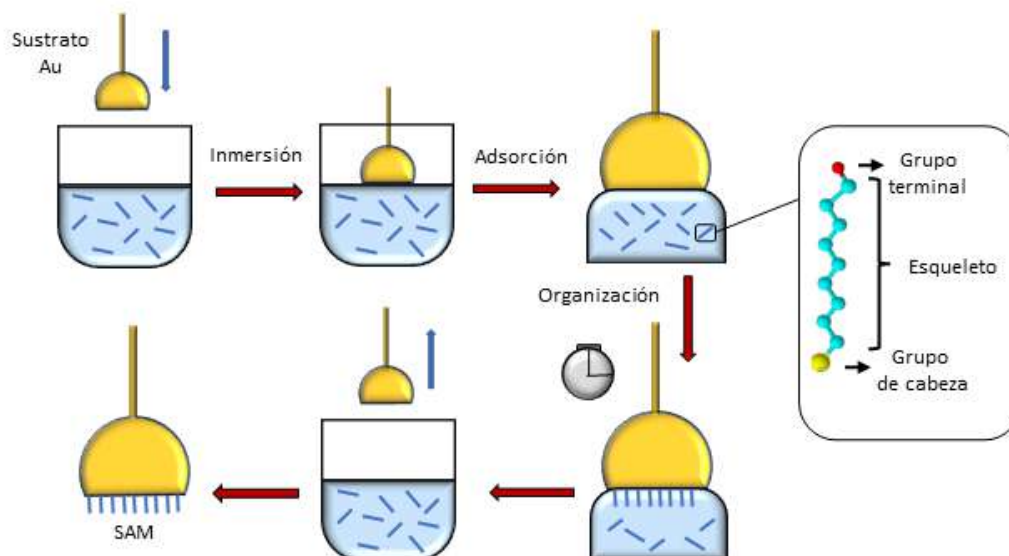


barrera física o electrostática, que además puede modificar sus propiedades ópticas y electrónicas, disminuir la reactividad superficial, e incluso actuar como un recubrimiento conductor o aislante, dependiendo de la naturaleza química del grupo terminal.

El origen del concepto SAM aparece en 1946, de la mano de Zisman [42]. En su primer trabajo en este tema describe la formación de una capa monomolecular a partir de una solución de surfactante por adsorción sobre una superficie metálica limpia, que posteriormente evaluó para determinar la relación entre la estructura molecular injertada y el ángulo de humectación. Pero no es hasta 1983 cuando este campo empieza a atraer el interés de varios grupos de investigación, a partir de los trabajos pioneros de Nuzzo y Allara [43-46]. En sus estudios iniciales demostraron que compuestos organosulfurados como los disulfuros de dialquilo podían utilizarse para formar monocapas muy ordenadas sobre superficies de oro desde soluciones diluidas. Posteriormente, se ha demostrado que los compuestos sulfuro-terminales, como los alcanotioles de cadena larga, también son capaces de dar lugar a ensamblajes organizados sobre superficies de oro. Desde entonces, se han estudiado SAMs formadas a partir de un incontable número de moléculas orgánicas sobre sustratos de distinta naturaleza. Hasta la fecha, las monocapas más extensamente caracterizadas han sido las alcanotioles de cadena larga sobre superficies de metales nobles [45-47]. Sin embargo, en la última década la formación de películas autoensambladas ha evolucionado en paralelo a los fascinantes progresos del ámbito de la nanotecnología, permitiendo manipular las propiedades superficiales e interfaciales de los materiales.

### 1.2.1. Formación de SAMs desde disolución.

Típicamente, el autoensamblaje de moléculas libres para formar una SAM se consigue a través de dos métodos: desde solución o desde fase vapor, siendo la primera opción la más empleada. Los sustratos limpios se sumergen en una solución, normalmente de concentración milimolar en la molécula deseada en un disolvente seleccionado en función de su solubilidad. El tiempo de formación de la monocapa puede establecerse desde minutos hasta horas, dependiendo del sistema en estudio. Con frecuencia, un periodo de incubación más largo permite que la película molecular se ensamble generando una fase sólida cristalina en la que se minimizan los defectos. Tras el tiempo deseado, los sustratos se retiran de la solución, se lavan varias veces con el mismo disolvente, y se secan (Esquema 4) [48].



**Esquema 4.** Formación de una SAM sobre un sustrato de oro.

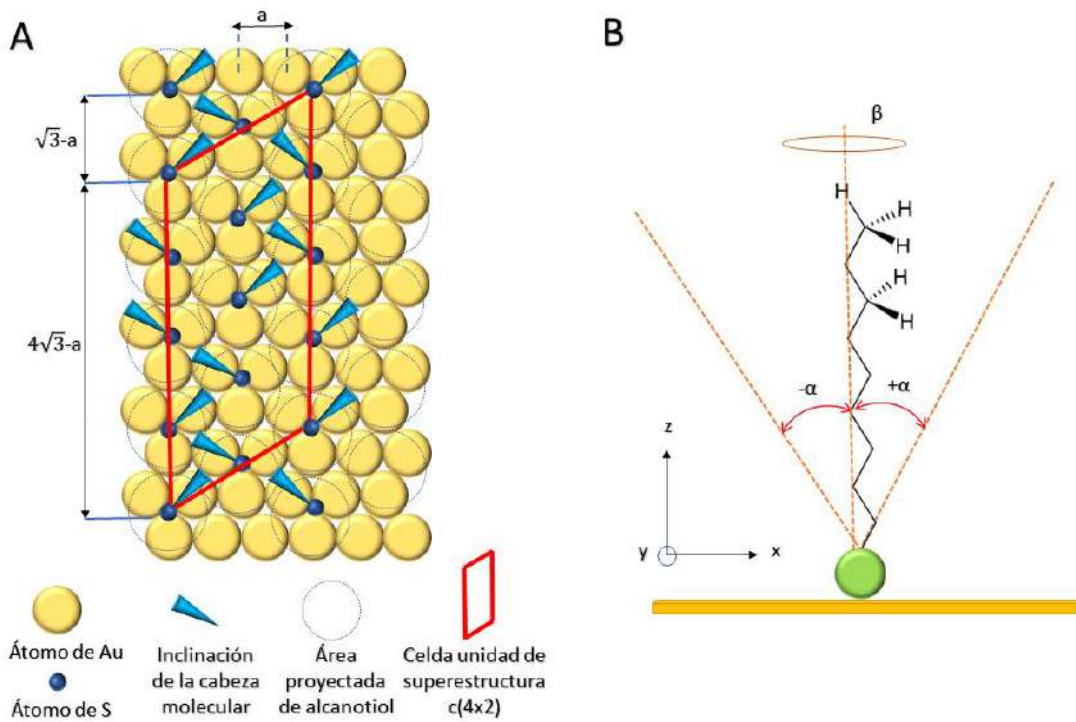
Además del tiempo de inmersión, hay otros factores experimentales que influyen en la cinética del ensamblaje y en la estructura de la película resultante, como son la temperatura, la concentración, la pureza y limpieza de la superficie y del disolvente o la longitud de la cadena, entre otros. Todos estos factores deben considerarse a fin de obtener recubrimientos que presenten las características deseadas.

### 1.2.2. Organización de SAMs. Estructura, ensamblaje y defectos.

La naturaleza del sustrato es uno de los parámetros más importantes en las propiedades finales de las SAMs. El oro es de las superficies más empleadas al tratarse de un metal noble, inerte y no tóxico, especialmente si se compara con otros como la plata o el cobre, lo que ayuda a evitar la contaminación superficial durante la formación de la SAM. Las moléculas con grupos tiol y disulfuro pueden unirse químicamente mediante enlaces covalentes a los tres metales citados, Cu, Ag y Au, debido a la configuración de sus orbitales moleculares, que posibilitan interacciones entre los orbitales d de sus átomos superficiales con los orbitales s de las moléculas que se adsorben [49].

La energía de un enlace covalente S-Au es del orden de 40-50 Kcal/mol [50]. La ordenación geométrica de los átomos de S en la superficie y la distancia entre los átomos vecinos establecen el límite de densidad molecular en la superficie del metal. Un recubrimiento completo de moléculas de alcanotioles sobre oro presenta una estructura ideal de  $(\sqrt{3} \times \sqrt{3})R30^\circ$  [51] (Esquema 5A). Sin embargo, en la mayoría de los sistemas no se alcanza este grado de empaquetamiento, ya que las moléculas tienden a adoptar una estructura que minimiza la energía libre de la capa orgánica. Por lo general, las

conformaciones obtenidas se componen de cadenas que presentan un alto grado de interacciones van der Waals y, en algunos casos, interacciones por puente de hidrógeno entre moléculas vecinas. La modificación de cualquier variable experimental afecta a estas interacciones, alterando la velocidad de formación, y con ello, la organización de la SAM. En la práctica, las condiciones experimentales estándar permiten obtener monocapas funcionalizadas cuyo comportamiento es aceptable en diversas aplicaciones. Sin embargo, los estudios fundamentales de las propiedades interfaciales persiguen minimizar los defectos en la estructura ensamblada, lo que no es tan sencillo [52]. Para obtener películas altamente ordenadas, se necesitan tiempos de inmersión mayores, cadenas alquílicas con esqueletos más largos, disoluciones modificadoras de mayor concentración y en las que además se evite la presencia de impurezas, así como sustratos con superficies muy limpias y bien definidas.

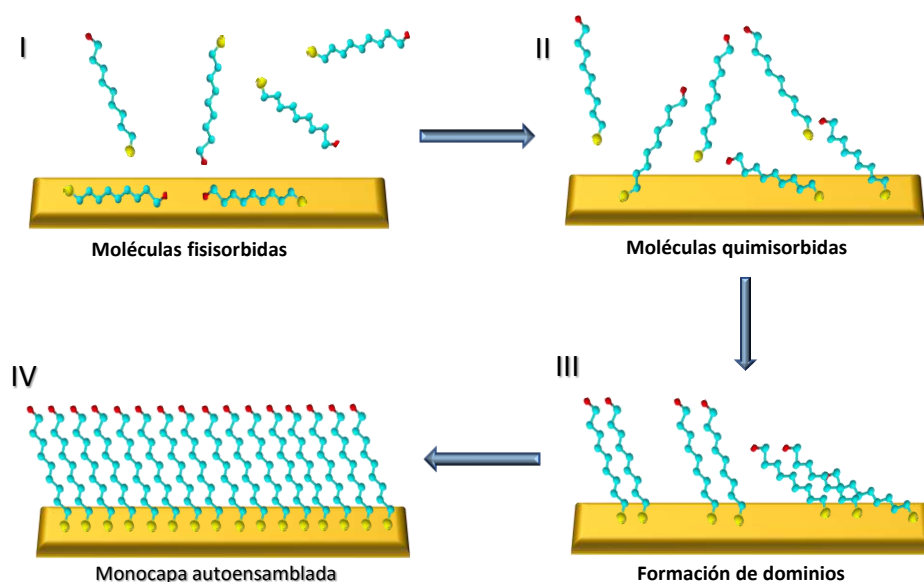


**Esquema 5.** (A) SAM de n-alcanotiol sobre un sustrato de Au(111) que da lugar a un recubrimiento completo, siguiendo el modelo estructural hexagonal  $(\sqrt{3} \times \sqrt{3})R30^\circ$ , donde los átomos de S se posicionan en los huecos trigonales libres entre átomos de Au. (B) Representación de una cadena de n-alcanotiol enlazada a la superficie en una conformación totalmente vertical, donde  $\alpha$  y  $\beta$  son los grados de libertad angulares de inclinación y torsión, respectivamente, para la conformación todo trans de la cadena.

Otros parámetros menos estudiados, como el disolvente a partir del que se produce el ensamblaje y la temperatura, han demostrado afectar a las propiedades de la película. En concreto, la estructura y polaridad del disolvente afectan al ensamblaje debido al balance entre las interacciones disolvente-sustrato y disolvente-adsorbato en el equilibrio dinámico que rige la adsorción del tiol [53]. Interacciones disolvente-sustrato más fuertes pueden

provocar que disminuya la velocidad de adsorción de los grupos tiol en el sustrato debido a la competencia que se produce con el desplazamiento de moléculas de disolvente de la superficie [54]. En los casos más estudiados, SAMs de n-alkanotioles, se ha encontrado que el uso de disolventes polares, que presentan poca solubilidad con estas moléculas, contribuye a la formación de empaquetamientos más compactos, con pocos huecos, pero a expensas de que puedan producirse fenómenos de fisiorción. Específicamente, mediante microscopía de efecto túnel se ha puesto de manifiesto que los disolventes polares mejoran la calidad de las SAMs de n-alkanotioles debido a las fuertes interacciones hidrofóbicas que acontecen entre las colas hidrofóbicas apolares, mientras que el uso de disolventes poco polares puede perturbar el proceso de ensamblaje y disminuir su compacidad [55]. Por otro lado, la presencia de tensioactivos con baja concentración micelar crítica en disoluciones acuosas contribuye a la formación de SAMs de n-alkanotioles altamente compactas al crear dominios hidrofóbicos que solubilizan las colas de las moléculas de alcano, facilitando su anclaje a la superficie del sustrato [56-59].

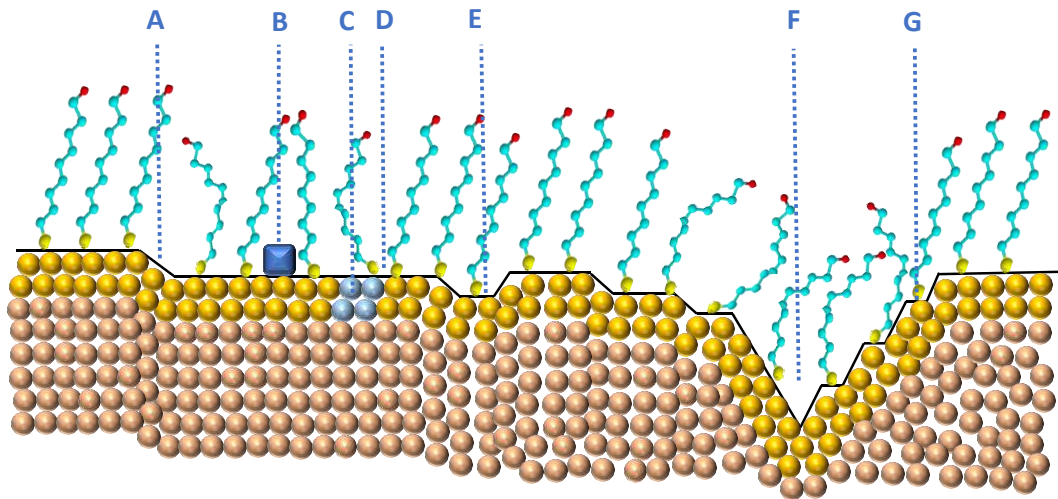
Las investigaciones disponibles en bibliografía sobre los disolventes empleados durante el autoensamblaje ponen de manifiesto el importante papel que representa a fin de obtener películas con empaquetamientos de calidad. En la actualidad, sigue siendo un reto comprender en detalle las complejas interacciones que tienen lugar entre el disolvente, la superficie y las moléculas tiol-terminales en el proceso de formación de SAMs, especialmente en aquellos casos en los que se usan esqueletos más complejos (Esquema 6).



**Esquema 6.** Representación de los pasos que componen el proceso de autoensamblaje: (I) fisiorción, (II) quimisorción, (III) formación de dominios y (IV) ensamblaje de la monocapa.

Dado que la formación de SAMs es un proceso controlado por la cinética y termodinámica de adsorción de la película, cabría esperar que todos los ensamblajes den

lugar a recubrimientos altamente organizados y con pocas irregularidades. Sin embargo, las estructuras reales han demostrado ser mucho más complejas que las teóricas, presentando con frecuencia defectos, que pueden tener un origen intrínseco o extrínseco. Los defectos intrínsecos están relacionados con la naturaleza de la SAM, considerada como un sistema dinámico con un comportamiento complejo, mientras que los defectos extrínsecos se deben a factores externos como la limpieza del sustrato, los métodos de preparación utilizados y la pureza de las soluciones de adsorbato, entre otros. La superficie del sustrato tiene un papel importante en este sentido. Así, los sustratos de oro policristalino muestran una estructura granulada, con diferentes caras y otras irregularidades. Incluso los sustratos monocristalinos de Au(111), que teóricamente presentan una superficie cristalina ideal, no son perfectamente planos y suelen estar ligeramente inclinados, presentando terrazas atómicamente planas separadas por escalones de altura atómica (Esquema 7).



**Esquema 7.** Representación esquemática de los defectos intrínsecos y extrínsecos frecuentemente presentes en monocapas autoensambladas reales formadas sobre sustratos macroscópicos de oro. (A) Defectos en los escalones del metal, (B) impurezas superficiales, (C) impurezas metálicas, (D) defectos en el límite de dos fases cristalinas, (E) islas de vacantes, (F) defectos en los límites de grano de Au, y (G) cadenas injertadas en escalones de la superficie.

### 1.2.3. SAMs de EGn.

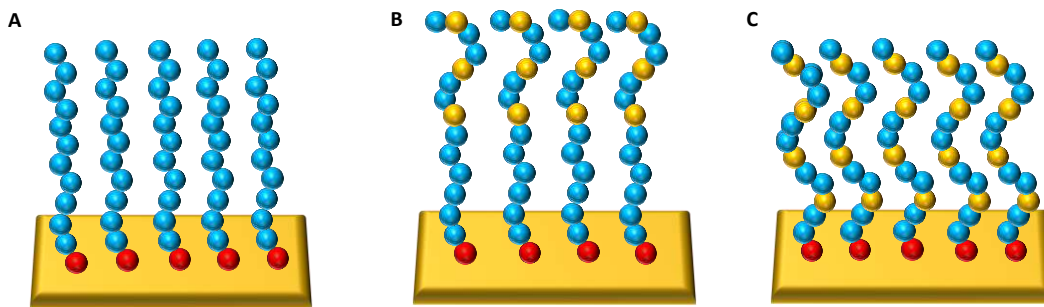
#### 2.3.1. SAMs Cn-EGn.

El gran esfuerzo que se ha hecho para comprender en profundidad muchas de las propiedades que rigen la organización de SAMs de n-alcanotioles, considerando todos los parámetros que pueden afectar al ensamblaje, sirve como punto de partida para numerosas investigaciones sobre formación de monocapas empleando otro tipo de moléculas. Uno de

los sistemas que más interés despierta son las capas moleculares que contienen unidades de EG en su estructura. Las moléculas de alcanotiol terminadas en grupos EGn son atractivas para el diseño de SAMs aprovechando la ventaja del espaciador alcano en la estructura, que potencia la organización de la película dando lugar con relativa facilidad a empaquetamientos compactos que exponen el grupo EGn-terminal al medio (Esquema 8). Este extremo EGn-terminal, en las citadas condiciones de anclaje, puede adoptar tanto una conformación helicoidal como todo-trans, dependiendo de diversos factores como son la naturaleza del sustrato [37, 60], el recubrimiento superficial [61, 62], el número de unidades EG [37, 62], y el disolvente [63]. Estos sistemas son de gran interés debido a su aplicabilidad en el campo biomédico. Así, las SAMs con estructuras EGn-terminales han demostrado minimizar la adsorción inespecífica de proteínas e inhibir la adhesión celular [37, 60, 64, 65], dependiendo de la cantidad de moléculas de agua que quedan retenidas en el interior de la película interactuando con las unidades EG, lo que afecta notablemente a la organización final [38, 66]. El hecho de que las películas formadas sean eficaces o no frente a la adsorción inespecífica de proteínas en función de su organización estructural ha despertado gran interés. Para analizar los factores que influyen en la resistencia a la adsorción de proteínas, se han estudiado en profundidad SAMs de alcanotioles EGn-terminales formadas sobre sustratos de Au y Ag [37, 60], encontrándose que la repulsión estérica, el volumen de exclusión, la rápida movilidad de las cadenas altamente hidratadas, la baja energía interfacial EG-agua y las interacciones débiles de los grupos EGn con las proteínas definen el comportamiento de las EGn-SAMs. Grunze et al.[37, 38] sugieren que la resistencia a la adsorción de proteínas es consecuencia de formación de una capa estable de moléculas de agua retenida en la interfase, que impide el contacto directo entre la superficie y las proteínas. Esto se debe a que el extremo EGn-terminal interactúa fuertemente con moléculas de agua, aumentando la densidad de enlaces por puente de hidrógeno, y previniendo con ello frente a la adsorción irreversible de proteínas.

Un ejemplo concreto en el que se han empleado SAMs EGn-terminales con un esqueleto alcano es en el diseño de membranas bicapa híbridas, capaces de retener agua y/o fragmentos de proteínas. Aunque la parte EGn-terminal, hidrofílica, debería mantener la tendencia lineal del esqueleto molecular dando lugar a empaquetamientos muy compactos debido a la coincidencia casi perfecta entre la sección transversal de ambas partes de la molécula, esto no sucede. Los fragmentos EGn-terminales muestran una conformación menos ordenada que la región de n-alcanotiol, debido a la presencia de átomos de oxígeno de los grupos éter. Sin embargo, experimentos IRRAS y medidas de elipsometría sugieren que las unidades EGn presentan una morfología cristalina de tipo laminar en una estructura helicoidal  $7/2$  ordenada y orientada normal a la superficie,

independientemente de la longitud del grupo alquilo [67, 68]. En base a estos resultados, Vanderah et al. pensaron que las mitades EGn-terminales podrían formar SAMs con una conformación helicoidal bien definida, sin necesidad de emplear un espaciador n-alcano. Así, sus siguientes trabajos son pioneros en el uso de moléculas tioladas que únicamente presentan unidades EG (EGn-SH) para formar SAMs, evaluando su conformación y su resistencia a la adsorción de proteínas [69, 70].



**Esquema 8.** Representación de una SAM formadas sobre sustratos de oro a partir de moléculas de (A) n-alkanotiol en conformación todo-trans, (B) n-alkanotiol OEG-terminal, donde el espaciador alcano facilita la formación de una estructura densamente empaquetada con un ordenamiento trans y las unidades EGn-terminales tienden a adquirir una conformación helicoidal, y (C) moléculas basadas en su totalidad en unidades EG, que dan lugar a ordenamientos que presentan una conformación helicoidal.

#### 1.2.3.2. EGn-SAMs

En la actualidad, la mayoría de las superficies modificadas empleando la técnica de formación de SAMs que contienen grupos EGn se forman a partir de moléculas de mercapto-etilenglicol (EGn-SH) sin espaciador alcano, dadas las potenciales aplicaciones que presentan. La organización se ve influenciada por el tamaño de la molécula, pero se ha demostrado que parámetros como la temperatura o la concentración salina de la disolución de formación también afectan al grado de empaquetamiento (Esquema 9).

Vanderah et al.[69] fueron los primeros en estudiar la influencia del disolvente en la estructura de la EG7-SAM, empleando técnicas de elipsometría, espectroscopía IR y EIS. En concreto, usaron tetrahidrofurano (THF) un disolvente no hidroxílico, etanol puro (EtOH) como disolvente hidroxílico, y una mezcla etanol/agua (EtOH95%), para determinar si el agua, incluso en pequeñas proporciones, influye en las propiedades finales de la SAM. La mejor organización estructural se encontró para la película formada en EtOH95%. Las medidas de EIS indican que la capa formada en este medio se comporta como un condensador casi ideal, mientras que las obtenidas en EtOH y THF presentan heterogeneidades que obligan a introducir un elemento de fase constante para explicar la

desviación con respecto a la idealidad. En términos de espesor, las capas obtenidas en EtOH y EtOH95% presentan grosores similares y reproducibles, mientras que para películas obtenidas en THF, los espesores son variables. Por último, los resultados de espectroscopía infrarroja fueron coherentes con las medidas de elipsometría, apuntando a la formación de películas altamente organizadas desde medios etanólicos y menos ordenadas cuando se preparaban desde THF. Estos resultados les permitieron concluir que las EG7-SAMs ensambladas en Au desde EtOH95% presentan una conformación helicoidal 7/2, similar a la que muestran las cadenas libres de EGn polimorfas. Sin embargo, el ensamblaje desde otros disolventes da lugar a películas menos compactas y con morfologías variables [70, 71]. Estos estudios sumados a los de Malysheva, demuestran que la organización estructural de las EGn-SAMs varía con n, obteniéndose películas helicoidales ordenadas para  $n > 4$ , mientras que el uso de moléculas que contienen menos de 6 unidades de EG en la cadena lleva a la formación de recubrimientos que son rápidamente penetrados por moléculas de agua [68, 70, 72, 73].



**Esquema 9.** Diagrama explicativo sobre la organización estructural de las EGN-SAMs sobre sustratos planos. A la derecha, se señalan las variables experimentales que definen el tipo de organización que las estructuras ensambladas adquieren. A la izquierda, se presentan potenciales aplicaciones de este tipo de recubrimientos en función del grado de empaquetamiento de la película polimérica.

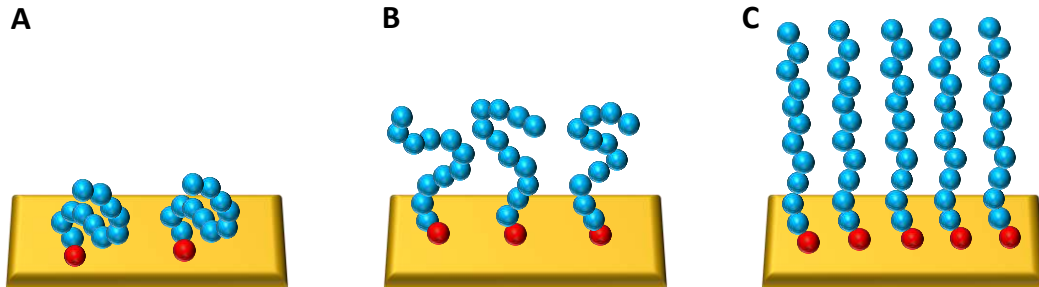


Más recientemente han aparecido nuevos estudios en este tema [74-77], en particular, en el desarrollo de biosensores electroquímicos, por lo que el estudio de las propiedades interfaciales es fundamental. Para ser de utilidad en esta aplicación, la película superficial debe permitir la transferencia electrónica entre el electrodo y las especies redox en disolución.

Son numerosos los trabajos recogidos en bibliografía en los que se emplean la CV para obtener información sobre la estructura y las propiedades de películas de EGN de varios espesores, en base a su grado de pasivación y a la permeación de pares redox de distinta naturaleza [78-80]. Más específicamente, se centran en estudiar el bloqueo que ejercen las películas frente a sondas redox en función del tamaño molecular y otras propiedades estructurales, o bien dependiendo de la solubilidad de las propias sondas. El sistema modelo EG7-SAM sobre electrodos de Au ha sido empleado por Doneux et al. [76, 77] para evaluar la influencia de la película ensamblada en el comportamiento de sistemas redox de esfera externa bien conocidos, como son  $[\text{Fe}(\text{CN})_6]^{3-/4-}$ ,  $[\text{Ru}(\text{NH}_3)_6]^{3+/2+}$ ,  $\text{Fc}(\text{MeOH})^{2+/0}$ , y  $[\text{IrCl}_6]^{2-/3-}$ . La EG7-SAM se comporta como una película que presenta poca impedancia en todos los sistemas, salvo en presencia de  $[\text{Fe}(\text{CN})_6]^{3-/4-}$  [81]. El efecto de inhibición particular en la transferencia electrónica del par  $[\text{Fe}(\text{CN})_6]^{3-/4-}$  se explicaría tanto en términos de hidratación de la SAM como de los aniones electroactivos. Con relación a esto último, Hotchen et al. [79] han encontrado que cadenas cortas de EGN ( $n = 4, 6$  y  $8$ ) bloquean de forma significativa la cinética de transferencia de carga del par  $[\text{Fe}(\text{CN})_6]^{3-/4-}$ , y atribuyeron esta inhibición a su insolubilidad en las películas basadas en EGN. De hecho, utilizando la especie hidrofóbica  $\text{Fc}(\text{MeOH})_2$ , soluble en EGN, se observa una transferencia electrónica reversible en presencia de las EGN-SAMs, apoyando la hipótesis anterior.

A pesar de la idoneidad de la molécula EG7-SH (y similares) para llevar a cabo estudios fundamentales que permiten ahondar en los mecanismos que rigen el ensamblaje y en las propiedades finales de las SAMs, en la mayoría de las aplicaciones biomédicas se precisa del uso de superficies PEGiladas con un número de unidades EGN muy superior a los empleados comúnmente en los estudios modelo. La investigación en el tipo de organización que estas cadenas adquieren al anclarse a las superficies metálicas que, como en el caso de las de menor tamaño, se enfocan en los efectos de la temperatura, el tiempo de inmersión o naturaleza del disolvente, entre otros. En la formación de estas SAMs la densidad de empaquetamiento ( $\sigma$ ) es uno de los parámetros más importantes, ya que define si las cadenas ancladas a la superficie se encuentran en una conformación más o menos extendida. En este sentido, el grado de hidratación de las unidades EG afecta notablemente al valor de  $\sigma$  [82]. Valores de  $\sigma$  pequeños indican que las cadenas están altamente hidratadas, adoptando una conformación de baja o muy baja densidad conocidas como

*mushroom* y *pancake*, respectivamente, mientras que a valores de  $\sigma$  más altos, las moléculas ancladas se encuentran estiradas, dando lugar a empaquetamientos compactos llamados *brush* (Esquema 10). En la mayoría de las aplicaciones se requiere que las películas de EGN adquieran este tipo de organización de alta densidad.



**Esquema 10.** Ilustración de los tres tipos de conformación de los polímeros anclados en superficie: (A) *pancake*, (B) *mushroom*, (C) *brush*.

El mayor problema que se encuentra al diseñar películas poliméricas basadas en moléculas de cadena larga sobre sustratos macroscópicos es el impedimento de las posiciones de anclaje que se produce por solapamiento cuando las moléculas se injertan en su conformación *random-coil*. Este solapamiento se produce cuando la distancia entre los puntos de unión de las cadenas a la superficie es comparable con el tamaño que presenta una molécula libre en la disolución modificadora [83] (Esquema 11A).

Para determinar la naturaleza del empaquetamiento se calcula el radio de Flory, que proporciona información sobre el tamaño de la cadena polimérica en su conformación *random-coil*, mediante la ecuación:

$$R_F = b \left( \frac{a \cdot N}{b} \right)^{1/2} \quad (1)$$

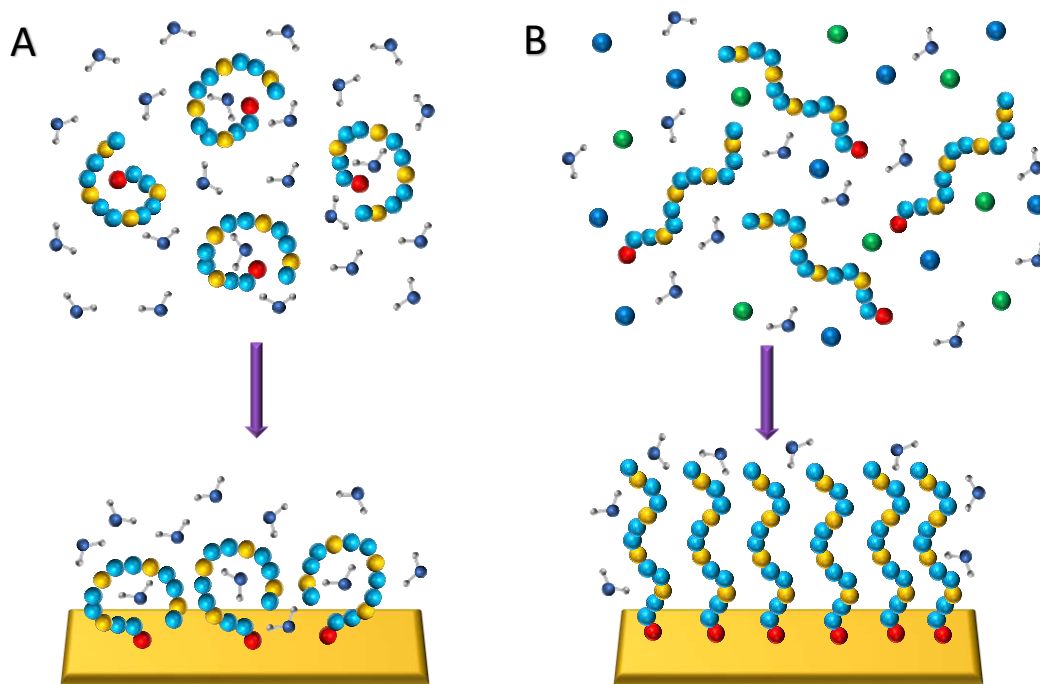
siendo  $a$  el tamaño del monómero ( $a=0.28$  nm para EGN en agua) [84],  $b$  la distancia de Kuhn ( $b=0.73$ ) [75] y  $N$  el número de monómeros en la cadena molecular. Por otro lado, la distancia entre centros de dos puntos de anclaje en la superficie,  $P$ , viene determinada por:

$$P = \left( \frac{1}{\sigma} \right)^{1/2} \quad (2)$$

La conformación tipo *mushroom* se caracteriza por presentar un recubrimiento pobre, con superficies que contienen un número relativamente pequeño de cadenas, con altura y tamaño definido por el radio de giro,  $R_F$ , a una distancia suficiente como para no interactuar entre sí. Conforme aumenta la densidad polimérica en la superficie, los valores de  $P$  pasan a estar muy por debajo de  $2R_F$ , indicando que las moléculas injertadas adquieren una conformación extendida y dan lugar a una capa espesa, tipo *brush*. El tamaño de esta estructura puede determinarse usando la relación de *Alexander de Gennes* [83],

$$H = \left(\frac{\sigma}{3}\right)^{1/3} \cdot b^{2/3} \cdot a \cdot N \quad (3)$$

Incluso con moléculas libres largas, se ha demostrado que es posible obtener recubrimientos muy compactos eligiendo las condiciones experimentales adecuadas. Una de las estrategias más útiles para aumentar  $\sigma$  en la película polimérica es emplear disoluciones que fueren a las moléculas libres a perder la conformación *random-coil*, adoptando su forma elongada. Esto puede conseguirse empleando disolventes pobres en relación a las cadenas a injertar [29], estableciendo condiciones cercanas a la fusión del polímero [85], o mediante la estrategia de empaquetamiento en el “punto de nube” ( *$\theta$ -point*) [29].



**Esquema 11.** Formación de SAM a partir de moléculas de EGn-SH. A temperatura ambiente en disolución acuosa (A), las cadenas se encuentran en conformación *random-coil*, y mantienen esta estructura al adsorberse en la superficie. (B) La adición de sales a la disolución provoca la deshidratación de las moléculas, facilitando que adopten una conformación extendida que da lugar a recubrimientos de alta densidad de empaquetamiento.

En síntesis, el punto de nube es una propiedad de fase que indica la temperatura a la que los polímeros dejan de ser miscibles en la disolución en que se encuentran. Este parámetro describe el ordenamiento de una cadena polimérica libre, en base a las interacciones que presenta con el disolvente, otros componentes del medio y el resto de las cadenas de la misma naturaleza. Se ha determinado que su valor puede modularse mediante diferentes variables experimentales, por ejemplo, en base a la estructura molecular [86] y a la concentración salina del entorno [87] (Esquema 11B).

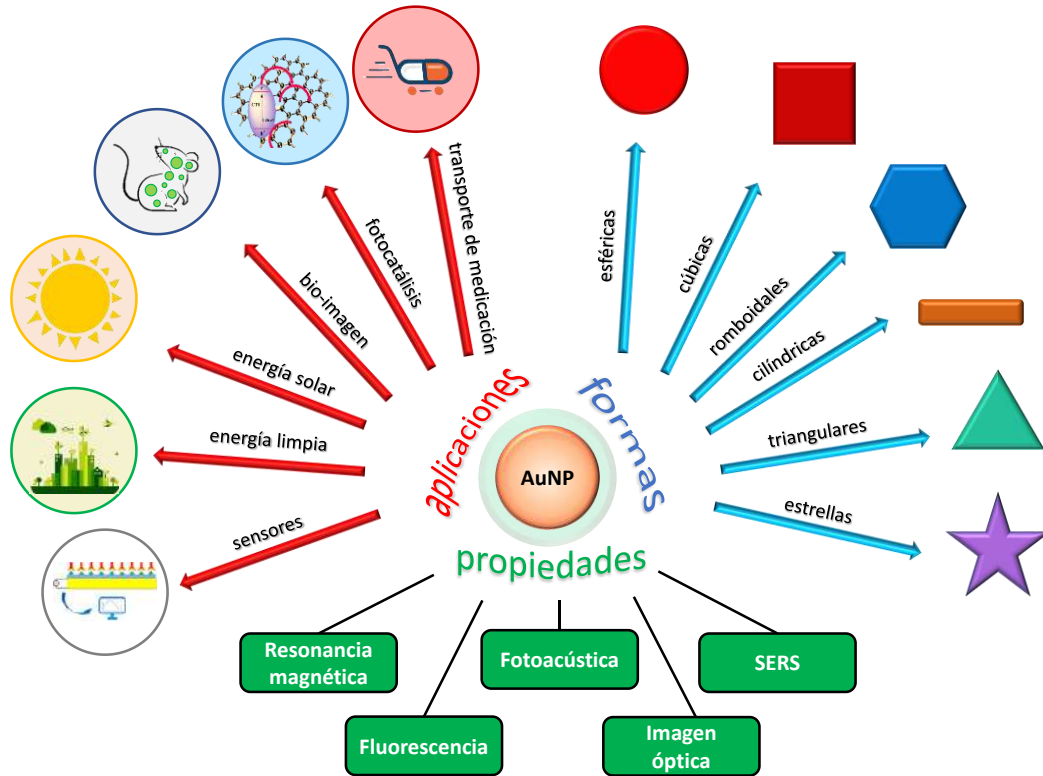
Emilsson et al. [74] han obtenido películas poliméricas basadas en EGN (de pesos moleculares entre 2 y 30 kDa) tipo *brush* bien definidas, desde disolución acuosa 0.9M Na<sub>2</sub>SO<sub>4</sub> a temperatura ambiente. La presencia de la sal en la disolución fuerza un equilibrio osmótico, haciendo que las cadenas poliméricas en conformación *random-coil* se deshidraten y pasen a estar estiradas, por lo que al anclarse en la superficie facilitan acomodar un número mayor de cadenas. La altura de las películas de EGN formadas en estas condiciones coincide con los valores calculados basados en un modelo similar al de *de Gennes* [88] para películas compactas en las que la altura es proporcional al peso molecular. Más recientemente, Ortiz et al. [75] han profundizado en esta estrategia evaluando  $\sigma$  en función de la concentración salina en la disolución modificadora. Encontraron que el mayor grado de empaquetamiento se obtiene cuando la película de EGN se forma en disolución salina 0.9 M en Na<sub>2</sub>SO<sub>4</sub>, y también observaron que la transición conformacional de *mushroom* a *brush* en las películas injertadas en la superficie sólo se produce a tiempos de formación largos, lo cual subraya la importancia del tiempo de adsorción para obtener recubrimientos que presenten conformaciones compactas.

### 1.3. NMs 3D: AuNPs.

Durante las últimas décadas las NP metálicas y, en especial las de Au, han atraído mucho interés debido a su alta relación superficie-volumen y a su pequeño tamaño, que hacen que presenten propiedades únicas [89]. Las AuNPs pueden prepararse por reducción de sales de Au(I) o Au(III) a Au(0). En cuanto a propiedades generales, los sustratos macroscópicos de oro son de color amarillo brillante y se caracterizan por ser extremadamente inertes, mientras que el Au coloidal puede presentar diversos colores en función del tamaño y la forma, sumado a propiedades ópticas, eléctricas y térmicas completamente diferentes. Estas propiedades son las que justifican que sean potenciales candidatos de aplicación en sistemas biológicos, en tareas tan diversas como la biodistribución de fármacos o la captación celular.

Las AuNPs destacan por sus propiedades de absorción y dispersión de la luz en el visible y en el infrarrojo cercano, debido al fenómeno de LSPR [90]. Estas propiedades ópticas justifican su uso como agentes de contraste en microscopía electrónica, y han motivado el diseño de nanoestructuras de diferentes formas. En la bibliografía actual es posible encontrar métodos de síntesis bien definidos que permiten obtener AuNPs esféricas de diferentes tamaños y con formas anisotrópicas como cilindros, triángulos, prismas o estrellas, entre otros (Esquema 13). Cada uno de estos tipos de AuNP presenta propiedades únicas que facilitan su uso en determinadas aplicaciones médicas, ya que mantienen la biocompatibilidad y una excelente química superficial. Gracias a esta última, es posible

formar recubrimientos moleculares en torno a las AuNPs a fin de introducir nuevas funciones o de proteger al NM frente a las inevitables interacciones con el medio biológico, como se ha comentado en el punto 1.1.



**Esquema 13.** Diagrama sobre AuNPs en el que se señalan las principales aplicaciones de estas nanoestructuras, las formas que pueden presentar en función de la metodología de síntesis empleada y las propiedades que hacen atractivo su uso en el campo biomédico.

En muchas de las aplicaciones en las que las AuNPs son interesantes es necesario que presenten una química superficial específica. Para ello, se recurre a la modificación superficial con polímeros, que ha demostrado que mejora considerablemente su uso en aplicaciones biomédicas, particularmente en el caso de distribución de fármacos y en la ingeniería de tejidos [91]. Además, los polímeros mejoran la estabilidad, dispersión y potencian la funcionalidad de las AuNPs, al ayudar a preservar las propiedades ópticas del núcleo de Au, e inducen respuestas frente a estímulos como la temperatura, el pH, la luz o enzimas y otras biomoléculas presentes en el medio [92]. El concepto de PEGilación explicado previamente es extensible a NPs. Así, es una estrategia clave que permite diseñar estructuras 3D para aplicaciones terapéuticas, que transportan y liberan de forma controlada fármacos, al mismo tiempo que aumenta de forma notable el tiempo de circulación del nanotransportador en el torrente sanguíneo, minimizando la opsonización por parte del sistema inmunitario.

### 1.3.1. Estabilidad coloidal de AuNPs.

Se entiende por dispersión coloidal al sistema conformado por dos fases, normalmente un líquido y partículas sólidas de diámetro comprendido entre  $10^{-9}$  y  $10^{-5}$  m. Se trata de una situación intermedia en la que el tamaño de partícula es demasiado grande como para que el comportamiento sea el de una disolución ordinaria, pero a su vez son lo suficientemente pequeñas como para que el movimiento browniano prevenga la sedimentación. Los coloides liofóbicos son aquellos que no poseen afinidad por el medio dispersante. Entre ellos se encuentran las AuNPs que son termodinámicamente inestables debido a la tendencia a disminuir que presentan su área interfacial y su energía libre superficial. Sin embargo, la velocidad de agregación puede ser muy lenta, lo que permite considerar al coloide como un sistema estable desde la óptica cinética. En el caso de AuNPs no modificadas superficialmente, la estabilidad coloidal depende totalmente de la carga electrostática. La pérdida de esta carga superficial puede conducir a que las suspensiones coloidales floculen, por lo que puede concluirse que, de forma general, las NPs coloidales no coagulan gracias a las fuerzas de repulsión electrostáticas.

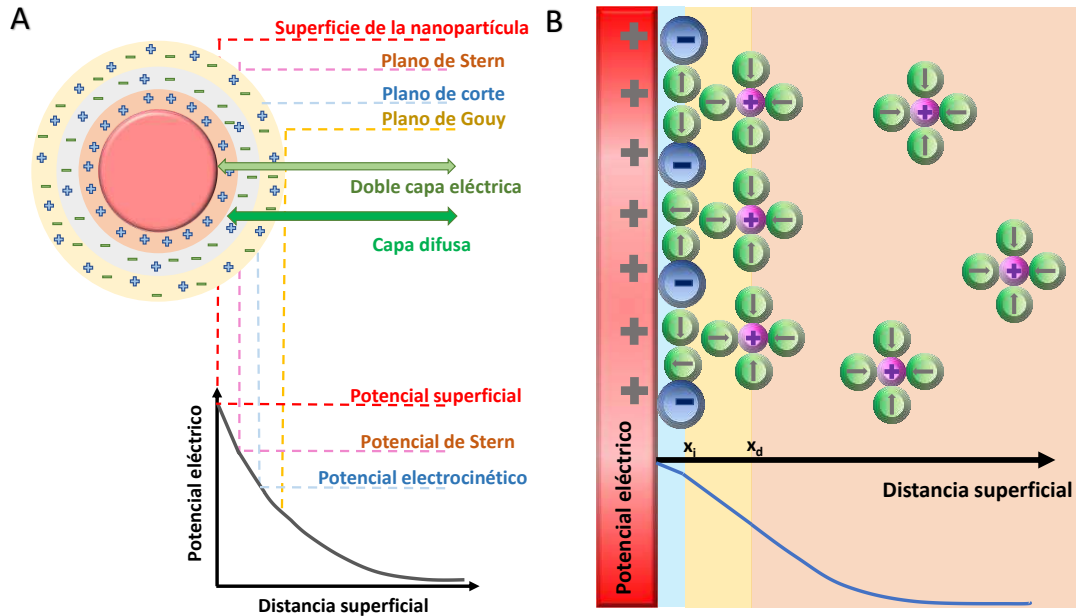
#### 1.3.1.1. Fenomenología de la doble capa eléctrica.

El entorno que rodea a las NPs cargadas e influye en las propiedades de su interfase ha sido extensamente estudiado. Generalmente, en este contexto se aplica el modelo de la doble capa formulado por Stern [93], que describe una capa fija en la superficie cargada (siguiendo el modelo de Helmholtz) [94] y una capa difusa de contraiones (modelo de Gouy-Chapman) [95, 96]. El espesor de esta capa difusa, que determina la cercanía de las partículas a escala nanométrica, depende en gran medida de la fuerza iónica de la disolución y puede caracterizarse en función del parámetro de Debye,  $\kappa$ , frecuentemente expresado como su inversa (longitud de Debye,  $\kappa^{-1}$ ). Así, considerando los iones como cargas puntuales,  $\kappa$  disminuye con el aumento de la fuerza iónica,  $I$ , que es dependiente de la concentración iónica. El aumento de esta fuerza se acompaña de la reducción de la estabilidad electrostática, que se debe a una aglomeración de las NPs por la atracción dominante van der Waals. Otro parámetro clave para definir el entorno de las NPs es la movilidad electroforética,  $\mu$ , y los valores derivados de la misma, como el potencial  $\zeta$ . Así, la carga adsorbida en la superficie metálica hace que haya un exceso local de contraiones (capa de Helmholtz o Stern) que deriva en la formación de la capa difusa alrededor de la partícula (capa de Gouy-Chapman). Esta capa la conforman contraiones que no se encuentran fuertemente unidos a la partícula, junto con iones de signo opuesto y moléculas de disolvente, aunque los primeros son mayoritarios. Esta distribución de cargas en la interfase

de la NP hace que el potencial eléctrico descienda lentamente a medida que aumenta la distancia a la superficie hasta anularse en el seno de la disolución (Esquema 14A).

Es sencillo describir el potencial  $\zeta$  en función de este modelo. Su valor, definido en el plano de corte, es una medida de la velocidad de desplazamiento de una partícula en presencia de un campo eléctrico, y es fuertemente dependiente de la naturaleza de los iones que rodean la AuNP. De hecho, en esta región, los iones y la partícula pueden considerarse una entidad, ya que se mueven en conjunto en caso de que se produzca un desplazamiento. Así, valores altamente negativos o positivos indican que las estructuras tienden a repelerse, y por tanto presentan elevada estabilidad coloidal. Por el contrario, valores bajos reflejan la ausencia de fuerzas capaces de mantener la distancia entre cuerpos, de modo que acaban acercándose y flocculan. Típicamente, el valor del potencial  $\zeta$  aceptado para evitar la floculación es de 30 mV (en valor absoluto). La estrecha relación entre el potencial  $\zeta$  y los iones del medio hace que sea fuertemente dependiente del pH en disolución acuosa. Una partícula con potencial  $\zeta$  negativo presente en un medio que se vuelva más alcalino tenderá a adquirir mayor carga negativa al aumentar los iones hidroxilo. Un incremento en el número de protones causará el efecto contrario. En base a esto se define el punto isoeléctrico de la partícula, que es normalmente el valor en que el sistema coloidal es menos estable.

El modelo mostrado en el Esquema 14B explica el comportamiento de la doble capa eléctrica partiendo de varias hipótesis: la superficie de las NPs se considera plana, infinita, y con carga uniforme e independiente de los iones; los iones se comportan como cargas puntuales; y la constante dieléctrica del disolvente es uniforme, teniendo en la doble capa el mismo valor que presenta en el seno de la disolución. Sin embargo, para la descripción exacta de la interfase de las NPs, las dos últimas hipótesis de partida llevan a resultados que no consiguen explicar de forma satisfactoria las interacciones de la doble capa. Por ello, se recurre al modelo de Gouy-Chapman-Stern-Grahame, en el que se considera que los iones (pueden estar solvatados) presentan un tamaño definido y, además, considera la existencia de campos eléctricos intensos ( $10^6$ - $10^8$  V/m) en las proximidades de la superficie, que pueden forzar la orientación dipolar de los disolventes, en especial en moléculas de agua.



**Esquema 14.** (A) Variación del potencial eléctrico en la interfase de las AuNP según el modelo de Gouy-Chapman-Stern. (B) Distribución de cargas aniónicas (azul), catiónicas (rosa) y moléculas de agua (verde, con sus dipolos orientados) en el modelo de Gouy-Chapman-Stern. En la parte inferior se esquematiza la variación del potencial eléctrico en función de lo anterior.

### 1.3.1.2. Teoría DLVO.

La teoría DLVO (llamada así por Derjaguin, Landau, Verwey y Overbeek) permite explicar la estabilidad coloidal en base al equilibrio entre las fuerzas opuestas de repulsión electrostática de Coulomb y de atracción tipo van der Waals [97].

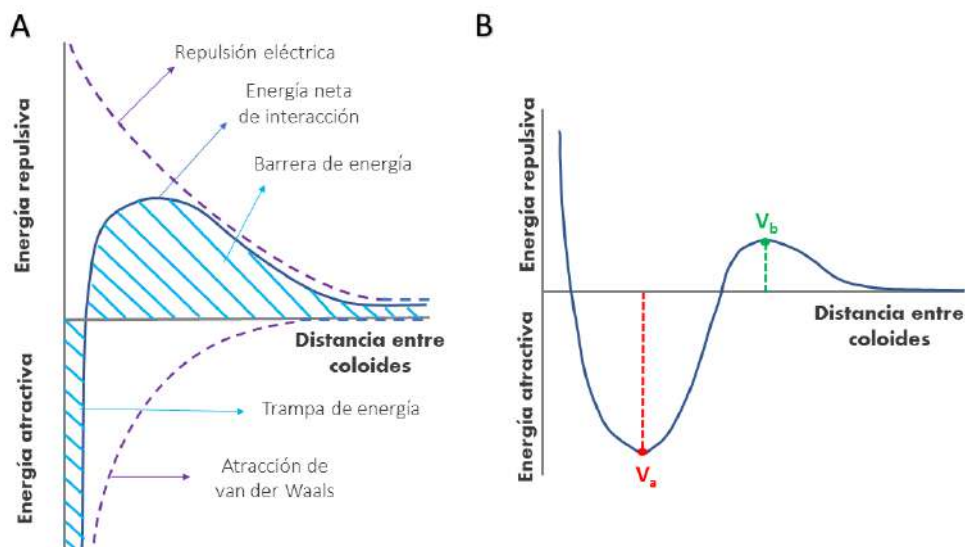
La repulsión electrostática comienza a ser importante al aproximarse los coloides y empezar a interferir la doble capa. La energía necesaria para superar la repulsión electrostática y forzar la unión de las partículas alcanza su valor máximo cuando las partículas se sitúan a una distancia muy corta (casi cero) y disminuye paulatinamente hasta cero según se aleja fuera de la doble capa. Por tanto, el valor máximo está relacionado con el potencial de la superficie. Por su parte, la atracción de van der Waals entre coloides es un efecto aditivo en el que, cada una de las NPs que componen el coloide experimenta la atracción de van der Waals del resto de partículas que componen el sistema. Así, la fuerza repulsiva entre las partículas del mismo signo es de naturaleza eléctrica, aumentando proporcionalmente con la carga y con el potencial electrocinético. La combinación de estas dos fuerzas se representa en la curva de energía neta de interacción (Esquema 15A). Dicho balance puede resultar en una fuerza atractiva o repulsiva (en función del medio de



dispersión y características de la interfase de la partícula, entre otras). La expresión de la energía potencial total es:

$$\Delta G_T(kT) = -\left(\frac{64C_0}{\kappa}\right)e^{-(\kappa h)} - \frac{A_H}{12\pi h^2} \quad (4)$$

donde  $C_0$  es la concentración de iones,  $h$  la distancia entre los coloides,  $A_H$  la constante de Hamaker del material coloidal y  $\kappa$  el parámetro de Debye. Si la barrera energética es superior a la energía de agitación térmica (aproximadamente  $10kT$ ) la energía cinética de las partículas no es suficiente para superarla, manteniéndose la estabilidad coloidal. La posición del mínimo de estabilidad indica la separación existente entre las partículas, que puede llegar a ser incluso de pocos Å, y permite distinguir entre diferentes tipos de interacciones: floculación, coagulación y agregación. Así, se habla de floculación para los acercamientos en los que el mínimo de energía equivalga a una separación relativamente larga y con poca profundidad; mientras que coagulación o agregación, normalmente empleados indistintamente, hacen referencia a un mayor acercamiento entre los cuerpos, con energía similar a la de cohesión o adhesión. Por tanto, para que se produzcan situaciones de floculación o coagulación entre partículas es necesario superar una energía,  $V_b$  (Esquema 15B).



**Esquema 15.** (A) Curva de energía neta resultante de la interacción entre dos partículas metálicas, combinación de energías electrostáticas e interacciones de tipo van der Waals. (B) Curva de energía neta típicas en coloides metálicos en las que, superada la barrera energética, las partículas evolucionan hacia sistemas más inestables.

La estabilidad coloidal resulta favorecida al incrementar la carga en la interfase (mediante especies adsorbidas, bien con agregación de especies activas o modificando la distribución de los iones presentes, por ejemplo, alterando el pH) y, por el contrario, la entrada de contraiones en la parte fija de la doble capa la disminuye, consecuencia de la

menor barrera energética. Superada esta última, se producen las interacciones coloidales. La intensidad de las interacciones de van der Waals son proporcionales a la profundidad del mínimo  $V_a$ , siendo mayor la energía necesaria para la separación de las partículas. En estas condiciones, la interacción neta es totalmente atractiva, lo que lleva a que esta región interna, a la que se aproximan de manera inevitable las partículas, se denomine comúnmente “trampa de energía” o “pozo de potencial.

### *1.3.1.3. Influencia de las fuerzas estéricas en la estabilidad coloidal.*

En los puntos 3.1.1 y 3.1.2 se ha asumido que la interfase de las partículas, sólida y homogénea, presenta límites perfectamente definidos. Sin embargo, en muchos casos esto no se cumple, existiendo interfases relativamente difusas, en las que los diferentes tipos de fuerzas se superponen. Esto se debe a la presencia de grupos enlazados a la superficie, termodinámicamente activos, que producen una “rugosidad dinámica” en la superficie de las partículas. En estas condiciones, el acercamiento entre partículas modifica la entropía del sistema derivando en una fuerza repulsiva conocida como “repulsión estérica” o “de solapamiento.” Estas capas adsorbidas constituyen una barrera estérica que aumenta la estabilidad de las dispersiones coloidales, evitando la coagulación. El efecto estérico producido, junto con el electrostático, son los métodos más usados para estabilizar suspensiones coloidales. Aunque la mayoría de los recubrimientos poliméricos estabilizan las nanoestructuras mediante efectos estéricos, es posible diseñar películas con carga, consiguiéndose así una coraza protectora de los coloides que evita la pérdida de estabilidad en ambos términos, estérico y electrostático, a partir de un único tipo de molécula.

Para conseguir NPs estabilizadas por efecto estérico, las películas poliméricas empleadas deben cumplir una serie de requisitos: a) la superficie de la NP debe quedar totalmente cubierta por el polímero; b) las fuerzas de unión de los ligandos poliméricos deben ser lo suficientemente fuertes como para evitar que sean desplazadas durante las colisiones derivadas del movimiento browniano; c) la capa formada debe ser lo suficientemente espesa ( $>3$  nm) para mantener el punto de máxima aproximación fuera del rango de acción de las fuerzas atractivas de van der Waals; y d) la parte de la molécula no anclada a la superficie, que puede ser de mayor o menor extensión, debe estar completamente solvatada por el disolvente. Una capa polimérica que presente estas características previene la coagulación desde dos vertientes: entrópica (o estérica) y entálpica [98]. Cuando dos partículas se aproximan, las cadenas de las capas poliméricas que las rodean comenzarán a interactuar cuando se sitúen lo suficientemente cerca. Este solapamiento entre las cadenas provoca cambios en la conformación del sistema, disminuyendo su capacidad de movimiento, esto es, sus grados de libertad, y por tanto

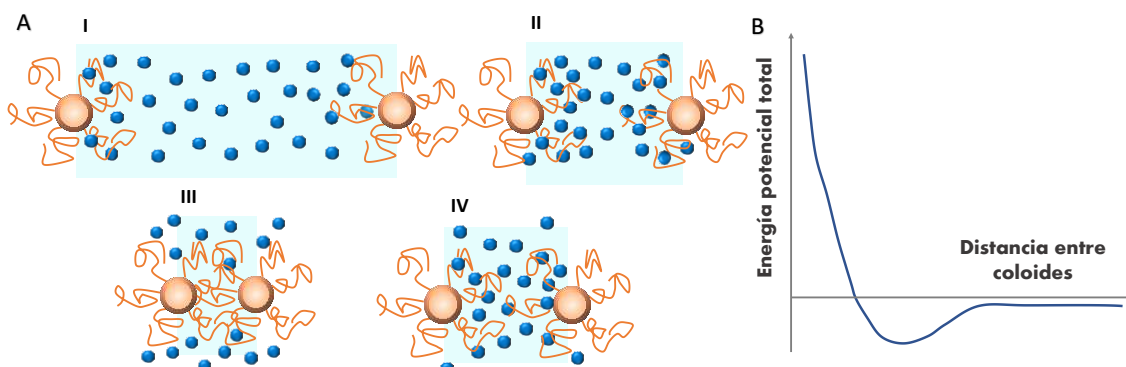
provocando una bajada en la entropía. Además, es frecuente que la capa polimérica que recubre la partícula contenga moléculas de disolvente fisisorbidas, que pasan a formar parte de la doble capa. Así, cuando dos coloides se aproximan y entrelazan sus cadenas, las moléculas de disolvente que las rodean son expulsadas, aumentando la concentración local de polímeros injertados en la superficie del NM. La desolvatación de los injertos poliméricos se traduce en el aumento de la energía de enlace inter-cadena, situación desfavorable para la entalpía del sistema. Esta situación energética adversa puede solventarse gracias a la presión osmótica: las moléculas de disolvente tienden a situarse en el espacio entre las partículas, resolviendo las cadenas poliméricas y restaurando parcialmente su libertad de movimiento (Esquema 16A).

A fin de evitar la situación energéticamente desfavorable anterior, los polímeros en bloque (*block polymer*) han demostrado ser una opción muy interesante: una parte de la molécula se ancla fuertemente a la superficie constituyendo una barrera estérica efectiva, mientras que el resto de la molécula, en caso de presentar alta afinidad por el disolvente, será solvatada (es decir, estabilizada electrostáticamente) de manera importante [99, 100].

Las fuerzas de repulsión estéricas que generan las cadenas poliméricas injertadas en la superficie de las partículas hacen que la curva de energía potencial neta presente un único mínimo (Esquema 16B). Las partículas protegidas pueden experimentar una agregación reversible, lo cual influye en todas sus propiedades (movilidad, estabilidad, transporte, biocompatibilidad, etc.) así como en las del entorno colindante. Esta estabilización electro-estérica que experimentan las partículas recubiertas con capas poliméricas se recoge en la teoría DLVO extendida, siendo el modelo teórico de Van Oss el que explica todas las interacciones que se producen en este sistema. En ella se contemplan también otras fuerzas repulsivas (como fuerzas de hidratación) y atractivas (como las hidrofóbicas o las magnéticas). Todas estas interacciones dependen de la naturaleza de las interfaces involucradas, como son el potencial  $\zeta$  y las distintas componentes de la energía libre superficial, por lo que es necesario evaluar las propiedades eléctricas y termodinámicas para la caracterización de estos sistemas [101]. Es importante puntualizar que las fuerzas de repulsión estéricas son un tipo concreto dentro de las llamadas interacciones ácido-base de Lewis (o interacciones electrón-receptor / electrón-donante), que tienen su origen en intercambios ácido-base entre las superficies de las NPs y el medio de dispersión. Se consideran así las interacciones no dispersivas y estructurales, gracias a las que es posible determinar de manera mucho más acertada la energía potencial neta del sistema en base al modelo extendido DLVO.

La descripción de este tipo de interacciones estéricas es compleja ya que depende de diferentes parámetros, como el grado de recubrimiento de la superficie coloidal, las

características del medio de dispersión y el mecanismo mediante el que las cadenas moleculares se enlazan a la superficie, además de la naturaleza de las moléculas seleccionadas para formar las capas protectoras.



**Esquema 16.** (A) (I) Dos partículas alejadas no presentan ningún tipo de interacción, y la película polimérica que recubre cada uno de los núcleos mantiene la estabilidad gracias al impedimento estérico. Si las partículas se acercan (II) y se sobrepasa una distancia que permita la interacción entre moléculas adsorbidas (III), pierden libertad de movimiento y se produce su desolvatación, desestabilizando el sistema en términos entrópico y entálpico. A fin de recuperar cierta estabilidad (IV), las cadenas injertadas en la superficie deben separarse, recuperando grados de libertad al ser resolvatadas por las moléculas de disolvente. (B) Representación de la curva de energía neta en función de la separación entre coloides estabilizados con películas poliméricas.

### 1.3.2. EGN-SAMs en sistemas 3D.

Muchas de las aplicaciones en las que las EGN-SAMs son de interés en sistemas *in vivo* requieren que éstas se encuentren injertadas en sistemas 3D, como son las AuNPs. Este tipo de partículas (EGN-AuNP) resulta atrayente en muchos campos de investigación debido al fenómeno LSPR [102], alta biocompatibilidad [103] y actividad catalítica [104].

Se cree que la naturaleza hidrofílica y la carga superficial neutra que presentan las moléculas de EGN evitan en gran medida la adsorción inespecífica de proteínas y el reconocimiento (y con ello, el rechazo) de las AuNPs por parte del sistema inmune [32]. Al igual que sucede en las películas formadas sobre sustratos 2D, el recubrimiento superficial ( $\sigma$ ) es uno de los parámetros más relevantes en su interacción con las proteínas y demás componentes del entorno biológico [105].

#### 1.3.2.1. Recubrimiento superficial y diámetro hidrodinámico de EGN-AuNP.

De forma similar a lo que sucede al anclar películas moleculares sobre superficies planas, es posible que los polímeros injertados en NPs adquieran dos regímenes distintos, *mushroom* y *brush* [83]. En el primero, las cadenas moleculares se comportan como entidades aisladas, y pueden considerarse como semiesferas cuyo tamaño viene dado por el radio de Flory

$$R_F = a \cdot N^{3/5} \quad (5)$$

donde  $N$  es el número de unidades EG en la cadena, y  $a$  su longitud (0.35 Å). Cuando  $\sigma$  presenta una conformación tipo *brush*, su espesor,  $L$ , viene determinado por

$$L = N \cdot a \cdot \left(\frac{a}{P}\right)^{2/3} \quad (6)$$

siendo  $P$  la distancia entre dos puntos de anclaje de la superficie. Cuando  $P$  está por encima de  $R_F$ , las cadenas tienen espacio para plegarse sobre la superficie de las AuNPs, dando lugar a una película delgada, con  $L$  pequeña. Por el contrario, si  $P < R_F$ , las moléculas se encuentran extendidas, formando una capa compacta [106]. En los casos en que  $L > 2R_F$ , se garantiza la obtención del régimen *brush* [107].

Para determinar el valor de  $\sigma$  en EGN-AuNPs se han empleado técnicas como la espectroscopía de resonancia magnética [108], el análisis termogravimétrico [105], la calorimetría isoterma de titulación [109], la ultracentrifugación analítica y el análisis de carbono orgánico total [110].

Otro parámetro interesante, estrechamente relacionado con el tamaño de la película polimérica es el diámetro hidrodinámico,  $D_H$ . Considerando que las cadenas de EGN ancladas a las AuNP esféricas, de diámetro  $D$ , presentan un comportamiento flexible, Vaknin et al. [111, 112] han propuesto la siguiente ecuación modelo para determinar el  $D_H$  de este tipo de NPs,

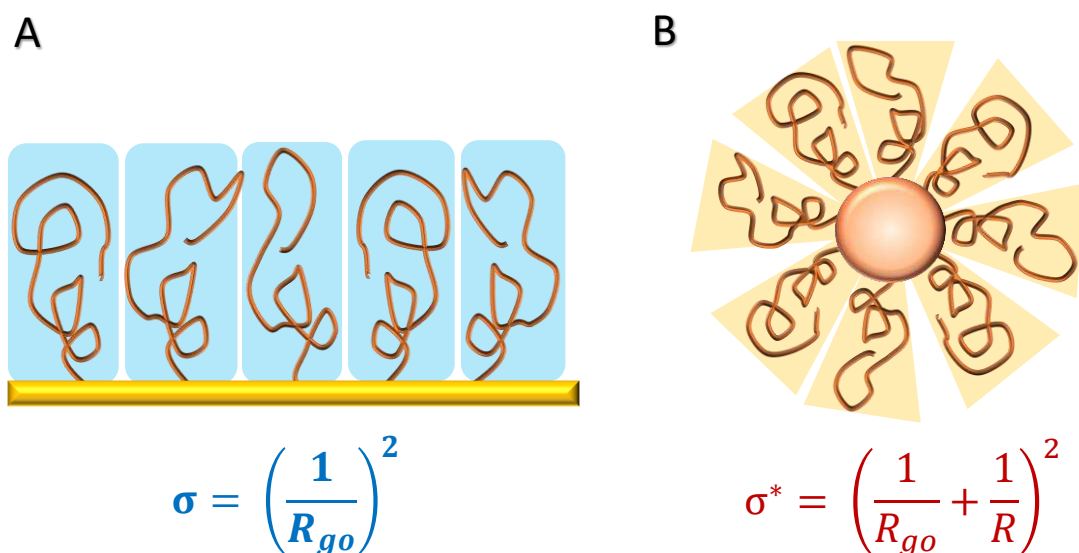
$$\left(\frac{D_H}{D}\right)^2 = 1 + 4 \cdot \frac{N \cdot b^2 \cdot \sigma^{1/2}}{D} \cdot (2w_0)^{1/4} \quad (7)$$

donde  $N$  es número de Kuhn de los monómeros,  $b$  la distancia de Kuhn ( $b=0.73$  para EGN) y  $w_0$  un parámetro de interacción adimensional de tres cuerpos ( $w_0 = 0.76$ ). El volumen hidrodinámico por molécula, fundamental para discernir el tipo de comportamiento que presentan las cadenas injertadas en la superficie, se obtiene dividiendo el volumen total de la corona polimérica que rodea la AuNP entre el número de moléculas ancladas. Se ha encontrado que para moléculas de EGN largas este valor es mayor del esperado si se asume que dichas moléculas están en una conformación tipo *brush*, ocupando en la superficie un volumen equiparable al de un cilindro cuya base es la huella molecular del EGN. El exceso de volumen determinado debe estar ocupado por moléculas de agua, libres o interaccionando estrechamente con las cadenas poliméricas, y este contenido en disolvente aumenta conforme lo hace la distancia a la superficie de la NP. Cálculos teóricos recientes han demostrado que el criterio adoptado para determinar el tipo de empaquetamiento en superficies planas es insuficiente para evaluar si se adopta un régimen tipo *brush* en NP, siendo necesario considerar la curvatura que estas presentan [113]. Estos cálculos han demostrado que la densidad del polímero es menor a medida que aumenta la distancia

radial, y mantienen un alto contenido en agua que únicamente disminuye en las proximidades de la superficie. El requisito de superposición a la altura del radio de giro del polímero,  $R_{go}$ , requiere modificar la estimación de la densidad de empaquetamiento para adoptar el régimen *brush*,

$$\sigma^* = \left( \frac{1}{R_{go}} + \frac{1}{R} \right)^2 \quad (8)$$

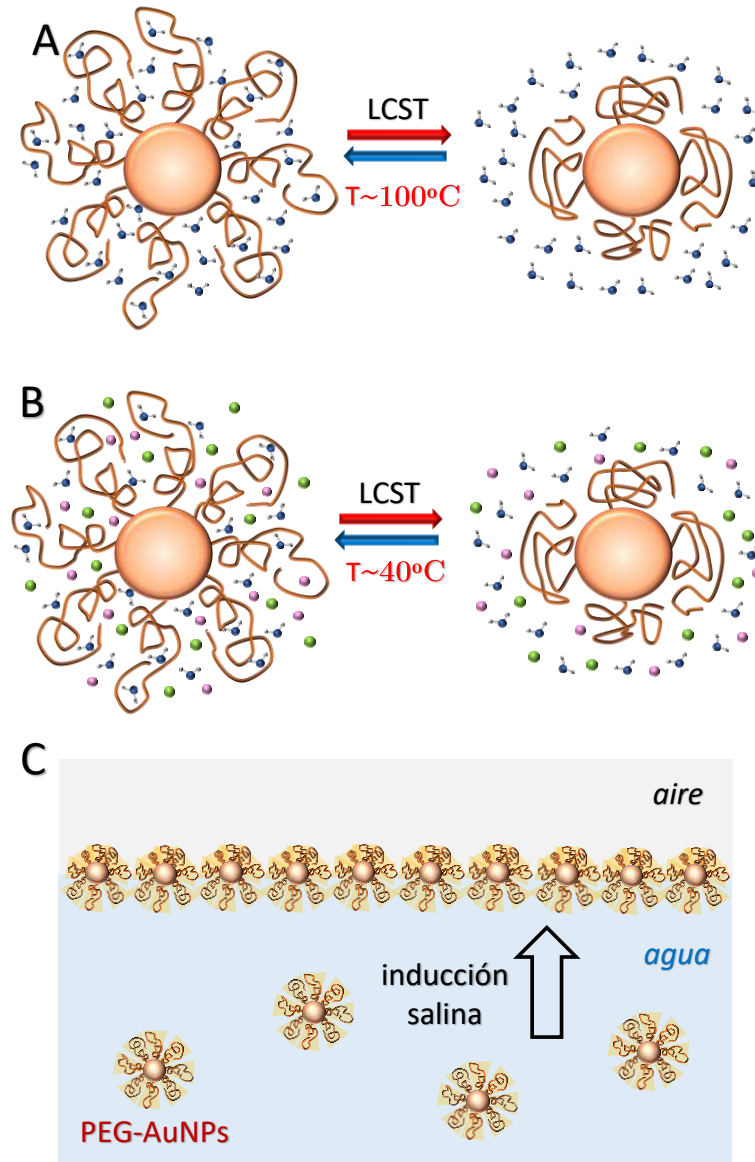
para NPs esféricas de radio  $R$ , teniendo en cuenta así la curvatura y el tamaño de la cadena polimérica en su conformación *coil* (Esquema 17). Cuando  $R \rightarrow \infty$ , se llega a la expresión típica de superficies planas,  $\sigma^* \approx 1/R_{go}^2$ . Por otro lado, para cadenas poliméricas muy largas en las que  $N \rightarrow \infty$ ,  $\sigma^* \approx 1/R^2$ , lo que implica que se necesita una densidad de injerto muy alta, que podría resultar poco realista para alcanzar el régimen *brush*.



**Esquema 17.** Representación esquemática indicando las diferencias para determinar la densidad de empaquetamiento en (A) sustratos planos y (B) NPs esféricas.

### 1.3.2.2. Respuesta frente a la temperatura y la concentración salina.

En AuNPs, a los parámetros de los que depende  $\sigma$  en sustratos macroscópicos, como el peso molecular de las cadenas de EGN o el disolvente, hay que sumar el tamaño y la forma de las NPs. Todos estos factores son determinantes de la estabilidad que muestra el sistema EGN-AuNP en suspensión en función del pH, concentración salina y temperatura [105, 114].



**Esquema 18.** Disposición de las cadenas poliméricas en EGN-AuNPs en suspensiones coloidales en función de la temperatura en (A) medio acuoso y (B) en presencia de determinadas concentraciones salinas. (C) Autoensamblaje 2D de EGN-AuNPs en la interfase causado por concentraciones altas de sales monovalentes.

Numerosos estudios han puesto de manifiesto que las EGN-AuNPs obtenidas empleando como ligandos EGN de diferente tamaño y empleando condiciones experimentales estándar, son estables tanto en un intervalo amplio de pH (2-12) en medio acuoso como en condiciones fisiológicas [115, 116]. Sin embargo, la respuesta a cambios térmicos de estos sistemas sí parece estar relacionada con el tipo de ensamblaje específico que presentan las cadenas de EGN. Así, el sistema binario agua-EGN muestra un diagrama de fase con una temperatura de solución crítica más baja (LCST, *Lower Critical Solution Temperature*) próxima a los 100°C. Este valor, relativamente alto, se debe principalmente a la formación de puentes de hidrógeno [117], y limita el uso de las EGN-AuNPs en

aplicaciones en las que se obtenga respuesta al modular la temperatura. Por encima de la LCST, la solvatación de las cadenas poliméricas no es suficiente para competir con las interacciones inter-cadena, lo que conduce a su colapso, pasando de una conformación *swelling*, en la que las cadenas están altamente hidratadas y expandidas, a que las cadenas se aglomeren, al no haber moléculas de disolvente entre ellas (Figura 18 A y B).

Los polímeros basados en EGN que han demostrado mayor sensibilidad a la temperatura son los derivados de metacrilato que presentan como grupo lateral una cadena corta de EG. En función de las características moleculares de las unidades monoméricas (longitud de la cadena, peso molecular o grupo terminal, entre otros) los recubrimientos poliméricos pueden ser insolubles en agua, fácilmente solubles hasta 100°C o termosensibles, con valores de LCST que varían en función de las propiedades anteriores [118]. En un estudio reciente de películas de EGN sobre NPs de SiO<sub>2</sub>, se ha demostrado que la LCST puede regularse entre 26°C y 90°C variando la longitud de la cadena lateral de este polímero [119].

Se ha encontrado que la presencia de sales en disolución puede reducir el valor de la LCST, permitiendo estudiar las propiedades termorresistentes del sistema a temperaturas más bajas, próximas a la fisiológica. Ijiri et al. [120] estudiaron este efecto en EGN-AuNP empleando Cn-EG7-álquil-terminales como ligando. Descubrieron que las NPs que no presentaban cabeza alquílica no se ensamblaban en el rango de temperatura 20-70°C, mientras que, en presencia de una cabeza alquílica de etilo, isopropilo o propilo, se producía el ensamblaje de las EGN-AuNP a temperaturas inferiores, indicando que la parte del ligando que queda expuesta a la interfase es fundamental en el comportamiento que exhibe el sistema en función de la temperatura. Posteriormente, estos mismos investigadores han demostrado que este proceso de ensamblaje controlado que experimentan las EGN-AuNP en medio acuoso tiene lugar mediante la hidratación y deshidratación de los fragmentos de EGN presentes en las moléculas injertadas en las NPs, fenómeno relacionado con la naturaleza del grupo de cabeza expuesto a la disolución y de la curvatura de la superficie, definida por el tamaño de las AuNPs [121].

Conscientes de la importancia de la densidad de empaquetamiento en las propiedades del sistema EGN-AuNP, Vaknin et al. han llevado a cabo una profunda investigación sobre la influencia que presentan diferentes concentraciones salinas [111, 112] y la temperatura de la disolución [122] en el injerto de las cadenas de EGN sobre la superficie de la AuNP. La presencia de iones en el medio hace que este disminuya su solubilidad por las cadenas de EGN, favoreciendo el autoensamblaje EGN-AuNP y la separación de fases. El mayor o menor efecto que ejerce un tipo de iones en particular sigue la serie de Hofmeister [123]. Se encuentra que pequeñas concentraciones de una sal divalente como el K<sub>2</sub>CO<sub>3</sub> provoca que



AuNPs recubiertas con EG18 y EG136 migren a la interfase vapor/disolución sin adquirir ninguna organización específica, pero, al aumentar la concentración salina, se produce un ordenamiento hexagonal de corto alcance, que acaba derivando en la formación de una estructura hexagonal cristalina altamente organizada. El  $D_H$  de estas NPs resulta independiente de la concentración salina, probablemente porque la película polimérica está protegida por una membrana semipermeable que mantiene constante su magnitud salina por encima del punto de nube [111]. Aumentando la concentración por encima de 1M, se observan precipitados macroscópicos 3D, que presentan orden de corto alcance, y que además son coherentes con que se produzcan ordenamientos con una simetría FCC entre las AuNPs más próximas, en los que las propiedades del ensamblaje están definidas por la longitud de la cadena polimérica [112].

Por otro lado, aunque las sales monovalentes como NaCl y KCl no producen separación de fase de los EGn a temperatura ambiente, sí son capaces de provocar, a concentraciones suficientemente altas, el autoensamblaje 2D de EGn-AuNPs en la interfase, lo que es coherente con la depleción de iones que se produce en los ordenamientos poliméricos *brush* a concentraciones salinas por debajo de las necesarias para lograr la separación de fases, generando un gradiente de presión osmótica que conduce al autoensamblaje 3D de estructuras supercristalinas (Esquema 18C) [124]. Mediante diferentes estrategias que incluyen la modificación de la concentración salina, el pH o la temperatura, se ha demostrado que también es posible modular el tipo de ensamblaje que adquiere el recubrimiento de EGn que rodean NPs de geometrías no esféricas, como nanocilindros o nanotriángulos [122, 125].

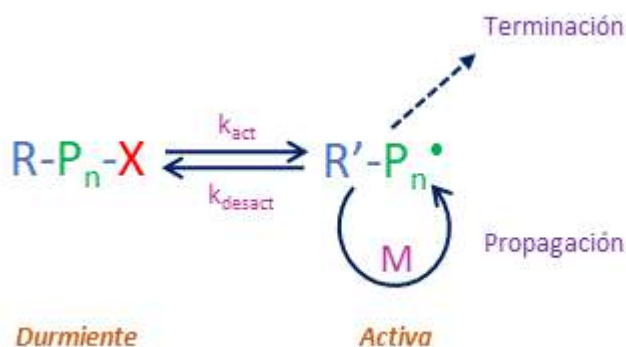
#### 1.4. Polimerización radical controlada.

La polimerización por radicales libres (FRP, *Free Radical Polymerization*) es una de las técnicas de polimerización más extendidas y durante mucho tiempo ha sido la estrategia más utilizada para la síntesis de polímeros tanto en el ámbito de la investigación como a escala industrial [126]. Una de las ventajas más atrayentes de este tipo de procesos es la posibilidad de obtener polímeros a partir de una amplia gama de monómeros, dando lugar a estructuras funcionalizadas que pueden incluir grupos ácido, hidroxilo o amino, entre otros. Además, es posible obtener un alto grado de conversión estableciendo las condiciones experimentales adecuadas. Sin embargo, las estrategias de polimerización por radicales libres presentan una importante desventaja: la amplia distribución del peso molecular de los polímeros formados. Esto se debe a que los radicales son especies extremadamente reactivas y tanto la reacción de terminación de cadena polimérica como de los radicales

libres son inevitables y dominan la FRP, lo que limita conseguir en su totalidad las características deseadas en los polímeros formados.

El desarrollo de las estrategias de polimerización radical (CRP, *Controlled Radical Polymerization*) ha sido clave para obtener polímeros con arquitectura totalmente controlada. En 1956, Swarcz [127] definió esta metodología como un procedimiento sin reacciones de transferencia ni terminación, lo que implica la posibilidad de producir polímeros con una estructura, composición, morfología y funcionalidad determinadas y de uso en aplicaciones específicas, como la administración de fármacos o el diseño de biosensores. La clave del éxito de las CRP se encuentra en el equilibrio que se establece entre los radicales libres que se propagan y las especies inactivas en estado latente, que se conocen como cadenas durmientes [128]. Manteniendo los fundamentos de las CRP, desde los años 90 se vienen desarrollando estrategias que pueden definirse como variantes de las primeras, a las que la IUPAC ha recomendado denominar Polimerización Radical de Desactivación Reversible (RDRP, *Reversible-Deactivation Radical Polymerization*) [129].

La cinética de reacción es la principal diferencia entre FRP y RDRP. Así, las FRP están dominadas por reacciones de transferencia y terminación de la cadena radicalaria, que presentan cinéticas de reacción muy rápidas y difíciles de controlar, y las RDRP se propagan mediante radicales que se desactivan de forma reversible, dando lugar a un equilibrio entre estados activo y durmiente (Esquema 19). En estas reacciones, el equilibrio está desplazado a la izquierda ( $k_{act} / k_{desact} \ll 1$ ), lo que reduce drásticamente la concentración de especies activas, y con ello la probabilidad de que sucedan reacciones de terminación radicalaria. De hecho, es posible reducir la cantidad de cadenas que sufren terminaciones radicalarias, que es casi del 100% en reacciones FRP a valores inferiores al 10% en RDRP. En estas últimas, el tiempo de vida de las moléculas activas se incrementa introduciendo largos periodos de inactividad ( $\sim 1$  min) entre breves etapas de propagación ( $\sim 1$  ms). Siguiendo esta estrategia, el tiempo de vida de las cadenas poliméricas en formación pasa de 1 s a 1 día, permitiendo obtener un sistema cuyas propiedades pueden controlarse [126].



**Esquema 19.** Equilibrio entre las especies activas y durmientes en RDRP.

El análisis del aumento del peso molecular durante la síntesis es una forma directa de diferenciar entre los mecanismos FRP y RDRP. Así, una reacción está cinéticamente controlada por FRP si da lugar a polímeros de alto peso molecular en tiempo corto. Por el contrario, en una reacción RDRP la evolución del peso molecular es más progresiva, siendo proporcional a la conversión de monómeros. A pesar de que la velocidad de iniciación es varios órdenes de magnitud más lenta que la de propagación, se ha demostrado que, bajo condiciones de polimerización “viva” controlada, es posible obtener polímeros con distribuciones de peso molecular estrechas [130]. La forma común de expresar la distribución de peso molecular de los polímeros se define en base a su dispersidad,  $\mathcal{D}$ ,

$$\mathcal{D} = \frac{M_w}{M_n} \quad (9)$$

donde  $M_w$  es el peso molecular promedio y  $M_n$  es el número molecular promedio de las cadenas poliméricas que componen la muestra. En general, el valor de  $\mathcal{D}$  debe estar por debajo de 1.5 para considerar que se produce una reacción RDRP eficiente [131].

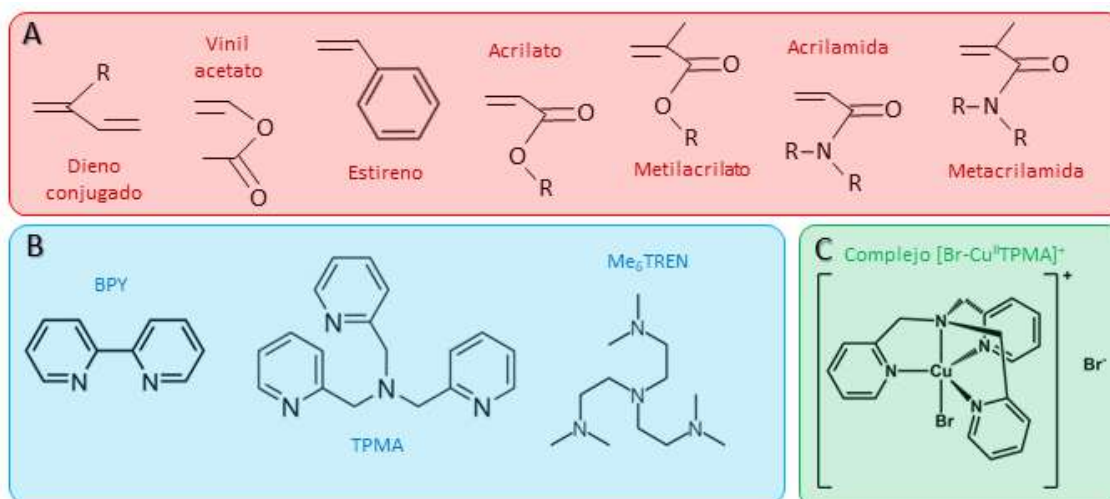
Manteniendo como principio el mecanismo de desactivación reversible, en los últimos 30 años se han desarrollado numerosas estrategias de polimerización, siendo las más utilizadas en la actualidad la polimerización mediada por nitróxidos (NMP, *Nitroxide-Mediated Polymerization*) [132], la polimerización por adición, fragmentación y transferencia reversible de cadena (RAFT, *Reversible Addition Fragmentation Chain Transfer*) [133], y la ATRP [134]. Las tres estrategias se clasifican como polimerizaciones vía radicales libres estables (SFRP, *Stable Free Radical Polymerization*) y, aunque todas presentan ventajas, en este trabajo se ha seleccionado la ATRP, cuya investigación se encuentra en constante avance y su aplicación está dando buenos resultados.

#### 1.4.1. ATRP.

El desarrollo de estrategias de ATRP ha supuesto un antes y un después en la química de los polímeros sintéticos, ya que se trata de un proceso altamente selectivo a los grupos funcionales y relativamente tolerante a la presencia de impurezas, lo que explica el interés. El principio general de esta estrategia se basa en el establecimiento de un rápido equilibrio dinámico entre una mínima cantidad de radicales libres en crecimiento junto con una mayoría de especies denominadas durmientes, temporalmente desactivadas. Los primeros trabajos de ATRP datan de 1995, de manera independiente por los grupos de Matyjaszewski [133] y Sawamoto [135], empleando sistemas catalíticos basados en cobre y rutenio, respectivamente. El sistema de reacción se considera multicomponente al estar formado por monómeros, iniciadores de reacción, complejos organometálicos

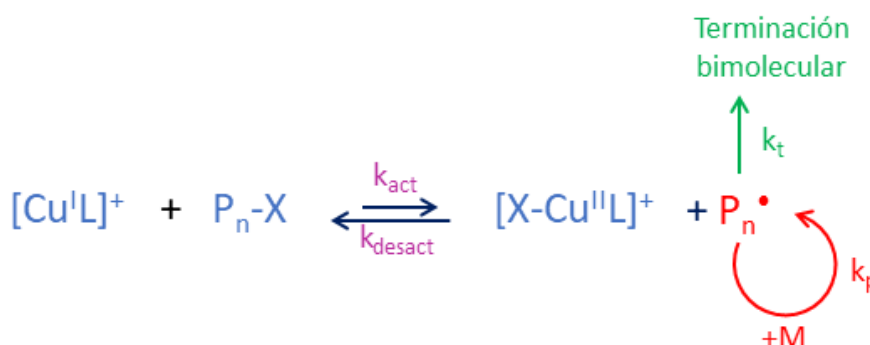
(catalizadores/ desactivantes), ligandos y, en ocasiones, aditivos o co-catalizadores, además del propio disolvente. Esta variabilidad de componentes explica la versatilidad del método, siendo posible llevar a cabo polimerizaciones a partir de una amplia gama de monómeros vinílicos, como los ésteres acrílicos, metacrilatos, acrilamidas, o acrilonitrilos, entre otros [136].

En los trabajos actuales se emplean, como catalizadores, complejos basados en metales de transición, principalmente cobre, con ligandos polidentados con grupos amino. A fin de modular de forma correcta el equilibrio entre las especies durmientes y en propagación, es fundamental que el metal central del complejo presente al menos dos estados de oxidación. Además, debe mostrar cierta afinidad por los halógenos y tener una esfera de coordinación capaz de expandirse para acomodar de forma selectiva átomos de esta naturaleza [137]. El cobre cumple todos estos requisitos, y además presentan un bajo coste, lo que explica que su uso sea generalizado. En su estado de oxidación más bajo (Cu(I)), tiene preferencia por las estructuras tetraédrica o plano-cuadrada, que se logra al combinarlo con ligandos tetra- o bi-dentados. Por su parte, el Cu(II) se coordina dando lugar a una estructura de bipirámide trigonal. Para formar complejos con estos centros metálicos, la elección de moléculas polidentadas basadas en un enlace N-donador, como las aminas alifáticas, reduce el coste de la catálisis e incrementa el grado de polimerización, manteniendo el control de la reacción. Los ligandos bidentados (2,2'-bipiridina o 4,4'-dimetil-2,2'-bipiridina) y tetradentados (tris (2-dimetil amino) etilamina (Me<sub>6</sub>TREN) y tris(2-piridilmetil) amina (TPMA)) son lo más usados en ATRP, siendo usados preferentemente en medios orgánico y acuoso, respectivamente (Esquema 20).



**Esquema 20.** Estructuras moleculares de (A) monómeros con diferentes grupos funcionales y (B) ligandos bidentados (BPY) y tetradentados (TPMA, Me<sub>6</sub>TREN), usados en reacciones ATRP. (C) Estructura de un complejo de Cu(II) coordinado con TPMA en presencia de iones haluro, Br<sup>-</sup>, en el medio, ocupando estos la quinta posición de coordinación.

La estructura y propiedades de los iniciadores de la reacción son esenciales para conseguir el éxito de la polimerización, garantizando que se produzca de forma controlada y a una velocidad razonable. Se trata de moléculas, de estructura general  $P_n-X$ , que deben contener un halógeno, generalmente un átomo de Br, que pueda ser transferido al complejo metálico, iniciando la polimerización. El mecanismo general de la reacción ATRP se representa en el Esquema 21. El iniciador se activa al producirse la rotura homolítica del enlace  $P_n-X$  a través de la oxidación del complejo catalítico generándose especies radicáticas ( $P_n\cdot$ ) y la forma no activa del catalizador, esto es, el complejo en su estado de oxidación más alto coordinado con el halógeno. Para que un iniciador sea capaz de generar un radical debe poseer un grupo atractor de electrones en el carbono  $\alpha$ , como el ciano, carbonilo o arilo, entre otros. Se trata de grupos que estabilizan las especies radicáticas por efecto inductivo o resonante. Sin embargo, la estabilidad de la especie activa se verá influenciada por el monómero a polimerizar y, por tanto, debe elegirse teniendo en cuenta su naturaleza.



**Esquema 21.** Esquema reacción ATRP.

Así, el mecanismo general ATRP se basa en un equilibrio entre una especie durmiente, generalmente un halogenuro de alquilo ( $R-X$ ), que actúa como iniciador, y las especies activas, los radicales libres  $R\cdot$ , en propagación, estableciéndose un equilibrio rápido entre los radicales que se propagan y las especies durmientes. Al mismo tiempo que se produce la rotura del enlace  $R-X$  por acción del catalizador, este sufre una oxidación reversible monoeléctrica y la consecuente transferencia del halógeno del iniciador. En la reacción inversa, los radicales libres en propagación reaccionan con la forma oxidada del complejo catalítico, que actúa desactivando la reacción, devolviendo el átomo de halógeno a la especie radicática, regenerando las especies durmientes y el catalizador activo. Este sistema en equilibrio está controlado por las constantes de activación y desactivación, siendo la segunda la de mayor magnitud a fin de mantener el control sobre la reacción. Esto hace que el equilibrio esté generalmente desplazado hacia la izquierda, en el sentido de la

desactivación, manteniéndose la funcionalidad del grupo terminal de las cadenas poliméricas en crecimiento y, al mismo tiempo, garantizando que haya una baja concentración de radicales libres en disolución para evitar las indeseables reacciones de terminación R-R, que provocarían el fin de la polimerización [138].

La velocidad de propagación la determina el equilibrio entre las reacciones de activación y desactivación, que son las que fijan las concentraciones de radicales activos en propagación. En medios orgánicos la constante de equilibrio del sistema ATRP,  $K_{ATRP}$  ( $K_{ATRP} = k_{act}/k_{desact}$ ) es pequeña, presentando valores del orden de  $10^{-4}$  [139], lo que indica que  $k_{act} < k_{desact}$ , manteniéndose el control de la reacción al haber una concentración de radicales libres baja. En medio acuoso el valor de esta constante es varios órdenes de magnitud mayor que en disolventes orgánicos, dificultando el control sobre la polimerización [140]. Además, la estabilidad de los complejos también se modifica en este entorno, ya que la especie  $[Cu^I L]^+$  tiende a desproporcionar, y los complejos desactivadores de la reacción basados en Cu(II) presentan baja halidofilicidad. Se han establecido estrategias para tratar de evitar estas desventajas. En primer lugar, el ligando TPMA es frecuentemente seleccionado para formar el complejo  $[Cu^{II} TPMA]^{2+}$  debido a que es estable en un amplio intervalo de pH, y a que el complejo que forma para catalizar la reacción,  $[Cu^I TPMA]^+$ , presenta baja desproporción. En este sentido, mantener el control del pH del medio durante el proceso de polimerización es fundamental. Por otro lado, la pobre halidofilicidad que muestra la especie desactivante  $[BrCu^{II} L]^+$ , que se disocia fácilmente en  $X\cdot$  y  $[Cu^{II} L]^{2+}$  dificultando el control de la polimerización, se puede prevenir empleando un exceso de iones haluro con respecto a la concentración de complejo (esto es,  $[X]^- / [Cu^{II} L]^{2+} \gg 1$ ) [138].

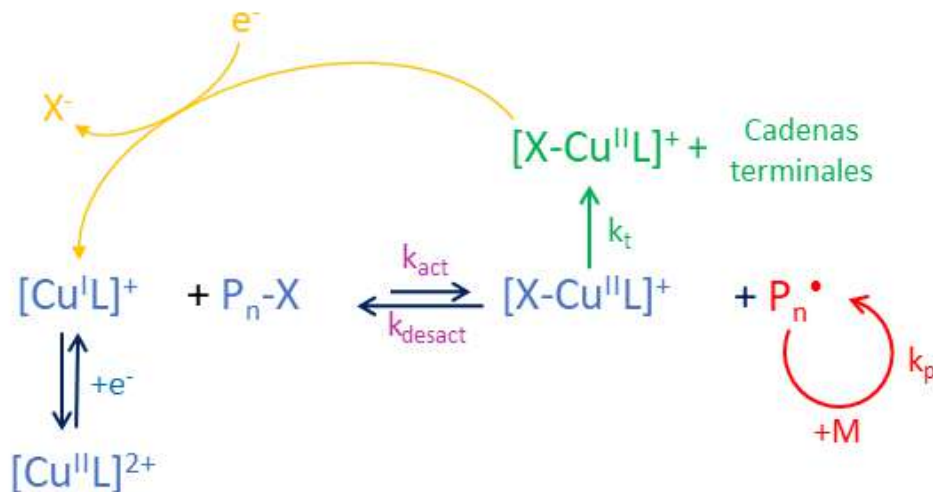
La ATRP se ha posicionado como uno de los métodos más fiables para diseñar polímeros con arquitecturas bien definidas, una composición funcional específica y baja polidispersidad. Con esta estrategia es posible obtener estructuras con aplicaciones en una amplia variedad de campos como el biomédico [141] y el desarrollo de NMs [142]. Otro de los grandes atractivos de esta metodología es que puede llevarse a cabo en condiciones experimentales suaves, incluyendo disolventes acuosos y temperatura ambiente [136, 138].

A lo largo de la última década, la técnica ATRP ha evolucionado a fin de convertirse en una técnica respetuosa con el medio ambiente. En este sentido, los sistemas catalizadores convencionales [128], han sido sustituidos por ligandos amino polidentados, que forman complejos con iones de cobre [143]. La clave de esta evolución está en el uso de pequeñas cantidades de complejos de cobre a partir de los cuales se producen continuamente las especies activadoras y desactivadoras de la reacción. En base a esto se han desarrollado varios métodos novedosos: ARGET- (*Activators ReGenerated by Electron Transfer*) [144], ICAR- (*Initiators for Continuous Activator Regeneration*) [145], SARA- (*Supplemental*

*Activator and Reducing Agent* ) [146], photo- [147], mecano- [148], sono- [149], y por mediación electroquímica (e-) [150] ATRP, que están demostrando ser enfoques eficaces que permiten reducir la concentración del catalizador hasta niveles de ppm. Esta última variante, eATRP, se considera la metodología más novedosa y prometedora.

#### 1.4.2. eATRP.

El uso de la electroquímica para generar radicales e iniciar polimerizaciones en la superficie de un electrodo es un tema detallado en la literatura [151]. En concreto, el primer trabajo sobre polimerización controlada electroquímicamente viene de la mano de Amatore [152] y a partir de él y hasta la fecha, diversos grupos de investigación están interesados en explorar todo lo relacionado con polimerizaciones vía eATRP, desde mecanismos de reacción fundamentales hasta optimización de condiciones experimentales que permitan obtener polímeros a medida, con buen rendimiento y baja polidispersidad.



**Esquema 22.** Mecanismo general de reacción e-ATRP.

En el Esquema 22 se presenta el mecanismo típico de una reacción eATRP catalizada por complejos de cobre con ligandos polidentados basados en nitrógeno para formar polímeros de elevado peso molecular en disolución. En ausencia de la limitación por transporte de masa, la polimerización se inicia cuando un potencial lo suficientemente negativo se aplica en el electrodo de trabajo, permitiendo la reducción del complejo de Cu(II) para producir el catalizador de la reacción, un complejo de Cu(I),  $[Cu^I L]^+$ , en las proximidades de la superficie. A continuación, el procedimiento es análogo al descrito anteriormente para una reacción ATRP: el catalizador activo  $[Cu^I L]^+$  reacciona con el iniciador  $P_n-X$ , presente en el medio de reacción, produciendo radicales,  $P_n^\bullet$ , y la forma desactivada del complejo de cobre,  $[X-Cu^{II}L]^+$ . Los radicales  $P_n^\bullet$  generados se propagan e

incrementan la longitud de la cadena molecular añadiendo una pequeña cantidad de monómeros, antes de ser capturados por el complejo  $[X-Cu^{II}L]^+$ , a partir del cual se produce de nuevo  $[Cu^I L]^+$  y la cadena durmiente  $P'_n-X$ .

La estrategia eATRP es una opción muy interesante en la que las condiciones de la reacción pueden modularse fácilmente aplicando el potencial o la corriente deseados. Además, si se mantiene el control sobre el pH y se evita la desproporción de los complejos catalizadores, es idónea para llevar a cabo reacciones en medio acuoso. La mayoría de trabajos se basan en la variación del potencial para controlar la ratio de los complejos, de modo que la relación entre las especies de Cu(II) y Cu(I) la determina el potencial aplicado, de acuerdo con la ecuación de Nernst,

$$E_{ap} = E^{\theta} + \frac{RT}{nR} \ln \frac{[XCu^{II}L]^+}{[XCu^I L]} \quad (10)$$

siendo  $E_{ap}$  el potencial aplicado,  $E^{\theta}$  el potencial de reducción estándar del par redox  $[XCu^{II}L]^+ / [XCu^I L]$ ,  $R$  la constante de los gases,  $T$  la temperatura, y  $F$  la constante de Faraday. El  $E_{ap}$  determina la cantidad de catalizador en el sistema, y por ende la velocidad de polimerización. El uso de un  $E_{ap}$  más negativo que  $E^{\theta}$  conduce a reacciones más rápidas al activarse un mayor número de radicales en propagación.

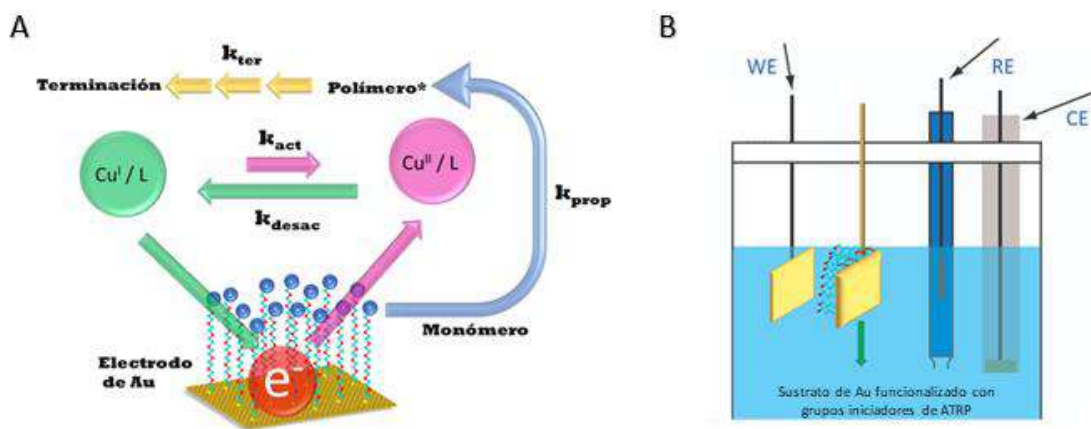
La implementación de métodos electroquímicos a la polimerización ATRP convencional implica una mejora en el control ya que es sencillo modular con exactitud la cantidad de catalizador activo en todo momento de la reacción. Además, cumple los objetivos de evolución hacia la química verde, al evitar el uso de agentes reductores y disolvente orgánicos y poder desarrollarse con eficacia en medio acuoso. Otra mejora que ofrece la alternativa eATRP es la posibilidad de tolerar pequeñas cantidades de oxígeno, algo imposible en la metodología ATRP convencional, debido a la fácil oxidación de Cu(I) a Cu(II) [153]. En el sistema eATRP, el complejo de Cu(II) formado es estable en disolución en presencia de oxígeno, aunque es aconsejable eliminar en la medida de lo posible este elemento ya que puede provocar reacciones redox paralelas que enmascaren los procesos principales.

### 1.4.3. SI-eATRP.

Aunque gran parte de las investigaciones en ATRP se basan en sintetizar polímeros en disolución homogénea, sus principios pueden extenderse a sustratos metálicos [154], proteínas [155], membranas [156], e incluso NPs [157]. Así, la SI-ATRP es una estrategia atractiva para funcionalizar una amplia variedad de sustratos. Se fundamenta en el crecimiento de una película polimérica a partir de cadenas individuales que se injertan en la superficie a través de un extremo (un grupo tiol en el caso de sustratos metálicos) y, por



el otro, crecen hacia la disolución (a partir de un grupo iniciador de la polimerización, frecuentemente -Br). El primer estudio de esta metodología se publicó en 1997 [158] y se ha ido desarrollando de manera importante hasta la actualidad. En la última década la variante electroquímica eATRP ha demostrado ser una alternativa muy interesante para generar películas poliméricas en superficie. Este procedimiento se inicia anclando las moléculas que contienen el grupo iniciador a la superficie del electrodo de trabajo, empleando para ello la formación de SAMs. Para que la SAM formada actúe como estructura adecuada para iniciar el crecimiento de la película polimérica es obligatorio que sea permeable al paso de corriente, facilitando la transferencia electrónica que activa el catalizador que desencadena el mecanismo de reacción (Esquema 23A).



**Esquema 23.** (A) Mecanismo de reacción SI-eATRP sobre un electrodo de Au. (B) Representación esquemática de la disposición de los electrodos y el sustrato modificado para polimerizar un sustrato no conductor mediante eATRP.

El tamaño de las moléculas empleadas (más específicamente, la distancia entre los grupos -SH y -Br) afecta a la conductividad de la superficie y a la densidad de empaquetamiento. Comúnmente, moléculas cortas (HS-C<sub>6</sub>-Br) dan lugar a SAMs con buenas propiedades de conducción eléctrica, pero que presentan algunos huecos o defectos. Por el contrario, moléculas más largas (HS-C<sub>15</sub>-Br) forman SAMs muy compactas, que bloquean totalmente la transferencia electrónica del par redox catalizador/desactivador. En estos casos, es posible formar monocapas mixtas con otros ligandos, permitiendo así el flujo de carga. Li et al.[159] fueron los primeros en presentar un sistema de este tipo. En concreto, describieron la preparación de polímeros tipo *brush* de PSPMA (poli (3-sulfopropilmetacrilato)) y PHEMA (poli (2-hidroxietilmetacrilato)) vía SI-eATRP desde un electrodo de oro modificado con una SAM mixta que incluía una molécula iniciadora de la polimerización, el DTBU y el 2-tionaftol como diluyente, gracias a la que se permitía el flujo de corriente. Con este trabajo pusieron de manifiesto no sólo la posibilidad de obtener películas compactas mediante SI-eATRP, sino también demostraron que la reacción podría

producirse en presencia de pequeñas cantidades de aire y que el medio de reacción podía ser reutilizado para formar polímeros en diferentes electrodos. Poco tiempo después, los mismos autores sugirieron una estrategia interesante para llevar a cabo polimerizaciones en superficie a partir de grupos de iniciación anclados a sustratos no conductores [160]. Para ello, el catalizador de Cu(I) se genera en un electrodo de trabajo desnudo, desde donde difunde al sustrato no conductor, modificado con moléculas que contienen grupos iniciadores de la polimerización, situado cerca del primero (Esquema 23B). Gracias al fenómeno de difusión de iones, se genera un gradiente de concentración entre las especies de Cu(I) y Cu(II) en el espacio creado entre el electrodo de trabajo y el sustrato no conductor modificado. La distancia entre ambos permite ajustar la cinética del crecimiento de la película polimérica.

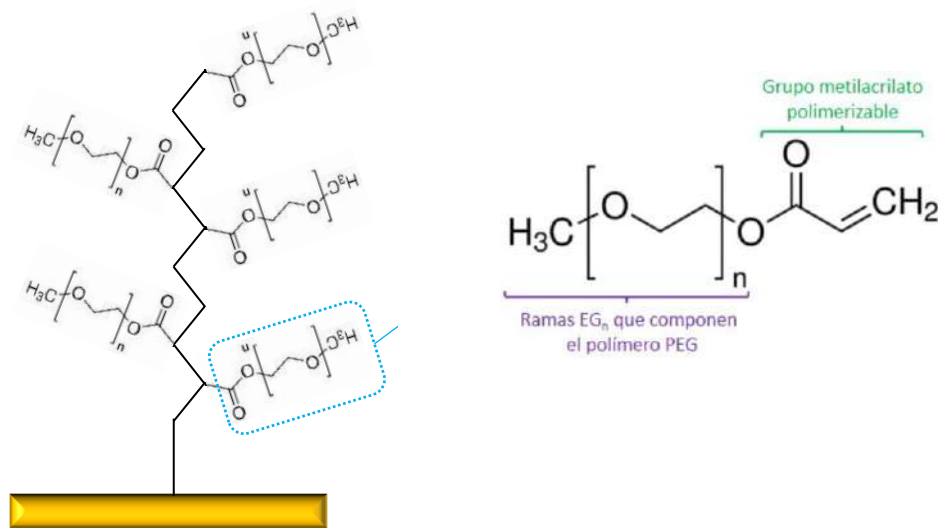
Un campo muy interesante, prácticamente inexplorado debido a las numerosas dificultades que presenta, es la formación de películas poliméricas para recubrir NPs metálicas previamente funcionalizadas con moléculas que contienen un grupo iniciador. Recientemente, Matyjaszewsky et al.[161] han descrito por primera vez la formación de películas poliméricas compactas a partir de diferentes monómeros sobre NPs de sílice mediante SI-eATRP, aunque empleando disolventes orgánicos para garantizar la solubilidad de las estructuras formadas. Hasta la fecha, no se han descrito polimerizaciones vía SI-eATRP de NPs en medio acuoso, estando la síntesis de este tipo de recubrimientos en su totalidad aún por desarrollarse.

#### 1.4.4. Formación de polímeros brush de EGn mediante SI-ATRP.

El diseño de películas poliméricas basadas en etilenglicol partiendo de monómeros que contienen uno o varios grupos EG en su estructura ha sido objeto de estudio desde la aparición de las primeras estrategias ATRP, y este interés se mantiene en la actualidad. Así, existen multiplicidad de monómeros comerciales disponibles, y muchos de ellos han sido aplicados de manera eficiente para obtener películas en superficie mediante SI-ATRP. Algunos de ellos son el dietilen-glicol-monometil-éter metacrilato (DEGMA,  $M_n=188$  g/mol)[162], el oligo (etilen-glicol) hidroxil metacrilato (HO-OEGMA,  $M_n=300$ ) [163], y múltiples variables del oligo (etilen-glicol) metil éter metacrilato (OEGMA) de una amplia variedad de pesos moleculares (300 g/mol [162], 560 g/mol y 1500 g/mol [164]). La estructura de estos monómeros (Esquema 24) la componen un esqueleto con un número variable de unidades EG junto con el metacrilato como grupo vinílico terminal a partir del que se produce la polimerización.

El primer trabajo en el que se demostró la posibilidad de formar recubrimientos poliméricos mediante SI-ATRP empleando monómeros EGn lo publican en 2005

Messersmith et al [165]. En concreto, parten de un iniciador catecólico injertado en superficies metálicas de estaño y acero inoxidable, a partir del que se polimerizan macromonómeros de metilmetacrilato con cadenas laterales de EGN. Las estructuras formadas alcanzaron un espesor de 100 nm, determinado por medidas de elipsometría. Además, demostraron que estas películas poliméricas eran capaces de evitar la adsorción de células de mamíferos, con lo que podían usarse para crear películas con patrones que presentasen regiones resistentes a la interacción celular y otras que la permitan. Experimentalmente, se llevó a cabo una reacción ATRP convencional, empleando agua como disolvente y CuBr como catalizador, bajo un flujo continuo de gas inerte y a temperatura ambiente.



**Esquema 24.** Representación de una cadena brush dentro de una película polimérica construida sobre un sustrato de Au usando OEGMA como monómero.

Durante los siguientes años se continuaron publicando trabajos en diferentes disciplinas, tanto de SI-ATRP como ATRP, para obtener películas con un elevado número de unidades EG. Así, surgieron también los primeros trabajos que tenían como fin sintetizar copolímeros. Uno de los más interesantes son los copolímeros bloque anfífilicos poli(metil metacrilato)-b-poli(poli(etilenglicol) metil éter metacrilato), sintetizados vía SI-ATRP por primera vez en 2009 [166], usando como plataforma nano-esferas de quitosano. Esta combinación de polímeros de distinta naturaleza es muy interesante dado que proporcionan al NM propiedades relacionadas con la naturaleza fisicoquímica de cada monómero.

La primera polimerización en superficie empleando monómeros OEGMA la propusieron Hosseiny y van Rijn [154], que demostraron la posibilidad de crecer películas mediante SI-eATRP en medio acuoso. Más específicamente, propusieron trabajar en

ausencia de electrolito soporte, consiguiendo películas de hasta 47 nm de espesor tras 2h de polimerización. Salvo este trabajo, no se encuentra bibliografía sobre el uso de la variante electroquímica de ATRP para obtener polímeros EGN a partir de sitios de iniciación injertados en electrodos, por lo que explorar el diseño de este tipo de estructuras desde una óptica novedosa y en consonancia con la química verde al llevarse a cabo de medio acuoso y con bajas concentraciones de catalizador, es esencial para el avance de la ciencia de superficies.

## 1.5. Bibliografía.

- [1] S. Bayda, M. Adeel, T. Tuccinardi, M. Cordani, F. Rizzolio, The history of Nanoscience and Nanotechnology: from chemical-physical applications to Nanomedicine, *Molecules* 25(1) (2020).
- [2] J.J. Gooding, S. Ciampi, The molecular level modification of surfaces: from self-assembled monolayers to complex molecular assemblies, *Chem. Soc. Rev.* 40(5) (2011) 2704-2718.
- [3] S.G. Zhang, Fabrication of novel biomaterials through molecular self-assembly, *Nature Biotechnol.* 21(10) (2003) 1171-1178.
- [4] K.E. Sapsford, W.R. Algar, L. Berti, K.B. Gemmill, B.J. Casey, E. Oh, M.H. Stewart, I.L. Medintz, Functionalizing nanoparticles with biological molecules: developing chemistries that facilitate nanotechnology, *Chem. Rev.* 113(3) (2013) 1904-2074.
- [5] V. Biju, Chemical modifications and bioconjugate reactions of nanomaterials for sensing, imaging, drug delivery and therapy, *Chem. Soc. Rev.* 43(3) (2014) 744-764.
- [6] J.W.G.P.A. Steed, *Supramolecular chemistry : from molecules to nanomaterials*, Wiley, Hoboken, NJ, 2012.
- [7] H. Yang, B. Yuan, X. Zhang, O.A. Scherman, Supramolecular chemistry at interfaces: host-guest interactions for fabricating multifunctional biointerfaces, *Accounts Chem. Res.* 47(7) (2014) 2106-2115.
- [8] P.M. Mendes, Stimuli-responsive surfaces for bio-applications, *Chem. Soc. Rev.* 37(11) (2008) 2512-2529.
- [9] H.L. Wang, X.T. Liang, J.T. Wang, S.J. Jiao, D.F. Xue, Multifunctional inorganic nanomaterials for energy applications, *Nanoscale* 12(1) (2020) 14-42.
- [10] C.S. Yuan, Y. Liu, T. Wang, M.J. Sun, X.G. Chen, Nanomaterials as smart immunomodulator delivery system for enhanced cancer therapy, *ACS Biomater. Sci. Eng.* 6(9) (2020) 4774-4798.
- [11] J. Yao, M. Yang, Y.X. Duan, Chemistry, biology, and mMedicine of fluorescent nanomaterials and related systems: new insights into biosensing, bioimaging, genomics, diagnostics, and therapy, *Chem. Rev.* 114(12) (2014) 6130-6178.
- [12] H.L. Gao, Q. He, The interaction of nanoparticles with plasma proteins and the consequent influence on nanoparticles behavior, *Expert Opin. Drug Del.* 11(3) (2014) 409-420.
- [13] A.E. Nel, L. Madler, D. Velegol, T. Xia, E.M.V. Hoek, P. Somasundaran, F. Klaessig, V. Castranova, M. Thompson, Understanding biophysicochemical interactions at the nano-bio interface, *Nat. Mater.* 8(7) (2009) 543-557.
- [14] M.P. Monopoli, C. Aberg, A. Salvati, K.A. Dawson, Biomolecular coronas provide the biological identity of nanosized materials, *Nat. Nanotechnol.* 7(12) (2012) 779-786.
- [15] S. Tenzer, D. Docter, S. Rosfa, A. Wlodarski, J. Kuharev, A. Rekić, S.K. Knauer, C. Bantz, T. Nawroth, C. Bier, J. Sirirattanapan, W. Mann, L. Treuel, R. Zellner, M. Maskos, H. Schild, R.H. Stauber, Nanoparticle size is a critical physicochemical determinant of the human blood plasma corona: a comprehensive quantitative proteomic analysis, *ACS Nano* 5(9) (2011) 7155-7167.

- [16] A. Salvati, A.S. Pitek, M.P. Monopoli, K. Prapainop, F.B. Bombelli, D.R. Hristov, P.M. Kelly, C. Aberg, E. Mahon, K.A. Dawson, Transferrin-functionalized nanoparticles lose their targeting capabilities when a biomolecule corona adsorbs on the surface, *Nat. Nanotechnol.* 8(2) (2013) 137-143.
- [17] P.C. Ke, S. Lin, W.J. Parak, T.P. Davis, F. Caruso, A decade of the protein corona, *ACS Nano* 11(12) (2017) 11773-11776.
- [18] P. Gopinath, S.U. Kumar, I. Matai, B. Bhushan, D. Malwal, A. Sachdev, P. Dubey, *Cancer Nanotheranostics*, Springer Singapore 2015.
- [19] Z.B. Li, X.F. Yu, P.K. Chu, Recent advances in cell-mediated nanomaterial delivery systems for photothermal therapy, *J. Mater. Chemistry B* 6(9) (2018) 1296-1311.
- [20] F. Schreiber, Structure and growth of self-assembling monolayers, *Prog. Surf. Sci.* 65(5-8) (2000) 151-256.
- [21] J.O. Zoppe, N.C. Ataman, P. Mocny, J. Wang, J. Moraes, H.A. Klok, Surface-Initiated controlled radical polymerization: state-of-the-art, opportunities, and challenges in surface and interface engineering with polymer brushes, *Chem. Rev.* 117(3) (2017) 1105-1318.
- [22] R. Barbey, L. Lavanant, D. Paripovic, N. Schuwer, C. Sugnaux, S. Tugulu, H.A. Klok, Polymer brushes via Surface-Initiated controlled radical polymerization: synthesis, characterization, properties, and applications, *Chem. Rev.* 109(11) (2009) 5437-5527.
- [23] D.M. Jones, W.T.S. Huck, Controlled surface-initiated polymerizations in aqueous media, *Adv. Mater.* 13(16) (2001) 1256-1259.
- [24] J. Kreuter, T. Hekmatara, S. Dreis, T. Vogel, S. Gelperina, K. Langer, Covalent attachment of apolipoprotein A-I and apolipoprotein B-100 to albumin nanoparticles enables drug transport into the brain, *J. Control. Release* 118(1) (2007) 54-58.
- [25] D.E. Owens, N.A. Peppas, Opsonization, biodistribution, and pharmacokinetics of polymeric nanoparticles, *Int J Pharmaceut.* 307(1) (2006) 93-102.
- [26] A. Abuchowski, T. Vanes, N.C. Palczuk, F.F. Davis, Alteration of immunological properties of bovine serum-albumin by covalent attachment of polyethylene-glycol, *J. Biol. Chem.* 252(11) (1977) 3578-3581.
- [27] A. Abuchowski, J.R. McCoy, N.C. Palczuk, T. Vanes, F.F. Davis, Effect of covalent attachment of polyethylene-glycol on immunogenicity and circulating life of bovine liver catalase, *J. Biol. Chem.* 252(11) (1977) 3582-3586.
- [28] P. Kingshott, H. Thissen, H.J. Griesser, Effects of cloud-point grafting, chain length, and density of PEG layers on competitive adsorption of ocular proteins, *Biomaterials* 23(9) (2002) 2043-2056.
- [29] M.L. Immordino, F. Dosio, L. Cattel, Stealth liposomes: review of the basic science, rationale, and clinical applications, existing and potential, *Int J Nanomed.* 1(3) (2006) 297-315.
- [30] A. Matsushima, Y. Kodera, M. Hiroto, H. Nishimura, Y. Inada, Bioconjugates of proteins and polyethylene glycol: potent tools in biotechnological processes, *J. Mol. Catal. B-Enzym.* 2(1) (1996) 1-17.
- [31] J.V. Jokerst, T. Lobovkina, R.N. Zare, S.S. Gambhir, Nanoparticle PEGylation for imaging and therapy, *Nanomedicine* 6(4) (2011) 715-728.
- [32] M.J. Roberts, M.D. Bentley, J.M. Harris, Chemistry for peptide and protein PEGylation, *Adv. Drug Deliver. Rev.* 54(4) (2002) 459-476.
- [33] R. Bhat, S.N. Timasheff, Steric exclusion is the principal source of the preferential hydration of proteins in the presence of polyethylene glycols, *Protein Sci.* 1(9) (1992) 1133-1143.
- [34] P. Bailon, W. Berthold, Polyethylene glycol-conjugated pharmaceutical proteins, *Pharm. Sci. Technol. To.* 1(8) (1998) 352-356.
- [35] C.D. Heyes, A.Y. Kobitski, E.V. Amirgoulova, G.U. Nienhaus, Biocompatible surfaces for specific tethering of individual protein molecules, *J. Phys. Chem. B* 108(35) (2004) 13387-13394.

- [36] P. Harder, M. Grunze, R. Dahint, G.M. Whitesides, P.E. Laibinis, Molecular conformation in oligo(ethylene glycol)-terminated self-assembled monolayers on gold and silver surfaces determines their ability to resist protein adsorption, *J. Phys. Chem. B* 102(2) (1998) 426-436.
- [37] R.L.C. Wang, H.J. Kreuzer, M. Grunze, Molecular conformation and solvation of oligo(ethylene glycol)-terminated self-assembled monolayers and their resistance to protein adsorption, *J. Phys. Chem. B* 101(47) (1997) 9767-9773.
- [38] R.A. Sperling, T. Pellegrino, J.K. Li, W.H. Chang, W.J. Parak, Electrophoretic separation of nanoparticles with a discrete number of functional groups, *Adv. Funct. Mater.* 16(7) (2006) 943-948.
- [39] J. Logie, S.C. Owen, C.K. McLaughlin, M.S. Shoichet, PEG-graft density controls polymeric nanoparticle micelle stability, *Chem. Mater.* 26(9) (2014) 2847-2855.
- [40] C. Brandenberger, C. Muehlfeld, Z. Ali, A.-G. Lenz, O. Schmid, W.J. Parak, P. Gehr, B. Rothen-Rutishauser, Quantitative evaluation of cellular uptake and trafficking of plain and polyethylene glycol-coated gold nanoparticles, *Small* 6(15) (2010) 1669-1678.
- [41] W.C. Bigelow, D.L. Pickett, W.A. Zisman, Oleophobic monolayer. 1. Films adsorbed from solution in non-polar liquids, *J. Coll. Sci.* 1(6) (1946) 513-538.
- [42] D.L. Allara, R.G. Nuzzo, Spontaneously organized molecular assemblies. 1. Formation, dynamics, and physical-properties of normal-alkanoic acids adsorbed from solution on an oxidized aluminum surface, *Langmuir* 1(1) (1985) 45-52.
- [43] R.G. Nuzzo, D.L. Allara, Adsorption of bifunctional organic disulfides on gold surfaces, *J. Am. Chem. Soc.* 105(13) (1983) 4481-4483.
- [44] E.B. Troughton, C.D. Bain, G.M. Whitesides, R.G. Nuzzo, D.L. Allara, M.D. Porter, Monolayer films prepared by the spontaneous self-assembly of symmetrical and unsymmetrical dialkyl sulfides from solution onto gold substrates - Structure, properties, and reactivity of constituent functional groups, *Langmuir* 4(2) (1988) 365-385.
- [45] M.D. Porter, T.B. Bright, D.L. Allara, C.E.D. Chidsey, Spontaneously organized molecular assemblies. 4. Structural characterization of normal-alkyl thiol monolayers on gold by optical ellipsometry, infrared-spectroscopy, and electrochemistry, *J. Am. Chem. Soc.* 109(12) (1987) 3559-3568.
- [46] J. Houk, G.M. Whitesides, Structure reactivity relations for thiol disulfide interchange, *J. Am. Chem. Soc.* 109(22) (1987) 6825-6836.
- [47] C.D. Bain, G.M. Whitesides, Formation of 2-component surfaces by the spontaneous assembly of monolayers on gold from solutions containing mixtures of organic thiols, *J. Am. Chem. Soc.* 110(19) (1988) 6560-6561.
- [48] B. Hammer, J.K. Norskov, Why gold is the noblest of all the metals, *Nature* 376(6537) (1995) 238-240.
- [49] R.G. Nuzzo, B.R. Zegarski, L.H. Dubois, Fundamental-studies of the chemisorption of organosulfur compounds on Au(111) - implications for molecular self-assembly on gold surfaces, *J. Am. Chem. Soc.* 109(3) (1987) 733-740.
- [50] G.E. Poirier, Characterization of organosulfur molecular monolayers on Au(111) using scanning tunneling microscopy, *Chem. Rev.* 97(4) (1997) 1117-1127.
- [51] S. Watson, M. Nie, L. Wang, K. Stokes, Challenges and developments of self-assembled monolayers and polymer brushes as a green lubrication solution for tribological applications, *RSC Adv.* 5(109) (2015) 89698-89730.
- [52] R. Yamada, H. Sakai, K. Uosaki, Solvent effect on the structure of the self-assembled monolayer of alkanethiol, *Chem. Lett.* (7) (1999) 667-668.
- [53] O. Dannenberger, M. Buck, M. Grunze, Self-assembly of n-alkanethiols: a kinetic study by second harmonic generation, *J. Phys. Chem. B* 103(12) (1999) 2202-2213.
- [54] A.H. Al Mamun, J.R. Hahn, Effects of solvent on the formation of octanethiol self-assembled monolayers on Au(111) at high temperatures in a closed vessel: a scanning tunneling microscopy and X-ray photoelectron spectroscopy study, *J. Phys. Chem. C* 116(42) (2012) 22441-22448.

- [55] D. Yan, J.A. Saunders, G.K. Jennings, Enhanced chain densities of n-alkanethiolate self-assembled monolayers on gold from aqueous micellar solutions, *Langmuir* 16(20) (2000) 7562-7565.
- [56] V. Ganesh, V. Lakshminarayanan, Self-assembled monolayers of alkanethiols on gold prepared in a hexagonal lyotropic liquid crystalline phase of triton X-100/water system, *Langmuir* 22(4) (2006) 1561-1570.
- [57] D. Garcia Raya, R. Madueno, M. Blazquez, T. Pineda, Formation of a 1,8-Octanedithiol self-assembled monolayer on Au(111) prepared in a lyotropic liquid-crystalline medium, *Langmuir* 26(14) (2010) 11790-11796.
- [58] D. Garcia Raya, C. Silien, M. Blazquez, T. Pineda, R. Madueno, Electrochemical and AFM study of the 2D-assembly of colloidal gold nanoparticles on dithiol SAMs tuned by ionic strength, *J. Phys. Chem. C* 118(26) (2014) 14617-14628.
- [59] S. Herrwerth, W. Eck, S. Reinhardt, M. Grunze, Factors that determine the protein resistance of oligoether self-assembled monolayers - Internal hydrophilicity, terminal hydrophilicity, and lateral packing density, *J. Am. Chem. Soc.* 125(31) (2003) 9359-9366.
- [60] M.W.A. Skoda, R.M.J. Jacobs, J. Willis, F. Schreiber, Hydration of oligo(ethylene glycol) self-assembled monolayers studied using polarization modulation infrared spectroscopy, *Langmuir* 23(3) (2007) 970-974.
- [61] S. Zorn, N. Martin, A. Gerlach, F. Schreiber, Real-time PMIRRAS studies of in situ growth of C(11)EG(6)OMe on gold and immersion effects, *Phys. Chem. Chem. Phys.* 12(31) (2010) 8986-8991.
- [62] L.Y. Li, S.F. Chen, J. Zheng, B.D. Ratner, S.Y. Jiang, Protein adsorption on oligo(ethylene glycol)-terminated alkanethiolate self-assembled monolayers: the molecular basis for nonfouling behavior, *J. Phys. Chem. B* 109(7) (2005) 2934-2941.
- [63] K.L. Prime, G.M. Whitesides, Adsorption of proteins onto surfaces containing end-attached oligo(ethylene oxide) - A model system using self-assembled monolayers, *J. Am. Chem. Soc.* 115(23) (1993) 10714-10721.
- [64] M.W.A. Skoda, F. Schreiber, R.A.J. Jacobs, J.R.P. Webster, M. Wolff, R. Dahint, D. Schwendel, M. Grunze, Protein density profile at the interface of water with oligo(ethylene glycol) self-assembled monolayers, *Langmuir* 25(7) (2009) 4056-4064.
- [65] R.L.C. Wang, H.J. Kreuzer, M. Grunze, The interaction of oligo(ethylene oxide) with water: a quantum mechanical study, *Phys. Chem. Chem. Phys.* 2(16) (2000) 3613-3622.
- [66] D.J. Vanderah, C.W. Meuse, V. Silin, A.L. Plant, Synthesis and characterization of self-assembled monolayers of alkylated 1-thiahexa(ethylene oxide) compounds on gold, *Langmuir* 14(24) (1998) 6916-6923.
- [67] D.J. Vanderah, C.P. Pham, S.K. Springer, V. Silin, C.W. Meuse, Characterization of a series of self-assembled monolayers of alkylated 1-thiaoligo (ethylene oxides)(4-8) on Gold, *Langmuir* 16(16) (2000) 6527-6532.
- [68] D.J. Vanderah, G. Valincius, C.W. Meuse, Self-assembled monolayers of methyl 1-thiahexa(ethylene oxide) for the inhibition of protein adsorption, *Langmuir* 18(12) (2002) 4674-4680.
- [69] D.J. Vanderah, J. Arsenault, H. La, R.S. Gates, V. Silin, C.W. Meuse, G. Valincius, Structural variations and ordering conditions for the self-assembled monolayers of HS(CH<sub>2</sub>CH<sub>2</sub>O)(3-6)CH<sub>3</sub>, *Langmuir* 19(9) (2003) 3752-3756.
- [70] D.J. Vanderah, T. Parr, V. Silin, C.W. Meuse, R.S. Gates, H.Y. La, G. Valincius, Isostructural self-assembled monolayers. 2. Methyl 1-(3-mercaptopropyl)-oligo(ethylene oxide)s, *Langmuir* 20(4) (2004) 1311-1316.
- [71] L. Malysheva, A. Onipko, R. Valiokas, B. Liedberg, First-principles modeling of oligo(ethylene glycol)-terminated and amide group containing alkanethiolates, *Appl. Surf. Sci.* 246(4) (2005) 372-376.
- [72] L. Malysheva, A. Onipko, T. Fyrner, H.H. Lee, R. Valiokas, P. Konradsson, B. Liedberg, Spectroscopic characterization and modeling of methyl- and hydrogen-terminated oligo(ethylene glycol) self-assembled monolayers, *J. Phys. Chem. C* 116(22) (2012) 12008-12016.

- [73] G. Emilsson, R.L. Schoch, L. Feuz, F. Hook, R.Y.H. Lim, A.B. Dahlin, Strongly stretched protein resistant poly(ethylene glycol) brushes prepared by grafting-To, *ACS Appl. Mater. Inter.* 7(14) (2015) 7505-7515.
- [74] R. Ortiz, S. Olsen, E. Thormann, Salt-induced control of the grafting density in poly(ethylene glycol) brush layers by a grafting-to approach, *Langmuir* 34(15) (2018) 4455-4464.
- [75] T. Doneux, L.Y. Cherif, C. Buess-Herman, Controlled tuning of the ferri/ferrocyanide electron transfer at oligo (ethylene glycol)-modified electrodes, *Electrochim. Acta* 219 (2016) 412-417.
- [76] T. Doneux, A. de Ghellinck, E. Triffaux, N. Brouette, M. Sferrazza, C. Buess-Herman, Electron transfer across an antifouling mercapto-hepta(ethylene glycol) self-assembled monolayer, *J. Phys. Chem. C* 120(29) (2016) 15915-15922.
- [77] R. Schlapak, D. Caruana, D. Armitage, S. Howorka, Semipermeable poly(ethylene glycol) films: the relationship between permeability and molecular structure of polymer chains, *Soft Matter* 5(21) (2009) 4104-4112.
- [78] C.E. Hotchen, I.J. Maybury, G.W. Nelson, J.S. Foord, P. Holdway, F. Marken, Amplified electron transfer at poly-ethylene-glycol (PEG) grafted electrodes, *Phys. Chem. Chem. Phys.* 17(17) (2015) 11260-11268.
- [79] K. Nekoueian, C.E. Hotchen, M. Amiri, M. Sillanpaa, G.W. Nelson, J.S. Foord, P. Holdway, A. Buchard, S.C. Parker, F. Marken, Interfacial electron-shuttling processes across monolayer grafted electrodes, *ACS Appl. Mater. Inter.* 7(28) (2015) 15458-15465.
- [80] A.L. Gui, E. Luais, J.R. Peterson, J.J. Gooding, Zwitterionic phenyl layers: finally, stable, anti-biofouling coatings that do not passivate electrodes, *ACS Appl. Mater. Inter.* 5(11) (2013) 4827-4835.
- [81] U.R. Dahal, Z.L. Wang, E.E. Dormidontova, Hydration and mobility of poly(ethylene oxide) brushes, *Macromolecules* 50(17) (2017) 6722-6732.
- [82] P.G. Degennes, Conformations of polymers attached to an interface, *Macromolecules* 13(5) (1980) 1069-1075.
- [83] F. Oesterhelt, M. Rief, H.E. Gaub, Single molecule force spectroscopy by AFM indicates helical structure of poly(ethylene-glycol) in water, *New J. Phys.* 1 (1999).
- [84] W. Taylor, R.A.L. Jones, Producing high-density high-molecular-weight polymer brushes by a "grafting to" method from a concentrated homopolymer solution, *Langmuir* 26(17) (2010) 13954-13958.
- [85] N. Zhang, R. Luxenhofer, R. Jordan, Thermoresponsive poly(2-oxazoline) molecular brushes by living ionic polymerization: kinetic investigations of pendant chain grafting and cloud point modulation by backbone and side chain length variation, *Macromol. Chem. Phys.* 213(9) (2012) 973-981.
- [86] G.C. Na, B.O. Yuan, H.J. Stevens, B.S. Weekley, N. Rajagopalan, Cloud point of nonionic surfactants: modulation with pharmaceutical excipients, *Pharmaceut. Res.* 16(4) (1999) 562-568.
- [87] S.T. Milner, Polymer brushes, *Science* 251(4996) (1991) 905-914.
- [88] G. Schmid, *Clusters and colloids: from theory to applications*, VCH Publisher, New York, USA, 1994.
- [89] J.M. Bingham, K.A. Willets, N.C. Shah, D.Q. Andrews, R.P. Van Duyne, Localized surface plasmon resonance imaging: simultaneous single nanoparticle spectroscopy and diffusional dynamics, *J. Phys. Chem. C* 113(39) (2009) 16839-16842.
- [90] H.R. Li, S. Pan, P. Xia, Y.X. Chang, C. Fu, W.J. Kong, Z.Y. Yu, K. Wang, X.Y. Yang, Z.P. Qi, Advances in the application of gold nanoparticles in bone tissue engineering, *J. Biol. Eng.* 14(1) (2020).
- [91] P.K. Deshmukh, K.P. Ramani, S.S. Singh, A.R. Tekade, V.K. Chatap, G.B. Patil, S.B. Bari, Stimuli-sensitive layer-by-layer (LbL) self-assembly systems: targeting and biosensory applications, *J. Control. Release* 166(3) (2013) 294-306.
- [92] O. Stern, The theory of the electrolytic double shift, *Z. Angew. Phys.* 30 (1924) 508-516.



- [93] I.H. Rhee, D.A. Dzombak, Surface complexation Gouy-Chapman modeling of binary and ternary cation exchange, *Langmuir* 14(4) (1998) 935-943.
- [94] D.L. Chapman, A contribution to the theory of electrocapillarity, *Philos. Mag.* 25(148) (1913) 475-481.
- [95] M. Gouy, On the constitution of the electric charge at the surface of an electrolyte, *C. R. Acad. Sci.* 149 (1909) 654-657.
- [96] H. Ohshima, The derjaguin-landau-verwey-overbeek (DLVO) theory of colloid stability, *Electrical Phenomena at Interfaces and Biointerfaces: Fundamentals and Applications in Nano-, Bio-, and Environmental Sciences* 27 (2012).
- [97] M. Kleman, O.D. Laverntovich *Stability of Colloidal Systems, Soft Matter Physics: An Introduction*, Springer Science & Business Media, New York (USA), 2003, pp. 519-559.
- [98] S. Edmondson, V.L. Osborne, W.T.S. Huck, Polymer brushes via surface-initiated polymerizations, *Chem. Soc. Rev.* 33(1) (2004) 14-22.
- [99] M. Krishnamoorthy, S. Hakobyan, M. Ramstedt, J.E. Gautrot, Surface-Initiated polymer brushes in the biomedical field: applications in membrane science, biosensing, cell culture, regenerative medicine and antibacterial coatings, *Chem. Rev.* 114(21) (2014) 10976-11026.
- [100] T. Tadros, *Interfacial forces in aqueous media*, John Wiley & Sons, New York (USA), 1995.
- [101] K.A. Willets, R.P. Van Duyne, Localized surface plasmon resonance spectroscopy and sensing, *Annu. Rev. Phys. Chem.* 58 (2007) 267-297.
- [102] L.A. Dykman, N.G. Khlebtsov, Uptake of engineered gold nanoparticles into mammalian cells, *Chem. Rev.* 114(2) (2014) 1258-1288.
- [103] M. Stratakis, H. Garcia, Catalysis by supported gold nanoparticles: beyond aerobic oxidative processes, *Chem. Rev.* 112(8) (2012) 4469-4506.
- [104] K. Rahme, L. Chen, R.G. Hobbs, M.A. Morris, C. O'Driscoll, J.D. Holmes, PEGylated gold nanoparticles: polymer quantification as a function of PEG lengths and nanoparticle dimensions, *RSC Adv.* 3(17) (2013) 6085-6094.
- [105] J.L. Perry, K.G. Reuter, M.P. Kai, K.P. Herlihy, S.W. Jones, J.C. Luft, M. Napier, J.E. Bear, J.M. DeSimone, PEGylated print nanoparticles: the impact of PEG density on protein binding, macrophage association, biodistribution, and pharmacokinetics, *Nano Lett.* 12(10) (2012) 5304-5310.
- [106] V.B. Damodaran, C.J. Fee, T. Ruckh, K.C. Papat, Conformational studies of covalently grafted poly(ethylene glycol) on modified solid matrices using X-ray photoelectron spectroscopy, *Langmuir* 26(10) (2010) 7299-7306.
- [107] D.R. Hristov, H. Lopez, Y. Ortin, K. O'Sullivan, K.A. Dawson, D.F. Brougham, Impact of dynamic sub-populations within grafted chains on the protein binding and colloidal stability of PEGylated nanoparticles, *Nanoscale* 13(10) (2021) 5344-5355.
- [108] W. Wang, Q.Q. Wei, J. Wang, B.C. Wang, S.H. Zhang, Z. Yuan, Role of thiol-containing polyethylene glycol (thiol-PEG) in the modification process of gold nanoparticles (AuNPs): stabilizer or coagulant?, *J. Colloid. Interf. Sci.* 404 (2013) 223-229.
- [109] D.N. Benoit, H.G. Zhu, M.H. Lillierose, R.A. Verm, N. Ali, A.N. Morrison, J.D. Fortner, C. Ayendano, V.L. Colvin, Measuring the grafting density of nanoparticles in solution by analytical ultracentrifugation and total organic carbon analysis, *Anal. Chem.* 84(21) (2012) 9238-9245.
- [110] H.H. Zhang, W.J. Wang, S. Mallapragada, A. Travesset, D. Vaknin, Macroscopic and tunable nanoparticle superlattices, *Nanoscale* 9(1) (2017) 164-171.
- [111] H. Zhang, W. Wang, M. Akinc, S. Mallapragada, A. Travesset, D. Vaknin, Assembling and ordering polymer-grafted nanoparticles in three dimensions, *Nanoscale* 9(25) (2017) 8710-8715.
- [112] U. Dahal, Z. Wang, E.E. Dormidontova, Hydration of spherical PEO-grafted gold nanoparticles: curvature and grafting density effect, *Macromolecules* 51(15) (2018) 5950-5961.

- [113] M. Retout, E. Brunetti, H. Valkenier, G. Bruylants, Limits of thiol chemistry revealed by quantitative analysis of mixed layers of thiolated-PEG ligands grafted onto gold nanoparticles, *J. Colloid Interf. Sci.* 557 (2019) 811-819.
- [114] D. Miyamoto, M. Oishi, K. Kojima, K. Yoshimoto, Y. Nagasaki, Completely dispersible PEGylated gold nanoparticles under physiological conditions: modification of gold nanoparticles with precisely controlled PEG-b-polyamine, *Langmuir* 24(9) (2008) 5010-5017.
- [115] X. Zhang, M.R. Servos, J.W. Liu, Ultrahigh nanoparticle stability against salt, pH, and solvent with retained surface accessibility via depletion stabilization, *J. Am. Chem. Soc.* 134(24) (2012) 9910-9913.
- [116] S. Saeki, N. Kuwahara, M. Nakata, M. Kaneko, Upper and lower critical solution temperatures in poly(ethyleneglycol) solutions, *Polymer* 17(8) (1976) 685-689.
- [117] J.-F. Lutz, Polymerization of oligo(ethylene glycol) (meth)acrylates: toward new generations of smart biocompatible materials, *J. Polym. Sci. A1* 46(11) (2008) 3459-3470.
- [118] Z.P. Du, X.F. Sun, X.M. Tai, G.Y. Wang, X.Y. Liu, Optimizing conditions of preparation of thermoresponsive SiO<sub>2</sub>-POEGMA particles via AGET-ATRP, *Appl. Surf. Sci.* 329 (2015) 234-239.
- [119] R. Iida, H. Mitomo, Y. Matsuo, K. Niikura, K. Ijiro, Thermoresponsive assembly of gold nanoparticles coated with oligo(ethylene glycol) ligands with an alkyl head, *J. Phys. Chem. C* 120(29) (2016) 15846-15854.
- [120] K. Xiong, H. Mitomo, X.M. Su, Y. Shi, Y. Yonamine, S. Sato, K. Ijiro, Molecular configuration-mediated thermo-responsiveness in oligo(ethylene glycol) derivatives attached on gold nanoparticles, *Nanoscale Adv.* 3(13) (2021) 3762.
- [121] H.J. Kim, W.J. Wang, A. Travesset, S.K. Mallapragada, D. Vaknin, Temperature-induced tunable assembly of columnar phases of nanorods, *ACS Nano* 14(5) (2020) 6007-6012.
- [122] Y.J. Zhang, P.S. Cremer, Interactions between macromolecules and ions: the Hofmeister series, *Curr. Opin. Chem. Biol.* 10(6) (2006) 658-663.
- [123] H.H. Zhang, W.J. Wang, S. Mallapragada, A. Travesset, D. Vaknin, Ion-Specific Interfacial Crystallization of Polymer-Grafted Nanoparticles, *Journal of Physical Chemistry C* 121(28) (2017) 15424-15429.
- [124] H.J. Kim, M.M. Hossen, A.C. Hillier, D. Vaknin, S.K. Mallapragada, W.J. Wang, Interfacial and bulk assembly of anisotropic gold nanostructures: implications for photonics and plasmonics, *ACS Appl. Nano Mater.* 3(8) (2020) 8216-8223.
- [125] K.D.T.P. Matyjaszewski, *Handbook of radical polymerization*, Wiley-Interscience, Hoboken, N.J., 2002.
- [126] M. Szwarc, The action of carbon black in stabilizing polymeric materials, *J. Polym. Sci.* 19(93) (1956) 589-590.
- [127] W.A. Braunecker, K. Matyjaszewski, Controlled/living radical polymerization: features, developments, and perspectives, *Prog. Polym. Sci.* 32(1) (2007) 93-146.
- [128] A.D. Jenkins, R.G. Jones, G. Moad, Terminology for reversible-deactivation radical polymerization previously called "controlled" radical or "living" radical polymerization (IUPAC recommendations 2010), *Pure Appl. Chem.* 82(2) (2010) 483-491.
- [129] L. Gold, Statistics of polymer molecular size distribution for an invariant number of propagating chains, *J. Chem. Phys.* 28(1) (1958) 91-99.
- [130] M. Szwarc, Living polymers, *Nature* 178(4543) (1956) 1168-1169.
- [131] J. Chiefari, Y.K. Chong, F. Ercole, J. Krstina, J. Jeffery, T.P.T. Le, R.T.A. Mayadunne, G.F. Meijs, C.L. Moad, G. Moad, E. Rizzardo, S.H. Thang, Living free-radical polymerization by reversible addition-fragmentation chain transfer: The RAFT process, *Macromolecules* 31(16) (1998) 5559-5562.
- [132] J.S. Wang, K. Matyjaszewski, Controlled living radical polymerization - Atom-transfer radical polymerization in the presence of transition-metal complexes, *J. Am. Chem. Soc.* 117(20) (1995) 5614-5615.

- [133] J.S. Wang, K. Matyjaszewski, Living controlled radical polymerization - Transition-metal catalyzed atom-transfer radical polymerization in the presence of a conventional radical initiator, *Macromolecules* 28(22) (1995) 7572-7573.
- [134] M. Kato, M. Kamigaito, M. Sawamoto, T. Higashimura, Polymerization of methyl-methacrylate with the carbon-tetrachloride dichlorotris (triphenylphosphine) ruthenium(II) methylaluminum bis(2,6-di-tert-butylphenoxide) initiating system - possibility of living radical polymerization, *Macromolecules* 28(5) (1995) 1721-1723.
- [135] K. Matyjaszewski, Atom transfer radical polymerization (ATRP): current status and future perspectives, *Macromolecules* 45(10) (2012) 4015-4039.
- [136] K. Matyjaszewski, J.H. Xia, Atom transfer radical polymerization, *Chem. Rev.* 101(9) (2001) 2921-2990.
- [137] M. Fantin, A.A. Isse, A. Gennaro, K. Matyjaszewski, Understanding the fundamentals of aqueous ATRP and defining conditions for better control, *Macromolecules* 48(19) (2015) 6862-6875.
- [138] W. Tang, Y. Kwak, W. Braunecker, N.V. Tsarevsky, M.L. Coote, K. Matyjaszewski, Understanding atom transfer radical polymerization: effect of ligand and initiator structures on the equilibrium constants, *J. Am. Chem. Soc.* 130(32) (2008) 10702-10713.
- [139] A. Simakova, S.E. Averick, D. Konkolewicz, K. Matyjaszewski, Aqueous ARGET ATRP, *Macromolecules* 45(16) (2012) 6371-6379.
- [140] P. Gurnani, S. Perrier, Controlled radical polymerization in dispersed systems for biological applications, *Progress in Polymer Science* 102 (2020).
- [141] K. Matyjaszewski, Advanced materials by atom transfer radical polymerization, *Adv. Mater.* 30(23) (2018).
- [142] T.G. Ribelli, F. Lorandi, M. Fantin, K. Matyjaszewski, Atom transfer radical polymerization: billion times more active catalysts and new initiation systems, *Macromol. Rapid Comm.* 40(1) (2019).
- [143] Y. Kwak, A.J.D. Magenau, K. Matyjaszewski, ARGET ATRP of methyl acrylate with inexpensive ligands and ppm concentrations of catalyst, *Macromolecules* 44(4) (2011) 811-819.
- [144] G. Wang, M. Schmitt, Z.Y. Wang, B. Lee, X.C. Pan, L.Y. Fu, J.J. Yan, S.P. Li, G.J. Xie, M.R. Bockstaller, K. Matyjaszewski, Polymerization-induced self-assembly (PISA) using ICAR ATRP at low catalyst concentration, *Macromolecules* 49(22) (2016) 8605-8615.
- [145] P. Chmielarz, P. Krysz, S. Park, K. Matyjaszewski, PEO-b-PNIPAM copolymers via SARA ATRP and eATRP in aqueous media, *Polymer* 71 (2015) 143-147.
- [146] M. Rolland, R. Whitfield, D. Messmer, K. Parkatzidis, N.P. Truong, A. Anastasaki, Effect of polymerization components on oxygen-tolerant photo-ATRP, *ACS Macro Lett.* 8(12) (2019) 1546-1551.
- [147] K.X. Liu, W.J. Zhang, L.X. Zong, Y.J. He, X.M. Zhang, M.Y. Liu, G. Shi, X.G. Qiao, X.C. Pang, Dimensional optimization for ZnO-based mechano-ATRP with extraordinary activity, *J. Phys. Chem. Lett.* 13(22) (2022) 4884-4890.
- [148] I. Zaborniak, P. Chmielarz, Ultrasound-mediated atom transfer radical polymerization (ATRP), *Materials* 12(21) (2019).
- [149] M. Fantin, F. Lorandi, A. Gennaro, A.A. Isse, K. Matyjaszewski, Electron transfer reactions in atom transfer radical polymerization, *Synthesis-Stuttgart* 49(15) (2017) 3311-3322.
- [150] D.W. Jenkins, S.M. Hudson, Review of vinyl graft copolymerization featuring recent advances toward controlled radical-based reactions and illustrated with chitin/chitosan trunk polymers, *Chem. Rev.* 101(11) (2001) 3245-3273.
- [151] V. Bonometti, E. Labbe, O. Buriez, P. Mussini, C. Amatore, Exploring the first steps of an electrochemically-triggered controlled polymerization sequence: activation of alkyl- and benzyl halide initiators by an electrogenerated Fe(II)Salen complex, *J Electroanal. Chem.* 633(1) (2009) 99-105.
- [152] J. Yeow, R. Chapman, A.J. Gormley, C. Boyer, Up in the air: oxygen tolerance in controlled/living radical polymerisation, *Chem. Soc. Rev.* 47(12) (2018) 4357-4387.

- [153] S.S. Hosseiny, P. van Rijn, Surface initiated polymerizations via e-ATRP in pure water, *Polymers* 5(4) (2013) 1229-1240.
- [154] M. Khan, J. Yang, C.C. Shi, J. Lv, Y.K. Feng, W. Zhang, Surface tailoring for selective endothelialization and platelet inhibition via a combination of SI-ATRP and click chemistry using Cys-Ala-Gly-peptide, *Acta Biomater.* 20 (2015) 69-81.
- [155] L.X. Xing, N.N. Guo, Y.T. Zhang, H.Q. Zhang, J.D. Liu, A negatively charged loose nanofiltration membrane by blending with poly (sodium 4-styrene sulfonate) grafted SiO<sub>2</sub> via SI-ATRP for dye purification, *Sep. Purif. Technol.* 146 (2015) 50-59.
- [156] A. Khabibullin, K. Bhangaonkar, C. Mahoney, Z. Lu, M. Schmitt, A.K. Sekizkardes, M.R. Bockstaller, K. Matyjaszewski, Grafting PMMA brushes from alpha-alumina nanoparticles via SI-ATRP, *ACS Appl. Mater. Inter.* 8(8) (2016) 5458-5465.
- [157] X.Y. Huang, M.J. Wirth, Surface-initiated radical polymerization on porous silica, *Anal. Chem.* 69(22) (1997) 4577-4580.
- [158] B. Li, B. Yu, W.T.S. Huck, F. Zhou, W. Liu, Electrochemically induced surface-initiated atom-transfer radical polymerization, *Angew. Chem. Int. Edit.* 51(21) (2012) 5092-5095.
- [159] B. Li, B. Yu, W.T.S. Huck, W. Liu, F. Zhou, Electrochemically mediated atom transfer radical polymerization on nonconducting substrates: controlled brush growth through catalyst diffusion, *J. Am. Chem. Soc.* 135(5) (2013) 1708-1710.
- [160] P. Chmielarz, J.J. Yan, P. Krys, Y. Wang, Z.Y. Wang, M.R. Bockstaller, K. Matyjaszewski, Synthesis of nanoparticle copolymer brushes via surface-initiated seATRP, *Macromolecules* 50(11) (2017) 4151-4159.
- [161] X.Q. Zhang, J.L. Zhang, L.L. Dong, S.X. Ren, Q.L. Wu, T.Z. Lei, Thermoresponsive poly(poly(ethylene glycol) methacrylate)s grafted cellulose nanocrystals through SI-ATRP polymerization, *Cellulose* 24(10) (2017) 4189-4203.
- [162] A.E. Rodda, F. Ercole, D.R. Nisbet, J.S. Forsythe, L. Meagher, Optimization of aqueous SI-ATRP grafting of poly(oligo(ethylene glycol) methacrylate) brushes from benzyl chloride macroinitiator surfaces, *Macromol. Biosci.* 15(6) (2015) 799-811.
- [163] X.W. Fan, L.J. Lin, P.B. Messersmith, Cell fouling resistance of polymer brushes grafted from Ti substrates by surface-initiated polymerization: effect of ethylene glycol side chain length, *Biomacromolecules* 7(8) (2006) 2443-2448.
- [164] X.W. Fan, L.J. Lin, J.L. Dalsin, P.B. Messersmith, Biomimetic anchor for surface-initiated polymerization from metal substrates, *J. Am. Chem. Soc.* 127(45) (2005) 15843-15847.
- [165] F. Tang, L.F. Zhang, J. Zhu, Z.P. Cheng, X.L. Zhu, Surface functionalization of chitosan nanospheres via surface-initiated AGET ATRP mediated by iron catalyst in the presence of limited amounts of air, *Ind. Eng. Chem. Res.* 48(13) (2009) 6216-6223.

# **Capítulo 2. Técnicas experimentales**



Para comprender el comportamiento tanto de los NMs híbridos como de las películas protectoras en sustratos macroscópicos que entran en contacto con el medio biológico es necesaria una caracterización químico-física que relacione los eventos observados en la bio-interfase con las propiedades superficiales de los mismos. Las características de las películas, capas o recubrimientos compactos, como son su orientación, topografía, índice de refracción, energía superficial o mojabilidad, afectan de manera importante a las propiedades de la interfase. Esto lleva a caracterizar las películas protectoras en términos de densidad superficial, volumen hidrodinámico, conformación y carga, entre otros. Conocidas las propiedades del NM, aparece el reto de identificar los cambios que tienen lugar en la interfase al exponerla al medio biológico, considerando que dicha exposición puede alterar las propiedades fisicoquímicas de la superficie al disminuir la estabilidad de la interfase. También es posible la aparición de cambios intrínsecos en la interfase debido a que una notable adsorción de moléculas circundantes podría considerarse que da lugar a un nuevo entorno.

La elección de una técnica de caracterización se basa en su capacidad de proporcionar la información deseada con suficiente resolución y sensibilidad. En este capítulo se presentan las diferentes metodologías empleadas para sintetizar y caracterizar las nanoestructuras estudiadas en la tesis, definiendo brevemente su fundamento teórico.

## **2.1. Experimentación electroquímica.**

La electroquímica ofrece herramientas importantes en la síntesis y caracterización de NMs, permitiendo obtener información tanto de los procesos superficiales que se desarrollan como de las propiedades que exhiben los recubrimientos obtenidos.

### **2.1.1. Técnicas electroquímicas.**

#### *2.1.1.1. Voltamperometría cíclica (CV).*

La CV podría considerarse la técnica más versátil al proporcionar información sobre los parámetros cinéticos y termodinámicos de los procesos de transferencia de carga en la interfase sólido-líquido controlando el potencial aplicado. También permite evaluar estructuras no electroactivas mediante, por ejemplo, sondas redox. Se basa en la aplicación de un potencial variable en el electrodo de trabajo, en un rango determinado, mientras se monitorizan éste y la corriente circulante, a una velocidad de barrido concreta y en dirección directa e inversa. Dependiendo del tipo de análisis, es posible realizar un único ciclo, un ciclo parcial o una secuencia de medidas para obtener los perfiles característicos intensidad-potencial ( $i$ - $E$ ) que tienen lugar en la interfase del electrodo de trabajo. El

análisis de las representaciones gráficas  $i$ - $E$ , conocidas como voltamperogramas o voltogramas, presentan potenciales de pico de los procesos e intensidades de corriente que permiten definir los mecanismos de las reacciones redox que acontecen, así como su reversibilidad, y detectar posibles reacciones secundarias. Nicholson y Shain [1] describieron matemáticamente los procesos observados en VC en función de la intensidad de corriente, haciendo posible detectar, por ejemplo, el tipo de control cinético (difusión o adsorción). Esto permite determinar si las estructuras a caracterizar son dependientes de la difusión de otras especies presentes en el medio.

### 2.1.1.2. Espectroscopia de impedancia electroquímica (EIS).

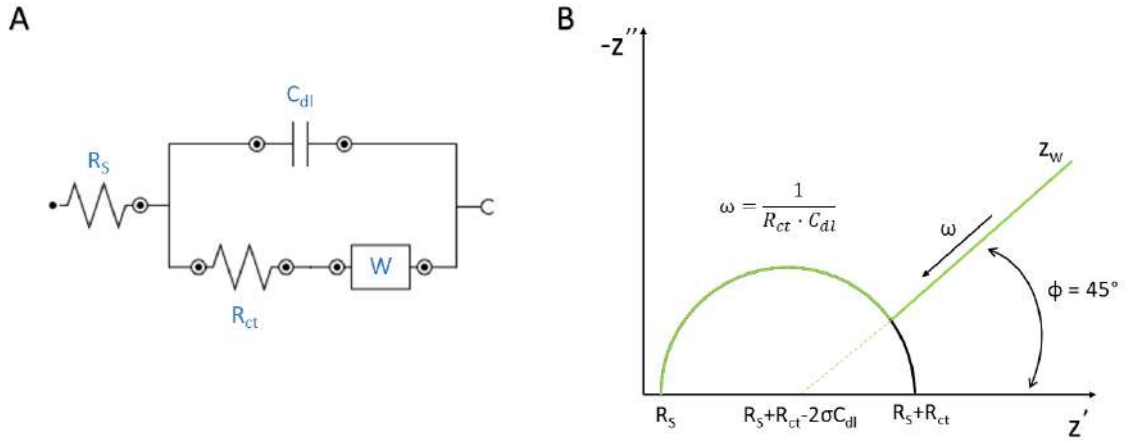
La EIS es una interesante técnica que proporciona información en base a la perturbación de la dinámica de un proceso electroquímico, basándose en las leyes de Faraday y Ohm ( $R=E/I$ ) para caracterizar un proceso químico mediante medidas eléctricas. Al igual que la resistencia ( $R$ ), la impedancia ( $Z$ ) es una medida de la capacidad de un circuito para resistir el flujo de la corriente eléctrica, desde un enfoque diferente. La  $Z$  se determina aplicando un potencial de corriente alterna (CA), esto es, una señal de excitación de pequeña amplitud (5-10 mV) sobre un potencial fijo de corriente continua (CC) a una celda electroquímica mientras se monitoriza la respuesta de la CA, que puede ser lineal o pseudo-lineal. Esta señal de CA asociada puede analizarse como una suma de funciones sinusoidales (serie de Fourier)

Así, es posible obtener una expresión análoga a la ley de Ohm para  $Z$ :

$$Z(\omega) = \frac{E_t}{I_t} = \frac{E_0 \text{sen}(\omega t)}{I_0 \text{sen}(\omega t + \phi)} = Z_0 \frac{\text{sen}(\omega t)}{\text{sen}(\omega t + \phi)} \quad (1)$$

donde  $\phi$  indica el cambio de fase,  $\omega$  es la frecuencia y  $t$ , el tiempo. Si el potencial aplicado es una función compleja (relación de Euler,  $E_t = E_0 \cdot e^{i\omega t}$ ), la impedancia se representa por un número complejo,  $Z(\omega) = Z_0 \cdot e^{i\omega\phi}$ , es decir, se compone de una parte real y otra imaginaria. Al representar la parte imaginaria ( $-Z''$ ) frente a la real ( $Z'$ ) se obtiene la representación de Nyquist, en la que cada punto corresponde a una determinada frecuencia. Sin embargo,  $Z(\omega)$  es normalmente una cantidad compleja con una magnitud y un cambio de fase que dependen de la frecuencia de la señal ( $Z(\omega) = |Z(\omega)| \cdot e^{i\omega\phi}$ ), lo que permite seleccionar un amplio rango de frecuencias para llevar a cabo la perturbación del potencial y obtener el espectro de Nyquist, que aporta información sobre el sistema a escalas de tiempo muy diferentes. La escala de frecuencias comúnmente usada es 100 kHz - 0.1 Hz.





**Esquema 1.** (A) Circuito equivalente tipo Randles y (B) representación de Nyquist para este circuito.

Analizando la dependencia de  $Z(\omega)$  con el potencial aplicado es posible aislar y distinguir la influencia de diferentes fenómenos físicos (como la capacidad, el transporte de masa o la difusión) y químicos (de transferencia electrónica o transferencia de carga) que tienen lugar en la interfase del electrodo. La interpretación de estos datos se consigue ajustando los datos EIS a un circuito eléctrico equivalente, cuyos elementos representan una base física de los procesos modelados en la interfase. El circuito de Randles es el modelo más común para representar un proceso de transferencia electrónica controlado por difusión en un electrodo desnudo, y en ocasiones este mismo circuito (o con algunas variaciones) permite evaluar el efecto de la presencia de películas en la superficie, que bloquean o inhiben la transferencia electrónica estudiada (Esquema 1).

En síntesis, la espectroscopía de impedancia permite caracterizar, identificar y estudiar las propiedades morfológicas y eléctricas de las diferentes películas formadas sobre superficies, así como evaluar el efecto que tienen sobre ellas procesos como la corrosión o la exposición a un medio biológico, entre otros. Esta técnica es particularmente valiosa para la caracterización de los huecos en la superficie de los NMs, ya que permite separar los efectos de la resistencia de la disolución, la carga de la doble capa y las corrientes debido a difusión u otros procesos que tengan lugar en ella [2].

### 2.1.1.3. Cronoamperometría.

La cronoamperometría mide la variación de la densidad de corriente con respecto al tiempo en función de un potencial aplicado. Frecuentemente, se comienza aplicando un potencial,  $E_1$ , en el que no se produce ningún proceso faradaico, seguido de un salto (escalón de potencial) hasta un potencial  $E_2$  que provoca cambios en la corriente en función del tiempo que se asocian a fenómenos que ocurren en la doble capa eléctrica. A partir de las curvas densidad de corriente-tiempo, es posible determinar el número de electrones

involucrados en los procesos redox, el área activa, los coeficientes de difusión de especies electroactivas o las especies iónicas que participan en la reacción redox.

En este trabajo se emplea la cronoamperometría como método de síntesis para obtener películas poliméricas mediante la estrategia SI-eATRP. Así, el potencial E2 debe modularse a fin de conseguir que sea lo suficientemente negativo como para generar el complejo catalizador de Cu(I), pero no demasiado, a fin de mantener el control sobre el crecimiento de la película.

#### 2.1.1.4. Balanza electroquímica de cuarzo (EQCM).

La microbalanza de cristal de cuarzo (QCM) es una técnica basada en la excitación de un piezoeléctrico mediante corriente alterna, generando una onda acústica que interacciona con el medio circundante. Se produce así un desplazamiento de fase y amplitud, en función de la frecuencia, que refleja la composición y propiedades del medio más próximo, por lo que la respuesta está determinada principalmente por las propiedades en la interfase. La ecuación que relaciona la variación de la frecuencia de resonancia con el grosor de la lámina de cuarzo y, consecuentemente con la especie que se adsorbe o desorbe en la superficie del sustrato se conoce como ecuación de Sauerbrey [3]

$$\Delta f = -\frac{2f_0^2}{A_r\sqrt{E_y\rho}}\Delta m \quad (2)$$

donde  $E_y$  es la constante de cizalla,  $A_r$ , el área del electrodo,  $\rho$ , la densidad del cristal de cuarzo y  $f_0$ , la resonancia de frecuencia del aire para este cristal. Experimentalmente, los cambios de masa (del orden de nanogramos) que se producen en la superficie del cristal de cuarzo pueden relacionarse con las variaciones de la frecuencia de resonancia de oscilación en la superficie de estos. Estos cristales de cuarzo se cortan de manera que un modo particular de vibración domine, siendo el corte AT el más utilizado. La frecuencia de resonancia se rige por el espesor del cristal, de manera que un aumento de este produce una disminución de la frecuencia de resonancia.

Esta última técnica es un ejemplo del auge que están teniendo los métodos electroquímicos acoplados a otras técnicas de caracterización, como espectroscópicas (UV-Vis [4], IR [5], Raman [6], rayos X [7]) o de caracterización superficial (TEM [8], AFM [9]). La incorporación de medidas electroquímicas a una microbalanza de cuarzo (EQCM) da lugar a una herramienta muy potente para la caracterización de superficies o la evaluación de procesos que tienen lugar en la interfase, permitiendo conocer de forma más detallada los procesos redox interfaciales a escala nanométrica.

### 2.1.2. Celdas y electrodos

La mayor parte de las medidas experimentales se llevaron a cabo en celdas de vidrio *Metrohm* con una capacidad de 25-50 ml de volumen. Se encuentran sujetas a una cabeza hermética con cinco entradas estando, en general, tres de ellas dedicadas a la configuración básica de tres electrodos y una cuarta entrada permite trabajar en atmósfera de nitrógeno. La quinta posición se empleó, en determinados experimentos, para monitorizar la temperatura o el pH.

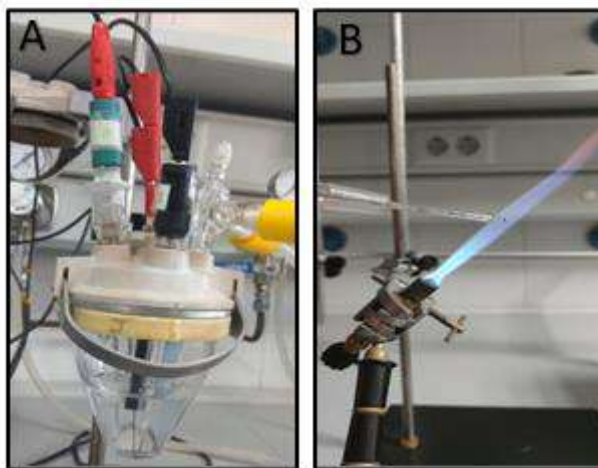


**Figura 1.** (A) Configuración típica de un sistema de tres electrodos. (B) Flameado de electrodo de Au poliorientado para su limpieza mecánica.

En la configuración básica de tres electrodos, se usó en todos los casos un electrodo de calomelanos ( $\text{Hg}/\text{Hg}_2\text{Cl}_2$ ) en  $\text{KCl}$  0.05 M y un electrodo auxiliar (o contraelectrodo) de Pt, de área superficial variable (Figura 1A). Por otro lado, en función del tipo de experimento se emplearon diferentes electrodos de trabajo (Figura 2):

*I) Electrodos monocristalinos poliorientados de oro.* De geometría esférica, se construyen a partir de un hilo de oro *Goodfellow* (99.998%), presentando un diámetro variable entre 1.5 y 2.5 mm, pero perfectamente definido para cada electrodo particular. Siguiendo el método de Clavilier [10], se emplea una llama de gas propano y oxígeno para conseguir electrodos monocristalinos de oro gracias a su elevada tensión superficial. El enfriamiento lento de este electrodo hace que las diferentes contribuciones superficiales den lugar a una superficie con orientaciones preferenciales. Así, estos electrodos se definen como monocristales de estructura cúbica centrada en las caras (FCC), en los que aparecen las facetas (111), (110) y (100), siendo la primera de ellas la más estable (de menor energía superficial).

*II) Electrodos monocristalinos de oro, Au(111).* Se emplearon electrodos comerciales *Arrandee™*, constituidos por una película de oro evaporado de  $250 \pm 50$  nm de espesor sobre

1.1±0.1 mm de vidrio borosilicato. Entre ambos se deposita una capa de cromo (2±1.5 nm) que mejora la adhesión del oro. El acondicionamiento previo de los mismos es análogo al de los electrodos poliorientados.

III) *Electrodos monocristalinos de oro, Au(111), Au(100) y Au(110)*. Además del monocristal comercial *Arrandee™*, se trabajó con electrodos cilíndricos de la marca *Metal Crystals & Oxides LTD*, de 3 mm de diámetro y 2 mm de espesor, con una cara pulida.

IV) *Electrodos policristalinos de oro (Au)*. Se emplean electrodos embutidos en teflón comerciales, de la casa *Metrohm*, de geometría circular con diámetros de 1.6 o 3.0 mm, y áreas geométricas de 0.020 y 0.071 cm<sup>2</sup>, respectivamente. En determinados experimentos se utilizó un electrodo policristalino cuadrado, de 1x1 cm y aproximadamente 1 mm de espesor, de fabricación artesanal.

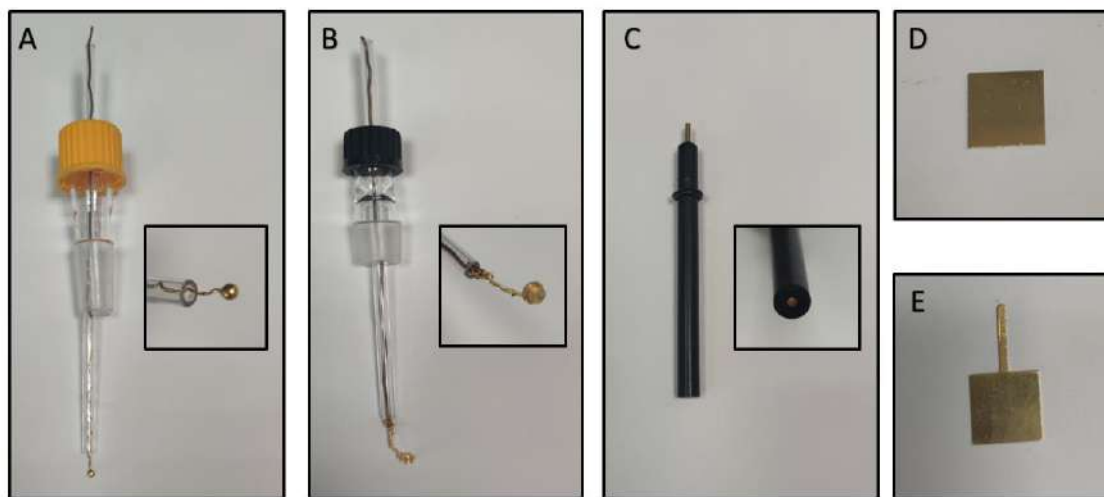
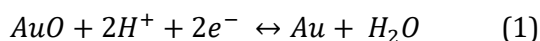
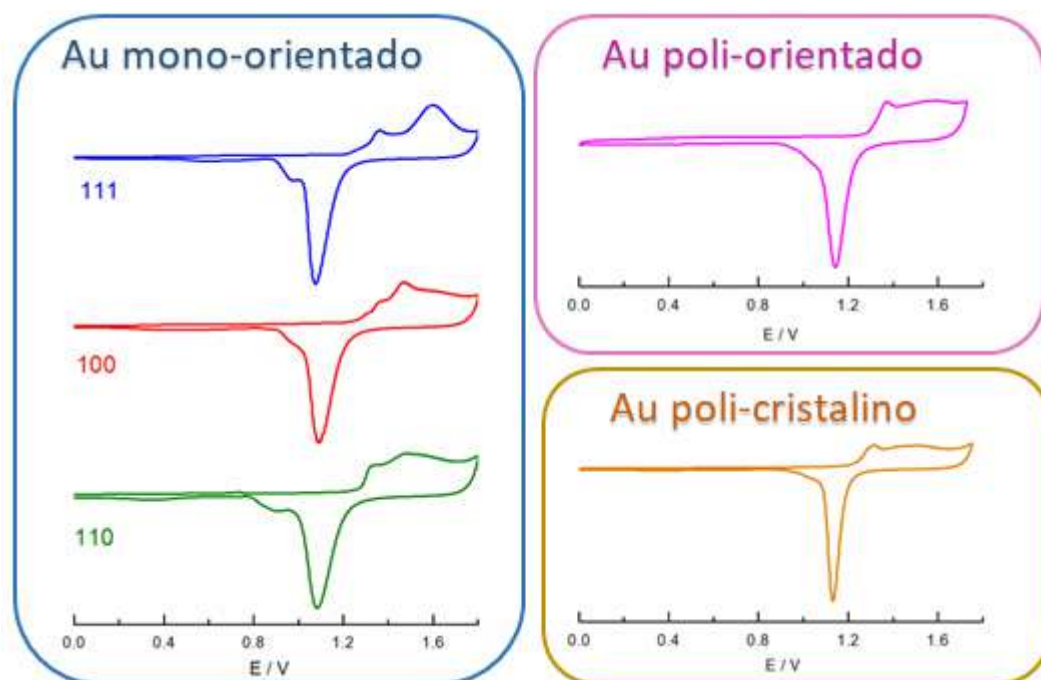


**Figura 2.** Diferentes electrodos de Au empleados: (A) monocristal poliorientado, (B) monocristal Au(100) de Metal Crystals & Oxides LTD, (C) y policristal comercial, (D) monocristal Au(111) Arrandee™ comercial y (E) policristal artesanal.

Antes de cada experimento, los diferentes electrodos de Au empleados se exponen a una llama de gas natural/aire hasta alcanzar su incandescencia durante unos 30 segundos y posteriormente se deja que alcance temperatura ambiente, para luego introducirlo en la celda electroquímica (Figura 1B). El estado de la superficie se evalúa registrando un voltograma cíclico en 0.01 M HClO<sub>4</sub>, que presenta una forma característica y bien definida para los diferentes tipos de electrodos de Au (Esquema 2). Este protocolo es el más apropiado para conseguir superficies limpias, ordenadas y altamente reproducibles. Además, a partir de estos voltogramas es posible determinar el área real, integrando el pico de reducción de los óxidos de oro,



Para determinar este área real, se asume que la densidad atómica en el caso de Au(111) es  $1.35 \cdot 10^{15}$  átomos/cm<sup>2</sup> (432  $\mu\text{C}/\text{cm}^2$ ), mientras que se reduce a  $1.2 \cdot 10^{15}$  átomos/cm<sup>2</sup> (390  $\mu\text{C}/\text{cm}^2$ ) para superficies policristalinas [11].



**Esquema 2.** Voltagramas cíclicos correspondientes a los distintos tipos de electrodo de Au empleados registrados en  $\text{HClO}_4$  0.01 M empleando un electrodo de referencia de hidrógeno. Velocidad de barrido: 0.1 V/s.

### 2.1.3. Instrumentación.

#### 2.1.3.1. CV, EIS y cronoamperometría.

Los estudios de CV, EIS y cronoamperometría se registraron en un sistema electroquímico Autolab (Ecochemie modelo Pgstat30) (Figura 3). El hardware lo conforman un potenciostato (Pgstat 30) y un generador de funciones e interfases (ACD/DAC 164), asociados a dos softwares: GPES 4.9 y FRA. Las técnicas de CV y cronoamperometría se controlan mediante el primero, mientras que el programa FRA permite el diseño de experimentos que lleven asociados medidas de frecuencia. Este sistema admite velocidades de barrido desde 0.01 a 50 V/s y desde 1mV/s a 10000 V/s utilizando el módulo de alta velocidad SCAN-GEN. Para las medidas EIS, es posible aplicar una señal de excitación de potencial sinusoidal de corriente de 5 mV a un potencial fijo CC en un rango de frecuencias de 100 kHz a 0.1 Hz.

Los programas GPES 4.9 y FRA, además de controlar las medidas experimentales, permiten analizar ciertos parámetros de los datos obtenidos. Con el primero es posible obtener los potenciales de pico, cargas, intensidades de corriente o anchura de pico de los voltagramas registrados. Por otro lado, FRA permite ajustar los resultados experimentales

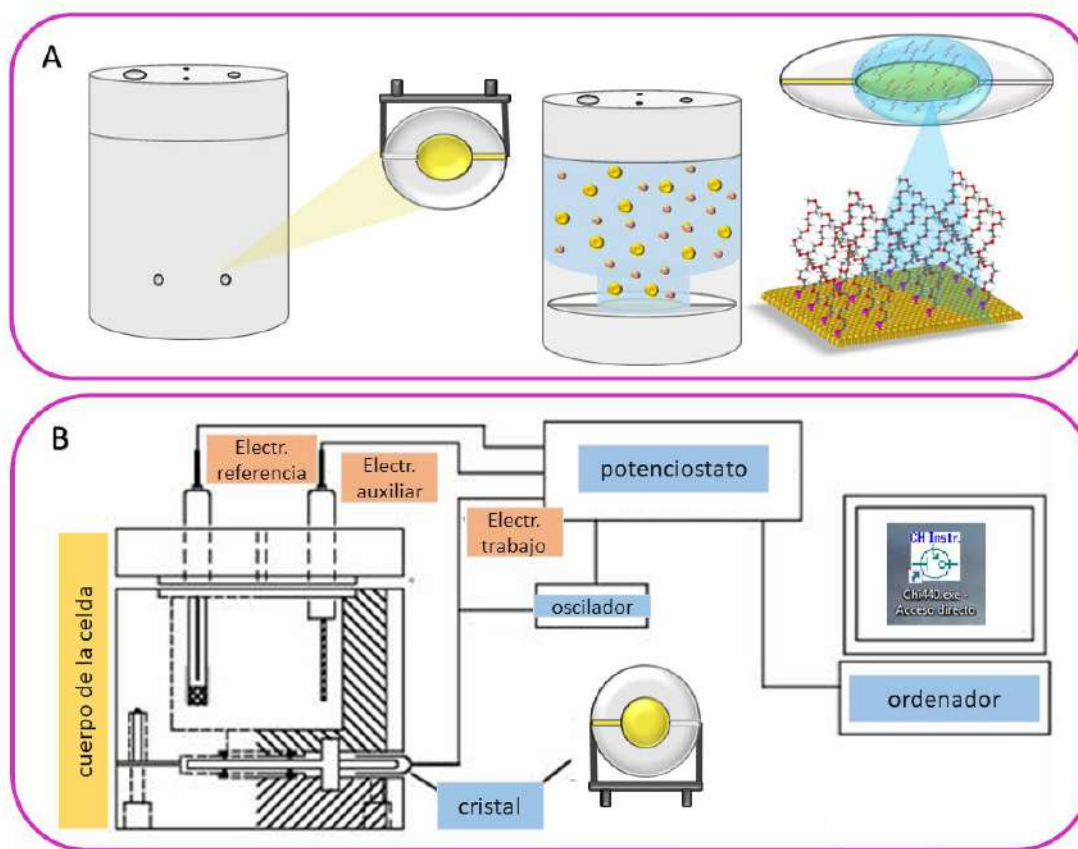
de las medidas de EIS a diferentes circuitos equivalentes, predefinidos o diseñados por el usuario, determinando así el valor de los componentes eléctricos equivalentes ( $R_s$ ,  $R_{ct}$ ,  $C_{dl}$ , etc).



**Figura 3.** Potenciostato Autolab (Ecochemie modelo Pgstat30).

#### 2.1.3.2 EQCM.

En los experimentos de EQCM se emplean una celda, equipo instrumental y programa de control distintos a los descritos en los apartados anteriores. En concreto, se trabaja con un potenciostato de la casa comercial *CHI Instruments*, modelo CHI440C, que lleva acoplada una microbalanza electroquímica de cuarzo con su propio programa, CHI440, para el registro y análisis de datos. Como electrodos de referencia y auxiliar se emplean calomelanos ( $Hg/Hg_2Cl_2$ ) en  $KCl$  0.05 M y Pt, respectivamente, cuyo tamaño y forma están adaptados a las características de la celda. El electrodo de trabajo es un disco de oro de 0.196  $cm^2$ . Más específicamente, se trata de un cristal de cuarzo cubierto por una capa de Ti de 100 Å y una capa de Au pulido de 1000 Å, que opera a una frecuencia de 8 MHz. La masa depositada se determina mediante la ecuación de Sauerbrey, usando una constante de calibración de 1.4 ng/Hz [12]. En el Esquema 3 se representa el tipo de celda empleado, así como un diagrama de los componentes generales de un equipo EQCM.



**Esquema 3.** (A) Representación de la celda EQCM y la interfase formada entre las moléculas de disolvente con la superficie del electrodo modificado. (B) diagrama de los componentes instrumentales en una medida EQCM.

### 2.3. Técnicas espectroscópicas.

En un sentido amplio, la espectroscopía se define como el estudio de la interacción de las ondas electromagnéticas con la materia con intercambio de energía. La radiación electromagnética está compuesta por campos eléctricos y magnéticos alternantes y perpendiculares entre sí que se propagan en línea recta y a velocidad constante en el vacío.

Estas técnicas son fundamentales en la caracterización de NMs, distinguiéndose frecuentemente entre técnicas de espectroscopía electrónica y vibracional. La primera relaciona la excitación de electrones desde el estado fundamental a estados excitados (absorción) y la relajación desde estados excitados al estado fundamental (emisión) con la estructura atómica, molecular o iónica. Por su parte, las frecuencias vibracionales se emplean para caracterizar los enlaces químicos, evaluando la interacción de fotones con especies en una muestra que resultan en la transferencia de energía hasta o desde la muestra a través de la excitación o desexcitación vibracional.

### 2.3.1. Espectroscopía UV-vis.

La espectrometría UV-vis se basa en la medida de propiedades ópticas (absorción, emisión y fluorescencia) que presentan las moléculas. Los espectros moleculares están generalmente constituidos por picos agudos, de modo que las posiciones de las líneas espectrales pueden ser determinadas con suficiente exactitud como para verificar la estructura electrónica de moléculas.

Desde el punto de vista de su uso en la caracterización de materiales, la profundidad de penetración de esta técnica (en torno a 50 nm, en la región del espectro UV-visible) hace que su aplicación en sustratos masivos sea limitada, pero sí permite caracterizar estructuras y materiales nanométricos con suficiente sensibilidad. Los espectros de absorción de suspensiones coloidales permiten determinar las propiedades ópticas de estos sistemas. Así, la LSPR es útil para conocer el tamaño de NPs en suspensión, la modificación de su interfase al estabilizarlas mediante recubrimientos moleculares e, incluso, fenómenos de agregación relacionados con la estabilidad de la suspensión, al observarse desplazamiento del plasmón a mayores longitudes de onda como consecuencia del acoplamiento en la resonancia del plasmón.

En este trabajo se ha empleado un espectrofotómetro Jasco V-570 para el registro de espectros UV-vis (Figura 4A). Este equipo permite además estudiar la región NIR (780 a 2500 nm). A fin de obtener la absorbancia óptima para las medidas experimentales (en el rango 0.5-0.8 u.a.) se emplean cubetas de cuarzo de 0.2 o 1.0 cm de paso óptico. Además, el acople de una cámara termostatazada Peltier ha permitido realizar estudios espectroscópicos en función de la temperatura (Figura 4B).

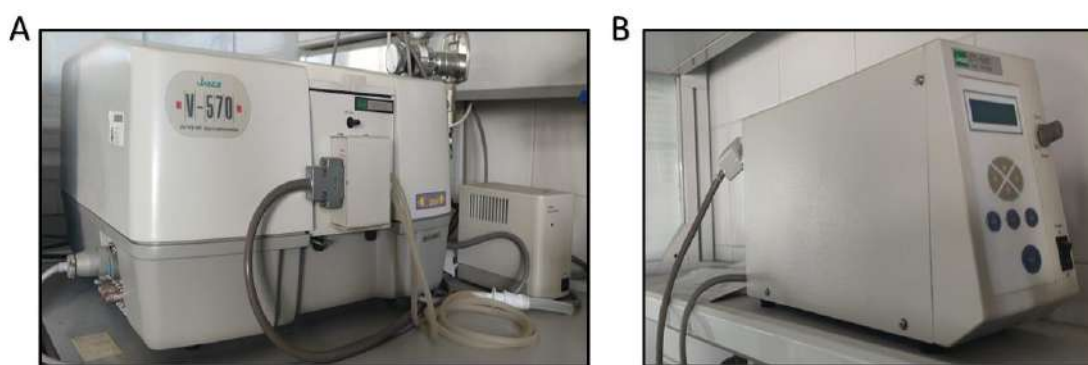


**Figura 4.** (A) Espectrofotómetro Jasco V-570 UV/Vis/NIR. (B) Termostato Peltier para el control de la temperatura en la celda de trabajo.



### 2.3.2. Espectroscopía IRRAS.

La espectroscopía IR se fundamenta en la absorción de frecuencias de luz infrarroja por moléculas y estructuras cristalinas. Esta absorción depende de la frecuencia de vibración de los enlaces entre los distintos átomos. La energía necesaria para que las moléculas y los cristales vibren, entre  $10^{12}$  y  $10^{14}$  Hz, se corresponde con la región IR del espectro electromagnético, y sólo los enlaces polares son capaces de interactuar con la radiación electromagnética. Al existir cargas parciales positivas y negativas en zonas diferenciadas de una molécula es posible que la componente eléctrica de la radiación electromagnética excite su energía vibracional, al mismo tiempo que se produce un cambio en el momento dipolar, lo que explica que la intensidad de la absorción dependa de la polaridad del enlace y que los enlaces no polares simétricos no se observen, ya que no interactúan con el campo eléctrico excitante. El cambio de energía registrado es específico para cada tipo de enlace y grupo de átomos involucrados en la vibración, lo que permite identificar y caracterizar la estructura irradiada.

La física clásica permite explicar, en muchos casos, los espectros IR en función de los movimientos vibratorios de las moléculas. En una molécula diatómica, los átomos se mantienen unidos debido al solapamiento de varios de sus orbitales dado que, a cierta distancia, se produce un balance entre las fuerzas atractivas y las interacciones repulsivas de los electrones del *core* de los dos átomos. Esta posición de equilibrio se puede modificar suministrando energía y, si se piensa en las moléculas como esferas sólidas conectadas por un resorte, puede explicarse mediante la ley de Hooke:

$$v = \frac{1}{2\pi} \sqrt{\frac{k}{\mu}} \quad (5)$$

$$\text{con } \mu = \frac{M_1 M_2}{M_1 + M_2} \quad (6)$$

que establece que las masas (átomos) vibran con unas frecuencias características que dependen de su masa reducida,  $\mu$ , y de la fortaleza del muelle (enlace químico),  $k$ . Esta aproximación se ha demostrado experimentalmente, siendo posible aplicarla con cierto éxito.

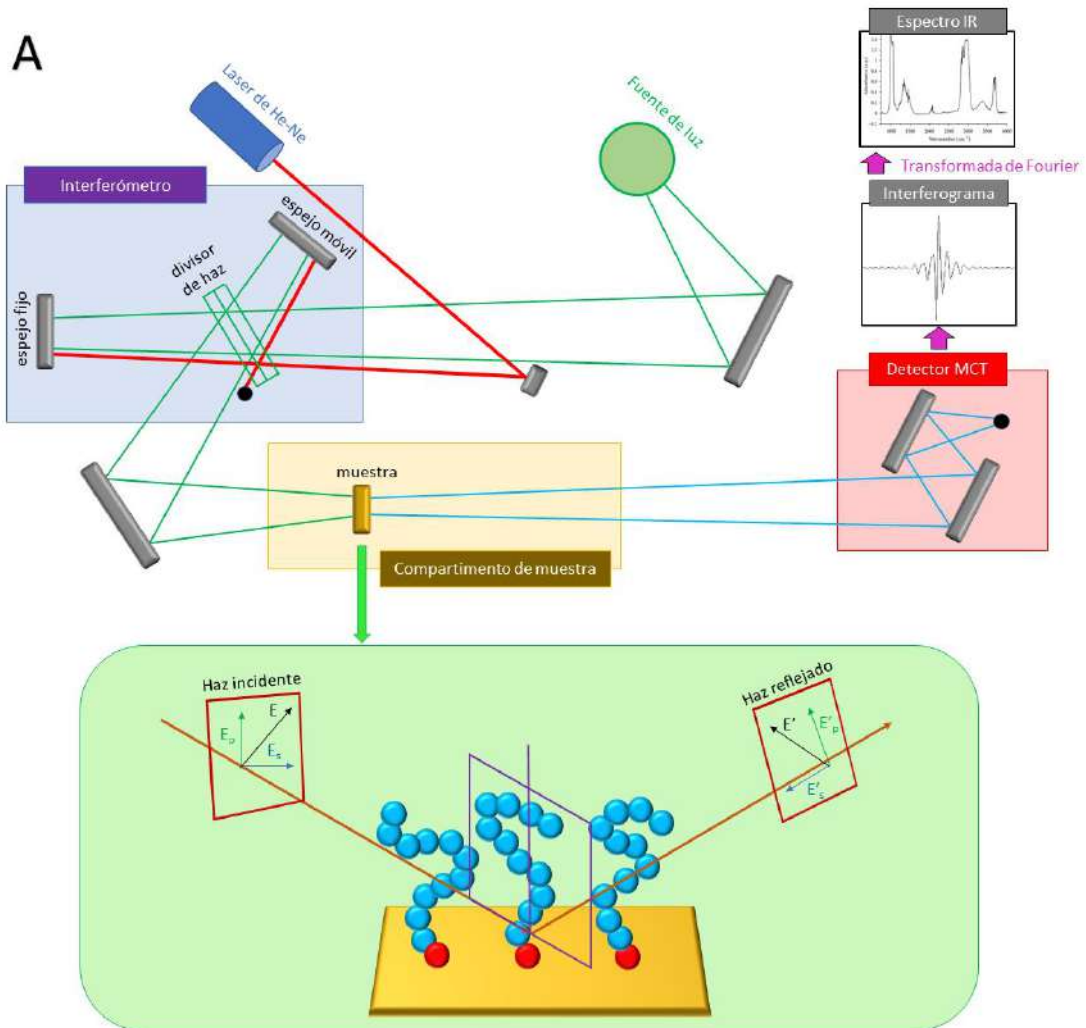
Las vibraciones en moléculas poliatómicas son mucho más complejas que en el caso descrito, ya que una molécula diatómica presenta un único modo de vibración (*stretching*). Asumiendo que cada átomo,  $N$ , de una molécula poliatómica puede desplazarse a lo largo de tres direcciones espaciales, éstas presentarán  $3N$  grados de libertad. Tres combinaciones de esos desplazamientos resultan en el movimiento espacial del centro de masas de la molécula, con lo que una molécula lineal de  $N$  átomos posee  $3N-5$  modos de vibración. Si la

molécula no es lineal, otras tres combinaciones de desplazamientos especifican la rotación de toda la molécula alrededor de su centro de masas, dando  $3N-6$  combinaciones de desplazamientos en los átomos que dejan el centro de masas y la orientación de la molécula inalterados, y siendo estas las distorsiones de interés de la molécula. Este número de movimientos se refieren a la molécula en su conjunto, aunque en muchos casos es posible definir la vibración como principalmente de tipo *stretching* (tensión) o de tipo *bending* (flexión). Las vibraciones de tensión se producen en el enlace entre dos átomos cuando estos se acercan y se alejan uno del otro, mientras que en los modos de flexión hay variación periódica en los ángulos entre los átomos.

La modalidad particular de espectroscopía IRRAS permite la caracterización de recubrimientos en superficies metálicas. Normalmente, para irradiar la muestra se emplea una geometría de reflexión con incidencia rasante (próxima a  $80^\circ$ ). La técnica se basa en la diferente absorción de la luz p- y s- polarizada de las capas delgadas absorbidas en superficies metálicas, que con la luz p-polarizada, pero no con la s-polarizada. El campo eléctrico de la primera es perpendicular a la dirección de propagación, mientras que el de la radiación p-polarizada es perpendicular a ambos, la componente s- y la dirección de propagación (Esquema 5A). Así, las moléculas localizadas en la superficie del sustrato experimentan la suma vectorial de ambos campos, debido a los haces incidente y reflejado. Experimentalmente, la sensibilidad se maximiza empleando ángulos de análisis altos, al aumentar el área analizada. [13]. Así, la espectroscopía IRRAS es especialmente útil para obtener información sobre la geometría de adsorción que presentan películas delgadas sobre superficies metálicas con alta sensibilidad.

Las medidas experimentales de espectroscopía infrarroja presentadas en este trabajo se realizaron con instrumento JASCO 6300 FTIR (Esquema 4B) equipado con un rayo láser sencillo (He-Ne). Generalmente se registró en el intervalo  $600-4000\text{ cm}^{-1}$ , en número de onda, quedando dentro de este rango todos los modos de vibración de las moléculas empleadas. La resolución de las medidas se estableció en 2 o  $4\text{ cm}^{-1}$ . El espectrofotómetro utilizado está equipado con un accesorio de reflectancia de la firma Pike Technologies (*VeeMAX™*) ensamblado en el compartimento de celda del de medida. Este complemento permite analizar las muestras haciendo incidir un rayo polarizado (p) a un ángulo variable, que se estableció entre  $60^\circ$  y  $80^\circ$ . Los datos se adquieren y analizan empleando el software Spectra Manager, asociado al equipo. Antes de cada experimento, el interferómetro y el compartimento de muestra se purgan con un flujo de aire seco (8L/min) que previamente ha circulado por un sistema de secado (K-MT LAB, Parker/Zandet GmbH&Co.KG). Con esto se pretende evitar que en el espectro IR aparezcan señales originadas por  $\text{H}_2\text{O}$ ,  $\text{CO}_2$  y otras

impurezas del medio sensibles a la técnica, que solapan con las propias de la muestra de interés y dificulten su caracterización.



**Esquema 4.** (A) Diagrama de componentes de un equipo de espectroscopía IRRAS. (B) Espectrofotómetro JASCO 6300 FTIR usado en este trabajo.

### 2.3.3. Espectroscopía XPS.

La espectroscopía XPS permite determinar la composición, tanto cualitativa como quasi-cuantitativa, y el estado químico de los elementos en la superficie de un material. Por tanto, se trata de una técnica adecuada para el estudio de películas finas sobre superficies e interfases, ya que permite la caracterización química y eléctrica con una profundidad máxima de análisis de 10 nm. Uno de los mayores atractivos de la espectroscopía XPS es su versatilidad, ya que posibilita el estudio de diferentes tipos de materiales como metales, aleaciones, cerámicos, polímeros, vidrios y, en general, cualquier superficie compatible con sistemas de ultra-alto vacío. Esto hace que sea útil en aplicaciones tan diversas como el análisis de deposición de capas y multicapas, tratamientos de superficies, corrosión, metalurgia, catálisis, electrónica y también en el campo biomédico.

El fundamento físico de esta técnica es el efecto fotoeléctrico que se origina al irradiar con rayos X de baja energía la superficie de una muestra. Esta radiación incidente provoca la fotoionización de los átomos de la muestra, emitiéndose fotoelectrones a partir de los niveles de energía determinados por la estructura electrónica del material. El registro de las energías cinéticas y el número de fotoelectrones que escapan de la superficie del material analizado proporciona información sobre la distribución y población de los niveles de energía electrónicos y, con esto, permite determinar qué elementos están presentes en la muestra, así como sus estados químicos y, en cierta medida, en qué cantidades están presentes [14].

La emisión de estos rayos X se suele realizar con fuentes de excitación que usan las líneas  $K\alpha_{1,2}$  de Mg o Al, con energías de 1253.6 y 1486 eV, respectivamente. Este proceso de fotoemisión (muy rápido, del orden de  $10^{-16}$  s) se describe según la ecuación de Einstein:

$$E_B = h\nu - KE \quad (7)$$

siendo  $E_B$  la energía de enlace del electrón en el átomo,  $h\nu$  la energía de la fuente de rayos X, y  $KE$  la energía cinética del electrón detectado por el espectrómetro del equipo de XPS. Esta ecuación es válida para gases (al ser la energía de enlace de un electrón igual a la energía de ionización) pero insuficiente para las fases condensadas. En sólidos, la superficie influye en la energía necesaria para remover un electrón del sistema, haciendo necesario añadir una contribución de energía adicional,  $\phi_{SP}$ , conocida como función trabajo. Esta función determina la energía mínima requerida para extraer un electrón desde el nivel de Fermi al vacío ( $E_F$  y  $E_0$ , respectivamente).

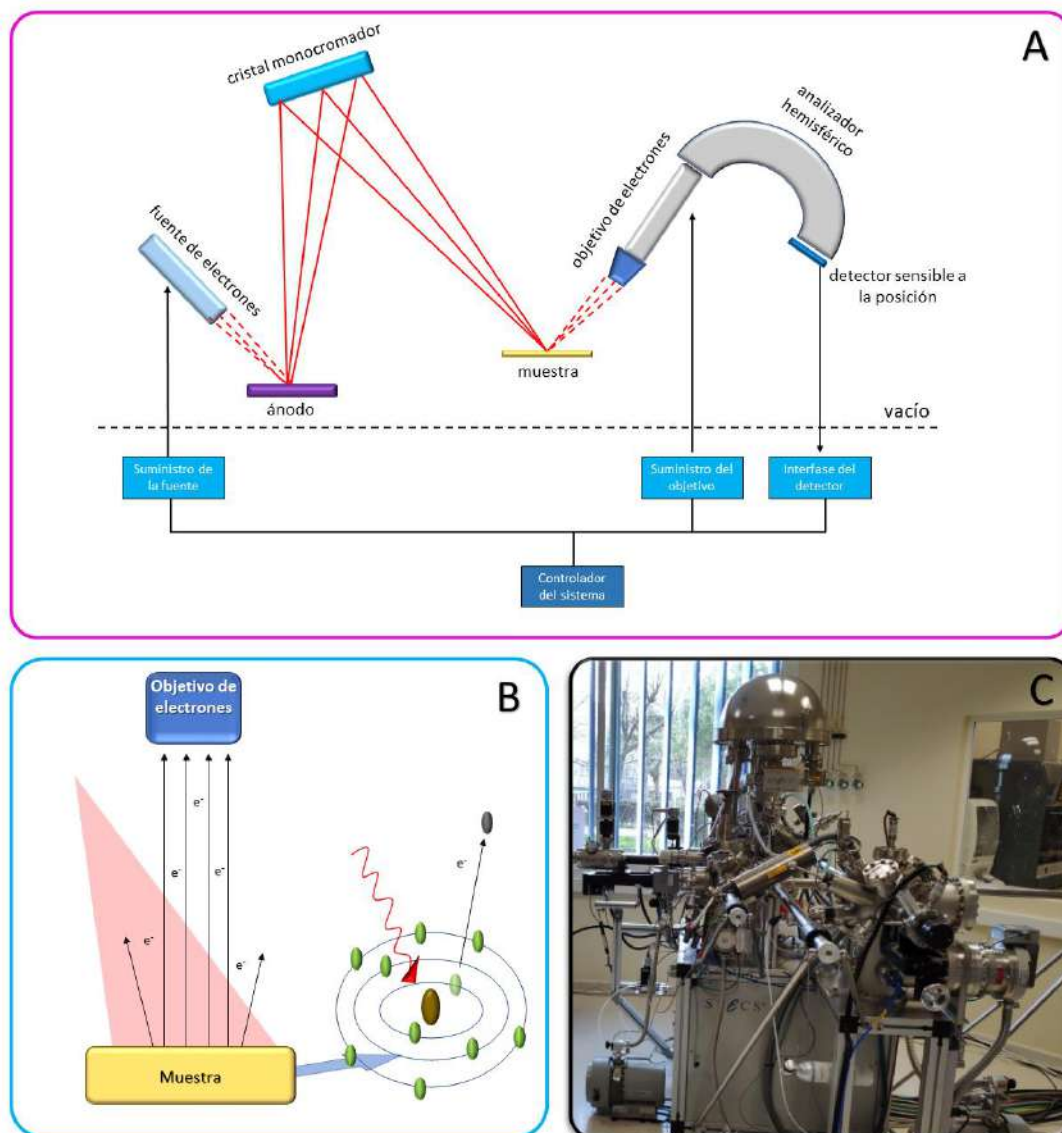
$$E_B^F = h\nu - KE - \phi_{SP} \quad (8)$$

$$\phi_{SP} = E_F - E_0 \quad (9)$$

El valor de este término se determina mediante un calibrado de la escala de energía del analizador a partir de un patrón con energías de enlace bien definidas, siendo frecuente emplear el oro metálico, cuyos valores de energía de enlace son  $E_F = 0$  eV y  $4f_{7/2} = 84$  eV.

Los equipos de espectroscopía XPS presentan como componentes primarios un sistema de ultra-alto vacío, una fuente de rayos X, un analizador de energía del electrón y un sistema de datos (Esquema 5A). La parte central del equipo es la cámara de vacío, donde se sitúa la muestra. Las condiciones de vacío son necesarias a fin de permitir que los electrones viajen desde la muestra hasta el detector sin colisionar con partículas gaseosas, garantizar la estabilidad de las especies presentes y mantener la funcionalidad de todas las componentes del instrumento (por ejemplo, la fuente de rayos X no es operativa en otras condiciones). La imperante necesidad de mantener estas condiciones durante la medida experimental justifica que, antes de cada experimento, la muestra a analizar se someta a un pretratamiento a vacío, operación lenta que suele llevar varias horas. Por otro lado, las fuentes de rayos X más utilizadas están equipadas con ánodos de Al o Mg, pudiendo estar o no la radiación monocromatizada, lo que proporciona una intensidad de radiación máxima al minimizarse la presencia de picos satélites próximos.

Las medidas de XPS recogidas en esta memoria se registraron con un espectrómetro SPECS Phoibos 150MCD (Servicio de Apoyo a la Investigación de la Universidad de Córdoba) utilizando radiación (12 kV, 300 V) de una fuente no monocromática de Mg  $K\alpha_{1,2}$  (1253.6 eV) y como sistema de vacío una cámara principal que trabaja con una presión mínima de  $5 \cdot 10^{-9}$  Pa. Para el registro de los espectros se usó un ángulo de  $90^\circ$  con respecto al plano de la superficie. El espectrómetro se calibró mediante la asignación de la energía de enlace (BE) de referencia de la línea de Au  $4f_{7/2}$  a 84 eV. Los barridos generales de la muestra fueron realizados en el rango comprendido entre 0 y 1100 eV (a una energía de 60 eV), presentando una desviación máxima de 0.2 eV en las BE. Para adquirir espectros de alta resolución (25 eV) se realizaron múltiples barridos en las regiones de interés. Finalmente, el análisis de los datos experimentales se realizó con el *software* CASA. Se eligió una línea de fondo *Shirley* y un ajuste no lineal con mínimos cuadrados adoptando distribuciones Gaussiana/Lorenziana para la deconvolución espectral.



**Esquema 5.** (A) Diagrama de los componentes de un espectrómetro XPS. (B) Proceso de fotoemisión de rayos X. (C) Espectrómetro SPECS Phoibos 150MCD.

## 2.4. Técnicas microscópicas.

A pesar de que podrían considerarse ligeramente invasivas, las técnicas microscópicas se han convertido en primordiales en todas las ramas de la investigación científica durante las últimas décadas. Uno de los principales retos asociados a la investigación de NMs es caracterizar, comprender y manipular las nanoestructuras de manera individual, considerando las partículas o cadenas moleculares individuales que componen una dispersión coloidal o película superficial en sustratos macroscópicos, respectivamente. Las técnicas microscópicas están demostrando ser una herramienta fundamental en este sentido, permitiendo tanto la determinación inequívoca de la forma y

tamaño de nanopartículas, como la rugosidad superficial y composición elemental de películas formadas sobre sustratos macroscópicos, entre otras características.

Dentro de estas técnicas, las microscopías electrónicas, tanto de barrido (SEM), como de transmisión (TEM), han permitido solventar el problema principal de la microscopía óptica. Por definición, la potencia amplificadora de un microscopio óptico está limitada por la longitud de onda de la luz visible. En cambio, los microscopios electrónicos utilizan electrones (cuya longitud de onda es mucho menor que la de la luz) para iluminar las muestras, lo que implica que pueden mostrar estructuras mucho más pequeñas. Así, mientras que la longitud de onda más corta de la luz visible es de alrededor de 4.000 Å, la longitud de onda de los electrones que se utilizan en los microscopios electrónicos se aproxima a 0.5 Å [15].

#### 2.4.1. Microscopía TEM.

La microscopía TEM emplea un haz de electrones acelerados (entre 200 y 800 KeV) a través de lentes electromagnéticas que inciden sobre muestras delgadas (<200 nm) situada en una columna de alto vacío. Menores espesores de muestra permiten obtener imágenes de mayor calidad. Los electrones incidentes con los que se irradia la muestra pueden rebotar, ser absorbidos por la misma o atravesarla. El análisis de las pérdidas específicas de los electrones del haz permite obtener información estructural, ya que el conjunto de electrones que atraviesa la muestra genera una imagen visible (proyectados sobre una pantalla fluorescente) o una imagen latente (si se registran en una placa fotográfica). En la caracterización de NMs, la microscopía TEM permite determinar la morfología, fases cristalinas, composición mayoritaria e impurezas de nanoestructuras (como nanopartículas con núcleos metálicos híbridas, láminas delgadas, grafenos o materiales mesoporosos, entre otros) y ultraestructuras de muestras biológicas.

Las micrografías TEM presentadas en este trabajo se han obtenido mediante un microscopio JEOL JEM 1400 de 120 kV equipado con una cámara de alta resolución Gatan ES1000 (11 megapixels y montaje lateral elevado) que permite obtener imágenes con gran amplitud de campo y excelente nitidez, localizado en el Servicio central de apoyo a la investigación (SCAI) de la Universidad de Córdoba (Figura 5A). Todas las muestras se prepararon depositando y evaporando gotas de las disoluciones de NMs en rejillas de Cu recubiertas de Formvar (400 mesh), de la firma Electron Microscopies Sciences. Para el análisis de las imágenes obtenidas se empleó el programa Image-Pro PLUS.

### 2.4.2. Microscopia SEM.

La microscopía electrónica SEM permite determinar de manera directa el tamaño de partícula o de grano de la muestra en imágenes 3D y con una resolución espacial de 1 a 3 nm. La mayoría de los equipos de última generación disponen de un analizador EDX (*Energy Dispersive X-ray*), que permite determinar los componentes químicos elementales *in situ* de cada una de las fases presentes en la muestra. Además, la posibilidad de realizar micrografías en dos y tres dimensiones (esto es, planas y en relieve) se emplea para obtener información estructural de interés, con un máximo de profundidad de 1  $\mu\text{m}$  (2D) y evaluar la topografía de la muestra (3D). Sin embargo, los microscopios SEM tienen menor capacidad de aumento y menor resolución en comparación con el TEM y, además, es imprescindible que las muestras sean conductoras, teniendo que someterse las aislantes a procesos de recubrimientos con metales, lo que puede conllevar a pérdida de información en su caracterización.

El modelo JSM7800F (JEOL) usado en este trabajo presenta una resolución de 1.2 nm a 1kV de aceleración y de 0.8 nm a 15 kV (Figura 5B). Está equipado con un detector de electrones secundarios que proporciona imágenes topográficas de la superficie de la muestra, un detector de electrones retrodispersados que genera imágenes en escala de grises relativas a los elementos constituyentes de la muestra, y un detector por dispersión de energías de Rayos X que permite el análisis cualitativo y semicuantitativo de los elementos constituyentes de la muestra.

Una de las características que mejor define a la microscopía electrónica de barrido es su excelente poder de resolución (3.5 nm y 300000x) que unido a la gran profundidad de campo y al efecto de sombreado le convierten en una herramienta de un alto potencial a la hora de realizar análisis tridimensionales de estructuras. Esto ha hecho posible emplear esta técnica para el evaluar las películas poliméricas de elevado espesor diseñadas en este trabajo.



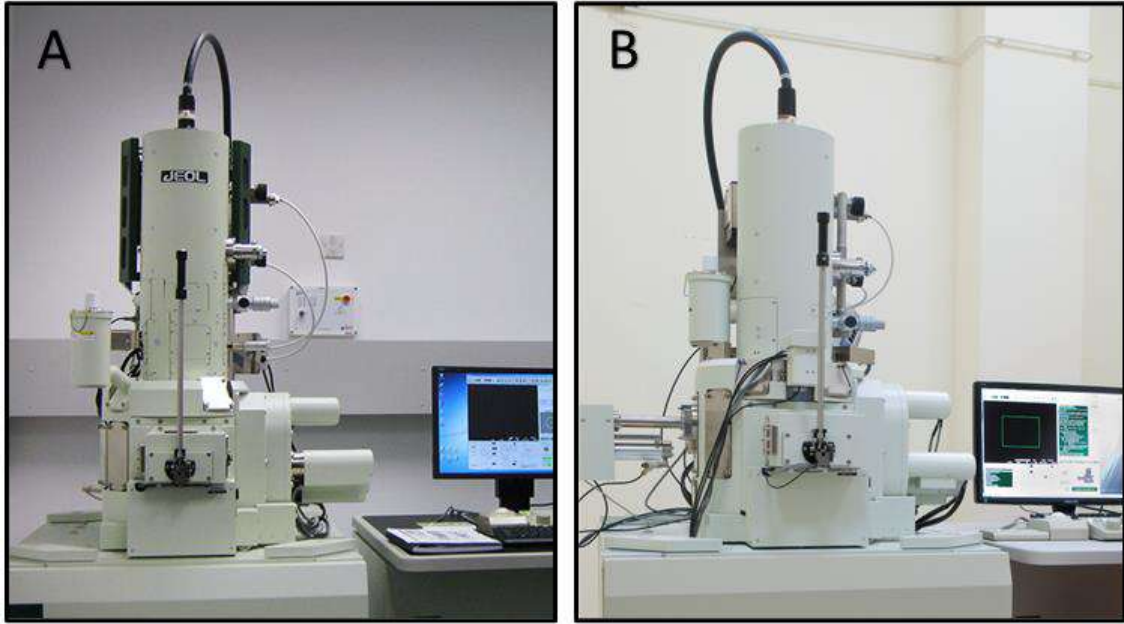


**Figura 5.** Microscópicos (A) JEOL JEM 1400 (TEM) y (B) JEOL JSM7800F (SEM).

## 2.5. Técnicas de DLS y medidas de potencial $\zeta$ .

DLS es una técnica no invasiva y bien establecida para medir el tamaño y la distribución de tamaño de muestras de partículas en suspensión por debajo de  $1\mu\text{m}$ , llegando los equipos de última tecnología a la escala subnanométrica. Experimentalmente, las muestras se irradian con luz láser, que se dispersa en todas las direcciones al alcanzar las partículas presentes. Como consecuencia del movimiento browniano las posiciones relativas de las partículas varían constantemente, originando cambios en las condiciones de interferencia y en la propia intensidad de dispersión. Así, las partículas pequeñas se mueven rápidamente y aceleran la variación de la intensidad de dispersión, y lo contrario se observa en las partículas grandes. Del análisis de estas fluctuaciones de intensidad se obtiene la velocidad del movimiento browniano y, en base a la relación de Stokes-Einstein, el tamaño de partícula expresado como diámetro hidrodinámico [16]:

$$D = \frac{kT}{3\pi\eta d_H} \quad (10)$$

donde  $D$  el coeficiente de difusión traslacional,  $\eta$  la viscosidad del medio,  $T$  la temperatura absoluta,  $k$  la constante de Boltzmann y  $d_H$  el diámetro hidrodinámico. Este último se define como el diámetro de una hipotética esfera sólida (esfera equivalente) que difunde con la misma velocidad que la muestra analizada. Por tanto, puede no corresponder exactamente al tamaño estructural real del NM (obtenido, por ejemplo, empleando técnicas de microscopía electrónica). Además, diferentes parámetros, como la viscosidad del medio, la

óptica del instrumento, la temperatura y el índice de refracción del material o concentración de la muestra, influyen en el resultado de la medida experimental.

Como se ha comentado en el capítulo anterior, el potencial  $\zeta$  es el potencial en el plano de corte de una partícula coloidal que se mueve bajo la acción del campo eléctrico. Su valor, que no puede medirse directamente, se deduce a partir de la movilidad electroforética de las partículas en presencia de un campo eléctrico,  $E$  (desplazándose, en función de su carga, al electrodo de carga opuesta). Cuando las fuerzas atractivas se compensan con la viscosidad del medio, las partículas se mueven a velocidad constante  $v$  que permite definir la movilidad electroforética  $\mu_e$ :

$$\mu_e = \frac{v}{E} \quad (11)$$

Teniendo en cuenta esta expresión,  $\zeta$  se calcula a partir de la ecuación de Henry:

$$\zeta = \frac{3\eta\mu_e}{2\varepsilon_r\varepsilon_0f(Ka)} \quad (12)$$

siendo  $\varepsilon_r$  la constante de permitividad dieléctrica relativa,  $\varepsilon_0$  la permitividad en el vacío,  $\eta$  la viscosidad y  $f(Ka)$  la función de Henry, cuyo valor viene determinado por el medio de dispersión.

Las medidas experimentales de DLS y  $\zeta$  se registran con el mismo instrumento. En este caso, se ha empleado el Zetasizer Nano ZSP, uno de los modelos más recientes de la casa comercial *Malvern Panalytical*, especialmente indicado para la caracterización de proteínas y nanopartículas con la máxima sensibilidad (Figura 6A). El sistema incorpora un analizador de tamaño de partícula y tamaño molecular de dos ángulos que permite la detección de agregados y de muestras con concentración muy baja o alta, utilizando la dispersión de luz dinámica con óptica de retrodispersión no invasiva (NIBS, *Non-Invasive Back Scatter*). La irradiación de la muestra se consigue con un láser de 633 nm de He-Ne y un autovalorador MPT-2. En función de la naturaleza de la muestra y del tipo de experimento, se emplearon cubetas de cuarzo o plástico, como las que se presentan en la Figura 6B. Los datos medidos son el promedio de al menos 20 barridos. Para el registro y posterior análisis de los diámetros hidrodinámicos promedio y potencial zeta de cada muestra se usó la versión más reciente del programa ZetaSizer.

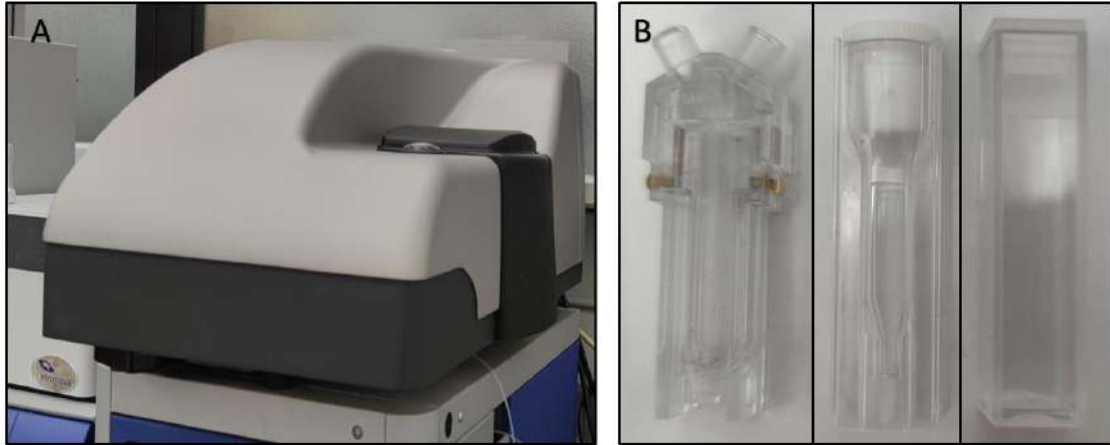


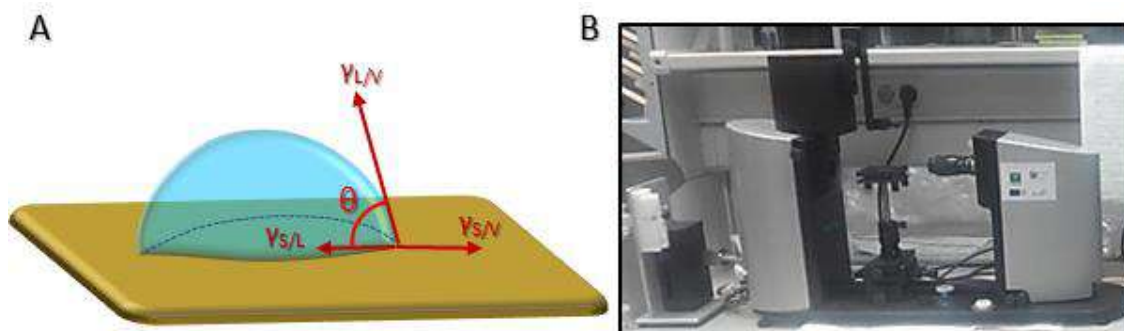
**Figura 6.** (A) Equipo Zetasizer Nano ZSP. (B) Cubetas empleadas para las medidas de DLS y potencial zeta.

## 2.6. Medidas de ángulo de contacto.

Las medidas de ángulo de contacto ( $\theta$ ) son muy interesante desde el punto de vista de la caracterización estructural de superficies, dado que las propiedades de mojabilidad, hidrofiliidad y humectación están directamente relacionadas con la estructura química y la topología superficial. Este parámetro se estudia en función de la energía de Gibbs entre la superficie de la monocapa y una gota de líquido depositada sobre ella. Por tanto, el valor de  $\theta$  depende tanto de la naturaleza de la superficie como de su estructura. Cuando el líquido es agua, las superficies hidrofóbicas se caracterizan por presentar valores altos, mientras que valores pequeños son propios de muestras hidrofílicas. Además, en una superficie hidrofóbica lisa,  $\theta$  aumenta conforme esta se vuelve rugosa.

Geoméricamente,  $\theta$  se define como el ángulo formado por un líquido en el límite trifásico donde confluyen un líquido, un gas y un sólido. En este punto trifásico actúan tres fuerzas diferentes (Esquema 6A). En función de la forma en que se realice la medida, se puede distinguir entre ángulo de contacto estático, dinámico y con corrección de rugosidad. Las medidas experimentales recogidas en este proyecto se realizan en base al primero, al ser la metodología más extendida para determinar ángulos de mojabilidad. Así, el ángulo de contacto estático (es decir, de gota sésil) se mide cuando la gota está asentada en la superficie y el límite trifásico permanece estático, siendo adecuado para evaluar superficies relativamente lisas y homogéneas. Los  $\theta$  estáticos también se utilizan para definir la energía libre superficial (esto es, la tensión superficial del sólido) del sustrato. El  $\theta$  estático ofrece una medición rápida, fácil y cuantitativa de la humectabilidad, basada en la ecuación de Young, que supone que las fuerzas interfaciales son termodinámicamente estables.

Los equipos empleados para medir  $\theta$  se conocen como tensiómetros ópticos. Se componen principalmente de una cámara, un dispensador de gotas, un soporte para la muestra y una fuente de luz. Actualmente, hay disponible una amplia gama de instrumentos, que presentan diferente grado de automatización. En este trabajo se utilizó un tensiómetro óptico Attension Theta (*Biolin Scientific*) equipado con cámara de alta velocidad (420 fps) (Figura 12B). Los parámetros de medida para el cálculo de la energía libre superficial se establecieron empleando el *software OneAttension*, eligiendo el modelo de Young-Laplace para obtener el perfil de gota adecuado.



**Esquema 6.** (A) Tensiones superficiales en una medida de ángulo de contacto. (B) Tensiómetro óptico Attension Theta.

## 2.7. Cromatografía de permeación en gel (GPC).

La importancia de la GPC en la caracterización de polímeros ha ido en aumento desde su aparición en los 60 de la mano de Moore et al. [17]. La garantía y el control de calidad durante la fase de producción y procesamiento han aumentado su importancia en muchos ámbitos de la industria. Así, el conocimiento exacto de los pesos moleculares y su distribución es importante tanto en la investigación de polímeros como en la industria, además de en el ámbito académico.

Otra forma de definir la técnica GPC es como la estrategia empleada para separar cadenas poliméricas individuales en base a su tamaño en disolución, dado que permite medir el peso molecular (MW, *Molecular Weight*) de muestras poliméricas naturales y sintéticas. La distribución de MW es un parámetro determinante en la mayoría de las propiedades físicas de los polímeros. Normalmente, las moléculas poliméricas se encuentran en disolución en conformación de bobina esférica, cuyo tamaño depende del MW. Estas moléculas se analizan introduciéndolas en un eluyente que fluye a través de una columna empacada con perlas porosas. El tamaño de los poros de las perlas es similar al de la cadena polimérica, que puede difundir a través de los mismos. Como resultado, las moléculas más largas eluyen primero ya que no pueden introducirse en muchos poros, mientras que lo contrario sucede con las más pequeñas, que presentan tiempos de retención

mayores. El tamaño de separación usado para calcular el MW de la muestra se determina mediante curvas de calibración que se construyen a partir de polímeros comerciales.

El mecanismo de separación de GPC se basa en el volumen de exclusión, a diferencia de lo que sucede en las cromatografías líquida y gaseosa, basadas en un equilibrio de distribución. Así, la separación conseguida en GPC se debe al volumen hidrodinámico de las moléculas de la muestra [18], que se puede determinar mediante experimentos de dispersión dinámica de luz midiendo el coeficiente de difusión. Es importante destacar que la separación en esta técnica se basa en el tamaño molecular y no es la masa molecular de las moléculas de la muestra.

Sin embargo, los tiempos de retención (o volumen de elución en términos de GPC) no son valores absolutos y no tienen correlación directa con la masa molecular de la muestra examinada; dependiendo de las condiciones de la medida (tipo de polímero, columna y eluyente, entre otros). El cálculo de los pesos molecular promedio en número ( $M_n$ , *Molecular number*) se determina mediante el conocido como método de *slice*, o método de cortes. Así, el pico del eluyente se separa haciendo cortes equidistantes en términos de volumen. A través de la calibración, el volumen de elución se transforma en masa molecular, y su valor debe ser corregido con la pendiente de la curva de calibración.

La distribución de masas,  $w(M)$  puede calcularse a partir de la señal del detector,  $S(V_e)$  y es el parámetro más importante para caracterizar polímeros. Éste se define como:

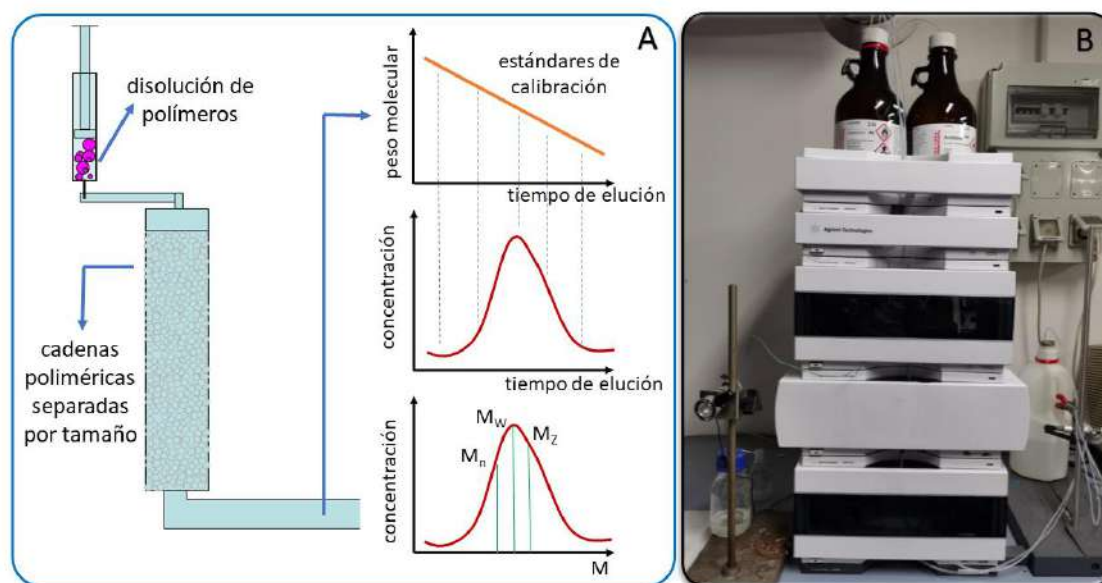
$$w(M) = \frac{dm}{dM} \quad (13)$$

siendo  $m$  la masa total. En función de valores medidos, puede reescribirse como:

$$w(M) \propto \frac{S(V_e)}{M(V_e) \cdot \sigma(V_e)} \quad (14)$$

donde  $S(V_e)$  es la señal del detector y  $\sigma(V_e)$  es la pendiente de la curva de calibración.

En este trabajo se empleó la técnica GPC para determinar el  $M_n$  y la dispersidad ( $\mathcal{D}$ ) de polímeros construidos a partir de monómeros comerciales con basados en etilenglicol mediante la estrategia de síntesis eATRP. Se usó el equipo Agilent 1260 Infinity Gel Permeation Chromatograph, equipado con un detector de índices de refracción (RID) y dos columnas PLgel Mixed-D (300 × 7.5 mm, 5  $\mu$ m) conectadas en serie. El Sistema de columnas se calibró con 12 estándares de poli (metil metacrilato) (PMMA) ( $M_n = 540$  a 210000  $\text{g}\cdot\text{mol}^{-1}$ ). Para el monómero usado en este trabajo, la columna y el detector se termostataron a 70 °C y 50 °C, respectivamente. Como eluyente se empleó una disolución 0.01 M de LiBr en DMF a una velocidad de flujo de 1 mL/min.



**Esquema 7.** (A) Representación esquemática de una medida en GPC. (B) Equipo Agilent 1260 Infinity.

## 2.8. Materiales y análisis de datos.

En todos los experimentos recogidos en este trabajo se ha utilizado agua ultrapura Milli-Q (Barnstead System), con una resistividad mínima de  $18.2 \text{ M}\Omega\cdot\text{cm}$ . El uso de agua no iónica es un factor crítico especialmente en el análisis electroquímico, siendo las técnicas empleadas muy sensibles a la presencia de especies electroactivas, incluso en cantidades del orden de ppm, por lo que deben evitarse.

En los apartados previos se ha hecho referencia al software empleado en cada técnica para el análisis y la interpretación de las medidas experimentales. Además de los citados, el programa de interpretación y representación de datos Origin 7.0 ha sido la herramienta básica empleada en este trabajo.

## 2.9. Bibliografía.

- [1] R.S. Nicholson, I. Shain, Theory of stationary electrode polarography. Single scan, cyclic methods applied to reversible-irreversible kinetic systems, *Analytical Chemistry* 36(4) (1964) 706-723.
- [2] R.P. Janek, W.R. Fawcett, A. Ulman, Impedance spectroscopy of self-assembled monolayers on Au(111): Sodium ferrocyanide charge transfer at modified electrodes, *Langmuir* 14(11) (1998) 3011-3018.
- [3] G. Sauerbrey, Verwendung von schwingquarzen zur wägung dünner schichten und zur mikrowägung, *Z. Phys.* 155(2) (1959) 206-222.
- [4] J. Tarabek, V. Kolivoska, M. Gal, L. Pospisil, M. Valasek, J. Kaminsky, M. Hromadova, Impact of the extended 1,1'-bipyridinium structure on the electron transfer and pi-dimer formation. Spectroelectrochemical and computational study, *J. Phy. Chem. C* 119(32) (2015) 18056-18065.
- [5] Y. Zhou, E.J. Reed, Structural phase stability control of monolayer  $\text{MoTe}_2$  with adsorbed atoms and molecules, *J. Phys. Chem. C* 119(37) (2015) 21674-21680.

- [6] H. Hajova, Z. Kominkova, A. Santidrian, O. Frank, L. Kubac, F. Josefik, M. Kalbac, Preparation and charge-transfer study in a single-walled carbon nanotube functionalized with poly(3,4-ethylenedioxythiophene), *J. Phys. Chem. C* 119(37) (2015) 21538-21546.
- [7] K.E. Silberstein, M.A. Lowe, B. Richards, J. Gao, T. Hanrath, H.D. Abruna, Operando X-ray scattering and spectroscopic analysis of germanium nanowire anodes in lithium ion batteries, *Langmuir* 31(6) (2015) 2028-2035.
- [8] X.H. Liu, J.Y. Huang, In situ TEM electrochemistry of anode materials in lithium ion batteries, *Energ. Environ. Sci.* 4(10) (2011) 3844-3860.
- [9] R. Wen, H.R. Byon, In situ monitoring of the Li-O<sub>2</sub> electrochemical reaction on nanoporous gold using electrochemical AFM, *Chem. Commun.* 50(20) (2014) 2628-2631.
- [10] J. Clavilier, R. Faure, G. Guinet, R. Durand, Preparation of mono-crystalline pt microelectrodes and electrochemical study of the plane surfaces cut in the direction of the (111) and (110) planes, *J. Electroanal. Chem.* 107(1) (1980) 205-209.
- [11] S. Trasatti, O.A. Petrii, Real surface-area measurements in electrochemistry, *Pure Appl. Chem.* 63(5) (1991) 711-734.
- [12] N.Y. Gu, L. Niu, S.J. Dong, Simultaneous determination of both the calibration constant in an electrochemical quartz crystal microbalance and the active surface area of a polycrystalline gold electrode, *Electrochem. Commun.* 2(1) (2000) 48-50.
- [13] P. Hollins, Infrared reflection-absorption spectroscopy, *Encyclopedia of Analytical Chemistry: Applications, Theory and Instrumentation* (2006).
- [14] J. Sharma, B.C. Beard, Fundamentals of X-ray photoelectron spectroscopy (XPS) and its applications to explosives and propellants, *Chemistry and Physics of Energetic Materials*, Springer 1990, pp. 569-585.
- [15] S. Amelinckx, D. Van Dyck, J. Van Landuyt, G. van Tendeloo, *Electron microscopy: principles and fundamentals*, John Wiley & Sons 2008.
- [16] M. Cappelletto, C.A. Capellari, S.H. Pezzin, L.A.F. Coelho, Stokes-Einstein relation for pure simple fluids, *J. Chem. Phys.* 126(22) (2007).
- [17] J.C. Moore, Gel permeation chromatography. 1. New method for molecular weight distribution of high polymers, *J. Polym. Sci. Part A 2(2PA)* (1964) 835-&.
- [18] Z. Grubisic, P. Rempp, H. Benoit, A universal calibration for gel permeation chromatography, *J. Polym. Sci. Pol. Lett.* 5(9PB) (1967) 753-759.





# Capítulo 3. Publicaciones



### 3.1. Artículo 1.

*Caracterización de monocapas autoensambladas de of O-(2-Mercaptoethyl)-O'-methyl-hexa(ethylene glycol) (EG7-SAM) en electrodos de oro.*





## Characterization of a self-assembled monolayer of O-(2-Mercaptoethyl)-O'-methyl-hexa(ethylene glycol) (EG7-SAM) on gold electrodes.

Miriam Chávez, Guadalupe Sánchez-Obrero, Rafael Madueño, José Manuel Sevilla, Manuel Blázquez, Teresa Pineda\*

Department of Physical Chemistry and Applied Thermodynamics, Institute of Fine Chemistry and Nanochemistry, University of Cordoba, Campus Rabanales, Ed. Marie Curie 2<sup>a</sup> Planta, E-14014 Córdoba, Spain.

### Abstract

The modification of surfaces by polyethylene glycol (EG<sub>n</sub>) is an approach used to reduce the antifouling effects of these materials in a biological medium. It has been found that the packing density and conformational order of these molecules in the films are crucial for the inhibition of unspecific protein adsorption. In this work, we present a study of the formation and characterization of a self-assembled monolayer of O-(2-Mercaptoethyl)-O'-methyl-hexa(ethylene glycol) (EG7-SAM) on either poly-oriented or Au(111) single crystal surfaces. The final properties of the formed EG7-SAMs are studied by examining the RD process as well as the electronic and ionic blocking behavior of these layers, under different experimental conditions, by using CV and EIS. Additional information of the structure, composition and organization is obtained by absorption-reflection infrared and X ray photoelectron spectroscopies and contact angle measurements. In contrast to the behavior observed with alkanethiols, the EG7-SAM shows the best final organization at a modification time of 1h. The antifouling properties of this EG7-SAM against the adsorption of the bovine serum albumin protein in a phosphate saline medium, has been evidenced by using the electrochemical quartz crystal microbalance technique.

**Keywords.** Polyethylene glycol, self-assembled monolayer, gold, cyclic voltammetry, electrochemical impedance spectroscopy, infrared spectroscopy, X ray photoelectronic spectroscopy, contact angle measurements, electrochemical quartz crystal microbalance.

## Introduction.

The covalent attachment of poly(ethylene glycol) chains (PEG or EGN, being n the number of EG units) to bioactive substances has been long defined as PEGylation [1] and recently, it has been applied to the modification of nanoparticle surfaces for its use in different fields to induce, on one hand, aqueous solubility, and on the other, to sterically shield nanoparticle surfaces to effectively minimize opsonisation and prolong blood circulation time *in vivo* [2,3]. Although these applications are based in the ability of avoiding protein unspecific adsorption, the factors that influence the interactions and circulation of PEGylated nanoparticles in the biological fluids are numerous and many efforts have been devoted to rationalized them. Molecular weight, surface density and conformation of the PEG chains are the most studied parameters and there is no doubt that is the precise knowledge of how they impact on the systemic administration that will lead to more efficacious products [3-5]. Complementary structural studies of these EG polymer layers on flat surfaces may help in understanding the suppressive effect for protein unspecific adsorption and in the translation to these drug delivery systems to the living systems [6,7].

Self-assembled monolayers (SAMs) of oligo(ethylene glycol) (OEG)-terminated alkanethiols on gold and silver substrates have been widely used to analyse the factors that influence the minimization of protein resistance [8-11] and within the facts responsible for this undesirable phenomenon, steric repulsion, large exclusion volume, rapid mobility of highly hydrated chains, low EG-water interfacial energy and weak interactions with the proteins have been mentioned. Earlier studies [8,12,13] comparing SAMs with short terminal EG segments to that of PEG, focussed on the steric repulsion model that attributes the protein resistance to the balance between this steric repulsion and the attractive forces. The steric repulsion has an elastic component caused by the compression and restriction of the EG segments and an osmotic component due to the loss of water by both the chains and the proteins. As the SAMs with the shorter EG terminal fragments have a more compact structure, the protein resistance was generally attributed to the osmotic component of the steric repulsion model. However, Grunze et al. [10,14] suggest that protein resistance of EG terminated SAMs is a consequence of the stability of the interfacial water layer, which prevent direct contact between the surface and the protein. Moreover, the conformation of the terminal strand contributes to the ability to bind water, being the helical but not the all-trans conformation the one which behaves as amphiphilic with respect to water, increasing the hydrogen bond density, and thus preventing irreversible protein adsorption.

SAMs formed with molecules containing an EG strand closer to the substrate binding and an alkane terminal portion have been used as models for hybrid bilayer membranes to allow for water and/or protein fragments incorporation. Although this hydrophilic spacer

should retain a linear framework and provide a good coverage due to the nearly perfect match between the cross-sectional area of the structures, a less ordered conformation than the alkanethiol portion is expected based on the presence of ether oxygen atoms in the skeleton. However, infrared and ellipsometry data suggest a lamellar-type crystal morphology in an ordered  $7/2$  helical structure oriented normal to the substrate independently of the length of the alkyl group [15,16]. These results make the authors to expect that the EG strands itself can form conformationally well-defined, helical SAMs and studied the conformation and the resistance to protein adsorption of chains that contain only EG units [17,18]. EG6-SAMs assembled on gold from 95 % EtOH solutions show well-ordered  $7/2$  helical conformation, similar to that of the folded chain crystal polymorph of PEG, and a behaviour that approaches to a near ideal capacitor but, when assembled from other solvents, the structure was found more variable and less ordered [18,19]. The EGn-SAMs structures vary with n, being helically ordered for  $n > 4$ , as seen by infrared spectroscopy and EIS data, whereas with less than 6 EG units in the chain, the films are rapidly penetrated by water [16,18,20,21].

The use of EGn films for the development of electrochemical biosensors requires that its interfacial structure allows electron transfer between the electrode and the redox species in solution. There have been many studies in the literature dealing with EGn films of various thickness attached to different electrode surfaces that uses the extent of passivation or permeation of redox pairs to draw information about the film structure and properties [22-24]. These studies focus on the sieving effect of the films as they allow the permeation of the molecules depending on molecular size [22] or the solubility of the redox probes into the film [23,24]. The attachment of thiolated EGn molecules of definite length on gold electrodes can serve as platform to better study these phenomena. In this sense, the studies of Doneux et al. [25,26] using an EG7-SAM on gold and applying electrochemical techniques showed that the film consists of a compact and fairly hydrated single monolayer with a peculiar behaviour that they explain on the basis of the hydration properties of the monolayer as well as the  $[\text{Fe}(\text{CN})_6]^{3-/4-}$  couple.

In the present work, the formation and characterization of a SAM of EG7 on either poly-oriented or single crystal gold electrodes and its behaviour against the unspecific adsorption of proteins employing different experimental techniques are performed. RD processes of the SAMs under different experimental conditions inform about their structural organization and compactness and the studies of the electronic and ionic blocking properties performed by using electrochemical techniques such as CV and EIS in the presence and absence of redox probes, complete this information. More insight on the film's properties are obtained by infrared and XPS spectroscopies and contact angle

measurements. Finally, the possible adsorption of proteins in the EG7-SAM is checked by electrochemical quartz crystal microbalance.

## Experimental section.

### Chemicals.

O-(2-Mercaptoethyl)-O'-methyl-hexa(ethylene glycol) (EG7), Potassium hexaferri-cyanide and potassium hexaferrocyanide ( $[\text{Fe}(\text{CN})_6]^{3-/4-}$ ), ferrocenemethanol and hexaamineruthenium chloride were purchased from Aldrich-Sigma (purity  $\geq 99\%$ ). The rest of the reagents were from Merck analytical grade. All solutions were prepared with deionized ultrapure water produced by Millipore system.

### Experimental Methods.

Electrochemical experiments were performed on an Autolab (Ecochemie model Pgstat30) instrument attached to a PC with proper software (GPES and FRA) for the total control of the experiments and data acquisition. A conventional three electrode cell comprising a platinum coil as counter electrode, a 50 mM KCl calomel (CE 50mM) as reference electrode and either a poly-oriented (po-Au) or a single crystal (111) gold (Au(111)), as the working electrodes, was used. The po-Au electrode was a homemade sphere obtained by melting a gold wire up to reach a diameter of approximately 2 mm and attached to the gold wire that serves as electrode connection. The Au(111) single crystal was from Arrandee™ (based on a 250 nm thick Au layer adhered to a 2.5 nm thin chromium layer deposited on a Borosilicate glass 11 x 11 mm flat surface). Before each experiment, the working electrodes were annealed in a natural gas flame to a light-red melt, cooling in air and then transferred to the electrochemical cell or to the working solutions. The state of the surface conditions was confirmed by cyclic voltammogram shapes taken in 0.01M HClO<sub>4</sub>. This surface treatment was the most appropriate for producing a surface that was clean, ordered, and reproducible. The real area of the gold electrodes was determined from the charge involved in the gold oxide reduction peak obtained under these conditions (A(po-Au) = 0.24 cm<sup>2</sup>).

Electrochemical impedance experiments were recorded in aqueous solutions of KNO<sub>3</sub> 0.1 M in the absence and presence of 1 mM  $[\text{Fe}(\text{CN})_6]^{3-/4-}$ . The later were obtained at the midpoint potential of the CV for the naked electrode, at 0.08 V. The spectra in the absence of the redox couple were recorded at different potentials. The frequency range used in all experiments was from 100 kHz to 0.1 Hz and the pulse amplitude was of 10 mV.



The electrochemical quartz crystal microbalance used was a CHI 400c series. The quartz crystals were covered by a layer of Ti of 100 Å and a layer of polished gold of 1000 Å. These crystals operate at 8 MHz. The mass deposited is obtained by using the Sauerbrey equation by using a calibration constant of 1.4 ng/Hz [27].

Infrared-reflection absorption spectroscopy (IRRAS) was measured by using a JASCO 6300 FTIR single (He-Ne) laser beam spectrometer in the 400-4000  $\text{cm}^{-1}$  wavenumber range, at a resolution of 4  $\text{cm}^{-1}$ . Spectra Manager software was employed for data collection and analysis. A Pike Technologies-VeeMAX™, variable angle specular reflectance accessory was used. Before measurements, the interferometer and sample compartment were purged with a flux of dry air of 8 l/min for half an hour. This flux was supplied by a compressed air adsorption dryer (K-MT LAB, Parker/Zandet GmbH&Co.KG). To record IRRAS spectra, Au-modified substrates were placed on a mask platform with an aperture of 10 mm in diameter to define the position and sampling dimensions where the beam spot was collimated. A p-polarized laser beam at a grazing angle of 80° was selected to interact with the sample surface for enhancement of the IR signals collected by the instrument MCT-detector.

XPS analysis was performed using an MCD SPECS Phoibos 150 spectrometer (from the Servicio Central de Apoyo a la Investigación (SCAI) of the Universidad de Cordoba) employing non-monochromatized (12 kV, 300 W) Mg K $\alpha$  radiation (1253.6 eV). The substrate, either clean or modified, was mounted on a steel sample holder and transferred to the XPS analytical chamber. The working pressure was less than  $5 \cdot 10^{-9}$  Pa. The spectra were collected using a take-off angle of 45° respect to the sample surface plane. The spectrometer was calibrated by the binding energy (BE) of the Au 4f $_{7/2}$  line at 84.0 eV. The standard deviation for the BE values was 0.2 eV. Survey scans were run in the 0-1100 eV range (pass energy 60 eV), and higher resolution scans were recorded for the C 1s, O 1s and S 2p regions. The analysis involved Shirley background subtraction, and whenever necessary, spectral deconvolution was carried out by nonlinear least-squares curve fitting adopting a Gaussian sum function, employing the software CASA-XPS.

Contact Angle (CA) Measurements were conducted by using an Optical Tensiometer Theta T200 device (Attension, Biolin Scientific) equipped with a high-speed camera (420 fps). The CA of the formed SAMs were measured in sessile drop method. The experiments were performed at room temperature and at open atmosphere. The results are given as an average of six measurements.

### Formation of the EG7-SAM.

The SAMs were formed by contacting the gold substrates with 1.0 mM EG7 EtOH solutions for the desired modification time. After the immersion time, the modified

electrode was thoroughly washed with EtOH and water and then drying under a nitrogen stream. The po-Au electrode was used in all the electrochemical experiments, unless otherwise stated and the Au(111) single crystal for IRRAS, XPS and Contact Angle measurements.

## Results and discussion

### Electrochemical characterization of the EG7-SAMs formed at different immersion times.

The RD process monitored by CV has long been used to inform about properties related to film stability and compactness, as well as to the suitability for the SAM preparation methods. We carried out preliminary experiments involving the evaluation of the influence of modification time in the SAMs properties. Figure 1 shows a set of CVs recorded with the freshly prepared EG7-SAMs in the potential range from  $-0.50$  to  $-1.30$  V, in KOH 0.1 M solutions. The EG7-SAM-Au substrates are removed from the formation solution (1 mM EG7 in EtOH), and subsequently washed and immersed in the working solution under potential controlled conditions (at  $-0.5$  V). When the current density at this potential becomes constant, the CVs are recorded. As a general behaviour, all the curves present a well visible although small peak (peak I) at higher potentials, and a last very intense peak (peak III) at lower potentials, that show some kind of fine structure that also changes with modification time (peak IV). Moreover, a small signal between these peaks (peak II) is observed. The peak potentials do not significantly vary at modification times lower than 1 h (Figure 1 b). At larger modification times the lower resolution of these peaks does not allow to draw a clear conclusion about its nature and will not be further commented.

The presence of well-defined peaks in the CVs for the RD process obtained at po-Au electrodes has been related to the breakage of the S-Au bond from gold facets of different crystalline orientations, from which at least the low-index facets Au(111), (100) and (110) have been clearly identified in SAMs formed at po-Au electrodes [28-32]. The direct relationship of the desorption potentials with the  $pzc$  for the different facets of the naked electrode would mean that the process is only governed by the interfacial electric field. However, the values of  $E_p - E_{pzc}$  are found to vary for the different facets and SAMs chemical composition being the existence of lateral attractive forces one of the main factors that affect this discrepancy. These lateral interactions also depend on the surface structure, including not only the type of facet but also the surface roughness [32]. Moreover, multiwave responses in RD processes carried out in smooth surfaces have been interpreted as the existence of domains of different sizes that desorb at different potentials due to variation in

cohesive interactions between chains as well as in permeability to counterions and solvent [33].

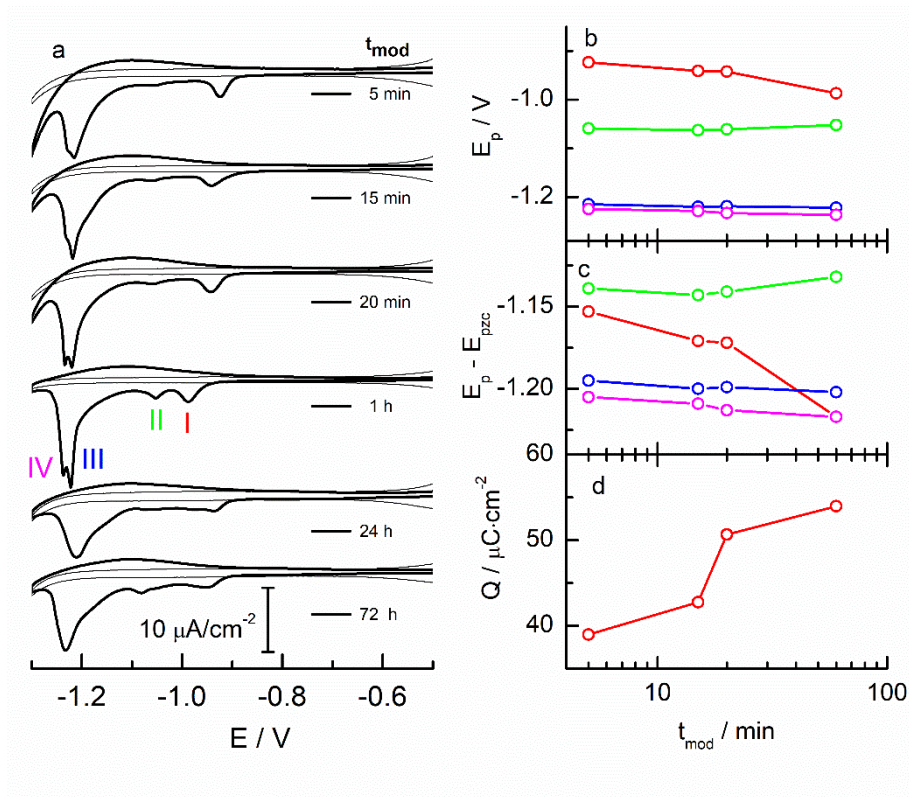


**Figure 1.** (a) CVs for the RD process of the EG7-SAM-po-Au formed at different modification times. The CVs are obtained in KOH 0.1 M; scan rate: 0.02 V/s (the thick and thin lines in each case correspond to the EG7-SAM and naked electrode, respectively); Plots of (b) peak potentials,  $E_p$ , (c)  $E_p - E_{pzc}$  and (d) the overall charge densities of the RD peaks as a function of modification time.

We have plotted  $E_p - E_{pzc}$  values at the different modification times for all the peaks obtained (Figure 1c) and the results show that all the peaks get closer in an interval of 60 mV ( $E_{pzc}$  values applied are +0.23, +0.08 and -0.02 V for (111), (100) and (110) facets of gold, respectively, that correspond to values measured in 10 mM  $\text{HClO}_4$  [32,34]). However, it is well known that the presence of the SAM on the electrode surface leads to large shifts on the  $E_{pzc}$  that depend on the surface coverage, the adsorption/desorption of ions and the surface dipole of the monolayer [35]. In the present analysis, the only object to subtract  $E_{pzc}$  values to the peak potentials is to see if these normalized values are only influenced for the gold facet where they were grown up or, on the contrary, there is additional phenomena playing a role in the occurrence of the peaks [36]. These results would indicate that peaks I and III/IV correspond to domains of molecules desorbed from the (111) and (110) facets, respectively, and that the fine structure observed (peaks III/IV) should be ascribed to the existence of domains with different lateral interactions. .

We have checked the surface recognition phenomenon by building an EG7-SAM on an Au(111) single crystal electrode and the results are plotted in Figure 2. As it can be observed, the unique peak shown at the Au(111) electrode at -0.99 V, coincides in potential with the peak I for the RD obtained at the po-Au electrode, confirming our hypothesis. Thus, influences of lateral interactions in the RD potential values for the molecules in these domains cannot be discarded.

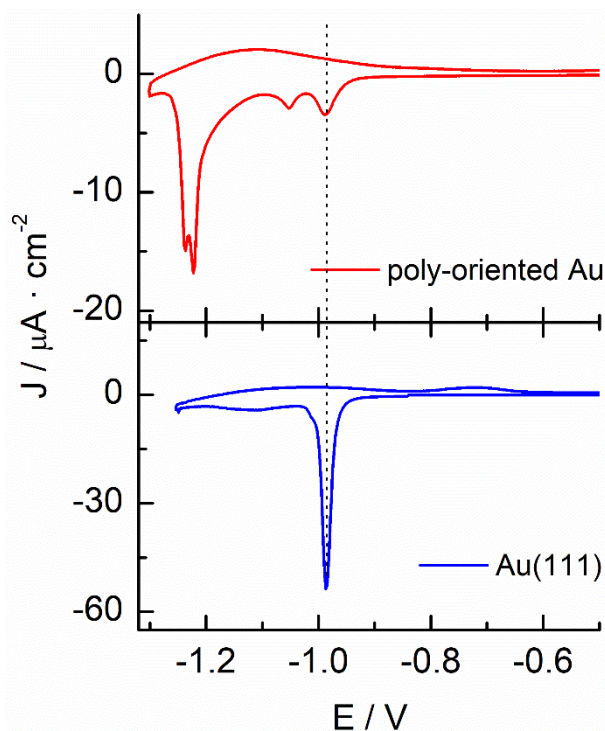
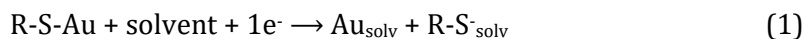


**Figure 2.** CVs for the RD process of the EG7-SAM formed in two different gold substrates at a modification time of 1 h, in KOH 0.1 M. Scan rate: 0.02 V/s.

The information on SAMs surface coverage based on RD processes is based in the widely accepted reaction [36-38],



where  $\text{Au}_{\text{solv}}$  and  $\text{R-S}_{\text{solv}}$  stand for the solvated thiolate and gold surface, respectively. This equation is a solvent substitution reaction that gives a chemical description of the initial and final states of the process and takes into account the energetic contributions involved in SAMs RD such as substrate-adsorbate, SAM-solvent, lateral interactions, substrate-solvent and surfactant solvation [32,36]. In this sense, the charge density,  $Q$ , should contain not only the faradaic charge due to the RD but also the double layer charging contribution. Moreover, it has been pointed out that although we use the reaction (1) to account for the RD process, the charge flowing to the interface per desorbed molecule is not an integer equal to the number of electron transferred from metal to the molecule but, this value depends on

electrode potential and the nature of the supporting electrolyte [39]. Thus, as an approximate tool, we measure the charge involved in the RD CVs of Figure 1 and the results are shown in Figure 1d. The charge densities obtained increase with modification time up to 1h and then, remain constant. Independent of the absolute values obtained, it can be said that the EG7 formed at shorter times should correspond to a sub-monolayer while at higher times, a saturated coverage is obtained. It is interesting to note that in the time interval of 20 to 60 min the EG7-SAM suffers a reductive process with well resolved peaks that loose resolution upon increasing modification time. If we accept that the presence of resolved peaks is related with the presence of domains with a preferential organization, it can be concluded that when the modification time is of 1h, the monolayer have reached the maximum charge density, that is, its maximum coverage, and the higher organization in domains. A roughly calculation of the surface coverage  $\Gamma$ , by taking into account the charge density obtained under this condition, gives us a value of  $5.7 \times 10^{-10} \text{ mol}\cdot\text{cm}^{-2}$  and an area per EG7 molecule of  $29 \pm 1 \text{ \AA}^2$ . A cross sectional area of  $21.38 \text{ \AA}^2/\text{EG}$  chain has been determined based on the X-ray unit cell dimensions of the crystalline polymer, and is presumed to be achieved for the alkylated EGN SAMs where the EG strands acquire the helical conformation [15], is not observed in the present system. This larger fingerprint of the EG7 molecules must be due to a lower compactness of the layer, probably due to the existence of a larger conformational freedom in the absence of alkyl chains in the molecules.

To get more insight into the properties, the following potential programs were applied to the EG7-SAM. First, the modified electrode is contacted with the alkaline solution at the initial potential (-0.4 V) and the scan to negative direction is initiated up to values where the complete monolayer is reductively desorbed. Then, the potential is scanned to positive values including the gold surface oxidation region and ended after scanning to negative values to the initial potential (Figure 3). Comparing to the blank profile, the EG7-SAM modified electrode shows, besides the RD peaks already commented, a small current density broad peak in the anodic frame (at -1.135 V) that could be ascribed to a partial re-adsorption of the desorbed EG7 molecules in the cathodic scan probably giving place to a sub-monolayer coverage that, however, does not affect in great extension the oxidation of the gold surface as the anodic peak at higher potentials almost coincides with that of the clean electrode. Second, the freshly modified electrode is now submitted to a potential scan in the positive direction to investigate if the presence of the EG7-SAM passivates the gold surface against oxidation. In fact, the CV shows that the onset for surface oxidation is displaced more than 250 mV in the presence of the monolayer (blue double arrow in the CV). At around 0.275 V, a burst of oxidation current is observed that should correspond to the oxidative desorption of the monolayer concomitant with the oxidation of the gold

surface. In the reverse scan, when the potential reaches the values for the RD, a small signal coinciding with the lowest potential peak obtained for the direct RD process is observed.

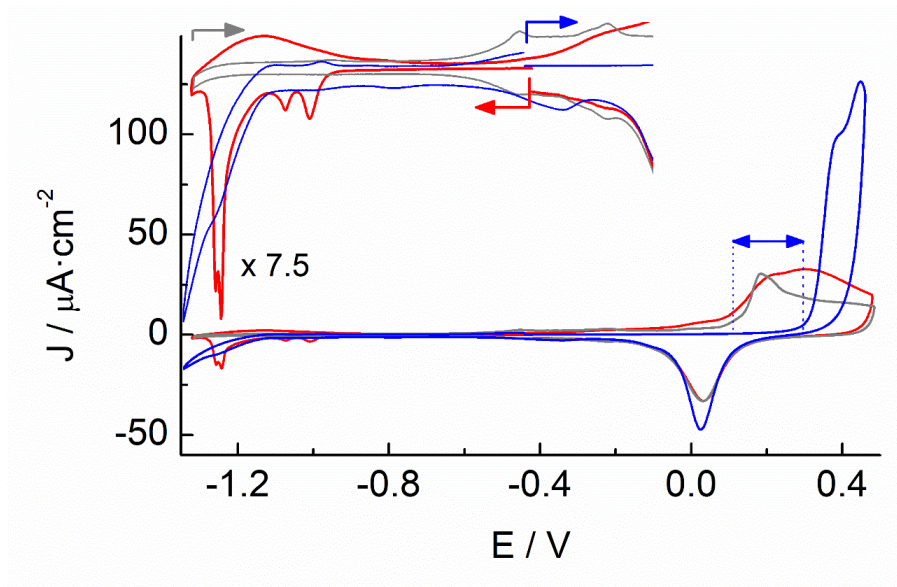


**Figure 3.** CVs for the reductive (red line) and oxidative (blue line) desorption processes of the EG7-SAM-Au, formed at a modification time of 1 hour. KOH 0.1 M, scan rate: 0.02 V/s. The grey curve represents the electrochemical profile for the naked gold electrode in the same medium. The inset shows an expanded view (in the Y axis direction) of the double layer region for the three curves showing coloured arrows to signal the direction of the scans and the trends of the current densities obtained.

### Blocking behaviour of EG7-SAM.

The EG7-SAM can be further characterized by analysing the effect on the heterogeneous electron transfer rate of some redox couples such as  $[\text{Fe}(\text{CN})_6]^{3-/4-}$ ,  $[\text{Ru}(\text{NH}_3)_6]^{3+/2+}$ ,  $\text{Fc}(\text{MeOH})_2^{0/+}$ . Whereas the CVs for  $[\text{Ru}(\text{NH}_3)_6]^{3+/2+}$  and  $\text{Fc}(\text{MeOH})_2^{0/+}$  redox probes are insensitive to the presence of the molecular layer (data not shown), that of  $[\text{Fe}(\text{CN})_6]^{3-/4-}$  shows important changes when compared to the naked electrode (Figure 4a). It can be observed that the electrochemical signal is completely suppressed when the EG7-SAM is present. Only a very small current density can be measured (see expanded view of the CVs in the insert) as it is typical for good blocking behaviour. However, the inhibition seems to be slightly weaker at immersion times higher than 1 h. The impedance data (Figure 4b) show the same trend, with a decrease in the diameter of the semicircle as the modification time increases. Under these experimental conditions, only the semicircle is seen, whereas the linear portion of the impedance spectrum is absent, indicating absence of diffusion.

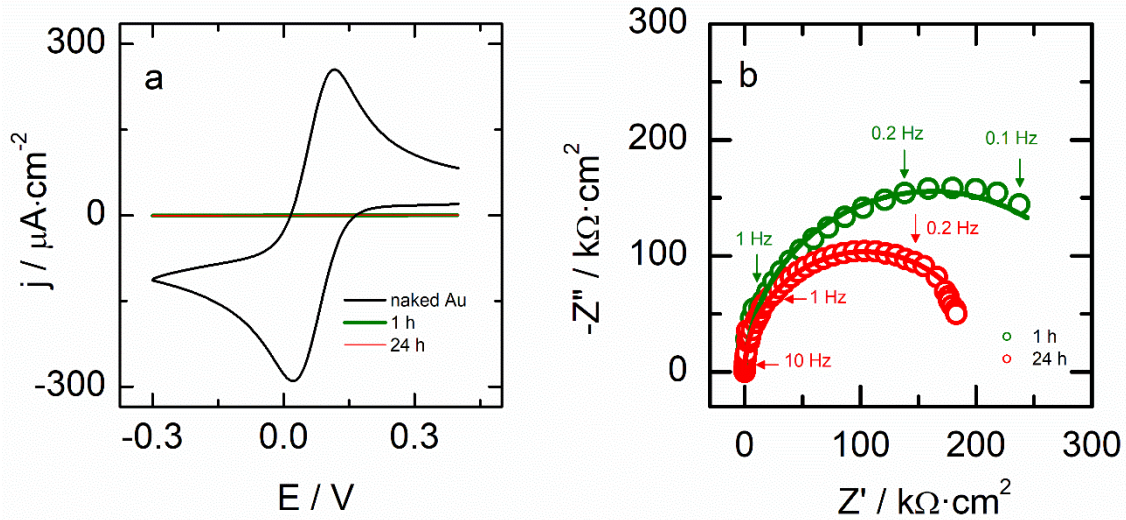


**Figure 4.** (a) CVs and (b) impedance spectra of 1 mM  $[\text{Fe}(\text{CN})_6]^{3-/4-}$  in  $\text{KNO}_3$  0.1 M in a naked and EG7-SAM po-Au electrode at different times of modification; scan rate for CVs is 0.1 V/s; the impedance spectra are recorded at the midpoint of the CV: 0.08 V. Some frequency values are indicated. Green and red open circles represent the experimental data and solid green and red lines are the best fits obtained by using a simplified Randles equivalent circuit, for the impedance spectra recorded for the EG7-SAM prepared at 1 and 24 h modification time, respectively.

Recently, Whitesides et al. [40] have examined the phenomenon of charge transport by tunnelling across SAMs of EGn of different chain lengths and have found that the attenuation factor  $\beta$  across these SAMs is much lower ( $\beta(\text{EGn}) = 0.29 \pm 0.02 \cdot n_{\text{atom}}^{-1}$ ) than the observed with alkanethiolates. If the exponential decrease with the chain length of the EG7 chain, with a tunnelling factor of  $\beta = 0.29$  per atom unit in the chain,  $d$ , is taken into account (equation 2), the apparent electron transfer rate constant,  $k_{\text{ap}}$ , obtained would be of around  $6.5 \cdot 10^{-5} \text{ cm} \cdot \text{s}^{-1}$  for a tunnelling transport mechanism by using a  $k_0$  value of 0.033 cm/s [211].

$$k_{\text{ap}} = k_0 \cdot e^{-\beta \cdot d} \quad (2)$$

The impedance spectra have been fitted by using a simplified Randles circuit (without Warburg element, as the spectra do not show diffusion features) and the charge transfer resistances have been obtained. From these data,  $k_{\text{ap}}$  values can be obtained by using equation (3):

$$k_{\text{ap}} = \frac{RT}{n^2 \cdot F^2 \cdot R_{\text{ct}} \cdot A \cdot c} \quad (3)$$

where  $R$  is the gas constant,  $T$  the temperature,  $F$  the Faraday constant,  $n$  the number of electrons,  $A$  the geometric area of the electrode and  $c$  the concentration of the redox pair. The  $k_{\text{ap}}$  values obtained for the EG7-SAMs formed at 1 and 24h modification time, are  $4.4 \cdot 10^{-7}$  and  $6.4 \cdot 10^{-7} \text{ cm} \cdot \text{s}^{-1}$ , respectively, that are much lower than the above given value based on the tunnelling mechanism. Although the occurrence of such a mechanism cannot be

discarded under these conditions, an additional concomitant effect must take place that produces this strong blockage of the ferricyanide redox probe by the EG7-SAM. This behaviour has already been described for this system by Doneux et al. [25,26], that investigated the heterogeneous electron transfer processes of different redox probes either positive, neutral, or negatively charged, across EG7-SAMs built on a polycrystalline gold electrode. They found that, as we also report in the present work, only the ferricyanide redox probe is affected, being its signal completely suppressed in the presence of an EG7-SAM. In an elegant approach, they demonstrated that this electron transfer inhibition is not due to a simple size or solubility driven permeation issue and recall the fact that the  $[\text{Fe}(\text{CN})_6]^{3-/4-}$  system is not an ideal outer-sphere redox couple. In contrast, they connect this behaviour to the impact of water molecules that play an important role in the change of the hydration shells of the oxidized and reduced form of this molecule, together with the reduced mobility of the water molecules in the EG7-SAM interface [42,43].

Now, the electrical properties of SAMs involve not only electronic but also ionic modes of conduction. The ionic insulating properties of n-alkanethiol SAMs have been largely studied employing EIS, in the absence of redox probes, as a way to test if the SAMs behave as an ideal parallel capacitor Helmholtz model either as a function of the applied potential or the medium chemical composition. In the present work, we have carried out impedance measurements as a function of the applied potential under the same experimental conditions of the experiments described in Figure 4 except that the redox probe was not present. The impedance spectra are represented as Bode phase plots to examine the values of the phase angle at low frequencies (c.a. 1 Hz) that is taken as a measure of the ideal capacitor system behaviour [44-46]. Figure 5a shows the variation of the phase angle values at 1 Hz with the applied potential for the EG7-SAM and for the naked gold electrodes. The CVs taken in the potential range of the electrochemical profile for the gold electrode in this media for the naked and the EG7-SAM modified electrodes are also shown (Figure 5b). The CVs for the reductive and the oxidative desorption included are obtained by starting the scan at -0.15 V and scanning in the negative or positive directions, respectively, using two different freshly prepared EG7-SAMs to see the stability potential range. The double layer capacitance,  $C_{dl}$ , has been recorded under the same experimental conditions and the results are plotted together with the values obtained from the fitting of the impedance spectra taken as a function of potential (by using a RC circuit, where R is the solution resistance and C the capacitance and adding a parallel R element when necessary to account for the ionic resistance). The potential interval where the  $C_{dl}$  values are almost constant ( $\sim 4.3 \pm 0.1 \mu\text{F}/\text{cm}^2$ ) and is almost coincident with that of constant current in the CV. In this way, we can evaluate the potential range of film stability and compare it with the data of phase angle



obtained. It is interesting to highlight that the phase angle approximately reaches the highest value of  $90^\circ$ , in a wide frequency range (see insert of Figure 5a) and that this behaviour is maintained in the potential interval that coincides with the stability of the film and with that where the ferricyanide probe is monitored (Figure 4). This behaviour agrees with results of EGN-SAMs studied by EIS under somewhat different experimental conditions (0.1 M potassium phosphate + 0.2 M potassium chloride) that show that the EG chains contact with nearest neighbours leaving little room for nonhelical conformations or penetration of solvent and/or ions [17-19].

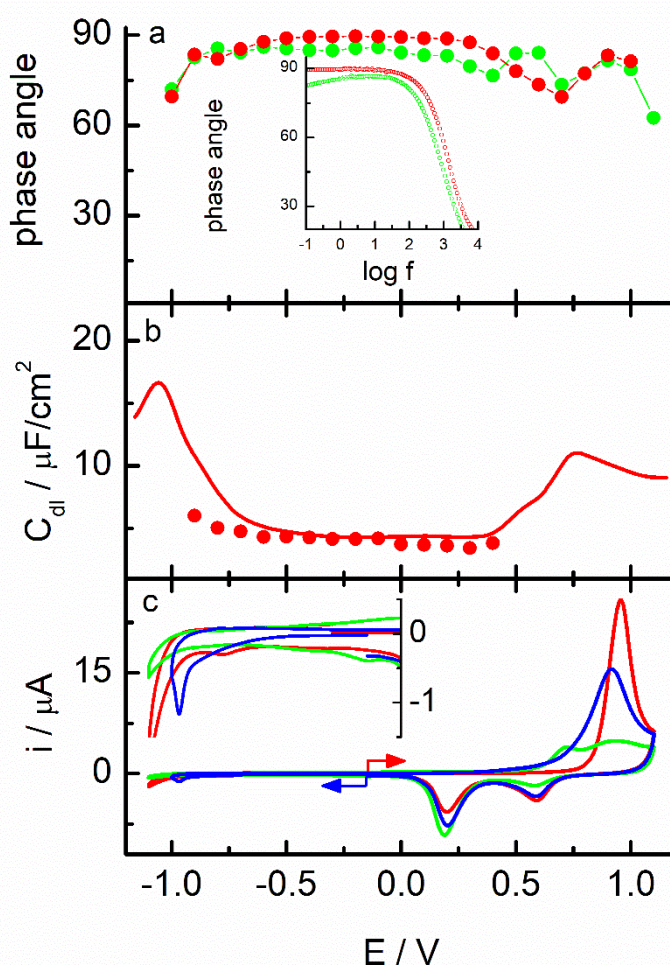


**Figure 5.** Insulating properties of the EG7-SAM gold electrode in  $\text{KNO}_3$  0.1M. (a) Phase angles taken at the frequency of 1 Hz for the naked (solid green circle) and EG7-SAM (solid red circle) electrodes as a function of potential. Insert: Bode plots obtained at  $-0.1$  V for the naked (green) and EG7-SAM (red) electrodes. (b) Double layer capacitance against potential recorded at a frequency of 500 Hz (solid red line) and capacitance values taken from the fitting of the impedance spectra (solid red circle). (c) CVs of the naked (green) and EG7-SAM gold electrodes recorded in the negative (blue) and positive (red) potential direction; scan rate: 0.02 V/s. Insert: enlarged view of the RD potential range.

These results together, allow us to conclude that the EG7-SAM have good blocking properties against electronic and ionic events in the potential range of SAM stability under neutral pH conditions.

### Infrared characterization of EG7-SAMs.

Infrared spectroscopy is one the most used techniques for the characterization of the EGn films and the assignation of the peaks for the different adopted structures of the chains within the SAMs is already well known [10,17-21,47-49]. One of the most addressed points has been the determination of the structural organization of the EGn chains in the films, as the helical conformation has been found to be less resistant to protein adsorption in comparison to the all-trans or disordered SAMs [17].

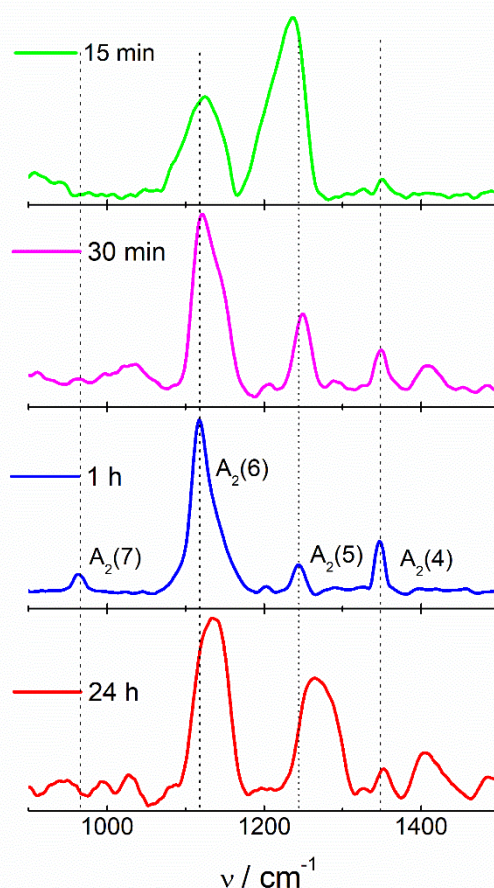


**Figure 6.** IRRAS spectra of the EG7-SAMs formed at different modification times on Au(111) single crystal surfaces recorded in the fingerprint region.

Figure 6 shows IRRAS of EG7-SAMs formed at different modification times on Au (111) single crystal surfaces. The fingerprint region has been used to prove the helical structure that it is characterized by the presence of a series of peaks at 1347, 1244, 1118 y 964  $\text{cm}^{-1}$  which belong to vibration modes parallel to the helix axis ( $A_2(4)$  to (7)) for a 7/2

helical axis structure in a normal orientation to the substrate and the absence of signals at 1360, 1280, 1234, 1149, 1116, 1061, 947 y 843  $\text{cm}^{-1}$ , related to vibration modes perpendicular to the chain axis ( $E_1(8)$  to (15)) [50]. As it can be observed in Figure 6, the EG7-SAM formed in 15 min shows two broad signals at 1124 and 1237  $\text{cm}^{-1}$ , and a well-defined but small peak at 1351  $\text{cm}^{-1}$ . These broad peaks should contain more than one single component corresponding to different modes of chain organization within the layer, either parallel or perpendicular vibration modes. At a modification time of 30 min, the peaks become narrower and new peaks emerge, which match with the different vibration's modes of the EG chains in a helical conformation. Upon increasing modification time to 1 h, the typical spectrum for the 7/2 helical structure is obtained. However, at larger modification times, the typical fingerprint disappears indicating that the structure gets less ordered, as it can be inferred from the broadening of the peaks.

The signals obtained for the EG7-SAM prepared in 1 h coincide with these of the well-ordered helical structure described for H- and  $\text{CH}_3$ -terminated EGn-SAMs, in particular, asymmetric COC-stretching +  $\text{CH}_2$ -rocking, asymmetric COC-stretching,  $\text{CH}_2$ -twisting,  $\text{CH}_2$ -wagging and  $\text{CH}_2$ -bending vibrations at 965, 1119, 1243, 1347 and 1462  $\text{cm}^{-1}$ , respectively [221, 222]. These findings agree with the electrochemical results that indicate that the optimum modification time for this EG7-SAM is of 1 h and indicate that the adopted conformation is the helical.

### Contact Angle Measurements.

Water contact angle measurements inform on the hydrophilic / hydrophobic character of the surfaces. We have measured the water contact angles of the EG7-SAMs formed at different modification times. The obtained values are gathered in Table 1. If the structure of the EG7 chain used in this study is considered, the contact angles must be sensitive to the organization of these molecules. Thus, the terminal methyl group, if exposed, will give a hydrophobic character to the layer in contrast to the possibility that they can be hidden in a disorganized structure. In fact, the EG7-SAM formed at 15 min shows a contact angle of  $49^\circ$  that increases up to values higher than  $60^\circ$  for the SAMs formed at longer times. Although higher values have been measured for similar structures [17], the observed increase is an indication of the exposure of the methyl terminal groups to the external SAM face.

**Table 1.** Water contact angles of EG7-SAMs at different modification times (standard deviations  $\pm 1^\circ$ )

Modification time	EG7-SAM-Au / $\theta_{(H_2O)}$
0	67
15 min	49
30 min	59
1 h	64
24 h	63

### XPS qualitative/quantitative characterization of t-OEG7.

To get more insight into the composition of the EG7-SAM formed on a gold electrode, we have carried out XPS experiments. The spectra show peaks corresponding to S 2p, C 1s and O 1s that can be obtained in high resolution as shown in Figure 7. The S 2p spectrum is dominated by a strong peak at 162.0 eV that can be deconvoluted by two S 2p<sub>3/2,1/2</sub> doublets characteristics of thiolate species bound to gold (161.8 and 163.0 eV) and free thiol or disulphur groups (163.8 and 165.0 eV), the first one representing an area higher than 80 % of the overall signal. This fact points to the preferent adsorption of the EG7 molecules to the gold surface via S-Au bonds [10,53-59]. The C 1s spectrum exhibits three components peaks at 284.6, 286.2 and 287.5 eV. The strongest peak at 286.2 eV is associated with the ether carbon atoms in the EG segments [60]. The O 1s spectrum also shows three components at 531.5, 532.6 and 533.7 eV. Similarly, the peak at 532.6 eV that represents the biggest contribution corresponds to the oxygen atoms in the EG segments.

The EG7-SAM characterized in this study is prepared from EG7 EtOH solutions. Thus, no water molecules are expected to be adsorbed in the SAM. However, EtOH molecules can be entrapped within the layer even after the just-prepared specimens are dried with a nitrogen stream. Thus, the extra peaks in the C 1s and O 1s signals can be due, on one side to molecules or fragments of EtOH [61] or to adventitious carbons coming from impurities within the SAMs.

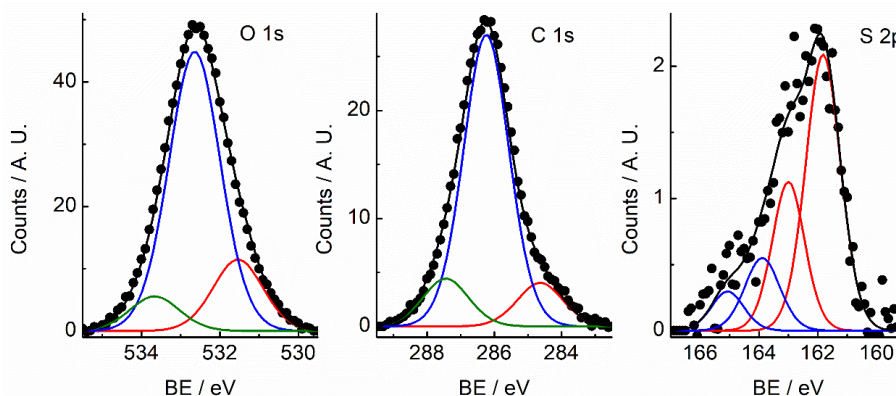


**Figure 7.** XPS spectra of the EG7-SAM gold electrode. The layer has been formed from an ethanolic solution in a modification time of 1 h. After modification, the modified substrate was dried with a nitrogen stream and subsequently maintained in a closed vial up to introduction in the vacuum XPS chamber.

### Adsorption of bovine serum albumin (BSA) on the EG7-SAM.

To ascertain if the EG7-SAM formed on gold, under the experimental conditions described in this work, suffers unspecific adsorption of proteins, we have used the electrochemical quartz crystal microbalance to analyse the behaviour upon contacting with a solution of the protein bovine serum albumin (BSA). Figure 8 shows the CV curves for the RD process of the as-prepared EG7-SAM and that after contacting with a solution of 10  $\mu\text{M}$  BSA for a long period of time (c.a., 2 hour), together with the frequency changes accompanying the electrochemical process.

The mass change accompanying the complete release of an EG7-SAM is of around 40 ng, if the packing density of the EG7 molecules is taken as the fingerprint of 29  $\text{\AA}^2$  per EG7 molecule determined above. The experimental mass change for the RD of the as-prepared SAM is of 29-30 ng. This value is close to the theoretical expected although, it cannot be ignored that this value can have some influences of the interfacial changes occurring simultaneously with the RD process. These processes include not only the replacement of the EG7 by water or electrolyte molecules [62] but also, the concomitant desorption of the water molecules co-adsorbed within the EG7-SAM [63]. The RD process is initiated after the frequency is equilibrated at the initial potential and as it can be observed, the value is kept constant up to the values where the desorption starts. At this point, coinciding with the voltammetric desorption peak, an abrupt increase in frequency, describing a sigmoidal shape, is observed. At lower potentials, the frequency slightly increases up to reaching a plateau. The traces obtained for the desorption of the EG7-SAM after being exposed to the protein BSA shows a similar shape with a total frequency change that equals this of the as-prepared SAM.

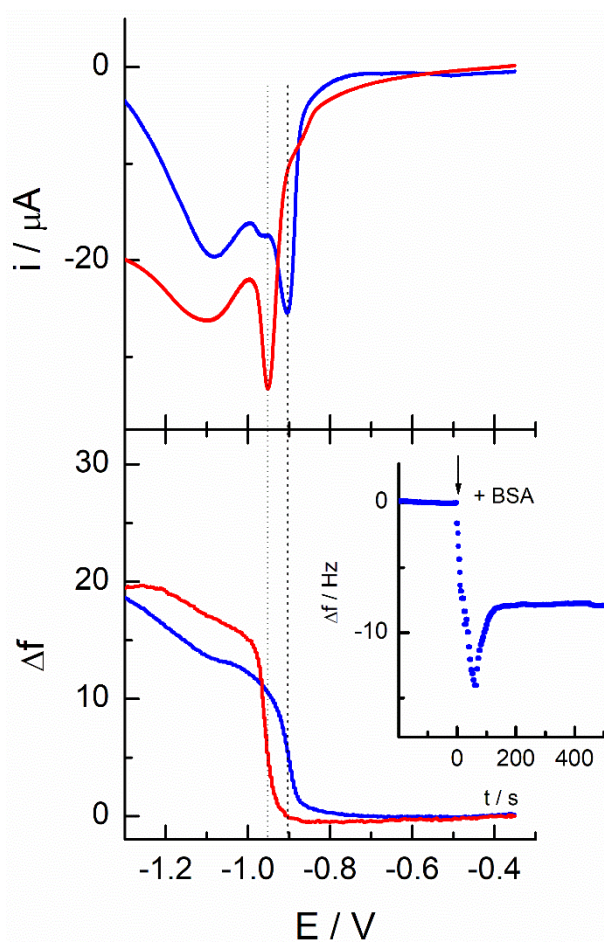


**Figure 8.** Electrochemical quartz crystal microbalance study of the RD process of an EG7-SAM on gold electrode, (red line) as-prepared and (blue line) after contacting with a BSA solution for 2 h. Inset: Changes in frequency of a EG7-SAM modified gold-quartz crystal upon introducing 10  $\mu\text{M}$  BSA solution in sodium phosphate buffer at pH 7.4.

The only found difference is that the RD takes place at around 50 mV higher potential. This is indicative of a decrease in the stability of the layer during the exposure to the protein solution, probably due to the interaction of some protein molecules that, in some way, disturbs the compactness of the layer. Moreover, the equivalence in the mass changes that accompany the desorption is an indication of the absence of adsorbed protein on the EG7-SAM. The insert of Figure 8 shows the frequency trace obtained when, after the SAM is equilibrated with a phosphate saline solution at pH 7.4, the BSA protein is added to this solution. At this point (marked with the arrow in Figure 8), the frequency suddenly decreases and after 1 min, starts increasing up to reach a constant value. The total frequency decrease accounts for a mass increase of 11-12 ng that supposes less than 10% of a BSA monolayer. Taking together this small value and the fact that this excess of mass is not monitored in the RD of the EG7-SAM, we think that the protein molecules are weakly adsorbed, if it does, and get released when the substrate is contacted with the solution used to carry out the RD process [69].

## Conclusions.

The EG7-SAM formed on a gold electrode from an ethanolic solution reaches a helical conformation at a modification time of 1 h. At longer times, the layer seems to acquire some disorganization, probably by the introduction of solvent molecules in the film structure. RD, IRRAS and contact angle measurements agree with this observation. While the RD shows well defined peaks that could be ascribed to ordered domains localized in different facets of the poly-oriented gold electrode, the IRRAS spectra taken in the fingerprint region show that the films prepared at modification times within 30 min and 1 h have the characteristic peaks of a helical conformation. The disorder obtained at longer times is, however, not translated to the contact angle values that keep constant under these conditions indicating that the disorganization of the helical conformation does not affect the terminal face of the film.

The compactness of the EG7-SAM is lower than that found in the EG<sub>n</sub>-alkanethiol terminated SAMs that show a fingerprint closer to these of the pure alkanethiol, probably forced by the presence of the long alkane chain that acts as an arm anchoring to the gold surface. However, the EG7-SAM formed in the present work exhibits good blocking properties against the ferrocyanide redox probe as well as good ionic insulating properties in neutral aqueous saline solutions.

Finally, the EG7-SAM prepared from EtOH solution with 1 h of immersion time resists the adsorption of the BSA protein as monitored by the quartz crystal microbalance. The mass change obtained after 2 h of contact with the BSA solution corresponds to less than 10 % of a BSA monolayer. However, when the protein solution is removed, the few adsorbed proteins are released, as it is demonstrated in the mass changes accompanying the RD process of the EG7-SAM recorded for a pristine and a SAM substrate submitted to protein adsorption. This is a confirmation of the weak strength of the protein adsorption phenomena in the EG7-SAM obtained under these experimental conditions.

*Acknowledgments.* We thank the Ministerio de Ciencia e Innovación (Project RED2018-102412-T Network of Excellence Electrochemical Sensors and Biosensors), Junta de Andalucía and Universidad de Córdoba (UCO-FEDER-2018: ref. 1265074-2B and Plan Propio, Submod. 1.2. P.P. 2019) for financial support of this work. M.C. acknowledges Ministerio de Universidades for FPU 17/03873 grant.

## References.

- [1] A. Abuchowski, J.R. McCoy, N.C. Palczuk, T. van Es, F.F. Davis, Effect of covalent attachment of polyethylene glycol on immunogenicity and circulating life of bovine liver catalase, *J. Biol. Chem.* 252(11) (1977) 3582-3586.
- [2] L. Kong, F. Campbell, A. Kros, DePEGylation strategies to increase cancer nanomedicine efficacy, *Nanoscale Horiz.* 4(2) (2019) 378-387.
- [3] Z. Hussain, S. Khan, M. Imran, M. Sohail, S.W.A. Shah, M. de Matas, PEGylation: a promising strategy to overcome challenges to cancer-targeted nanomedicines: a review of challenges to clinical transition and promising resolution, *Drug Deliv. Transl. Res.* 9(3) (2019) 721-734.
- [4] J.S. Suk, Q. Xu, N. Kim, J. Hanes, L.M. Ensign, PEGylation as a strategy for improving nanoparticle-based drug and gene delivery, *Adv. Drug Deliver. Rev.* 99 (2016) 28-51.
- [5] J.V. Jokerst, T. Lobovkina, R.N. Zare, S.S. Gambhir, Nanoparticle PEGylation for imaging and therapy, *Nanomedicine* 6(4) (2011) 715-728.
- [6] M. Tanaka, T. Sawaguchi, Y. Hirata, O. Niwa, K. Tawa, C. Sasakawa, K. Kuraoka, Properties of modified surface for biosensing interface, *J. Colloid Inter. Sci.* 497 (2017) 309-316.
- [7] R. Ortiz, S. Olsen, E. Thormann, Salt-Induced Control of the Grafting Density in Poly(ethylene glycol) Brush Layers by a Grafting-to Approach, *Langmuir* 34(15) (2018) 4455-4464.
- [8] K.L. Prime, G.M. Whitesides, Adsorption of Proteins onto Surfaces Containing End-Attached Oligo(Ethylene Oxide) - A Model System Using Self-Assembled Monolayers, *J. Am. Chem. Soc.* 115(23) (1993) 10714-10721.
- [9] S. Herrwerth, W. Eck, S. Reinhardt, M. Grunze, Factors that determine the protein resistance of oligoether self-assembled monolayers - Internal hydrophilicity, terminal hydrophilicity, and lateral packing density, *J. Am. Chem. Soc.* 125(31) (2003) 9359-9366.
- [10] P. Harder, M. Grunze, R. Dahint, G.M. Whitesides, P.E. Laibinis, Molecular conformation in oligo(ethylene glycol)-terminated self-assembled monolayers on gold and silver surfaces determines their ability to resist protein adsorption, *J. Phys. Chem. B* 102(2) (1998) 426-436.
- [11] M.W.A. Skoda, F. Schreiber, R.A.J. Jacobs, J.R.P. Webster, M. Wolff, R. Dahint, D. Schwendel, M. Grunze, Protein Density Profile at the Interface of Water with Oligo(ethylene glycol) Self-Assembled Monolayers, *Langmuir* 25(7) (2009) 4056-4064.
- [12] S.I. Jeon, J.H. Lee, J.D. Andrade, P.G. Degennes, Protein Surface Interactions in the Presence of Polyethylene Oxide. 1. Simplified Theory, *J. Colloid Inter. Sci.* 142(1) (1991) 149-158.
- [13] K. Feldman, G. Hahner, N.D. Spencer, P. Harder, M. Grunze, Probing resistance to protein adsorption of oligo(ethylene glycol)-terminated self-assembled monolayers by scanning force microscopy, *J. Am. Chem. Soc.* 121(43) (1999) 10134-10141.
- [14] R.L.C. Wang, H.J. Kreuzer, M. Grunze, Molecular conformation and solvation of oligo(ethylene glycol)-terminated self-assembled monolayers and their resistance to protein adsorption, *J. Phys. Chem. B* 101(47) (1997) 9767-9773.
- [15] D.J. Vanderah, C.W. Meuse, V. Silin, A.L. Plant, Synthesis and Characterization of Self-Assembled Monolayers of Alkylated 1-Thiahexa(ethylene oxide) Compounds on Gold, *Langmuir* 14(24) (1998) 6916-6923.
- [16] D.J. Vanderah, C.P. Pham, S.K. Springer, V. Silin, C.W. Meuse, Characterization of a series of self-assembled monolayers of alkylated 1-thiaoligo (ethylene oxides)(4-8) on Gold, *Langmuir* 16(16) (2000) 6527-6532.
- [17] D.J. Vanderah, G. Valincius, C.W. Meuse, Self-assembled monolayers of methyl 1-thiahexa(ethylene oxide) for the inhibition of protein adsorption, *Langmuir* 18(12) (2002) 4674-4680.
- [18] D.J. Vanderah, J. Arsenault, H. La, R.S. Gates, V. Silin, C.W. Meuse, G. Valincius, Structural variations and ordering conditions for the self-assembled monolayers of HS(CH<sub>2</sub>CH<sub>2</sub>O)(3-6)CH<sub>3</sub>, *Langmuir* 19(9) (2003) 3752-3756.



- [19] D.J. Vanderah, T. Parr, V. Silin, C.W. Meuse, R.S. Gates, H. La, G. Valincius, Isostructural Self-Assembled Monolayers. 2. Methyl 1-(3-Mercaptopropyl)-oligo(ethylene oxide)s, *Langmuir* 20(4) (2004) 1311-1316.
- [20] L. Malysheva, A. Onipko, R. Valiokas, B. Liedberg, First-Principle DFT and MP2 Modeling of Infrared Reflection–Absorption Spectra of Oriented Helical Ethylene Glycol Oligomers, *J. Phys. Chem. B* 109(27) (2005) 13221-13227.
- [21] L. Malysheva, A. Onipko, T. Fyrner, H.-H. Lee, R.n. Valiokas, P. Konradsson, B. Liedberg, Spectroscopic Characterization and Modeling of Methyl- and Hydrogen-Terminated Oligo(ethylene glycol) Self-Assembled Monolayers, *J. Phys. Chem. C* 116(22) (2012) 12008-12016.
- [22] R. Schlapak, D. Caruana, D. Armitage, S. Howorka, Semipermeable poly(ethylene glycol) films: the relationship between permeability and molecular structure of polymer chains, *Soft Matter* 5(21) (2009) 4104-4112.
- [23] C.E. Hotchen, I.J. Maybury, G.W. Nelson, J.S. Foord, P. Holdway, F. Marken, Amplified electron transfer at poly-ethylene-glycol (PEG) grafted electrodes, *Phys. Chem. Chem. Phys.* 17(17) (2015) 11260-11268.
- [24] K. Nekoueian, C.E. Hotchen, M. Amiri, M. Sillanpää, G.W. Nelson, J.S. Foord, P. Holdway, A. Buchard, S.C. Parker, F. Marken, Interfacial Electron-Shuttling Processes across KolliphorEL Monolayer Grafted Electrodes, *ACS Appl. Mater. Interfaces* 7(28) (2015) 15458-15465.
- [25] T. Doneux, L. Yahia Cherif, C. Buess-Herman, Controlled Tuning of the Ferri/Ferrocyanide Electron Transfer at Oligo(Ethylene Glycol)-Modified Electrodes, *Electrochim. Acta* 219 (2016) 412-417.
- [26] T. Doneux, A. de Ghellinck, E. Triffaux, N. Brouette, M. Sferrazza, C. Buess-Herman, Electron Transfer Across an Antifouling Mercapto-hepta(ethylene glycol) Self-Assembled Monolayer, *J. Phys. Chem. C* 120(29) (2016) 15915-15922.
- [27] N. Gu, L. Niu, S. Dong, Simultaneous determination of both the calibration constant in an electrochemical quartz crystal microbalance and the active surface area of a polycrystalline gold electrode, *Electrochem. Commun.* 2(1) (2000) 48-50.
- [28] R. Madueno, J.M. Sevilla, T. Pineda, A.J. Roman, M. Blazquez, A voltammetric study of 6-mercaptapurine monolayers on polycrystalline gold electrodes, *J. Electroanal. Chem.* 506(2) (2001) 92-98.
- [29] D.F. Yang, C.P. Wilde, M. Morin, Electrochemical desorption and adsorption of nonyl mercaptan at gold single crystal electrode surfaces, *Langmuir* 12(26) (1996) 6570-6577.
- [30] S. Yoshimoto, T. Sawaguchi, F. Mizutani, I. Taniguchi, STM and voltammetric studies on the structure of a 4-pyridinethiolate monolayer chemisorbed on Au(100)-(1×1) surface, *Electrochem. Commun.* 2(1) (2000) 39-43.
- [31] K. Arihara, T. Ariga, N. Takashima, T. Okajima, F. Kitamura, K. Tokuda, T. Ohsaka, Multiple voltammetric waves for reductive desorption of cysteine and 4-mercaptobenzoic acid monolayers self-assembled on gold substrates, *Phys. Chem. Chem. Phys.* 5(17) (2003) 3758-3761.
- [32] T. Doneux, M. Steichen, A. De Rache, C. Buess-Herman, Influence of the crystallographic orientation on the reductive desorption of self-assembled monolayers on gold electrodes, *J. Electroanal. Chem.* 649(1-2) (2010) 164-170.
- [33] S.S. Wong, M.D. Porter, Origin of the multiple voltammetric desorption waves of long-chain alkanethiolate monolayers chemisorbed on annealed gold electrodes, *J. Electroanal. Chem.* 485(2) (2000) 135-143.
- [34] D.M. Kolb, J. Schneider, Surface Reconstruction in Electrochemistry - Au(100)-(5×20), Au(111)-(1×23) and Au(110)-(1×2), *Electrochim. Acta* 31(8) (1986) 929-936.
- [35] P. Ramirez, R. Andreu, A. Cuesta, C.J. Calzado, J.J. Calvente, Determination of the potential of zero charge of Au(111) modified with thiol monolayers, *Anal. Chem.* 79(17) (2007) 6473-6479.
- [36] R.C. Salvarezza, P. Carro, The electrochemical stability of thiols on gold surfaces, *J. Electroanal. Chem.* 819 (2018) 234-239.

- [37] C.A. Widrig, C. Chung, M.D. Porter, The electrochemical desorption of n-alkanethiol monolayers from polycrystalline gold and silver electrodes, *J. Electroanal. Chem.* 310(1-2) (1991) 335-59.
- [38] O. Azzaroni, M.E. Vela, G. Andreasen, P. Carro, R.C. Salvarezza, Electrodesorption Potentials of Self-Assembled Alkanethiolate Monolayers on Ag(111) and Au(111). An Electrochemical, Scanning Tunneling Microscopy and Density Functional Theory Study, *J. Phys. Chem. B* 106(47) (2002) 12267-12273.
- [39] T. Laredo, J. Leitch, M. Chen, I.J. Burgess, J.R. Dutcher, J. Lipkowski, Measurement of the Charge Number Per Adsorbed Molecule and Packing Densities of Self-Assembled Long-Chain Monolayers of Thiols, *Langmuir* 23(11) (2007) 6205-6211.
- [40] M. Baghbanzadeh, C.M. Bowers, D. Rappoport, T. Žaba, L. Yuan, K. Kang, K.-C. Liao, M. Gonidec, P. Rothmund, P. Cyganik, A. Aspuru-Guzik, G.M. Whitesides, Anomalous Rapid Tunneling: Charge Transport across Self-Assembled Monolayers of Oligo(ethylene glycol), *J. Am. Chem. Soc.* 139(22) (2017) 7624-7631.
- [41] D. Garcia-Raya, R. Madueno, J. Manuel Sevilla, M. Blazquez, T. Pineda, Electrochemical characterization of a 1,8-octanedithiol self-assembled monolayer (ODT-SAM) on a Au(111) single crystal electrode, *Electrochim. Acta* 53(27) (2008) 8026-8033.
- [42] C. Dicke, G. Hähner, pH-Dependent Force Spectroscopy of Tri(ethylene Glycol)- and Methyl-Terminated Self-Assembled Monolayers Adsorbed on Gold, *J. Am. Chem. Soc.* 124(42) (2002) 12619-12625.
- [43] H.I. Kim, J.G. Kushmerick, J.E. Houston, B.C. Bunker, Viscous "Interphase" Water Adjacent to Oligo(ethylene glycol)-Terminated Monolayers, *Langmuir* 19(22) (2003) 9271-9275.
- [44] E. Boubour, R.B. Lennox, Insulating Properties of Self-Assembled Monolayers Monitored by Impedance Spectroscopy, *Langmuir* 16(9) (2000) 4222-4228.
- [45] E. Boubour, R.B. Lennox, Potential-Induced Defects in n-Alkanethiol Self-Assembled Monolayers Monitored by Impedance Spectroscopy, *J. Phys. Chem. B* 104(38) (2000) 9004-9010.
- [46] E. Boubour, R.B. Lennox, Stability of  $\omega$ -Functionalized Self-Assembled Monolayers as a Function of Applied Potential, *Langmuir* 16(19) (2000) 7464-7470.
- [47] H.-H. Lee, Z. Ruzele, L. Malysheva, A. Onipko, A. Gutes, F. Bjorefors, R. Valiokas, B. Liedberg, Long-Chain Alkylthiol Assemblies Containing Buried In-Plane Stabilizing Architectures, *Langmuir* 25(24) (2009) 13959-13971.
- [48] R. Valiokas, L. Malysheva, A. Onipko, H.H. Lee, Z. Ruzele, S. Svedhem, S.C.T. Svensson, U. Gelius, B. Liedberg, On the quality and structural characteristics of oligo(ethylene glycol) assemblies on gold: An experimental and theoretical study, *J. Electron Spectros. Relat. Phenomena* 172(1-3) (2009) 9-20.
- [49] L. Malysheva, A. Onipko, B. Liedberg, Ab Initio Modeling of Defect Signatures in Infrared Reflection-Absorption Spectra of SAMs Exposing Methyl- and Hydrogen-Terminated Oligo(ethylene glycols), *J. Phys. Chem. A* 112(4) (2008) 728-736.
- [50] M. Kobayashi, M. Sakashita, Morphology Dependent Anomalous Frequency-Shifts of Infrared-Absorption Bands of Polymer Crystals - Interpretation in Terms of Transition Dipole -Dipole Coupling Theory, *J. Chem. Phys.* 96(1) (1992) 748-760.
- [51] T. Miyazawa, Y. Ideguchi, K. Fukushima, Molecular Vibrations and Structure of High Polymers. 3. Polarized Infrared Spectra, Normal Vibrations and Helical Conformation of Polyethylene Glycol, *J. Chem. Phys.* 37(12) (1962) 2764-2776.
- [52] T. Yoshihara, S. Murahashi, H. Tadokoro, Normal Vibrations of Polymer Molecules of Helical Conformation. 4. Polyethylene Oxide + Polyethylene-D4 Oxide, *J. Chem. Phys.* 41(9) (1964) 2902-2911.
- [53] Y.L. Jeyachandran, T. Weber, A. Terfort, M. Zharnikov, Application of Long Wavelength Ultraviolet Radiation for Modification and Patterning of Protein-Repelling Monolayers, *J. Phys. Chem. C* 117(11) (2013) 5824-5830.
- [54] D.G. Castner, K. Hinds, D.W. Grainger, X-ray photoelectron spectroscopy sulfur 2p study of organic thiol and disulfide binding interactions with gold surfaces, *Langmuir* 12(21) (1996) 5083-5086.

- [55] M.M. Walczak, C.A. Alves, B.D. Lamp, M.D. Porter, Electrochemical and X-ray photoelectron spectroscopic evidence for differences in the binding sites of alkanethiolate monolayers chemisorbed at gold, *J. Electroanal. Chem.* 396(1-2) (1995) 103-114.
- [56] F. Schreiber, Structure and growth of self-assembling monolayers, *Prog. Surf. Sci.* 65(5-8) (2000) 151-256.
- [57] C.D. Bain, E.B. Troughton, Y.T. Tao, J. Evall, G.M. Whitesides, R.G. Nuzzo, Formation of Monolayer Films by the Spontaneous Assembly of Organic Thiols from Solution onto Gold, *J. Am. Chem. Soc.* 111(1) (1989) 321-335.
- [58] R.G. Nuzzo, B.R. Zegarski, L.H. Dubois, Fundamental-Studies of the Chemisorption of Organosulfur Compounds on Au(111) - Implications for Molecular Self-Assembly on Gold Surfaces, *J. Am. Chem. Soc.* 109(3) (1987) 733-740.
- [59] H. Rieley, G.K. Kendall, F.W. Zemicael, T.L. Smith, S. Yang, X-ray Studies of Self-Assembled Monolayers on Coinage Metals. 1. Alignment and Photooxidation in 1,8-Octanedithiol and 1-Octanethiol on Au, *Langmuir* 14(18) (1998) 5147-5153.
- [60] C. Palegrosdemange, E.S. Simon, K.L. Prime, G.M. Whitesides, Formation of Self-Assembled Monolayers by Chemisorption of Derivatives of Oligo(Ethylene Glycol) of Structure HS(CH<sub>2</sub>)<sub>11</sub>(OCH<sub>2</sub>CH<sub>2</sub>)META-OH on Gold, *J. Am. Chem. Soc.* 113(1) (1991) 12-20.
- [61] Z. Liu, T. Duchoň, H. Wang, D.C. Grinter, I. Waluyo, J. Zhou, Q. Liu, B. Jeong, E.J. Crumlin, V. Matolín, D.J. Stacchiola, J.A. Rodriguez, S.D. Senanayake, Ambient pressure XPS and IRRAS investigation of ethanol steam reforming on Ni-CeO<sub>2</sub>(111) catalysts: an in situ study of C-C and O-H bond scission, *Phys. Chem. Chem. Phys.* 18(25) (2016) 16621-16628.
- [62] T. Kawaguchi, H. Yasuda, K. Shimazu, M.D. Porter, Electrochemical Quartz Crystal Microbalance Investigation of the Reductive Desorption of Self-Assembled Monolayers of Alkanethiols and Mercaptoalkanoic Acids on Au, *Langmuir* 16(25) (2000) 9830-9840.
- [63] M. Yoshimoto, K. Honda, S. Kurosawa, M. Tanaka, Dynamic Properties of Self-Assembled Monolayers of Mercapto Oligo(ethylene oxide) Methyl Ether on an Oscillating Solid-Liquid Interface, *J. Phys. Chem. C* 118(29) (2014) 16067-16073.



### 3.2. Artículo 2.

*Monocapas autoensambladas de O-(2-Mercaptoethyl)-O'-methyl-hexa(ethylene glycol) (EG7-SAM) en electrodos de oro. Efectos de la naturaleza de la disolución/electrolito en la formación y propiedades bloqueantes frente a la transferencia electrónica.*





**Self-assembled monolayers of O-(2-Mercaptoethyl)-O'-methyl-hexa(ethylene glycol) (EG7-SAM) on gold electrodes. Effects of the nature of solution/electrolyte on formation and electron transfer blocking characteristics.**

Miriam Chávez, Guadalupe Sánchez-Obrero, Rafael Madueño, José Manuel Sevilla, Manuel Blázquez, Teresa Pineda\*

Department of Physical Chemistry and Applied Thermodynamics, Institute of Fine Chemistry and Nanochemistry, University of Cordoba, Campus Rabanales, Ed. Marie Curie 2<sup>a</sup> Planta, E-14014 Córdoba, Spain.

**Abstract**

The self-assembly of O-(2-Mercaptoethyl)-O'-methyl-hexa(ethylene glycol) (EG7) on gold substrates produces monolayers whose structure should depend primarily on the solvents used for their formation. Although this should be also the case for any self-assembled monolayer (SAM) system, the presence of oxygen atoms in the EG7 chains brings about specific interactions with the solvent molecules other than just the van der Waals interactions taking place with alkanethiols. In this work we investigate the effects of the nature of the solutions for EG7-SAM formation in the RD processes using gold substrates either polycrystalline or single crystal electrodes. The patterns obtained in polycrystalline substrates are compared to the peaks observed at gold single crystal electrodes and it has been found that the main peaks correspond to the molecules desorbed from the different gold facets contained in the polycrystalline substrate. These single peaks are in fact composed of two contributions that can be explained as the presence of domains where the EG7 molecules are organized with different orientations, giving place to intermolecular interactions of different magnitude. The blocking properties of these films are strongly determined by the nature of the electrolyte used for the analysis and not by the solvent used in their formation. Although no experimental evidence of the specific interaction and/or retention inside the film of Na<sup>+</sup> or phosphate or both ions is obtained, a specific effect that accounts for an electron transfer rate constant of an order of magnitude lower than the obtained with other electrolytes is observed. These results can contribute to increase the understanding of the relationship between the EG7-SAMs structure and functionalities.

**Keywords.** Polyethylene glycol, self-assembled monolayer, gold electrode, cyclic voltammetry, electrochemical impedance spectroscopy, contact angle measurements.

## Introduction.

The construction of multifunctional interfaces with tailored properties is an important research topic that is nowadays attracting the attention in the field of biocompatible and functional materials. Self-assembled monolayers (SAMs) constitute one of the most utilized strategies to create functional interfaces due to the easy preparation and the huge number of molecules available to assemble on different solid surfaces [1,2]. The dynamic equilibrium governing the adsorption of thiols on solid surfaces is influenced by the solvent-substrate and the solvent-adsorbate interactions, and the rates of formation depend on the magnitude of these interactions that can be tuned by the solvent-adsorbate interaction strength [1]. In this sense, the use of polar solvents that present low solubility for alkanethiols can contribute to their assembly at the substrate surface [3,4]. Results obtained by scanning tunneling microscopy have shown that solvents of high polarity improve the quality of alkanethiol SAMs due to the strong hydrophobic interactions between the nonpolar hydrophobic tails, whereas the low polarity solvents can disturb the tight packing of the monolayer [5]. The presence of surfactants of low critical micellar concentration in water solutions has demonstrated to contribute to the formation of highly compact alkanethiol SAMs by providing hydrophobic domains that solubilize the alkane tails and facilitate their delivery to the substrate surface [6-13].

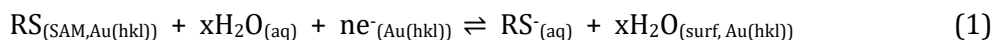
Oligo-ethylene glycol (OEG)-terminated alkanethiols have been widely used to form SAMs taking the advantage of the long alkane arm that directs the organization of the molecules resulting in compact layers that expose the OEG-terminal to the medium. The OEG portion, under these conditions, can adopt either a helical or an all-trans conformation depending on factors such as the type of substrate [14,15], the surface coverage [16,17], the number of EG units [15,17] and the solvent [18]. These SAMs have demonstrated to minimize the unspecific adsorption of proteins and inhibit cell attachment [14,15,19,20] depending on the amount of water associated with the OEG chains that ultimately depends on its conformation [21,22].

Most of the surfaces modified with ethylene glycol used in the actual applications employ mercapto-poly-ethylene glycol (EGn) molecules that lack the alkane arm, and the organization of these layers results obviously different and dependent on other parameters such as temperature or the presence of different salts in the formation solution [23,26]. One of the shortest EGn chains available is O-(2-Mercaptoethyl)-O'-methyl-hexa(ethylene glycol) (EG7) and can be used as a model for the characterization of the EGn-SAMs. We have recently reported that the EG7-SAM formed from an EG7 ethanolic solution acquires the best structural performance at a modification time of 1h. Under these conditions, the cyclic voltammograms for the RD process obtained from a polyoriented (PO) gold electrode shows



a set of discrete peaks that cannot be only explained on the basis of the desorption from different defined gold facets present in the surface, but the existence of different degrees of intermolecular interactions need to be introduced in the scene [27]. Dealing with the use of EGN layers on electrochemical biosensors to avoid the nonspecific adsorption phenomenon and the drawback of inhibition of the heterogeneous electron transfer kinetics, Doneux et al. [28,29] studied the electrochemical performance of the EG7-SAM using different outer sphere redox probes such as  $[\text{Fe}(\text{CN})_6]^{3-/4-}$ ,  $[\text{Ru}(\text{NH}_3)_6]^{3+/2+}$ ,  $\text{Fc}(\text{MeOH})^{2+/0}$ , and  $[\text{IrCl}_6]^{2-/3-}$ , to investigate the monolayer barrier properties. They found that the EG7-SAM behaves as a low impedance film [30] with all the assayed redox probes except for the  $[\text{Fe}(\text{CN})_6]^{3-/4-}$  system. They interpreted the high electron transfer inhibition in terms of the hydration properties of both the monolayer and the electroactive anions. In an earlier study by Vanderah et al. [31] on the influence of the solvent used for the SAM formation on the structure of the EG7-SAM, as characterized by ellipsometry, infrared reflection-absorption spectroscopy (IRRAS) and EIS, they choose within a nonhydroxylic solvent as THF, a hydroxylic EtOH and also select an EtOH/water mixture, EtOH<sub>95</sub>, to discern the effect of the presence of water in the formation solution. The best performance was found for the layer produced from the EtOH<sub>95</sub> solution. Moreover, whereas the EG7-SAMs formed from EtOH and EtOH<sub>95</sub> showed the same thickness, that from THF solvent present a variable value, indicating a more irregular structure. Similarly, the layer formed from EtOH<sub>95</sub> behaves as an almost perfect capacitor but for those from EtOH and THF, the heterogeneity obliges to introduce the constant phase element to account for the deviation of that ideal behavior. Finally, infrared spectroscopy revealed a highly organized structure for both layers formed in EtOH and a less ordered film when formed in THF.

Pioneering works on alkanethiol SAMs RD processes have already established the type of information that can be obtained in relation to SAMs stability and organization [32-38], and now it is widely accepted that the process can be considered as a solvent substitution reaction,



that involves the different energetic contributions such as substrate-adsorbate, intermolecular lateral, substrate-SAM-solvent, free surfactant-solvent and substrate-solvent interactions [38-41].

In this context and taking the EG7-SAM as a model for the PEGylated surfaces, we have explored its electrochemical behavior by going deeper into the RD processes by using different gold substrates. To this end, the EG7-SAMs are formed in different media, from these already described by Vanderah et al. [31] to the sodium phosphate aqueous solution. Moreover, these EG7-SAMs are also characterized by EIS in different neutral media to find

out the influence of the electrolyte in the electrochemical response of the  $[\text{Fe}(\text{CN})_6]^{3-/4-}$  redox probe. Whereas the solvent used for the formation of the SAM influences the structure as observed in the RD signatures, the blocking ability against the redox probe is not affected. In contrast, the electrolyte solution used for this analysis tunes the electrochemical response influencing the apparent electron transfer rate constant values.

## Experimental section.

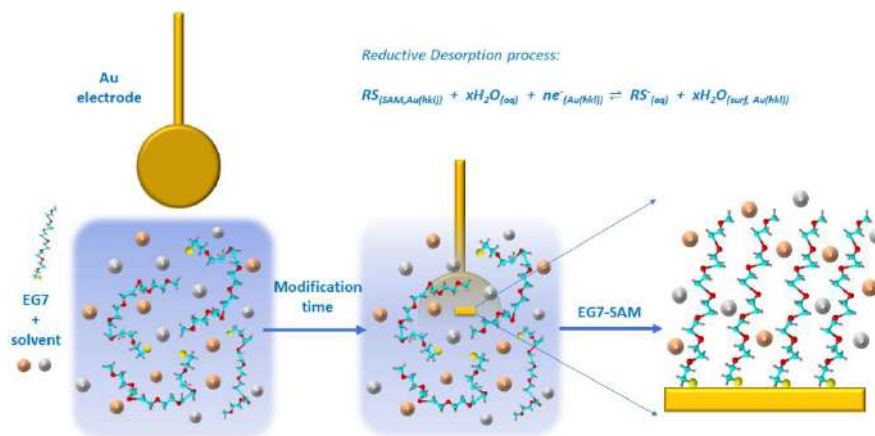
### Chemicals.

O-(2-Mercaptoethyl)-O'-methyl-hexa(ethylene glycol) (EG7), Potassium hexaferricyanide and potassium hexaferrocyanide ( $[\text{Fe}(\text{CN})_6]^{3-/4-}$ ), were purchased from Aldrich-Sigma (purity  $\geq 99\%$ ). The rest of the reagents were from Merck analytical grade. All the aqueous solutions were prepared with deionized ultrapure water produced by Millipore system.

### Experimental methods.

Electrochemical experiments were performed on an Autolab (Ecochemie model Pgstat30) instrument attached to a PC with proper software (GPES and FRA) for the total control of the experiments and data acquisition. A conventional three electrode cell comprising a platinum coil as counter electrode, a 50 mM KCl calomel (CE 50mM) as reference electrode and either a poly-oriented (PO gold) or single crystals gold (Au(111), Au(100) and Au(110)), as the working electrodes, were used. The PO gold electrode was a homemade sphere obtained by melting a gold wire up to reach a diameter of approximately 2mm and attached to the gold wire that serves as electrode connection. The single crystals were 3mm diameter and 2mm thick cylinders from Metal Crystals & Oxides LTD, with a polished side. A gold wire, mounted at the rear end, allowed easier handling of the crystal. Before each electrochemical measurement, the electrodes were annealed in a natural gas flame to a light-red melt for about 20 s and, after a short period of cooling in air, quenched in ultrapure water. The electrodes were then transferred into the electrochemical cell with a droplet of water adhering to it to prevent contamination and were contacted with the solution by the meniscus method, under potential controlled conditions. Each surface of the single crystals used in this study showed the well-known characteristic voltammograms in 0.01 M  $\text{HClO}_4$  solutions. The real area of the gold electrodes were determined from the charge involved in the gold oxide reduction peaks obtained under these conditions ( $A_{(\text{PO gold})} = 0.24 \text{ cm}^2$ ;  $A_{(\text{Au}(111))} = 0.09 \text{ cm}^2$ ;  $A_{(\text{Au}(100))} = 0.09 \text{ cm}^2$ ;  $A_{(\text{Au}(110))} = 0.10 \text{ cm}^2$ ).

For electrode modification, the gold electrodes were immersed in the EG7 solutions (either of pure EtOH or 95 % EtOH (EtOH<sub>95</sub>) or tetrahydrofuran (THF) or sodium phosphate (NaPi) 1 M) for a modification time of 1 h (Scheme 1). After extensive washing with water or blank electrolyte, they were transferred to the electrochemical cell, to carried out the CV or EIS experiment.



**Scheme 1.** Formation of EG7-SAM on an Au electrode.

The cyclic voltammograms for the RD processes were recorded in KOH 0.1 M solutions and these for the evaluation of the electron transfer in aqueous solutions were of sodium phosphate (NaPi) 0.1 M at pH 7.4, KNO<sub>3</sub> 0.1 M and KCl 0.1 M in the presence of 1 mM [Fe(CN)<sub>6</sub>]<sup>3-/4-</sup>. The EIS measurements were obtained at the midpoint potential of the cyclic voltammogram registered for the naked electrode (at 0.08 V), using an amplitude rms of 10 mV and a frequency interval from 0.1 to 10000 Hz.

Contact Angle measurements were conducted by using an Optical Tensiometer Theta T200 device (Attension, Biolin Scientific) equipped with a high-speed camera (420 fps). The CA of the formed SAMs was measured in sessile drop method. The experiments were performed at room temperature and at open atmosphere. The results are given as an average of six measurements.

## Results and discussion.

### RD of EG7-SAMs formed in different media.

We have previously reported results on the characterization of a compact EG7-SAM formed from EtOH solution by using electrochemical and spectroscopic techniques [27]. In particular, the results of the RD process monitored by CV show a set of peaks with a shape that depends on the modification time. In a first approximation, the peaks are ascribed to the desorption of portions of monolayer from the different facets existing in the PO gold

whose peak potentials follow the trend of the potential of zero charge ( $pzc$ ) of these naked facets. However, there are some details in the cyclic voltammograms that cannot be explained only on this basis. To get more insight into this system, we first studied the RD process of the EG7-SAM formed in different solvents on a PO gold electrode. Considering previous results on the organization of this SAM formed from EtOH, EtOH<sub>95</sub> and THF, characterized by electrochemical impedance and infrared spectroscopies [31], and that formed from a 1 M NaPi solution analyzed by CV [28,29], the RD processes of the SAMs formed under the same experimental conditions are here examined.

Figure 1 shows the cyclic voltammograms for these RD processes that show that, although all of them share the multi-peak shape, they differ in the shape and in the potentials of the individual peaks. Moreover, there is no clear trend on the peak potential variations. While the SAM formed from EtOH, EtOH<sub>95</sub> and THF present a similar pattern with four peaks, that formed from 1 M NaPi aqueous solution shows only three peaks that are displaced 50 mV in the positive direction. However, the charge densities involved in the overall RD peaks are almost equal and independent on the nature of the solvent used for its formation.

Pioneering works using single crystal gold electrodes to ascribe the multipeak voltammetry obtained at polycrystalline gold electrodes tried to explain the differences in peak potential as different energetics of the Au-S bond on the various single crystal gold facets. Thus, the differences in potential were correlated to the potential of zero charge of the naked surfaces [33,37]. In this context, many systems have been analyzed and the peaks have been assigned to monolayer domains desorbed from Au(111), Au(100) and Au(110) facets [36,38,42-44]. Moreover, the type of sulfur adsorption sites depending on the ordering of the surface gold atoms in the facet, either reconstructed or unreconstructed, was also entered in the discussion, indicating that the cohesive interactions between neighboring adsorbates would vary with these different binding sites thus influencing the packing density [45]. Recently, the classical way of considering the peak potential of the RD as a measure of the Au-S bond energy was reinforced by considering the different contributions included in the energy change between the initial and final states of the RD reaction represented by reaction (1). This equation is a substitution reaction between the adsorbate and the solvent [38,39]. Thus, the adsorbate-surface interaction involves the Au-S bond that should be directly correlated with the crystallographic orientation. However, the different interactions of the adsorbates whether in the adsorbed state or free in solution would affect the energetics of desorption.

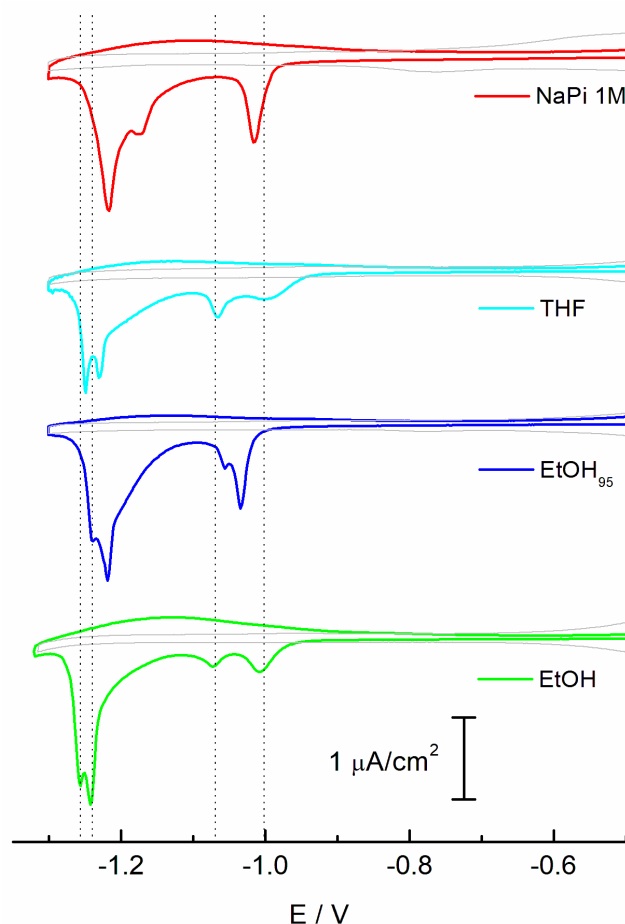


**Figure 1.** Cyclic voltammograms for the RD process of the EG7-SAM on PO gold electrodes in KOH 0.1 M solution. The grey line represents the blank profiles obtained in the same solution.  $v = 20$  mV/s. The SAMs have been formed in different solvents as labeled, at a modification time of 1 h.

Studies by Cometto et al. [41,46] on the electrochemical stability of alkanethiol SAMs of different chain length on planar and curved surfaces compare the position of the RD peaks obtained on Au(111) and Au(100) single crystal electrodes. They found that the differences in the RD potentials in these substrates increase with the alkanethiol chain length, suggesting a preferential adsorption of the SAMs on the Au(100). Analyzing the different contributions of the interactions taking place in the RD process, they found that the shift in the potential for a given SAM formed on different surfaces depends on the substrate-adsorbate interactions that are determined by the energy of the Au-S bond, the adsorbate-adsorbate interaction determined by the lateral interactions mainly consisting of vdW forces, the different thiol-solvent interactions in the adsorbed state that depends on the *pzc* of the SAM, the solvation energy of the free alkanethiols and the solvent-substrate interactions that again depend on the *pzc* of the naked gold surfaces.

To get more insight into the nature of the peaks obtained for the desorption of monolayer domains from different gold facets and correlate them for the SAMs formed

under different solvent conditions, we have carried out a study of the formation of EG7-SAM in the different media described above, and its RD processes using Au(111), Au(100) and Au(110) single crystal electrodes.

Starting with the EG7-SAM formed in EtOH, we obtain a single peak at -0.99 V (peak 1) on the Au(111) surface that is very close to the first peak in the PO gold as already reported [27]. The process on Au(100) and Au(110) show broad peaks at -1.21 and -1.20 V (peak 3 and 4), respectively (Figure 2). Besides these, a small peak at -0.985 V is seen in the Au(100) surface at potentials close to peak 1 on the Au(111) facet. A small peak at -1.07 V (peak 2) is also obtained at the Au(110) that is also coincident with the second peak on the PO gold surface. It is interesting to note that the peaks 3 and 4 are shifted to higher potentials (~40 mV) in respect to these corresponding in the PO gold electrode. These features are also observed in the cyclic voltammograms recorded for the EG7-SAM formed in THF (Figure 2).

The trend obtained for the EG7-SAM formed in NaPi presents important differences. First, only three peaks appear in the cyclic voltammogram for the PO gold. The first one is sharp and is comprised in the potential interval where the main peak in Au(111) and the smaller peaks in Au(100) and Au(110) appear (peaks 1 and 2). It must be noted that, in contrast to what happens in the PO gold, the main peak in Au(111) is broad and seems to be formed by two overlapped peaks. Second, the lower potential peaks in PO gold are almost coincident with the main peaks at (100) and (110) surfaces. Finally, the EG7-SAM formed in EtOH<sub>95</sub> presents an Au(111) peak that occurs at 85 mV higher potential than the first peak in the PO gold surface. The rest of the peaks in the single crystals lay very close to those of the PO gold electrode.

Figure 3 shows the above commented peak potentials for the PO and the single crystal electrodes and, as it can be observed, the potentials for each peak are within the intervals of 55 to 80 mV, indicating that they can represent similar energetic situations.

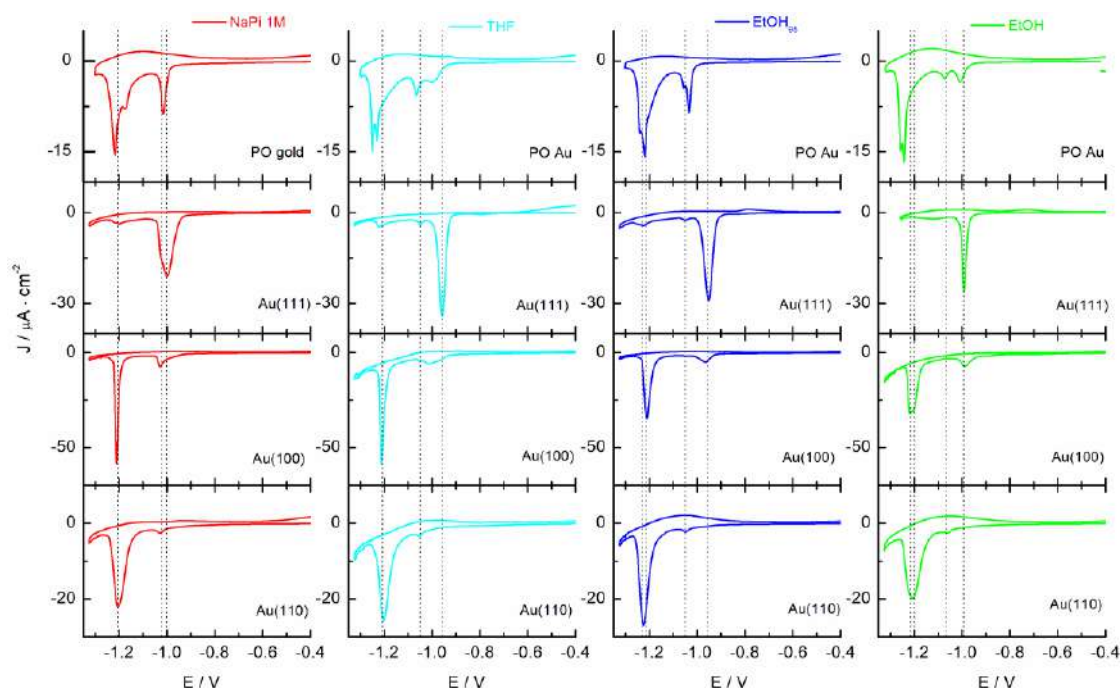


**Figure 2.** Cyclic voltammograms for the RD processes of the EG7-SAMs on PO gold and Au(111), Au(100) and Au(110) single crystal electrodes in KOH 0.1 M solution.  $v = 20$  mV/s. The SAMs have been formed in different solvents as labeled, at a modification time of 1 h.

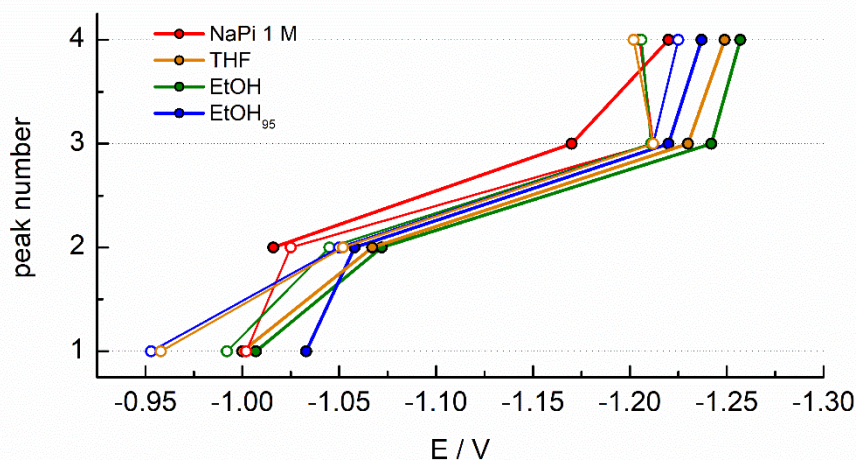


**Figure 3.** Potential values for the different peaks observed in the RD process of EG7-SAM on a PO (solid circles) and single crystal (empty circles) gold electrodes. While the PO gold electrode peaks (1, 2, 3 and 4) correspond to these observed in the cyclic voltammograms, these for the single crystals are: 1, main peak in Au(111); 2, small first peak in Au(110); 3, main peak in Au(100); 4, main peak in Au(110).

As observed in Figure 2, most of the main peaks obtained in the RD process at single crystal electrodes seems to contain more than one contribution. To get more information about the origin of the peaks, and after eliminating the background currents, we have carried out a deconvolution of these peaks, by using Lorentzian curves (Figure S1). We have used three contributions to fit the cyclic voltammograms that are named as peak 1, 2 and 3 in Figure 4, where the peak potential, the half width, and the percentage of area for each

component are represented. The cyclic voltammogram recorded for the EG7-SAM formed in NaPi in a Au(111) single crystal, can be fitted with two peaks at -0.99 and -1.02V with a half width of around 30 mV and a charge density that supposes 53 and 34 % of the total charge, and a third peak at -1.19 V of very low charge (~12%) that should correspond to molecules desorbed from step or defect sites on the (111) facet. This double contribution observed in the single crystal and absent in the peak obtained at the same potentials in the PO surface, must be assigned to monolayer domains with different intermolecular interactions that can be produced when larger terraces exist on the Au(111) single crystal surface as it should be the case, in comparison to the PO gold surface. In the case of EtOH as solvent, two contributions are also present with similar half width but being the second contribution of lower significance. The cyclic voltammograms of the SAMs built in EtOH<sub>95</sub> or THF also show this second type of contribution, but both are of very low charge density in comparison to the first one.

The curves obtained with Au(100) show a first peak between -1.025 V and -0.97 V that are very close to the second contribution of the (111) facet and involve a charge density lower than 20 % of the total amount measured. The main peak, although very sharp requires the introduction of two signals that are also of a very low width (half width of less than 20 mV), and these are of the same magnitude in the case of the SAMs prepared in EtOH and THF and of a ratio 60:30 in the SAMs prepared in NaPi or EtOH<sub>95</sub>. It can be thought that the first peak observed in the (100) facet should have an origin on either, a small portion of reconstructed hexagonal surface or some stepped sites that would show a similar energetic than the (111) domain that we obtain as a second contribution in that facet. The presence of two domains with different molecular interactions on the (100) facet could explain the presence of the double contribution in the main peak. The fact that the SAMs formed in NaPi and EtOH<sub>95</sub> present a major contribution in the higher potential peak that is assigned as less energetic, can be ascribed to the effect of water molecules on the organization of the layer. In the case of EtOH and THF, the absence of water in the formation solution avoids this and the adsorbed molecules should share conformation.



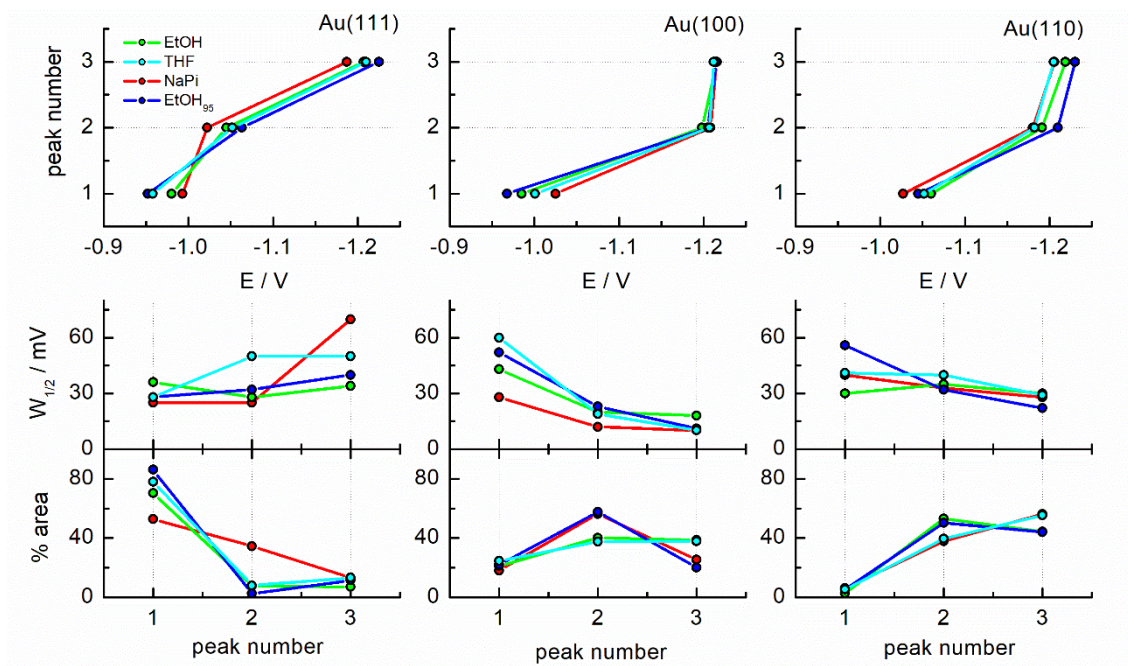


**Figure 4.** Parameters obtained in the deconvolution of the cyclic voltammograms RD main peaks recorded in the Au(111), Au(100) and Au(110) single crystal electrodes. The potentials of the three contributions (peaks 1, 2 and 3 in decreasing potential order) are plotted in the top graphics. The lower panel gathers the half width and the percentage area of every deconvoluted peak for the three single crystal surfaces.

In the deconvolution of the RD with Au(110), besides the first small peak at -1.045 V that coincides with the more negative potential region where the (111) peaks are obtained, a broad signal at more negative potential is observed for all the SAMs independent on the solvent used in the formation solution. The peak is also deconvoluted introducing two contributions of similar widths and area ratio.

The presence of multi-wave voltammetry in the RD peaks of long alkanethiol SAMs has been observed in Au(111) single crystal electrodes [27,34,36,38,42], and the features have been assigned to the sequential desorption from sites with different binding energies [34,36], or monolayer domains with different sizes and stability [35], or depletion micelles that can be formed on the double layer region [33,36,47,48], and finally, they have been ascribed to the relative importance of the different intermolecular interactions that are present through the monolayer [49]. Thus, the deconvolution of the main peaks including two contributions should be explained as the presence of domains where the EG7 molecules are organized with different orientations that give place to intermolecular interactions of different magnitude. If we consider that the length of the EG7-SH chain can be longer than the hexadecanethiol, that gives place to multi-wave voltammetry at Au(111) single crystal gold electrodes [35], it is expected that, under some circumstances, the same behavior can be found in the EG7-SAM on the three single crystal faces studied in this work.

One interesting aspect of the EG7-SAMs formed on different single crystal facets is that the charge densities involved in the RD process are similar independent on the formation media but somewhat different for each facet, being of around 20% higher for Au(111) and Au(100), and 5% lower than that for the PO gold electrode (Table S1). By taking into account the surface atomic densities ( $1.39 \times 10^{15}$ ,  $1.20 \times 10^{15}$ , and  $0.85 \times 10^{15}$ , for the Au(111), (100) and (110) planes, respectively) [50], and the surfaces coverages determined from the charge densities, the coverages obtained are of 0.30, 0.33 and 0.39 for Au(111), Au(100) and Au(110), respectively.

### Contact angles measurements of the EG7-SAMs.

The water contact angles of these EG7-SAMs have been measured and the results are gathered in table 1. The highest values obtained for the SAMs formed in ethanolic solutions point to a higher exposure of the methyl groups to the interface. A lower value is measured for the EG7-SAM formed in NaPi that probably reflect the higher content of water on the topmost layer even though the experiment is made with a dried surface. The lowest value obtained for the SAM formed in THF can be related to the less organized structure that is presumed in this media in agreement with previous work [31], and that can allow the exposure of some EG units to the external surface creating a more hydrophilic environment.

**Table 1.** Water contact angles measured for the EG7-SAMs assembled in different modification solvents.

Modification solvent	Contact angle / $\theta_{(H_2O)}$
<b>NaPi 1M</b>	$53.3 \pm 1.2$
<b>THF</b>	$48.2 \pm 2.4$
<b>EtOH<sub>95</sub></b>	$61.0 \pm 2.1$
<b>EtOH</b>	$71.3 \pm 3.1$

### Evaluation of the blocking behavior of the EG7-SAMs formed in different media.

Another interesting point to check is the electrochemical response of these SAMs against the redox pair  $[\text{Fe}(\text{CN})_6]^{3-/4-}$ . We choose this redox probe because recent works have shown that, while other systems as  $[\text{Ru}(\text{NH}_3)_6]^{3+/2+}$ ,  $\text{Fc}(\text{MeOH})_2^{+/0}$  and  $[\text{IrCl}_6]^{2-/3-}$ , maintain their reversible behavior and are not inhibited by the presence of the monolayer, the  $[\text{Fe}(\text{CN})_6]^{3-/4-}$  electron transfer is completely suppressed at the EG7-SAM prepared in NaPi 1M solution [27-29].

The experimental strategy used here is the preparation of the EG7-SAMs in the different media used in the above section (NaPi 1 M, EtOH, EtOH<sub>95</sub> and THF) and their evaluation by CV and EIS by using the [Fe(CN)<sub>6</sub>]<sup>3-/4</sup> redox probe in three different solutions (c.a., NaPi 0.1 M at pH 7, KNO<sub>3</sub> 0.1 M and KCl 0.1 M). As previously reported [28,29], the inhibition of the electron transfer signal is complete when the cyclic voltammogram of the EG7-SAM formed in 1 M NaPi is recorded in a NaPi 0.1 M solution (Figure 5). A strong inhibition, although lower than the above, is also observed when the [Fe(CN)<sub>6</sub>]<sup>3-/4</sup> redox pair is explored in either KNO<sub>3</sub> or KCl 0.1 M solutions. The Nyquist plots obtained under the same experimental conditions are also included in Figure 5 and the results for the rest of experimental conditions are included in Figure S2, where the data are also represented as Bode plots to highlight the observed changes. The impedance data show the typical semicircles representing the charge transfer resistance with total absence of the Warburg element, indicating no diffusion contribution. The spectra have been fitted by using a Randles equivalent circuit (either with or without Warburg component) and the results are included in Table SI. The capacitor has been substituted by a constant phase element to improve the fitting and account for deviations from ideal capacitive behavior (CPE = (Q(iω)<sup>n</sup>)<sup>-1</sup>, where Q and n are the magnitude and exponent parameter of the CPE). We have used Eqn. (1) to calculate the effective capacitance,

$$C = \frac{n \sqrt{\frac{Q}{(R_s^{-1} + R_{CT}^{-1})^{1-n}}}}{\quad} \quad (1)$$

where R<sub>s</sub> and R<sub>CT</sub> are the solution and the charge transfer resistance obtained from fitting the impedance spectra. The capacitance values are gathered in Table 2. Table 3 gathers the electron transfer rate constant values obtained by using Eqn. (2).

$$k_{ap} = \frac{RT}{n^2 \cdot F^2 \cdot R_{CT} \cdot A \cdot c} \quad (2)$$

where R is the gas constant, T the temperature, F the Faraday constant, n the number of electrons, A the geometric area of the electrode and c the concentration of the redox pair and R<sub>CT</sub> the charge transfer resistance obtained in the fits (Table S1).

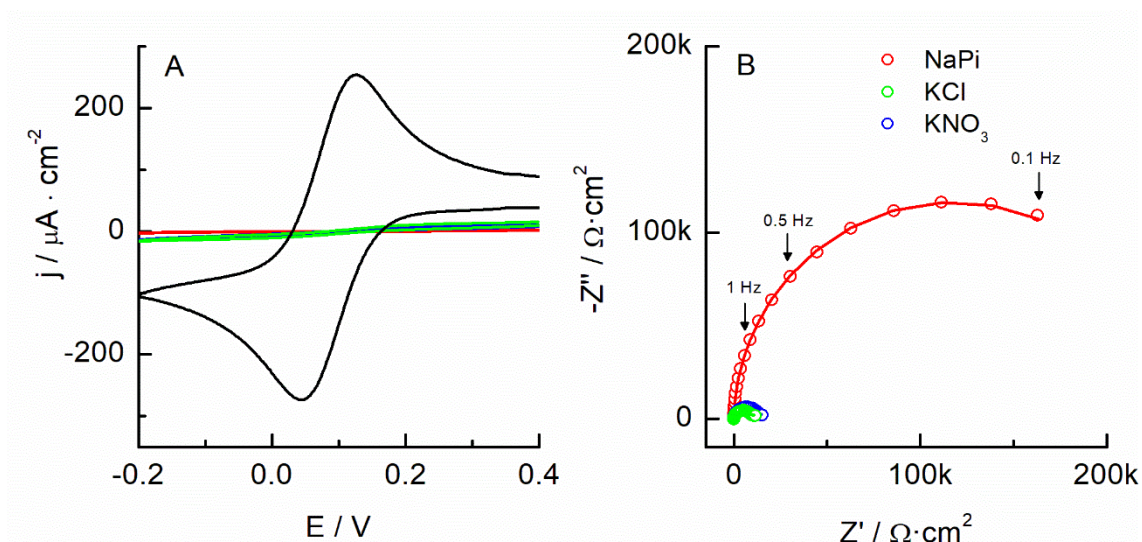


**Figure 5.** (A) Cyclic voltammograms recorded at a scan rate of 0.1 V/s, and (B) impedance spectra of 1 mM  $\text{K}_3\text{Fe}(\text{CN})_6$  and 1 mM  $\text{K}_4[\text{Fe}(\text{CN})_6]$  in 0.1 M electrolyte solutions (as indicated in the figure label) in the presence of EG7-SAMs formed in 1M NaPi at pH 7.4. The black line corresponds to the curve recorded with the naked gold electrode.

**Table 2.** Double layer capacitance of the EG7-SAM, determined by using Eqn. (1), and the data obtained in the fitting of impedance spectra of EG7-SAM PO gold electrodes prepared in four different media and evaluated in 1 mM  $[\text{Fe}(\text{CN})_6]^{3-/4}$  in three electrolyte solutions.

<i>Cdl</i> / $\mu\text{F} \cdot \text{cm}^{-2}$	Evaluation media		
	Formation media	NaPi	$\text{KNO}_3$
NaPi 1 M	3.9	4.2	4.3
THF	5.0	4.9	4.9
$\text{EtOH}_{95}$	4.1	5.0	5.0
EtOH	5.2	4.2	5.2

**Table 3.** Electron transfer rate constants ( $k_{ap}$ ) of the  $[\text{Fe}(\text{CN})_6]^{3-/4}$  redox probe, determined by using Eqn. (2), and the  $R_{ct}$  data obtained in the fitting of impedance spectra of EG7-SAM PO gold electrodes prepared in four different media and evaluated in 1 mM  $[\text{Fe}(\text{CN})_6]^{3-/4}$  in three electrolyte solutions (Table S1).

$k_{ap}$ ( $\times 10^6$ ) / $\text{cm} \cdot \text{s}^{-1}$	Evaluation media		
	Formation media	NaPi	$\text{KNO}_3$
NaPi 1 M	0.5	9.3	13.4
THF	0.4	3.4	4.9
$\text{EtOH}_{95}$	0.9	2.4	2.6
EtOH	0.5	4.5	4.7

It can be seen that the as-prepared EG7-SAM blocks the  $[\text{Fe}(\text{CN})_6]^{3-/4}$  electron transfer similarly, and thus, the electron transfer rate constants are practically independent of the nature of the solvent employed in the formation solution. However, a strong dependence on the electrolyte used for the electrochemical evaluation is observed. Whereas the stronger inhibition is always obtained when the experiment is run in NaPi 0.1 M solutions, an increase in the electron transfer rate constant of an order of magnitude is observed when the redox probe is assayed in either  $\text{KNO}_3$  or  $\text{KCl}$  solutions.

The peculiar blocking behavior of  $[\text{Fe}(\text{CN})_6]^{3-/4}$  redox probe that has been interpreted in terms of the hydration properties of both the monolayer and the electroactive anions [28], together with the classical view of the existence of repulsive interactions that affect the concentration profiles of the redox probe in the surrounding of the electron transfer active sites [51-54], can help in the understanding of this phenomenon.

In contrast to what has been observed for the RD processes, the inhibition of the electron transfer of the redox probe is not much influenced by the nature of the solvent employed in the formation of the EG7-SAM. Only little differences are obtained that, most of them, are within the experimental variability of these systems. We expected some influence of the presence of water in the formation solution but, probably, the small amount of these molecules that remains within the EG7 assembled chains is not reflected in the external face of the layer. Deeply investigations on this topic have evidenced that during EGn-SAM growth in aqueous solutions, and under conditions of high surface coverage, the increased binding of thiol molecules constitute a driving force for structural changes within the monolayer that press out the water molecules that are previously interacting with the EG groups. This effect is considered to occur at higher temperature but, under room temperature conditions as these used in our work, this driving force should not operate and the water molecules interacting with the EG moieties maintain these rather strong interactions [55]. In this respect, even assuming that compact monolayers are formed in the four solutions employed, the EG7-SAMs formed in  $\text{EtOH}_{95}$  and NaPi solutions should contain certain water molecules within the chains. Moreover, although it has been found that once the monolayers are dried and newly immersed in water solutions, they are impermeable to water molecules [17], when they are examined by infrared spectroscopy under a water layer, some changes in the peak frequencies along with peak broadening are observed that are interpreted as penetration of some water molecules into the external monolayer region that result in the formation of hydrogen bonds with the oxygen atoms of the EG moieties [16,17,20,55,56]. The strong interaction between the EG units with water may then establish a transition of structured aqueous layer at the film/liquid interface [21] independently of the fact that the SAMs were formed in aqueous solutions or not.

At this point, it is interesting to note the important effect of the electrolyte used for the electrochemical evaluation of the SAMs by the  $[\text{Fe}(\text{CN})_6]^{3-/4}$  redox probe. As the electrochemical measurement is made after equilibrating the modified electrode with the solution, there is plenty of time for the water molecules and the electrolyte ions to interact with the external region of the EG7-SAM. The slightly negative charge measured for EGN films [57,58] can allow the interaction with cations, in this case the  $\text{Na}^+$  or  $\text{K}^+$  ions, that exist in a high concentration in the electrolyte. To explore the existence of a long-range structured water layer adjacent to the EGN interface, Dicke et al. [59] made force-distance measurements under different electrolyte solutions. They employed both chaotropic and kosmotropic ions following the Hofmeister series to investigate their influence on water structure and the possible interaction with the EG units of the SAM, but they could not find a conclusive effect as all the ions studied showed a similar trend independent of their position in the series. The necessity of certain amount of space for a complexation between the EG units and the cations that should not be available in the densely packed SAM was used as the reason for the lack of effects.

However, the role of different ions in the formation of two-phase systems with EGN polymers is well documented and a different ability is found for  $\text{Na}^+$  and  $\text{K}^+$  and even for phosphate salts. These effects are explained on the basis of their position on the Hofmeister series and their free energy of hydration. Thus, the presence of these salts can decrease the amount of water available in the vicinity of the monolayer changing the structure of the interface [60]. If the structural changes in the external region of the EG7-SAM are dependent on the ability of the ions to make the layer more impermeable to the redox probe, the observed differences in the electron transfer rate constants of the  $[\text{Fe}(\text{CN})_6]^{3-/4}$  redox probe could be explained. To ascertain if this effect is produced by the  $\text{Na}^+$  or the phosphate ions, apart from the studies in  $\text{KNO}_3$  and  $\text{KCl}$ , we have also studied the influence of other salts like  $\text{NaCl}$  or  $\text{KPi}$ . Under these conditions, the same behavior is observed allowing us to conclude that is only the combination effect of  $\text{Na}^+$  and phosphate ions that provoke the stronger inhibition of the  $[\text{Fe}(\text{CN})_6]^{3-/4}$  electron transfer.

To find out if after exposure of the EG7-SAMs to the electrolyte solutions, some ions can remain adhered to the external region of the monolayer, X-ray photoelectronic spectra have been recorded for EG7-SAMs that have been contacted overnight with each of the electrolyte solutions used in this work. In any of the cases, we could detect the presence of them as it has been the case reported in earlier studies dealing with the same propose [59]. Moreover, no changes in the composition and/or binding energies of the S 2p, C 1s and O 1s signals corresponding to the SAMs were detected that could allow some conclusions about the presence of those ions in the monolayer that could explain the observed behavior. Figure

S3 shows the spectra obtained in high resolution for the S 2p, C 1s and O 1s, for the EG7-SAMs formed in EtOH<sub>95</sub> and NaPi 1 M, after being in contact overnight with the electrolyte solution. The S 2p spectra are dominated by the peak at 162 eV corresponding to the thiolate species bound to gold, as it was observed for the EG7-SAM formed in EtOH [27]. However, an increase in the ratio of free thiol or di-sulfur groups in the deconvoluted spectra is found in respect to the SAM formed in the absence of water (25-30 % in the present case, whereas less than 20 % of the area corresponding to the high energy peaks, in the case of EtOH). The spectra obtained for the C 1s and O 1s are deconvoluted with three components being the strongest peaks assigned to the carbon and oxygen atoms in the EG segments. The rest of components are ascribed to adventitious carbons or oxygen functions coming from impurities that are very difficult to eliminate. The presence of some water molecules that remains within the SAM (~532.5 eV [61]) cannot be discarded.

## Conclusions.

Compact EG7-SAMs can be formed from EtOH, EtOH<sub>95</sub>, THF and NaPi 1 M aqueous solutions of EG7 on gold substrates as evidenced by the analysis of the RD processes. When using a PO gold electrode, subtle differences are observed in the shape and potentials of the various peaks that are ascribed to the different interactions of the solvent with the EG7 chains and the probable retention of some water molecules within the self-assembled chains. The formation of EG7-SAMs on low index gold single crystals allows us to assign the peaks to different facets of gold and speculate on the existence of possible interactions that give place to different organization depending on the size of the domains within the monolayer.

The differences observed in the RD processes of the EG7-SAMs formed in various solvents are not translated into the blocking behavior of these films as analyzed by CV and EIS of the [Fe(CN)<sub>6</sub>]<sup>3-/4</sup> redox pair in different electrolytes. A stronger inhibition of the electron transfer of the probe is obtained in NaPi 0.1 M aqueous solution in comparison with the other electrolytes such as KNO<sub>3</sub>, KCl, NaCl and KPi. There must be specific interactions between the Na<sup>+</sup> or phosphate or both ions that can change either the structure of the topmost region of the monolayer establishing specific interactions with the ether oxygens, or the structure of the water film directly interacting with the monolayer. However, no experimental evidence has been found for any of these possibilities, concluding that a repulsion effect for an increase of the negative charge in the monolayer that occurs in the presence of NaPi must be responsible for this stronger inhibition of the electron transfer. In this respect, a recent study investigating the breakdown of protein resistance in OEG-terminated alkanethiol SAMs [62], has proposed that trivalent ions replace the structured

water molecules coupled in an interfacial water layer to the SAM, as a possible mechanism in overcoming the protein resistance.

*Acknowledgements.* We thank the Ministerio de Ciencia e Innovación (Project RED2018-102412-T Network of Excellence Electrochemical Sensors and Biosensors), Junta de Andalucía and Universidad de Córdoba (UCO-FEDER-2018: ref. 1265074-2B and Plan Propio, Submod. 1.2. P.P. 2019) for financial support of this work. M.C. acknowledges Ministerio de Universidades for FPU 17/03873 grant.

## References.

- [1] J.C. Love, L.A. Estroff, J.K. Kriebel, R.G. Nuzzo, G.M. Whitesides, Self-Assembled Monolayers of Thiolates on Metals as a Form of Nanotechnology, *Chem. Rev.* 105(4) (2005) 1103-1169.
- [2] A. Ulman, Formation and Structure of Self-Assembled Monolayers, *Chem. Rev.* 96(4) (1996) 1533-1554.
- [3] R. Yamada, H. Sakai, K. Uosaki, Solvent effect on the structure of the self-assembled monolayer of alkanethiol, *Chem. Lett.* (7) (1999) 667-668.
- [4] T.W. Schneider, D.A. Buttry, Electrochemical quartz crystal microbalance studies of adsorption and desorption of self-assembled monolayers of alkyl thiols on gold, *J. Am. Chem. Soc.* 115(26) (1993) 12391-7.
- [5] A.H.A. Mamun, J.R. Hahn, Effects of Solvent on the Formation of Octanethiol Self-Assembled Monolayers on Au(111) at High Temperatures in a Closed Vessel: A Scanning Tunneling Microscopy and X-ray Photoelectron Spectroscopy Study, *J. Phys. Chem. C* 116(42) (2012) 22441-22448.
- [6] D. Yan, J.A. Saunders, G.K. Jennings, Enhanced Chain Densities of n-Alkanethiolate Self-Assembled Monolayers on Gold from Aqueous Micellar Solutions, *Langmuir* 16(20) (2000) 7562-7565.
- [7] D. Yan, J.A. Saunders, G.K. Jennings, Kinetics of Formation for n-Alkanethiolate Self-Assembled Monolayers onto Gold in Aqueous Micellar Solutions of C12E6 and C12E7, *Langmuir* 18(26) (2002) 10202-10212.
- [8] D. Yan, J.A. Saunders, G.K. Jennings, Formation and Stability of Hexadecanethiolate SAMs Prepared in Aqueous Micellar Solutions of C12E6, *Langmuir* 19(22) (2003) 9290-9296.
- [9] V. Ganesh, V. Lakshminarayanan, Self-Assembled Monolayers of Alkanethiols on Gold Prepared in a Hexagonal Lyotropic Liquid Crystalline Phase of Triton X-100/Water System, *Langmuir* 22(4) (2006) 1561-1570.
- [10] D. García Raya, R. Madueno, M. Blázquez, T. Pineda, Formation of a 1,8-Octanedithiol Self-Assembled Monolayer on Au(111) Prepared in a Lyotropic Liquid-Crystalline Medium, *Langmuir* 26(14) (2010) 11790-11796.
- [11] D. Garcia Raya, C. Silien, M. Blázquez, T. Pineda, R. Madueño, Electrochemical and AFM Study of the 2D-Assembly of Colloidal Gold Nanoparticles on Dithiol SAMs Tuned by Ionic Strength, *J. Phys. Chem. C* 118(26) (2014) 14617-14628.
- [12] A.R. Puente Santiago, T. Pineda, M. Blázquez, R. Madueño, Formation of 2-D Crystalline Intermixed Domains at the Molecular Level in Binary Self-Assembled Monolayers from a Lyotropic Mixture, *J. Phys. Chem. C* 120(16) (2016) 8595-8606.
- [13] A.R. Puente Santiago, G. Sánchez-Obrero, T. Pineda, M. Blázquez, R. Madueño, Influence of Patterning in the Acid-Base Interfacial Properties of Homogeneously Mixed CH<sub>3</sub>- and COOH-Terminated Self-Assembled Monolayers, *J. Phys. Chem. C* 122(5) (2018) 2854-2865.



- [14] S. Herrwerth, W. Eck, S. Reinhardt, M. Grunze, Factors that determine the protein resistance of oligoether self-assembled monolayers - Internal hydrophilicity, terminal hydrophilicity, and lateral packing density, *J. Am. Chem. Soc.* 125(31) (2003) 9359-9366.
- [15] P. Harder, M. Grunze, R. Dahint, G.M. Whitesides, P.E. Laibinis, Molecular conformation in oligo(ethylene glycol)-terminated self-assembled monolayers on gold and silver surfaces determines their ability to resist protein adsorption, *J. Phys. Chem. B* 102(2) (1998) 426-436.
- [16] M.W.A. Skoda, R.M.J. Jacobs, J. Willis, F. Schreiber, Hydration of oligo(ethylene glycol) self-assembled monolayers studied using polarization modulation infrared spectroscopy, *Langmuir* 23(3) (2007) 970-974.
- [17] S. Zorn, N. Martin, A. Gerlach, F. Schreiber, Real-time PMIRRAS studies of in situ growth of C(11)Eg(6)OMe on gold and immersion effects, *Phys. Chem. Chem. Phys.* 12(31) (2010) 8986-8991.
- [18] L.Y. Li, S.F. Chen, J. Zheng, B.D. Ratner, S.Y. Jiang, Protein adsorption on oligo(ethylene glycol)-terminated alkanethiolate self-assembled monolayers: The molecular basis for nonfouling behavior, *J. Phys. Chem. B* 109(7) (2005) 2934-2941.
- [19] K.L. Prime, G.M. Whitesides, Adsorption of Proteins onto Surfaces Containing End-Attached Oligo(Ethylene Oxide) - A Model System Using Self-Assembled Monolayers, *J. Am. Chem. Soc.* 115(23) (1993) 10714-10721.
- [20] M.W.A. Skoda, F. Schreiber, R.A.J. Jacobs, J.R.P. Webster, M. Wolff, R. Dahint, D. Schwendel, M. Grunze, Protein Density Profile at the Interface of Water with Oligo(ethylene glycol) Self-Assembled Monolayers, *Langmuir* 25(7) (2009) 4056-4064.
- [21] R.L.C. Wang, H.J. Kreuzer, M. Grunze, Molecular conformation and solvation of oligo(ethylene glycol)-terminated self-assembled monolayers and their resistance to protein adsorption, *J. Phys. Chem. B* 101(47) (1997) 9767-9773.
- [22] R.L.C. Wang, H.J. Kreuzer, M. Grunze, The interaction of oligo(ethylene oxide) with water: a quantum mechanical study, *Phys. Chem. Chem. Phys.* 2(16) (2000) 3613-3622.
- [23] M. Chavez, A. Fernandez-Merino, G. Sanchez-Obrero, R. Madueno, J.M. Sevilla, M. Blazquez, T. Pineda, Distinct thermoresponsive behaviour of oligo- and poly-ethylene glycol protected gold nanoparticles in concentrated salt solutions, *Nanoscale Adv.* 3(16) (2021) 4767-4779.
- [24] G. Emilsson, R.L. Schoch, L. Feuz, F. Höök, R.Y.H. Lim, A.B. Dahlin, Strongly Stretched Protein Resistant Poly(ethylene glycol) Brushes Prepared by Grafting-To, *ACS Appl. Mater. Interfaces* 7(14) (2015) 7505-7515.
- [25] R. Ortiz, S. Olsen, E. Thormann, Salt-Induced Control of the Grafting Density in Poly(ethylene glycol) Brush Layers by a Grafting-to Approach, *Langmuir* 34(15) (2018) 4455-4464.
- [26] G. Sanchez-Obrero, M. Chavez, R. Madueno, M. Blazquez, T. Pineda, J.M. Lopez-Romero, F. Sarabia, J. Hierrezuelo, R. Contreras-Caceres, Study of the self-assembly process of an oligo(ethylene glycol)-thioacetyl substituted theophylline (THEO) on gold substrates, *J. Electroanal. Chem.* 823 (2018) 663-671.
- [27] M. Chávez, G. Sánchez-Obrero, R. Madueño, J.M. Sevilla, M. Blázquez, T. Pineda, Characterization of a self-assembled monolayer of O-(2-Mercaptoethyl)-O'-methyl-hexa(ethylene glycol) (EG7-SAM) on gold electrodes, *J. Electroanal. Chem.* 880 (2021) 114892.
- [28] T. Doneux, A. de Ghellinck, E. Triffaux, N. Brouette, M. Sferrazza, C. Buess-Herman, Electron Transfer Across an Antifouling Mercapto-hepta(ethylene glycol) Self-Assembled Monolayer, *J. Phys. Chem. C* 120(29) (2016) 15915-15922.
- [29] T. Doneux, L. Yahia Cherif, C. Buess-Herman, Controlled Tuning of the Ferri/Ferrocyanide Electron Transfer at Oligo(Ethylene Glycol)-Modified Electrodes, *Electrochim. Acta* 219 (2016) 412-417.
- [30] A.L. Gui, E. Luais, J.R. Peterson, J.J. Gooding, Zwitterionic Phenyl Layers: Finally, Stable, Anti-Biofouling Coatings that Do Not Passivate Electrodes, *ACS Appl. Mater. Interfaces* 5(11) (2013) 4827-4835.

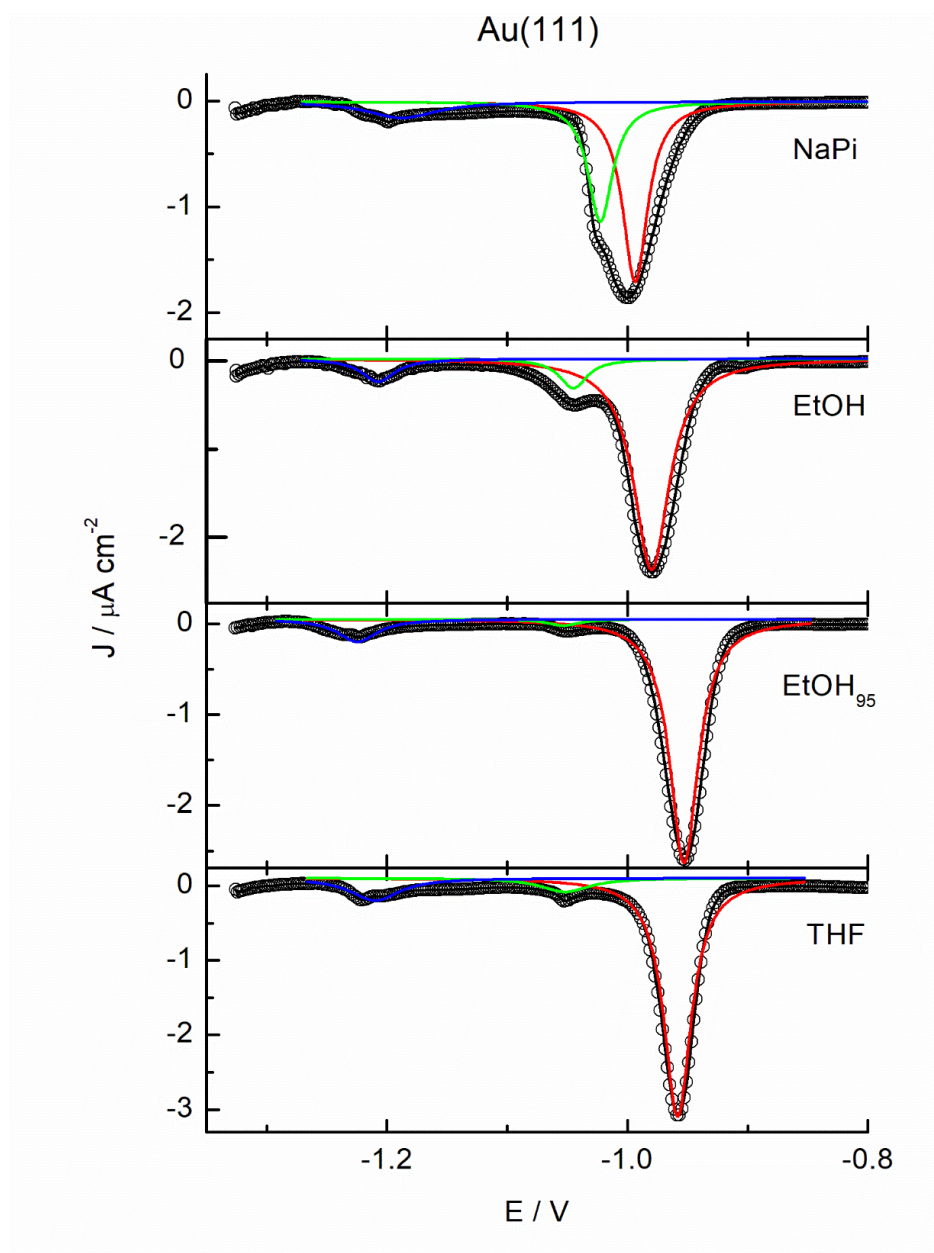
- [31] D.J. Vanderah, G. Valincius, C.W. Meuse, Self-assembled monolayers of methyl 1-thiahexa(ethylene oxide) for the inhibition of protein adsorption, *Langmuir* 18(12) (2002) 4674-4680.
- [32] C.A. Widrig, C. Chung, M.D. Porter, The electrochemical desorption of n-alkanethiol monolayers from polycrystalline gold and silver electrodes, *J. Electroanal. Chem.* 310(1-2) (1991) 335-59.
- [33] C.J. Zhong, J. Zak, M.D. Porter, Voltammetric reductive desorption characteristics of alkanethiolate monolayers at single crystal Au(111) and (110) electrode surfaces, *J. Electroanal. Chem.* 421(1-2) (1997) 9-13.
- [34] M.M. Walczak, C.A. Alves, B.D. Lamp, M.D. Porter, Electrochemical and X-ray photoelectron spectroscopic evidence for differences in the binding sites of alkanethiolate monolayers chemisorbed at gold, *J. Electroanal. Chem.* 396(1-2) (1995) 103-114.
- [35] C.J. Zhong, M.D. Porter, Fine structure in the voltammetric desorption curves of alkanethiolate monolayers chemisorbed at gold, *J. Electroanal. Chem.* 425(1-2) (1997) 147-153.
- [36] S.S. Wong, M.D. Porter, Origin of the multiple voltammetric desorption waves of long-chain alkanethiolate monolayers chemisorbed on annealed gold electrodes, *J. Electroanal. Chem.* 485(2) (2000) 135-143.
- [37] D.F. Yang, C.P. Wilde, M. Morin, Electrochemical desorption and adsorption of nonyl mercaptan at gold single crystal electrode surfaces, *Langmuir* 12(26) (1996) 6570-6577.
- [38] T. Doneux, M. Steichen, A. De Rache, C. Buess-Herman, Influence of the crystallographic orientation on the reductive desorption of self-assembled monolayers on gold electrodes, *J. Electroanal. Chem.* 649(1-2) (2010) 164-170.
- [39] T. Laredo, J. Leitch, M. Chen, I.J. Burgess, J.R. Dutcher, J. Lipkowski, Measurement of the Charge Number Per Adsorbed Molecule and Packing Densities of Self-Assembled Long-Chain Monolayers of Thiols, *Langmuir* 23(11) (2007) 6205-6211.
- [40] O. Azzaroni, M.E. Vela, G. Andreasen, P. Carro, R.C. Salvarezza, Electrodesorption Potentials of Self-Assembled Alkanethiolate Monolayers on Ag(111) and Au(111). An Electrochemical, Scanning Tunneling Microscopy and Density Functional Theory Study, *J. Phys. Chem. B* 106(47) (2002) 12267-12273.
- [41] N. Arisnabarreta, G.D. Ruano, M. Lingenfelder, E.M. Patrino, F.P. Cometto, Comparative Study of the Adsorption of Thiols and Selenols on Au(111) and Au(100), *Langmuir* 33(48) (2017) 13733-13739.
- [42] R. Madueno, J.M. Sevilla, T. Pineda, A.J. Roman, M. Blazquez, A voltammetric study of 6-mercaptopurine monolayers on polycrystalline gold electrodes, *J. Electroanal. Chem.* 506(2) (2001) 92-98.
- [43] S. Yoshimoto, T. Sawaguchi, F. Mizutani, I. Taniguchi, STM and voltammetric studies on the structure of a 4-pyridinethiolate monolayer chemisorbed on Au(100)-(1×1) surface, *Electrochem. Commun.* 2(1) (2000) 39-43.
- [44] K. Arihara, T. Ariga, N. Takashima, T. Okajima, F. Kitamura, K. Tokuda, T. Ohsaka, Multiple voltammetric waves for reductive desorption of cysteine and 4-mercaptopbenzoic acid monolayers self-assembled on gold substrates, *Phys. Chem. Chem. Phys.* 5(17) (2003) 3758-3761.
- [45] D. Grumelli, L.J. Cristina, F.L. Maza, P. Carro, J. Ferrón, K. Kern, R.C. Salvarezza, Thiol Adsorption on the Au(100)-hex and Au(100)-(1 × 1) Surfaces, *J. Phys. Chem. C* 119(25) (2015) 14248-14254.
- [46] F.P. Cometto, Z. Luo, S. Zhao, J.A. Olmos-Asar, M.M. Mariscal, Q. Ong, K. Kern, F. Stellacci, M. Lingenfelder, The van der Waals Interactions of n-Alkanethiol-Covered Surfaces: From Planar to Curved Surfaces, *Angew. Chem. Int. Ed.* 56(52) (2017) 16526-16530.
- [47] M. Byloos, H. Al-Maznai, M. Morin, Formation of a Self-Assembled Monolayer via the Electrospreading of Physisorbed Micelles of Thiolates, *J. Phys. Chem. B* 103(31) (1999) 6554-6561.
- [48] D.F. Yang, H. AlMaznai, M. Morin, Vibrational study of the fast reductive and the slow oxidative desorptions of a nonanethiol self-assembled monolayer from a Au(111) single crystal electrode, *J. Phys. Chem. B* 101(7) (1997) 1158-1166.

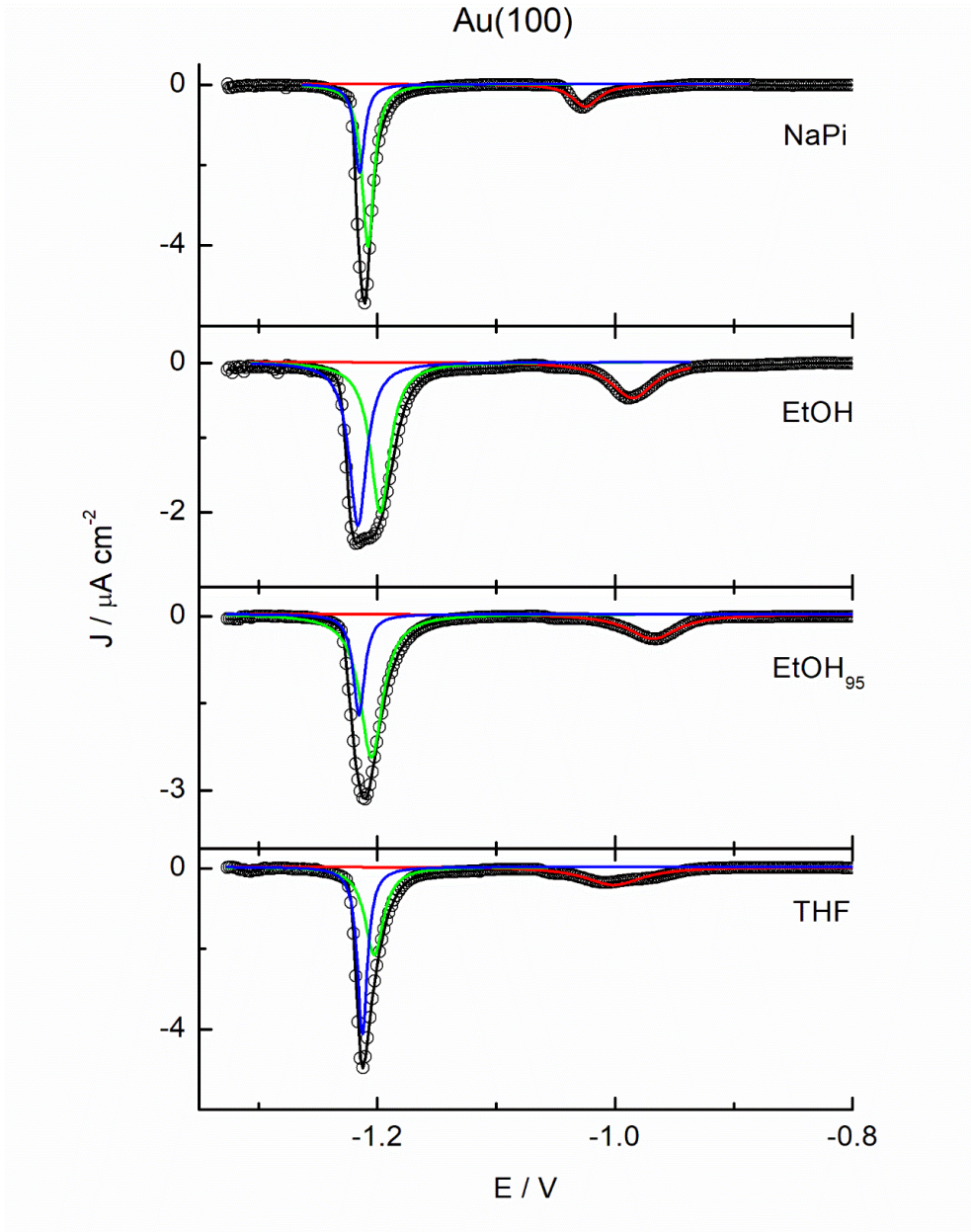
- [49] I. Thom, M. Buck, On the interpretation of multiple waves in cyclic voltammograms of self-assembled monolayers of n-alkane thiols on gold, *Z. Phys. Chem.* 222(5-6) (2008) 739-754.
- [50] X. Gao, G.J. Edens, F.-C. Liu, M.J. Weaver, A. Hamelin, Sensitivity of Electrochemical Adlayer Structure to the Metal Crystallographic Orientation: Potential-Dependent Iodide Adsorption on Au(100) in Comparison with Other Low-Index Surfaces, *J. Phys. Chem.* 98(33) (1994) 8086-8095.
- [51] K. Takehara, H. Takemura, Y. Ide, Electrochemical Studies of the Terminally Substituted Alkanethiol Monolayers Formed on a Gold Electrode - Effects of the Terminal Group on the Redox Responses of Fe(Cn)6-N-3-, Ru(Nh3)H-6-3+ and Ferrocenedimethanol, *Electrochim. Acta* 39(6) (1994) 817-822.
- [52] T.H. Degefa, P. Schon, D. Bongard, L. Walder, Elucidation of the electron transfer mechanism of marker ions at SAMs with charged head groups, *J. Electroanal. Chem.* 574(1) (2004) 49-62.
- [53] J.M. Campina, A. Martins, F. Silva, Selective Permeation of a Liquidlike Self-Assembled Monolayer of 11-Amino-1-undecanethiol on Polycrystalline Gold by Highly Charged Electroactive Probes, *J. Phys. Chem. C* 111(14) (2007) 5351-5362.
- [54] R. Madueno, D. Garcia-Raya, A.J. Viudez, J.M. Sevilla, T. Pineda, M. Blazquez, Influence of the solution pH in the 6-mercaptapurine self-assembled monolayer (6MP-SAM) on a Au(111) single-crystal electrode, *Langmuir* 23(22) (2007) 11027-11033.
- [55] S. Zorn, M.W.A. Skoda, A. Gerlach, R.M.J. Jacobs, F. Schreiber, On the Stability of Oligo(ethylene glycol) (C11EG6OMe) SAMs on Gold: Behavior at Elevated Temperature in Contact with Water, *Langmuir* 27(6) (2011) 2237-2243.
- [56] M. Zolk, F. Eisert, J. Pipper, S. Herrwerth, W. Eck, M. Buck, M. Grunze, Solvation of Oligo(ethylene glycol)-Terminated Self-Assembled Monolayers Studied by Vibrational Sum Frequency Spectroscopy, *Langmuir* 16(14) (2000) 5849-5852.
- [57] H.J. Kreuzer, R.L.C. Wang, M. Grunze, Hydroxide ion adsorption on self-assembled monolayers, *J. Am. Chem. Soc.* 125(27) (2003) 8384-8389.
- [58] C. Dicke, G. Hähner, pH-Dependent Force Spectroscopy of Tri(ethylene Glycol)- and Methyl-Terminated Self-Assembled Monolayers Adsorbed on Gold, *J. Am. Chem. Soc.* 124(42) (2002) 12619-12625.
- [59] C. Dicke, G. Hähner, Interaction between a Hydrophobic Probe and Tri(ethylene glycol)-Containing Self-assembled Monolayers on Gold Studied with Force Spectroscopy in Aqueous Electrolyte Solution, *J. Phys. Chem. B* 106(17) (2002) 4450-4456.
- [60] S.C. Silvério, O. Rodríguez, J.A. Teixeira, E.A. Macedo, The Effect of Salts on the Liquid-Liquid Phase Equilibria of PEG600 + Salt Aqueous Two-Phase Systems, *J. Chem. Eng. Data* 58(12) (2013) 3528-3535.
- [61] X.-P. He, X.-W. Wang, X.-P. Jin, H. Zhou, X.-X. Shi, G.-R. Chen, Y.-T. Long, Epimeric Monosaccharide-Quinone Hybrids on Gold Electrodes toward the Electrochemical Probing of Specific Carbohydrate-Protein Recognitions, *J. Am. Chem. Soc.* 133(10) (2011) 3649-3657.
- [62] M.W.A. Skoda, N.F. Conzelmann, M.R. Fries, L.F. Reichart, R.M.J. Jacobs, F. Zhang, F. Schreiber, Switchable  $\beta$ -lactoglobulin (BLG) adsorption on protein resistant oligo (ethylene glycol) (OEG) self-assembled monolayers (SAMs), *J. Colloid Interface Sci.* 606 (2022) 1673-1683.

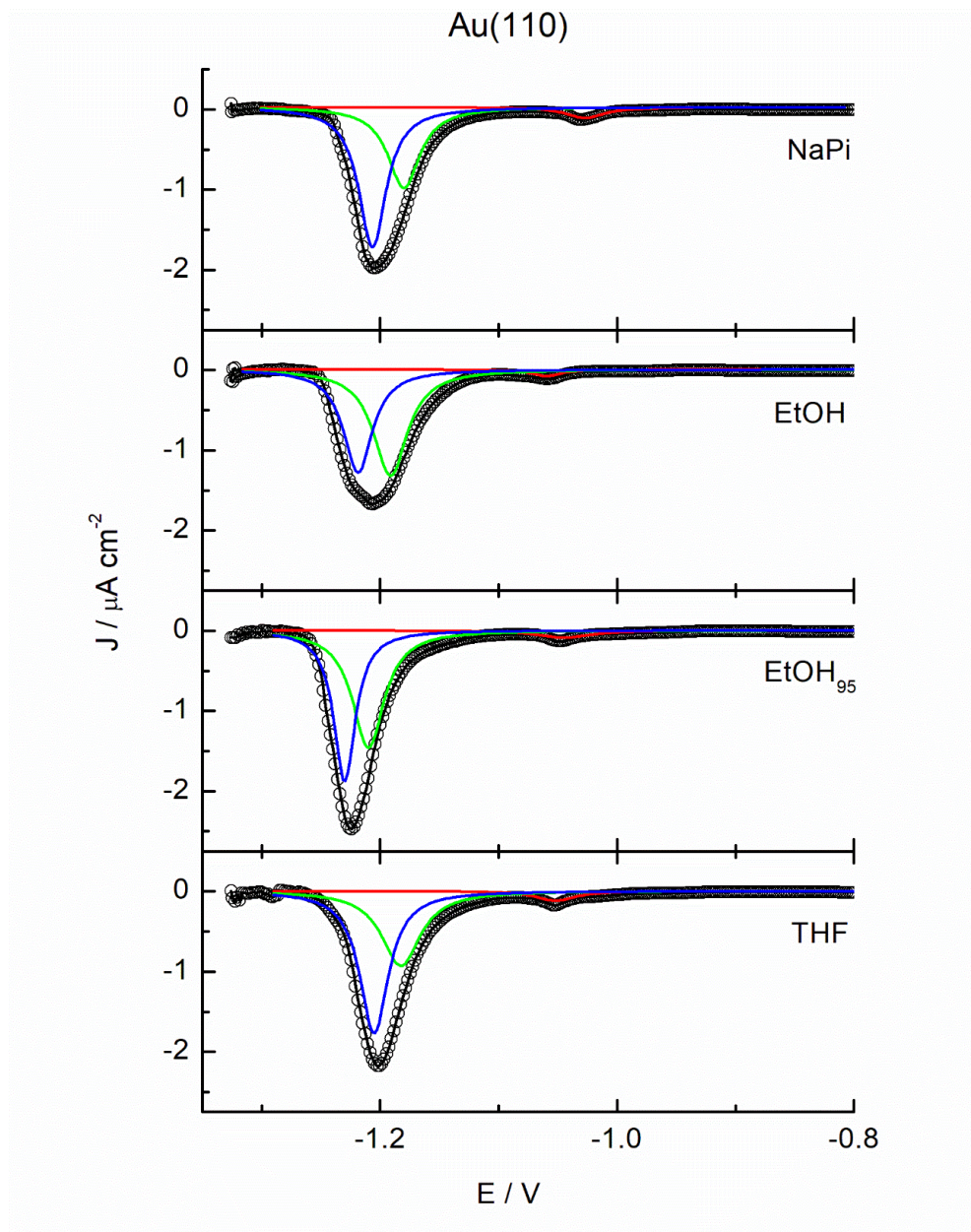
## **Supporting information**

## Deconvolution of cyclic voltammetric peaks for the RD of EG7-SAM on single crystal gold electrodes.

The RD peaks obtained for the EG7-SAMs at different gold single crystal surfaces were background subtracted and submit to a deconvolution process by using Lorentzian curves. This fit has been made to find out the main contributions of the different components to the multipeak voltammetry. All these fittings have been carried out by using the curves obtained at 0.02 V/s as they generally present the best resolution in CV of this process when recorded at this scan rate.



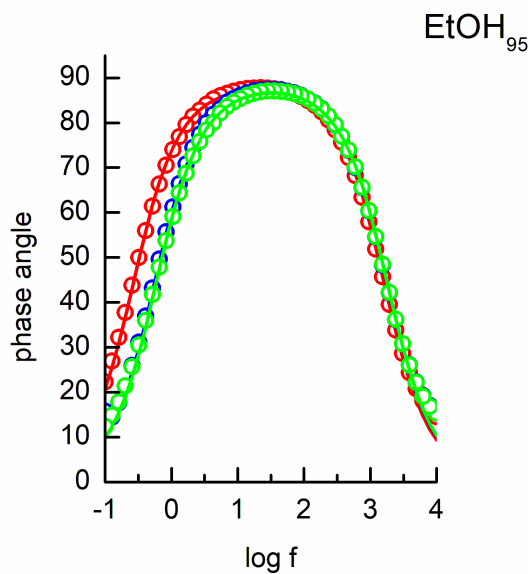
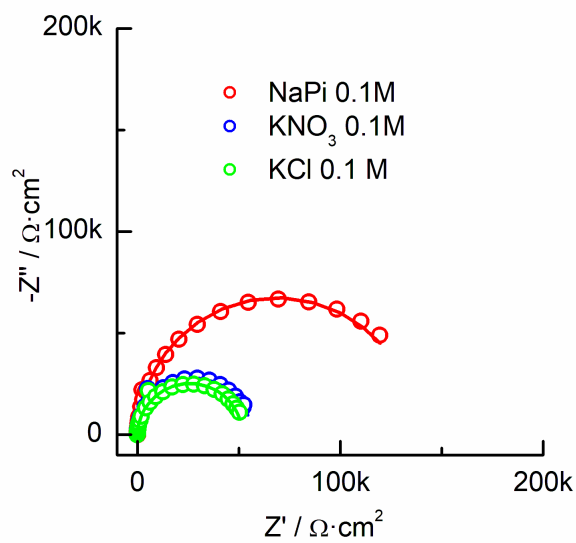
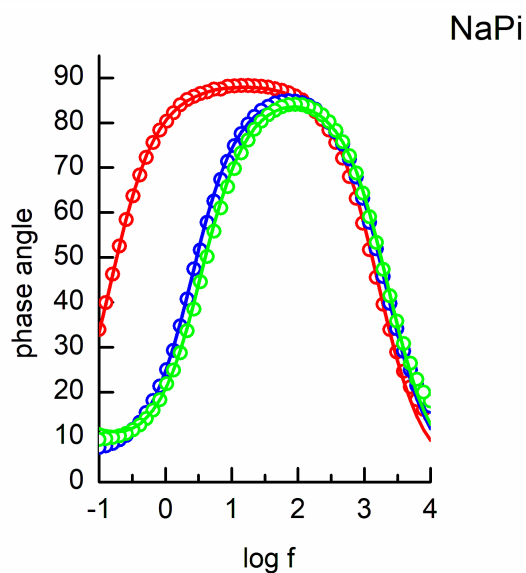
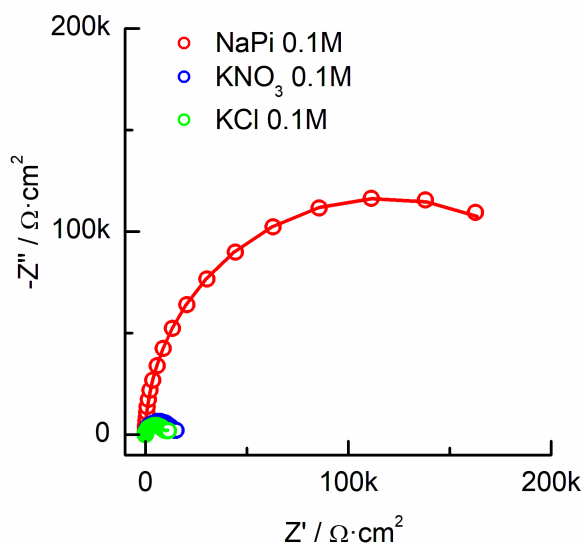
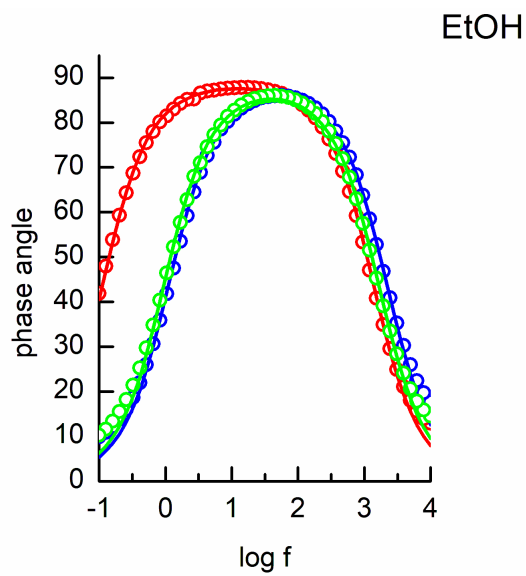
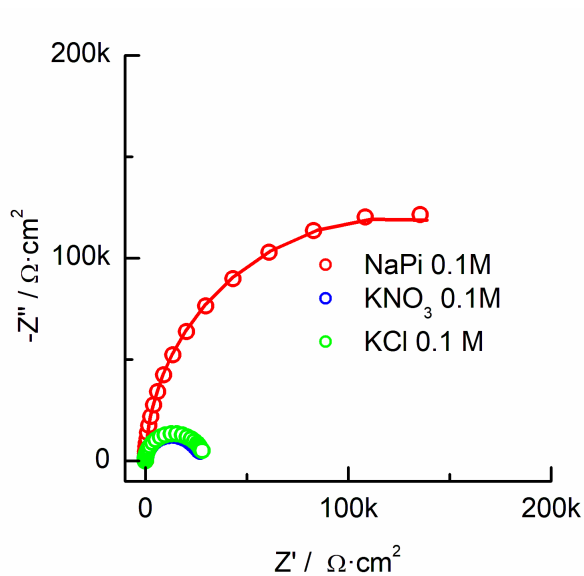




**Figure S1.** Deconvolution of the CVs for the RD processes of EG7-SAMs formed in different solvents and recorded with Au(111), Au(100) and Au(110) single crystal electrodes. The fitting procedure has been made by using Lorentzian curves.

### Electrochemical impedance spectroscopy of EG7-SAMs.

Blocking behaviour against a 1 mM  $K_3Fe(CN)_6$  and 1 mM  $K_4[Fe(CN)_6]$  in 0.1 M electrolyte solutions of the layers formed in different media. Nyquist and Bode plots. Circles are the experimental data and lines correspond to the best fits. The fits have been made by using the Randle's equivalent circuit (either with or without Warburg element).





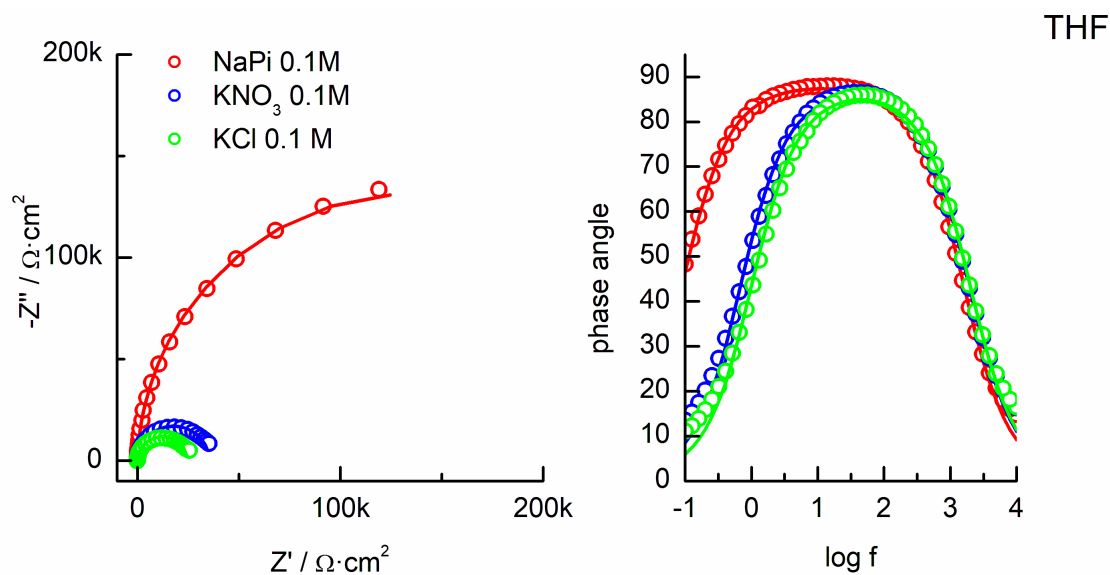


**Figure S2.** Blocking behaviour of the EG7-SAMs formed in different solvents: impedance spectra of 1 mM  $K_3Fe(CN)_6$  and 1 mM  $K_4[Fe(CN)_6]$  in 0.1 M electrolyte solutions (as indicated in the figure label) in the presence of EG7-SAMs.

**Table S1.** Charge densities obtained from the RD process of the EG7-SAMs formed in different solvent solutions.

Electrode / electrolyte	Charge densities / $\mu C / cm^{-2}$			
	NaPi 1 M	EtOH	EtOH <sub>95</sub>	THF
PO-gold	63.0	60.1	66.2	66.0
Au(111)	78.6	79.8	79.4	78.6
Au(100)	77.5	76.1	72.9	74.7
Au(110)	62.5	62.0	63.0	62.5

**Table S2.** Fitting parameters obtained from the fits represented in Figure S2.

Formation media	Evaluation media											
	NaPi 0.1 M				KNO <sub>3</sub> 0.1 M				KCl 0.1 M			
	$R_s / \Omega$	$R_{CT} / k\Omega$	$Q \cdot 10^5$	n	$R_s / \Omega$	$R_{CT} / k\Omega$	$Q \cdot 10^5$	n	$R_s / \Omega$	$R_{CT} / k\Omega$	$Q \cdot 10^5$	n
NaPi 1 M	122	1114	7.73	0.990	88	253	8.18	0.984	79	128	8.32	0.981
THF	95	1353	9.75	0.981	79	177	9.67	0.977	77	123	9.47	0.975
EtOH <sub>95</sub>	115	626	8.03	0.987	88	255	9.85	0.991	85	235	9.78	0.987
EtOH	108	1183	10.2	0.984	81	65	8.15	0.977	87	45	10.2	0.980

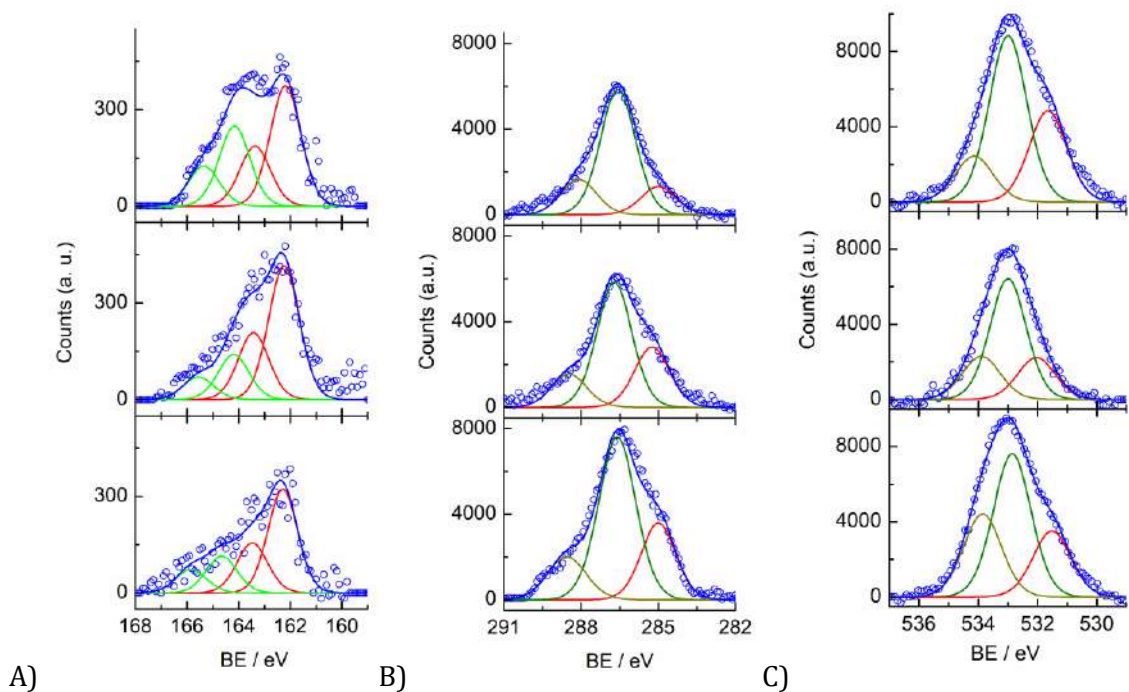


**Figure S3.** XPS spectra of the EG7-SAM gold electrodes. The EG7-SAM has been formed (A) in EtOH<sub>95</sub> solution, (B, C) in 1 M NaPi solution, with a modification time of 1 h. After modification, the EG7-SAM substrates (A, B) were washed and transferred to a 0.1 M NaPi solution at pH 7.4 overnight. After that, the samples were washed and dried with a nitrogen stream and subsequently maintained in a closed vial up to introduction in the vacuum XPS chamber.

### 3.3. Artículo 3.

*Evaluación mediante espectroscopía de impedancia electroquímica del efecto del potencial y la naturaleza del electrolito en la integridad de monocapas autoensambladas de O-(2-Mercaptoetil)-O'-metil-hexa(etilenglicol) (EG7-SAM)*



Effects of the potential and the electrolyte nature in the integrity of the O-(2-Mercaptoethyl)-O'-methyl-hexa(ethylene glycol) self-assembled monolayer by electrochemical impedance spectroscopy.

Miriam Chávez, Guadalupe Sánchez-Obrero, Rafael Madueño, José Manuel Sevilla, Manuel Blázquez, Teresa Pineda\*

Departamento de Química Física y Termodinámica Aplicada, Instituto Químico para la Energía y el Medioambiente, Universidad de Córdoba, Campus Rabanales, Ed. Marie Curie 2<sup>a</sup> Planta, E-14014 Córdoba, Spain

**ARTICLE UNDER REVIEW**

## Abstract

This work addresses an in-deep study of the ionic conductive properties of the EG7-SAM by EIS in a range of experimental conditions including different aqueous electrolytes and wide potential intervals. The measurements are made in the absence of electroactive probes to get information about the ionic ingress or dynamics into the film. The SAMs stability potential regions comprised between the potentials for reductive and oxidative desorption processes are here limited and re-defined as regions where ionic ingress occur and these where the ionic permeability does not take place. This distinction leads to a much smaller region where the SAM behaves as an ideal capacitor. Moreover, these features are dependent on the solution pH and electrolyte in contact with the SAM. The temperature effects on the ionic conductivity are also addressed resulting in differences in behavior of complementary parameters. Capacitance spectroscopy analysis of the EG7-SAM helps in the characterization of these films. Thus, information about processes occurring in different time scales (or frequencies) can be obtained through the proposed analysis. Putting all the results together, a new perspective of the SAMs conductive properties can be obtained that will be very useful in the choice of a determined layer for specific applications.

## Introduction

The self-assembly of alkanethiol molecules on metal surfaces has been studied in the last several decades as model systems for highly compact and well-organized monolayers with specific properties that mostly depend on the alkane chain length and their compacity [1-3]. The presence of terminal functional groups in the alkane chain breaks in some way the organization, and introduces some degree of disorder that is somewhat compensated by the applications generated by these functionalities [4, 5]. In a search for new purposes, some groups have investigated the properties of self-assembled monolayers (SAMs) with other molecular skeletons than the alkane chain such as these formed by oligophenyls or oligo(phenylene ethylenes) [6-9]. Another interesting type of SAMs is comprised by these formed by an alkane chain terminated with one or several ethylene glycol units (EGn-C-SAMs) that have been studied for long time due to their resistance to protein adsorption [10-12]. The EGn portion of these SAMs seems to adopt a well-organized structure, either with helicoidal or all-trans conformations, mostly due to the presence of the long chain arm that help the terminal EGn groups in their organization. The final structure, however, has been shown to depend on the nature of the substrate, the surface coverage, the number of EG units and the solvent [13-17].

We are recently studying the self-assembly of mercapto-poly-ethylene glycol (EGn) molecules lacking the alkane arm [18-22], to add some light into their conformational behavior. Through the RD process of the O-(2-Mercaptoethyl)-O'-methyl-hexa(ethylene glycol) (EG7-SAM) formed from EtOH solution at different modification times, the best performance for this film has been found to be of 1h [18]. The reason for this is that the longer time contacting with the ethanolic solution could allow the introduction of some solvent molecules that alter the helicoidal conformation, as it has been confirmed by infrared spectroscopy. When the EG7-SAM is formed from different solvents either organic or aqueous solutions, the RD signal shows subtle differences that were assigned to different interactions of the solvent with the EG7 chains, probably by retention of some water molecules within the self-assembled chains. A comparison of the EG7-SAM formed in a polyoriented gold substrate with these formed at low index single crystal gold electrodes, manifests some signs of the existence of different interactions and, therefore, different organization as a function of the domain size within the monolayer. The electronic blocking properties of the EG7-SAM against the ferrocyanide redox probe are not sensitive to the different conformations obtained with the various solvent used in the formation. In contrast, the blocking behavior is dependent on the nature of the electrolyte used to study it. A specific role of the sodium or phosphate ions is concluded that could be ascribed to induced changes in the topmost region of the monolayer or the structure of the water film directly interacting with the monolayer.

The lower potential perturbation used in EIS makes this technique very suitable for the analysis of the SAMs in the presence of redox probes as well as in their absence. Thus, in the absence of electroactive redox pairs, the impedance measurements can inform about the ionic permeability of the monolayers. In this way, the ionic insulating properties of alkanethiol SAMs have been evaluated with this technique [23-26] pointing that the well packed SAMs exhibit strong barriers to ionic penetration with phase angles close to  $90^\circ$  in a wide frequency range of  $1\text{Hz} < f < 1000\text{Hz}$ , the theoretical values for an ideal capacitor behavior. Thus, the phase angle values at an ion-diffusion related frequency (1Hz) are taken as an evidence of the presence of ionic conduction when the values are lower than  $88^\circ$  [23]. When these measurements are made at different potentials, a critical value is found that separates potential regions in which the SAM behaves as an ionic insulator and can be modeled as a Helmholtz capacitor from that at which ion penetration into the SAM is activated [24]. This approach has been addressed to alkanethiol SAMs [23,24,26-28] and terminal functionalized alkanethiol SAMs [25,26,29]. When a wide potential range is analyzed, a region where the SAM becomes leaky is always found [27,28]. More recently, complex capacitance spectroscopy has also been used to better characterize these

monolayers and resolve an ionic relaxation process that can be used as a fingerprint for the monolayer properties [30-32].

These findings encourage us to further study the electrochemical behavior of the EG7-SAMs by using the approaches of EIS of these films in the absence of redox pairs. A pioneering work examined the impedance spectra of the EG7-SAM formed in three different EG7 solutions (THF, Ethanol and 95% ethanol) at the potential of 0 V, and a difference in the insulating properties was obtained depending on the nature of the formation solution [33]. In the present work, we accomplish a thorough study of the EG7-SAM formed in ethanolic or in sodium phosphate 1 M solutions by using EIS in the absence of redox pairs in aqueous solutions either acid, alkaline or neutral to analyze their ionic conductive properties. Moreover, the temperature effects on the SAMs properties in a neutral electrolyte evidence interesting differences in behavior depending on the frequencies where the phenomena are monitored. We also used the complex capacitance approach to further characterize the properties of these EG7-SAMs that could serve as a model for the EGn-SAMs of different chain lengths, to gain more insight into the structure and functional properties of these films.

## **Experimental section.**

### Chemicals.

O-(2-Mercaptoethyl)-O'-methyl-hexa(ethylene glycol) (EG7), was purchased from Aldrich-Sigma (purity  $\geq 99\%$ ). The rest of the reagents were from Merck analytical grade. All the aqueous solutions were prepared with deionized ultrapure water produced by Millipore system.

### Experimental methods

Electrochemical experiments were performed on an Autolab (Ecochemie model Pgstat30) instrument attached to a PC with proper software (GPES and FRA) for the total control of the experiments and data acquisition. A conventional three electrode cell comprising a platinum coil as counter electrode, a 50 mM KCl calomel (CE 50mM) as reference electrode and a poly-oriented (PO gold) as working electrode, were used. The PO gold electrode was a homemade sphere obtained by melting a gold wire up to reach a diameter of approximately 2mm and attached to the gold wire that serves as electrode connection. Before each electrochemical measurement, the electrodes were annealed in a natural gas flame to a light-red melt for about 20 s and, after a short period of cooling in air, quenched in ultrapure water. The surface of the PO gold used in this study showed the well-



known characteristic voltammograms in 0.01 M HClO<sub>4</sub> solutions. The real area of the electrode was determined from the charge involved in the gold oxide reduction peaks obtained under these conditions ( $A_{(PO_{gold})} = 0.24 \text{ cm}^2$ ).

For electrode modification, the gold electrodes were immersed in the EG7 ethanolic solution or in 1 M sodium phosphate (NaPi) for a modification time of 1 h. After extensive washing with water or blank electrolyte, they were transferred to the electrochemical cell, to carried out the CV or electrochemical EIS experiments. The EIS experiments were made at different potentials using an amplitude rms of 10 mV and a frequency interval from 0.1 to 10000 Hz.

## Results and discussion.

In a recent work, we have reported that the blocking properties of the EG7-SAMs against the ferrocyanide redox probe are somewhat dependent of the nature of the formation solution but strongly dependent on the electrolyte used to check the redox responses [20]. The presence of a sodium phosphate electrolyte produces the lowest apparent electron transfer rate constant and the comparison with other electrolytes points to a combined effect of Na<sup>+</sup> and phosphate ions at blocking the ferrocyanide electron transfer. In this regard, complementary information on these permeability properties can be found by using EIS in the absence of redox couples. We have recorded the impedance spectra of the EG7-SAM formed in an ethanolic solution in a wide potential region, and in aqueous solutions under different experimental conditions. In these studies, the starting point is the definition of the potential intervals where the EG7-SAM is stable that is limited by the reductive and the oxidative desorption processes at low and high potentials, respectively.

In the case of the EG7-SAM exposed to an acid medium (10 mM HClO<sub>4</sub>), we record the cyclic voltammograms starting at a potential where the monolayer is presumably stable (at +0.6 V) and scan either in the positive or negative direction (Figure 1b and c). Under these conditions, the current density is maintained low and constant up to potentials higher than +1.2 V where the formation of surface oxides on the naked electrode starts (Figure 1a). The stability region ends, however, after additional 100-200 mV are scanned, with the development of a strong oxidative current that is interpreted as the oxidative desorption of the monolayer. This fact has been already found in other SAMs in agreement with a protection effect of the monolayer against gold surface oxidation [18,34-38]. The RD is recorded by scanning in the negative direction and observing the cathodic peaks at potentials lower than +0.3 V. Therefore, the EG7-SAM should maintain its integrity in the

potential interval from +0.3 to +1.4 V under acidic conditions. We thus make a wide-ranging study in this potential interval to obtain more information on the SAM electrochemical integrity by recording the impedance spectra at potentials included in the above defined stability region.

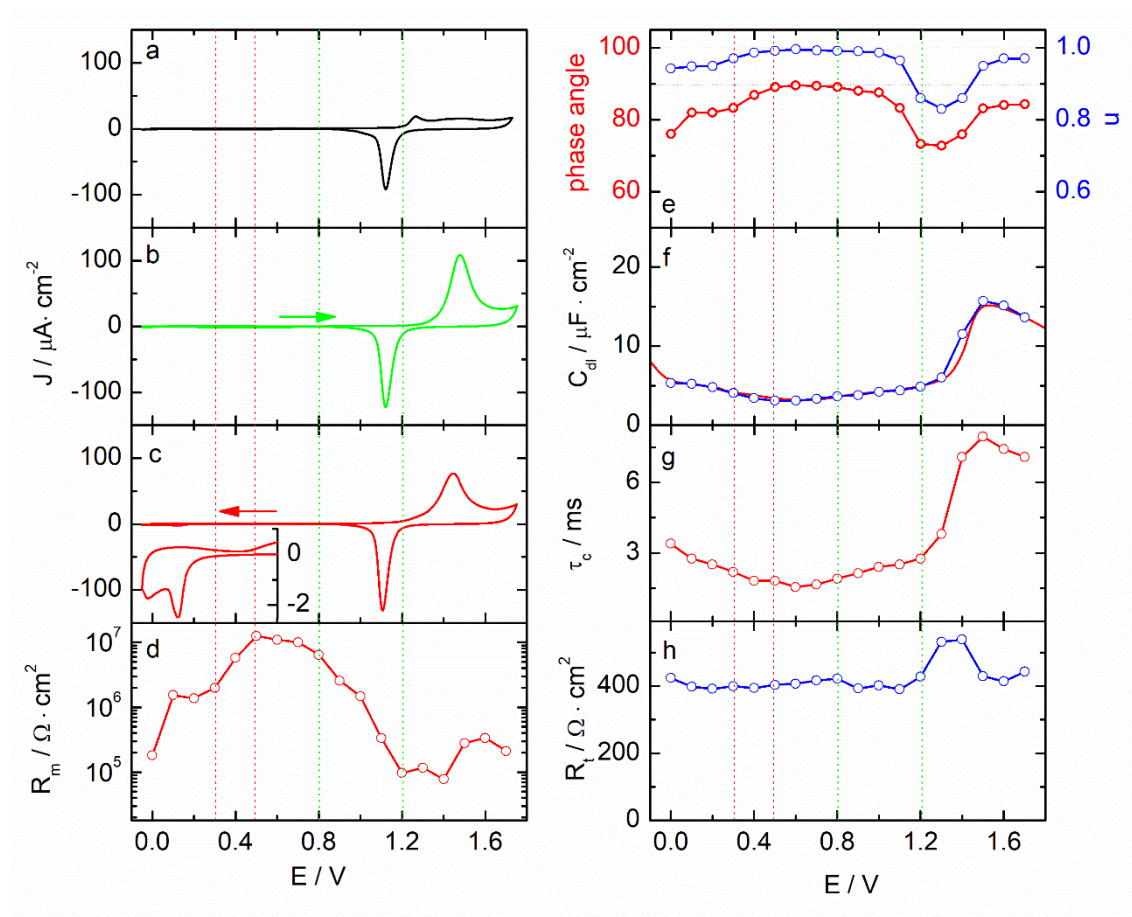


**Figure 1.** Cyclic voltammograms for the naked (a) and EG7-SAM modified gold electrode starting at +0.6 V and scanning to positive (b) and negative potentials (c) to record the oxidative and RD processes, respectively. The inset in (c) shows the enlargement of the RD process to show the onset of the reduction peaks. The arrows show the direction of the scans. (d) Monolayer resistance ( $R_m$ ) and (e) CPE coefficients ( $n$ ) obtained in the fitting analysis of the impedance spectra by using a  $R(RC)$  equivalent circuit. In (e), the phase angle measured at the frequency of 1Hz is also shown. (f) The capacitance curve obtained at the frequency of 500 Hz is plotted (—) together with the values obtained by using the Nyquist complex capacitance curves (—○—); the characteristic relaxation times ( $\tau_c$ ) (g) and the resistances  $R_t$  (h) of the process (see explanation in the text). Experiments are recorded in an  $HClO_4$  10 mM solution in the absence of redox probes.

Figure 2 includes impedance Nyquist plots acquired at three different potentials (+0.4, +0.6 and +1.0 V) with the EG7-SAM in a 10 mM  $HClO_4$  solution. At +0.6 V, a potential that is in the middle of the SAMs stability region, we obtain the highest value of impedance indicating that the layer shows a good packing density resulting in a greater ionic barrier

under these conditions. At potentials either positive or negative, the observed deviation or tilt of the impedance trace at lower frequencies would indicate an increase of SAMs ionic permeability and a deviation from the ideal capacitor behavior. These features are better observed when the impedance data are plotted as Bode representations, where the value of the phase angle obtained at 1 Hz is taken as a measure of the presence or absence of ionic permeability within the SAM as this frequency can be correlated with the diffusion phenomenon that occurs in this time scale [23]. The spectrum represented as Bode phase angle plot at +0.6 V shows the typical behavior of a dielectric layer that is usually modeled by a series resistance,  $R_s$ , due to solution, leads, and contacts, in series with a capacitor associated with the monolayer. While the phase angle is close to  $90^\circ$  in a wide frequency interval covering from 0.1 to 100 Hz, the spectra registered at lower or higher potentials show a decrease in the phase angle at lower frequencies. Under these conditions, a parallel resistance,  $R_m$ , must be introduced in the RC circuit representing the ideal capacitor behavior, to account for this deviation. As it has been described for well packed alkanethiol SAMs [27], the resistance of the monolayer,  $R_m$ , when the electroactive species are absent, is infinite and there should not be current flow across the interface. The potential perturbation under these conditions only results in transient currents due to charging of the monolayer capacitance, and this behavior is obtained in the present system from the phase angle close to  $90^\circ$  observed in the potential range between +0.4 and +1.0 V. Outside this range, the phase angle at low frequencies start to decrease. The values of phase angles measured at 1 Hz, that are taken as a measure of the ideal capacitive behavior [23-25] are plotted in Figure 1e. The departure of the phase angle at lower frequencies from  $90^\circ$  has been explained as the presence of a conductive pathway parallel to the monolayer capacitance associated with ion permeability of the SAM [26,39].

The values of the impedance modulus at 0.1 Hz are not very sensitive to the potential (Figure 2b) with values of around  $3 - 4 \times 10^5 \Omega \cdot \text{cm}^2$  that are closer to these of  $10^6 \Omega \cdot \text{cm}^2$  obtained for octadecanethiol SAMs that seems to be one of the highest compact and insulating monolayers studied [279, 280, 288]. The slopes of these spectra are the unity in all the cases studied. The behavior of long chain alkanethiol SAMs for long time were modeled with a parallel plate capacitor, but soon was found that the SAMs became leaky capacitors at certain potentials. Thus, the necessity of introducing the parallel resistance,  $R_m$ , is an indication of ion penetration into the SAM, that are observable at lower frequencies, at these potentials [26-28,41].

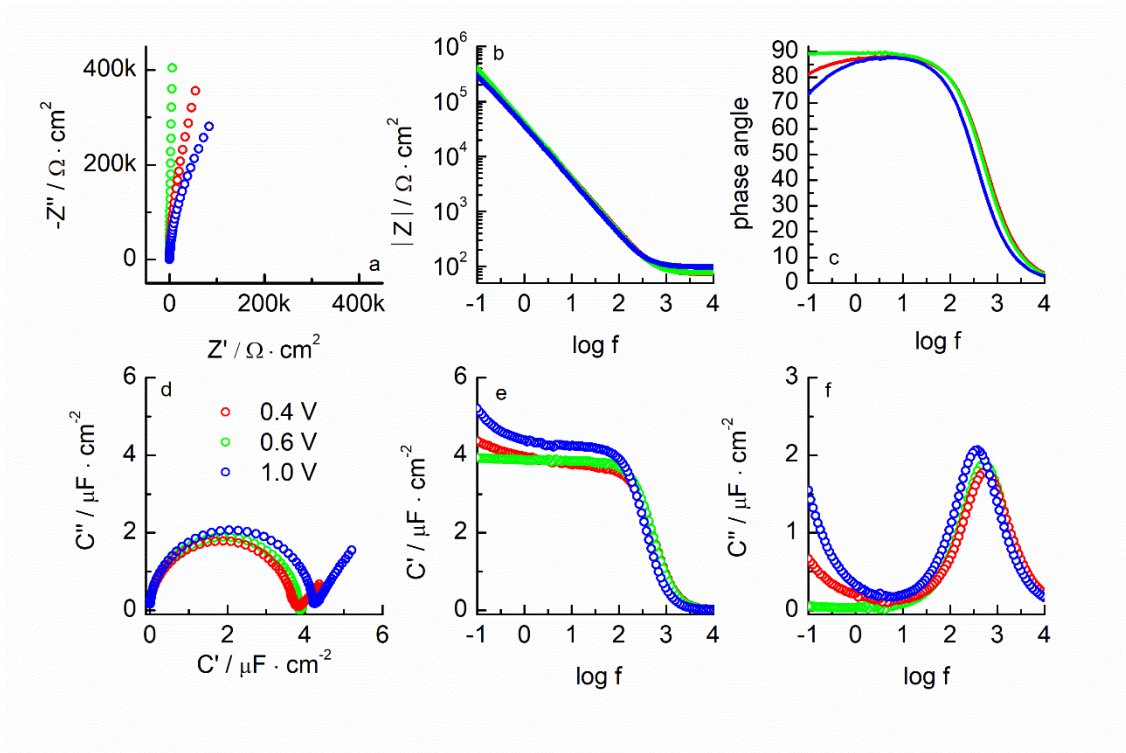


**Figure 2.** Impedance spectra recorded for the EG7-SAM in 10 mM  $\text{HClO}_4$  medium at different potential values, and plotted as Nyquist impedance (a), impedance (b), phase angle (c), Nyquist capacitive diagram (d) complex (e) and real capacitance (f) represented in Bode forms.

The impedance spectra have been fitted by using an equivalent circuit  $R(RQ)$ , consisting in a resistance ( $R_s$ ) in series with a constant phase element (CPE), with  $Z = 1/Q(i\omega)^n$ , in parallel with the resistance of the monolayer ( $R_m$ ). The use of the CPE element in place of the capacitor is made to consider possible heterogeneities in the SAM-electrolyte interface. The CPE exponent  $n$  is close to 1 in the potential range coinciding with that in which the measured phase angle at 1 Hz is close to  $90^\circ$  (Figure 1e), indicating a very good performance for the EG7-SAM at these potentials. The  $R_m$  values are plotted in Figure 1d and, as it can be observed, they are of the order of  $10^7 \Omega \cdot \text{cm}^2$  in the potential interval from +0.5 to +0.7 V, as expected for a good dielectric layer. At lower potentials, the resistance decreases in an exponential manner with an inverse slope of 248 mV/dec, up to the onset potential for the RD process. A similar behavior is observed at higher potentials, from +0.7 to +1.2 V, now coinciding the end with the onset of the oxidative desorption ( $\partial \log R_m / \partial E = 215 \text{ mV/dec}$ ). The decrease in resistance has been analyzed for alkanethiol SAMs in the low potential region and explained as the SAMs behaving as leaky capacitors, and its exponential dependence interpreted as a barrier associated with ion penetration that is dependent on the magnitude of the electric field across the monolayer [27]. It is interesting to note that,

as it also happens in the case of alkanethiols, the capacitance curve presents a low and constant value ( $3.2 \mu\text{F}/\text{cm}^2$ ) in the complete stability range (Figure 1f).

Another way to examine the impedance data is generating capacitance spectra (from the complex impedance function) that highlights the storage characteristics of the interface rather than the resistive terms as emphasized in normal EIS [30,31]. As the terms are phasorially related,  $Z^*(\omega) = Z' + jZ''$ , with  $\omega = 2\pi f$ , the angular frequency, and its inverse the admittance,  $Y^*(\omega) = 1 / Z^*(\omega)$ , we determine the capacitance function according to:

$$C^*(\omega) = (j\omega)^{-1} \cdot Y^*(\omega)$$

$$C^*(\omega) = \frac{Y''}{\omega} - \frac{jY'}{\omega} = C' + jC''$$

where the real part ( $C'(\omega)$ ) of the complex capacitance function is related to the imaginary part of the admittance, and the imaginary part ( $C''(\omega)$ ) is related to the real part of the admittance.

Following these transformations, we also plotted the impedance data in Figure 2d-f as Bode and complex plane capacitance plots. The real part of the capacitance gives the capacitance of the cell measured at low frequency, and the imaginary capacitance the losses in the form of energy dissipation [40,42]. When these magnitudes are plotted against the frequency, it can be seen that  $C'(\omega)$  increases monotonically from zero to a maximum value that represents the low frequency capacitance  $C_{LF}$ , whereas  $C''(\omega)$  shows a peaked shape. This latter plot also allows the determination of  $C_{LF}$  ( $C''_{max}$  in the peak equals  $\frac{1}{2} C_{LF}$ ). When the values of the determined capacitances coincide, this indicates a near homogeneous dielectric relaxation. On the other hand, the frequency at the peak maximum allows the estimation of the relaxation time constant,  $\tau_0$  ( $\tau_0 = 1 / (2\pi f_0)$ , where  $f_0$  is the peak value in the imaginary capacitance plot).

Following these transformations, Bueno et al. have proposed a model to obtain more information about the capacitive and resistive elements of the SAMs, the film charging fingerprint [30,32]. This model is based on the analysis of the impedance data in the middle frequency region, that is observed as a semicircle in the complex capacitance spectra and is interpreted as a capacitive response originated from the entrapment of ions within the film, probably in the formation process or upon contact with the supporting electrolyte. They would generate ionic relaxation features that can be quantified by two terms in series combination,  $R_t$  and  $C_t$ , the latter being the ionic capacitance that is intrinsically associated with  $R_t$ , the resistance linked to rotational voltage perturbations within the film, where  $C_t \cdot R_t$

resolved as  $\tau_t$ , represents a fingerprint of the SAM/electrolyte function. We have measured, on one hand, the peak maximum in the imaginary capacitance vs frequency spectra and determined  $\tau_t$  in all the potential range of EG7-SAM stability. On the other hand, the capacitance  $C_t$  is measured in the complex capacitance plots, as the semicircle's diameter, and from these data,  $R_t$  values were also determined (Figure 1f-h). We have found roughly constant values for these magnitudes ( $C_t = 3.2 \mu\text{F}/\text{cm}^2$ ,  $R_t = 400 \Omega \cdot \text{cm}^2$ ,  $\tau_t = 1.6 \text{ ms}$ ) in a wide potential interval, with an increase at potentials coinciding with the reductive and oxidative desorption processes.

A similar study with the EG7-SAM formed under the same previous experimental conditions but recording the impedance spectra in an alkaline media (0.1 M KOH) (Figure 3) has also been carried out. The stability interval is again indicated by the potentials of the reductive and oxidative desorption processes, resulting from -0.9 to +0.3 V. The analysis of the spectra gives values for the phase angle measured at 1 Hz that reach the maximum value of  $89.3^\circ$  in the potential range of -0.7 to -0.1 V with a similar trend that the CPE exponent  $n$  that also gets the maximum value of unity, in agreement with an ideal capacitor behavior. The decrease of these magnitudes at potentials coinciding with the reductive and oxidative desorption processes is observed as it happens in acid media. Although there is an interval of around 200 mV where the phase angle decreases at potentials approaching the reductive peak, the high resistance measured because of the lack of current flow through the interface, does not substantially decrease. In contrast to the observed leakage phenomenon observed in acid medium the EG7-SAM maintains its integrity up to the faradaic process starts. In the high potential region, however, there is an exponential decrease in  $R_m$  (inverse slope  $\partial \log R_m / \partial E = 290 \text{ mV/dec}$ ) that could indicate the increased ionic permeability of the SAM. The capacitance curves obtained for the EG7-SAM in alkaline media (Figure 3f) also show the typical behavior observed in acid medium with values of  $3.6 \mu\text{F}/\text{cm}^2$ , as the lowest value. Figure 3 also shows the results of the analysis of the complex capacitance spectra with data in accordance with these found in acid media ( $C_t = 3.6 \mu\text{F}/\text{cm}^2$ ,  $R_t = 120 \Omega \cdot \text{cm}^2$ ,  $\tau_t = 0.5 \text{ ms}$ ).

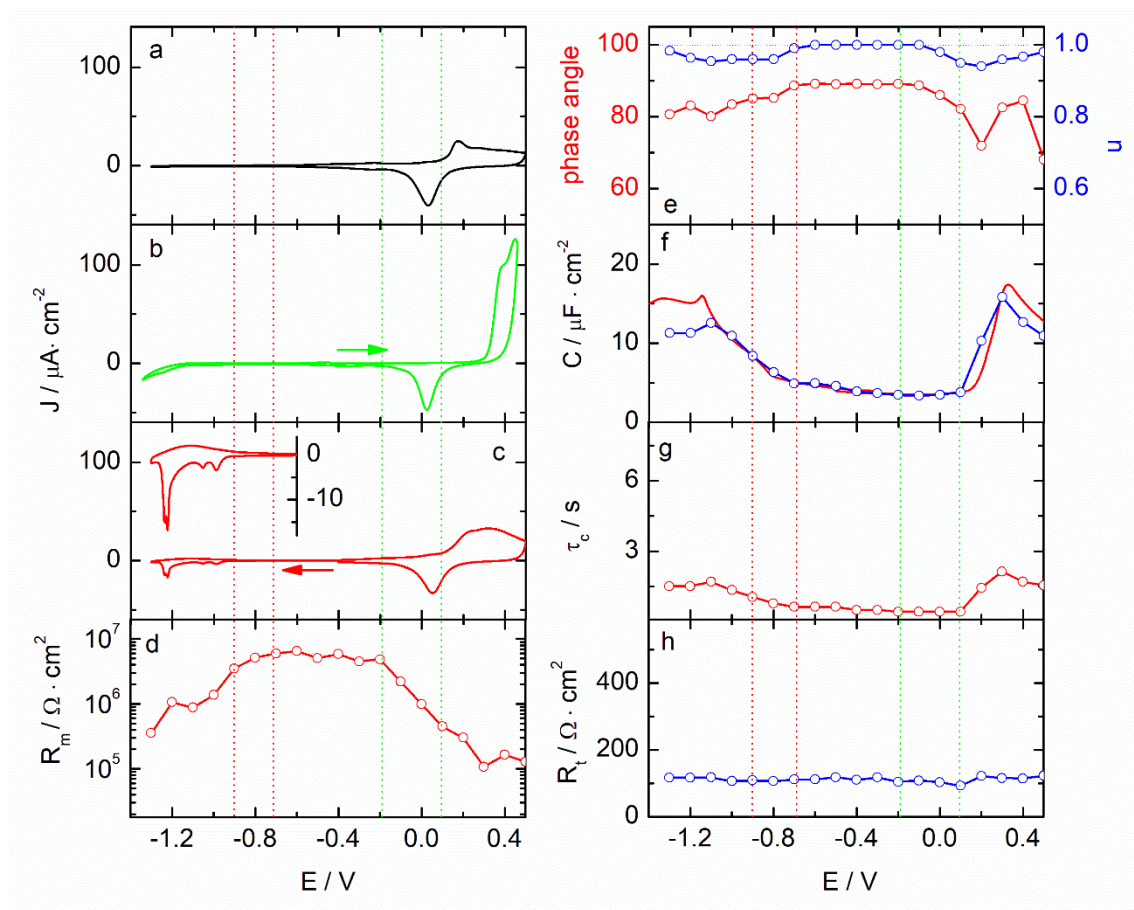


**Figure 3.** Cyclic voltammograms for the naked (a) and EG7-SAM modified gold electrode starting at  $-0.4$  V and scanning to positive (b) and negative potentials (c) to record the oxidative and RD processes, respectively. The inset in (c) shows the enlargement of the RD process to show the onset of the reduction peaks. The arrows show the direction of the scans. (d) Monolayer resistance ( $R_m$ ) and (e) CPE coefficients ( $n$ ) obtained in the fitting analysis of the impedance spectra by using a  $R(RQ)$  circuit. In (e), the phase angle measured at the frequency of 1Hz is also shown. (f) The capacitance curve obtained at the frequency of 500 Hz is plotted (—) together with the values obtained by using the Nyquist complex capacitance curves (—○—); the characteristic relaxation times ( $\tau_c$ ) (g) and the resistances  $R_t$  (h) of the process (see explanation in the text). Experiments are recorded in a KOH 0.1 M solution in the absence of redox probes.

To complement the whole pH interval for aqueous solutions, we have carried out a parallel study in a neutral media in the presence of 0.1 M  $KNO_3$  electrolyte that is one of the most used in electrochemical studies in aqueous solutions. We found that in the potential range from  $-0.4$  to  $+0.7$  V, the EG7-SAM is stable in the presence of 0.1 M  $KNO_3$  electrolyte, as judged by the lack of faradic currents up to the oxidative or reductive processes take place. However, although the onset for oxidative desorption is clearly observed, the reduction of the monolayer seems to be less resolved. In fact, from  $-0.4$  to  $-0.7$  V there is a smooth increase in the current density that could be interpreted as the reduction of the less energetically bound molecules or simply to the increase in capacitance due to the entrance of ions or solvent molecules into the film. In fact, when we analyze the impedance spectra

by using an R(RQ) circuit, the highest resistances due to the impediment of current flow are only seen in a small potential interval, decreasing in an exponential manner with an inverse slope of 307 mV/dec in the potential interval of -0.4 to -0.8 V. Under these circumstances, however, the leakage of the capacitor should be concomitant with the desorption of the layer. Again, the positive potential region becomes leaky when the potentials approach the region of the oxidative process, and these mentioned leaky processes leave only a very small region from -0.4 to 0.0 V where the SAM avoid the entrance of ions. Other parameters would indicate a better performance of the EG7-SAM in  $\text{KNO}_3$  electrolyte such as the phase angle at 1 Hz or the CPE exponent that are close to the ideal capacitor behavior in a wider potential range. In agreement with these results are the values obtained from the complex capacitance analysis where values of  $C_t = 4.3 \mu\text{F}/\text{cm}^2$ ,  $R_t = 180 \Omega \cdot \text{cm}^2$ ,  $\tau_t = 1 \text{ ms}$  are found in a wider potential interval.

In line with these results obtained in aqueous neutral solutions, we have also studied the EG7-SAM formed in NaPi 1M solution and examined in NaPi 0.1 M at pH 7.4, to see if the observed behavior against the ferricyanide redox probe under these conditions has some parallelism with the impedance results in the absence of redox probes. Figure 4 contains the results obtained in this medium together with these in  $\text{KNO}_3$  0.1 M to highlight the possible differences. The oxidative and RD processes of the EG7-SAM in NaPi 0.1 M are less resolved with onsets at lower and higher potentials, respectively, than these in  $\text{KNO}_3$ . Moreover, the phase angle never reaches the  $88^\circ$  being around  $2^\circ$  lower than those observed in  $\text{KNO}_3$  in all the potential interval. A similar difference is found with the CPE exponent that is lower than the unity. This heterogeneity is translated into a higher value of the capacitance that shows the higher value measured for the EG7-SAM (around  $8.5 \mu\text{F}/\text{cm}^2$ ) when compared with  $\text{KNO}_3$  electrolyte and even with alkaline or acidic media. As the relaxation time is of the same order of magnitude in both electrolytes (Figure 4g), the  $R_t$  values ( $R_t = 85 \Omega \cdot \text{cm}^2$ ) also differ being much lower in the NaPi electrolyte.



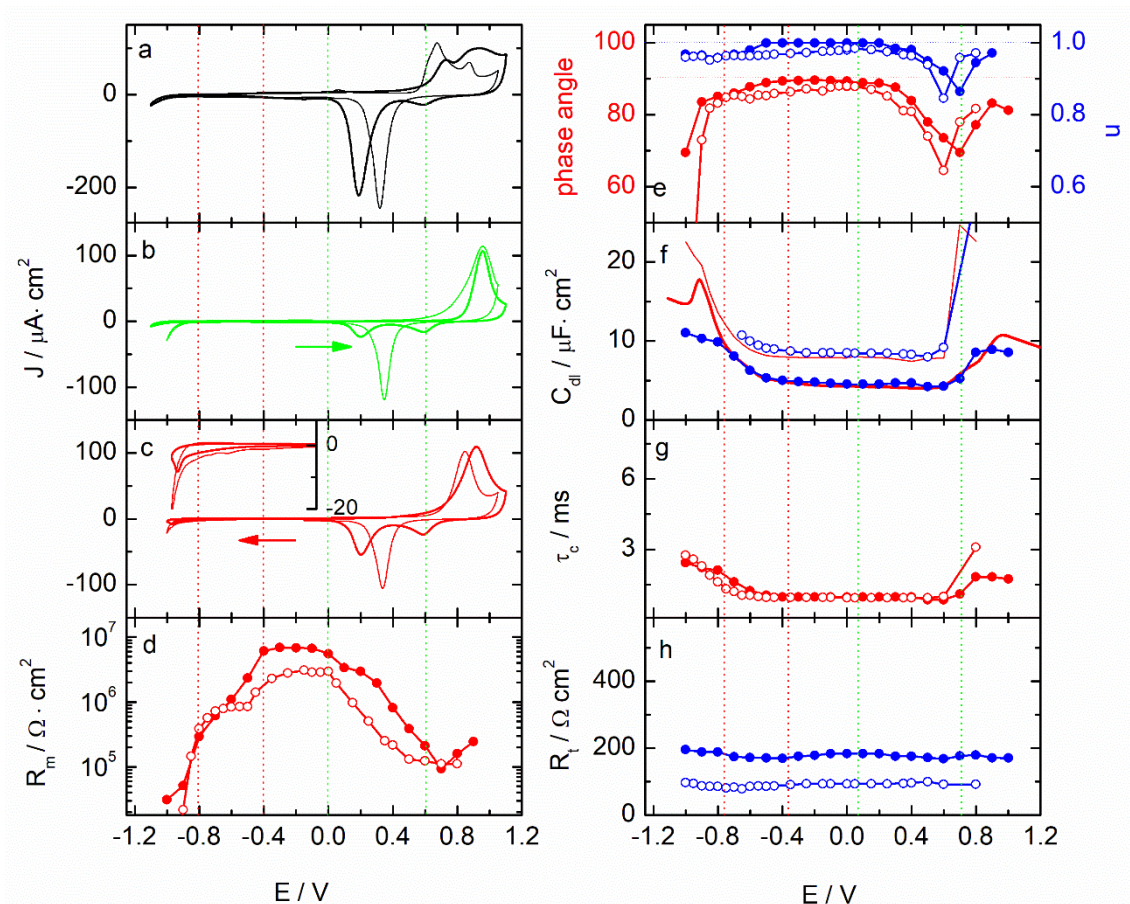


**Figure 4.** Cyclic voltammograms for the naked (a) and EG7-SAM modified gold electrode starting at  $-0.4$  V and scanning to positive (b) and negative potentials (c) to record the oxidative and RD processes, respectively. The inset in (c) shows the enlargement of the RD process to show the onset of the reduction peaks. The arrows show the direction of the scans. (d) Monolayer resistance ( $R_m$ ) and (e) CPE coefficients ( $n$ ) obtained in the fitting analysis of the impedance spectra by using a  $R(RQ)$  circuit. In (e), the phase angle measured at the frequency of 1Hz is also shown. (f) The capacitance curve obtained at the frequency of 500 Hz is plotted (—; - -) together with the values obtained by using the Nyquist complex capacitance curves (—●—; —○—); the characteristic relaxation times ( $\tau_c$ ) (g) and the resistances  $R_t$  (h) of the process (see explanation in the text). Experiments are recorded in a 0.1 M  $KNO_3$  (thicker lines and solid circles) and 0.1 M  $NaPi$  solution at pH 7.4 (thinner lines and empty circles) in the absence of redox probes.

As a rule, the EG7-SAM presents a potential region of stability higher than 1 V where the current density measured by CV is low and constant with total absence of faradaic signals in different aqueous electrolyte solutions. These regions, however, do not behave identically against the ionic insulation properties as obtained by EIS analysis. Although a small region of higher  $R_m$  values, that is where the SAM presents the highest insulation character, is always present, only in alkaline media we find no leakage up to the RD occurs. In acid and neutral media, either  $KNO_3$  or  $NaPi$  electrolytes, this phenomenon seems to occur but due to the lack of resolution in the peaks for the RD process in the latter case, it can be convoluted with the formation of pinholes upon the less strongly bound molecules

are desorbed. The specific interactions of the hydroxyl anions accompanied by their hydration shells with the methoxy-terminated EGn-SAMs [43] should provide a strong barrier for ion penetration up to potentials where the Au-S bond is finally broken. This slightly negatively charged layer of hydrated hydroxyl groups can be well organized on the top-most region of the EG7-SAM exposed to alkaline solutions and resist the changes in the electric field when the potential changes negatively in respect to the zero-charge potential. Moreover, the structure of the EG7 skeleton possess a strong dipole moment that could compensate for the potential changes by acquiring a different orientation [44]. In contrast, the leakage behavior observed in the high potential region, reported in this paper for the first time for these EG7-SAM and never mentioned for the alkanethiol SAMs in the literature, is observed under all the experimental conditions studied, either acid, alkaline or neutral media. This finding indicates that care must be taken when defining the stability intervals for SAMs only in the basis of low and constant capacitance values that is taken as a proof of high compacity.

The capacitance analysis made gives us some information on the EG7-SAM behavior when exposed to different media. Although the relaxation time constants are very close, the values of  $R_t$  obtained from them show some differences. In particular, in the case of acid medium, the highest value of  $400 \text{ } \Omega \cdot \text{cm}^2$  is found that could be interpreted as a bigger resistance to rotational perturbations for the ions within the film. In connection with this, we can also note the smaller value obtained for  $R_t$  for the EG7-SAM formed in NaPi and exposed to the same electrolyte. This fact together with the higher capacitance value points to a higher interaction of the ions with the film that confers some permeability. This is in contrast to the reported high electronic blocking behavior observed for this SAM formed in NaPi and analyzed in the same electrolyte against the ferrocyanide redox probe [20].

To gain more insight into the EG7-SAM properties, we have measured the impedance spectra as a function of temperature in a  $\text{KNO}_3$  solution. The spectra are recorded at  $-0.25 \text{ V}$ , a potential in which the  $R_m$  is maxima, and presumably no leakage occurs. The temperature was changed from  $10$  to  $80 \text{ } ^\circ\text{C}$ . As it is shown in Figure 5, the EG7-SAM maintains the same properties at low temperatures but at  $t > 30 \text{ } ^\circ\text{C}$ , the film begins to be permeated by ions as seen by the decrease of  $R_m$ . The same trend is followed by the phase angle measured at  $1 \text{ Hz}$  and the CPE exponent  $n$ . At  $80 \text{ } ^\circ\text{C}$ , the temperature is reversed, and the mentioned parameters start to increase reaching almost the initial values at  $10 \text{ } ^\circ\text{C}$ .

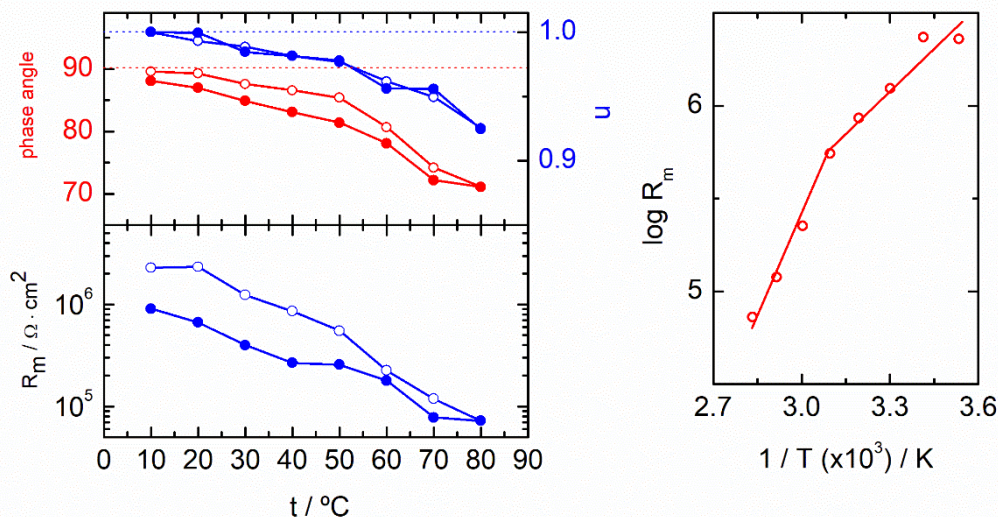


**Figure 5.** Left: Effect of temperature in the phase angle measured at the frequency of 1 Hz, the CPE coefficient ( $n$ ) and the monolayer resistance ( $R_m$ ) obtained in the fitting analysis of the impedance spectra by using a R(RQ) circuit. Right: Variation of the logarithmic of  $R_m$  as a function of the inverse of the absolute temperature. The impedance spectra were recorded at different temperatures from 10 to 80 °C and immediately going back to 10 °C on a EG7-SAM in a 0.1 M  $\text{KNO}_3$  solution; Empty and solid circles represent the data for the direct and the reverse temperature scans respectively.

The analysis of the monolayer resistance,  $R_m$ , indicates a nearly reversible behavior. At low temperatures, the EG7-SAM behaves like an ideal capacitor and at certain temperature value, the resistance starts to decrease as an indication of capacitor leakage. Two trends can be distinguished, the first one showing a lower energy barrier (0.3 eV) for ion ingress in the monolayer and the second one with a higher value (0.6 eV) corresponding to the higher temperature interval. This transition that occurs at around 50 °C would be due to a change in the lateral interactions that make the film less permeable to ions. These special interactions existing in the EGn-SAMs where water molecules play an important role, should explain this transition temperature where the water molecules would acquire a higher mobility after weakening and/or breaking hydrogen bonds and allowing the ions entrance. It seems that at highest temperatures the ion ingress is more demandant, maybe because the possible interaction sites are occupied, or the channels topography do not allow the process. This fact is compatible with the reversibility of this phenomenon, as the water would newly interact with the EGn chains when the mobility decreases at lower temperatures.

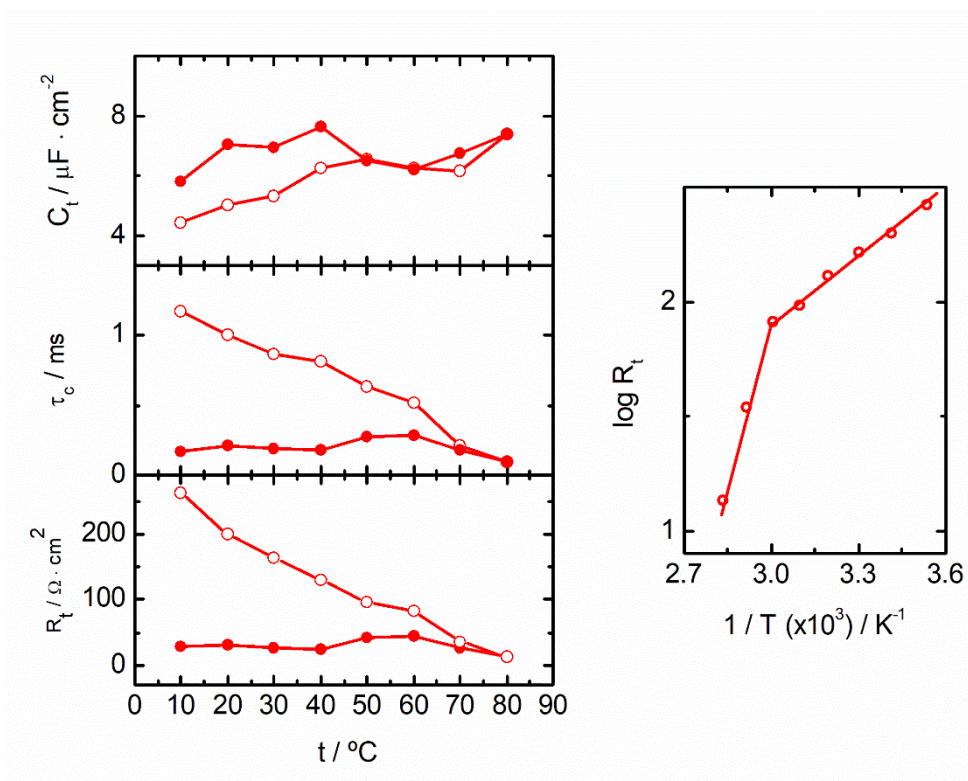


**Figure 6.** Left: Results of the analysis of the capacitance spectra of EG7-SAM formed in ethanol solution. The capacitance, relaxation time and its coupled resistance are plotted against temperature. The spectra were recorded in a 0.1 M  $\text{KNO}_3$  solution. Right: Variation of the logarithmic of  $R_t$  as a function of the inverse of the absolute temperature. The impedance spectra were recorded at different temperatures from 10 to 80  $^\circ\text{C}$  and immediately going back to 10  $^\circ\text{C}$  on a EG7-SAM in a 0.1 M  $\text{KNO}_3$  solution; empty and solid circles represent the data for the direct and the reverse temperature scans respectively.

This reversibility is not observed in the parameters obtained in the analysis of the capacitance spectra. The capacitance increases with temperature and maintain almost that highest value in the temperature descending ramp. Moreover, the relaxation time,  $\tau_t$ , and the resistance,  $R_t$ , decrease up to 0.1 ms and  $12 \Omega \cdot \text{cm}^2$  and do not recover the initial values upon reverting temperature. The smaller value of  $R_t$  would indicate that the ions inside the film do not offer resistance to the changes in the field at least in the high-to-medium frequency region that is where we detect these features.

The logarithmic analysis of the resistance,  $R_t$ , as a function of temperature (Figure 6) shows linear trends with a change in the slopes at around 60  $^\circ\text{C}$ . From this plot we can determine the energy for the activation barrier being of 0.9 and 0.2 eV for the resistances measured in the medium-to-high frequency ranges. The higher activation barrier found for the ions to respond to the changes in the applied field in the pristine EG7-SAM is in agreement with the difficulty to rotate as they accommodate within the chains in parallel with the hydrogen bonding networks existing in the film. However, when this network is

broken, they would find a different situation that permit them to move more freely in response to the changes in the applied field in the time scale of observation.

In a former report dealing with octadecanethiol SAM a constancy of the monolayer capacitance with temperature has been found [28]. Moreover, the monolayer resistance is temperature sensitive only in the potential region where the SAM behaves as a leaky capacitor. Thus, the differences observed in our system should be related to the different molecular composition and structure together with the specific interactions taking place within the SAM.

## Conclusions.

We have presented an in-dept study of the EG7-SAM ion permeability by EIS in different electrolyte aqueous solutions in the absence of redox probes. The interval of SAM's stability defined by CV as the potentials where the current density is low and constant, comprised between the oxidative and RD processes does not inform about the permeability of ions through the SAM. However, EIS analysis defines the real region where the SAM does not allow the ingress of ions and these that demonstrate a leakage behavior, that are situated at potential previous to the reductive and oxidative desorption potentials. The leakage in the potential region closer to the RD has been already reported for alkanethiol SAMs [279, 280] but this at positive potentials is defined for the first time in this work and for the EG7-SAM. There is no doubt that this feature can exist for all the SAMs, formed by either alkanethiol or other different skeleton as the EGn studied in this work.

The different behavior observed in the various pH or electrolytes also indicates that these features need to be taken into account when using these monolayer systems in applications that need precise conductive properties.

The additional information obtained by analyzing the signals by capacitance spectroscopy is also very helpful to fully understand the SAMs properties and, in particular, the EGn-SAMs that are becoming very important in different fields.

The finding that this later capacitance analysis manifests the loss of reversibility whereas the direct analysis of the measured parameters shows that the effects of temperature in the SAMs are reverted indicates that these properties deserve a thorough study to get a deeper information.

*Acknowledgements.* We thank the Ministerio de Ciencia e Innovación (Project RED2018-102412-T Network of Excellence Electrochemical Sensors and Biosensors), Junta de Andalucía and Universidad de Córdoba (UCO-FEDER ref. 1265074-2B and Plan Propio,

Submod. 1.2.) for financial support of this work. M.C. acknowledges Ministerio de Universidades for FPU 17/03873 grant.

## References .

- [1] A. Ulman, *An Introduction to Ultrathin Organic Films: From Langmuir-Blodgett to Self-assembly*, Academic Press, New York, 1991.
- [2] A. Ulman, Formation and Structure of Self-Assembled Monolayers, *Chem. Rev.* 96(4) (1996) 1533-1554.
- [3] J.C. Love, L.A. Estroff, J.K. Kriebel, R.G. Nuzzo, G.M. Whitesides, Self-Assembled Monolayers of Thiolates on Metals as a Form of Nanotechnology, *Chem. Rev.* 105(4) (2005) 1103-1169.
- [4] F. Schreiber, Structure and growth of self-assembling monolayers, *Prog. Surf. Sci.* 65(5-8) (2000) 151-256.
- [5] K.L. Prime, G.M. Whitesides, Self-assembled organic monolayers: model systems for studying adsorption of proteins at surfaces, *Science* 252(5009) (1991) 1164.
- [6] C.M. Bowers, D. Rappoport, M. Baghbanzadeh, F.C. Simeone, K.C. Liao, S.N. Semenov, T. Zaba, P. Cyganik, A. Aspuru-Guzik, G.M. Whitesides, Tunneling across SAMs Containing Oligophenyl Groups, *J. Phys. Chem. C* 120(21) (2016) 11331-11337.
- [7] M. Zharnikov, Femtosecond Charge Transfer Dynamics in Monomolecular Films in the Context of Molecular Electronics, *Acc. Chem. Res.* 53(12) (2020) 2975-2984.
- [8] E. Zojer, A. Terfort, M. Zharnikov, Concept of Embedded Dipoles as a Versatile Tool for Surface Engineering, *Acc. Chem. Res.* 55(13) (2022) 1857-1867.
- [9] H. Valkenier, E.H. Huisman, P.A. van Hal, D.M. de Leeuw, R.C. Chiechi, J.C. Hummelen, Formation of High-Quality Self-Assembled Monolayers of Conjugated Dithiols on Gold: Base Matters, *J. Am. Chem. Soc.* 133(13) (2011) 4930-4939.
- [10] E. Ostuni, R.G. Chapman, R.E. Holmlin, S. Takayama, G.M. Whitesides, A survey of structure-property relationships of surfaces that resist the adsorption of protein, *Langmuir* 17(18) (2001) 5605-5620.
- [11] S. Lowe, N.M. O'Brien-Simpson, L.A. Connal, Antibiofouling polymer interfaces: poly(ethylene glycol) and other promising candidates, *Polymer Chem.* 6(2) (2015) 198-212.
- [12] R. Konradi, C. Acikgoz, M. Textor, Polyoxazolines for Nonfouling Surface Coatings - A Direct Comparison to the Gold Standard PEG, *Macromol. Rapid Commun.* 33(19) (2012) 1663-1676.
- [13] S. Herrwerth, W. Eck, S. Reinhardt, M. Grunze, Factors that determine the protein resistance of oligoether self-assembled monolayers - Internal hydrophilicity, terminal hydrophilicity, and lateral packing density, *J. Am. Chem. Soc.* 125(31) (2003) 9359-9366.
- [14] P. Harder, M. Grunze, R. Dahint, G.M. Whitesides, P.E. Laibinis, Molecular conformation in oligo(ethylene glycol)-terminated self-assembled monolayers on gold and silver surfaces determines their ability to resist protein adsorption, *J. Phys. Chem. B* 102(2) (1998) 426-436.
- [15] M.W.A. Skoda, R.M.J. Jacobs, J. Willis, F. Schreiber, Hydration of oligo(ethylene glycol) self-assembled monolayers studied using polarization modulation infrared spectroscopy, *Langmuir* 23(3) (2007) 970-974.
- [16] S. Zorn, N. Martin, A. Gerlach, F. Schreiber, Real-time PMIRRAS studies of in situ growth of C(11)Eg(6)OMe on gold and immersion effects, *Phys. Chem. Chem. Phys.* 12(31) (2010) 8986-8991.
- [17] L.Y. Li, S.F. Chen, J. Zheng, B.D. Ratner, S.Y. Jiang, Protein adsorption on oligo(ethylene glycol)-terminated alkanethiolate self-assembled monolayers: The molecular basis for nonfouling behavior, *J. Phys. Chem. B* 109(7) (2005) 2934-2941.

- [18] M. Chávez, G. Sánchez-Obrero, R. Madueño, J.M. Sevilla, M. Blázquez, T. Pineda, Characterization of a self-assembled monolayer of O-(2-Mercaptoethyl)-O'-methyl-hexa(ethylene glycol) (EG7-SAM) on gold electrodes, *J. Electroanal. Chem.* 880 (2021) 114892.
- [19] M. Chavez, A. Fernandez-Merino, G. Sanchez-Obrero, R. Madueno, J.M. Sevilla, M. Blazquez, T. Pineda, Distinct thermoresponsive behaviour of oligo- and poly-ethylene glycol protected gold nanoparticles in concentrated salt solutions, *Nanoscale Adv.* 3(16) (2021) 4767-4779.
- [20] M. Chávez, G. Sánchez-Obrero, R. Madueño, J.M. Sevilla, M. Blázquez, T. Pineda, Self-assembled monolayers of O-(2-Mercaptoethyl)-O'-methyl-hexa(ethylene glycol) (EG7-SAM) on gold electrodes. Effects of the nature of solution/electrolyte on formation and electron transfer blocking characteristics, *J. Electroanal. Chem.* 914 (2022) 116303.
- [21] M. Chávez, G. Sánchez-Obrero, R. Madueño, J.M. Sevilla, M. Blázquez, T. Pineda, Electrochemical evaluation of the grafting density of self-assembled monolayers of polyethylene glycol of different chain lengths formed by the grafting to approach under conditions close to the cloud point, *J. Electroanal. Chem.* 913 (2022) 116294.
- [22] G. Sanchez-Obrero, M. Chavez, R. Madueno, M. Blazquez, T. Pineda, J.M. Lopez-Romero, F. Sarabia, J. Hierrezuelo, R. Contreras-Caceres, Study of the self-assembly process of an oligo(ethylene glycol)-thioacetyl substituted theophylline (THEO) on gold substrates, *J. Electroanal. Chem.* 823 (2018) 663-671.
- [23] E. Boubour, R.B. Lennox, Insulating Properties of Self-Assembled Monolayers Monitored by Impedance Spectroscopy, *Langmuir* 16(9) (2000) 4222-4228.
- [24] E. Boubour, R.B. Lennox, Potential-Induced Defects in n-Alkanethiol Self-Assembled Monolayers Monitored by Impedance Spectroscopy, *J. Phys. Chem. B* 104(38) (2000) 9004-9010.
- [25] E. Boubour, R.B. Lennox, Stability of  $\omega$ -Functionalized Self-Assembled Monolayers as a Function of Applied Potential, *Langmuir* 16(19) (2000) 7464-7470.
- [26] R.P. Janek, W.R. Fawcett, A. Ulman, Impedance spectroscopy of self-assembled monolayers on Au(111): Evidence for complex double-layer structure in aqueous NaClO<sub>4</sub> at the potential of zero charge, *J. Phys. Chem. B* 101(42) (1997) 8550-8558.
- [27] H. Sahalov, B. O'Brien, K.J. Stebe, K. Hristova, P.C. Searson, Influence of Applied Potential on the Impedance of Alkanethiol SAMs, *Langmuir* 23(19) (2007) 9681-9685.
- [28] B. O'Brien, H. Sahalov, P.C. Searson, The temperature dependence of the impedance of alkanethiol self-assembled monolayers, *Appl. Physics Lett.* 97(4) (2010).
- [29] D.K. Peng, S.T. Yu, D.J. Alberts, J. Lahann, Switching the Electrochemical Impedance of Low-Density Self-Assembled Monolayers, *Langmuir* 23(1) (2007) 297-304.
- [30] M.S. Góes, H. Rahman, J. Ryall, J.J. Davis, P.R. Bueno, A Dielectric Model of Self-Assembled Monolayer Interfaces by Capacitive Spectroscopy, *Langmuir* 28(25) (2012) 9689-9699.
- [31] P.R. Bueno, G. Mizzon, J.J. Davis, Capacitance Spectroscopy: A Versatile Approach To Resolving the Redox Density of States and Kinetics in Redox-Active Self-Assembled Monolayers, *J. Phys. Chem. B* 116(30) (2012) 8822-8829.
- [32] J. Lehr, J.R. Weeks, A. Santos, G.T. Feliciano, M.I.G. Nicholson, J.J. Davis, P.R. Bueno, Mapping the ionic fingerprints of molecular monolayers, *Phys. Chem. Chem. Phys.* 19(23) (2017) 15098-15109.
- [33] D.J. Vanderah, G. Valincius, C.W. Meuse, Self-assembled monolayers of methyl 1-thiahexa(ethylene oxide) for the inhibition of protein adsorption, *Langmuir* 18(12) (2002) 4674-4680.
- [34] R. Madueno, J.M. Sevilla, T. Pineda, A.J. Roman, M. Blazquez, A voltammetric study of 6-mercaptapurine monolayers on polycrystalline gold electrodes, *J. Electroanal. Chem.* 506(2) (2001) 92-98.
- [35] R. Madueno, D. Garcia-Raya, A.J. Viudez, J.M. Sevilla, T. Pineda, M. Blazquez, Influence of the solution pH in the 6-mercaptapurine self-assembled monolayer (6MP-SAM) on a Au(111) single-crystal electrode, *Langmuir* 23(22) (2007) 11027-11033.

- [36] D. García Raya, R. Madueno, M. Blazquez, T. Pineda, Formation of a 1,8-Octanedithiol Self-Assembled Monolayer on Au(111) Prepared in a Lyotropic Liquid-Crystalline Medium, *Langmuir* 26(14) (2010) 11790-11796.
- [37] D. Garcia-Raya, R. Madueno, M. Blazquez, T. Pineda, Formation of 1,8-Octanedithiol Mono- and Bilayers under Electrochemical Control, *J. Phys. Chem. C* 114(8) (2010) 3568-3574.
- [38] Z. Gonzalez-Granados, G. Sanchez-Obrero, R. Madueño, J.M. Sevilla, M. Blazquez, T. Pineda, Formation of Mixed Mono layers from 11-Mercaptoundecanoic Acid and Octanethiol on Au(111) Single Crystal Electrode under Electrochemical Control, *J. Phys. Chem. C* 117(46) (2013) 24307-24316.
- [39] L.V. Protsailo, W.R. Fawcett, Studies of electron transfer through self-assembled monolayers using impedance spectroscopy, *Electrochim. Acta* 45(21) (2000) 3497-3505.
- [40] F. Ben Amara, E.R. Dionne, S. Kassir, C. Pellerin, A. Badia, Molecular Origin of the Odd–Even Effect of Macroscopic Properties of n-Alkanethiolate Self-Assembled Monolayers: Bulk or Interface?, *J. Am. Chem. Soc.* 142(30) (2020) 13051-13061.
- [41] L.V. Protsailo, W.R. Fawcett, Electrochemical Impedance Spectroscopy at Alkanethiol-Coated Gold in Propylene Carbonate, *Langmuir* 18(23) (2002) 8933-8941.
- [42] H. Randriamahazaka, K. Asaka, Electromechanical Analysis by Means of Complex Capacitance of Bucky-Gel Actuators Based on Single-Walled Carbon Nanotubes and an Ionic Liquid, *J. Phys. Chem. C* 114(41) (2010) 17982-17988.
- [43] H.J. Kreuzer, R.L.C. Wang, M. Grunze, Hydroxide ion adsorption on self-assembled monolayers, *J. Am. Chem. Soc.* 125(27) (2003) 8384-8389.
- [44] A.V. Sarode, A.C. Kumbharkhane, Dielectric relaxation study of poly(ethylene glycols) using TDR technique, *J. Mol. Liquids* 164(3) (2011) 226-232.



### 3.4. Artículo 4.

*Evaluación electroquímica de la densidad de empaquetamiento formadas mediante la aproximación grafting to de monocapas autoensambladas de polietilenglicol de diferente longitud de cadena en condiciones próximas al punto de nube.*





## Electrochemical evaluation of the grafting density of self-assembled monolayers of polyethylene glycol of different chain lengths formed by the grafting to approach under conditions close to the cloud point.

Miriam Chávez, Guadalupe Sánchez-Obrero, Rafael Madueño, José Manuel Sevilla, Manuel Blázquez, Teresa Pineda\*

Department of Physical Chemistry and Applied Thermodynamics, Institute of Fine Chemistry and Nanochemistry, University of Cordoba, Campus Rabanales, Ed. Marie Curie 2<sup>a</sup> Planta, E-14014 Córdoba, Spain

### Abstract

Grafting densities of polymers on gold surfaces are important parameters that inform about the chain conformation adopted by the chains, either mushroom or brush conformation. Most of the literature reports on this topic are based on ellipsometry measurements with other few results obtained from surface plasmon resonance or quartz crystal microbalance. In this work, we report the use of cyclic voltammetry of the RD process of mercapto-polyethylene glycol self-assembled monolayers (EGn-SAMs) to get the grafting densities of these polymers with different chain lengths (c.a. EG136, EG45 and EG18). When the EGn-SAMs are formed from aqueous solutions where the polymer chains are highly hydrated, an excess of charge density is obtained that apart from the capacitive contribution found in these processes, include an extra charge due to the hydrogen evolution reaction (HER) produced by the high ratio of water contained in the film that reduces concomitantly with the SAM RD process. However, preparing the EGn-SAM in the presence of high salt concentrations that lowers the water content within the chains, that is, using the cloud point strategy, very realistic grafting density values are obtained. The RD profiles of the EGn-SAMs completely change from a broad peak with high charge density to a structured peak that allows us the determination of grafting density values. Capacitance curves and the behavior of the electrochemical process of the  $\text{Fe}(\text{CN})_6^{3-/4-}$  redox pair in the presence of the films are also in agreement with the CV results. The grafting density values obtained by this methodology are higher than those reported for these SAMs by using other techniques but agree with the footprints expected for these chains when organized in a brush conformation. Moreover, they also are close to the values obtained by thermogravimetric analysis of the same films built on gold nanoparticles that behave as planar surfaces.

**Keywords.** Poly- ethylene glycol; self-assembled monolayer; grafting density; cloud point; reductive desorption.

## Introduction.

Self-assembled monolayers of alkanethiols (C-SAMs) and oligo (ethylene glycol)-terminated alkanethiols (EG-C-SAMs) formed on noble metal surfaces have been widely studied because of their organized structures and capability to be tailored with different chemical functionalities in the exposed interface [1-4]. The fact that poly(ethylene glycol) (EGn) has demonstrated to prevent protein unspecific adsorption has stimulated great efforts in research dealing with the adsorption on different solid surfaces, through a strategy known as PEGylation [5], to make these surfaces biocompatible.

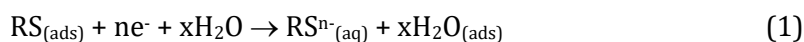
Most of the studies of biocompatibility have used EG-C-SAMs as model systems since the alkanethiol arm forces the organization of the whole molecule and adopting the EGn portion a helicoidal or all-trans conformation [6-11]. Thus, the influence of the number of EG moieties, the terminal group and the nature of the metal substrate have been studied to find out the origin of the biocompatibility of these films. However, most of the PEGylated surfaces used in biological systems are built with EGn chains devoid of the alkane arm, and most frequently with larger EGn than those used in the model studies. Thus, knowledge on the organization of these layers is still necessary to get more insight into the actual structure when EGn is directly attached to metal surfaces. One of the most important parameters in the characterization of these polymer films is the grafting density ( $\sigma$ ) as it will define if the chains are in more or less extended conformations. In this sense, EGn hydration is an important factor determining the structure and the values of the  $\sigma$  parameter [12]. At lower  $\sigma$ , the chains are well hydrated and adopt the mushroom conformation whereas at higher  $\sigma$  values, the chains stretch away from the surface leading to the loss of hydration, and the brush regime is reached.

Grafting densities of EGn polymers on gold surfaces have been determined by using different experimental techniques and protocols. Upon decreasing EGn solubility by either increasing temperature or ionic strength, higher surfaces coverages are obtained [13]. Ex situ ellipsometry and neutron reflectometry techniques were first used to obtain  $\sigma$  values of EGn-SH molecules (with n from 18 to 120) on gold surfaces, that resulted higher than the theoretically calculated for the unperturbed chains under high- and low-solubility conditions. The driving force for chemisorption through the thiol group was considered to be sufficient for the coverage to proceed beyond the close-packed mushroom regime, forcing the chains to adopt an extended brush conformation [13].

The major problem found for the grafting of polymer chains to a surface starts when the binding reaches saturation because the overlap of coils. This overlapping occurs when the distance between grafting points is comparable to the coil size in solution [14,15]. One of the most useful approaches for increasing the  $\sigma$  values of polymers is to use dispersions

where the individual coils are shrunk. This can be reached by using either less favorable solvents [16], or under polymer melt conditions [17,18], or by the “cloud point” grafting strategy [16]. Thus, the grafting process of EGn polymers in 0.9 M Na<sub>2</sub>SO<sub>4</sub> at room temperature results in well-defined brushes of high density, and this is explained as due to an osmotic balance that, in the presence of salt, makes the polymer shrinks and more coils can then fit on the surface [19]. The height of these brushes, prepared with EGn of molecular weights from 2 to 30 kDa, agrees with the calculated values based on a model similar to the “de Gennes” [20] for strongly stretched brushes in which the height is proportional to the molecular weight [243]. Recently, Ortiz et al. [21] have verified this strategy by controlling the grafting density under different salt concentrations and found that the highest value is obtained when the EGn film is formed in the presence of 0.9 M Na<sub>2</sub>SO<sub>4</sub> aqueous solution, and observed the conformational transition from mushroom to brush only when the grafting process proceeded during long periods, emphasizing the importance of adsorption time to obtain high  $\sigma$  and the brush conformation.

The *grafting to* approach for attaching polymer chains with a terminal thiol group on a gold surface follows the self-assembly strategy consisting in contact the metal surface with a solution of the thiol derivative for a determined time. This procedure readily produces SAMs of the polymer due to the main interaction of the thiol group with the gold surface atoms. One important parameter of these SAMs is the surface coverage (or  $\sigma$ ) and, therefore, the footprint of the molecules. The literature on this topic reports the determination of these parameters as well as the thickness of the EGn films by using experimental techniques such as quartz crystal microbalance (QCM) and surface plasmon resonance (SPR) [19,21], and ellipsometry [13,17,22]. However, the strategy to obtain SAM surface coverages by using electrochemical techniques, has not yet been reported for this kind of systems. In this sense, the RD process of the SAM is a tool that gives this information based on the following reaction [23]:



where (*ads*) and (*aq*) refer to thiols in chemisorbed and solvated states, respectively. The reaction (1) is a solvent substitution reaction and, although for years has been treated as monoelectronic, is now accepted that this assumption depends on the specific system and the experimental conditions considered [24].

Pioneering work of Porter et al. [25] described the RD process of alkanethiol SAMs as a tool to determine desorption potentials and surface coverages. This desorption potential was found to depend on the chain length and the intermolecular interactions that are also related to the chain lengths [24,26]. The RD process as studied by CV on a gold single crystal electrode is usually observed as a single peak whose charge density accounts for the

reduction of the R-S-Au bond taking into account the reaction (1). Moreover, it is also believed that the overall charge density contains a capacitive current that has been determined as a 20 % of the total charge density measured [27-29].

When polycrystalline or polyoriented gold electrodes are used, a set of peaks are obtained for the RD process that are mainly ascribed to the desorption of SAMs patches attached to the different gold facets present in these electrode surfaces [30-34]. Nonetheless, there are some cases in which multi-wave voltammetry has been also observed in the RD of SAMs of long alkanethiols in Au(111) single crystal electrodes. These multi-wave voltammetric signals have been suggested to be due to the sequential desorption from sites with different binding energies [33,34], monolayer domains with different sizes and stability [35], and depletion micelles that are formed in the double layer region [33,36-38]. By using second harmonic generation (SHG) combined with CV, Buck et al. [24] have proposed the intermolecular interactions as the origin of multi-wave behavior in n-alkanethiol desorption from single crystal surfaces. The double peak found for alkanethiols of intermediate lengths cannot be explained by a separation of capacitive and faradaic contributions as it was previously stated [37]. These two contributions are not separated and occurs through all the desorption process whenever the desorbed molecules remain at the interface, and the peak splitting is a consequence of the relative importance of the molecular interactions.

In the present work, we studied the RD processes of EGn-SAMs (with  $n = 18, 45$  and  $136$ ) formed by the *grafting to* method on polyoriented gold (PO) and Au(111) single crystal electrodes by the CV technique. We find that the charge density of the RD peaks obtained for the SAMs formed from EGn water solutions are higher than the expected for compact SAMs. However, the formation of these SAMs in the presence of high sodium phosphate (NaPi) concentrations (close to the EGn cloud point, i.e. under  $\theta$ -conditions) gives results that allows us to determine more realistic  $\sigma$  values.

## Experimental section.

### Materials.

Poly(ethylene glycol) methyl thiol of MW 800, 2000 and 6000 (EGn,  $n = 18, 45$  and  $136$ ) were purchased from Sigma. The rest of the reagents were from Merck analytical grade. All solutions were prepared with deionized ultrapure water produced by a Millipore system.

The EGn solutions used for the grafting experiments were prepared by mixing the polymers with water or NaPi aqueous solutions. Different concentrations of salt were

prepared to estimate the cloud points for the different polymers as defined by the initiation of phase separation (Figure S1).

The polymers were grafted to the gold surfaces by immersing the clean electrodes in the different polymer solutions and left overnight for surface modification at room temperature. Thereafter, the electrodes were thoroughly washed with water and dried with a N<sub>2</sub> flow.

## Experimental methods.

Electrochemical experiments were performed on an Autolab (Ecochemie model Pgstat 30) instrument attached to a PC with proper software (GPES and FRA) for the total control of the experiments and data acquisition. A conventional three electrode glass cell comprising a platinum coil as counter electrode, a 50 mM KCl calomel (CE 50mM) as reference electrode and either a polyoriented (PO) or an (111) single crystal gold (Au(111)), as the working electrodes, was used. The PO gold electrode was a homemade sphere obtained by melting a gold wire up to reach a diameter of approximately 2 mm, attached to a gold wire that serves as electrode connection. The Au(111) single crystal was a cylinder of 3-mm diameter and 2 mm thick from Metal Crystals and Oxides Ltd., Cambridge, England, with a polished side. A gold wire mounted at its far tip, allowed easier handling of the crystal. Before each electrochemical measurement, the electrodes were annealed in a small Bunsen burner to light red melt for about 20 s and, after a short period of cooling in air, quenched in ultrapure water. The electrode was then transferred into the electrochemical cell with a droplet of water adhering to it to prevent contamination. The surface condition was confirmed by a cyclic voltammogram in 0.01 HClO<sub>4</sub>, and the real surface area was determined from the gold oxide reduction peak obtained under these conditions ( $A(\text{PO gold}) = 0.24 \text{ cm}^2$ ;  $A(\text{Au}(111)) = 0.07 \text{ cm}^2$ ).

The cyclic voltammograms for the RD processes were recorded in KOH 0.1 M solutions and these for the evaluation of the electron transfer in aqueous solutions were of 0.1 M KNO<sub>3</sub> in the presence of [Fe(CN)<sub>6</sub>]<sup>3-/4-</sup> 1 mM in each component. The EIS measurements were obtained at the midpoint potential of the cyclic voltammogram registered for the naked electrode (at 0.08 V), using an amplitude rms of 10 mV and a frequency interval from 0.1 to 10000 Hz.

XPS analysis was performed using an MCD SPECS Phoibos 150 spectrometer (from the Servicio Central de Apoyo a la Investigación (SCAI) of the Universidad de Cordoba) employing non-monochromatized (12 kV, 300 W) Mg K $\alpha$  radiation (1253.6 eV). The substrate, either clean or modified, was mounted on a steel sample holder and transferred to the XPS analytical chamber. The working pressure was less than 5·10<sup>-9</sup> Pa. The spectra

were collected using a take-off angle of 45° respect to the sample surface plane. The spectrometer was calibrated by the binding energy (BE) of the Au 4f<sub>7/2</sub> line at 84.0 eV. The standard deviation for the BE values was 0.2 eV. Survey scans were run in the 0-1100 eV range (pass energy 60 eV), and higher resolution scans were recorded for the C 1s, O 1s and S 2p regions. The analysis involved Shirley background subtraction, and whenever necessary, spectral deconvolution was carried out by nonlinear least-squares curve fitting adopting a Gaussian sum function, employing the software CASA-XPS.

Contact Angle (CA) Measurements were conducted by using an Optical Tensiometer Theta T200 device (Attension, Biolin Scientific) equipped with a high-speed camera (420 fps). The CAs of the formed SAMs were measured in sessile drop method. The experiments were performed at room temperature and at open atmosphere. The results are given as an average of six measurements.

## Results and discussion.

The grafting of the polymer chains on the gold substrates was carried out as described in the experimental section. The films prepared overnight showed the best electrochemical performance and reproducible results and, therefore, this modification time has been chosen for the experiments. These EGn-SAMs are characterized by CV following a potential program that allows to record the RD process. Thus, the EGn-SAM electrode is contacted with the electrolyte solution under potential controlled conditions at a value where the film is stable and, when the equilibrium is reached, the voltammetric curve is recorded. The RD process of the EG136-SAM formed on a poly-oriented (PO) gold electrode from a solution of EG136 0.18 mM in water is plotted in Figure 1. The CV shows a broad reductive peak at -1.01 V (width at half height = 72 mV) that involves a charge density of 115  $\mu\text{C}/\text{cm}^2$ . This charge density is too high to explain the desorption of an EG136-SAM even considering that the packing density is similar to that of alkanethiols (this process involves a charge density of around 70  $\mu\text{C}/\text{cm}^2$ ) [39]. Unexpectedly, the RD of the EG136-SAM formed under the same experimental conditions but using a single crystal Au(111) electrode also shows a broad peak (width at half height = 90 mV) slightly displaced in potential at -1.02 V (Figure 1). Most of the RD peaks obtained from SAMs composed of alkanethiols or other mercaptoderivatives built at Au(111) surfaces appear as a sharp peak at the highest potential within these included in the sometimes resolved broad peaks obtained at polycrystalline gold electrodes. Moreover, using PO gold electrodes, a set of discrete peaks, being the first one ascribed to the desorption from (111) facets, is frequently observed [30,31,40]. The above results intrigue us for the following three reasons: the excess of



charge density, the lack of discreteness of the peaks in PO electrode and the much broader peak in Au(111) electrode.

To get more insight into the origin of these features we have carried out experiments using different concentrations of EG136 in the SAM forming solutions. Whereas from 10 mM to the actual 0.18 mM EG136 concentrations the same behavior is observed, lowering the concentration to 0.018 mM, completely changes the RD profile. A set of peaks that remember the pattern obtained for EG7-SAM [31] in the PO gold electrode as well as a single sharp peak in the Au(111) electrode are now recorded (Figure 1).

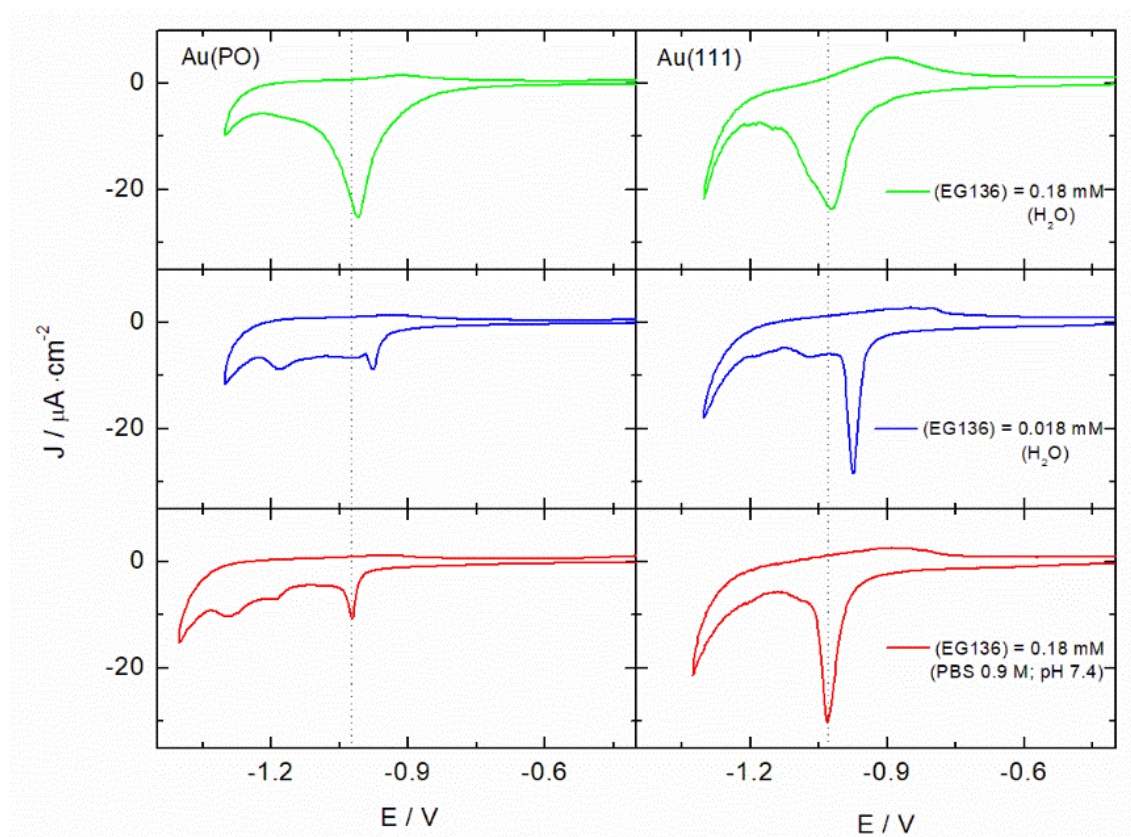


**Figure 1.** CVs for the RD process of the EG136-SAM at PO and Au(111) electrodes formed in solutions of different EG136 concentrations and in the absence and presence of NaPi salt;  $v = 0.02$  V/s.

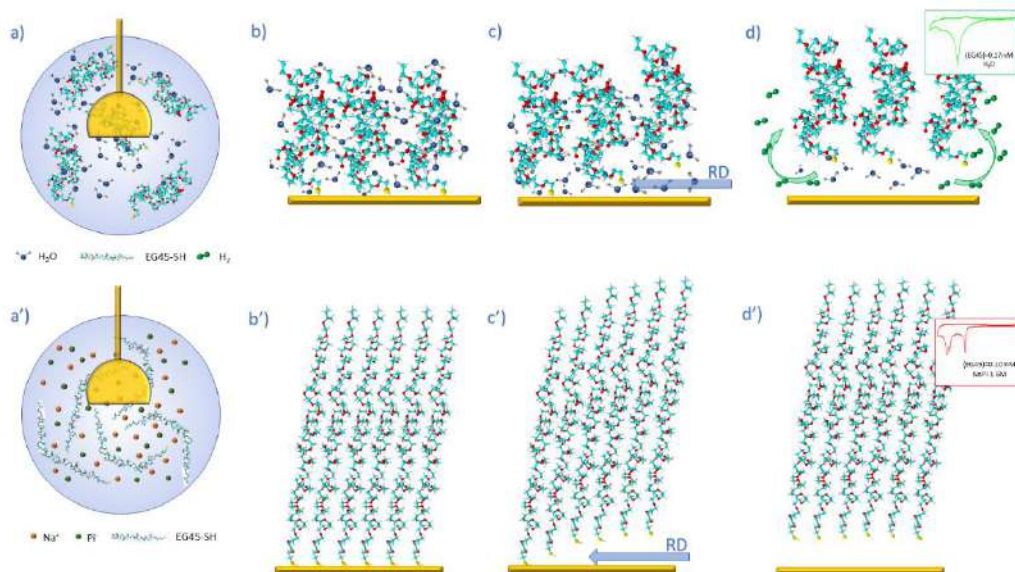
Higher charge densities than that corresponding to the RD of a complete monolayer obeying the reaction (1) have been previously found, and ascribed to the concomitant reduction of either R-S-S-R species that can be formed from free R-SH groups that remain into the SAMs or the reaction of the second thiol groups that are present in the form of intralayer disulfide bonds at the SAM interface when using dithiol derivatives [41-43]. In the case of EG136-SAM, the presence of free molecules in the polymeric film that are not able to reach the gold surface and complete the grafting reaction cannot be discarded at least in solutions of high concentrations. We have carried out XPS of these layers formed

under these various experimental conditions and we have found that, in the case of the SAMs formed in solutions of the highest concentrations, a measurable ratio of either free S-H or disulfide exists in the layer (Figure S2). It is not expected that they correspond to disulfide species as the same phenomenon that impedes the diffusion of the chains to reach the gold surface or to leave the film, would also hinder the encounter of two chains in the film to form them. Thus, this extra contribution must be due to some free EG136-SH chains trapped into the film. However, the SAMs formed at lower EGn concentrations or in the presence of NaPi do not show that contribution.

In a study of RD of a homologous series of pyridine-terminated thiols with aromatic backbones in Au(111) electrodes, Rohwerder et al. [44,45] found multi-wave voltammetry with an extraordinary high reductive charge that gives unrealistic surface coverage values even if the non-Faradaic excess charges of around 20-30% due to the drastic change of capacity from the modified and unmodified substrate were taken into consideration [27,46-48]. They assigned this excess of charge to a parallel Faradaic reaction by noting that the RD process takes place within the H<sub>2</sub> evolution potential region and suggested that this reaction can occur concomitantly with the RD of the SAM at least when the potentials of the later become more negative as it was the case. Apparently, the RD process has a catalytic effect on the H<sub>2</sub> evolution reaction (HER) [44,45]. By combining experiments of CV, in situ ellipsometry, and hydrodynamic voltammetry, the concomitant oxidation of H<sub>2</sub> with the desorption of the monolayer is proposed. This rapid HER in respect to that taking place on a bare gold electrode, is thought to involve the orientation of water molecules in the gap created between the gold surface and the suspended reduced monolayer, accompanied by the diffusion of the positively charged electrolyte counter ions.

In our case, the EG136-SAMs formed from water solutions containing high EG136 concentrations should contain a high fraction of water. It is well known that the conformation of grafted chains on a surface depends on the chain density [13,49], and this is influenced by the actual conformation of the polymer in solution. As water is a good solvent for EGn polymers, they will be in a random coil conformation or unperturbed state where the polymer chains are interacting with water mainly by H-bonds. This conformation is transferred to the adsorbed state [12] and it is believed that the chains adopt the mushroom conformation that, on the other hand, supposes a low grafting density. Under these conditions the polymer layer contains a high ratio of water that can be reduced at the same potentials of the RD process. Thus, the water content in the SAM is high and it can be reduced in parallel with the SAM RD (Scheme 1). Only one peak appears in the voltammograms, in contrast to what happens with pyridine-terminated aromatic thiols that, after the consumption of the initially adsorbed water layer, water transport into inner

plane requires to overcome the large electrolyte-blocking SAM domains and the catalyzed HER appears as a separated lower potential peak.



**Scheme 1.** Model for EGN-SAM formation and its RD process. Formation of the EGN-SAM in water (a) and under near cloud point conditions (a'); (b, b', c, c', d and d') the formed SAM is submitted to a potential scan to produce the RD process.

One necessary fact for this process to happen is that the molecular layer does not diffuse away from the surface, remaining at the interface forming patches or micelles. This can be the case for EG136 as shown in Figure S3. When the RD experiment is run starting at potentials of SAM stability and going to lower values up to the S-Au bonds are completely reduced, and then the scan continues to high potentials covering the oxidation of the gold surface atoms, the extra anodic charge obtained in respect to that of the oxidation of the gold surface, should correspond to the Au-S oxidation reaction [27,38]. A CV corresponding to the direct oxidation of a newly prepared EG136-SAM together with one for the bare electrode are also shown for comparison (Figure S3). The charge density recorded at high potentials is higher than that corresponding to the oxidation of the gold surface and lower than that involved in the oxidation of a complete monolayer. Thus, this is a confirmation that a great portion of the monolayer is retained at the electrode interface after the RD process.

This result can give the idea that the RD is not appropriate to determine the surface coverage of the polymer SAMs as we cannot separate the contribution of the rapid HER, if it is the case, from the actual RD charge density. However, it is well known that when the polymers are dissolved in poor solvents, the excluded volume expansion is reduced, and the chains adopt a more extended conformation (Scheme 1). Here, we use the method of

changing the ionic strength of the EGN solutions by adding increasing concentrations of NaPi up to reach the solution cloud point. By using solutions of (EGn) = 0.17 mM, the cloud point in the presence of NaPi is determined for EG136, EG45 and EG18 that are the chains studied in this work. Whereas EG18 resists NaPi concentrations higher than 4 M without phase separation, EG45 and EG136 solution turbidity is produced at (NaPi) > 1.6 and 0.9 M, respectively.

When the RD of a EG136-SAM formed in a 0.9 M NaPi solution is recorded, a CV showing a set of well-defined peaks (Figure 1, PO gold electrode) with a first sharp peak at -1.02 V that is displaced 40 mV more negative than the same peak for the SAM formed in a low EG136 concentration in the absence of salt is obtained. A similar behavior is observed for the RD from an Au(111) single crystal electrode. This effect is explained as a higher stability of the SAM formed from the high ionic strength solution in comparison to that formed in water.

Figure 2 shows the CVs for the RD of EG136-SAMs formed in solutions of different salt concentrations. Increasing salt concentration, the shape of the CVs changes from the broad peak obtained in water to the multi-peak in the presence of salt. The charge density drastically decreases when adding salt to the formation solution and follows a smoothly increase up to 45  $\mu\text{C}/\text{cm}^2$  at higher salt concentrations.

Concomitant with the changes in the RD profiles, the water contact angle values of the EG136-SAMs vary from  $29.5 \pm 5.2^\circ$  to  $36.1 \pm 4.1^\circ$  for the films formed in the absence and presence of salt (close to the cloud point), respectively. This is also an indication of the better organization of the molecules in the film exposing the terminal groups to the solution when the brush conformation is favored.

A similar behavior is obtained for the EG45-SAM. Whereas an excess of charge density together with an unresolved RD peak are obtained for the EG45-SAMs formed in water and in the presence of 0.9 M NaPi, a structured multi-peak curve is obtained when the SAM is formed in the presence of 1.6 M NaPi. The charge density obtained under these experimental conditions is of 46.5  $\mu\text{C}/\text{cm}^2$ . Again, the CV recorded for the EG45-SAM prepared in a diluted water solution shows the multi-peak pattern although the charge density is too low, indicating the formation of a partial monolayer.

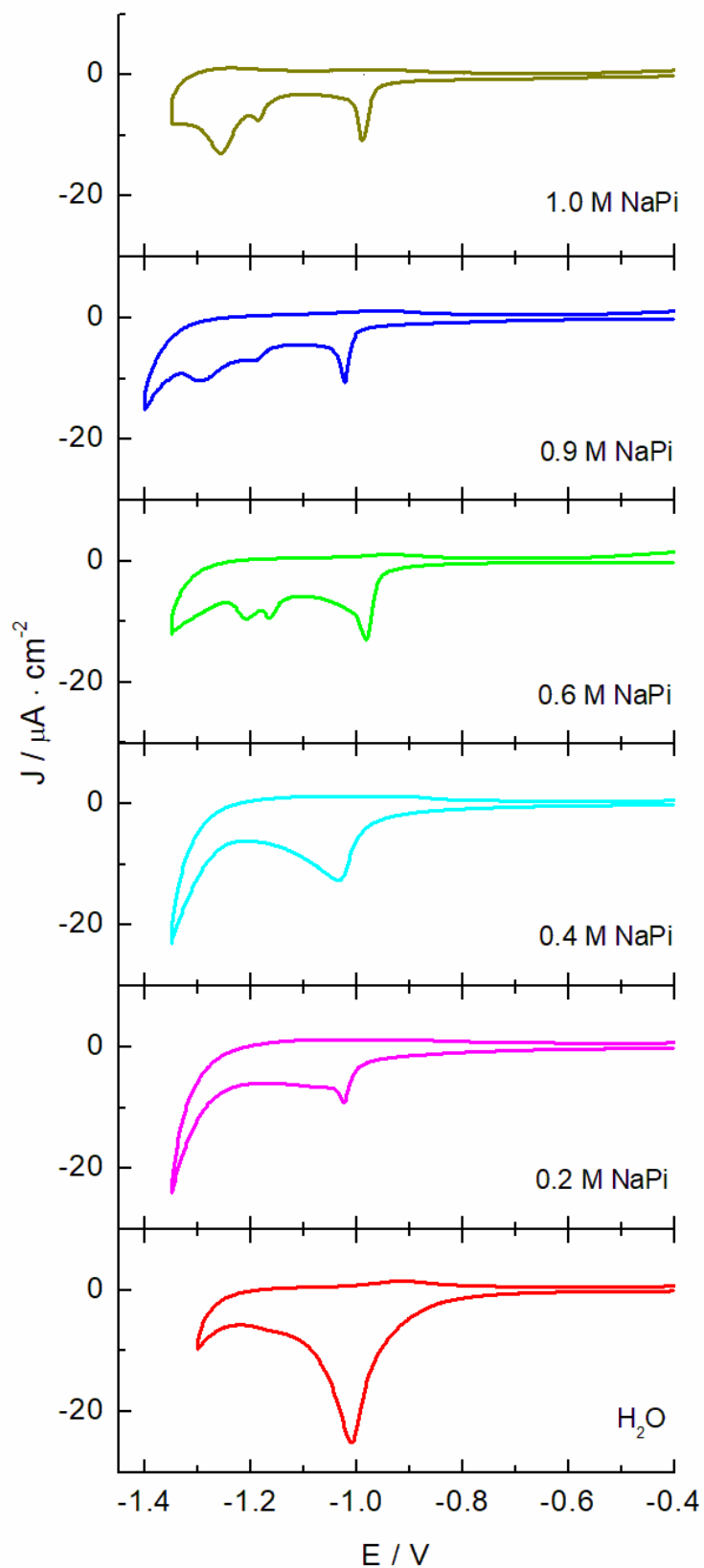


**Figure 2.** CVs for the RD process of the EG136-SAM at PO electrodes formed in solutions of different NaPi salt concentrations; (EG136) = 0.18 mM;  $v = 0.02$  V/s.

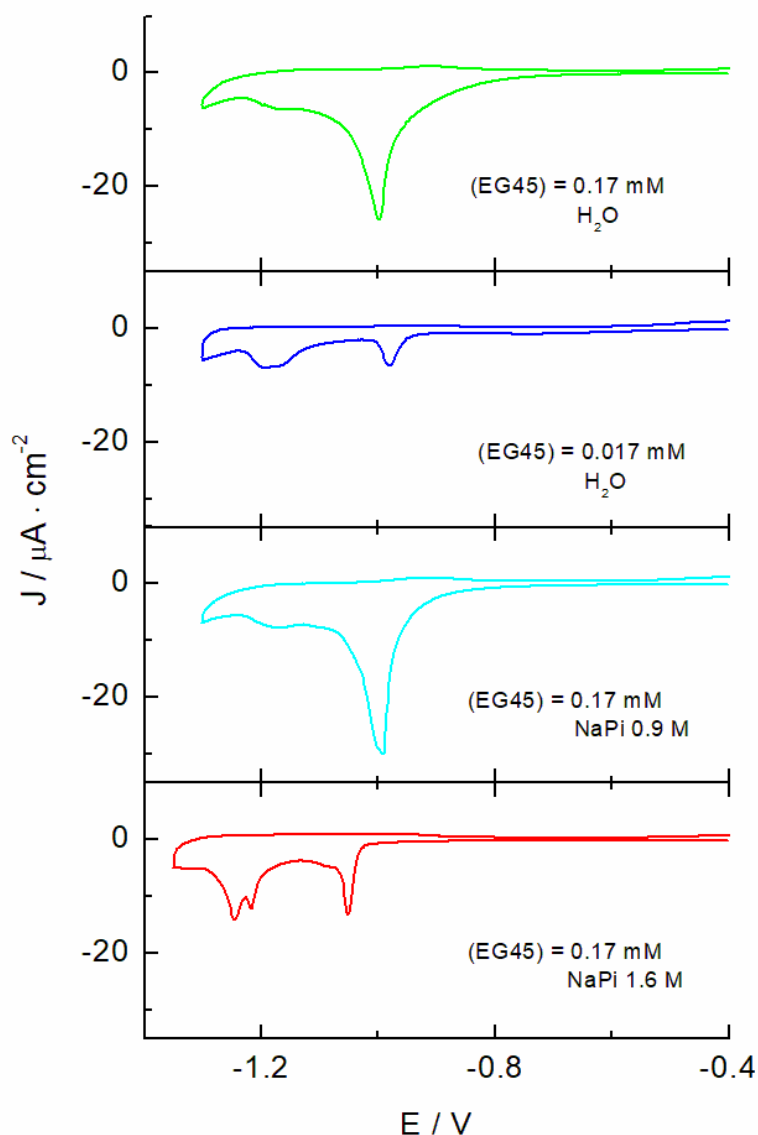


**Figure 3.** CVs for the RD process of the EG45-SAM at PO electrodes formed in solutions of different EG45 concentrations and in the absence and presence of NaPi salt;  $v = 0.02$  V/s.

In the case of EG18-SAMs, the multi-peak curves are recorded for the SAM formed in water as well as in the presence of 4 M NaPi. The charge density measured is of  $61.5 \mu\text{C}/\text{cm}^2$ . The only observed difference is the higher stability that supposes the small displacement of the potential ( $\sim 30$  mV) to more negative values for the later. The shorter chain length of the EG18 may be sufficient to avoid the effect of the excluded volume effect and the accumulation of water into the film is not produced as it happens with EG45 and EG136 molecules.

Another evidence of the different behavior of the RD of the EGN-SAMs as a function of the chain length formed in the absence and presence of NaPi is found from double layer capacitance curves (Figure 5). The general pattern shown for these curves is the low and constant capacity value in the potential interval of SAM stability, indicating the existence of

a compact layer that should behave as an ideal capacitor, followed for a hump coinciding with the potentials for SAM RD processes. It is interesting to observe that the peak recorded at lower potentials strongly differs from the SAMs prepared in pure water EGN solutions or in the presence of NaPi at concentrations just below the cloud point. This higher capacity signals should be correlated with the higher charge densities obtained in the voltammetric RD profiles for the SAMs formed in pure water solutions.

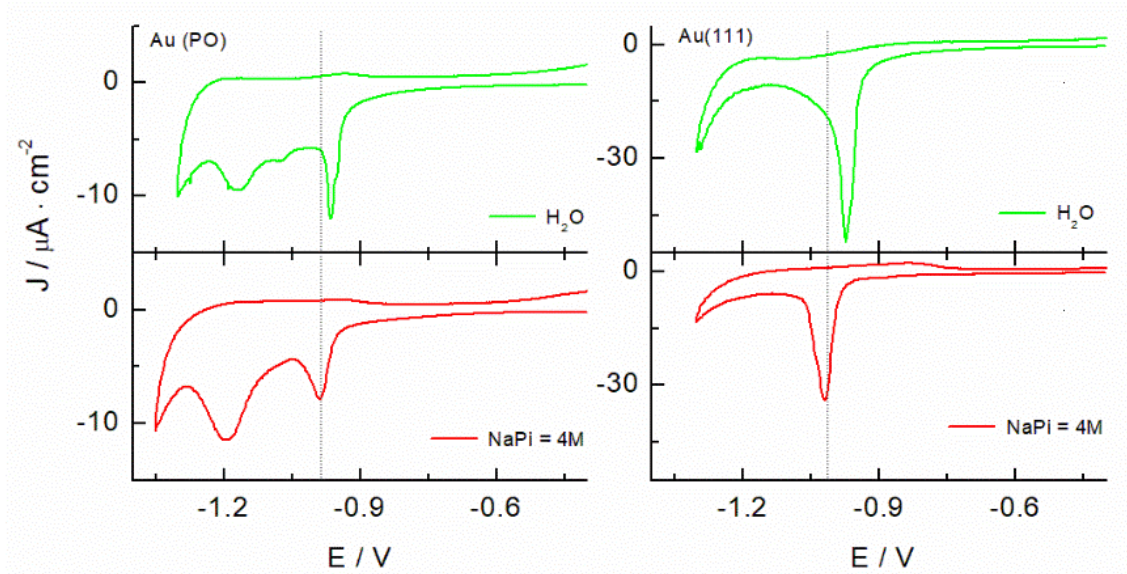


**Figure 4.** CVs for the RD process of the EG18-SAM at Au(PO) and Au(111) electrodes formed in solutions of different NaPi salt concentrations. (EG18) = 0.18 mM;  $v = 0.02$  V/s.

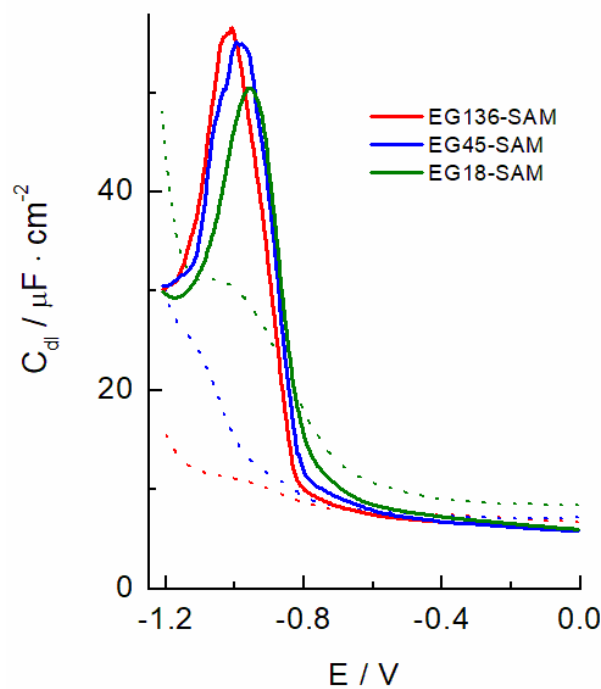


**Figure 5.** Double layer capacity curves for the EGn-SAMs formed in EGn water (solid lines) or aqueous NaPi solutions (dashed lines) at the concentrations just below the cloud points (4 M for EG18, 1.6 M for EG45 and 0.9 M for EG136).

The charge densities obtained from the RD processes by using the cloud point grafting strategy can be used to get information about the surface coverage and conformation of the polymer SAMs. Table 1 gathers the grafting density values ( $\sigma$ ) for the EG136-, EG45-, and EG18-SAMs obtained directly from the charge densities after correction of the capacitive contribution ( $Q = nF\Gamma$ , where  $\Gamma$  is the surface coverage of the SAM). In a recent study of the grafting density of EG113 by using surface plasmon resonance (SPR) measurements in the presence of various  $\text{Na}_2\text{SO}_4$  salt concentrations, values ranging from 0.26 to 1.60 chains  $\text{nm}^{-2}$  have been obtained for the films formed in water and up to 0.6 M  $\text{Na}_2\text{SO}_4$ , respectively [21]. In that work, the importance of the modification time to obtain a high coverage is highlighted as deduced by comparison with other studies [13,17,19,22,50,51]. The methodologies used to build these EGn films include the use of changing temperature or the presence of different salt concentrations to reach the cloud point conditions as we have made in this work. However, the techniques used to obtain the grafting density values were SPR [19,21], X ray photoelectronic spectroscopy [51] and most of them, ellipsometry [13,17,22,50]. It seems that these techniques give lower coverage values than those obtained by electrochemical RD processes. However, if we compare the  $\sigma$  values obtained in the present work with those reported for AuNPs surfaces and determined by thermogravimetric analysis, we found a better correlation [52,53]. In fact, the size of the AuNPs used in these works are large and the system should behave close to a planar surface showing similar  $\sigma$  values [54,55].

**Table 1.** Molecular and conformational parameters of the EGn chains in the SAMs.

	$\sigma /$ chains· $\text{nm}^2$	Footprint / $\text{Å}^2$	$R_F /$ nm	H / nm	L / nm	(H/L)x100
<b>EG136</b>	2.25	44.4	5.27	28.0	38.1	73.6
<b>EG45</b>	2.30	43.5	3.03	9.35	12.1	73.4
<b>EG18</b>	3.07	32.6	1.92	4.12	5.1	81.7
<b>EG7<sup>(1)</sup></b>	3.43	29.0	1.20	1.66	2.0	72.3

<sup>(1)</sup> Data taken from ref. [31].

Under the experimental conditions used to obtain the grafting densities of Table 1, i.e., cloudy point or  $\theta$ -conditions, the theoretical values of the Flory radius, that gives the coil size of the polymer, can be determined by:



$$R_F = b \left( \frac{a \cdot N}{b} \right)^{1/2} \quad (1)$$

where  $a$  is the monomer size ( $a = 0.28$  nm for polyethylene glycol in water) [321],  $b$  is the Kuhn length ( $b = 0.73$ ) [75], and  $N$  is the number of monomer in the chain. The exponent  $1/2$  has been given for  $\theta$ -solvent conditions. The distance between the center of grafting points in the surface is given by  $P = (1/\sigma)^{1/2}$ , and these values are much lower than  $2R_F$ , leading us to conclude that the EGN chains are in an extended conformation forming a thick layer. By using the Alexander de Gennes scaling relation [300]:

$$H = \left( \frac{\sigma}{3} \right)^{1/3} \cdot b^{2/3} \cdot a \cdot N \quad (2)$$

the brush heights  $H$  can be found. The  $H$  values gathered in Table 1 would correspond to the EGN molecules exposed to a good solvent as it is the case. In fact, although the SAMs are formed under  $\theta$ -conditions, the RD experiments are carried out in 0.1 M KOH solutions that would correspond to good solvent conditions. Thus, the equilibration of the EGN layers with this solution should lead to the elongation of the chains to be accommodated with the different environment. The obtained values, although higher than  $2R_F$ , account for the 70-80 % of the theoretical length for a helicoidal conformation of the chains, confirming this hypothesis.

Another interesting piece of information can be obtained by analyzing the blocking properties of these layers. It has been shown that the electrochemical signal of a redox species in solution is decreased when the electrode active area is either reduced or completely blocked as the approach of the species to the electrode surface is prevented [43,57]. The analysis of these signals is a good tool to determine the presence and nature of defects in the layers [58]. We have carried out cyclic voltammetric experiments of the  $\text{Fe}(\text{CN})_6^{3-/4-}$  redox pair as it has been shown to be very sensitive to the presence of EGN layers on electrodes [31].

As it is shown in Figure 6, the redox response in CV is completely suppressed when the gold electrode is covered by EG136-SAM formed either in water or in 0.9 M NaPi. The curves are typical of cases that involve a tunneling mechanism and, in a first approximation, would agree with the absence of defects or pinholes in the layers. However, EIS is a more sensitive tool and allows the determination of the charge transfer resistance of the redox probe in the presence of the monolayer and thus, the surface coverage. The impedance signals obtained for the redox pair in the presence of EG136-SAM show, on one hand, the typical semicircle that indicates a high charge transfer resistance, and on the other, the absence of straight line at low frequencies showing the absence of diffusion of the redox pair to the electrode surface. It is observed that the semicircle diameter is higher for the SAM formed under conditions near the cloud point indicating higher compactness. A similar

behavior is shown by the EG45- and EG18-SAMs, although in these cases the difference in the semicircle diameter is bigger, pointing to an even higher compactness of the layers formed under near cloud point conditions in respect to these formed in water.

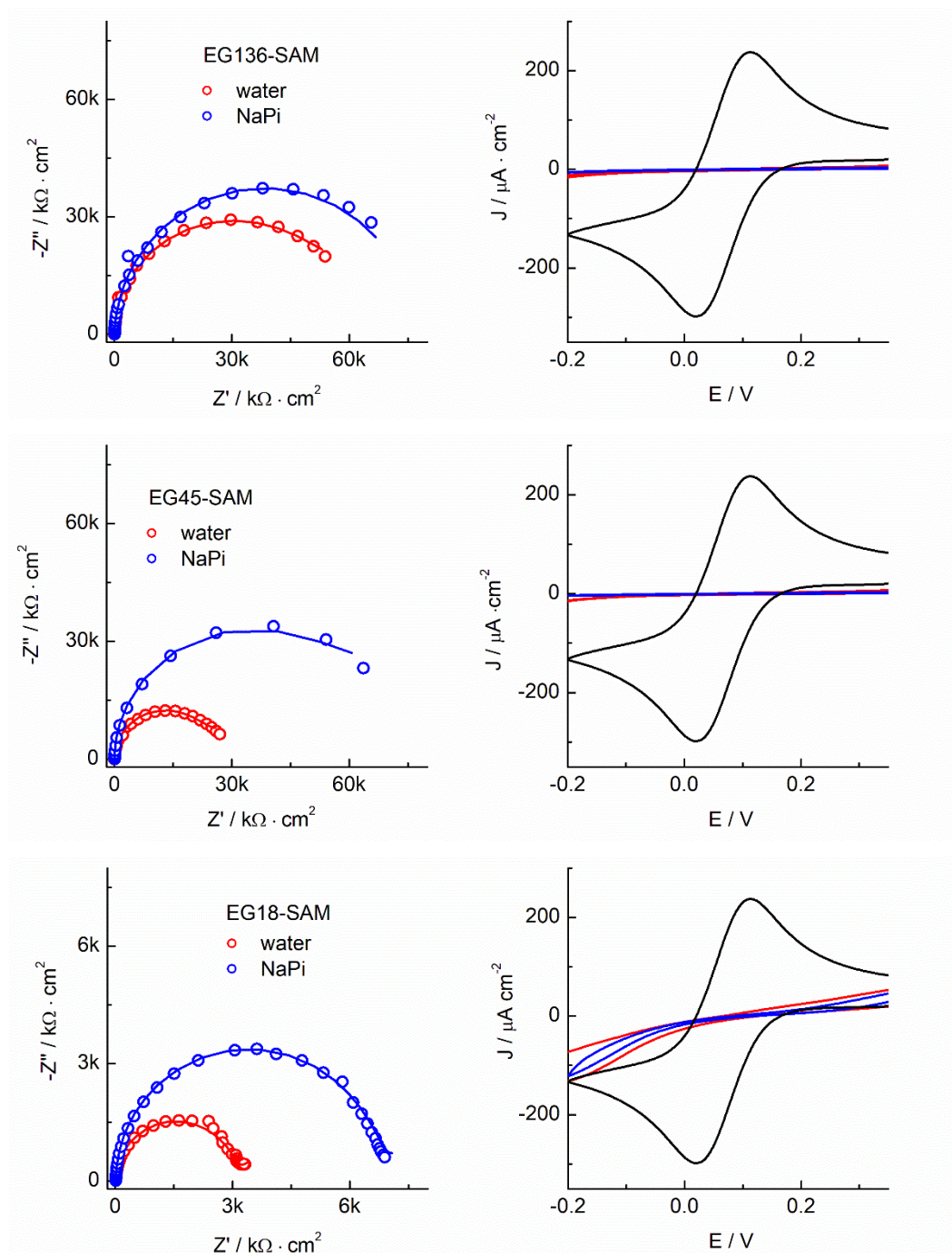


**Figure 6.** Electrochemical response of the  $\text{Fe}(\text{CN})_6^{3-/4-}$  redox pair (1mM in each component) in 0.1 M  $\text{KNO}_3$  in the presence of EGn-SAMs formed in water (0.18 mM EGn) and/or 0.9 M NaPi for EG136; 1.6 M NaPi for EG45 and, 4 M NaPi for EG18. Left: Electrochemical impedance spectra. The circles are the experimental data and the lines are the results of the fitting analysis; Right: Cyclic voltammograms recorded at the scan rate of 0.1 V/s; the black line corresponds to the response at the bare electrode.

The fitting of the spectra by using a Randle's equivalent circuit allows to determine the charge transfer resistance,  $R_{CT}$ . The  $R_{CT}$  can be related to the apparent surface coverage ( $\theta$ ) if we assume that electron transfer reactions occur only at the uncovered surface. Thus, the apparent fractional coverage of the electrode can be estimated by using equation (3) [57,59],

$$\theta = 1 - \left( \frac{R_{CT}^{bare}}{R_{CT}^{SAM}} \right) \quad (3)$$

where  $R_{CT}^{bare}$  is the value corresponding to the gold bare surface and  $R_{CT}^{SAM}$  these determined in the presence of the SAMs. The surfaces coverage values obtained are gathered in Table 2.

**Table 2.** Charge transfer resistances and apparent surface coverages estimated by eqn. (3) for the EGn-SAMs formed under different experimental conditions.

Formation media	$R_{CT} / k\Omega \cdot cm^2$		Surface coverage, $\theta$	
	H <sub>2</sub> O	NaPi	H <sub>2</sub> O	NaPi
<b>EG136</b>	268.9	320	0.9999	0.9999
<b>EG45</b>	114.6	282	0.9998	0.9999
<b>EG18</b>	16.6	31.7	0.9988	0.9993

These apparent surface coverages indicate a strong blocking effect of the EGn-SAMs against the  $Fe(CN)_6^{3-/4-}$  redox pair. Only in the case of the EG18-SAM and, in particular, when formed in a water solution, the presence of pinholes is presumed. This analysis allows us to conclude that the EGn layers, either formed in absence or presence of high salt concentrations, have compact structures and they don't present defects at least to be detected by the  $Fe(CN)_6^{3-/4-}$  redox pair. The higher  $R_{CT}$  values measured for the SAMs formed under cloud point conditions would agree with the increased grafting density proposed in our model.

## Conclusions.

This work proposes a strategy to determine grafting densities of EGn molecules of different chain length by a simple experiment consisting in the analysis of the RD process of the SAM. The method uses the cloud point approach to build films in a brush conformation increasing in this way the grafting density of the SAMs. The high propensity of EGn chains to interact with water molecules provokes the formation of the films that contain a high ratio of water and present a mushroom conformation. The addition of high salt concentrations to the EGn solutions allows the shrinking of the chains and a better

organization of the formed films. This phenomenon is clearly observed by comparing the RD profiles of the SAMs formed in the absence and presence of the salt at concentrations close to their cloud points and is confirmed by EIS analyzing the behavior of the  $\text{Fe}(\text{CN})_6^{3-/4-}$  redox pair. This methodology then, serves to recognize the formation of the highly organized brush conformation by analyzing the shape of the cyclic voltammogram, and to determine a more realistic grafting density values than those reported in the literature by using ellipsometry [13,17,22,50] and surface plasmon resonance [19,21] techniques, within others. The procedure can be extended to other polymer chains of different chemical nature that can form SAMs on metal surfaces by the grafting to approach methodology.

*Acknowledgements.* We thank the Ministerio de Ciencia e Innovación (Project RED2018-102412-T Network of Excellence Electrochemical Sensors and Biosensors), Junta de Andalucía and Universidad de Córdoba (UCO-FEDER-2018: ref. 1265074-2B and Plan Propio, Submod. 1.2. P.P. 2019) for financial support of this work. M.C. acknowledges Ministerio de Universidades for FPU 17/03873 grant.

## References.

- [1] A. Ulman, Formation and Structure of Self-Assembled Monolayers, Chem. Rev. (Washington, D. C.) 96(4) (1996) 1533-1554.
- [2] J.C. Love, L.A. Estroff, J.K. Kriebel, R.G. Nuzzo, G.M. Whitesides, Self-Assembled Monolayers of Thiolates on Metals as a Form of Nanotechnology, Chem. Rev. 105(4) (2005) 1103-1169.
- [3] P.S. Weiss, Functional Molecules and Assemblies in Controlled Environments: Formation and Measurements, Acc. Chem. Res. 41(12) (2008) 1772-1781.
- [4] J.E. Raynor, J.R. Capadona, D.M. Collard, T.A. Petrie, A.J. Garcia, Polymer brushes and self-assembled monolayers: Versatile platforms to control cell adhesion to biomaterials (review), Biointerphases 4(2) (2009) FA3-FA16.
- [5] A.S. Karakoti, S. Das, S. Thevuthasan, S. Seal, PEGylated Inorganic Nanoparticles, Angew. Chem. Int. Ed. 50(9) (2011) 1980-1994.
- [6] R.L.C. Wang, H.J. Kreuzer, M. Grunze, Molecular conformation and solvation of oligo(ethylene glycol)-terminated self-assembled monolayers and their resistance to protein adsorption, J. Phys. Chem. B 101(47) (1997) 9767-9773.
- [7] P. Harder, M. Grunze, R. Dahint, G.M. Whitesides, P.E. Laibinis, Molecular conformation in oligo(ethylene glycol)-terminated self-assembled monolayers on gold and silver surfaces determines their ability to resist protein adsorption, J. Phys. Chem. B 102(2) (1998) 426-436.
- [8] S. Tokumitsu, A. Liebich, S. Herrwerth, W. Eck, M. Himmelhaus, M. Grunze, Grafting of alkanethiol-terminated poly(ethylene glycol) on gold, Langmuir 18(23) (2002) 8862-8870.
- [9] S. Herrwerth, W. Eck, S. Reinhardt, M. Grunze, Factors that determine the protein resistance of oligoether self-assembled monolayers - Internal hydrophilicity, terminal hydrophilicity, and lateral packing density, J. Am. Chem. Soc. 125(31) (2003) 9359-9366.
- [10] J. Fick, R. Steitz, V. Leiner, S. Tokumitsu, M. Himmelhaus, M. Grunze, Swelling behavior of self-assembled monolayers of alkanethiol-terminated poly(ethylene glycol): A neutron reflectometry study, Langmuir 20(10) (2004) 3848-3853.

- [11] M.W.A. Skoda, F. Schreiber, R.A.J. Jacobs, J.R.P. Webster, M. Wolff, R. Dahint, D. Schwendel, M. Grunze, Protein Density Profile at the Interface of Water with Oligo(ethylene glycol) Self-Assembled Monolayers, *Langmuir* 25(7) (2009) 4056-4064.
- [12] U.R. Dahal, Z. Wang, E.E. Dormidontova, Hydration and Mobility of Poly(ethylene oxide) Brushes, *Macromolecules* 50(17) (2017) 6722-6732.
- [13] L.D. Unsworth, Z. Tun, H. Sheardown, J.L. Brash, Chemisorption of thiolated poly(ethylene oxide) to gold: surface chain densities measured by ellipsometry and neutron reflectometry, *J. Colloid Interf. Sci.* 281(1) (2005) 112-121.
- [14] P.G. de Gennes, Conformations of Polymers Attached to an Interface, *Macromolecules* 13(5) (1980) 1069-1075.
- [15] P.G. de Gennes, Polymers at an interface; a simplified view, *Adv. Colloid Interf. Sci.* 27(3) (1987) 189-209.
- [16] P. Kingshott, H. Thissen, H.J. Griesser, Effects of cloud-point grafting, chain length, and density of PEG layers on competitive adsorption of ocular proteins, *Biomaterials* 23(9) (2002) 2043-2056.
- [17] W. Taylor, R.A.L. Jones, Producing High-Density High-Molecular-Weight Polymer Brushes by a "Grafting to" Method from a Concentrated Homopolymer Solution, *Langmuir* 26(17) (2010) 13954-13958.
- [18] W. Taylor, R.A.L. Jones, Protein Adsorption on Well-Characterized Polyethylene Oxide Brushes on Gold: Dependence on Molecular Weight and Grafting Density, *Langmuir* 29(20) (2013) 6116-6122.
- [19] G. Emilsson, R.L. Schoch, L. Feuz, F. Höök, R.Y.H. Lim, A.B. Dahlin, Strongly Stretched Protein Resistant Poly(ethylene glycol) Brushes Prepared by Grafting-To, *ACS Appl. Mater. Interfaces* 7(14) (2015) 7505-7515.
- [20] S.T. Milner, Polymer Brushes, *Science* 251(4996) (1991) 905.
- [21] R. Ortiz, S. Olsen, E. Thormann, Salt-Induced Control of the Grafting Density in Poly(ethylene glycol) Brush Layers by a Grafting-to Approach, *Langmuir* 34(15) (2018) 4455-4464.
- [22] L.D. Unsworth, H. Sheardown, J.L. Brash, Protein-Resistant Poly(ethylene oxide)-Grafted Surfaces: Chain Density-Dependent Multiple Mechanisms of Action, *Langmuir* 24(5) (2008) 1924-1929.
- [23] T. Laredo, J. Leitch, M. Chen, I.J. Burgess, J.R. Dutcher, J. Lipkowski, Measurement of the Charge Number Per Adsorbed Molecule and Packing Densities of Self-Assembled Long-Chain Monolayers of Thiols, *Langmuir* 23(11) (2007) 6205-6211.
- [24] I. Thom, M. Buck, On the interpretation of multiple waves in cyclic voltammograms of self-assembled monolayers of n-alkane thiols on gold, *Z. Phys. Chem.* 222(5-6) (2008) 739-754.
- [25] C.A. Widrig, C. Chung, M.D. Porter, The electrochemical desorption of n-alkanethiol monolayers from polycrystalline gold and silver electrodes, *J. Electroanal. Chem.* 310(1-2) (1991) 335-59.
- [26] D.W. Hatchett, R.H. Uibel, K.J. Stevenson, J.M. Harris, H.S. White, Electrochemical measurement of the free energy of adsorption of n-alkanethiolates at Ag(111), *J. Am. Chem. Soc.* 120(5) (1998) 1062-1069.
- [27] D.F. Yang, C.P. Wilde, M. Morin, Electrochemical desorption and adsorption of nonyl mercaptan at gold single crystal electrode surfaces, *Langmuir* 12(26) (1996) 6570-6577.
- [28] D.F. Yang, C.P. Wilde, M. Morin, Studies of the electrochemical removal and efficient re-formation of a monolayer of hexadecanethiol self-assembled at an Au(111) single crystal in aqueous solutions, *Langmuir* 13(2) (1997) 243-249.
- [29] T. Kakiuchi, H. Usui, D. Hobarra, M. Yamamoto, Voltammetric Properties of the Reductive Desorption of Alkanethiol Self-Assembled Monolayers from a Metal Surface, *Langmuir* 18(13) (2002) 5231-5238.

- [30] R. Madueno, J.M. Sevilla, T. Pineda, A.J. Roman, M. Blazquez, A voltammetric study of 6-mercaptapurine monolayers on polycrystalline gold electrodes, *J. Electroanal. Chem.* 506(2) (2001) 92-98.
- [31] M. Chávez, G. Sánchez-Obrero, R. Madueño, J.M. Sevilla, M. Blázquez, T. Pineda, Characterization of a self-assembled monolayer of O-(2-Mercaptoethyl)-O'-methyl-hexa(ethylene glycol) (EG7-SAM) on gold electrodes, *J. Electroanal. Chem.* 880 (2021) 114892.
- [32] T. Doneux, M. Steichen, A. De Rache, C. Buess-Herman, Influence of the crystallographic orientation on the reductive desorption of self-assembled monolayers on gold electrodes, *J. Electroanal. Chem.* 649(1-2) (2010) 164-170.
- [33] S.S. Wong, M.D. Porter, Origin of the multiple voltammetric desorption waves of long-chain alkanethiolate monolayers chemisorbed on annealed gold electrodes, *J. Electroanal. Chem.* 485(2) (2000) 135-143.
- [34] M.M. Walczak, C.A. Alves, B.D. Lamp, M.D. Porter, Electrochemical and X-ray photoelectron spectroscopic evidence for differences in the binding sites of alkanethiolate monolayers chemisorbed at gold, *J. Electroanal. Chem.* 396(1-2) (1995) 103-114.
- [35] C.J. Zhong, M.D. Porter, Fine structure in the voltammetric desorption curves of alkanethiolate monolayers chemisorbed at gold, *Journal of Electroanalytical Chemistry* 425(1-2) (1997) 147-153.
- [36] C.J. Zhong, J. Zak, M.D. Porter, Voltammetric reductive desorption characteristics of alkanethiolate monolayers at single crystal Au(111) and (110) electrode surfaces, *J. Electroanal. Chem.* 421(1-2) (1997) 9-13.
- [37] M. Byloos, H. Al-Maznai, M. Morin, Formation of a Self-Assembled Monolayer via the Electrospreading of Physisorbed Micelles of Thioliates, *J. Phys. Chem. B* 103(31) (1999) 6554-6561.
- [38] D.F. Yang, H. AlMaznai, M. Morin, Vibrational study of the fast reductive and the slow oxidative desorptions of a nonanethiol self-assembled monolayer from a Au(111) single crystal electrode, *J. Phys. Chem. B* 101(7) (1997) 1158-1166.
- [39] M.M. Walczak, D.D. Popenoe, R.S. Deinhammer, B.D. Lamp, C.K. Chung, M.D. Porter, Reductive Desorption of Alkanethiolate Monolayers at Gold - A Measure of Surface Coverage, *Langmuir* 7(11) (1991) 2687-2693.
- [40] G. Sanchez-Obrero, M. Chavez, R. Madueno, M. Blazquez, T. Pineda, J.M. Lopez-Romero, F. Sarabia, J. Hierrezuelo, R. Contreras-Caceres, Study of the self-assembly process of an oligo(ethylene glycol)-thioacetyl substituted theophylline (THEO) on gold substrates, *J. Electroanal. Chem.* 823 (2018) 663-671.
- [41] M.L. Carot, M.J. Esplandiu, F.P. Cometto, E.M. Patrino, V.A. Macagno, Reactivity of 1,8-octanedithiol monolayers on Au(1 1 1): Experimental and theoretical investigation, *J. Electroanal. Chem.* 579(1) (2005) 13-23.
- [42] M.J. Esplandiu, H. Hagenstrom, D.M. Kolb, Functionalized Self-Assembled Alkanethiol Monolayers on Au(111) Electrodes: 1. Surface Structure and Electrochemistry, *Langmuir* 17(3) (2001) 828-838.
- [43] D. Garcia-Raya, R. Madueno, J. Manuel Sevilla, M. Blazquez, T. Pineda, Electrochemical characterization of a 1,8-octanedithiol self-assembled monolayer (ODT-SAM) on a Au(111) single crystal electrode, *Electrochim. Acta* 53(27) (2008) 8026-8033.
- [44] M.I. Muglali, A. Bashir, A. Terfort, M. Rohwerder, Electrochemical investigations on stability and protonation behavior of pyridine-terminated aromatic self-assembled monolayers, *Phys. Chem. Chem. Phys.* 13(34) (2011) 15530-15538.
- [45] M.I. Muglali, A. Erbe, Y. Chen, C. Barth, P. Koelsch, M. Rohwerder, Modulation of electrochemical hydrogen evolution rate by araliphatic thiol monolayers on gold, *Electrochim. Acta* 90 (2013) 17-26.
- [46] Y.-T. Long, H.-T. Rong, M. Buck, M. Grunze, Odd-even effects in the cyclic voltammetry of self-assembled monolayers of biphenyl based thiols, *J. Electroanal. Chem.* 524-525 (2002) 62-67.
- [47] T. Kawaguchi, H. Yasuda, K. Shimazu, M.D. Porter, Electrochemical Quartz Crystal Microbalance Investigation of the Reductive Desorption of Self-Assembled Monolayers of Alkanethiols and Mercaptoalkanoic Acids on Au, *Langmuir* 16(25) (2000) 9830-9840.

- [48] T.W. Schneider, D.A. Buttry, Electrochemical quartz crystal microbalance studies of adsorption and desorption of self-assembled monolayers of alkyl thiols on gold, *J. Am. Chem. Soc.* 115(26) (1993) 12391-7.
- [49] S. Alexander, Adsorption of chain molecules with a polar head a scaling description, *J. Phys. France* 38(8) (1977) 983-987.
- [50] D.F. Marruecos, M. Kastantin, D.K. Schwartz, J.L. Kaar, Dense Poly(ethylene glycol) Brushes Reduce Adsorption and Stabilize the Unfolded Conformation of Fibronectin, *Biomacromolecules* 17(3) (2016) 1017-1025.
- [51] R. Ogaki, O.Z. Andersen, G.V. Jensen, K. Kolind, D.C.E. Kraft, J.S. Pedersen, M. Foss, Temperature-Induced Ultradense PEG Polyelectrolyte Surface Grafting Provides Effective Long-Term Bioresistance against Mammalian Cells, Serum, and Whole Blood, *Biomacromolecules* 13(11) (2012) 3668-3677.
- [52] M. Chavez, A. Fernandez-Merino, G. Sanchez-Obrero, R. Madueno, J.M. Sevilla, M. Blazquez, T. Pineda, Distinct thermoresponsive behaviour of oligo- and poly-ethylene glycol protected gold nanoparticles in concentrated salt solutions, *Nanoscale Adv.* 3(16) (2021) 4767-4779.
- [53] K. Rahme, L. Chen, R.G. Hobbs, M.A. Morris, C. O'Driscoll, J.D. Holmes, PEGylated gold nanoparticles: polymer quantification as a function of PEG lengths and nanoparticle dimensions, *RSC Adv.* 3(17) (2013) 6085-6094.
- [54] A. Jimenez, A. Sarsa, M. Blazquez, T. Pineda, A Molecular Dynamics Study of the Surfactant Surface Density of Alkanethiol Self-Assembled Monolayers on Gold Nanoparticles as a Function of the Radius, *J. Phys. Chem. C* 114(49) (2010) 21309-21314.
- [55] E. Reyes, R. Madueño, M. Blazquez, T. Pineda, Facile Exchange of Ligands on the 6-Mercaptopurine-Monolayer Protected Gold Clusters Surface, *J. Phys. Chem. C* 114(38) (2010) 15955-15962.
- [56] F. Oesterhelt, M. Rief, H.E. Gaub, Single molecule force spectroscopy by AFM indicates helical structure of poly(ethylene-glycol) in water, *New Journal of Physics* 1 (1999).
- [57] H.O. Finklea, D.A. Snider, J. Fedyk, E. Sabatani, Y. Gafni, I. Rubinstein, Characterization of Octadecanethiol-Coated Gold Electrodes as Microarray Electrodes by Cyclic Voltammetry and Ac-Impedance Spectroscopy, *Langmuir* 9(12) (1993) 3660-3667.
- [58] H.O. Finklea, S. Avery, M. Lynch, T. Furtch, Blocking oriented monolayers of alkyl mercaptans on gold electrodes, *Langmuir* 3(3) (1987) 409-413.
- [59] R.P. Janek, W.R. Fawcett, A. Ulman, Impedance Spectroscopy of Self-Assembled Monolayers on Au(111): Sodium Ferrocyanide Charge Transfer at Modified Electrodes, *Langmuir* 14(11) (1998) 3011-3018.

**Supporting information.**



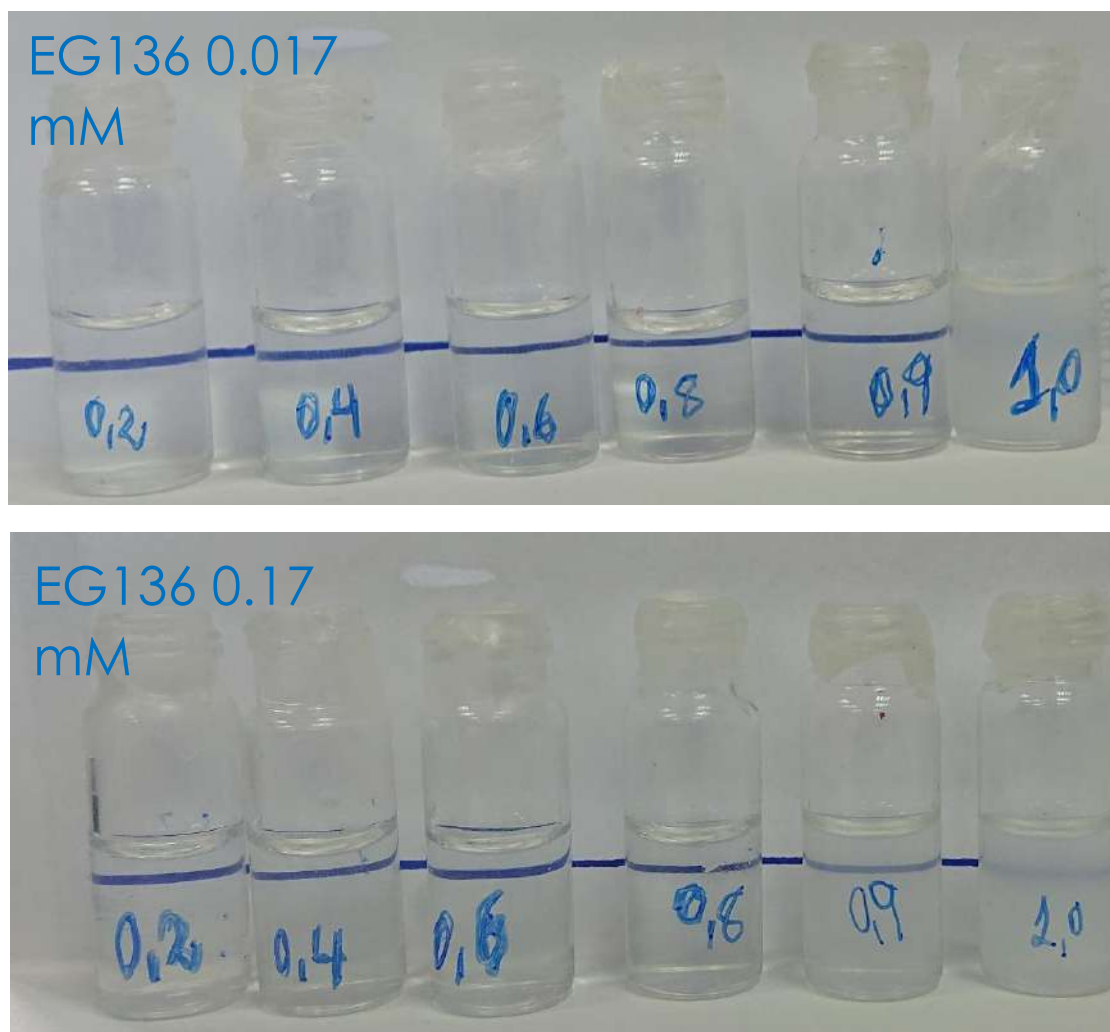


**Figure S1.** Photography of EG136 solutions of different concentrations and in the presence of various NaPi salt concentrations to show the cloud point.

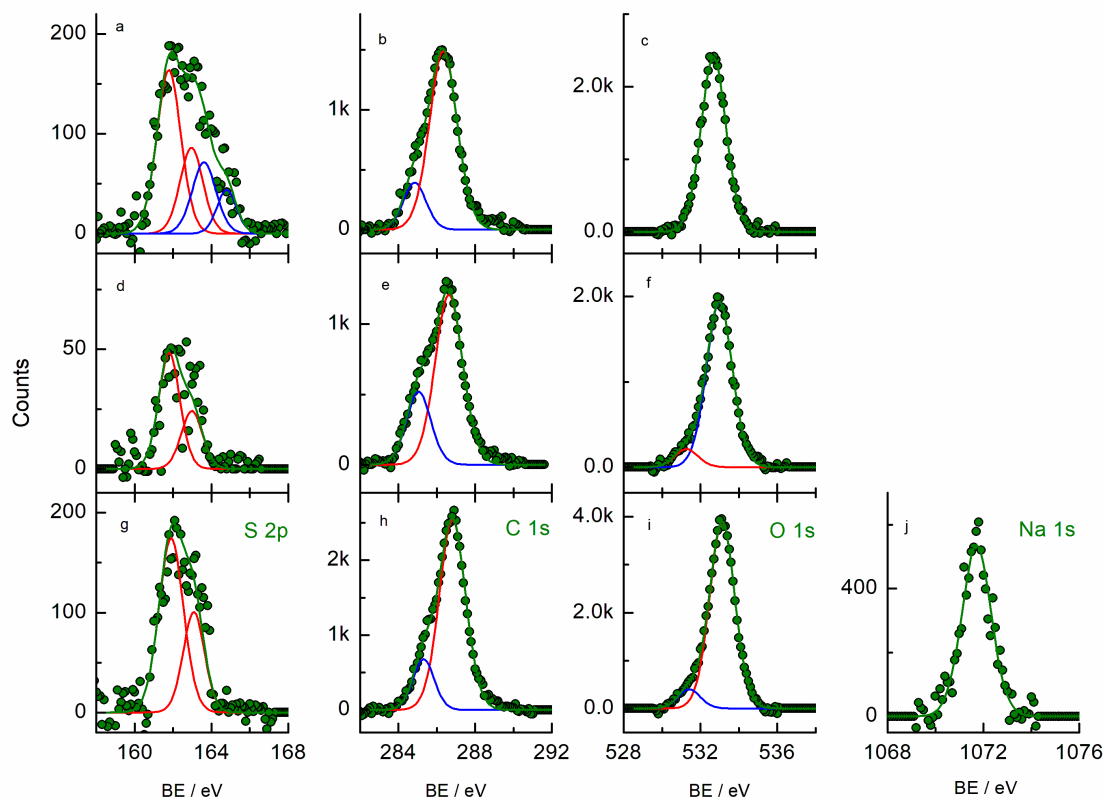


**Figure S2.** High resolution scans of XPS spectra recorded in the regions of S 2p, C 1s, O 1s and Na 1s, of EG136-SAMs formed in solutions of 0.18 mM (a, b, c), 0.018 mM (d, e, f) and 0.18 mM and NaPi 0.9 M.

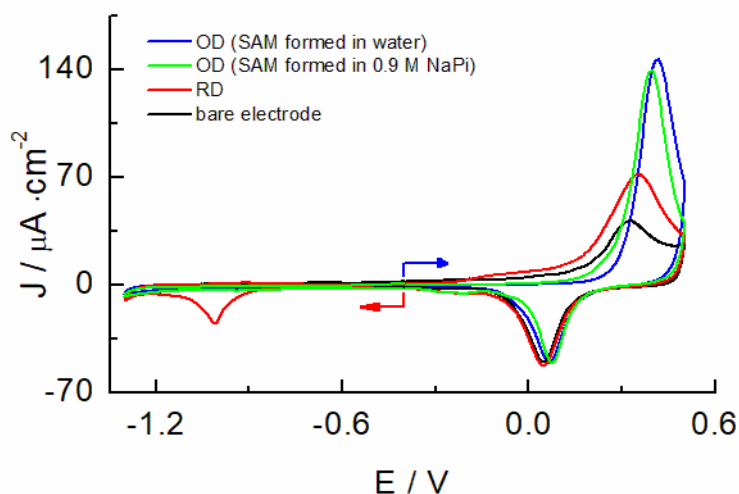


**Figure 3S.** CVs of EG136-SAMs formed from a 0.18 mM EG136 in water in the absence (blue line: oxidative desorption; red line: RD) and presence (green line: oxidative desorption) of 0.9 M NaPi salt. The black line corresponds to the bare electrode.

### 3.5. Artículo 5.

*Evaluación electroquímica de la densidad de empaquetamiento formadas mediante la aproximación grafting to de monocapas autoensambladas de polietilenglicol de diferente longitud de cadena en condiciones próximas al punto de nube.*



Issue 16, 2021



From the journal:  
**Nanoscale Advances**

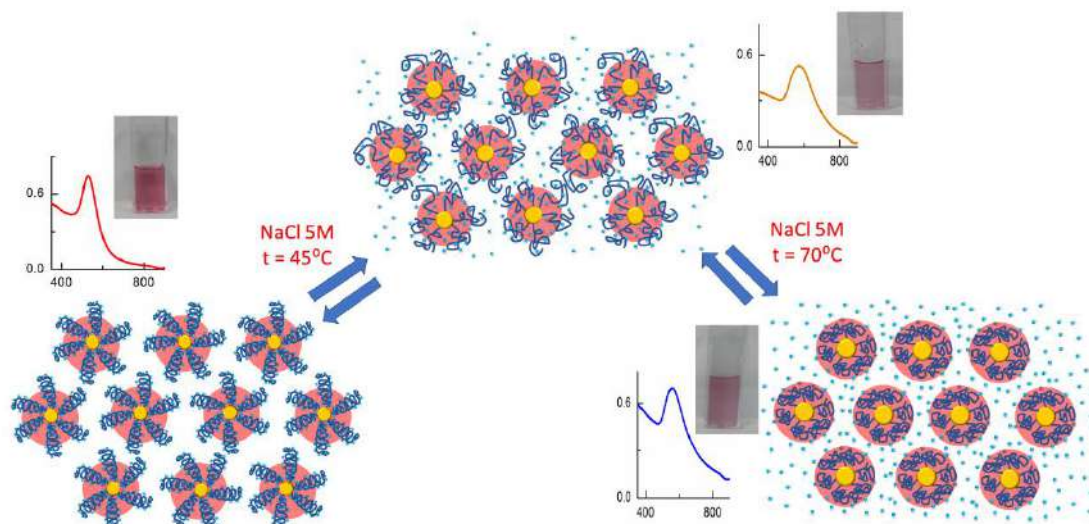
## **Distinct thermoresponsive behaviour of oligo- and poly-ethylene glycol protected gold nanoparticles in concentrated salt solutions.**

Miriam Chávez, Ángela Fernández-Merino, Guadalupe Sánchez-Obrero, Rafael Madueño, José Manuel Sevilla, Manuel Blázquez, Teresa Pineda\*

Department of Physical Chemistry and Applied Thermodynamics, Institute of Fine Chemistry and Nanochemistry, University of Cordoba, Campus Rabanales, Ed. Marie Curie 2<sup>a</sup> Planta, E-14014 Córdoba, Spain

### **Abstract**

In this work, methoxy terminate oligo- and polyethylene glycol of different chain lengths (EGn, n = 7, 18, 45 and 136) are grafted on AuNP surfaces under conditions that they attain maximum grafting densities. These EGn-AuNPs gain stability in respect to the pristine c-AuNPs in aqueous solutions and in a wide temperature interval and they form stable suspensions in solutions of high NaCl concentrations. To show the thermoresponsive properties of these EGn-AuNPs, temperature titrations experiments are carried out in the presence of increasing amounts of salts. The concentrations of NaCl are chosen by checking the stability of the EGn-AuNPs at room temperature and choosing the highest concentrations that allow them to form stable suspensions. The analysis of the temperature titration experiments monitored by UV-visible spectroscopy and dynamic light scattering allows us to establish the existence of transitions from individual to assembled nanoparticles, the reversibility of the temperature transitions and hysteretic behaviour in these systems. While EG7-AuNPs only show reversible temperature transitions in the presence of 5 mM NaCl, EG18-AuNPs do up to 1 M NaCl, becoming only partially reversible in 2 M NaCl. The titrations of EG45-AuNPs in 3 and 5 M NaCl, show irreversible temperature transitions. Finally, EG136-AuNPs present a complex and interesting behaviour with two temperature transitions, the first one showing hysteresis and the second being reversible.



**Graphical abstract**

## Introduction.

Surface-grafted polymers or polymer brushes are currently used in macroscopic and nanoscopic surfaces such as gold nanoparticles (AuNPs) as they confer many interesting properties that are necessary in their applications for *in vivo* systems. One of these properties is biocompatibility and a very popular strategy followed to endow NMs with it, is by surrounding their surface with polyethylene glycol of different chain lengths (EGn), a process known as PEGylation [1,2]. It is considered that the hydrophilic and uncharged nature of EGn molecules help to avoid in a great extent the unspecific adsorption of proteins and the recognition by the immune system [3]. These stealth properties of the EGn protected AuNPs (EGn-AuNPs) are believed to be determined by the length and grafting density of the chains in the surface, and recently, it has been reported that the specific chemical properties of the ligands are the major driving force determining the composition of the protein corona that ultimately will be responsible for the prolongation of the blood circulation time and the immune response of the nanoparticles [4,5]. One of the most important parameters determining the interaction of nanoparticles with proteins is the grafting density of the EGn used to protect the surface and therefore its related chain conformation [6]. To determine de grafting density, many approximations have been reported that include nuclear magnetic resonance spectroscopy [5,7,8], thermogravimetric analysis [6], isothermal titration calorimetry [9], analytical ultracentrifugation and total organic carbon analysis [10], within others. The chain conformation of the surface-grafted polymer dictates the interfacial properties, and as described within the Alexander-de-Gennes theory [11, 12], the good solvents

make the interactions with the solvent preferred over these with other polymer chains. Thus, under low grafting densities, there are no lateral constraints, and the polymer adopts a swollen conformation, behaving like a free polymer in solution, and the Flory radius describes the size of the random coil that is formed by such a polymer in solution [13]. This structure is called mushroom conformation. When the grafting density is high, the polymer chains are forced into a stretched or brush conformation [14].

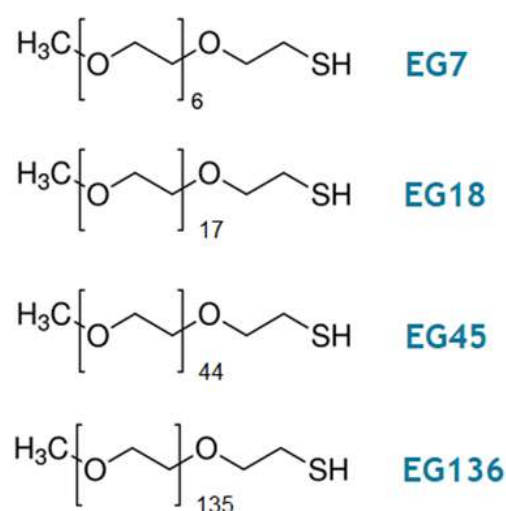
The grafting densities of EGn in AuNPs are influenced by the EGn molecular weight and the size of the nanoparticle and are mainly responsible for the stabilization of the EGn-AuNPs in solutions of different pH, salt concentrations and temperature [6, 8]. In this sense, the thermoresponsive properties of these polymers can be studied by analysing their assembly behaviour. The EGn-water system shows a phase diagram of the close-loop type with a lower critical solution temperature (LCST) at around 100 °C that is mainly due to the formation of hydrogen bonds [15]. This limits the use of EGn polymers for the temperature triggered assembly of polymer grafted nanoparticles. However, the presence of salts can lower the LCST [16] and allows to study their thermoresponsive properties at lower temperature ranges. In a study of AuNPs coated with short EGn ligands terminated with alkyl heads, Ijiro et al. found that when the alkyl head was absent, the nanoparticles did not assemble in the range from 20 to 70 °C but, with either ethyl, iso-propyl or propyl-headed EGn-AuNPs, the assembly took place at lower temperatures, indicating that the part of the ligand displayed on the outermost surface is important on the thermoresponsive behavior [17]. Recently, they have demonstrated that this thermoresponsive assembly/ disassembly process in water takes place through the hydration/dehydration of the EGn portion in a manner dependent on the hydrophobicity at their terminus and the surface curvature of the different size AuNPs employed. Also, by using molecular dynamics simulations they show that the surface curvature tuned the distribution of the hydrophobic terminus in the normal direction along the surface, leading to variations in molecular configurations and that, the smaller the curvature the higher the local density, promoting the bending of the ligand molecules configuration and stabilizing the hydrophobic terminus in the relatively dense EGn moiety [18]. These results are in agreement with the observed behaviour for gold nanorods that shows a two-step assembly/disassembly with temperature, induced by stepwise dehydration, that depends on the nanorod diameter but is independent on its length [19].

EG18- and EG45-AuNPs form clusters at high ionic strength ( $K_2SO_4$ ) and elevated temperature as a result of collapse of the surface-grafted EGn molecules [20, 21]. Another way to obtain thermoresponsive polymers at lower temperature is to form a statistical polymer constituted by EG and propylene oxide (PO) groups that are modified by a dihydrolipoic acid terminal to attach to an AuNP surface. The transition temperature of these polymers can be tuned by adjusting the ratio between EG and PO, the size of the nanoparticle and the salt concentration [22]. Moreover, the steric hindrance generated by the reorganization of flexible hydrophilic polymer brushes during interparticle association is critical for the morphological selectivity in the assembly [23].

Taking advantage of the hydrophobic/hydrophilic tuneable characteristics of the PEG polymers depending on the experimental conditions, Vaknin et al. have dedicated great efforts to elucidate the influence of different salt concentrations [24-28] and temperature of the suspensions [29-31] in the interfacial assembly of EGn-AuNPs. The addition of ions to the solution impinges a poor solvent character for the polymers that could provoke the self-assembly of the EGn-AuNPs and its phase separation. The specific effect of ions, in general, follows the Hofmeister series. In fact, the presence of low level  $K_2CO_3$  salt concentration makes the EG18- and EG136-AuNPs to migrate to the vapor/solution interface without any specific organization but, when the salt concentration increases, short range hexagonal order develops, finally acquiring a highly ordered hexagonal crystallinity. The hydrodynamic radius of these EGn-AuNPs is found to be independent of salt concentration probably because the polymer corona can be protected by an effective semipermeable membrane that maintains a constant salt concentration up to the  $\theta$ -point [24]. When the concentration increases above 1 M, 3D macroscopic precipitates are induced that exhibit short range order and are consistent with a *fcc* symmetry with the nearest-neighbour distance in the assemblies dominated by the polymer length [25]. Although monovalent salts as NaCl and KCl do not cause phase separation of PEG at room temperature, they lead to 2D self-assembly of EGn-AuNPs at the interface, consistent with the depletion of ions in the polymer brush at concentrations lower than the necessary for bulk phase separation, generating an osmotic pressure gradient that drives the self-assembly. However, they do not induce 3D assembly into supercrystals [26]. Different strategies that include salt concentration, interpolymer complexation, pH and temperature changes demonstrate that the self-assembly of structures other than spheres is also possible as it has been observed for gold nanorods [29] and gold nanotriangles [30] grafted with an EGn polymer corona.



In this work, we present a study of the stability of EGn-AuNPs formed with methoxy-terminated oligo- or poly-ethylene glycol of different chain length (Scheme 1). The EGn-AuNPs have been prepared under conditions that guarantee the highest grafting density for the different chain length employed. A characterization by using UV-visible spectroscopy, dynamic light scattering (DLS) and zeta-potential measurements in an aqueous medium is first made to define the nanoparticle properties. The influence of the ionic strength and temperature in the stability of the suspensions, pointing to the reversibility of the observed changes, is reported. The monitorization of the aggregation phenomena is made by following the changes in the LSPR bands as well as the hydrodynamic sizes of the EGn-AuNPs by DLS.



**Scheme 1.** Oligo- and poly- (ethylene glycol) methyl ether thiol, EGn, where n is the number of monomer units per chain, used in this work.

## Experimental section.

### Chemicals.

Hydrogen tetrachloroaurate (III) trihydrate ( $\text{HAuCl}_4$ ), sodium citrate, O-(2-Mercaptoethyl)-O'-methyl-hexa(ethylene glycol) (EG7) and poly(ethylene glycol) methyl ether thiol (MW 800, EG18; MW 2000, EG45; MW 6000, EG136) were purchased from Aldrich-Sigma (purity  $\geq 99\%$ ). The rest of the reagents were from Merck analytical grade. All solutions were prepared with deionized ultrapure water produced by a Millipore system (Mili-Q Direct-8).

### Synthesis of c-AuNPs and surface modification.

The synthesis of citrate-capped gold nanoparticles (c-AuNPs) has been carried out by following the classic Turkevich method [32]. In brief, 50 mL of 1 mM HAuCl<sub>4</sub> was brought to a boil under stirring. By the addition of 5 mL 38.8 mM sodium citrate, the colour of the mixture changes from pale yellow to burgundy. Boiling was continued for 10 min and then the solution was cooled to room temperature under stirring. Finally, c-AuNPs are stored in the dark at room temperature, remaining quite stable for several weeks.

The pristine c-AuNPs were diluted in Milli-Q water to reach 3.5 nM concentration and the pH was fitted to 7.5-8.0 with NaOH. Then a 2-fold excess of EGn-SH ligand in respect to the necessary to cover the AuNP surface, was added under vigorous stirring. This concentration was determined by considering the total gold atoms in the nanoparticle surfaces and using a footprint of 20 Å<sup>2</sup>/molecule (this footprint is lower than the observed on flat surfaces [33, 34] and ensures that the concentration ratio is sufficient). The mixture was left overnight under shaking to allow for a maximum molecular self-assembly. To remove unreacted thiolate molecules, the mixture was submitted to three washing steps consisting of centrifugation (at 12000 rpm for 15 min), removal of supernatant and addition of water. The EGn-AuNPs obtained under these conditions are kept in the dark at room temperature and remain stable for weeks.

### Characterization of AuNPs.

The c- and EGn-AuNPs were imaged by transmission electron microscopy (TEM) (JEOL JEM 1400 instrument (Servicio Central de Apoyo a la Investigación (SCAI) Universidad de Córdoba) operating at 80–120 kV and the images analysed using Image Pro Plus software. Samples were prepared onto Formvar-coated Cu grids (400 mesh, Electron Microscopy Sciences). Each TEM grid was immersed in ca. 1 nM EGn-AuNPs solution for an hour, then dunked in water to wash away unattached particles and finally air dried at room temperature.

The grafting density of EGn-AuNPs was determined by thermogravimetric analysis (TGA), by using a Mettler Toledo thermogravimetric analyser. The EGn-AuNP samples (10 mg) were prepared by first drying the washed solutions at 60 °C for 4 hours previous to TGA measurements. The temperature was varied between 20 °C and 800 °C at 10 °C /min under nitrogen atmosphere flowing at 40 mL/min. The amount of EGn was calculated by using the ratio of weight loss occurring between 300 °C and 450 °C, considered to correspond to the degradation of EGn, to the weight remaining at 450 °C that correspond to AuNPs [6, 35]. The AuNPs volume, mass, and surface area are calculated assuming an ideal spherical shape with a diameter of 25 nm. The weight loss assigned to the polymer corona and the weight remaining at 450 °C are averaged by the EGn and the AuNP molar mass,

respectively, to determine the amount of EGn grafted per nanoparticle. This ratio is divided by the AuNP surface area to obtain the grafting density,  $\sigma$ , and its reverse, the footprint of the EGn molecules.

The size, size distribution and zeta-potential of the particles were determined by dynamic light scattering (DLS) (Malvern Zetasizer Nano, ZSP) with 633 nm He–Ne laser. The measured data are the average of at least 20 runs. The average hydrodynamic diameter ( $D_H$ ) and mean zeta potential of each sample were computed using the software provided by the manufacturer.

The extinction spectra were recorded using a Jasco V-670 UV-vis-NIR spectrophotometer. The studies of the temperature effects were made by fitting a Peltier temperature controller, and a rate of 0.5 °C/min programme was selected.

## Results and discusión.

### Ligand exchange of c-AuNPs by EGn polymer chains.

The ligand exchange of c-AuNPs by EGn-SH molecules of different chain lengths ( $n = 7, 18, 45$  and  $136$ ) readily takes place on nanoscopic gold surfaces. In this work, we have used c-AuNPs of 25 nm diameter synthesized by the classical Turkevich method (Figure S1), and the exchange reactions are carried out under the experimental conditions described in the experimental section, that allow to reach a maximum surface coverage. UV-visible spectroscopy shows a small shift of the LSPR band of ca. 2-3 nm in respect to the c-AuNPs, regardless of the polymer chain length (Figure S2). This shift in the maximum wavelength is produced by the change of the refractive index of the layer immediately surrounding the AuNP surface [36]. The presence of the polymer corona around the AuNP is perceived through the increase in dispersibility of the EGn-AuNPs in comparison to the c-AuNPs that becomes somewhat aggregated upon deposition on the TEM grid (Figure S1).

TGA of the EGn-AuNP samples has been carried out to get information on the extent of grafting density of the different EGn molecules (see experimental section). Table 1 gathers the molecular parameters obtained by TGA. The grafting density ( $\sigma$ ) decreases with the increase in chain length, and consequently the footprint increases. A value of 20.7 Å<sup>2</sup> is found for EG7, that is somewhat lower than the footprint of this molecule adsorbed in macroscopic gold [34] and determined by RD of the EG7-self assembled monolayer on a gold electrode. By using the theoretical surface area of the AuNP of 25 nm diameter, the number of EGn molecules per nanoparticle is calculated.

**Table 1.** Molecular parameters obtained by ATG.

	% weight loss	$\sigma / \text{nm}^2$	Footprint/ $\text{\AA}^2$	EGn / AuNP
<b>EG7</b>	2.9	4.82	20.7	9470
<b>EG18</b>	5.5	3.90	25.6	7660
<b>EG45</b>	9.9	3.28	30.5	6430
<b>EG136</b>	9.5	1.04	96.1	2040

**Table 2.** Properties of EGN molecules and hydrodynamic diameters ( $D_H$ ) and Z-potentials as measured by DLS.

	MW/Da	$D_H/\text{nm}$	L/nm	Hel/nm	Trans/nm	Zeta-potential/ mV
<b>EG7</b>	356	28.4	1.7	1.9	2.5	-28.5 $\pm$ 1.3
<b>EG18</b>	800	28.4	1.7	5.0	6.4	-10.8 $\pm$ 2.4
<b>EG45</b>	2000	37.2	6.1	12.5	16.0	-10.2 $\pm$ 2.3
<b>EG136</b>	6000	59.7	17.3	37.8	48.4	-6.9 $\pm$ 1.0

**Table 3.** Conformational parameters of the EGN chains in EGN-AuNPs as calculated by using eqn. 1 to 3.

	$R_f / \text{nm}$	P / nm	$D_H^{(1)} / \text{nm}$	$D_H^{(2)} / \text{nm}$	$V_{\text{molec}} / \text{nm}^3$
<b>EG7</b>	1.1	0.455	29.1	28.8	0.40
<b>EG18</b>	2.0	0.506	34.8	34.5	0.50
<b>EG45</b>	3.4	0.552	48.2	46.0	2.91
<b>EG136</b>	6.7	0.980	72.9	57.1	50.56

(1) Determined by using eqn. 2.

(2) Determined by using eqn. 4.

To evaluate the EGN shell formed around the AuNP and the existence of any aggregation phenomena, we use the DLS technique. After modification, larger  $D_H$  values in respect to the c-AuNPs were obtained, which can be attributed to the presence of the surface grafted EGN layer. Table 2 contains information on the EGN molecular weights, experimental hydrodynamic diameters ( $D_H$ ) and calculated thickness (L) for the different EGN-AuNPs. The L values increase with the chain length in a nonlinear fashion. The theoretical length values for these molecules by assuming a brush regime with the chains adopting either a helicoidal or an all-trans conformation that suppose an incremental of 2.78  $\text{\AA}$  or 3.56  $\text{\AA}$  per monomer, respectively [37] are also gathered to compare with the experimental values. Finally, the zeta-potential measured for the different EGN-AuNPs are also included. Comparing to the c-AuNPs that show a negative value of -44 mV due to the presence of citrate anions protecting the surface, the zeta-potential values are increasing from the shorter to the higher chain, as expected for the neutral characteristics of the EGN molecules. The AuNP surface modification with mercapto-derivatives is believed to take place by the exchange of the

citrate anions by the thiol group and, therefore, most of the citrate anions are displaced from the surfaces and thus, an increase of the zeta-potential values [38-41] that are consistent with these reported for EGn-coated AuNPs is found [6, 42, 43].

The two regimes described by polymers attached to a surface are the mushroom regime, that occurs at very low grafting density and the brush regime that develops when the grafting densities are high.<sup>11, 12</sup> In the mushroom regime, the chains behave as isolated chains in solution, and can be thought as hemispheres with a size given by the Flory radius:

$$R_F = a \cdot N^{3/5} \quad (1)$$

where N is the number of monomers in the chain and a is the monomer length (0.35 Å).

When the polymer enters the brush regime, the thickness of the brush can be given by:

$$L = N \cdot a \left(\frac{a}{P}\right)^{2/3} \quad (2)$$

where P is the distance between the grafting points in the surface,

$$P = \left(\frac{1}{\sigma}\right)^{1/2} \quad (3)$$

The conformation should be in a mushroom regime when P is greater than R<sub>F</sub>, as the chains have space to fold back over the AuNP surface, resulting in a thin layer (small L). In contrast, when P is lower than R<sub>F</sub>, the EGn should exist in a brush regime with the chains stretching out from the AuNP surface resulting a thick layer (large L).<sup>44</sup> In the case that L > 2R<sub>F</sub>, the dense brush regime is obtained [45]. By using the grafting densities σ determined by TGA (Table 1), the values of P and L are determined by using eqn. 2 and 3 (Table 3). As it can be observed, the values of P obtained by using eqn. 3 are lower than R<sub>F</sub>, indicating that the attached molecules are in the brush conformation.

On the basis of the behaviour of EGn in the presence of salts [46, 47], and considering that EGn-AuNPs consist of flexible chains covalently grafted at the AuNP core of diameter D, Vaknin et al. [24, 25] have modelled the effective hydrodynamic diameter D<sub>H</sub> for spherical nanoparticles by eqn. 4,

$$\left(\frac{D_H}{D}\right)^2 = 1 + 4 \cdot \frac{N \cdot b^2 \cdot \sigma^{1/2}}{D} \cdot (2w_o)^{1/4} \quad (4)$$

where N is now the number of Kuhn monomers, b is the Kuhn length (b = 0.724 nm for EGn), σ is the grafting density and w<sub>o</sub> is a dimensionless three body interaction (w<sub>o</sub> = 0.76). The values of D<sub>H</sub> obtained by eqn. 4 are also gathered in Table 3. These values are of the same order of those determined by eqn. 3 and to these obtained by DLS (Table 2).

The hydrodynamic volumes per molecule determined by dividing the EGn corona volume, as obtained through the experimental D<sub>H</sub> values, by the number of molecules grafted on the surface, as determined from TGA, are higher than expected if we assume that the EGn molecules are in a brush conformation occupying a cylinder whose base is the footprint of the molecule, and this excess is much larger for EG136. The excess of volume

must be occupied by either free or bound water molecules whose presence would be more important with increasing the distance from the AuNP surface. Recent theoretical calculations have demonstrated that the criterion for planar surfaces is insufficient to assess the achievement of the brush regime and that the curvature needs to be considered [48, 49]. They demonstrate that the polymer density decreases with the radial distance, and they remain well hydrated with a decrease in the fraction of free water only close to the surface. The requirement of overlapping at the height of the radius of gyration of the polymer,  $R_{go}$ , leads to a modified estimate for the required grafting density to achieve the brush regime,  $\sigma^* \approx (1/R_{go} + 1/R)$  for spherical nanoparticles of radius  $R$ , taking into account the surface curvature as well as the polymer coil dimension [48, 49].

### Stability of the EGn-AuNPs in aqueous solutions.

The obtained EGn-AuNPs have been examined in aqueous solution of different pH by UV-visible spectroscopy. The LSPR band does not shift when the pH is changed from alkaline to neutral and weakly acid media. Figure 1 shows the variations of LSPR wavelength and extinction peak intensity for the EGn-AuNPs as a function of pH. Only in the case of EG7-AuNPs, an increase of the LSPR wavelength is observed at  $pH < 5$  that is parallel with a decrease in extinction because of the aggregation of the nanoparticles in this medium. However, in comparison with the behaviour of the citrate-AuNPs, 38, 41 a higher stability is conferred by the presence of the EG7 protecting layer. Moreover, the aggregation phenomenon is reverted when the pH of the solution is changed to neutral or alkaline values.

The stability of the EGn-AuNPs as indicated by the position of the LSPR wavelength is preserved under these acidic media for the longer EGn chains, although a small decrease in extinction is also observed at  $pH < 3$ .

When these EGn-AuNPs aqueous neutral solutions are exposed to temperature changes from 5 to 90 °C, no changes in the LSPR bands are observed for EG18-, EG45- and EG136-AuNPs. However, the EG7-AuNPs, although keep stable up to 85 °C, experiment an abrupt displacement from 522 nm to 536 nm with the concomitant emergence of a band near 740 nm when the temperature reaches 90 °C. Upon descending the temperature from this value, with the same rate as the ascending ramp, the spectrum returns to the initial shape, probing that the induced temperature aggregation of the EG7-AuNPs is completely reversible (Figure 2).

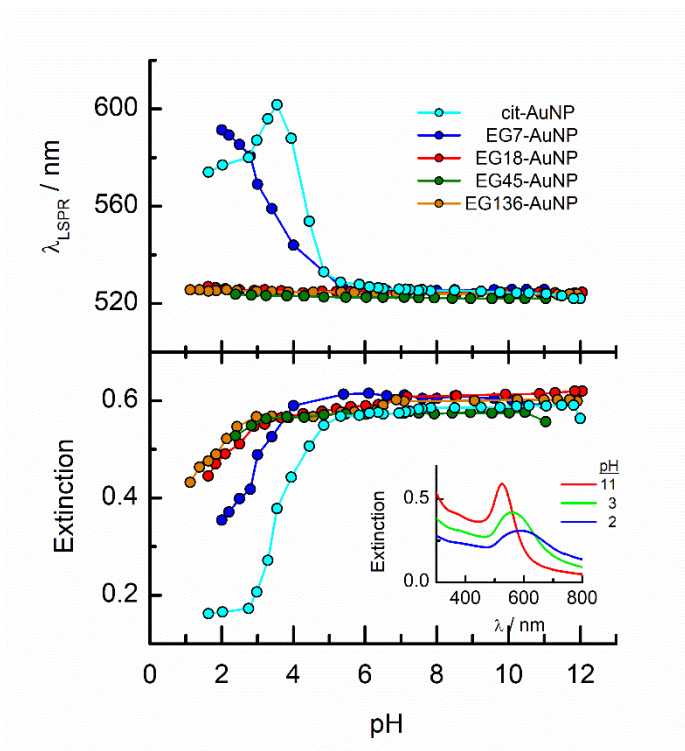


**Figure 1.** Effects of the solution pH on the LSPR wavelength and extinction of the EGn-AuNPs in aqueous solution. The pH was adjusted by adding aliquots of either NaOH or HCl diluted solutions. The experiments were run at room temperature (22 °C). *Inset:* Spectra of EG7-AuNPs at different solution pH.

One way to check the goodness of the protection of these AuNPs against aggregation is to study the effects of the presence of salts in the LSPR band parameters (Figure 3). It is well known that the EGn-AuNPs continue stable in solution in the presence of 1 M NaCl when the grafting density of the chains is appropriate [50]. As it can be observed, either the wavelength or the extinction peak of the EG136-AuNP and EG45-AuNPs spectra accomplish with this condition and do not change up to 1 M NaCl salt concentration. The behaviour observed for EG7-AuNPs in the presence of increasing NaCl concentration deserves some comments. Whereas the LSPR band obtained in water shows the typical shape for a well dispersed solution, when the concentration of salt is greater than 0.1 M, an increase of the scatter at longer wavelength is detected (Figure 3, inset). At higher concentrations, a small band at around 800 nm appears that remains in equilibrium with that for the individual particles. These features are kept in the presence of 1 M NaCl. Interestingly, the band at 522 nm is maintained indicating that the individual EG7-AuNPs coexist with some big aggregates.

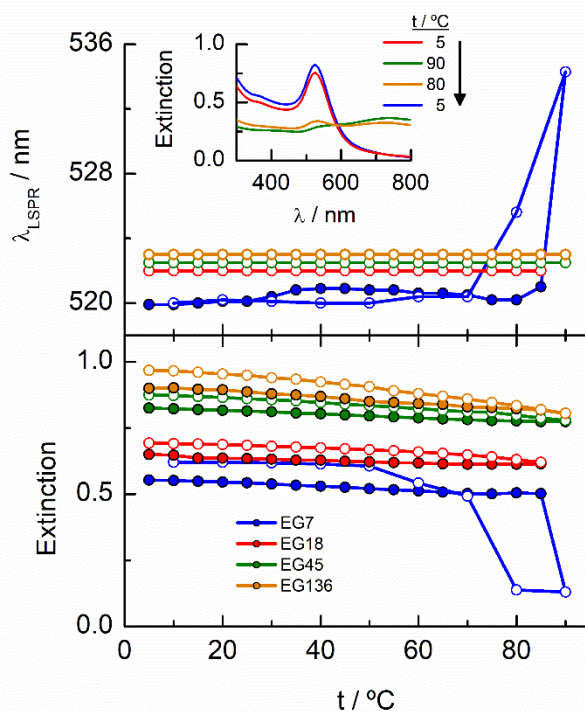


**Figure 2.** Temperature titration curves for EGN-AuNPs in neutral aqueous solutions (no additional salt is added other than that necessary to get a neutral medium). Changes in the LSPR extinction and wavelength. The direct (solid circle) and reverse (empty circle) temperature scans are plotted. Inset: Spectra of EG7-AuNPs at different temperatures (the arrow indicates the direction of the temperature change).

DLS measurements of EG7-AuNPs dispersions in water and in the presence of 0.1 M NaCl confirm this idea. The  $D_H$  in water is of 28.4 nm while, in the presence of salt, a first signal at 29 nm accompanied with a second one of much higher value ( $\sim 720$  nm) that should correspond to these aggregates of bigger size (Figure S3) are observed in the size distribution plot. However, these aggregates should exist in a low concentration as the number distribution plot of these signals shows only the peak of lower diameter indicating that these are the most abundant in the dispersion.

EG18-AuNPs show a different and more common behaviour. The LSPR band centred at 522 nm for the dispersion in water shifts to longer wavelength at NaCl concentrations higher than 0.2 M. This wavelength shift is accompanied by a new band at around 600 nm that overlaps with the original one. The  $D_H$  value obtained in water is of 28.4 nm and does not change in the presence of 0.15 M NaCl and even higher concentrations (1 M).

The influence is more pronounced for divalent salts as  $\text{CaCl}_2$ . EG18-AuNPs exhibit a displacement of the LSPR band to higher values at very low  $\text{CaCl}_2$  concentration, and this change is paralleled with a decrease in the extinction peak following the normal behaviour of loss of stability and irreversible precipitation in the presence of salts. The EG7-AuNPs behave somewhat different. An important increase in the extinction peak concomitant with



a small displacement of the band to lower wavelength is observed at concentrations higher than 2 mM. The observed wavelength displacement is however apparent and seems to be due to the influence of the scattering that is being produced in the presence of  $\text{CaCl}_2$  (Figure 3, inset). This effect is ascribed to the decrease in transmittance due to Rayleigh scattering of the polymers amplified by the LSPR band of the AuNP when the presence of the salt make the water to be a poor solvent after breaking of the polymer-water H-bonds and probably exposing a more hydrophobic surface [51].

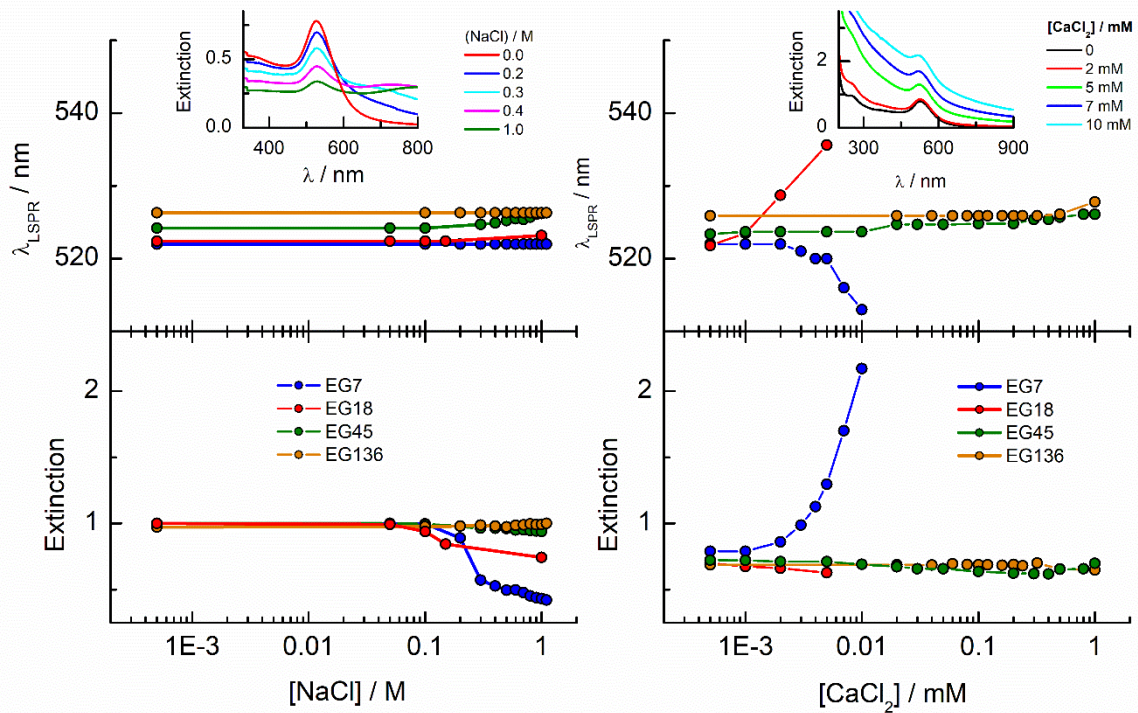


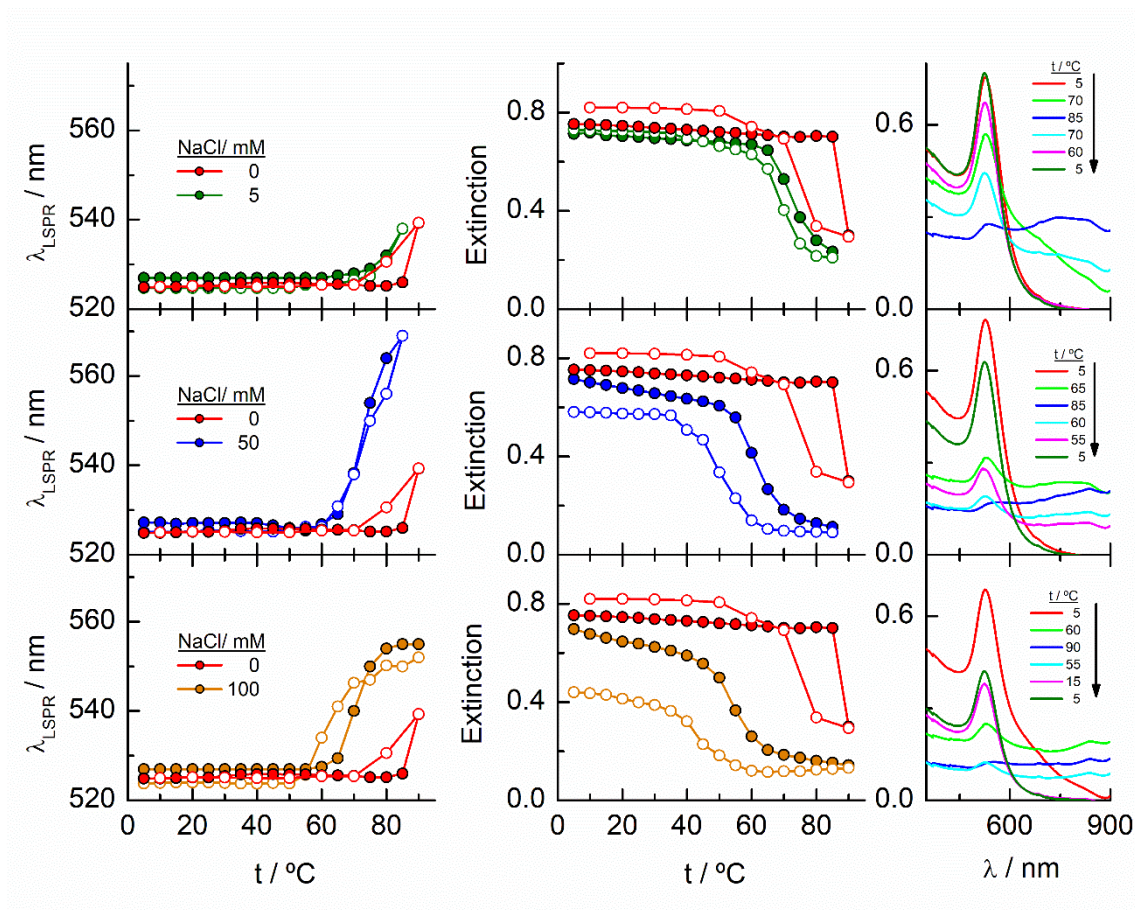
**Figure 3.** Effects of the salt's addition in the stability of EGN-AuNPs as seen by UV-visible spectroscopy. The insets show spectra of EG7-AuNPs in the presence of different concentrations of salts. The experiments were run at room temperature (22 °C).

The EG7-AuNPs have the highest grafting density of the nanoparticles studied in this work, and a corona thickness that is around 90% of the theoretically calculated for an extended conformation. Moreover, the lower zeta-potential measured for these nanoparticles would indicate that most of the citrate anions remain in the surface, probably competing for the sites of water molecules (Tables 1 and 2). Although the grafting densities decrease as the EGN chains increase in length, the brush conformation seems to be adopted upon attaching to the nanoparticle surface. However, the thicknesses are lower than half of the theoretical for the extended conformation. As the curvature of AuNP does not change through the experiment, this difference must be ascribed to the decrease of polymer density with the radial distance and the higher hydration of the chains that can be responsible for the higher zeta-potential measured for these EGN-AuNPs.

## Effect of temperature in the stability of EGn-AuNPs in the presence of high NaCl concentrations.

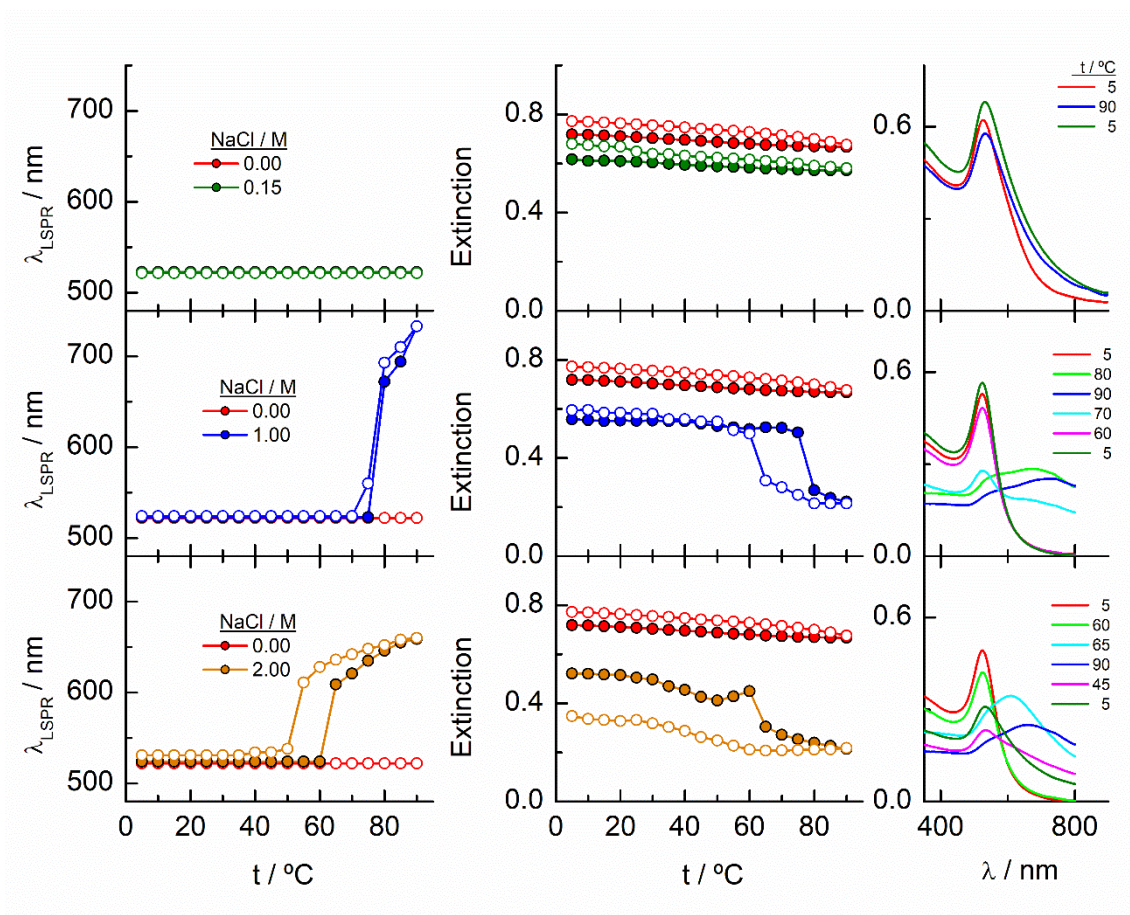
The results described above invite us to carry out a deeper study of these systems in the presence of different salt concentrations as a function of temperature. The high LCST of the system EGn-water [15] is explained by the existence of H-bonds between the polymer and water, and the loss of these interactions either with increasing temperature or in the presence of salts or both, contributes to the entropic loss that make the water a poor solvent and, consequently, to the conformational transition of the nanoparticle attached polymers that provokes the lowering of the LCST of the system. As shown in Figure 2, the EG18-, EG45- and EG136-AuNPs present high stability in aqueous solution upon changing temperature from 5 to 90 °C. EG7-AuNPs, however, experiment some changes that are visible in the spectra at temperature higher than 85 °C and in the presence of salt (Figure 2 and 3, inset).

Figure 4 shows the analysis of the UV-visible spectra for EG7-AuNPs in the presence of 5, 50 and 100 mM NaCl as a function of temperature. At the very low concentration of 5 mM, the feature observed at 85 °C in pure water is now seen at lower temperature. The displacement of the LSPR band is concomitant with a decrease in extinction that becomes restored upon reverting the temperature. The transition temperature ( $T_A$ ), observed at 72 °C is displaced by 5 °C in the decreasing temperature ramp. Suspensions of EG7-AuNPs in the presence of 50 or 100 mM NaCl follow a similar behaviour exhibiting the expected trend of decreasing  $T_A$  at 62 and 54 °C, respectively. Although the maximum LSPR band reaches its original value when returning to ambient temperature, the extinction peak does not recuperate these values. The reverse curves show transitions that are 10-12 °C lower than the direct ones, and more importantly, they do not reach the initial values (intensity loss of 20 and 40%, respectively). The shape of the spectra representing the unstable dispersions are similar, indicating that the same phenomena are being produced under these conditions. These spectral shapes suggest the presence of a mixture of aggregates and individual particles at temperatures higher and in the transition region. Theoretical treatments of these nanoparticle associations point to the formation of long chains of AuNPs that start to interact as a consequence of the loss of H-bonds between the EG7 chains and water, in the presence of salt and upon increasing temperature. Following Pileni's reported equation,<sup>53</sup> the peak with maximum at 850 nm (Figure 4, spectra obtained in the presence of 0.05 and 0.1 M NaCl at temperatures higher than  $T_A$ ) would correspond to a linear arrangement of EG7-AuNPs with an aspect ratio of 5.



**Figure 4.** Changes in the LSPR wavelength and extinction of EG7-AuNPs as a function of temperature in the presence of different NaCl concentrations. Full circles represent the ascending temperature and empty circles, the descending temperature data. The spectra plotted in the graphs on the right correspond to these that are significant of the changes produced with temperature.

As commented in relation to Figure 2 for EG7-AuNPs, the DLS data obtained agree with this idea. In fact, whereas the  $D_H$  values in water do not change with temperature up to 80 °C (the higher temperature that can be measured in our system), these obtained in the presence of 100 mM NaCl, show two peaks, being the first at ~29 nm more important in the intensity plot than that at ~720 nm. While the first peak does not appreciably change, the second one decreases up to values of ~300 nm at higher temperature (Figure S3). These features would indicate that the firstly formed big aggregates are somewhat broken in smaller ones. Although the trend in the reverse temperature ramp is to reach the same conditions of the initial state, the decrease in size is only apparent if the 40% reduction in extinction in the UV-visible spectra is interpreted as precipitation of the big aggregates that is accelerated at high temperature and therefore, they cannot be monitored under these conditions. When the temperature goes down, the bigger aggregates have longer lifetimes and can be accounted for in the DLS measurement.



**Figure 5.** Changes in the LSPR wavelength and extinction of EG18-AuNPs as a function of temperature in the presence of different NaCl concentrations. Full circles represent the ascending temperature and empty circles, the descending temperature data. The spectra plotted in the graphs on the right correspond to these that are significative of the changes produced with temperature.

EG18-AuNPs have also been studied as a function of temperature in the presence of 0.15, 1 and 2 M NaCl (Figure 5). While the system is stable in all the temperature range studied, when only 0.15 M NaCl is present, a strong displacement of the LSPR band to higher values accompanied of an extinction decrease are observed at 75 °C when the salt concentration is 1 M. The reverse scan shows a retention of these aggregates up to lower temperatures, but they terminated dissolving, and the initial state is completely recovered. When the salt concentration is increased to 2 M, a transition at 60 °C is observed that, although partially tend to go to the initial state, concludes with an extinction loss. The reverse transition determined either in the wavelength or in the extinction curve, takes place at around 10 °C lower temperature that the direct one.

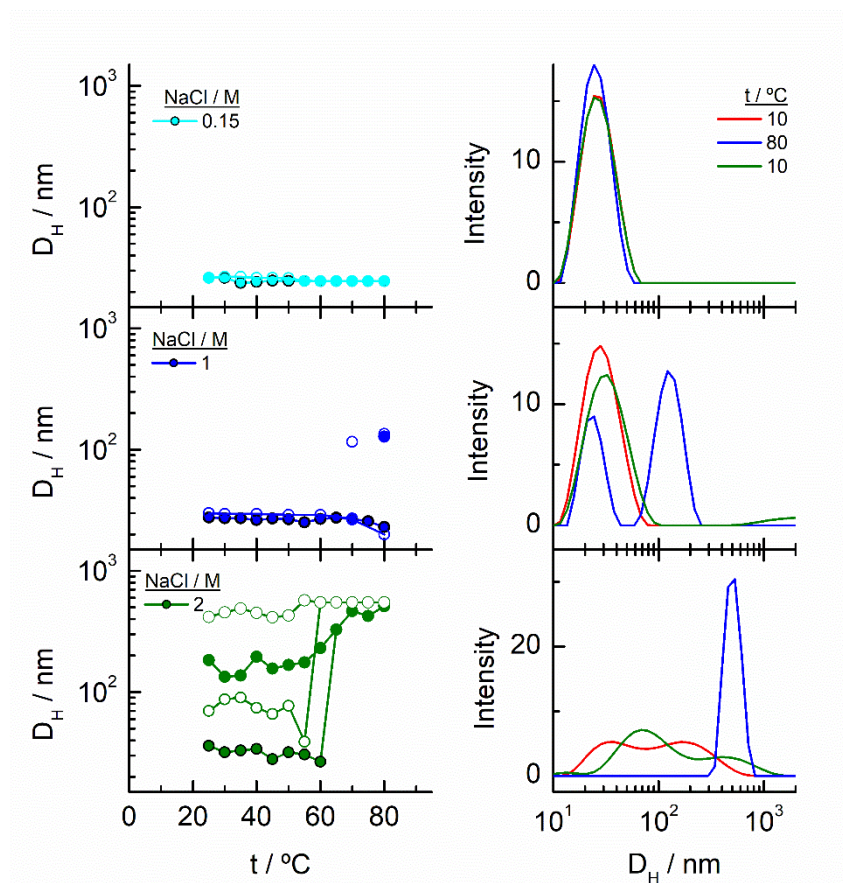


**Figure 6.** Changes in the hydrodynamic diameters of EG18-AuNPs as a function of temperature in the presence of different NaCl concentrations. Full circles represent the ascending temperature and empty circles, the descending temperature data. The intensity distribution of  $D_H$  plotted in the graphs on the right correspond to these that are significant of the changes produced with temperature.

To gain more insight into the different processes occurring in these temperature titrations experiments, we have studied these systems by DLS. EG18-AuNPs in the presence of 0.15 and 1 M NaCl show  $D_H$  values of 29 nm, similar to these found in water, and they do not change with temperature in the measured interval (20-80 °C) (Figure 6). However, in solutions of 1 M NaCl at 80 °C, the intensity plot shows two peaks that should be related to some assembly process under these conditions, in agreement with absorption data. The results obtained with solutions of 2 M NaCl are more complex. A mixture of peaks (with maxima at 36 and 180 nm) is obtained at the lowest temperature and they evolve with some irregularities up to 65 °C where they coalesce in a peak at higher size values (~400-500 nm). The reverse scan shows a parallel behaviour: one peak up to 60 °C that splits in two peaks that remain in their values up to room temperature. These transitions are almost coincident with those observed by UV-visible spectroscopy. We note, however, that the plot of number distribution vs  $D_H$  shows the peak of lower  $D_H$  up to the transition and after that, the one of

higher  $D_H$ , and a parallel behaviour in the reverse titration, thus indicating the predominance of the individual and aggregated EG18-AuNPs at lower and higher temperature, respectively. However, concomitant with these changes a precipitation of the larger aggregates should take place judging by the loss of extinction at the end of the titration.

When the AuNPs are protected by longer EGN chains, the dispersions present much higher stability in the presence of salt, allowing to increase the NaCl concentration up to 5M.

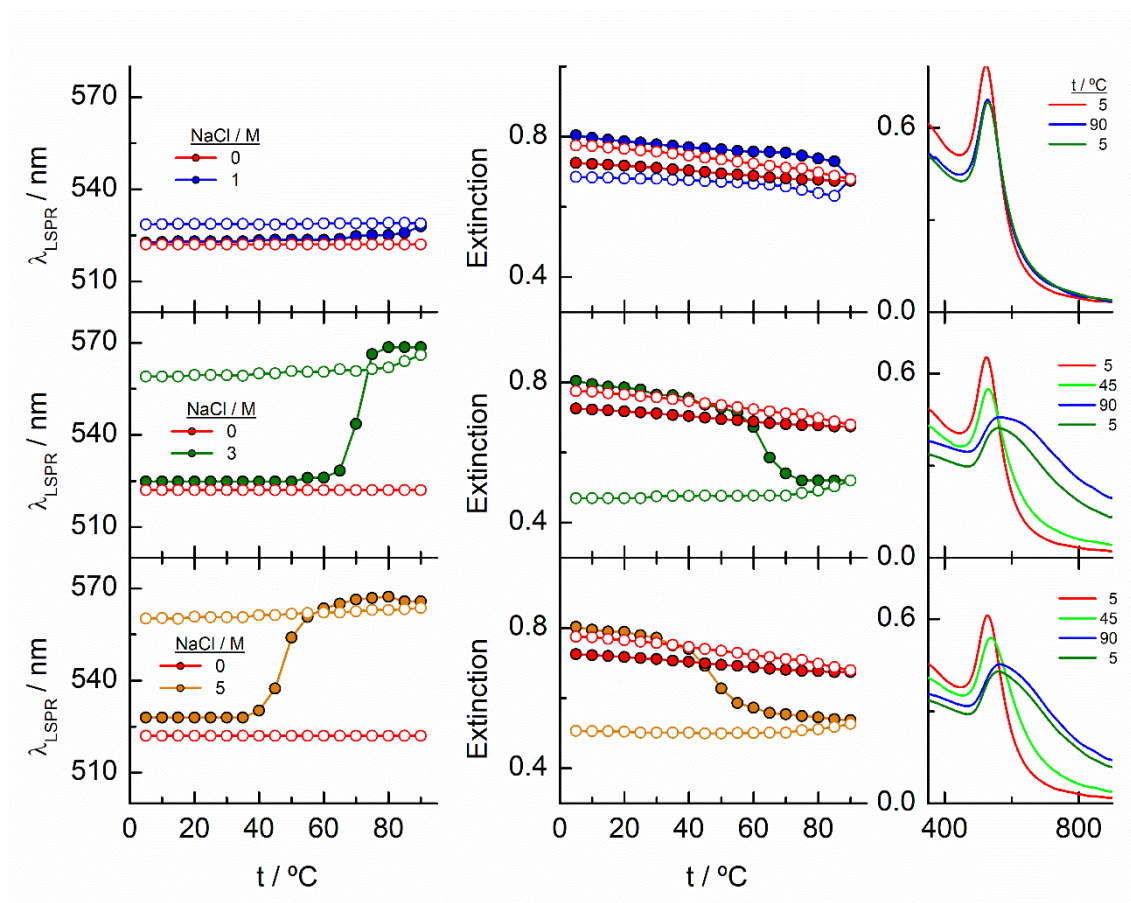


**Figure 7.** Changes in the LSPR wavelength and extinction of EG45-AuNPs as a function of temperature in the presence of different NaCl concentrations. Full circles represent the ascending temperature and empty circles, the descending temperature data. The spectra plotted in the graphs on the right correspond to these that are significant of the changes produced with temperature.

Figure 7 shows the analysis of the results obtained for EG45-AuNPs in the presence of 1, 3 and 5 M NaCl. No changes in the shape of the spectra obtained with the lowest concentration are observed in the temperature scan from 5 to 90 °C and vice versa. However, when the same experiments are run in the presence of 3 and 5 M salt concentration, transitions at 70 and 47 °C (measured in the wavelength trace), respectively, are obtained. Although in the direct scan, the curves seem similar to these observed for

EG18-AuNPs, the phenomenon produced should be different. On one hand, the aggregates being formed from 45 to 90 °C do not disaggregate when the temperature is reversed (the wavelength and extinction keep almost constant in the reverse scan). On the other hand, the shape of the spectra is somewhat different to that for EG7- and EG18-AuNPs aggregates and are unchanged upon lowering the temperature to the initial value. These shapes have been related with the formation of tight clusters 54 that should be more difficult to dissolve.

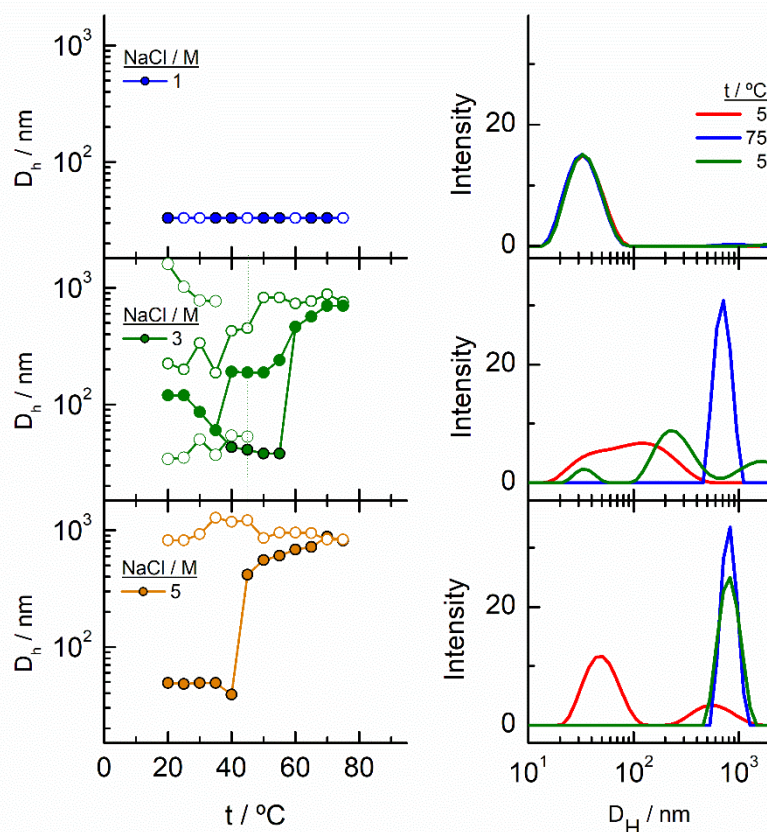


**Figure 8.** Changes in the hydrodynamic diameters of EG45-AuNPs as a function of temperature in the presence of different NaCl concentrations. The intensity distribution of DH plotted in the graphs on the right correspond to these that are significant of the changes produced with temperature.

In the DLS titrations of EG45-AuNPs (Figure 8) we do not observe any transition in 1M NaCl and a similar behaviour of that observed in 3 and 5 M salt concentration by UV-visible spectroscopy, with transitions at 57 and 42 °C, respectively. However, the observed compartment is somewhat more complex in the case of 2 M NaCl. At room temperature, the intensity distribution plot shows a broad envelop that seems to be composed of two contributions, and this feature continues up to 35 °C where they are resolved into two peaks at 45 and 195 nm. Increasing the temperature, they continue up to 60 °C where they coalesce in a signal of size higher than 450 nm. In the reverse scan this unique peak is

monitored at high temperature, and down to 45 °C, a mixture of two or three signals are observed up to reaching room temperature. If we take in mind the loss of extinction observed in the UV-visible titration experiment under the same experimental conditions, it can be concluded that a massive precipitation of the aggregates should occur, and the measured sizes correspond to the aggregates that remain in the suspension before they precipitate. The titration of EG45-AuNPs in the presence of 5 M NaCl is less complex as only one species is observed through the temperature scan. Moreover, the behaviour is the same to that shown by UV-visible spectroscopy. The DLS equivalent number distribution plots agree with the predominant existence of individual particles in 1 M NaCl solutions, the exchange between individual and aggregates upon the transition in 3 M, and in the ascending ramp in 5 M NaCl whereas, only the peaks corresponding to big aggregates are seen in the descending ramp of the later.

Finally, the behaviour observed for EG136-AuNPs substantially differs from these described above (Figure 9). Some aggregation is observed at 85 °C in 1 M NaCl solutions as detected by a displacement of the LSPR band to longer wavelength that is accompanied by some scatter at around 900 nm. The individual nanoparticles are soon obtained upon lowering the temperature to 75 °C. The presence of 3 or 5 M NaCl brings about some specific changes as a function of temperature with transitions at 60 and 45 °C in the ascending ramp, respectively, that make the system to evolve up to a state that is maintained in an interval of around 15 °C. The displacement of wavelength produced upon this transition (~40 nm) would indicate the formation of aggregates of small size and with certain spherical symmetry [54]. Increasing further the temperature, a decrease in wavelength (of around 20 nm, with transition points of 83 and 67 °C, respectively) brings the system to a new state that remains constant up to the highest temperature studied (90 °C). Interestingly, the evolution of the assemblies in the reversed ramp follows the same trend up to the second transition, where the spectra shift to the longest wavelength observed (~590 nm) for these EG136-AuNPs, up to the first transition, to achieve the initial state at room temperature. An interesting point to note is the clear observation of a hysteresis phenomenon under these conditions, related with the first transition. Then, while the second transition is completely reversible, the first one requires lowering the temperature 10-15 °C down in respect to that in the direct ramp. Again, the shape of the spectra can give some idea about the kind of aggregation that takes place in the presence of high salt concentrations. In fact, the spectrum observed in the interval of 50-65 °C would represent the formation of small clusters that, with increasing temperature, experiment a rise in extinction that is mainly due to Rayleigh scattering. This phenomenon is related to the behaviour of the polymer chains more than with an evolution of the cluster size [51]. In fact, the extinction continues increasing up to



the highest temperature and follows exactly the same trend in the reverse ramp. This high temperature together with the presence of salt would make the chains to experiment an additional dehydration and collapse achieving the EG136-AuNPs cloud point under these conditions (Scheme 2).

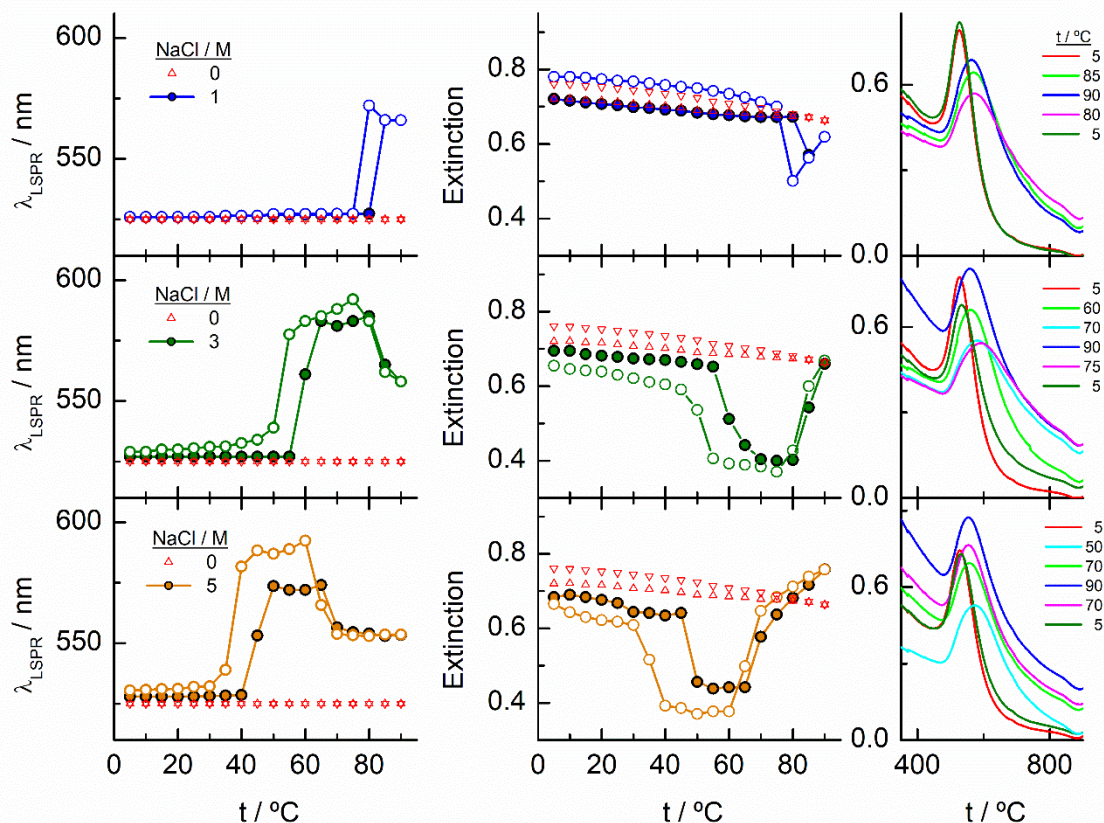
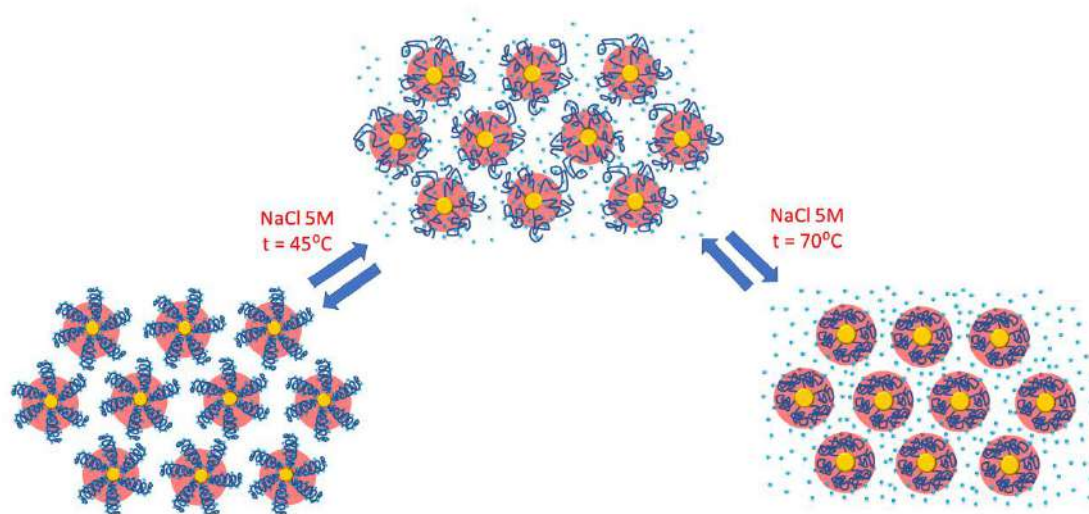


**Figure 9.** Changes in the LSPR wavelength and extinction of EG136-AuNPs as a function of temperature in the presence of different NaCl concentrations. Full circles represent the ascending temperature and empty circles, the descending temperature data. The spectra plotted in the graphs on the right correspond to these that are significant of the changes produced with temperature.

The phenomenon of bistability and its related hysteresis have been reported for nanoparticles functionalized with specific ionizable ligands and takes place through a delicate balance between van der Waals and electrostatic interparticle interactions. The overall interaction potential features an energy barrier at finite separation that generates hysteresis when the magnitude to overcome the aggregate to the dispersed state differs from that to overcome the reverse step [55]. Temperature induced hysteresis has been also observed for AuNPs during reversible clustering pointing out that the rate of heating and cooling altered its magnitude, applying this fact as a method to distinguish the kinetics and thermodynamic regimes [56]. Within the systems studied in this work, we observe this phenomenon in the case of EG136-AuNPs in the presence of 1, 3 and 5 M NaCl, although is

more evident at the highest concentration. In the other EGn-AuNPs analysed there are some signs of the existence of hysteresis, but the simultaneous precipitation avoids its observation.



**Scheme 2.** Temperature transitions of EG136-AuNPs.

The observed trend with temperature in the  $D_H$  values of the EG136-AuNPs in the presence of salts partially agrees with the results of UV-visible spectroscopy (Figure 10). The only peak measured in 1 M NaCl in all the temperature scan corresponds to the findings of unchanged wavelength and extinction up to high temperature values. The suspension in 3 M NaCl shows only one peak in all the temperature range studied but it changes in size describing a transition at 57 °C in the direct scan to higher hydrodynamic diameters (close to 1000 nm) indicating the formation of big aggregates. These clusters of nanoparticles, however, must not strongly couple as the wavelength shift is very small. Moreover, the presence of strong Rayleigh scatter after the second transition points in this direction. In contrast, in the presence of 5 M NaCl, two peaks are observed from the lower temperature, being the largest one (at sizes higher than 600 nm) in a small ratio (not seen in the number distribution plot). After the transition, the peaks collapse, and only the larger size aggregates remain. The reverse scan shows only one peak that start to decrease at a temperature coinciding with that observed for the first transition in UV-visible spectroscopy (~36 °C). The feature observed at temperatures higher than 70-80 °C in absorption spectroscopy cannot be seen in DLS as the maximum temperature reached by our system is of 75-80 °C. However, the high reversibility obtained in this portion of the curve would agree with the Rayleigh scatter being responsible for this effect. We have made photographs of the EG136-AuNPs suspensions at 20, 60 and 75 °C to corroborate the kind of phenomenon taking place as the temperature increases. The inset in Figure 10 shows the

changes in colour of the suspension that goes from the red wine normally observed for the individually dispersed nanoparticles (left, 20 °C) to the violet when there is some aggregation (middle, 60 °C) and finally to the cloudy aspect (right, 75 °C), confirming our suggestions.

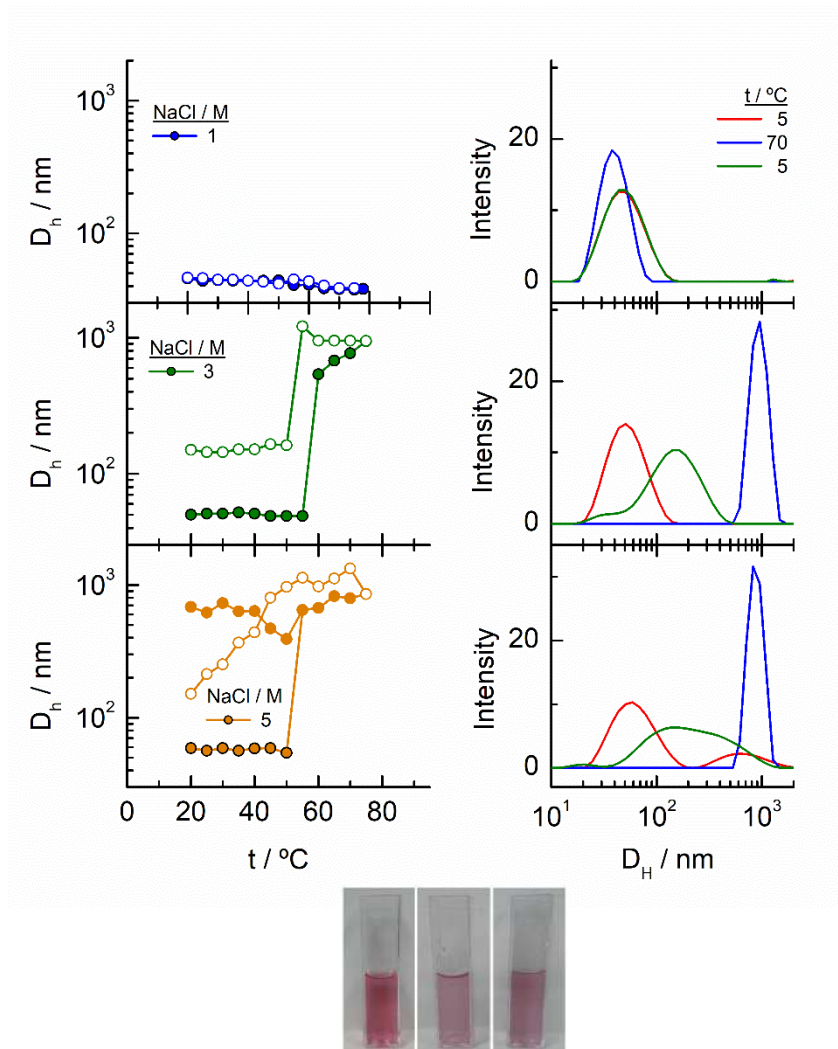


**Figure 10.** Left: Changes in the hydrodynamic diameters of EG136-AuNPs as a function of temperature in the presence of different NaCl concentrations. The spectra plotted in the graphs on the right correspond to these that are significant of the changes produced.

## Conclusions.

EGn-AuNPs prepared by ligand exchange from c-AuNPs present an increased stability in aqueous suspensions in a wide pH and temperature ranges. As it has previously been reported, the stability of EGN-AuNPs strongly depends on the grafting density [6, 8], and we show in this work that for a specific nanoparticle core size, the chain length has also some influence. In fact, even though longer chains graft to the surface with larger footprints than the shorter ones, they confer higher stabilization, as it is typical for colloidal steric

stabilization by neutral polymer chains. Once the optimal conditions for EGN grafting are achieved, the EGN-AuNPs suspensions resist the presence of certain salt concentrations. While all the prepared nanoparticles practically withstand up to 1 M NaCl, the EG7- and EG18-AuNPs lose dispersity in the presence of relatively low concentrations of CaCl<sub>2</sub>, an effect that should be ascribed to the divalent cation.

The presence of NaCl in the EGN-AuNPs suspensions also influence the thermo-sensitivity differently. EG7-AuNPs show transitions from the individual to aggregated nanoparticles strongly dependent on the NaCl concentration, presenting reversibility only in very low concentration (5 mM NaCl). Increasing chain length, the suspensions resist the presence of higher salt concentrations. The EG18-AuNPs shows a reversible temperature transition in 1 M NaCl but become only partially reversible in the presence of 2 M NaCl. The formation of big aggregates (as seen by DLS) and its precipitations in the later conditions should be responsible for the loss of material upon restoring the initial conditions. Although the EG45-AuNPs do not assembled in the presence of 3 and 5 M NaCl at room temperature, they suffer temperature transitions to the formation of aggregates that do not dissolve upon lowering the temperature. The bigger aggregates suddenly precipitate and cannot be monitored neither by UV-visible spectroscopy nor DLS, and the smaller ones remain suspended upon reaching the initial conditions.

The larger chain EG136 confers the most interesting behaviour to the AuNPs suspensions. First, the EG136-AuNPs experiment a reversible transition at around 85 °C in 1 M NaCl. With increasing NaCl concentration to 3 and 5 M, the systems show two transitions in the temperature range studied. The first transition at lower temperature would lead to the formation of small aggregates that can keep suspended in a temperature interval of 15 °C and then evolve to an assembled state where the metal cores are not coupled as the LSPR wavelength decrease from the value adopted after the first transition. Under these conditions, a Rayleigh scattering is observed that is ascribed to the effects of the salt dehydrating the polymer chains and making them to collapse. While this second transition is completely reversible, the first one shows a hysteretic behaviour that supposes an incremental energy barrier to overcome for the aggregates to reach the disassembled AuNPs in respect to that for the assembly. These findings encourage us to go deeply into the control of the hysteretic behaviour of the EG136-AuNPs to find applications in the various fields that depend on this phenomenon.<sup>56</sup>

*Conflicts of interest.* There are no conflicts to declare.

*Author contributions*

Conceptualization, M.C., A. F-M, T.P.; Methodology, M.C., A. F-M, T.P., M.B., J.M. S.; Formal analysis, M.C., A. F-M, T.P., R.M., G. S-O; Investigation, M.C., A. F-M, T.P. M.B., J.M. S., R. M., G. S-O.; Writing-original draft preparation, M.C., A. F-M, T.P.; Funding acquisition, T.P., M. B. All authors have read and agreed to the published version of the manuscript.

*Acknowledgements.* We thank the Ministerio de Ciencia e Innovación (Project RED2018-102412-T Network of Excellence Electrochemical Sensors and Biosensors), Junta de Andalucía and Universidad de Córdoba (UCO-FEDER-2018: ref. 1265074-2B and Plan Propio, Submod. 1.2. P.P. 2019) for financial support of this work. M.C. and A. F-M. acknowledge Ministerio de Universidades for FPU 17/03873 grant and the Universidad de Córdoba for Contrato Predoctoral grant, respectively.

## References.

- [1] D. Matsukuma, H. Otsuka, Chapter 13 - PEGylation for biocompatible surface, in: H. Ohshima, K. Makino (Eds.), *Colloid and Interface Science in Pharmaceutical Research and Development*, Elsevier, Amsterdam, 2014, pp. 261-283.
- [2] A.S. Karakoti, S. Das, S. Thevuthasan, S. Seal, PEGylated Inorganic Nanoparticles, *Angew. Chem. Int. Ed.* 50(9) (2011) 1980-1994.
- [3] J.V. Jokerst, T. Lobovkina, R.N. Zare, S.S. Gambhir, Nanoparticle PEGylation for imaging and therapy, *Nanomedicine* 6(4) (2011) 715-728.
- [4] R. Cai, J. Ren, Y. Ji, Y. Wang, Y. Liu, Z. Chen, Z. Farhadi Sabet, X. Wu, I. Lynch, C. Chen, Corona of Thorns: The Surface Chemistry-Mediated Protein Corona Perturbs the Recognition and Immune Response of Macrophages, *ACS Appl. Mater. Interfaces* 12(2) (2020) 1997-2008.
- [5] D.R. Hristov, H. Lopez, Y. Ortin, K. O'Sullivan, K.A. Dawson, D.F. Brougham, Impact of dynamic subpopulations within grafted chains on the protein binding and colloidal stability of PEGylated nanoparticles, *Nanoscale* 13(10) (2021) 5344-5355.
- [6] K. Rahme, L. Chen, R.G. Hobbs, M.A. Morris, C. O'Driscoll, J.D. Holmes, PEGylated gold nanoparticles: polymer quantification as a function of PEG lengths and nanoparticle dimensions, *RSC Adv.* 3(17) (2013) 6085-6094.
- [7] J. Lu, Y. Xue, R. Shi, J. Kang, C.-Y. Zhao, N.-N. Zhang, C.-Y. Wang, Z.-Y. Lu, K. Liu, A non-sacrificial method for the quantification of poly(ethylene glycol) grafting density on gold nanoparticles for applications in nanomedicine, *Chem. Sci.* 10(7) (2019) 2067-2074.
- [8] M. Retout, E. Brunetti, H. Valkenier, G. Bruylants, Limits of thiol chemistry revealed by quantitative analysis of mixed layers of thiolated-PEG ligands grafted onto gold nanoparticles, *J. Coll. Inter. Sci.* 557 (2019) 807-815.
- [9] W. Wang, Q.-Q. Wei, J. Wang, B.-C. Wang, S.-h. Zhang, Z. Yuan, Role of thiol-containing polyethylene glycol (thiol-PEG) in the modification process of gold nanoparticles (AuNPs): Stabilizer or coagulant?, *J. Coll. Interface Sci.* 404 (2013) 223-229.
- [10] D.N. Benoit, H.G. Zhu, M.H. Lilierose, R.A. Verm, N. Ali, A.N. Morrison, J.D. Fortner, C. Ayendano, V.L. Colvin, Measuring the Grafting Density of Nanoparticles in Solution by Analytical Ultracentrifugation and Total Organic Carbon Analysis, *Anal. Chem.* 84(21) (2012) 9238-9245.
- [11] P.G. de Gennes, Conformations of Polymers Attached to an Interface, *Macromolecules* 13(5) (1980) 1069-1075.
- [12] S. Alexander, Adsorption of chain molecules with a polar head a scaling description, *J. Phys. France* 38(8) (1977) 983-987.

- [13] P.J. Flory, The Configuration of Real Polymer Chains, *J. Chem. Phys.* 17(3) (1949) 303-310.
- [14] P.G. de Gennes, Polymers at an interface; a simplified view, *Adv. Colloid Interf. Sci.* 27(3) (1987) 189-209.
- [15] S. Saeki, N. Kuwahara, M. Nakata, M. Kaneko, Upper and lower critical solution temperatures in poly (ethylene glycol) solutions, *Polymer* 17(8) (1976) 685-689.
- [16] P.U. Kenkare, C.K. Hall, Modeling of phase separation in PEG-salt aqueous two-phase systems, *Aiche J.* 42(12) (1996) 3508-3522.
- [17] R. Iida, H. Mitomo, Y. Matsuo, K. Niikura, K. Ijiro, Thermoresponsive Assembly of Gold Nanoparticles Coated with Oligo(Ethylene Glycol) Ligands with an Alkyl Head, *J. Phys. Chem. C* 120(29) (2016) 15846-15854.
- [18] K. Xiong, H. Mitomo, X. Su, Y. Shi, Y. Yonamine, S.-i. Sato, K. Ijiro, Molecular configuration-mediated thermo-responsiveness in oligo(ethylene glycol) derivatives attached on gold nanoparticles, *Nanoscale Adv.* (2021).
- [19] R. Iida, H. Mitomo, K. Niikura, Y. Matsuo, K. Ijiro, Two-Step Assembly of Thermoresponsive Gold Nanorods Coated with a Single Kind of Ligand, *Small* 14(14) (2018) 1704230.
- [20] D. Zambo, G.Z. Radnoczi, A. Deak, Preparation of Compact Nanoparticle Clusters from Polyethylene Glycol-Coated Gold Nanoparticles by Fine-Tuning Colloidal Interactions, *Langmuir* 31(9) (2015) 2662-2668.
- [21] D. Zámbo, S. Pothorszky, D.F. Brougham, A. Deák, Aggregation kinetics and cluster structure of amino-PEG covered gold nanoparticles, *RSC Advances* 6(32) (2016) 27151-27157.
- [22] C. Durand-Gasselín, M. Capelot, N. Sanson, N. Lequeux, Tunable and Reversible Aggregation of Poly(ethylene oxide-st-propylene oxide) Grafted Gold Nanoparticles, *Langmuir* 26(14) (2010) 12321-12329.
- [23] L. Cheng, J. Song, J. Yin, H. Duan, Self-Assembled Plasmonic Dimers of Amphiphilic Gold Nanocrystals, *J. Phys. Chem. Lett.* 2(17) (2011) 2258-2262.
- [24] H.H. Zhang, W.J. Wang, S. Mallapragada, A. Travesset, D. Vaknin, Macroscopic and tunable nanoparticle superlattices, *Nanoscale* 9(1) (2017) 164-171.
- [25] H. Zhang, W. Wang, M. Akinc, S. Mallapragada, A. Travesset, D. Vaknin, Assembling and ordering polymer-grafted nanoparticles in three dimensions, *Nanoscale* 9(25) (2017) 8710-8715.
- [26] H. Zhang, W. Wang, S. Mallapragada, A. Travesset, D. Vaknin, Ion-Specific Interfacial Crystallization of Polymer-Grafted Nanoparticles, *J. Phys. Chem. C* 121(28) (2017) 15424-15429.
- [27] S. Nayak, M. Fieg, W.J. Wang, W. Bu, S. Mallapragada, D. Vaknin, Effect of (Poly)electrolytes on the Interfacial Assembly of Poly(ethylene glycol)-Functionalized Gold Nanoparticles, *Langmuir* 35(6) (2019) 2251-2260.
- [28] W. Wang, H.J. Kim, W. Bu, S. Mallapragada, D. Vaknin, Unusual Effect of Iodine Ions on the Self-Assembly of Poly(ethylene glycol)-Capped Gold Nanoparticles, *Langmuir* 36(1) (2020) 311-317.
- [29] H.J. Kim, W.J. Wang, A. Travesset, S.K. Mallapragada, D. Vaknin, Temperature-Induced Tunable Assembly of Columnar Phases of Nanorods, *ACS Nano* 14(5) (2020) 6007-6012.
- [30] H.J. Kim, M.M. Hossen, A.C. Hillier, D. Vaknin, S.K. Mallapragada, W.J. Wang, Interfacial and Bulk Assembly of Anisotropic Gold Nanostructures: Implications for Photonics and Plasmonics, *ACS Appl. Nano Mater.* 3(8) (2020) 8216-8223.
- [31] H.J. Kim, W.J. Wang, S.K. Mallapragada, D. Vaknin, The Effects of Temperature on the Assembly of Gold Nanoparticle by Interpolymer Complexation, *J. Phys. Chem. Lett.* 12(5) (2021) 1461-1467.
- [32] J. Turkevich, P.C. Stevenson, J. Hillier, A Study of the Nucleation and Growth Processes in the Synthesis of Colloidal Gold, *Discuss. Faraday Soc.* (11) (1951) 55-75.
- [33] G. Sanchez-Obrero, M. Chavez, R. Madueno, M. Blázquez, T. Pineda, J.M. Lopez-Romero, F. Sarabia, J. Hierrezuelo, R. Contreras-Caceres, Study of the self-assembly process of an oligo(ethylene glycol)-thioacetyl substituted theophylline (THEO) on gold substrates, *J. Electroanal. Chem.* 823 (2018) 663-671.

- [34] M. Chávez, G. Sánchez-Obrero, R. Madueño, J.M. Sevilla, M. Blázquez, T. Pineda, Characterization of a self-assembled monolayer of O-(2-Mercaptoethyl)-O'-methyl-hexa(ethylene glycol) (EG7-SAM) on gold electrodes, *J. Electroanal. Chem.* 880 (2021) 114892.
- [35] C.A. Simpson, A.C. Agrawal, A. Balinski, K.M. Harkness, D.E. Cliffel, Short-Chain PEG Mixed Monolayer Protected Gold Clusters Increase Clearance and Red Blood Cell Counts, *ACS Nano* 5(5) (2011) 3577-3584.
- [36] A.C. Templeton, J.J. Pietron, R.W. Murray, P. Mulvaney, Solvent refractive index and core charge influences on the surface plasmon absorbance of alkanethiolate monolayer-protected gold clusters, *J. Phys. Chem. B* 104(3) (2000) 564-570.
- [37] P. Harder, M. Grunze, R. Dahint, G.M. Whitesides, P.E. Laibinis, Molecular conformation in oligo(ethylene glycol)-terminated self-assembled monolayers on gold and silver surfaces determines their ability to resist protein adsorption, *J. Phys. Chem. B* 102(2) (1998) 426-436.
- [38] B. Cárdenas, G. Sanchez-Obrero, R. Madueño, J.M. Sevilla, M. Blázquez, T. Pineda, Influence of the Global Charge of the Protein on the Stability of Lysozyme-AuNP Bioconjugates, *J. Phys. Chem. C* 118(38) (2014) 22274-22283.
- [39] F. Canaveras, R. Madueño, J.M. Sevilla, M. Blazquez, T. Pineda, Role of the Functionalization of the Gold Nanoparticle Surface on the Formation of Bioconjugates with Human Serum Albumin, *J. Phys. Chem. C* 116(18) (2012) 10430-10437.
- [40] E. Reyes, R. Madueño, M. Blazquez, T. Pineda, Facile Exchange of Ligands on the 6-Mercaptopurine-Monolayer Protected Gold Clusters Surface, *J. Phys. Chem. C* 114(38) (2010) 15955-15962.
- [41] A.J. Viudez, R. Madueno, T. Pineda, M. Blazquez, Stabilization of gold nanoparticles by 6-mercaptopurine monolayers. Effects of the solvent properties, *J. Phys. Chem. B* 110(36) (2006) 17840-17847.
- [42] M. Schollbach, F. Zhang, F. Roosen-Runge, M.W.A. Skoda, R.M.J. Jacobs, F. Schreiber, Gold nanoparticles decorated with oligo(ethylene glycol) thiols: Surface charges and interactions with proteins in solution, *J. Coll. Interface Sci.* 426 (2014) 31-38.
- [43] G. Zhang, Z. Yang, W. Lu, R. Zhang, Q. Huang, M. Tian, L. Li, D. Liang, C. Li, Influence of anchoring ligands and particle size on the colloidal stability and in vivo biodistribution of polyethylene glycol-coated gold nanoparticles in tumor-xenografted mice, *Biomaterials* 30(10) (2009) 1928-1936.
- [44] J.L. Perry, K.G. Reuter, M.P. Kai, K.P. Herlihy, S.W. Jones, J.C. Luft, M. Napier, J.E. Bear, J.M. DeSimone, PEGylated PRINT Nanoparticles: The Impact of PEG Density on Protein Binding, Macrophage Association, Biodistribution, and Pharmacokinetics, *Nano Lett.* 12(10) (2012) 5304-5310.
- [45] V.B. Damodaran, C.J. Fee, T. Ruckh, K.C. Popat, Conformational Studies of Covalently Grafted Poly(ethylene glycol) on Modified Solid Matrices Using X-ray Photoelectron Spectroscopy, *Langmuir* 26(10) (2010) 7299-7306.
- [46] H.D. Willauer, J.G. Huddleston, R.D. Rogers, Solute Partitioning in Aqueous Biphasic Systems Composed of Polyethylene Glycol and Salt: The Partitioning of Small Neutral Organic Species, *Ind. Eng. Chem. Res.* 41(7) (2002) 1892-1904.
- [47] J.G. Huddleston, H.D. Willauer, R.D. Rogers, Phase Diagram Data for Several PEG + Salt Aqueous Biphasic Systems at 25 °C, *J. Chem. Eng. Data* 48(5) (2003) 1230-1236.
- [48] U. Dahal, Z. Wang, E.E. Dormidontova, Hydration of Spherical PEO-Grafted Gold Nanoparticles: Curvature and Grafting Density Effect, *Macromolecules* 51(15) (2018) 5950-5961.
- [49] U. Dahal, E.E. Dormidontova, Chain Conformation and Hydration of Polyethylene Oxide Grafted to Gold Nanoparticles: Curvature and Chain Length Effect, *Macromolecules* 53(19) (2020) 8160-8170.
- [50] Y. Liu, M.K. Shipton, J. Ryan, E.D. Kaufman, S. Franzen, D.L. Feldheim, Synthesis, Stability, and Cellular Internalization of Gold Nanoparticles Containing Mixed Peptide-Poly(ethylene glycol) Monolayers, *Anal. Chem.* 79(6) (2007) 2221-2229.

- [51] M.-Q. Zhu, L.-Q. Wang, G.J. Exarhos, A.D.Q. Li, Thermosensitive Gold Nanoparticles, *J. Am. Chem. Soc.* 126(9) (2004) 2656-2657.
- [52] R.W. Taylor, R. Esteban, S. Mahajan, R. Coulston, O.A. Scherman, J. Aizpurua, J.J. Baumberg, Simple Composite Dipole Model for the Optical Modes of Strongly-Coupled Plasmonic Nanoparticle Aggregates, *J. Phys. Chem. C* 116(47) (2012) 25044-25051.
- [53] A. Brioude, X.C. Jiang, M.P. Pileni, Optical Properties of Gold Nanorods: DDA Simulations Supported by Experiments, *J. Phys. Chem. B* 109(27) (2005) 13138-13142.
- [54] R.W. Taylor, T.-C. Lee, O.A. Scherman, R. Esteban, J. Aizpurua, F.M. Huang, J.J. Baumberg, S. Mahajan, Precise Subnanometer Plasmonic Junctions for SERS within Gold Nanoparticle Assemblies Using Cucurbit[n]uril "Glue", *ACS Nano* 5(5) (2011) 3878-3887.
- [55] D. Wang, B. Kowalczyk, I. Lagzi, B.A. Grzybowski, Bistability and Hysteresis During Aggregation of Charged Nanoparticles, *J. Phys. Chem. Lett.* 1(9) (2010) 1459-1462.
- [56] J. Kruse, S. Merkens, A. Chuvilin, M. Grzelczak, Kinetic and Thermodynamic Hysteresis in Clustering of Gold Nanoparticles: Implications for Nanotransducers and Information Storage in Dynamic Systems, *ACS Appl. Nano Mater.* 3(9) (2020) 9520-9527.



**Supporting information.**

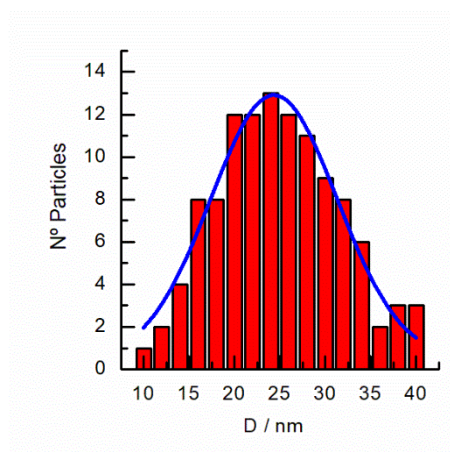
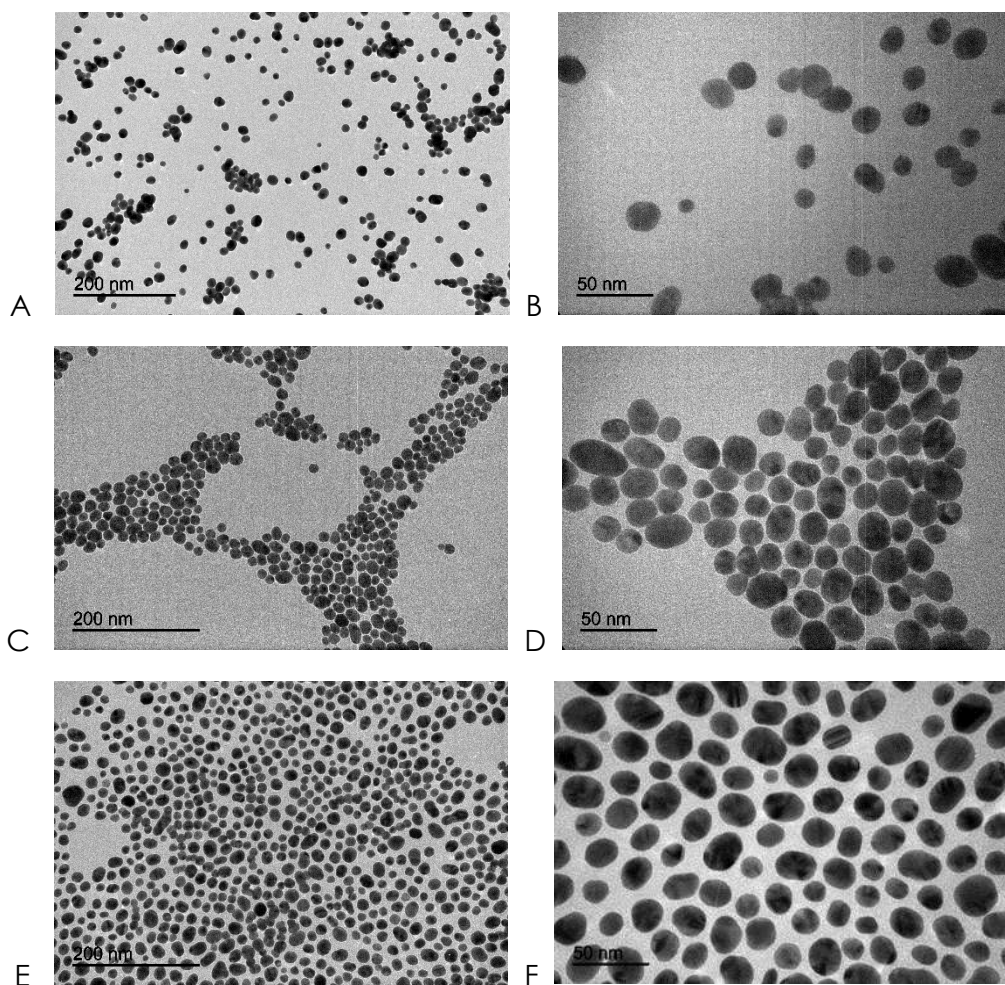


**Figure S1.** TEM images of AuNPs: (A, B): c-AuNPs; (C,D) EG18-AuNPs; (E, F) EG136-AuNPs. Size distribution of the AuNPs.

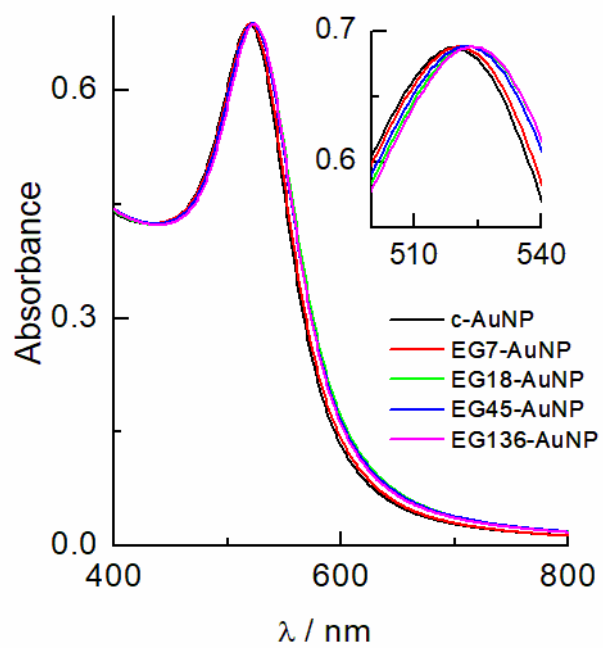


**Figure S2.** UV-visible spectra of AuNPs modified with EGN of different chain length.

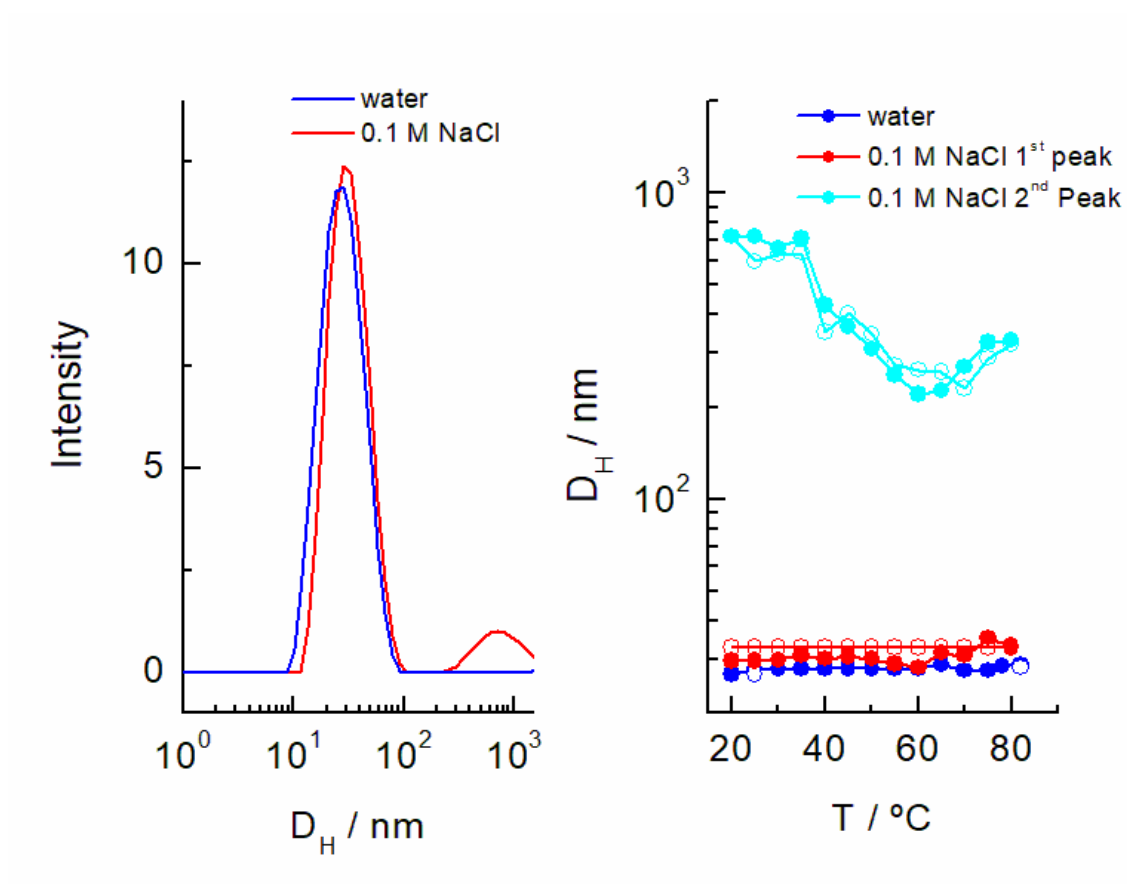


**Figure S3.** (A) Size distribution of EG7-AuNPs; (B) Hydrodynamic diameters of EG7-AuNPs as a function of temperature under different conditions.

### 3.6. Artículo 6.

*Caracterización de autoensamblajes de Bis[2-(2-bromoisobutyryloxy) undecyl] disulphide (DTBU) en superficies de oro con potenciales usos en polimerizaciones tipo superficies inicializadas mediante transferencia atómica radicalaria (SI-ATRP).*





## Characterization of self-assembled Bis[2-(2-bromoisobutyryloxy) undecyl] disulphide (DTBU) on gold surfaces suitable for use in surface-initiated atom transfer radical polymerization (SI-ATRP)

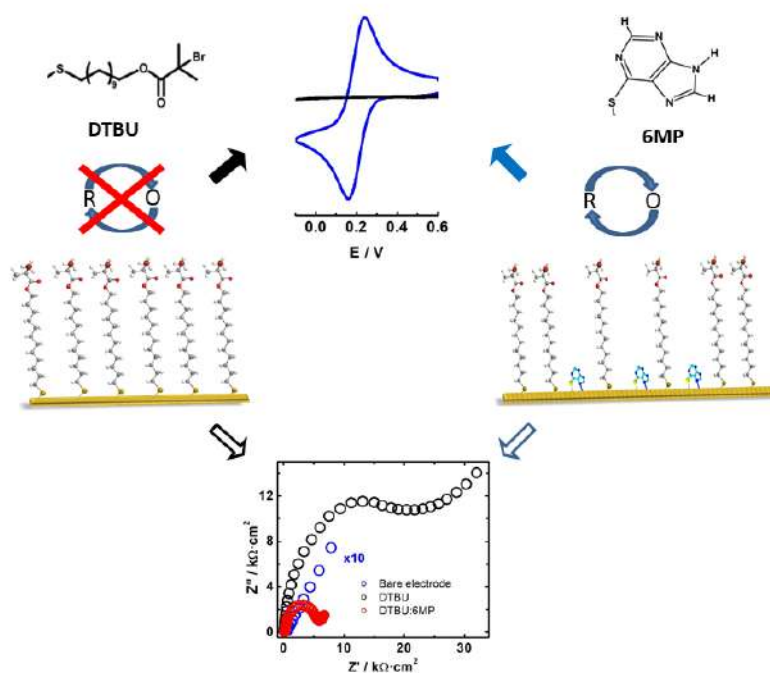
Miriam Chávez, Laura Fuentes-Rodríguez, Guadalupe Sánchez-Obrero, Rafael Madueño, José Manuel Sevilla, Manuel Blázquez, Teresa Pineda\*

Department of Physical Chemistry and Applied Thermodynamics, Institute of Fine Chemistry and Nanochemistry, University of Cordoba, Campus Rabanales, Ed. Marie Curie 2<sup>a</sup> Planta, E-14014 Córdoba, Spain

### Abstract

Bis[2-(2-bromoisobutyryloxy) undecyl] disulphide (DTBU) is an initiator for surface-initiated atom transfer radical polymerization (SI-ATRP) able to functionalize metal surfaces through formation of self-assembled monolayers (SAM). The goal of this work is the making monolayers with the DTBU initiator on gold polycrystalline electrodes and their study by electrochemical methods as cyclic voltammetry (CV), capacity-potential curves (C-E), electrochemical impedance spectroscopy (EIS), and angle contact measurements for their characterization. Information of the integrity and permeability of the monolayers has been obtained by capacitance-potential measurements and impedance spectra. Also, the blocking effect of the physical barrier that SAM can produce to different redox probes is explored by using voltammetry and impedance. DTBU forms a compact monolayer whose main features are related with heterogeneous chain structures, having a non-polar hydrocarbon internal part and a polar head group. This is confirmed by X-ray photoelectron spectroscopy (XPS) which shows the presence of the elements of the DTBU adsorbate of SAM. Moreover, mixed monolayers of DTBU and 6-mercaptopurine (6MP) have been prepared and characterized, to check if the thiol facilitates electron exchange through monolayers. On this approach, different DTBU:6MP ratios have been employed and characterized studying IRRAS spectra, electrochemical properties, and contact angle on the modified surface. These mixed monolayers provide optimal conditions for adaptation and use in e-ATRP.

**Keywords.** DTBU radical polymerization initiator; self-assembled monolayers; 6-mercaptopurine 6MP; mixed monolayers; cyclic voltammetry; electrochemical impedance spectroscopy; contact angle; XPS; IRRAS.



**Graphical abstract**

## Introduction.

Atom transfer radical polymerization (ATRP) is one of the polymerization techniques used to produce polymers in a controlled manner [1-5], both from the point of view of the polydispersity and the nature and structure of the final product as copolymers, linear, branched structures, etc. This radical polymerization initiated on a surface (SI-ATRP) providing a way to functionalize a wide variety of substrates with polymers [6]. Its versatility and tolerance towards a wide variety of functional groups has turned this reaction into a synthesis technique widely used to prepare brush polymers [7-11] special relevance due to their applications in the field of nanomedicine [12,13].

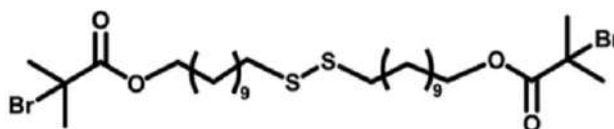
The self-assembled monolayers (SAM) represent a suitable approach to the design of surface chemistry in a wide range of metal substrates since the assembly of small molecules offers a convenient, simple, and highly versatile system to modify the intrinsic properties of the surface [14-17]. Also, properties such as mechanical stability, electrical conductivity, activation potential and reactivity are essential in the initiator bound to the substrate to obtain a good yield and control in the polymerization reaction.

One of the basic objectives of the studies on the formation of a SAM with an initiator molecule for the SI-ATRP, and with electrochemical mediation (e-ATRP), is to find the experimental conditions on the surface where the electronic transfer itself of redox catalyst is facilitated, typically a copper complex with the associated pair Cu(II)/Cu(I) [10, 11]. Li et al., have studied this aspect, after observing that, although short chains seem a good option



because of the poorer packaging of SAM that facilitates electronic transfer [18], the polymer growth with these chains is very limited.

On the other hand, chains like those of DTBU (Bis[2-(2-bromoisobutyryloxy) undecyl] disulphide (Scheme 1) inhibit the transfer of the catalyst pair, so the alternative was to assemble a mixed monolayer with a conductive molecule such as 2-thionaphthiol (2-NAT) together with the DTBU [10], obtaining polymer films homogeneous brush. This strategy allowed not only to create charge transfer spaces for the redox reaction through the 2-NAT domains, but also to assemble high quality initiator monolayers for the formation of dense brush-type polymers.

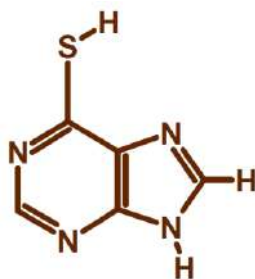


**Scheme 1.** DTBU molecule

The aim of this work is to obtain functionalized gold surfaces with self-assembled monolayers of initiator of the radical polymerization reaction with atomic transfer (SI-ATRP).

Attention is focused on the determination of the experimental conditions that allow to control the conditioning of the surface. The DTBU molecule is an initiator with the thiol function that allows it to form a self-assembled monolayer on a metal surface, leaving exposed the active center that produces the primary radicals for polymerization.

In this work, polycrystalline gold electrodes were chosen. The characterization of this monolayer by electrochemical methods, contact angle measurements, and XPS and IRRAS, has been performed, where chain interactions play an important role. Also, the formation of mixed monolayers formed with DTBU and 6-mercaptapurine (6MP) has been tested. This last molecule (Scheme 2), has been extensively studied for the formation of self-assembled monolayers on gold and other metallic substrates [19-22], showing that it does not produce blocking effect against molecules such as potassium ferricyanide, except in alkaline medium, due to the formation of a negatively charged monolayer through nitrogen N(9)-H ionization.



**Scheme 2.** 6-mercaptapurine molecule

On the other hand, as it has been above reported, the self-assembled DTBU molecule significantly limits the electron transfer by the packing formed on the metallic surface. Therefore, under the usual experimental conditions, 6MP is a good candidate for the formation of mixed monolayers with DTBU for use in e-ATPR.

## Experimental.

### Chemicals.

Bis[2-(2-bromoisobutyryloxy) undecyl] disulphide (DTBU), 6-mercaptapurine (6MP), ferrocene-methanol,  $K_4Fe(CN)_6$  and  $Ru(NH_6)Cl_3$  were from Sigma-Aldrich. Other reagents such as perchloric acid ( $HClO_4$ , 70%), potassium hydroxide (KOH), ETOH and potassium nitrate ( $KNO_3$ ) were from Merck (analytical quality). All solutions were prepared with deionized water produced by Millipore system.

### Methods.

Electrochemical experiments were performed using an Autolab (Ecochemie model Pgstat30) instrument attached to a PC with proper software (GPES and FRA) for the total control of the experiments and data acquisition.

The measurements of EIS were carried out at different contacted potentials ( $E_{dc}$ ) in a frequency range of 10 kHz to 0.1 Hz and with a potential modulation amplitude (r.m.s.) of 5 mV. The differential capacity-potential curves were obtained by impedance measurements performed at a perturbation frequency  $f = 49$  Hz. The differential capacity was calculated as  $C_d = 1/(\omega Z'')$ , with  $Z''$  being the imaginary part of the total impedance and  $\omega = 2\pi f$  being the angular frequency of the perturbation.

For the electrochemical studies Metrohm thermostated electrochemical cells are used under an inert atmosphere of nitrogen, for which this gas was bubbled for 15-20 minutes. A configuration of three electrodes is used. As work electrode (WE) a BAS polycrystalline gold electrode of BioAnalytical System, Kenilworth, UK, of 1.6 mm diameter, or a flat square

plate ( $1 \times 1 \text{ cm}^2$ ) of polycrystalline gold, or a gold single crystal with approximately 3-mm diameter and 2-mm thick cylinders with a flat polished side oriented in the (111) surface was used. As auxiliary, a Pt electrode (CE) and a reference electrode (RE) of Ag/AgCl 3M, or a reversible hydrogen electrode (RHE) used for the experiments of determination of the real area. To guarantee the reproducibility of the electrode surface, a treatment was applied. The polycrystalline working electrode was polished with a suspension of  $\text{Al}_2\text{O}_3$  ( $0.05 \mu\text{m}$ ) in a polisher (Buehler, Metaserv-2000), rinsed and treated with ultrasound in ultra-pure water for 10 minutes. The surface condition was confirmed by a cyclic voltammogram in  $0.01 \text{ M HClO}_4$ , and the real surface area was determined from the stripping reduction peak of oxides and hydroxide on the gold electrode surface [23,24]. This treatment was the most appropriate for producing a clean and very reproducible surface.

The formation of self-assembled monolayers (SAM) of DTBU, 6MP and mixed DTBU: 6MP were prepared by contacting a fresh clean gold substrate with ethanolic solutions of the mercaptoderivatives at a total concentration of  $1 \text{ mM}$ , overnight, at room temperature and protected from light. The modified electrodes, once removed from the thiol ethanolic solution, were cleaned by stirring for 15 minutes, or sonicating for 2 minutes, on pure EtOH.

X-ray photoelectronic spectroscopy (XPS) analysis was performed with a SPECS Phoibos 150 MCD spectrometer from SCAI, University of Cordoba, using non monochromatized ( $12 \text{ kV}$ ,  $300 \text{ W}$ ) Mg KR radiation ( $1253.6 \text{ eV}$ ). The spectra were analyzed following previous reported procedure [25].

IRRAS characterization. A  $250 \text{ nm}$  thick Au layer adhered to a  $2.5 \text{ nm}$  thin chromium layer deposited on a Borosilicate glass  $11 \times 11 \text{ mm}$  flat surface were used as Au coated substrates (Gold-Arrandee™) for the Infrared Reflection-Absorption Spectroscopy (IRRAS) measurements. IRRA spectra were recorded on a JASCO 6300 FTIR single (He-Ne) laser beam spectrometer in the  $400\text{--}4000 \text{ cm}^{-1}$  wavenumber range at a resolution of  $4 \text{ cm}^{-1}$ , and the data were acquired by the integrated software (Spectra Manager) [25].

For the determination of the contact angle, an optical Thei tensiometer (Attension, Biolin Scientific) equipped with a high-speed camera (420 fps) was used, with a disposable pipette tip. Milli-Q water was used as measuring fluid. Experimentally, the measurement was made by dropping a constant volume ( $2 \mu\text{L}$ ) onto a solid surface (flat electrode) and recording the image of the drop.

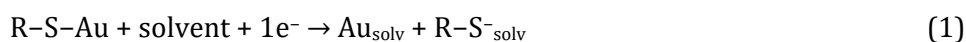
## Results and discussion.

### Electrochemical characterization.

#### RD of the DTBU-SAM.

The modification of the gold surface was carried out by self-assembly following the protocol described in the experimental section. The assembly involves the breaking of the S-S bond [16] obtaining a SAM.

Interesting information about SAM properties can be derived by using electrochemical techniques. In this sense, the RD of the molecules bound by an Au-S bond can be monitored by CV and the electrochemical profile allows an estimation of the DTBU surface coverage according to the equation (1).



where  $\text{Au}_{\text{solv}}$  and  $\text{R-S}^-_{\text{solv}}$  stand for solvated gold surface and thiolate, respectively. This equation represents a solvent substitution reaction that takes into account the energetic contributions involved in SAMs RD such as substrate-adsorbate, SAM-solvent, lateral interactions, substrate-solvent and surfactant solvation [26]. In this sense, the charge density, should contain not only the faradaic charge due to the RD but also the double layer charging contribution. Moreover, it has been pointed out that although we use the reaction (1) to account for the RD process, the charge flowing to the interface per desorbed molecule is not an integer equal to the number of electron transferred from metal to the molecule but, this value depends on electrode potential and the nature of the supporting electrolyte [27].

Figure 1 (top) shows the I-E curves obtained by CV of the RD of DTBU as well as the blank electrolyte, an aqueous solution of 0.1 M KOH.

The scanning starts at -0.1 V (double layer region), in the cathodic direction to -1.15 V. In this potential interval appears a peak with a shoulder associated to the RD. A roughly calculation of the surface coverage  $\Gamma$ , by taking into account the charge density obtained under this condition ( $s = 78.0 \text{ mC/cm}^2$ ), gives a value of  $8.1 \times 10^{-10} \text{ mol}\cdot\text{cm}^{-2}$  and an area per DTBU molecule of  $21 \pm 1 \text{ \AA}^2$ , values that correspond to those of a complete monolayer of aliphatic chain thiols [14]. The calculated results on the surface area of DTBU molecules in SAM from RD, schematically suggest a typical vertical disposition as in chain alkanethiols according to reference [14] which includes a possible tilt angle with respect to the surface normal. In any case, the arrangement of DTBU on the gold surface is such that it forms a compact monolayer.

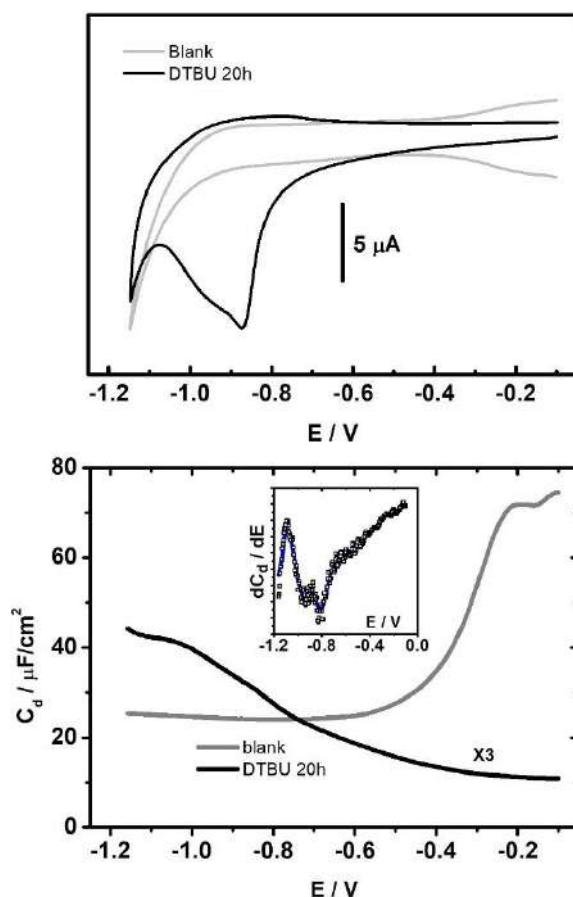


**Figure 1.** (Top) Voltammogram of the RD of DTBU monolayer on gold electrode in contact with an aqueous solution KOH 0.1 M. In gray, voltammogram of the bare gold electrode. (Bottom) C-E curves of the RD of DTBU ( $C_d \times 3$ ) and bare electrode (gray). Aqueous solution KOH 0.1 M. frequency 49 Hz. Inset: First derivative of the C-E curve (square). The smoothing operation of the derivative curve (solid line).

The capacitance-potential curves of DTBU/Au have been recorded on 0.1 M KOH solution, under experimental conditions of total surface coverage. Figure 1 (bottom) shows a potential scanning in the direction of the RD. The great difference between the C-E curve of modified and bare electrode is a decrease in the differential capacity caused by the interaction of DTBU with the polycrystalline gold surface. Also, the C-E curve for the DTBU monolayer in the cathodic potential range shows a profile in which, a gradual and stepped evolution is shown from -0.2 V, suggesting that other processes before RD are observed.

The differential capacity in the potential range -0.1 to -0.2 V is  $3.6 \text{ mF/cm}^2$ , a value close to those obtained with alkanethiols with a non-polar hydrocarbon chain which exposed polar terminal groups [28]. It has been tried to improve resolution of the capacitance variation taking its first derivative, curve (inset). The obtained profile indicates that the measurement of capacity potential, unlike the current potential, is sensitive to three transitions in the potential region between -0.4 and -1.0 V. It should be noted that  $C_d$  is obtained as  $-1/wZ''$ , so  $dC_d/dE$  is the derivative of the inverse of the impedance  $Z''$

(imaginary part), thus sensitive to faradic and non-faradic processes on the electrode surface. The change at more negative potentials where RD takes place, suggests that the formation of a complete and compact monolayer of DTBU on gold surface involves a strong intermolecular interaction.

#### Study of the integrity of DTBU SAM using EIS.

EIS allows to study the electrode-electrolyte interface describing it as an ideal electric double layer (DL), i.e., the Helmholtz model, or whether it deviates due to surface heterogeneity by current leakage at different scale of time [29]. The composition and concentration of the electrolyte may play a role in its behavior, which is often analyzed by the variation of the phase angle with AC polarization frequency.

The formation of DTBU monolayers is verified by XPS spectra (Appendix A) in the region of interest confirming the presence of the key elements of the adsorbate-substrate structure (Fig. A1).

Figure 2 shows the Bode plots for the DTBU SAM/Au interface obtained after 20 hours of modification at several DC potentials in the cathodic region. The impedance spectrum for the bare electrode at -0.2 V (grey line). shows a maximum phase angle close to 80°, which suggests that the polycrystalline gold surface behaves like a non-ideal DL and is represented by a constant phase element (CPE). This might be caused by the intrinsic heterogeneity and surface roughness of the polycrystalline substrate.

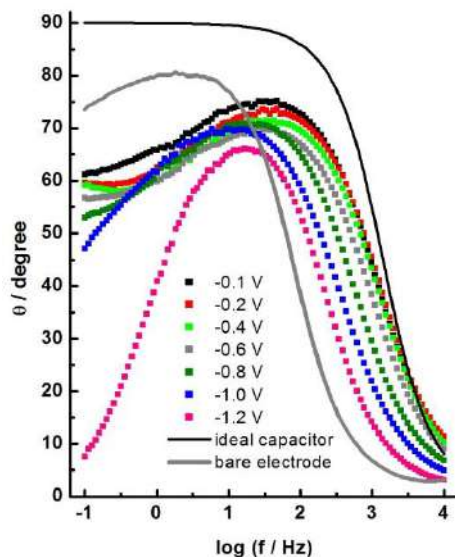


**Figure 2.** Bode representation of the DTBU-SAM/Au in 0.1 M KOH in the range of potentials from the SAM stability zone, at the least negative edge, to the RD, at the most negative. Bode representation of the Au(s)/KOH(ac) 0.1M interface (grey). Ideal capacitor (black). Modification time 20 hours.

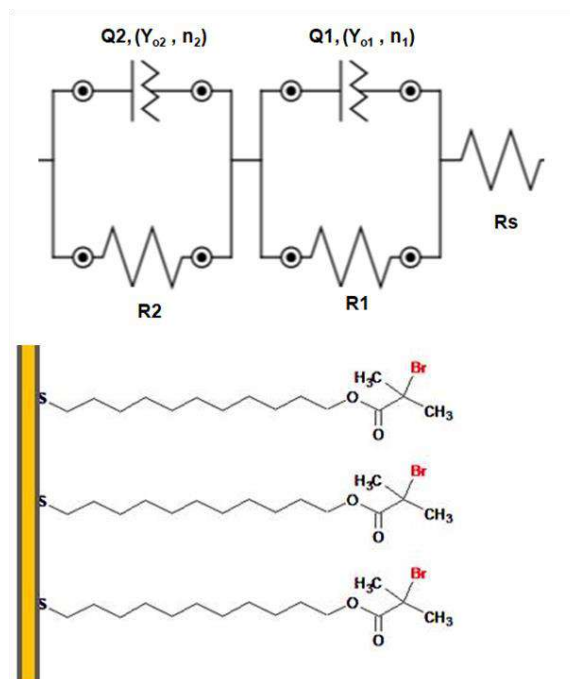
The theoretical variation of the phase angle with the polarization frequency for an ideal DL is also shown in Fig 2. This simulation assumes a capacitance as that found in the CE curves at less negative potentials, where no faradic response takes place. However, a large deviation from ideal behaviour is observed in the presence of the DTBU film. A maximum phase angle of 70-75° suggests a double layer typical of the solid heterogenous surface. The deviations from ideal capacitive behaviour can be empirically represented by the so-called “constant phase element” (CPE) having the following dependence on frequency and containing the double-layer capacitance quantity,  $Y_0$  [29]

$$Z(\text{CPE}) = 1/(jY_0\omega)^n$$

the parameter  $n$  is related to the phase angle  $q$  by  $q = n(\pi/2)$ .  $n = 1$  corresponds to true capacitance behaviour. Moreover, the observed transitions at low frequencies reveal the complexity of this interface. This behaviour suggests that the DTBU chain structure must also be considered. The heterogeneous structure is composed by a non-polar hydrocarbon skeleton inside the SAM and a polar head containing oxygen and bromine atoms. To understand this complex behaviour as reveals  $\theta$ -log  $f$  curves is necessary to bear in mind that structure, nature, and elements of the DTBU long chain play a main role.

In view of the electrochemical results and considering the structure of the DTBU chain, an equivalent circuit has been selected for the Bode plot fitting, which is appropriate in monolayer with polarity differences on the chains [30,31]. It allows to obtain information from the Au/DTBU interface. It is a combination of elements in series,  $R_s(Q1R1)$ , and  $(Q2R2)$ , with parallel arrangement of the elements enclosed in parentheses.  $R_s$  representing the resistance of the solution, and  $QR$  an interface with CPE ( $Q1$  and  $Q2$ ) elements. The (1) and the (2) indexes refer to the surface and inside the monolayer, respectively, where the ions can partially or totally penetrate due to the potential permeability suggested by the electrochemical data. In Scheme 3 a representation of the combination of elements and the configuration of the DTBU monolayer is shown.

An acceptable fitting is obtained which suggests that the interface behaves in agreement with the scheme that considers the structure of DTBU. Other equivalent circuits such as those used in similar systems containing film or porous material on electrode surfaces described in the reference [29] have been tested, showing no improvement in the fit. Table 1 summarizes the results of the parameters obtained in the best fitting.



**Scheme 3.** Equivalent circuit and representation of the DTBU monolayer on polycrystalline gold electrode.

Figure 3 shows the fittings of the Bode-phase curves, under the experimental conditions tested (KOH 0.1 M and KNO<sub>3</sub> 0.1 M), according to the equivalent circuit.

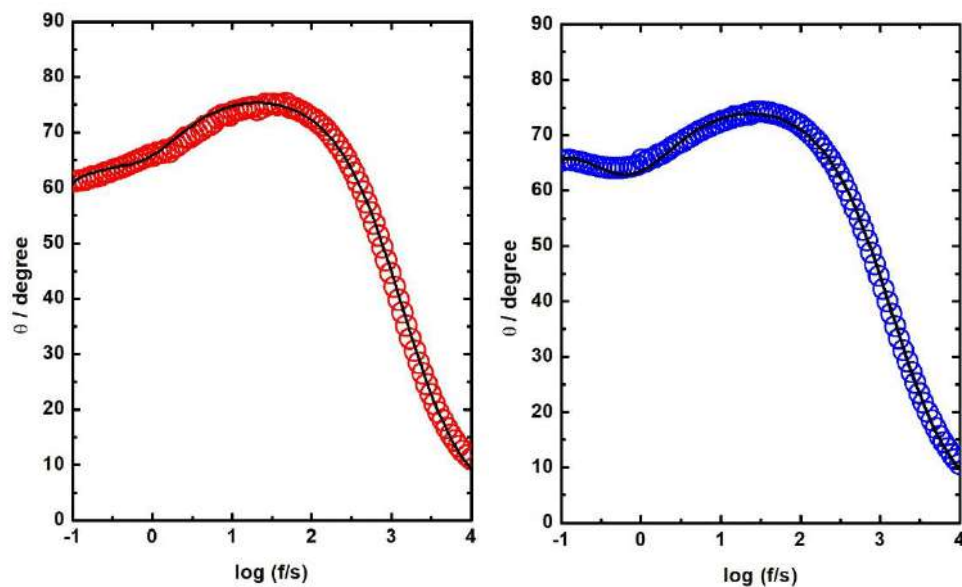


**Figure 3.** Bode representation and fitting with Rs (R1Q1) (R2Q2). Experimental values (○) equivalent circuit curve (-). E<sub>dc</sub> = -0.1V. Au/DTBU monolayer in KOH (left) and KNO<sub>3</sub> (right) at 0.1M.



**Table 1.** EIS Best Fitting Parameters of the Au/DTBU monolayer in KOH and KNO<sub>3</sub> 0.1 M

Au/DTBU	R <sub>s</sub> / W·cm <sup>2</sup>	Y <sub>o1</sub> ·10 <sup>8</sup> /W <sup>1/ns</sup>	n <sub>1</sub>	R <sub>1</sub> / kW·cm <sup>2</sup>	Y <sub>o2</sub> ·10 <sup>8</sup> /W <sup>-1/ns</sup>	n <sub>2</sub>	R <sub>2</sub> / kW·cm <sup>2</sup>
<b>KOH 0.1 M</b>	35.0	6.32	0.853	18.6	7.57	0.887	593
<b>KNO<sub>3</sub> 0.1 M</b>	33.6	15.3	0.851	7.51	16.01	0.866	519

It is worth noting that the values found for n<sub>1</sub> and n<sub>2</sub> are consistent with a CPE where the phase angle does not reach 80° in any case. Moreover, R<sub>1</sub> and R<sub>2</sub> have high values, according to the nature of DTBU being those of R<sub>2</sub> which correspond to the hydrophobic inside of the aliphatic chain.

Bode phase curves of the bare electrode show sensitivity on the inflection point at high frequency as compared to the modified substrate. On a first approach, this behaviour can be modelled assuming a simple scheme with an ideal double layers (DL) that provides a quantitative relationship between capacitance of bare and modified electrodes at high frequency. For a fixed value of phase angle, θ<sub>1/2</sub> would be the ordinate of the inflection point. It can be written

$$f_m(q_{1/2})/f_o(q_{1/2}) = C_o/C_m$$

Applying to the DTBU SAM interface, the subscripts (o) and (m) refer to the bare gold and modified electrode, respectively. However, if you consider that the interface behaves like a CPE with similar values of n for Au and Au/DTBU, it can be demonstrated that it does not add extra complexity.

In Bode curves of Figure 2, one has analysed the displacement of f<sub>m</sub>(θ<sub>1/2</sub>) with the potential. The determination of C<sub>m</sub> from this frequency indicates an almost coincident variation with potential as compared with the differential capacity-potential curves determined by impedance measurements (Table 2).

**Table 2.** C<sub>d</sub> experimental values and C<sub>m</sub> calculated values from EIS at different potentials of the Au-DTBU/KOH (ac) 0.1 M interface. t<sub>mod</sub> = 20 h

E / V	-0.1	-0.2	-0.4	-0.6	-0.8	-1.0	-1.2
<b>C<sub>d</sub> / mF/cm<sup>2</sup></b>	3.6	3.7	4.4	6.1	9.0	13.2	25.7
<b>C<sub>m</sub> / mF/cm<sup>2</sup></b>	3.6	3.5	4.1	5.4	8.5	13.5	24.9

Blocking effect of DTBU monolayers.

To examine the blocking properties of the SAM interface of DTBU, a study of several redox probes has been carried out. Therefore, CV and EIS of Fe(CN)<sub>6</sub><sup>3-/4-</sup>, Ru(NH<sub>3</sub>)<sub>6</sub><sup>3+/2+</sup> and

FcMeOH have been employed both with the bare and modified electrodes. It is known that the heterogenous electron transfer of the redox pairs is sensitive to the blockage that occurs on the metal surface with self-assembled monolayers. The observed behavior is able to detect the presence and nature of defects revealing information on the organization of the monolayer [32].

The selected probes show difference in the electrical charge of the reagent molecule (negative, positive, and neutral), and in the nature of the redox pairs and the solvation properties [33,34]. Figure 4 (left) shows the voltammograms of  $\text{Fe}(\text{CN})_6^{3-/4-}$  1 mM in  $\text{KNO}_3$  0.1 M onto bare gold electrode, and after 20 h of modification with DTBU. On the right of the Figure 4 is shown EIS (Nyquist plot) in the same experimental conditions. A potential DC corresponding to the average between the peak potentials of the couple  $\text{Fe}(\text{CN})_6^{3-/4-}$  was applied.

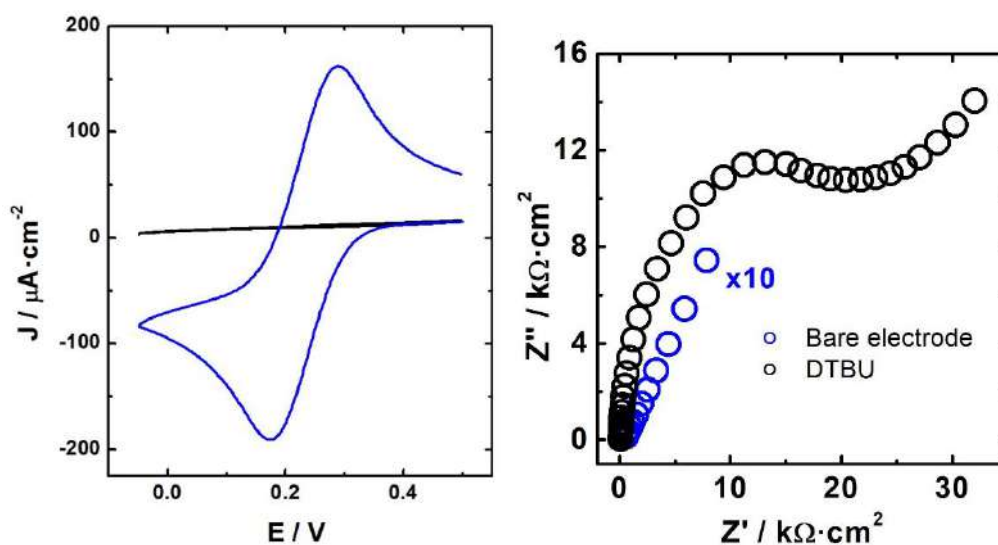


**Figure 4.** (left) CV of  $\text{Fe}(\text{CN})_6^{3-/4-}$  1 mM in  $\text{KNO}_3$  0.1 M for bare gold electrode (blue), after 20 h of modification with DTBU (black). Scan rate 0.1 V/s. (right) EIS (Nyquist plot) of  $\text{Fe}(\text{CN})_6^{3-/4-}$  in the same experimental.  $E_{\text{dc}} = +0.22$  V.

With the bare gold electrode, the redox pair is clearly appreciated. The presence of DTBU after 20h of modification gives rise to a total reduction of the current by a blocking effect. The impedance spectra show great sensitivity to the modification of the gold electrode with DTBU. It is observed an arc at high frequency indicative of the appreciable increase of the resistance to the charge transfer in comparison with the bare electrode (Figure 4, right). For  $\text{Ru}(\text{NH}_3)_6^{3+/2+}$  and FcMeOH, no significant changes are observed either in the voltammogram or in the impedance spectrum with respect to the bare electrode (Appendix A).

A Randles circuit has been used with a CPE to model the electric double layer in the fitting of the impedance spectra. The greatest sensitivity to modification of the electrode is

highlighted with the  $\text{Fe}(\text{CN})_6^{3-/4-}$  redox probe where  $R_{\text{CT}}$  increases by more than two magnitude orders in the presence of DTBU monolayer. The values of  $n$  for the modified electrode oscillate between 0.8 and 0.9 assuming a CPE electric double layer.

RD of mixed SAM of DTBU and 6MP.

The RD of DTBU-6MP mixed monolayers on the polycrystalline gold electrode in 0.1 M KOH has been studied. The modification was also carried out in EtOH solutions by using a 1 mM total concentration of thiols and a modification time of 20 h (overnight). The voltammogram of 6MP monolayer has also been recorded under the same experimental conditions for comparison. Figure 5 shows the voltammograms of the RD in the different proportions of modification studied.

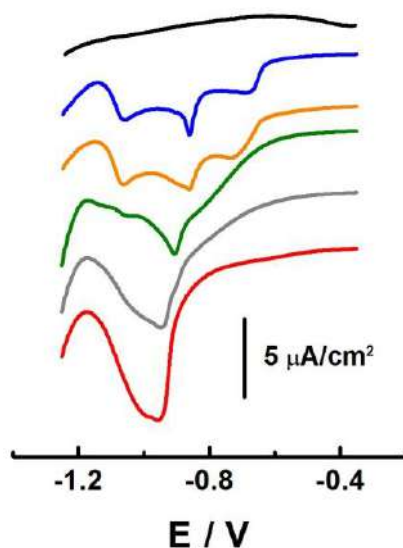


**Figure 5.** RD of the mixed SAM of DTBU and 6MP after 20 h of modification. Scan rate 20 mV/s. Top to bottom: Blank electrolyte; DTBU:6MP ratio: 0:100; 10:90; 30:70; 90:10; 100:0.

The RD of 6MP has already been studied by our research group [20]. In Figure 5, there are up to three partially overlapped peaks in the RD profile of the 6MP. The approximate peak potentials are -0.67, -0.86 and -1.05 V. These values are close to those obtained with a polyfaceted gold and they matches with those obtained with single crystal facets of Au(111), Au(100) and Au(110), respectively. The onset of the RD faradic current of the 6MP occurs -0.58 V, showing a faradic process extended to negative potentials with a surface charge density of  $66 \pm 8$  mC/cm<sup>2</sup>. The RD profile of DTBU, has already been described in previous sections, the onset is close to -0.75 V and the surface charge density  $78 \pm 6$  mC/cm<sup>2</sup>.

The voltammograms corresponding to the mixtures in the different proportions show an increase of overlapping and a loss of resolution of the peaks, although overall a displacement of the faradic current is observed in the cathode direction as the proportion

of DTBU increases. For these mixed monolayers the difficulty for determining the surface charge density increases, obtaining values that range between 65-70 mC/cm<sup>2</sup>. This feature indicates that as the proportion of 6MP increases, so does the proportion on the surface of electrode.

### Study of the integrity and the blocking effect of the mixed layers DTBU:6MP.

IRRAS spectra of mixed DTBU:6MP monolayers have been recorded (Appendix A), indicating that 6MP is present in a significant proportion on the surface as expected from the modifying mixture. The bands assigned to the C-N stretching mode of the 6MP rings stand out in the spectrum, at 1690 cm<sup>-1</sup> which is a clear indicator of the interaction of 6MP with the gold surface (appendix A). The integrity of the mixed monolayers has been studied through EIS and analyzed from the Bode phase representation. Figure 6 shows the impedance spectra  $\theta$ -log f for 6MP, DTBU and selected mixtures for  $E_{dc} = 0.0$  V. Similar results have been found at potentials -0.2, -0.1, +0.1 and +0.2 V.

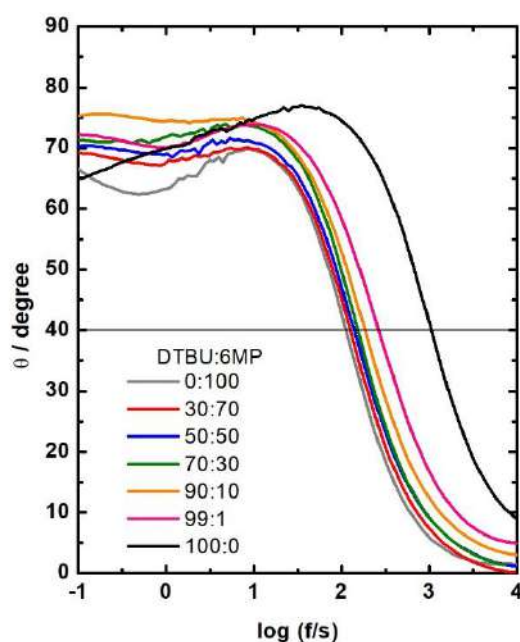


**Figure 6.** Bode plot for DTBU, 6MP and DTBU:6MP ratio 30:70, 50:50, 70:30, 90:10 y 99:1.  $E_{dc} = 0.0$  V.

All the spectra have a profile with the characteristic displacement of the inflection point as those obtained for DTBU. It is observed that for 6MP SAM the value of  $f(q_{1/2})$  at high frequencies (2.04) takes place a decade below of that to DTBU (3.04). On the other hand, for the different ratio, this parameter gradually moves to higher frequencies as the amount of DTBU increases. The figure shows a horizontal line that marks the angle 40°, the same

reference as when the comparison between the differential capacity of the bare electrode versus the modified electrode with DTBU was made. If we accept the capacity-frequency relationship as in the previous case, we can write the relation  $C_{m1}/C_{m2} = f_{m2}/f_{m1}$ , where  $m_1$  and  $m_2$  are the symbols used for the two monolayers to be compared. In mixed monolayers, a model with a parallel combination of the differential capacity to each SAM is used, so that the total capacity is the sum of the individual contribution weighted by the number of molecules of each on the surface [34]. Thus, it can be written:

$$C = C_{DTBU} \cdot C_{DTBU} + C_{6MP} \cdot C_{6MP}$$

where  $C_{DTBU}$  and  $C_{6MP}$  are the capacitances of pure DTBU and 6MP SAM, respectively. Considering the binary mixture on the surface, with  $C_{DTBU} + C_{6MP} = 1$ , and combining with the previous equations, an expression is reached that allows to estimate the composition at the interface:

$$\chi_{6MP} = \frac{f_{6MP}}{f} \frac{(f_{DTBU} - f)}{(f_{DTBU} - f_{6MP})}$$

whit  $f$  being the value of  $f(q_{1/2})$  for any given mixed monolayer of DTBU and 6MP and the rest of symbols having its usual meaning. Under the modification conditions of the gold electrode with both molecules, the proportion of 6MP onto electrode surface is higher than that of modification mixture in all cases. This is suggested by the low gradual displacement of  $f(q_{1/2})$  that can be observed in Figure 6.

### Contact angle measurements.

The hydrophilic/hydrophobic character of the DTBU-SAM and mixed monolayers with 6MP has been studied by contact angle (CA) measurements. The variation of the contact angle with the 6MP composition in solution is shown in Figure 7. The representation is practically linear, which would be in accordance with a surface composition like that of the solution mixture, and which is in accordance with Cassie model [35], which indicates that there is no selective fixation (attachment) from one of the thiols.

However, this interpretation is in marked contrast what was observed by EIS that suggests the preferential binding of 6MP over DTBU and considering this behaviour, it is possible to label the surface composition of the mixed SAM that give rise the cyclic voltametric profiles (Figure 5). This is also in agreement with the significative perturbation of the IR spectrum in the presence of a small proportion of 6MP in the thiol mixture (Figure A2-C). Figure 7 compares the surface concentration of 6MP with the proportion in solution being able to appreciate this fact. This type of deviation has been explained in terms of the formation of random surface structures, without domain location, and solvation differences of exposed heads to the medium (water). The lower proportion of DTBU on the surface is

compensated by the predominance of the hydrophobic effect [16,36], which due to the larger size limits water access to 6MP (Scheme 4). This behavior results on an apparent proportionality between contact angle and composition in solution as observed in the figure.

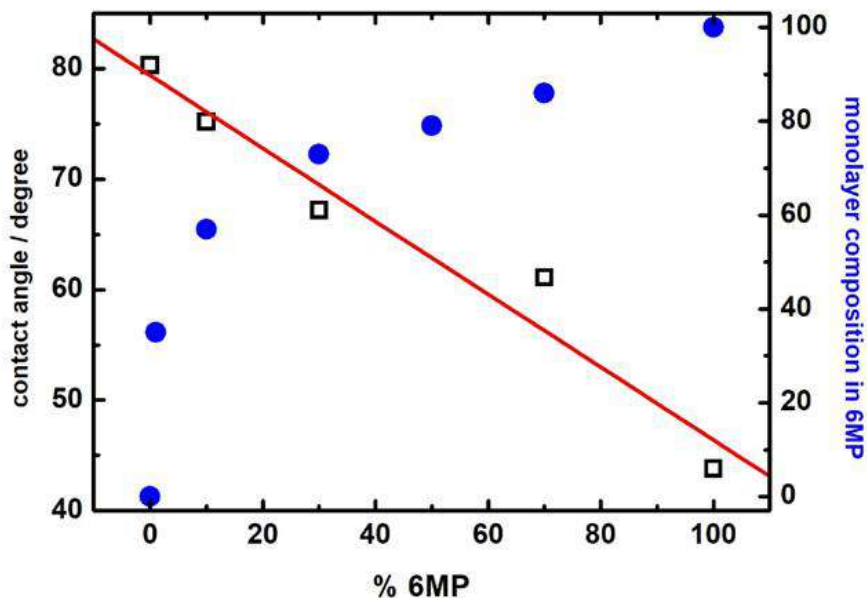
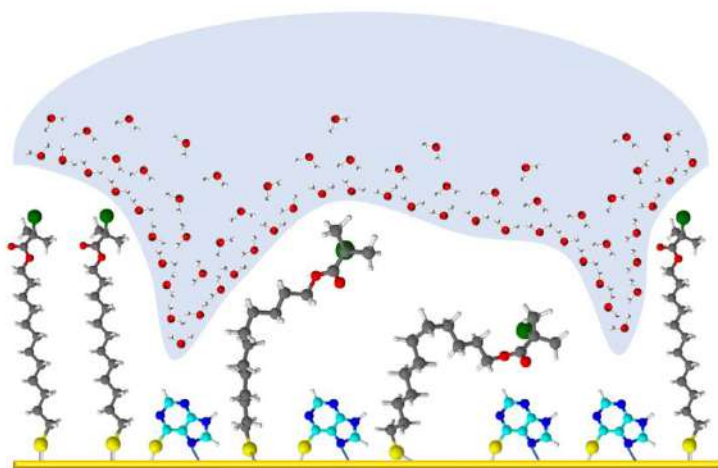


**Figure 7.** Contact angle on DTBU and 6MP monolayers and mixed monolayers DTBU:6MP in different ratios. (•) experimental CA; (□) Linear Fit; (·) % 6MP on the surface.



**Scheme 4.** Mixed monolayer DTBU:6MP. Limitation of access to water and hydrophobic effect.

The collected results suggest examining the conductive properties of the mixed SAMs. Accordingly, the blocking effect of DTBU:6MP monolayers, against the  $\text{Fe}(\text{CN})_6^{3-/4-}$  redox

probe has been explored, for possible changes in the rate of the electron transfer. Figure 8 shows the impedance spectrum of the redox probes on a mixed monolayer 90:10 as compared to that obtained with bare electrode and of the DTBU and 6MP monolayers.

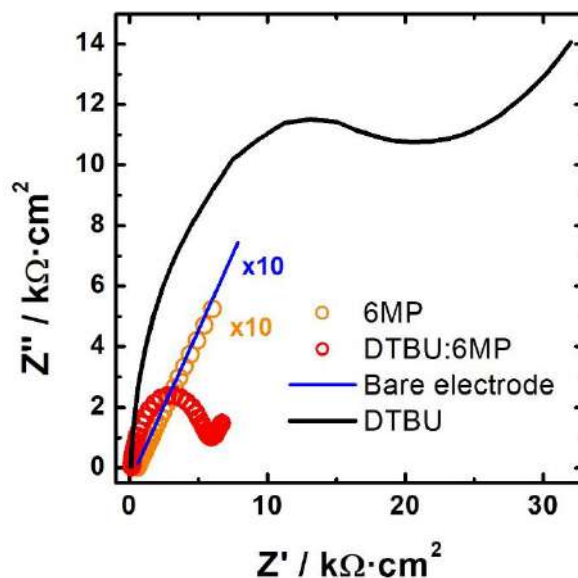


**Figure 8.** EIS (Nyquist plot) of  $\text{Fe}(\text{CN})_6^{3-/4-}$  1 mM in  $\text{KNO}_3$  0.1 M for bare gold electrode (blue), self-assembled monolayer with DTBU (black), SAM with 6MP (orange) and mixed monolayer DTBU:6MP from a ratio 90:10 in solution (red).  $E_{\text{dc}} = +0.22$  V.

A semicircle at high frequencies is observed which indicates that the resistance to electron transfer is higher than to the bare electrode, although it is much lower than that obtained with the DTBU monolayer.

However, for a 6MP SAM, no appreciable differences are observed with respect to the bare electrode, highlighting the diffusion line in the entire frequency range. Considering a Randles circuit, a very low value of  $R_{\text{ct}}$ , 0.010 kW, is obtained by fitting. This feature suggests the choice of this molecule in the preparation of mixed monolayers to activate the DTBU response as an initiator

The value obtained for the resistance to charge transfer for a mixed monolayer DTBU:6MP is 0.791 kW, clearly higher than the obtained value either with a bare electrode (0.031 kW) and with an Au-6MP, but it is lower by a factor to 8 with respect to that corresponding to the DTBU monolayer. This last result shows that the presence of 6MP increases the rate of the electronic transfer of redox couple such as  $\text{Fe}(\text{CN})_6^{3-/4-}$  and, therefore, the DTBU-6MP mixed monolayer provide the optimal conditions for its adaptation and use in e-ATPR.

## Conclusions.

DTBU, initiator in ATRP polymerization reactions, forms self-assembled monolayers on Au substrates through the S-Au bond as it is confirmed by XPS. The peaks associated to the RD of the SAM (for  $t_{\text{MOD}}$  overnight) is coherent with a compact monolayer with a molecule footprint of  $20.5 \text{ \AA}^2$ . The C-E curves support this characterization, with a differential capacity of  $3.6 \text{ mF/cm}^2$  for the SAM. In consequence, DTBU is postulated as a good candidate to be an initiator in SI-ATRP.

The studies on the integrity of DTBU on polycrystalline gold reveal the presence of a film whose characteristics are defined by a non-polar site near the surface and a polar character by exposed groups to the solution. The phase angle at high frequency is sensitive to the dielectric properties of the electric double layer of the modified electrode, establishing an excellent correlation between transition frequency  $f(q_{1/2})$  and differential capacity. At low frequencies, variations dependent on the potential are observed which suggest a certain permeability of formed SAMs. The  $\text{Fe}(\text{CN})_6^{3-/4-}$  redox probe suffers a significative limitation in the electron transfer by the presence of a DTBU compact monolayer.

The IRRAS studies of mixed monolayers DTBU:6MP, indicate that 6MP is present in higher proportion on the surface as expected from the modification mixture. The bands assigned to the C-N stretching mode of the 6MP rings stand out in the spectrum, at  $1690 \text{ cm}^{-1}$  that is a clear indication of the interaction of 6MP with gold surface. For a 90:10 ratio, the estimated proportion of 6MP on the electrode surface by frequency transition  $f(q_{1/2})$  in EIS measurements, exceeds that of DTBU. In this mixed monolayer, the  $\text{Fe}(\text{CN})_6^{3-/4-}$  probe has a charge transfer resistance an order of magnitude lower that the corresponding to the DTBU monolayer. This feature provides optimal conditions for its adaptation and use in e-ATRP.

DTBU and DTBU-6MP SAMs contact angle measurements suggest the formation of random structures on the surface. The differences in the solvation of the exposed heads to the environment (water), leads to a more hydrophobic predominant effect, providing conditions that also favor radical polymerization on the electrode surface.

*Acknowledgements.* We thank the Ministerio de Ciencia e Innovación (Project RED2018-102412-T Network of Excellence Electrochemical Sensors and Biosensors), Junta de Andalucía and Universidad de Cordoba (UCO-FEDER ref. 1265074-2B and Plan Propio, Submod. 1.2.) for financial support of this work. M.C. acknowledges Ministerio de Universidades for FPU 17/03873 grant.



## References.

- [1] J.S. Wang, K. Matyjaszewski, Controlled Living Radical Polymerization - Atom-Transfer Radical Polymerization in the Presence of Transition-Metal Complexes, *J. Am. Chem. Soc.* 117(20) (1995) 5614-5615.
- [2] M. Kato, M. Kamigaito, M. Sawamoto, T. Higashimura, Polymerization of Methyl-Methacrylate with the Carbon-Tetrachloride Dichlorotris(Triphenylphosphine)Ruthenium(II) methylaluminum Bis(2,6-Di-Tert-Butylphenoxide) Initiating System - Possibility of Living Radical Polymerization, *Macromolecules* 28(5) (1995) 1721-1723.
- [3] V. Percec, B. Barboiu, Living Radical Polymerization of Styrene Initiated by Arenesulfonyl Chlorides and Cu-I(BPY) (N)Cl, *Macromolecules* 28(23) (1995) 7970-7972.
- [4] R. Barbey, L. Lavanant, D. Paripovic, N. Schuwer, C. Sugnaux, S. Tugulu, H.A. Klok, Polymer Brushes via Surface-Initiated Controlled Radical Polymerization: Synthesis, Characterization, Properties, and Applications, *Chem. Rev.* 109(11) (2009) 5437-5527.
- [5] J.O. Zoppe, N.C. Ataman, P. Mocny, J. Wang, J. Moraes, H.A. Klok, Surface-Initiated Controlled Radical Polymerization: State-of-the-Art, Opportunities, and Challenges in Surface and Interface Engineering with Polymer Brushes (vol 117, pg 1105, 2017), *Chem. Rev.* 117(5) (2017) 4667-4667.
- [6] S. Edmondson, V.L. Osborne, W.T.S. Huck, Polymer brushes via surface-initiated polymerizations, *Chem. Soc. Rev.* 33(1) (2004) 14-22.
- [7] K. Matyjaszewski, P.J. Miller, N. Shukla, B. Immaraporn, A. Gelman, B.B. Luokala, T.M. Siclovan, G. Kickelbick, T. Vallant, H. Hoffmann, T. Pakula, Polymers at interfaces: Using atom transfer radical polymerization in the controlled growth of homopolymers and block copolymers from silicon surfaces in the absence of untethered sacrificial initiator, *Macromolecules* 32(26) (1999) 8716-8724.
- [8] W.X. Huang, J.B. Kim, M.L. Bruening, G.L. Baker, Functionalization of surfaces by water-accelerated atom-transfer radical polymerization of hydroxyethyl methacrylate and subsequent derivatization, *Macromolecules* 35(4) (2002) 1175-1179.
- [9] K. Matyjaszewski, H.C. Dong, W. Jakubowski, J. Pietrasik, A. Kusumo, Grafting from surfaces for "Everyone": ARGET ATRP in the presence of air, *Langmuir* 23(8) (2007) 4528-4531.
- [10] B. Li, B. Yu, W.T.S. Huck, F. Zhou, W.M. Liu, Electrochemically Induced Surface-Initiated Atom-Transfer Radical Polymerization, *Angew. Chem.-Int. Ed.* 51(21) (2012) 5092-5095.
- [11] B. Li, B. Yu, W.T.S. Huck, W.M. Liu, F. Zhou, Electrochemically Mediated Atom Transfer Radical Polymerization on Nonconducting Substrates: Controlled Brush Growth through Catalyst Diffusion, *J. Am. Chem. Soc.* 135(5) (2013) 1708-1710.
- [12] M. Mullner, Molecular Polymer Brushes in Nanomedicine, *Macromol. Chem. Phys.* 217(20) (2016) 2209-2222.
- [13] M. Mullner, K. Yang, A. Kaur, E.J. New, Aspect-ratio-dependent interaction of molecular polymer brushes and multicellular tumour spheroids, *Polymer Chem.* 9(25) (2018) 3461-3465.
- [14] F. Schreiber, Structure and growth of self-assembling monolayers, *Prog. Surf. Sci.* 65(5-8) (2000) 151-256.
- [15] J.C. Love, L.A. Estroff, J.K. Kriebel, R.G. Nuzzo, G.M. Whitesides, Self-assembled monolayers of thiolates on metals as a form of nanotechnology, *Chem. Rev.* 105(4) (2005) 1103-1169.
- [16] E. Albayrak, S. Karabuga, G. Bracco, M.F. Danisman, 11-Hydroxyundecyl octadecyl disulfide self-assembled monolayers on Au(111), *Appl. Surf. Sci.* 311 (2014) 643-647.
- [17] S.M. Flores, A. Shaporenko, C. Vavilala, H.-J. Butt, M. Schmittel, M. Zharnikov, R. Berger, Control of surface properties of self-assembled monolayers by tuning the degree of molecular asymmetry, *Surf. Sci.* 600(14) (2006) 2847-2856.
- [18] J.J. Gooding, F. Mearns, W.R. Yang, J.Q. Liu, Self-assembled monolayers into the 21(st) century: Recent advances and applications, *Electroanalysis* 15(2) (2003) 81-96.

- [19] T. Pineda, J.M. Sevilla, A.J. Roman, R. Madueno, M. Blazquez, Modification of metal substrates and its application to the study of redox proteins, *Stability and Stabilization of Biocatalysts* 15 (1998) 697-702.
- [20] R. Madueno, J.M. Sevilla, T. Pineda, A.J. Roman, M. Blazquez, A voltammetric study of 6-mercaptapurine monolayers on polycrystalline gold electrodes, *J. Electroanal. Chem.* 506(2) (2001) 92-98.
- [21] R. Madueno, D. Garcia-Raya, A.J. Viudez, J.M. Sevilla, T. Pineda, M. Blazquez, Influence of the solution pH in the 6-mercaptapurine self-assembled monolayer (6MP-SAM) on a Au(111) single-crystal electrode, *Langmuir* 23(22) (2007) 11027-11033.
- [22] J.M. Sevilla, T. Pineda, R. Madueno, A.J. Roman, M. Blazquez, Characterization of 6-mercaptapurine monolayers on Hg surfaces, *J. Electroanal. Chem.* 442(1-2) (1998) 107-112.
- [23] S. Trasatti, O.A. Petrii, Real Surface-area Measurements in Electrochemistry, *Pure Appl. Chem.* 63(5) (1991) 711-734.
- [24] M. Lukaszewski, M. Soszko, A. Czerwinski, Electrochemical Methods of Real Surface Area Determination of Noble Metal Electrodes - an Overview, *Int. J. Electrochem. Sci.* 11(6) (2016) 4442-4469.
- [25] M. Chávez, G. Sánchez-Obrero, R. Madueño, J.M. Sevilla, M. Blázquez, T. Pineda, Characterization of a self-assembled monolayer of O-(2-Mercaptoethyl)-O'-methyl-hexa(ethylene glycol) (EG7-SAM) on gold electrodes, *J. Electroanal. Chem.* 880 (2021) 114892.
- [26] R.C. Salvarezza, P. Carro, The electrochemical stability of thiols on gold surfaces, *J. Electroanal. Chem.* 819 (2018) 234-239.
- [27] T. Laredo, J. Leitch, M.H. Chen, I.J. Burgess, J.R. Dutcher, J. Lipkowski, Measurement of the charge number per adsorbed molecule and packing densities of self-assembled long-chain monolayers of thiols, *Langmuir* 23(11) (2007) 6205-6211.
- [28] A.R. Puente-Santiago, G. Sanchez-Obrero, T. Pineda, M. Blazquez, R. Madueno, Influence of Patterning in the Acid-Base Interfacial Properties of Homogeneously Mixed CH<sub>3</sub>- and COOH-Terminated Self-Assembled Monolayers, *J. Phys. Chem. C* 122(5) (2018) 2854-2865.
- [29] B.E. Conway, Impedance Behavior of Electrochemical Supercapacitors and Porous Electrodes, in: E. Barsoukov, J.R. Macdonald (Eds.), *Impedance Spectroscopy: Theory, Experiment, and Applications*, 2nd Edition, Wiley, New Jersey, 2005, pp. 495-496.
- [30] S. Gritsch, P. Nollert, F. Jahnig, E. Sackmann, Impedance spectroscopy of porin and gramicidin pores reconstituted into supported lipid bilayers on indium-tin-oxide electrodes, *Langmuir* 14(11) (1998) 3118-3125.
- [31] A.E. Vallejo, C.A. Gervasi, Impedance analysis of ion transport through gramicidin channels in supported lipid bilayers, *Bioelectrochemistry* 57(1) (2002) 1-7.
- [32] E. Boubour, R.B. Lennox, Insulating properties of self-assembled monolayers monitored by impedance spectroscopy, *Langmuir* 16(9) (2000) 4222-4228.
- [33] T. Doneux, A. de Ghellinck, E. Triffaux, N. Brouette, M. Sferrazza, C. Buess-Herman, Electron Transfer Across an Antifouling Mercapto-hepta(ethylene glycol) Self-Assembled Monolayer, *J. Phys. Chem. C* 120(29) (2016) 15915-15922.
- [34] G. Sanchez-Obrero, M. Chavez, R. Madueno, M. Blazquez, T. Pineda, J.M. Lopez-Romero, F. Sarabia, J. Hierrezuelo, R. Contreras-Caceres, Study of the self-assembly process of an oligo(ethylene glycol)-thioacetyl substituted theophylline (THEO) on gold substrates, *J. Electroanal. Chem.* 823 (2018) 663-671.
- [35] A.B.D. Cassie, Contact Angles, *Discussions of the Faraday Society* 3 (1948) 11-16.
- [36] Y.J. Liu, N.M. Navasero, H.Z. Yu, Structure and reactivity of mixed co-carboxyalkyl/alkyl monolayers on silicon: ATR-FTIR spectroscopy and contact angle titration, *Langmuir* 20(10) (2004) 4039-4050.

**Supporting information.**

## Spectroscopic characterization.

### X-ray Photoelectron Spectroscopy analysis.

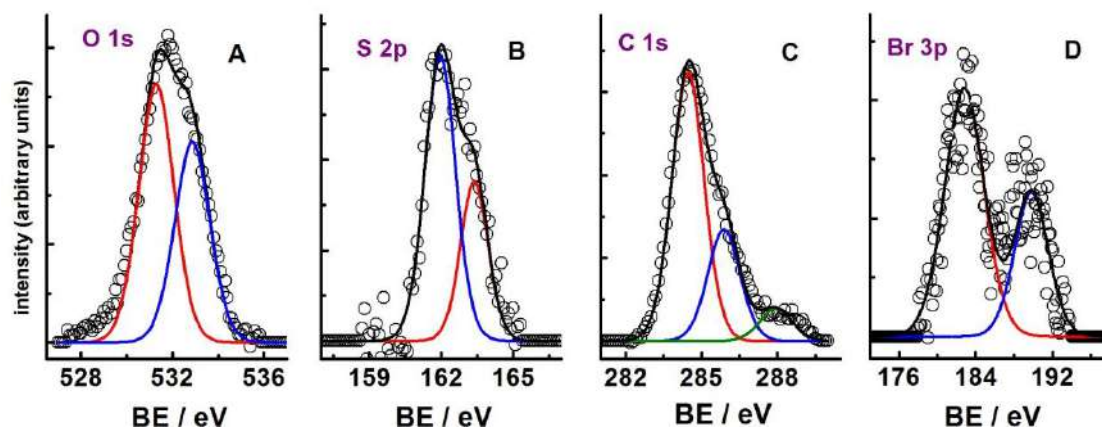


**Figure A1.** O 1s, S 2p, C 1s and Br 3p XPS spectra of DTBU on gold electrode. The spectra are decomposed into the individual contributions (see text).

Figure A1 provides the X-ray photoelectron spectra for the regions of interest verifying the presence of each element found in the adsorbate structures. Figure A1-A confirms the presence of oxygen of DTBU monolayers with two different O 1s peaks, at 531.5, and 533.2 eV, corresponding to  $\underline{O}-C=O$  and  $O-C=\underline{O}$ , respectively [1]. The S 2p region (Figure A1-B) consists of a slightly asymmetric peak centered at a BE of 162.0 eV. This peak can be deconvoluted with a doublet of Gaussian peaks, with an intensity ratio of 2:1 and a separation of 1.4 eV. The BE fitted values, 162.0 and 163.4 eV, correspond to the S 2p<sub>3/2</sub> and S 2p<sub>1/2</sub> levels, respectively. These values coincide with those found for thiols interacting strongly with Au in 2D and 3D SAMs [2]. In Figure 1A-C, the radical initiator films show three different C 1s peaks at 284.5, 286, and 288 eV, corresponding to alkyl chain hydrocarbons, C–O–C, and C=O. Figure 1A-D shows the Br 3p peaks at 182 and 190 eV for the radical initiator film, which would correspond to Br 3p<sub>3/2</sub> and Br 3p<sub>1/2</sub> levels, respectively [3]. Therefore, the S 2p<sub>3/2</sub> BE data provide the best evidence that gold is partially oxidized, and that the gold-sulfur bond is covalent in character. The remaining regions of the XPS spectrum of interest verify the presence of the elements of the DTBU adsorbate of SAM.

### FT-IRRAS spectra.

Figure A2 shows the IRRAS spectra recorded between 1000 and 3000 cm<sup>-1</sup> that contain most of the signals corresponding to DTBU and 6-MP.

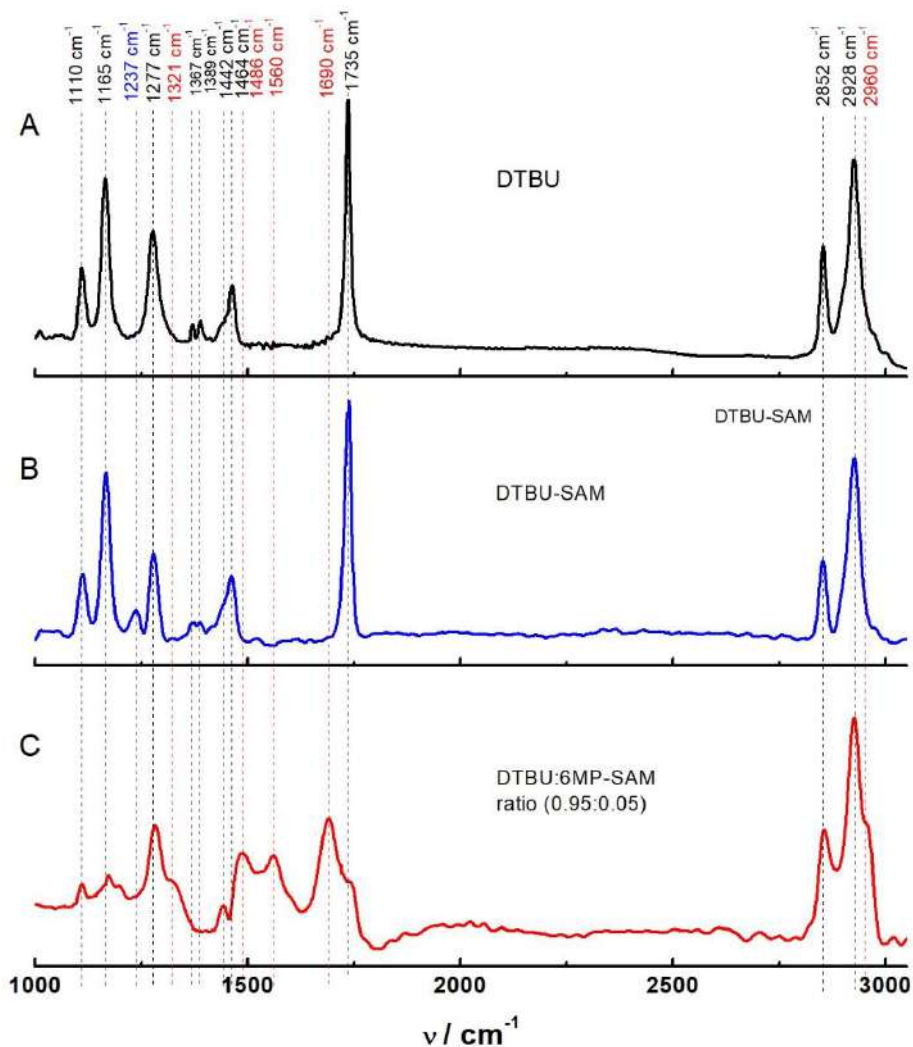


**Figure A2.** Infrared spectra of DTBU in KBr solid (black, A) and self-assembled in Au(111) substrate (blue, B). In red (C) the IR of self-assembled in Au(111) substrate of mixed monolayer DTBU:6MP in the ratio 95:5

The comparison between the spectra of the DTBU in KBr (Figure A2-A) and the DTBU chemisorbed on the gold surface (Figure A2-B) indicates few changes. Only the appearance of the band at 1237  $\text{cm}^{-1}$  and the consequent decrease of the band at 1277  $\text{cm}^{-1}$  in the adsorption of DTBU on gold are relevant, suggesting a fine structure associated with the vibration modes of the CH<sub>2</sub> twist and rock deformations in the molecule chain. Table A1 summarizes the bands assignment of the IR spectra of DTBU together those that appear of the 6MP in the mixed monolayer (Figure A2-C).

**Table A1.** IR bands in the region 1000-3100  $\text{cm}^{-1}$  for DTBU [350] and 6MP [351, 352] in the spectra of the Figure A2.

$\nu / \text{cm}^{-1}$	Assignment	Sample
1110	$\underline{\text{C}}-\underline{\text{O}}-\text{R}$ ester stretching	DTBU
1165	$\underline{\text{O}}-\underline{\text{C}}=\text{O}$ ester symmetric stretching	
1237	CH <sub>2</sub> twist/rock deformation	DTBU SAM
1277	$\underline{\text{O}}-\underline{\text{C}}=\text{O}$ ester asymmetric stretching, CH <sub>2</sub> twist/rock deformation	DTBU
1321	CH <sub>2</sub> wagging deformation	DTBU-6MP-SAM
1367	CH <sub>3</sub> isobutyl s'' symmetric stretching	DTBU
1389	CH <sub>3</sub> isobutyl s' symmetric stretching	
1442	CH <sub>2</sub> scissoring deformation	
1464	CH <sub>3</sub> asymmetric stretching	
1486	C-N 6MP ring stretching	
1560	C-N 6MP ring stretching	DTBU-6MP-SAM
1690	C-N 6MP ring stretching bond to gold	
1735	C=O ester stretching	
2852	C-H symmetric stretching of CH <sub>2</sub>	DTBU
2928	C-H asymmetric stretching of CH <sub>2</sub>	
2960	C-H 6MP ring stretching	
2960	C-H 6MP ring stretching	DTBU-6MP-SAM

In contrast to what was previously observed, the presence of 6MP in a small proportion in the mixture with DTBU results in a mixed monolayer, whose spectrum (Figure A2-C) is very different of that DTBU (Figure A2-B). The intensities and broadness of the DTBU bands are affected, and a set of new signals corresponding to 6MP appears. In particular, the bands at 1486, 1560 and 1690  $\text{cm}^{-1}$  that are assigned to the C-N stretching modes of the 6MP rings, the latter being a clear indicator of the interaction of 6MP with the surface of Au [4]. In addition, a prominent shoulder appears at 2960  $\text{cm}^{-1}$  that is assigned to the C-H tension in the ring. In the region of low frequency, it is of interest the appearance of a shoulder highlighted at 1321  $\text{cm}^{-1}$  that corresponds to the CH<sub>2</sub> deformation of the DTBU chains (wagging). This fact, together with the decrease and disappearance of other bands of the chain of this molecule, suggests a great influence of 6MP on the mixed monolayer. Since the DTBU: 6MP initial ratio is 95:5, a homogeneous macroscopic distribution of 6MP is suggested on the surface covered by mixed SAM such that DTBU chain interactions decrease despite 6MP being the minor initial component.

## Electrochemical results. Redox pair.

For the  $\text{Ru}(\text{NH}_3)_6^{3+/2+}$  and FcMeOH probes, no significant changes are observed in both the voltammograms and the profiles of the Nyquist plots on the DTBU films compared to that observed on the bare electrode (Figure A3).

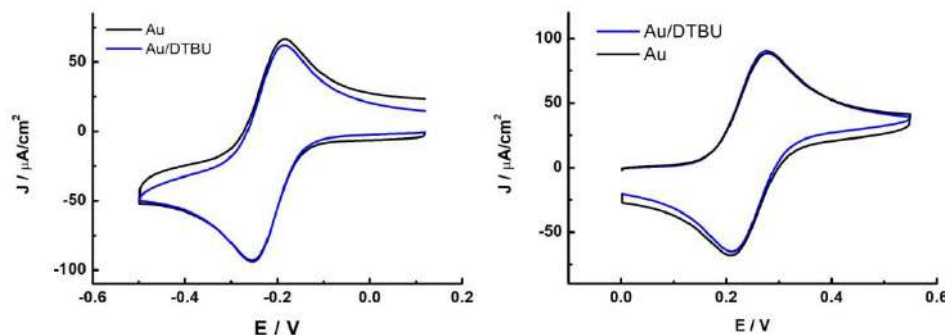


**Figure A3.** CV of  $\text{Ru}(\text{NH}_3)_6^{3+/2+}$  (left) y ferrocene-methanol (right) 1 mM in  $\text{KNO}_3$  0.1 M on bare Au, and Au-DTBU SAM. 0.1 V/s.

This behavior suggests that these probes penetrate at least up to distances, with respect to the electrode, which does not appreciably disrupt the rate of the electronic transfer. A Randles circuit has been used using a CPE to represent the electric double layer for the fits of the impedance spectra. Table A2 summarizes the results for the charge transfer resistance,  $R_{CT}$ , and the parameter  $n$  of the interface, determined according to the fit made.

**Table A2.**  $R_{CT}$  and  $n$  parameters of the fitting (Randles circuit) of the impedance spectrum of the redox probes studied.

EIS	$\text{Fe}(\text{CN})_6^{3-/4-}$ ( $E_{dc}=+0.220\text{V}$ )		$\text{Ru}(\text{NH}_3)_6^{3+/2+}$ ( $E_{dc}=0.190\text{V}$ )		FcMeOH ( $E_{dc}$ $=+0.245\text{V}$ )	
C. Randles	$n$ (CPE)	$R_{CT}/k\Omega$	$n$ (CPE)	$R_{CT}/k\Omega$	$n$ (CPE)	$R_{CT}/k\Omega$
Au	0.9275	0.031	0.9689	0.0640	0.9300	0.110
Au/DTBU	0.8804	6.33	0.9193	0.0414	0.9114	0.085

The greatest sensitivity to modification of the electrode is highlighted with the  $\text{Fe}(\text{CN})_6^{3-/4-}$  pair where  $R_{CT}$  increases notably in the presence of DTBU monolayer. The values of  $n$  for the modified electrode oscillate around 0.8 and 0.9, according to the type behavior of a CPE to represent the electric double layer.

## References Appendix A.

- [1] D. Briggs, G. Beamson, XPS Studies of the Oxygen-1S and Oxygen-2S levels in a Wide-Range of Functional Polymers, *Anal. Chem.* 65(11) (1993) 1517-1523.
- [2] M.C. Bourg, A. Badia, R.B. Lennox, Gold-sulfur bonding in 2D and 3D self-assembled monolayers: XPS characterization, *J. Phys. Chem. B* 104(28) (2000) 6562-6567.
- [3] Q.J. Yu, X.H. Ma, Z. Lan, M.Z. Wang, C.J. Yu, Structure Transition of CuOX Nanoparticles in Copper-Silica Nanocomposites, *J. Phys. Chem. C* 113(17) (2009) 6969-6975.
- [4] A.J. Viudez, R. Madueno, T. Pineda, M. Blazquez, Stabilization of gold nanoparticles by 6-mercaptopurine monolayers. Effects of the solvent properties, *J. Phys. Chem. B* 110(36) (2006) 17840-17847.



### 3.7. Artículo 7.

*Formación de películas poliméricas tipo brush de poli(etilenglicol) empleando ATRP por mediación electroquímica iniciada en superficie (SI-eATRP).*



**Efficient formation poly(ethylene glycol) polymer brushes on gold electrodes via surface initiated electrochemical mediated ATRP (SI-eATRP)**

Miriam Chávez<sup>1\*</sup>, Jie Luo<sup>2</sup>, Marco Fantin<sup>2</sup>, Abdirisak A Isse<sup>2</sup>, Guadalupe Sánchez-Obrero<sup>1</sup>, Rafael Madueño<sup>1</sup>, José Manuel Sevilla<sup>1</sup>, Manuel Blázquez<sup>1</sup>, Teresa Pineda<sup>1</sup>

(1) Departamento de Química Física y Termodinámica Aplicada, Instituto Químico para la Energía y el Medioambiente, Universidad de Córdoba, Campus Rabanales, Ed. Marie Curie 2<sup>a</sup> Planta, E-14014 Córdoba, Spain

(2) Department of Chemical Sciences, University of Padova, Via Marzolo 1, 35131, Padova, Italy

**ARTICLE UNDER REVIEW**

## Abstract.

Electrochemically mediated surface-initiated atom transfer radical polymerization (SI-eATRP) is an interesting *grafting from* technique used to grow, in a controlled way, polymeric films from a wide range of surfaces, including metal substrates. Aqueous SI-eATRP offers an appealing strategy for the preparation of polymers by using water-soluble monomers, departing from oxidatively stable catalyst complex.

The goal of this work is to tailor compact poly-(oligo(ethylene glycol)methacrylate) (p-OEGMA) brushes on gold electrodes by combining the formation of self-assembled monolayers (SAMs) containing a suitable ATRP initiator molecule, and the SI-eATRP polymerization approach. We have investigated the effects of the SAM-initiator nature, the applied potential, and the duration of the polymerization process on the properties of the grafted p-OEGMA-brushes. In addition, we employ electrochemical quartz micro balance measurements to evidence the living character of the polymerization.

The final properties of the tailored p-OEGMA-brush are studied by CV and EIS, obtaining information of the electronic and ionic blocking behaviour of these films, under different experimental conditions. We get further information of structural conformation, composition and organization from different characterization techniques: IRRAS and XPS spectroscopies, contact angle measurements, and SEM and AFM microscopies. These techniques allow us to confirm that an efficient formation of p-OEGMA-brushes via SI-eATRP is achieved. Thus, the designed SI-eATRP system offers an interesting option to functionalize a wide variety of substrates with water-soluble and biocompatible monomers. Such coatings present potential applications in various fields, including biomedical applications.

*Keywords:* biocompatible polymers; SI-eATRP; electrochemistry; water-soluble polymers; poly-ethylene glycol; electrochemistry; surface chemistry; polymer brushes

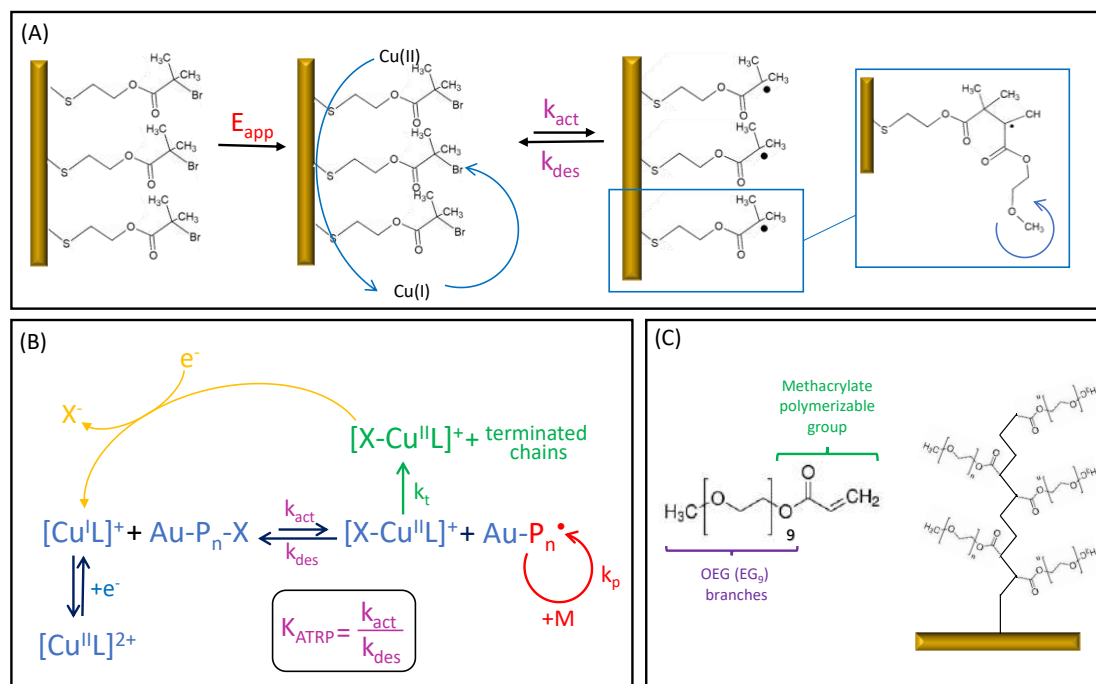
## Introduction.

Atom transfer radical polymerization (ATRP) is one of the most reliable methods for tailoring polymers of well-defined architectures, specific functional composition and low polydispersity [1,2], allowing the design of structures that could be implemented on different fields such as the biomedical [3-5] including the development of NMs [2,6]. Another aspect that makes ATRP attractive is that it can be carried out under mild experimental conditions, including aqueous media and room temperature [1,7] evolving in an environmentally friendly way [8,9]. A key for this evolution is the use of small amounts of copper complexes, from which the activator and deactivator species are continuously

produced. A wide variety of novel methods have been developed on that basis: ARGET- [10,11], ICAR- [12,13], SARA- [14,15], photo- [16,17], mechano- [18,19], sono- [20,21], and electrochemically mediated (e-) [22-29] ATRP have proven to be effective approaches that allow to reduce catalyst concentration down to ppm levels. Although these strategies have been created for solution polymerization, the same principles can be extended to polymerization from metal substrates [30-32], protein [33,34], membranes [35,36], and even nanoparticle surfaces [37,38], through ATRP initiated from a surface (SI-ATRP) that is an useful strategy to functionalize such a variety of substrates.

The Scheme 1 outlines the mechanism of electrochemically SI-ATRP (SI-eATRP), catalyzed by Cu complexes of multidentate nitrogen-based ligands (L), for tailoring polymer brushes on gold substrates bearing the initiator molecules. In the absence of mass transport limitations, the electrochemical reaction starts once an appropriate potential is applied to the working electrode, allowing the reduction of Cu(II) complex to produce the Cu(I) based-catalyst,  $[\text{Cu}^{\text{I}}\text{L}]^+$ , at the vicinity of the surface. Then, active  $[\text{Cu}^{\text{I}}\text{L}]^+$  reacts with the initiator molecules at the surface ( $\text{Au-P}_n\text{-X}$ ), producing  $\text{Au-P}_n\cdot$  radicals, and the deactivator complex,  $[\text{X-Cu}^{\text{II}}\text{L}]^+$ . The generated  $\text{Au-P}_n\cdot$  propagates and increases the length of the molecular chain by adding monomer units, before being caught by  $[\text{X-Cu}^{\text{II}}\text{L}]^+$ , generating again  $[\text{Cu}^{\text{I}}\text{L}]^+$  and the dormant  $\text{Au-P}_n\text{-X}$  molecular chain. The equilibrium constant  $K_{\text{ATRP}}$  must be shifted to the left to retain chain-end functionality and low radical concentration, thus maintaining control over the reaction. However, polymerizations in aqueous media present large  $K_{\text{ATRP}}$ , so keeping control over the process is more complicated than in organic solvents [39]. In addition, aqueous medium is awkward because the  $[\text{Cu}^{\text{I}}\text{L}]^+$  catalyst tend to disproportionation and the Cu deactivator complexes present poor halidophilicity [138]. Different strategies are commonly employed to avoid these drawbacks, as the use of tris(2-pyridylmethyl)amine (TPMA) to obtain the complex  $[\text{Cu}^{\text{II}}\text{TPMA}]^{2+}$  that presents high stability in a wide pH range, while its catalyst form,  $[\text{Cu}^{\text{I}}\text{TPMA}]^+$  presents a slow disproportionation. The poor halidophilicity of the deactivator  $[\text{XCu}^{\text{II}}\text{L}]^+$ , which leads to dissociation to  $\text{X}^-$  and  $[\text{Cu}^{\text{II}}\text{L}]^{2+}$  and hinders the control over the polymer growth, can be prevented by using a large excess of halide ions in respect to the complex (i.e.  $[\text{X}^-]/[\text{Cu}^{\text{II}}\text{TPMA}]^{2+} \gg 1$ ) [7,40].

Thus, SI-eATRP is an appealing option as the polymerization conditions can be easily modulated by selecting an applied potential,  $E_{\text{app}}$ , that modulate the ratio  $\text{Cu(II)}/\text{Cu(I)}$  according to the Nernst equation and so the polymerization rate. Such electrochemical setup has been successfully applied to tailoring polymers such as poly-/oligo-(ethylene glycol) (meth)acrylates, hydroxyethyl methacrylate, and (meth)acrylamides on metal substrates [30,31].



**Scheme 1.** SI-eATRP mechanism: (A) in the presence of DTBE-SAM. (B) Whole mechanism. (C) Molecular structure of the OEGMA monomer and schematic representation of the bottlebrush tailored from the surface.

Many studies have been focused on the improvement of surface properties by using poly-ethylene glycol (EGn)-based molecules, across the PEGylation strategy [41], due to their excellent antifouling abilities, biodegradability, and biocompatibility. We have dedicated a great effort to study EGn films employing the *grafting to* approach through the formation of self-assembled monolayers (SAMs) [42-45]. The self-assembly methodology starts with EGn-SH molecules of a definite size that upon contact with the gold metal surface can bind through an Au-S bond. Depending on several factors, the anchored chains adopt a specific conformation that ultimately define the grafting density. In contrast, by using the *grafting from* strategy, such as SI-eATRP, the grafted PEG-based molecular chain would present a different structural organization since they are not linear EGn molecules, but tailored structures made of a carbon-carbon backbone with oligo(ethylene glycol) ethyl ether methacrylate (OEGMA) branches (Scheme 1C), thus obtaining p-OEGMA brushes. We thus find that SI-eATRP is an attractive tailoring strategy because it provides well-controlled ATRP synthesis of homogeneous, compact films of high quality.

A key feature on SI-eATRP is the nature and chemical properties of the initiator molecules. As they are attached to the electrode surface in the form of a SAM (**Scheme 1A**) they can block the electron transfer of the redox catalyst in solution. Thus, it is required that the selected initiator structure permits the electron transfer of the catalyst. In this sense, the long chain molecule 11,11'-dithiobis[1-(2-bromo-2-methylpropionyloxy)undecane]

(DTBU) that have been widely used in conventional SI-ATRP is not appropriate as the DTBU-SAM completely block the electron transfer of the catalyst [31]. A nice approach is to build a mixed monolayer that include other molecules that would introduce charge transfer pathways to facilitate the electron exchange. In a recent work, we have found that 6-mercaptopurine (MP) is useful to prepare mixed monolayers with DTBU for SI-eATPR [46]. Another approach is to use molecules with the same terminal functional group but shorter alkane arm (2,2'-dithio-bis[1-(2-bromo-2-methylpropionyloxy)ethane] (DTBE)) as they allow the electron transfer of the catalyst [30].

In the present work, we use the SI-eATRP approach to tailor ethylene glycol-based polymer brushes (p-OEGMA) on either poly-crystalline or single crystal gold electrodes. We use  $[\text{BrCu}^{\text{I}}\text{TPMA}]^+ / [\text{BrCu}^{\text{I}}\text{TPMA}]$  as complex, oligo(ethylene glycol) methyl ether methacrylate (OEGMA<sub>500</sub>) as monomer, and tetraethylammonium bromide (TEABr) as supporting electrolyte. The role of the initiator structure and the polymerization conditions (through the parameters  $E_{\text{app}}$  and reaction time) on the properties of the tailored p-OEGMA-brush are investigated. Specifically, electrochemical techniques such as CV, chronoamperometry, EQCM and EIS, in the presence and absence of redox probes, are used to generate and evaluate the electronic and ionic blocking properties of the polymer films. For further characterization of the structures, we have employed IRRAS and XPS spectroscopies, contact angle measurements, SEM and AFM.

## Experimental section.

### Chemicals.

Bis[2-(2'-bromoisobutyryloxy)ethyl]disulfide (DTBE), bis [2-(2'-bromoisobutyryloxy) undecyl] disulfide (DTBU), tris(2-pyridylmethyl)amine (TPMA), 6-mercaptopurine monohydrate (6MP), tetraethylammonium bromide (TEABr), potassium hexaferricyanide ferrocenemethanol, and hexaamineruthenium chloride were purchased from Sigma-Aldrich (purity  $\geq 99\%$ ) and used without further purifications. Oligo(ethylene glycol) methyl ether methacrylate (OEGMA) monomer (average  $M_n$  500, Sigma-Aldrich) was purified by passing it through a column filled with basic aluminium oxide, to remove commercial inhibitors. Then, it was stored at 4°C and promptly used. The rest of the reagents were from Merck analytical grade. All solutions were prepared with deionized ultrapure water produced by Millipore system (Mili-Q).

### Experimental methods.

Electrochemical experiments were performed on an Autolab (Ecochemie model Pgstat30) instrument attached to a PC with proper software (GPES and FRA) for the total

control of the experiments and data acquisition. All electrochemical experiments were performed under inert atmosphere of  $N_2$  at room temperature. Except for polymerization experiments, a conventional three electrode cell comprising a platinum coil as counter electrode, a 50 mM KCl calomel (CE 50 mM) as reference electrode and either a polycrystalline (p-Au) or a single crystal (111) gold (m-Au) as the working electrodes (WE), were used. For polymerizations, the platinum coil counter electrode was substituted for a graphite rod. Moreover, it was separated from the working solution by a glass frit containing the same electrolyte solution used in the WE compartment, and a methylcellulose gel saturated with  $Et_4NBF_4$ . The p-Au electrode was a flat square plate ( $1 \times 1 \text{ cm}^2$ ). The m-Au single crystal was from Arrandee™ (based on a 250 nm thick Au layer adhered to a 2.5 nm thin chromium layer deposited on a Borosilicate glass  $11 \times 11 \text{ mm}$  flat surface). Before each experiment, the WE were annealed in a natural gas flame to a light-red melt, cooling down in air and then transferred to the electrochemical cell. Surface conditions were confirmed by CV shapes recorded in 0.01 M  $HClO_4$ . This treatment was the most appropriate for generating a surface that was clean, ordered, and reproducible.

The CVs and EIS for the evaluation of the electron transfer of redox probes were recorded in aqueous solutions of  $KNO_3$  0.1 M in the presence of 1 mM  $[Fe(CN)_6]^{3-/4-}$  at 0.1 V/s scan rate. The EIS experiments were recorded at the midpoint potential of the CV for the naked electrode (0.08 V). The spectra in the absence of the redox couples were recorded in aqueous solutions of 0.1 M  $NaClO_4$  at different potentials. The frequency range used in all experiments was from 100 kHz to 0.1 Hz and the pulse amplitude of 10 mV.

The EQCM used was a CHI 400c series. The quartz crystals were covered by a layer of Ti of 100 Å and a layer of polished gold of 1000 Å. These crystals work at 8 MHz. The mass deposited was obtained by the Sauerbrey equation by using a calibration constant of 1.4 ng/Hz [47].

Gel permeation chromatography (GPC) was used to determine the number average molecular weight ( $M_n$ ) and polydispersity (PDI,  $\mathcal{D}$ ) values, using an Agilent 1260 Infinity GPC, equipped with a refractive index detector and two PLgel Mixed-D columns ( $300 \text{ mm} \times 5 \mu\text{m}$ ) connected in series. The column compartment and the detector were thermostated at 70°C and 50°C, respectively. The eluent was a 10 mM solution of LiBr in DMF at a flow rate of 1 mL/min. The column system was calibrated with 12 linear poly(methyl methacrylate) (PMMA) commercial standards ( $M_n=640-1560000$ ). Monomer conversion was determined by  $^1H$ -NMR spectroscopy with a Bruker 200 MHz instrument, using  $D_2O$  as solvent and different internal standards depending on the experiment.

Infrared-reflection absorption spectroscopy (IRRAS) was measured on a JASCO 6300 FTIR single (He-Ne) laser beam spectrometer in the  $400-4000 \text{ cm}^{-1}$  wavenumbers range at



a resolution of  $4\text{ cm}^{-1}$ . The data were acquired and further analysed by the integrated software (Spectra Manager). A variable angle specular reflectance accessory (Pike Technologies-VeeMAX™) enabled samples to be analysed with a p-polarized laser incident beam at a grazing angle of  $80^\circ$ . The reflected IR signal was collected by a MCT-detector. Prior to the measurements, the interferometer and the sample compartments were purged with a dry and free  $\text{CO}_2$  air flux of  $8\text{ L/min}$  supplied by a compressed air adsorption dryer (K-MT LAB, Parker/Zandet GmbH&Co.KG).

XPS analysis was performed using an MCD SPECS Phoibos 150 spectrometer (from the Servicio Central de Apoyo a la Investigación (SCAI) of the Universidad de Córdoba) employing non-monochromatized ( $12\text{ kV}$ ,  $300\text{ W}$ ) Mg Ka radiation ( $1253.6\text{ eV}$ ). The substrate was mounted on a steel sample holder and transferred to the XPS analytical chamber. The working pressure was less than  $5 \cdot 10^{-9}\text{ Pa}$ . The spectra were collected using a take-off angle of  $45^\circ$  respect to the sample surface plane. The spectrometer was calibrated by the binding energy (BE) of the Au  $4f_{7/2}$  line at  $84.0\text{ eV}$ . The standard deviation for the BE values was  $0.2\text{ eV}$ . Survey scans were run in the  $0\text{-}1100\text{ eV}$  range (pass energy  $60\text{ eV}$ ), and higher resolution scans were recorded for the C  $1s$ , O  $1s$  and Au  $4f$  regions. The analysis involved Shirley background subtraction, and whenever necessary, spectral deconvolution was carried out by nonlinear least-squares curve fitting adopting a Gaussian sum function, employing the software CASA-XPS.

Contact Angle measurements were conducted by using an Optical Tensiometer Theta T200 device (Attension, Biolin Scientific) equipped with a high-speed camera ( $420\text{ fps}$ ), with a disposable pipette tip. Measurements were performed in sessile drop method. Milli-Q water was used as measuring fluid. Experimentally, the measurement was made by dropping a constant volume ( $2\ \mu\text{L}$ ) onto modified m-Au electrodes and recording the image of the drop. The results are given as an average of at least six measurements.

Scanning electron micrographs (SEM) were obtained using a JEOL JSM 6300 SEM (from the Servicio Central de Apoyo a la Investigación (SCAI), Universidad de Córdoba), equipped with a field emission electron gun. The magnification of the focus was varied until obtain good resolution and a clear signal of the growth polymer was recorded. Thereupon, micrographics in different regions of the substrate were taken.

Atomic Force Microscopy (AFM). Surface topography and adhesion images were acquired in the quantitative imaging (QI) mode using a JPK Nanowizard 4 AFM instrument with a Vortis Advanced SPM controller (JPK Instruments, Germany). Antimony (n) doped silicon probes, coated with reflective aluminum and nominal frequency  $320\text{ kHz}$ , nominal spring constant  $37\text{ N/m}$ , and tip radius  $<10\text{ nm}$ , were used (TESPA-V2 Bruker). Images were acquired at a  $256 \times 256$  pixels resolution with a fixed force setpoint of  $5\text{ nN}$  and an

indentation speed of 60  $\mu\text{m/s}$ . The spring constant of the cantilever was calibrated before every experiment by using the thermal noise method implemented in the JPK software Calibration Manager. p-OEGMA-brushes samples were measured in air at 24 °C inside a low-noise acoustic enclosure. Scan areas from 1 to 25  $\mu\text{m}^2$  were found adequate for the structure characterization of the films on at least 5 different spots of the m-Au substrates and its subsequent statistical analysis. Height of the films from different sections of the line profiles, average, mean and RMS roughness were determined from the analysis of the topographic images by using the JPK Data Processing software (JPKSPM v.7.0.163).

### Formation of Self-assembled monolayer for SI-eATRP

The SAMs of the initiator molecules were prepared by overnight immersion of freshly annealed substrates in an ethanolic thiol solution containing the initiator, either DTBE (1 mM) or a mixture of DTBU:6MP (90/10) at a total concentration of 1 mM.

### Electrochemically Mediated ATRP of OEGMA

The detailed procedure for p-OEGMA-brush formation on a conventional cell is described below. First, the polymerization solution containing  $\text{CuBr}_2$  (1 mM), TPMA (1 mM), TEABr (0.1M) and OEGMA monomer (10% vol) was prepared, and the pH was kept constant (c.a. pH = 6.0) during all the process. After bubbling nitrogen for at least 30 min, a CV was recorded to check the extent of electron transfer and to select the  $E_{\text{app}}$  to perform the polymerization. By the application of the appropriate potential, the catalyst  $[\text{Cu}^{\text{I}}\text{TPMA}]^+$  is generated in the vicinity of the WE. Considering that in SI-eATRP the initiator molecules are anchored to the WE surface, stirring was avoided to keep active  $[\text{Cu}^{\text{I}}\text{TPMA}]^+$  species near them. At the end of the electrolysis, the p-OEGMA-brush decorated Au electrodes were gently washed with water and dried under a nitrogen-flow before any other experiment.

### EQCM evaluation of the SI-eATRP

Polymerization experiments were performed in an EQCM to evaluate the kinetics and the living character of eATRP. EQCM experiments were conducted starting with an electrode covered with a homogeneous initiator monolayer, to create an easy-reproducible starting surface. Before each experiment, the sensor was allowed to equilibrate at OCP, and then, the SI-eATRP reaction was initiated by the application of the appropriated potential. The working solution contains the same components as in the conventional setup.

## Results and Discussion

### Electrochemical evaluation of the reaction medium

Preliminary experiments were run by recording CVs of the copper redox complex as a screening method to select the appropriate conditions to perform the polymerization reaction (Figure 1) [22]. Due to the well-known low bromidophilicity of  $[\text{Cu}^{\text{II}}\text{TPMA}]^{2+}$  in aqueous solutions [48], we add a large excess of  $\text{Br}^-$  ions relative to the catalyst complex (i.e. 100-fold molar excess), ensuring a large excess of  $[\text{BrCu}^{\text{II}}\text{TPMA}]^+$  deactivator species in solution [27]. Accordingly, the observed signal is due to the electron transfer of  $[\text{BrCu}^{\text{II}}\text{TPMA}]^+ / [\text{BrCu}^{\text{I}}\text{TPMA}]$  redox couple. The half wave potential of  $[\text{BrCu}^{\text{II}}\text{TPMA}]^{2+} / [\text{BrCu}^{\text{I}}\text{TPMA}]^+$  redox couple on the bare p-Au surface was  $E_{1/2} = -0.39$  V, with a difference between anodic and cathodic peak potentials of ca. 90 mV, in agreement with literature [23]. Upon addition of OEGMA, a positive shift of 40 mV ( $E_{1/2} = -0.35$  V) is observed, probably caused by the change in the dielectric constant of the medium, which also affects the diffusion coefficient ( $D$ ) and the electron transfer rate constant ( $k_0$ ) of the redox pair (Table S1) [49,50].

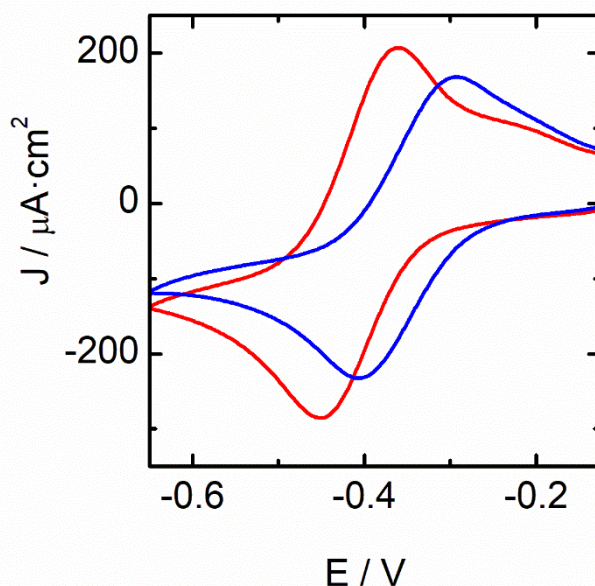


**Figure 1.** CVs of 1 mM  $[\text{BrCu}^{\text{II}}\text{TPMA}]^+ / [\text{BrCu}^{\text{I}}\text{TPMA}]^+$  in 0.1 M TEABr aqueous solution in the absence (red) and in the presence of 10 %vol OEGMA monomer.

#### Tailoring an ATRP-initiator to the electrode surface

As the platform from which the SI-eATRP reaction will be performed must enable the electron transfer of the catalyst redox pair to generate the active form at the surface, we first check this by using different SAMs (Figure 2). As it has already been reported [31] the DTBU-SAM completely inhibits the catalyst electron transfer (Figure 2A), a mixed SAM where the DTBU is diluted with a more conductive molecule such as 6MP [51] has been prepared [46]. Likewise, the DTBE-SAM allows the electron transfer of the catalyst complex, in this case, due to the thinner formed film (Figure 2).

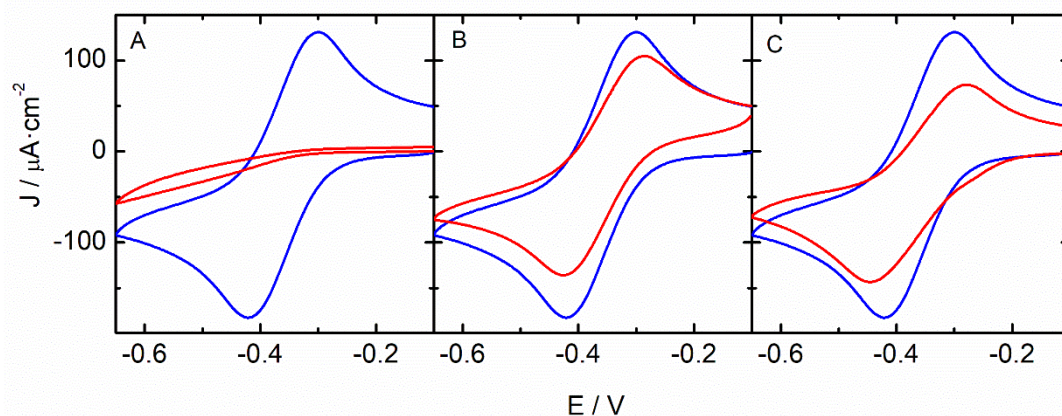


**Figure 2.** CVs of 1 mM  $[\text{BrCu}^{\text{II}}\text{TPMA}]^+ / [\text{BrCu}^{\text{I}}\text{TPMA}]^+$  redox pair in 0.1 M TEABr aqueous solution in the presence of 10 %vol OEGMA monomer, in naked p-Au electrode (blue line) and in the presence of different initiator-films: (A) DTBU-SAM, (B) DTBU:MP-SAM and (C) DTBE-SAM.

The important parameters affecting the overall properties of a polymer layer grafted from a surface by the eATRP approach, are the  $E_{\text{app}}$  at which the reaction is performed and the time of polymerization ( $t_p$ ). It is believed that the number-average molar mass of the brushes grafted from surfaces are of the same order of magnitude than those obtained on bulk systems, whose sizes are obtained by GPC [52,53]. Therefore, to establish a comparison with the surface-initiated experiments, we have found interesting to evaluate the effect of different  $E_{\text{app}}$  on the sizes of p-OEGMA-brushes prepared on homogeneous aqueous media.

To establish a potential range to evaluate the eATRP polymerization reaction, we recorded CVs on a naked p-Au electrode in the absence and presence of 2-hydroxyethyl 2-bromoisobutyrate (HEBiB), a water-soluble initiator, in solution (Figure S1). As expected, in the presence of HEBiB the cathodic peak markedly increases, while the anodic one almost disappears, as expected for a catalyst system [40]. Along the course of the reaction at the different  $E_{\text{app}}$ , aliquots were analysed by GPC (Figure S2) and  $^1\text{H}$  NMR to obtain the relative  $M_w$ ,  $M_w/M_n$ , and monomer conversion (Table S2 and S3). It can be observed that by applying higher potentials, we can improve the control over the process, obtaining lower polydispersity and almost complete monomer conversion, whereas the opposite trend is observed by using lower  $E_{\text{app}}$  values.

#### Monitorization of SI-eATRP by EQCM

The growth of p-OEGMA-brushes under SI-eATRP approach have been monitored by EQCM. As  $E_{\text{app}}$  modulate the amount of available catalyst and control the reaction speed, we have chosen two values, the first being one where the reaction does not take place and the second one varying within the interval in which the reaction proceeds. Then, we can change the course of the reaction in an “on - off” fashion [23]. We have noted that at  $E_{\text{app}} > -0.25$  V

no current is measured indicating that active  $[\text{Cu}^{\text{I}}\text{TPMA}]^+$  species are not produced, and the reaction does not initiate ( $E_{\text{app}}^{\text{off}} = -0.1 \text{ V}$ ). Now, to evaluate the “*living character*” of the polymerization system, we selected as second value,  $E_{\text{app}}^{\text{on}} = E_{1/2} = -0.35 \text{ V}$  (see Figure 2). The cumulative EQCM profile for p-OEGMA-brush growth (Figure 3) shows that upon applying  $E_{\text{app}}^{\text{on}} = -0.35 \text{ V}$ , the generation of the catalyst at the electrode surface is initiated, and immediately triggers a decrease in frequency. After 30 min a mass accumulation of  $0.11 \text{ ng}\cdot\text{s}^{-1}$  was obtained. At that time, the potential was newly changed to  $-0.10 \text{ V}$ , and almost no frequency changes were detected. Again, upon going back to  $-0.35 \text{ V}$ , approximately the same growing rate was registered. The observed behaviour clearly indicates that the SI-eATRP reaction system that we propose herein can be switched “*on*” and “*off*” by the application of the proper potential, evidencing the *living character* of the process. The quantification of the mass accumulation on the electrode surface during the first two hours of polymerization was consistent, indicating that free radical formation was negligible in comparison to radical propagating chains formation. If the reaction is continued by more than 3h, the incremental frequency slowed down until negligible mass increase was detected. This effect must be related to the higher thickness of the formed p-OEGMA brush, which can inhibit the catalyst formation, although the possible termination of the polymerization reactions cannot be discarded [1,54,55].

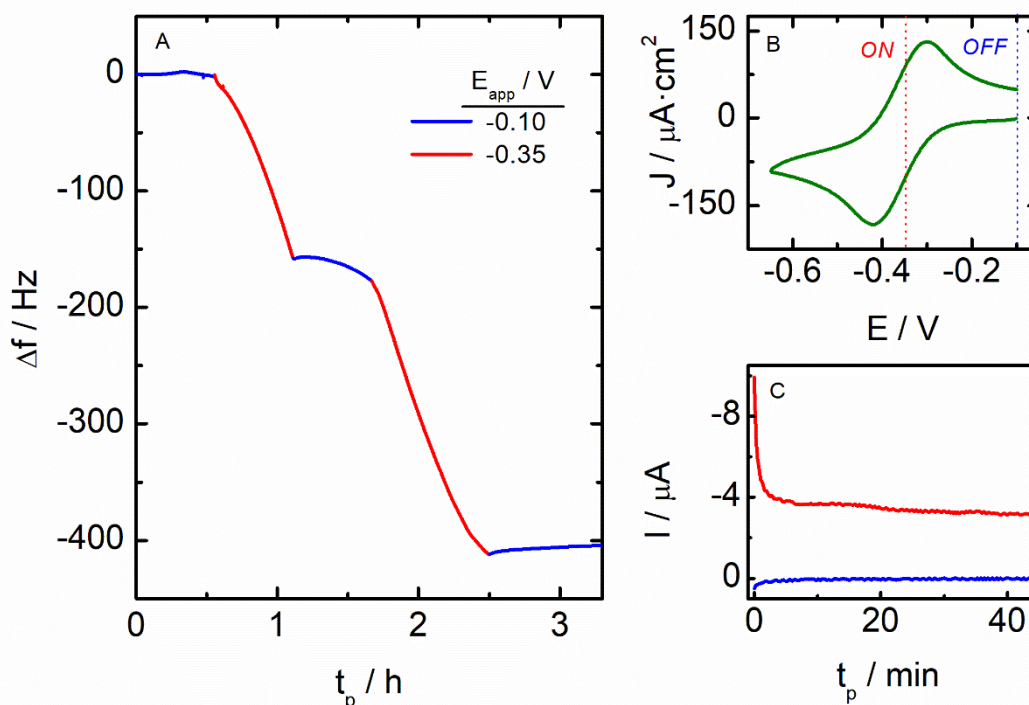


**Figure 3.** (A) Cumulative EQCM profile of p-OEGMA-brush growth. Red lines correspond to  $E_{\text{app}}^{\text{on}} = -0.35 \text{ V}$  (at which the p-OEGMA-brush is growing) and blue lines to periods recorded at  $E_{\text{app}}^{\text{off}} = -0.10 \text{ V}$ . (B) Schematic representation of CV of the  $[\text{BrCu}^{\text{I}}\text{TPMA}]^+ / [\text{BrCu}^{\text{II}}\text{TPMA}]^+$  redox pair: dotted lines represent the  $E_{\text{app}}$  values, and (C) chronoamperometric curves in response to the  $E_{\text{app}}^{\text{on}} / E_{\text{app}}^{\text{off}}$  potentials.

The chronoamperometric curves recorded at different  $E_{app}$  are similar in shape (Figure S3), showing the initial decay of current that indicate the production of the active catalyst  $[Cu^+TPMA]^+$ . This is followed for a steady current due to the regeneration of the complex that is immediately reduced in the vicinity of the working electrode and thus, the current never decreases to zero. The amount of stable current measured depends on both,  $E_{app}$  and the dissociation constant of the  $[BrCu^+TPMA]$  complex, from which the activator  $[Cu^+TPMA]^+$  is obtained (Scheme S1) [23]. We have also analyzed the simultaneous frequency changes and the corresponding mass increases measured in an interval of 2h polymerization time (Table 1). Lower  $E_{app}$  produced faster reactions that eventually lead to the complete loss of control over the polymerization due to radical-radical termination reactions [7]. When the polymerization reactions were performed within the interval  $-0.34 < E_{app} < -0.27$  V, an almost steady growth was observed, whereas at lower  $E_{app}$  a much higher frequency decrease is observed that is translated into a higher mass rise that can suppose the loss of polymerization control. Under these conditions, it is possible that the increase of mass corresponds not only to the formed polymer but also to some monomers trapped into the brushes as the reaction becomes very fast.

**Table 1.** Frequency changes and corresponding mass increases during the polymerization at different  $E_{app}$ .

$E_{app}$ / V	$-\Delta f$ / Hz	Mass rise / $ng \cdot s^{-1}$
<b>-0.27</b>	120	0.023
<b>-0.28</b>	130	0.025
<b>-0.30</b>	135	0.026
<b>-0.32</b>	140	0.027
<b>-0.34</b>	182	0.035
<b>-0.35</b>	567	0.110
<b>-0.36</b>	650	0.126
<b>-0.38</b>	760	0.148

Although the frequency changes measured correspond to an apparent mass increase which includes not only the formation of the p-OEGMA-film, but also the mass of solvent and other molecules that might be trapped in between, we have performed a rough approximation of the thickness of the obtained polymer brushes according to Eq. (1) [56],

$$\Gamma = d \cdot \rho_0 \quad (1)$$

where  $\Gamma$  is the surface concentration of p-OEGMA-chains, determined from EQCM measurements, and  $\rho_0$  is a fixed density value related to the nature of the molecules within the layer and  $d$  is the thickness of the film. Assuming that the major contribution of mass

increase is due to the polymer anchored at the electrode surface, we use the commonly employed density for PEG-based structures of  $1.08 \text{ g}\cdot\text{cm}^{-3}$ . The results are plotted in Figure 4.

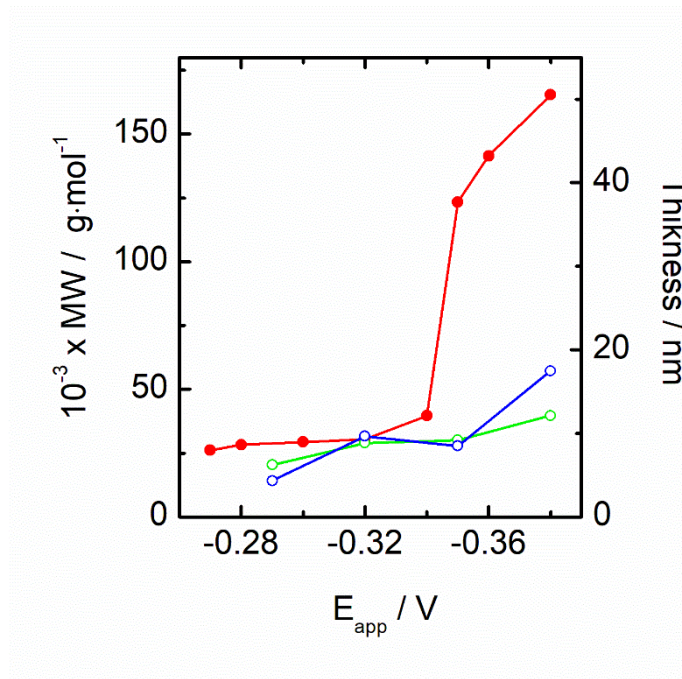
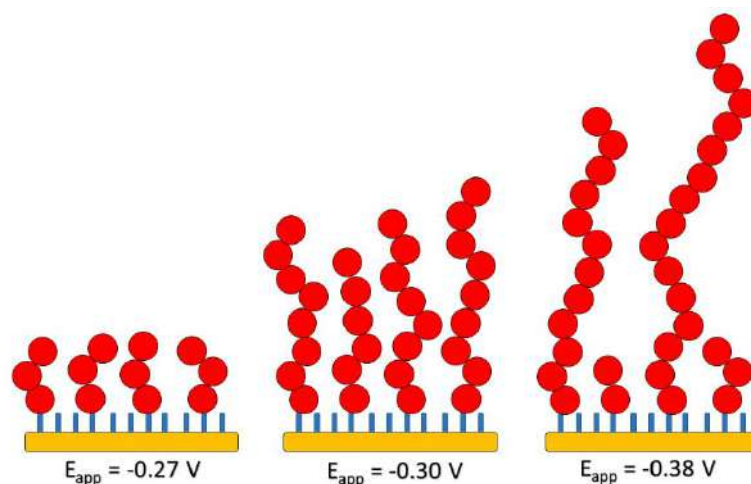


**Figure 4.** p-OEGMA thicknesses and MWs (red) determined by using equation (1) and grafting density of  $0.22 \text{ chains}/\text{nm}^2$ , respectively for the brushes formed at different  $E_{app}$ . MWs (green and blue) determined by eATRP (Table S3) are shown for comparison.

The determined thicknesses suggest, in a first approximation, that the control over the polymerization is maintained and that mass deposition clearly increases when using more negative  $E_{app}$  values. These apparent thicknesses present a balanced and progressive increase from 7 to 12 nm ( $-0.27 \text{ V} > E_{app} > -0.34 \text{ V}$ ). At lower potentials, the thickness increases abruptly indicating some loss of control in the polymerization reaction. Previous work dealing with the growth of OEGMA brushes by SI-ATRP [57] has reported the grafting density of the p-OEGMA brushes being on average  $0.22 \text{ chains}/\text{nm}^2$ , in agreement with other experimental determinations [58,59]. This grafting density supposes a compact packing of the p-OEGMA brushes that can be achieved when the attaching points on the surface are not limiting, as it is the present case. Considering this grafting density and the thickness determined above, an apparent MW for the p-OEGMA growth from the DTBE-SAM surface as a function of  $E_{app}$  can be determined (Figure 4). As commented above, the mass determined by EQCM is the wet mass that should contain the water molecules and other solution components that remain interacting with the OEGMA moieties, therefore, the determined MWs must be bigger than the real ones. Thus, we can conclude that the p-OEGMA obtained in the potential range  $-0.27 \text{ V} < E_{app} < -0.34 \text{ V}$  growth under polymerization

control, whereas at  $E_{app} < -0.34$  V the control is suddenly lost, and the polymers acquire a much higher molecular weight. However, the high mass rise measured under these conditions (Table 1) should be due not only to the formed polymer but also to trapped monomers within the film. Figure 4 also shows the MW of the p-OEGMA homogeneously growth in solution by eATRP, that are closer to the brushes formed under controlled conditions. Thus, we can conclude that the idoneous potential to perform the polymerization under these experimental conditions are those closed to the  $E_{1/2}$  of the  $[\text{BrCu}^{\text{II}}\text{TPMA}]^+ / [\text{BrCu}^{\text{I}}\text{TPMA}]^+$  redox pair and, when using lower values, the control over the reaction starts to get loss, increasing heterogeneity and surface roughness (**Scheme 2**).



**Scheme 2.** Schematic representation of p-OEGMA-brush tailored by using different  $E_{app}$ . The application of more negative potentials produces faster film formation, but at the expense of losing some control over the reaction. This results in the formation of thicker polymer films, but with more heterogeneities and defects.

Electrochemical characterization of p-OEGMA brushes.

The formed p-OEGMA-brushes growth from p-Au-SAM surfaces have been analysed through their effect on the heterogeneous electron transfer rate of different redox couples such as  $[\text{Fe}(\text{CN})_6]^{3-/4-}$ ,  $[\text{Ru}(\text{NH}_3)_6]^{3+/2+}$  and  $\text{Fc}(\text{MeOH})^{0/+}$ . In previous works, we and others have reported that  $[\text{Ru}(\text{NH}_3)_6]^{3+/2+}$  and  $\text{Fc}(\text{MeOH})^{0/+}$  redox probes are insensitive to the presence of several EGn-SAMs [42-44,60,61]. Despite the presumed different organization of the films formed through *grafting from* mechanisms, we found that these p-OEGMA-coatings show the same trend and they are only sensitive to the  $[\text{Fe}(\text{CN})_6]^{3-/4-}$  redox couple. We have analysed the influence of  $E_{app}$  and the polymerization time in the polymer formation by CV and EIS (Figure 5). For  $E_{app}$  of -0.30 and -0.35 V and 1.5 h of polymerization time, we obtain a strong but not complete inhibition of the electron transfer of  $[\text{Fe}(\text{CN})_6]^{3-/4-}$  redox couple. The extent of this partial blocking effect is better observed in the Nyquist plot. These spectra are fitted by using a Randles equivalent circuit (Scheme S3). We detect an increase of the semicircle diameter with decreasing  $E_{app}$  (Figure 5B) or longer



polymerization times (Figure 5D), by using -0.35 V as  $E_{app}$ . The presence of the linear region at low frequencies on the Nyquist plots points to the existence of some defects or pinholes that enable diffusion of the redox couple [62]. Charge transfer resistance,  $R_{ct}$ , extracted from the fitting are gathered in Table 2 and 3, and from them, the apparent rate constants ( $k_{app}$ ) of  $[Fe(CN)_6]^{3-/4-}$  probe in the presence of p-OEGMA brushes are determined by using Eq. (2) [63],

$$k_{app} = \frac{RT}{n^2 F^2 R_{ct} A c} \quad (2)$$

where R is the gas constant, T the temperature, F the Faraday constant, n the number of electrons, A the geometric area of the electrode and c the concentration of the redox couple. All the evaluated p-OEGMA-brushes produce a reduction on the  $k_{app}$  of at least two orders of magnitude comparing to bare gold ( $\sim 0.02 \text{ cm}\cdot\text{s}^{-1}$ ) [396]. Despite these values indicate that the polymer-brush exerts a significant blockage of the redox probe, tunnelling mechanism can be overlooked as significant currents are measured in the cyclic voltammograms. Additionally, we can use  $R_{ct}$  values to estimate the surface coverage ( $\theta$ ) by assuming that the registered current is due to the presence of defects in the film, by using Eqn. (3) [62,65]:

$$\theta = 1 - \frac{R_{ct}^{bare}}{R_{ct}^{p-OEGMA}} \quad (3)$$

It is interesting to note that  $R_{ct}$  values of the mixed initiator monolayer used in these studies, DTBU:MP-SAM, is comparable to that of the bare gold electrode. In this way, the calculated surface coverage (Tables 2 and 3), is mainly attributed to the presence of p-OEGMA brush onto the electrode. Consistently, we obtain lower apparent rate constants and greater surface coverages for the p-OEGMA films tailored by using more negative potentials or longer times during the electrolysis.

At this point, it is interesting to note that the electronic blocking properties of the p-OEGMA brushes grafted from a mixed DTBU:MP- or a DTBE-SAM are very similar with values of  $k_{app}$  of  $8.6\cdot 10^{-5}$  and  $4.4\cdot 10^{-5} \text{ cm}\cdot\text{s}^{-1}$ , respectively. Based on these results, we can conclude that, despite the nature of the initiator SAM, the tailored p-OEGMA brushes should be very similar, at least in respect to the properties that inhibit the electron transfer of the  $[Fe(CN)_6]^{3-/4-}$  redox probe. This fact has been also reported for SI-ATRP [66] with the finding that all the p-OEGMA films were resistant to protein adsorption independently of the initiator structure.

In this respect, we have tried the growth of p-OEGMA from a homogeneous DTBU-SAM by using an indirect method (Scheme S4). Now, the WE is used only to generate the catalyst and it is placed in a close distance of the DTBU-SAM substrate from which the polymer can grow. Thus, once the potential is applied, active  $[Cu^I TPMA]^+$  catalyst is

generated at the naked p-Au surface that diffuses and reaches the initiator-modified surface [67]. The resultant polymer presents a higher resistance to  $[\text{Fe}(\text{CN})_6]^{3-/4-}$  electron transfer when compared with those described above (Figure S4). The EIS signal obtained in the presence of this layer only shows a semicircle covering the complete frequency range, indicating absence of diffusion and probably, absence of defects, pointing out that we have tailored a compact and pinhole-free structure. The measured  $R_{\text{ct}} = 127.8 \text{ k}\Omega\cdot\text{cm}^2$  is almost two orders of magnitude larger than those obtained by the SI-eATRP approach.

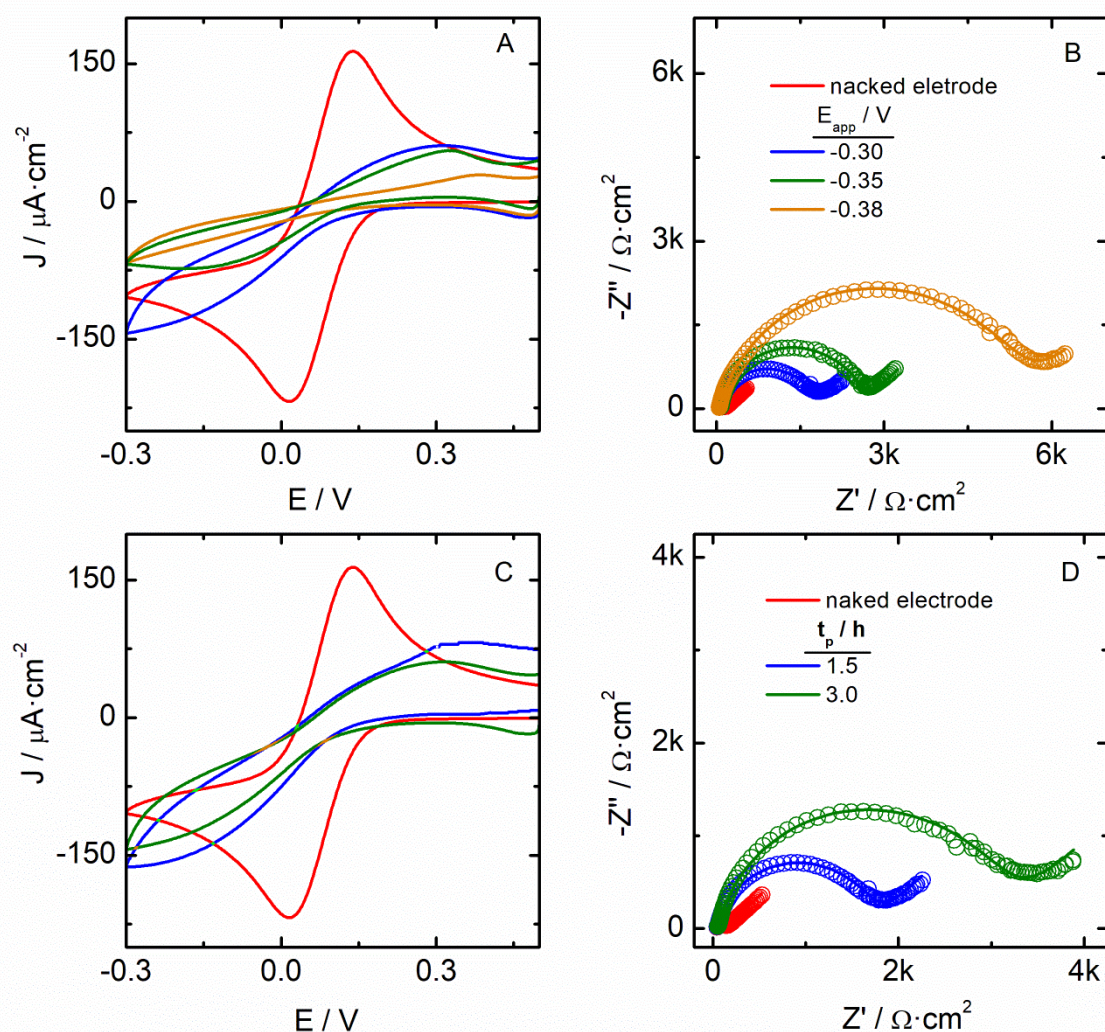


**Figure 5.** CVs (A,C) and EIS (B,D) of 1mM  $\text{K}_4[\text{Fe}(\text{CN})_6]$  in 0.1 M  $\text{KNO}_3$  in the presence of p-OEGMA-brushes formed varying the  $E_{\text{app}}$  (A,B) (and using 1.5h as polymerization time) or the polymerization time (C,D), with  $E_{\text{app}} = -0.35 \text{ V}$ . The red signals correspond to DTBU:6MP-SAM.

As a whole, these results indicate that there are clear differences on the blocking properties of p-OEGMA brush polymer growth by SI-eATRP when compared with those obtained by the grafting to approach of self-assembly using EGN-SH molecules [42-44]. By

SI-eATRP, we are probably tailoring thicker but also more heterogeneous films in comparison to those formed by employing the self-assembly strategy of grafting polymer molecules of definite chain lengths.

**Table 2.**  $R_{ct}$  data obtained by fitting EIS of 1mM  $[\text{Fe}(\text{CN})_6]^{3-/4-}$  in the presence of p-OEGMA brush formed varying  $E_{app}$ ; Electron transfer rate constants ( $k_{app}$ ) and surface coverage of p-OEGMA-brush determined by using Eqn. (2) and (3), respectively.

$E_{app} / \text{V}$	$R_{ct} / \text{k}\Omega \cdot \text{cm}^2$	Surface coverage, $\theta$	$k_{app} \cdot 10^4 / \text{cm} \cdot \text{s}^{-1}$
-0.30	1.7	0.932	1.6
-0.35	2.5	0.955	1.1
-0.38	5.4	0.979	0.51

**Table 3.**  $R_{ct}$  data obtained by fitting EIS of 1mM  $[\text{Fe}(\text{CN})_6]^{3-/4-}$  in the presence of p-OEGMA-brush formed varying the polymerization time by using an  $E_{app} = -0.35 \text{ V}$ ; Electron transfer rate constants ( $k_{app}$ ) and surface coverage of p-OEGMA-brush determined by using Eqn. (2) and (3), respectively.

Polym. time / h	$R_{ct} / \text{k}\Omega \cdot \text{cm}^2$	Surface coverage, $\theta$	$k_{app} \cdot 10^4 / \text{cm} \cdot \text{s}^{-1}$
1.5	1.7	0.932	1.6
3.0	3.1	0.963	0.86

Nevertheless, we must also consider the conformation of OEGMA chains within the film. Based on our study of the EG7-SAM on gold electrodes, we state that SAMs formed by using EGn-SH molecules tend to produce a surface packing in which EGn strands reach a helical conformation. Such structural organization generates highly hydrated interfaces in which water molecules show reduced mobility [42]. As water is a good solvent for EGn-based polymers, many H-bond interactions must take place within the film. Thus, we can suggest that the polymer brushes obtained by SI-eATRP are made up of branches growing parallel to the surface, among which empty volumes can be generated. These volumes could be occupied by water molecules which present higher mobility than those trapped within p-OEGMA chains and serve as channels for  $[\text{Fe}(\text{CN})_6]^{3-/4-}$  redox probes to diffuse to the electrode surface.

Another interesting property of the polymer films is the ability of ionic conduction. This can be checked by using the EIS technique in the absence of redox probes. We have measured the impedance spectra of the p-OEGMA film in 0.1 M  $\text{NaClO}_4$  electrolyte in a wide potential interval (Figure 6). The spectra represented as Bode phase angle plot show the typical behavior of a dielectric layer that is usually modeled by a series resistance,  $R_s$ , due to solution, leads, and contacts, in series with a capacitor associated with the monolayer.

While the phase angle is almost constant in a wide frequency interval (approximately  $80^\circ$ ), it never reaches the  $90^\circ$  value that would indicate an ideal capacitive behavior. This feature is indicative of a heterogeneous interface and should be represented by a constant phase element (CPE). Moreover, the spectra show an important decrease in phase angle at lower frequencies. Under these conditions, a parallel resistance,  $R_m$ , must be introduced in the RC circuit representing the capacitor behavior, to account for this deviation. As it has been described for well packed alkanethiol SAMs [68], the resistance of the monolayer,  $R_m$ , when the electroactive species are absent is infinite and there should not be current flow across the interface [69,70]. The phase angle and the capacitance values are almost constant independently of potential for p-OEGMA brushes growth from the DTBE-SAM. A variation of the phase angle reaching values as low as  $70^\circ$  at low and high potentials together with an increase in capacitance,  $6.1 \pm 0.7 \mu\text{F}\cdot\text{cm}^{-2}$ , in comparison with the  $4.0 \pm 0.5 \mu\text{F}\cdot\text{cm}^{-2}$  value obtained for the p-OEGMA growth from DTBE-SAM points to a more heterogeneous layer when DTBU:MP-SAM (Figure 6C). The same trend is observed for  $R_m$  ( $0.64$  and  $0.24 \text{ M}\Omega\cdot\text{cm}^2$ , for DTBE and DTBU:MP, respectively) indicating that ions diffusion is more probable in the later (Figure 6D). These results together suggest the presence of defects that enable the ingress of ions through the films as detected in the low frequency regime. These defects or channels facilitate the ionic permeability, and this should be related to the swelling behaviour of p-OEGMA-brushes. In fact, before the polymerization, water molecules are interacting with OEGMA monomer units and such interactions are maintaining once monomers are tailored, thus solvent molecules remain inside the formed film [71]. Moreover, under potential application and changing the frequency around it, the interactions can be disturbed, appearing new channels within the polymer brush that facilitate the movement of ions and/or solvent.

### Surface Characterization of p-OEGMA brushes.

To go deeply into the chemical composition of the p-OEGMA brushes growth via SI-eATRP, we have performed XPS measurements. Figure 7A shows the surveys of the p-OEGMA and the DTBE-SAM where it was grafted from for comparison. As it can be observed, there are important differences such as the lack of signal of the Au 4f signal that become attenuated by the presence of the thick p-OEGMA film evidencing that the polymer layer is thicker than the testing depth of the XPS. Moreover, p-OEGMA film survey shows stronger peaks corresponding to C 1s and O 1s that are recorder in higher resolution to be deconvoluted for a quantitative determination (Figure 7B). The carbon/oxygen molar ratio obtained is of 2.4, which agrees with the theoretical of 2.1. Similar C/O ratios have been reported for comparable p-OEGMA-films tailored by conventional ATRP [56,72]. The

deconvolution of the high-resolution C 1s spectrum gives three contributions (ether carbon atoms (CH<sub>2</sub>-O) at 286.4 eV, aliphatic carbon (CH<sub>2</sub>-CH<sub>2</sub>), at 285.0 eV and a small amount of carboxylate carbon (C=O) at 288.8 eV). In a similar way, the O 1s main peak shows two components, the biggest contribution at 532.8 eV corresponding to ether group (C-O), and a second signal ascribed to carbonyl (C=O) groups. It is important to note the absence of a copper signal, so that we can assume that no significant amount of such element, in any of its forms, remains within the tailored film.

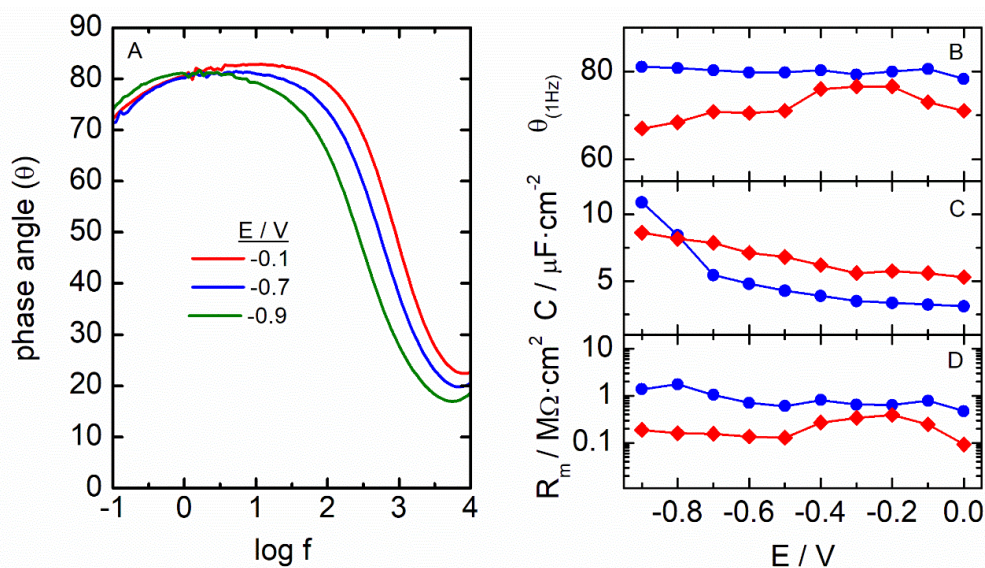


**Figure 6.** (A) Bode plots of p-OEGMA-brush grown using DTBE-SAM as initiator monolayer recorded in 0.1M NaClO<sub>4</sub> at different applied potentials. (B) Phase angles taken at the frequency of 1 Hz for the p-OEGMA-brush tailored from DTBE-SAM (blue) and DTBU:MP-SAM (red). (C) Double layer capacitance and (D) Monolayer resistance,  $R_m$ , versus applied potential taken from the fitting of the impedance spectra.

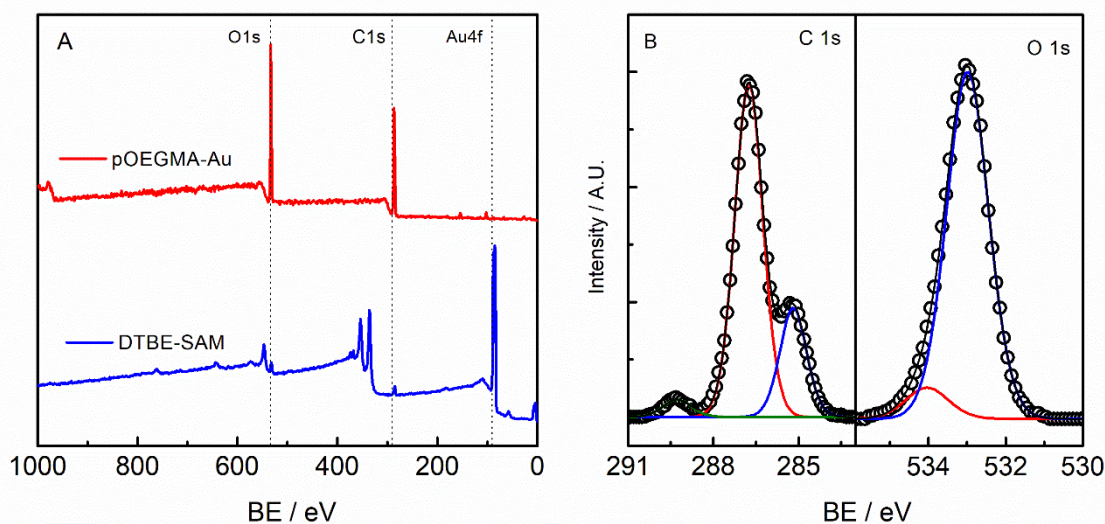


**Figure 7.** (A) Survey spectra of DTBE-SAM and pOEGMA-film growth from it. (B) High resolution scans recorded in the regions of C 1s and (C) O 1s for p-OEGMA brush.

Infrared absorption-reflection spectroscopy (IRRAS) can also add some information on the structure and conformation of the molecules in the film. The bulk spectrum of the OEGMA monomer is shown for comparison with the p-OEGMA film in Figure 8. Characteristic bands due to symmetric and asymmetric C-H stretching modes appears at ca. 2943 and 2875  $\text{cm}^{-1}$ , respectively. The C=O stretching band (1731  $\text{cm}^{-1}$ ) presents a slightly displacement from its position on the monomer (1715  $\text{cm}^{-1}$ ) and a broadening that can be due to the interaction through H-bonds in the polymer. In addition, we also detect peaks usually assigned to CH<sub>2</sub> bending (1450  $\text{cm}^{-1}$ ), CH<sub>2</sub> wagging (1350  $\text{cm}^{-1}$ ), and overlapping CH<sub>2</sub> twisting vibrations (1320-1240  $\text{cm}^{-1}$ ). The position and intensity of these later peaks that are in the fingerprint region and inform about the possibility of a helicoidal or all-trans conformation of the ethylene glycol chains [73], agree with an orientation almost parallel to the surface that precludes a further analysis of their conformation (Scheme 1C).

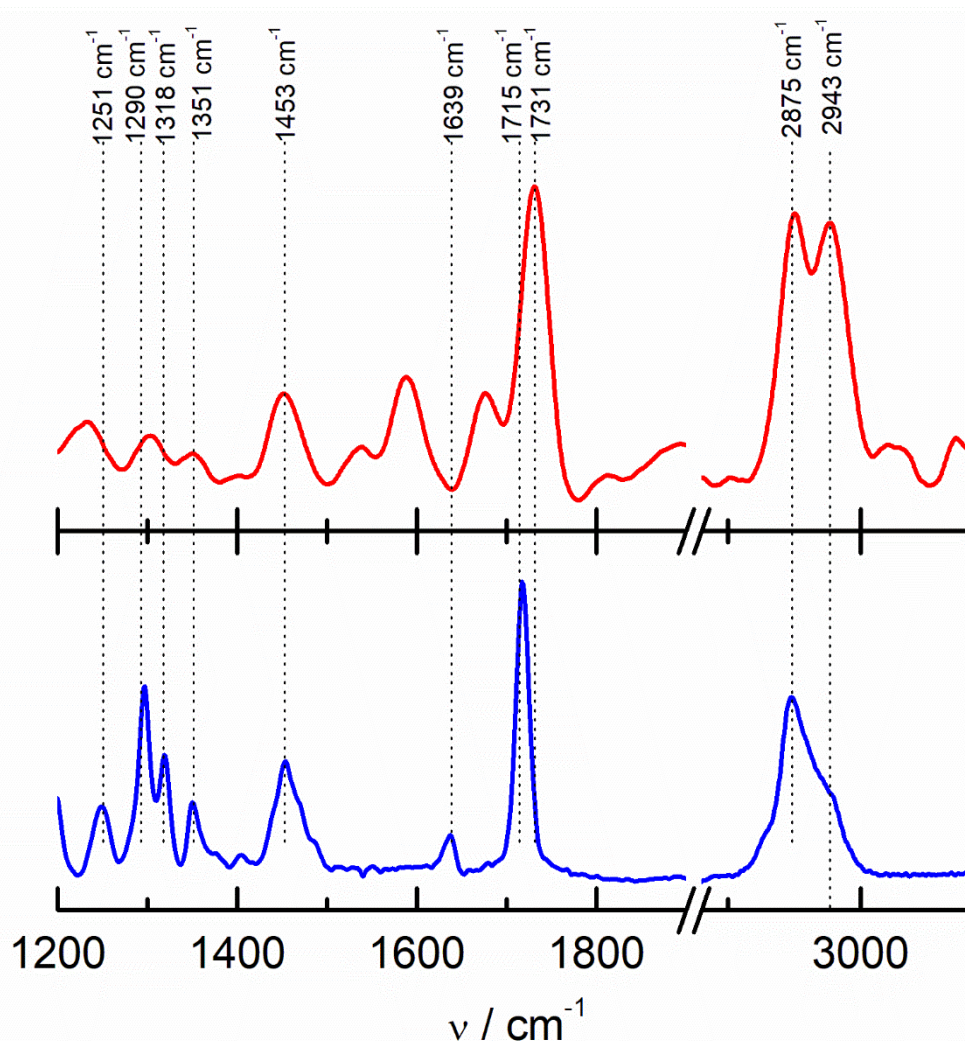


**Figure 8.** IRRAS spectra of free-monomer (blue) and p-OEGMA brush (red).

The hydrophilic nature of the p-OEGMA films differ from the hydrophobic character of the initiators SAM surfaces. Thus, water contact angles can give us a valuable information on the presence of these films on the surface. In fact, static contact angles measured for DTBE- and DTBU:MP-SAM are  $67^\circ$  and  $75^\circ$ , respectively. We have measured the contact angles of p-OEGMA formed at different  $E_{app}$ , and at different times during the polymerization process. However, the measured contact angles were always comprised within the range of  $46^\circ$  to  $53^\circ$ , despite the conditions. It seems that the p-OEGMA brushes tailored by the SI-eATRP method are compact enough to modify the wettability of the surface which becomes notably hydrophilic under all the checked conditions [66,72,74]. However, in comparison to the EG136-SAMs that show contact angles of 29 to  $36^\circ$ , a less hydrophilic character is found in the present case.

Finally, we have examined the polymer films by Sem and AFM. Representative images are shown in Figure S5 where it can be seen that the analysed samples contain large smooth homogeneous regions, without visible pinholes or defects (Figure S5A) together with some less compact and clearly more heterogenous patches (Figure S5B) that are easily distinguishable from the naked gold substrate (Figure S5C). A similar view offers the AFM images. Height images recorded at different regions are shown in Figure S6, together with the evaluation of the roughness-length plot. Interestingly, we found two patterns on the tailored film. On one side, we detect a homogeneous layer of  $18.3 \pm 7.3$  nm height, measured from the bottom of the substrate, which covers the entire surface. From it, the polymeric brush continued growing in a more irregular manner, giving a structural map that presents regions reaching between 32.9 and 51.5 nm total height. Roughness parameters,  $R_q$  and  $R_a$ ,  $3.70 \pm 0.49$  nm and  $5.95 \pm 0.90$  nm, respectively, are consisting with the latter, confirming the formation of a brush with uneven surface topography. In addition, the obtained heights are in agreement with the average thickness of p-OEGMA film determined with EQCM data and built under the same polymerization conditions, revealing the heterogeneity of the p-OEGMA films growth under these conditions.

## Conclusions.

We have effectively tailored p-OEGMA brushes onto gold substrates by SI-eATRP, a *grafting from* approach. EQCM has proved the living character of the polymerization setup proposed herein and allowed us to further investigate the effect of the  $E_{app}$  on the polymerization rate. The obtained results indicate that there is a wide potential range in which the control over the polymerization is retained. Thus, p-OEGMA brushes tailored by

applying such potential values result in relatively uniform surfaces. However, p-OEGMA films electronic blocking properties as measured by using a redox probe, as well as its ionic insulating properties, suggest the existence of some pinholes and/or channels within the formed film, that allow both, the electron transfer of  $[\text{Fe}(\text{CN})_6]^{3-/4-}$  redox probe, and the movement of ion/solvent through the film. The obtained films show similar properties despite the nature of the initiator-SAM used for grafting the polymer, although some small differences can be found when analyzing the ionic permeability that indicates that the p-OEGMA grafted from a DTBU:6MP-SAM is somewhat more heterogeneous.

The mass deposition measured by EQCM allow us the estimation of the average thickness of p-OEGMA brushes that are similar to these obtained by AFM measurements. The analysis of the topography and surface roughness suggest that the tailored films present some imperfections. SEM, AFM, XPS and CA measurements are also consistent with the formation of thick but not completely homogeneous layers. Moreover, IRRAS points to the formation of brushes with the ethylene glycol chains attached to a central chain in an orientation almost parallel to the substrate surfaces. It is interesting to note that no copper deposition has been detected by either EQCM or XPS measurements. This is essential to validate the SI-eATRP setup proposed herein. Based on the results obtained in this work, we are able to tailor quality p-OEGMA brushes that are potential candidates to be applied on a huge range of fields.

## References.

- [1] K. Matyjaszewski, Atom Transfer Radical Polymerization (ATRP): Current Status and Future Perspectives, *Macromolecules* 45(10) (2012) 4015-4039.
- [2] K. Matyjaszewski, Advanced Materials by Atom Transfer Radical Polymerization, *Adv. Mater.* 30(23) (2018).
- [3] P. Gurnani, S. Perrier, Controlled radical polymerization in dispersed systems for biological applications, *Progress Polymer Sci* 102 (2020).
- [4] Y. Miura, Controlled polymerization for the development of bioconjugate polymers and materials, *J. Mater. Chem. B* 8(10) (2020) 2010-2019.
- [5] D.J. Siegwart, J.K. Oh, K. Matyjaszewski, ATRP in the design of functional materials for biomedical applications, *Progress Polymer Sci* 37(1) (2012) 18-37.
- [6] W.W. He, L. Cheng, L.F. Zhang, Z. Liu, Z.P. Cheng, X.L. Zhu, A versatile  $\text{Fe}_3\text{O}_4$  based platform via iron-catalyzed AGET ATRP: towards various multifunctional nanomaterials, *Polymer Chem.* 5(2) (2014) 638-645.
- [7] M. Fantin, A.A. Isse, A. Gennaro, K. Matyjaszewski, Understanding the Fundamentals of Aqueous ATRP and Defining Conditions for Better Control, *Macromolecules* 48(19) (2015) 6862-6875.
- [8] W.A. Braunecker, K. Matyjaszewski, Controlled/living radical polymerization: Features, developments, and perspectives, *Progress Polymer Sci.* 32(1) (2007) 93-146.
- [9] T.G. Ribelli, F. Lorandi, M. Fantin, K. Matyjaszewski, Atom Transfer Radical Polymerization: Billion Times More Active Catalysts and New Initiation Systems, *Macromol. Rapid Commun.* 40(1) (2019).



- [10] Y. Kwak, A.J.D. Magenau, K. Matyjaszewski, ARGET ATRP of Methyl Acrylate with Inexpensive Ligands and ppm Concentrations of Catalyst, *Macromolecules* 44(4) (2011) 811-819.
- [11] P.V. Mendonca, J.P.M. Ribeiro, C.M.R. Abreu, T. Guliashvili, A.C. Serra, J.F.J. Coelho, Thiourea Dioxide As a Green and Affordable Reducing Agent for the ARGET ATRP of Acrylates, Methacrylates, Styrene, Acrylonitrile, and Vinyl Chloride, *Acs Macro Letters* 8(3) (2019) 315-319.
- [12] D. Konkolewicz, A.J.D. Magenau, S.E. Averick, A. Simakova, H.K. He, K. Matyjaszewski, ICAR ATRP with ppm Cu Catalyst in Water, *Macromolecules* 45(11) (2012) 4461-4468.
- [13] G. Wang, M. Schmitt, Z.Y. Wang, B. Lee, X.C. Pan, L.Y. Fu, J.J. Yan, S.P. Li, G.J. Xie, M.R. Bockstaller, K. Matyjaszewski, Polymerization-Induced Self-Assembly (PISA) Using ICAR ATRP at Low Catalyst Concentration, *Macromolecules* 49(22) (2016) 8605-8615.
- [14] D. Konkolewicz, Y. Wang, M. Zhong, P. Krys, A.A. Isse, A. Gennaro, K. Matyjaszewski, Reversible-Deactivation Radical Polymerization in the Presence of Metallic Copper. A Critical Assessment of the SARA ATRP and SET-LRP Mechanisms, *Macromolecules* 46(22) (2013) 8749-8772.
- [15] P. Chmielarz, P. Krys, S. Park, K. Matyjaszewski, PEO-b-PNIPAM copolymers via SARA ATRP and eATRP in aqueous media, *Polymer* 71 (2015) 143-147.
- [16] X. Jiang, J. Wu, L. Zhang, Z. Cheng, X. Zhu, Highly Active ppm Level Organic Copper Catalyzed Photo-Induced ICAR ATRP of Methyl Methacrylate, *Macromol. Rapid Commun.* 35(21) (2014) 1879-1885.
- [17] M. Rolland, R. Whitfield, D. Messmer, K. Parkatzidis, N.P. Truong, A. Anastasaki, Effect of Polymerization Components on Oxygen-Tolerant Photo-ATRP, *Acs Macro Letters* 8(12) (2019) 1546-1551.
- [18] M. Cvek, J. Kollar, M. Mrlik, M. Masar, P. Suly, M. Urbanek, J. Mosnacek, Surface-initiated mechano-ATRP as a convenient tool for tuning of bidisperse magnetorheological suspensions toward extreme kinetic stability, *Polymer Chem.* 12(35) (2021) 5093-5105.
- [19] K.X. Liu, W.J. Zhang, L.X. Zong, Y.J. He, X.M. Zhang, M.Y. Liu, G. Shi, X.G. Qiao, X.C. Pang, Dimensional Optimization for ZnO-Based Mechano-ATRP with Extraordinary Activity, *J. Phys. Chem. Letters* 13(22) (2022) 4884-4890.
- [20] I. Zaborniak, P. Chmielarz, Ultrasound-Mediated Atom Transfer Radical Polymerization (ATRP), *Materials* 12(21) (2019).
- [21] I. Zaborniak, P. Chmielarz, Temporally Controlled Ultrasonication-Mediated Atom Transfer Radical Polymerization in Miniemulsion, *Macromol. Chem. Phys.* 220(17) (2019).
- [22] A.J.D. Magenau, N.C. Strandwitz, A. Gennaro, K. Matyjaszewski, Electrochemically Mediated Atom Transfer Radical Polymerization, *Science* 332(6025) (2011) 81.
- [23] A.J.D. Magenau, N. Bortolamei, E. Frick, S. Park, A. Gennaro, K. Matyjaszewski, Investigation of Electrochemically Mediated Atom Transfer Radical Polymerization, *Macromolecules* 46(11) (2013) 4346-4353.
- [24] P. Chmielarz, M. Fantin, S. Park, A.A. Isse, A. Gennaro, A.J.D. Magenau, A. Sobkowiak, K. Matyjaszewski, Electrochemically mediated atom transfer radical polymerization (eATRP), *Prog. Polym. Sci.* 69 (2017) 47-78.
- [25] P. Chmielarz, S. Park, A. Simakova, K. Matyjaszewski, Electrochemically mediated ATRP of acrylamides in water, *Polymer* 60 (2015) 302-307.
- [26] F. Lorandi, M. Fantin, A.A. Isse, A. Gennaro, Electrochemically mediated atom transfer radical polymerization of n-butyl acrylate on non-platinum cathodes, *Polymer Chem.* 7(34) (2016) 5357-5365.
- [27] M. Fantin, F. Lorandi, A. Gennaro, A.A. Isse, K. Matyjaszewski, Electron Transfer Reactions in Atom Transfer Radical Polymerization, *Synthesis* 49(15) (2017) 3311-3322.
- [28] F. De Bon, S. Marenzi, A.A. Isse, C. Durante, A. Gennaro, Electrochemically Mediated Aqueous Atom Transfer Radical Polymerization of N,N-Dimethylacrylamide, *ChemElectroChem* 7(6) (2020) 1378-1388.

- [29] J. Luo, C. Durante, A. Gennaro, A.A. Isse, Electrochemical study of the effect of Al<sup>3+</sup> on the stability and performance of Cu-based ATRP catalysts in organic media, *Electrochim. Acta* 388 (2021).
- [30] S.S. Hosseiny, P. van Rijn, Surface Initiated Polymerizations via e-ATRP in Pure Water, *Polymers* 5(4) (2013) 1229-1240.
- [31] B. Li, B. Yu, W.T.S. Huck, F. Zhou, W.M. Liu, Electrochemically Induced Surface-Initiated Atom-Transfer Radical Polymerization, *Angew. Chem., Int. Ed.* 51(21) (2012) 5092-5095.
- [32] G. Lu, Y.M. Li, C.H. Lu, Z.Z. Xu, Corrosion protection of iron surface modified by poly(methyl methacrylate) using surface-initiated atom transfer radical polymerization (SI-ATRP), *Colloid Polym. Sci.* 288(14-15) (2010) 1445-1455.
- [33] M. Khan, J. Yang, C.C. Shi, J. Lv, Y.K. Feng, W. Zhang, Surface tailoring for selective endothelialization and platelet inhibition via a combination of SI-ATRP and click chemistry using Cys-Ala-Gly-peptide, *Acta Biomaterialia* 20 (2015) 69-81.
- [34] G. Bayramoglu, B.F. Senkal, M. Yilmaz, M.Y. Arica, Immobilization and stabilization of papain on poly(hydroxyethyl methacrylate-ethylenglycol dimethacrylate) beads grafted with epoxy functional polymer chains via surface-initiated-atom transfer radical polymerization (SI-ATRP), *Bioresour. Technol.* 102(21) (2011) 9833-9837.
- [35] L.X. Xing, N.N. Guo, Y.T. Zhang, H.Q. Zhang, J.D. Liu, A negatively charged loose nanofiltration membrane by blending with poly (sodium 4-styrene sulfonate) grafted SiO<sub>2</sub> via SI-ATRP for dye purification, *Sep. Purif. Technol.* 146 (2015) 50-59.
- [36] J.C. Dai, Y.C. Dong, C. Yu, Y.X. Liu, X.G. Teng, A novel Nafion-g-PSBMA membrane prepared by grafting zwitterionic SBMA onto Nafion via SI-ATRP for vanadium redox flow battery application, *J. Membr. Sci.* 554 (2018) 324-330.
- [37] A. Khabibullin, K. Bhangaonkar, C. Mahoney, Z. Lu, M. Schmitt, A.K. Sekizkardes, M.R. Bockstaller, K. Matyjaszewski, Grafting PMMA Brushes from alpha-Alumina Nanoparticles via SI-ATRP, *ACS Appl. Mater. Interfaces* 8(8) (2016) 5458-5465.
- [38] J.J. Yan, T. Kristufek, M. Schmitt, Z.Y. Wang, G.J. Xie, A. Dang, C.M. Hui, J. Pietrasik, M.R. Bockstaller, K. Matyjaszewski, Matrix-free Particle Brush System with Bimodal Molecular Weight Distribution Prepared by SI-ATRP, *Macromolecules* 48(22) (2015) 8208-8218.
- [39] A. Simakova, S.E. Averick, D. Konkolewicz, K. Matyjaszewski, Aqueous ARGET ATRP, *Macromolecules* 45(16) (2012) 6371-6379.
- [40] M. Fantin, A.A. Isse, K. Matyjaszewski, A. Gennaro, ATRP in Water: Kinetic Analysis of Active and Super-Active Catalysts for Enhanced Polymerization Control, *Macromolecules* 50(7) (2017) 2696-2705.
- [41] A.S. Karakoti, S. Das, S. Thevuthasan, S. Seal, PEGylated Inorganic Nanoparticles, *Angew. Chem. Int. Ed.* 50(9) (2011) 1980-1994.
- [42] M. Chávez, G. Sánchez-Obrero, R. Madueño, J.M. Sevilla, M. Blázquez, T. Pineda, Characterization of a self-assembled monolayer of O-(2-Mercaptoethyl)-O'-methyl-hexa(ethylene glycol) (EG7-SAM) on gold electrodes, *J. Electroanal. Chem.* 880 (2021) 114892.
- [43] M. Chávez, G. Sánchez-Obrero, R. Madueño, J.M. Sevilla, M. Blázquez, T. Pineda, Self-assembled monolayers of O-(2-Mercaptoethyl)-O'-methyl-hexa(ethylene glycol) (EG7-SAM) on gold electrodes. Effects of the nature of solution/electrolyte on formation and electron transfer blocking characteristics, *J. Electroanal. Chem.* 914 (2022) 116303.
- [44] M. Chávez, G. Sánchez-Obrero, R. Madueño, J.M. Sevilla, M. Blázquez, T. Pineda, Electrochemical evaluation of the grafting density of self-assembled monolayers of polyethylene glycol of different chain lengths formed by the grafting to approach under conditions close to the cloud point, *J. Electroanal. Chem.* 913 (2022) 116294.
- [45] M. Chavez, A. Fernandez-Merino, G. Sanchez-Obrero, R. Madueno, J.M. Sevilla, M. Blazquez, T. Pineda, Distinct thermoresponsive behaviour of oligo- and poly-ethylene glycol protected gold nanoparticles in concentrated salt solutions, *Nanoscale Adv.* 3(16) (2021) 4767-4779.
- [46] M. Chavez, L. Fuentes-Rodriguez, G. Sanchez-Obrero, R. Madueno, J.M. Sevilla, M. Blazquez, T. Pineda, Characterization of self-assembled Bis 2-(2-bromoisobutyryloxy) undecyl disulphide (DTBU)

on gold surfaces suitable for use in surface-initiated atom transfer radical polymerization (SI-ATRP), *J. Electroanal. Chem.* 918 (2022).

[47] N. Gu, L. Niu, S. Dong, Simultaneous determination of both the calibration constant in an electrochemical quartz crystal microbalance and the active surface area of a polycrystalline gold electrode, *Electrochem. Commun.* 2(1) (2000) 48-50.

[48] A. Michieletto, F. Lorandi, F. De Bon, A.A. Isse, A. Gennaro, Biocompatible polymers via aqueous electrochemically mediated atom transfer radical polymerization, *J. Polym. Sci.* 58(1) (2020) 114-123.

[49] J.E.B. Randles, Kinetics of Rapid Electrode Reactions, *Discuss. Faraday Soc.* 1 (1947) 11-19.

[50] R.S. Nicholson, Theory and Application of Cyclic Voltammetry for Measurement of Electrode Reaction Kinetics, *Anal. Chem.* 37(11) (1965) 1351-1355.

[51] R. Madueno, D. Garcia-Raya, A.J. Viudez, J.M. Sevilla, T. Pineda, M. Blazquez, Influence of the solution pH in the 6-mercaptopyrimidine self-assembled monolayer (6MP-SAM) on a Au(111) single-crystal electrode, *Langmuir* 23(22) (2007) 11027-11033.

[52] K. Matyjaszewski, N.V. Tsarevsky, Nanostructured functional materials prepared by atom transfer radical polymerization, *Nature Chem.* 1(4) (2009) 276-288.

[53] E.M. Benetti, S. Zapotoczny, J. Vancso, Tunable thermoresponsive polymeric platforms on gold by "photoiniferter"-based surface grafting, *Adv. Mater.* 19(2) (2007) 268-271.

[54] M. Fantin, F. Lorandi, T.G. Ribelli, G. Szczepaniak, A.E. Enciso, C. Fliedel, L. Thevenin, A.A. Isse, R. Poli, K. Matyjaszewski, Impact of Organometallic Intermediates on Copper-Catalyzed Atom Transfer Radical Polymerization, *Macromolecules* 52(11) (2019) 4079-4090.

[55] N. Ayres, Polymer brushes: Applications in biomaterials and nanotechnology, *Polymer Chem.* 1(6) (2010) 769-777.

[56] H.W. Ma, M. Wells, T.P. Beebe, A. Chilkoti, Surface-initiated atom transfer radical polymerization of oligo(ethylene glycol) methyl methacrylate from a mixed self-assembled monolayer on gold, *Adv. Funct. Mater.* 16(5) (2006) 640-648.

[57] B.R. Coad, Y. Lu, V. Glattauer, L. Meagher, Substrate-Independent Method for Growing and Modulating the Density of Polymer Brushes from Surfaces by ATRP, *ACS Applied Materials & Interfaces* 4(5) (2012) 2811-2823.

[58] K. Ohno, Y. Kayama, V. Ladmiral, T. Fukuda, Y. Tsujii, A Versatile Method of Initiator Fixation for Surface-Initiated Living Radical Polymerization on Polymeric Substrates, *Macromolecules* 43(13) (2010) 5569-5574.

[59] W. Feng, R. Chen, J.L. Brash, S. Zhu, Surface-Initiated Atom Transfer Radical Polymerization of Oligo(ethylene glycol) Methacrylate: Effect of Solvent on Graft Density, *Macromolecular Rapid Communications* 26(17) (2005) 1383-1388.

[60] T. Doneux, L. Yahia Cherif, C. Buess-Herman, Controlled Tuning of the Ferri/Ferrocyanide Electron Transfer at Oligo(Ethylene Glycol)-Modified Electrodes, *Electrochim. Acta* 219 (2016) 412-417.

[61] T. Doneux, A. de Ghellinck, E. Triffaux, N. Brouette, M. Sferrazza, C. Buess-Herman, Electron Transfer Across an Antifouling Mercapto-hepta(ethylene glycol) Self-Assembled Monolayer, *J. Phys. Chem. C* 120(29) (2016) 15915-15922.

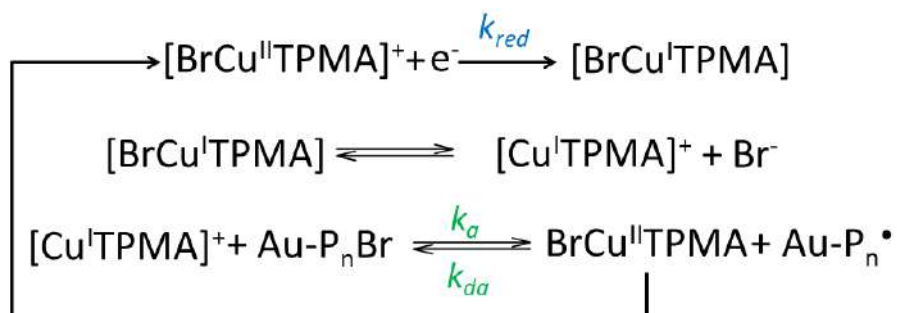
[62] H.O. Finklea, D.A. Snider, J. Fedyk, E. Sabatani, Y. Gafni, I. Rubinstein, Characterization of Octadecanethiol-Coated Gold Electrodes as Microarray Electrodes by Cyclic Voltammetry and Ac-Impedance Spectroscopy, *Langmuir* 9(12) (1993) 3660-3667.

[63] A.J. Bard, L.R. Faulkner, *Electrochemical Methods: Principles and Applications*, 2<sup>a</sup> ed., John Wiley and Sons, New York, 2001.

[64] J. Kuta, E. Yeager, Influence of Cations on Electrode-Kinetics of Ferricyanide Ferrocyanide System on Rotating Gold Electrode, *J. Electroanal. Chem.* 59(1) (1975) 110-112.

- [65] R.P. Janek, W.R. Fawcett, A. Ulman, Impedance Spectroscopy of Self-Assembled Monolayers on Au(111): Sodium Ferrocyanide Charge Transfer at Modified Electrodes, *Langmuir* 14(11) (1998) 3011-3018.
- [66] A.A. Brown, N.S. Khan, L. Steinbock, W.T.S. Huck, Synthesis of oligo(ethylene glycol) methacrylate polymer brushes, *Eur. Polym. J.* 41(8) (2005) 1757-1765.
- [67] B. Li, B. Yu, W.T.S. Huck, W. Liu, F. Zhou, Electrochemically Mediated Atom Transfer Radical Polymerization on Nonconducting Substrates: Controlled Brush Growth through Catalyst Diffusion, *J. Am. Chem. Soc.* 135(5) (2013) 1708-1710.
- [68] H. Sahalov, B. O'Brien, K.J. Stebe, K. Hristova, P.C. Searson, Influence of Applied Potential on the Impedance of Alkanethiol SAMs, *Langmuir* 23(19) (2007) 9681-9685.
- [69] E. Boubour, R.B. Lennox, Insulating Properties of Self-Assembled Monolayers Monitored by Impedance Spectroscopy, *Langmuir* 16(9) (2000) 4222-4228.
- [70] E. Boubour, R.B. Lennox, Potential-Induced Defects in n-Alkanethiol Self-Assembled Monolayers Monitored by Impedance Spectroscopy, *J. Phys. Chem. B* 104(38) (2000) 9004-9010.
- [71] S. Zorn, M.W.A. Skoda, A. Gerlach, R.M.J. Jacobs, F. Schreiber, On the Stability of Oligo(ethylene glycol) (C(11)EG(6)OMe) SAMs on Gold: Behavior at Elevated Temperature in Contact with Water, *Langmuir* 27(6) (2011) 2237-2243.
- [72] X. Shi, Y. Wang, D. Li, L. Yuan, F. Zhou, Y. Wang, B. Song, Z. Wu, H. Chen, J.L. Brash, Cell Adhesion on a PEOGMA-Modified Topographical Surface, *Langmuir* 28(49) (2012) 17011-17018.
- [73] M. Kobayashi, M. Sakashita, Morphology Dependent Anomalous Frequency-Shifts of Infrared-Absorption Bands of Polymer Crystals - Interpretation in Terms of Transition Dipole -Dipole Coupling Theory, *J. Chem. Phys.* 96(1) (1992) 748-760.
- [74] B.S. Lee, J.K. Lee, W.J. Kim, Y.H. Jung, S.J. Sim, J. Lee, I.S. Choi, Surface-initiated, atom transfer radical polymerization of oligo(ethylene glycol) methyl ether methacrylate and subsequent click chemistry for bioconjugation, *Biomacromolecules* 8(2) (2007) 744-749.

## Supporting Information.



**Scheme S1.** Catalytic Electrochemical-chemical reactions of copper complex present on the working solution.  $[\text{BrCu}^{\text{II}}\text{TPMA}]^+$  is the deactivator complex,  $[\text{Cu}^{\text{I}}\text{TPMA}]^+$  is the active catalyst, and  $[\text{BrCu}^{\text{I}}\text{TPMA}]$  and  $[\text{Cu}^{\text{II}}\text{TPMA}]^{2+}$  are inactive species.

**Table S1.** Diffusion coefficient (D) and electron transfer rate constants ( $k_0$ ) for  $[\text{BrCu}^{\text{II}}\text{TPMA}]^+ / [\text{BrCu}^{\text{I}}\text{TPMA}]^+$  in TEABr 0.1 M aqueous solution in the absence and presence of OEGMA monomer  $\text{H}_2\text{O} : \text{OEGMA } 90:10$  %vol.

	<b>H<sub>2</sub>O solution</b>	<b>H<sub>2</sub>O solution + OEGMA</b>
<b>D / cm<sup>2</sup>·s<sup>-1</sup></b>	$3.10 \cdot 10^{-6}$	$1.25 \cdot 10^{-6}$
<b>k<sub>0</sub> / cm·s<sup>-1</sup></b>	$9.85 \cdot 10^{-3}$	$3.27 \cdot 10^{-3}$

Evaluation of eATRP process in the presence of a free initiator in solution.

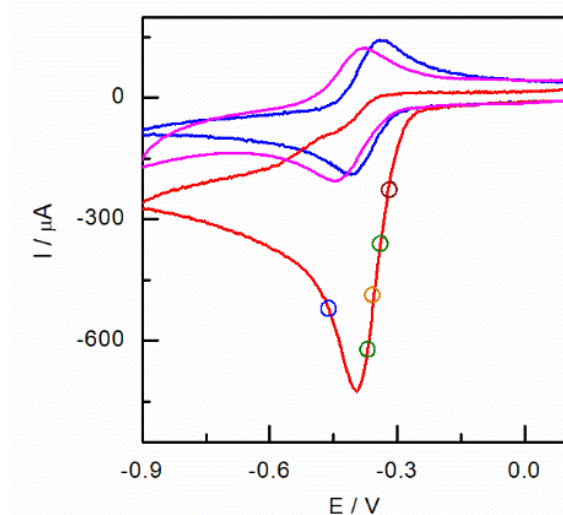


**Figure S1.** Cyclic voltammograms of 1 mM  $[\text{Cu}^{\text{II}}\text{TPMA}]^{2+} / [\text{Cu}^{\text{I}}\text{TPMA}]^+$  in  $\text{H}_2\text{O} : \text{OEGMA}$  solution 90:10 (blue), after the addition of 2 mM HEBiB (red), and after 4h reaction (pink). Circles indicate the potentials evaluated in the experiments.

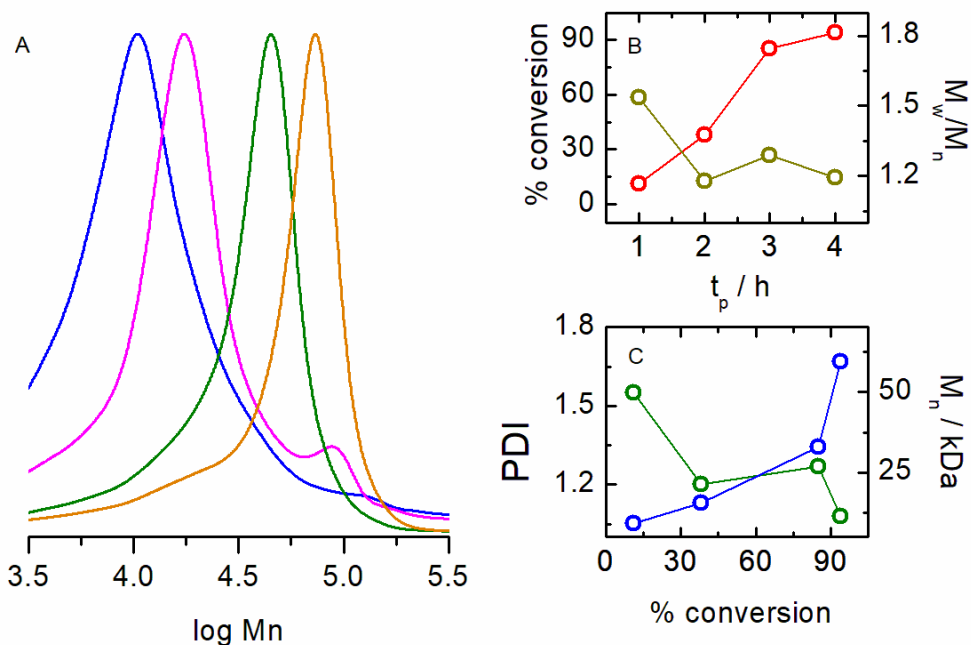


**Figure S2.** Time evolution of the GPC traces for eATRP of p-OEGMA brush formation grafted on HEBiB: 1 h (blue) to 4h (orange) polymerization.  $E_{app} = -0.29$  V. (B) Evolution of the conversion % (red) and molecular weight (brown) with time. (C) Evolution of molecular weight (blue) and molecular weight distribution (green) with conversion.

**Table S2.** Results of the effect of  $E_{app}$  in the eATRP of OEGMA with  $[BrCu^{II}TPMA]^+/[Cu^{I}TPMA]^+$  as catalytic system. All experiments were carried out in  $H_2O$ : OEGMA 90:10 %vol in the presence of 0.1 M TEABr as supporting electrolyte.

$E_{app} / V$	$\Delta E / V$	$t / h$	%conv	$M_n$ th	$M_n$ app	PDI, $\bar{D}$
-0.29	0.06	4	94	50500	59422	1.09
-0.32	0.03	4	92	46700	58797	1.08
-0.35	0.00	3	89	47770	54733	1.12
-0.38	-0.03	3	85	45630	70354	1.18
-0.51	-0.16	2	79	42400	97286	1.51

**Table S3.** Results of the polymerization after 2h.

$E_{app} / V$	$\Delta E / V$	$t / h$	%conv	$M_n$ th	$M_n$ app	PDI, $\bar{D}$
-0.29	0.06	2	38	20415	14225	1.18
-0.32	0.03	2	54	28986	31636	1.12
-0.35	0.00	2	56	30057	27837	1.21

<b>-0.38</b>	-0.03	2	74	39725	57253	1.08
<b>-0.51</b>	-0.16	2	79	42400	97286	1.51

Evaluation of the  $E_{app}$  on the polymerization. Current-time curves.

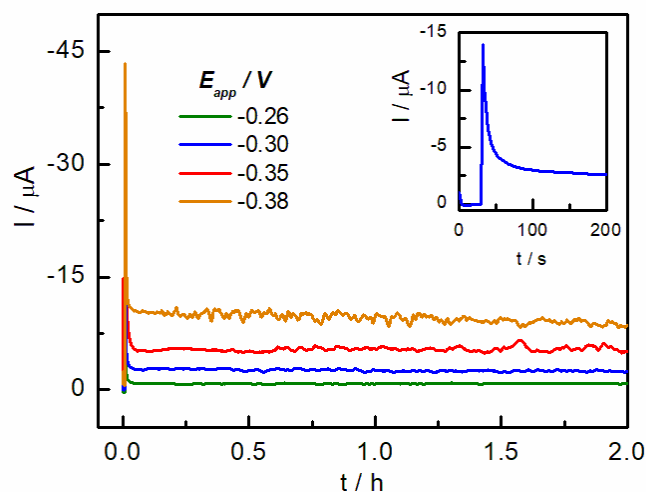
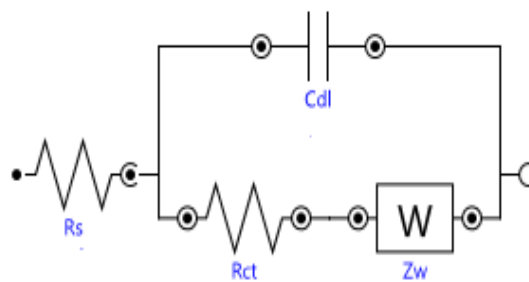


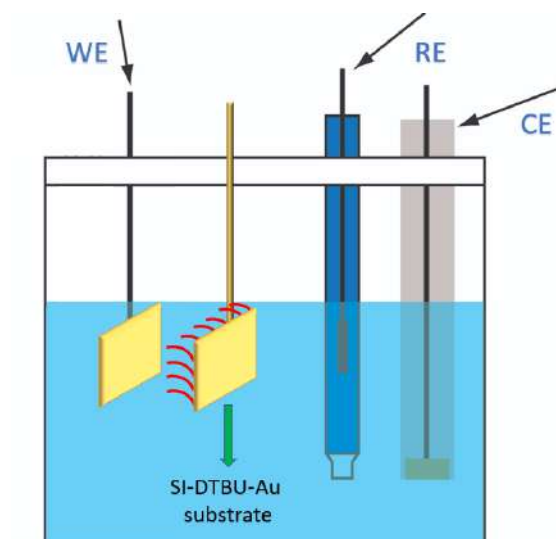
**Figure S3.** Current-time curves of  $[\text{BrCu}^{\text{II}}\text{TPMA}]^+$  oxidation as a function of  $E_{app}$  recorded on EQCM cell. Inset: magnification of the plot at the beginning of the experiment ( $E_{app} = -0.35$  V)



**Scheme 3.** Electrochemical impedance spectra, in the presence of ferricyanide probe, recorded in this work were fitted by using a Randles circuit. It consists of a double layer capacity ( $C_{dl}$ ) in parallel to a charge transfer resistance ( $R_{ct}$ ) and Warburg impedance ( $Z_w$ ).



SI-eATRP from DTBU-SAM through catalyst diffusion.



**Scheme S4.** Schematic representation of diffusion process to control eATRP for the indirect tailoring of p-OEGMA-brush. We have prepared polymer brushes from a DTBU-decorated brushes from a DTBU-decorated m-Au electrode in an indirect manner. Through catalyst diffusion, it is possible to control the eATRP reaction. Both the distance and the angle at which the DTBU-SAM decorated electrode is positioned strongly affect the kinetics of the polymer growth. Thus, we placed a DTBU-SAM decorated m-Au parallel to the naked p-Au working electrode, at ca. 0.5 cm.

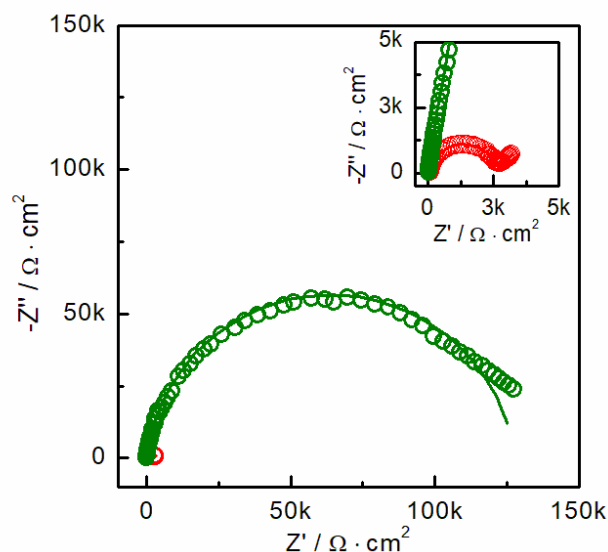


**Figure S4.** Impedance spectra of 1 mM  $K_4[Fe(CN)_6]$  in 0.1 M  $KNO_3$  in the presence of p-OEGMA-brush formed from DTBU-SAM Au substrate placed close to a naked p-Au electrode as WE (green) and p-OEGMA-brush formed from DTBE-SAM via conventional SI-eATRP (red). Polymerization conditions:  $E_{app} = -0.35$  V, 3h reaction time.

### Scanning electron microscopy characterization.

Representative SEM micrographs taken at different positions of p-POEGMA-brush grafted. All the sowed images present a focus magnification of  $\times 2000$ . We analyzed p-OEGMA brushes tailored by varying the  $E_{app}$ , polymerization time, and initiator surfaces, and not notable differences were obtained from the images recorded.

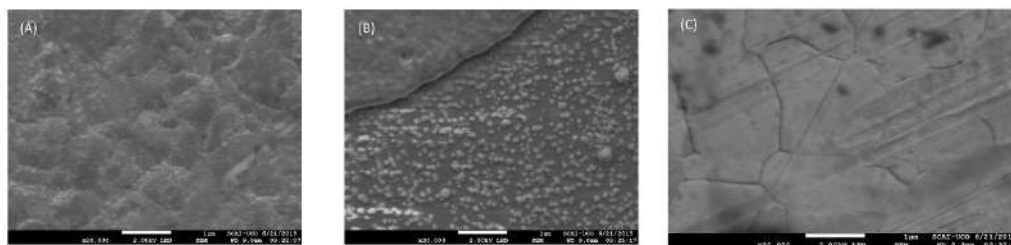


**Figure S5.** (A) p-OEGMA-brush homogeneous region micrograph taken by SEM, (B) p-OEGMA-brush region presenting defect, and (C) naked m-Au crystal using the same magnification. Polymerization conditions:  $E_{app} = -0.35$  V, 3h reaction time.

### Atomic force microscopy characterization.

We have recorded height images for various scanning scales of a polymer brush tailored by using  $E_{app} = -0.35$  V and 3h reaction time. Some representative examples are presented below.

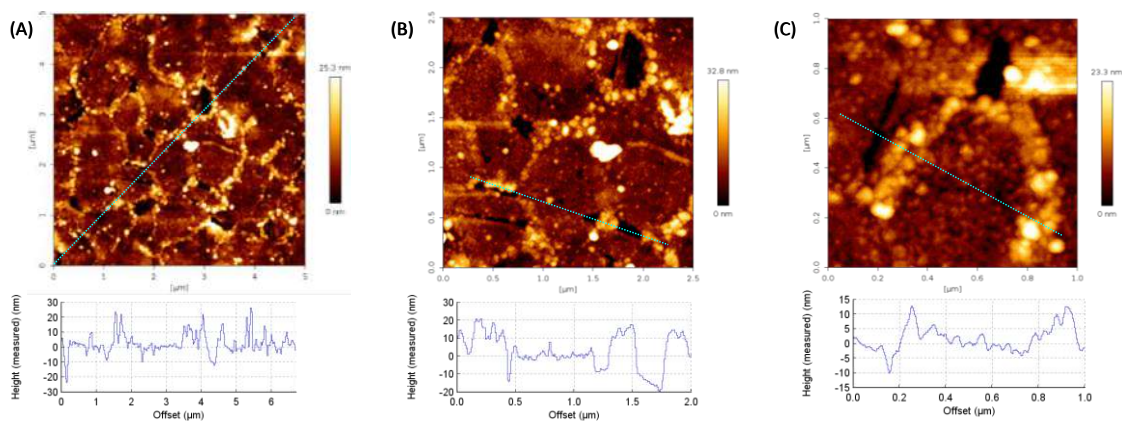


**Figure S6.** (A, B, C) (top) AFM images of p-OEGMA-brush and (A,B,C) (bottom) roughness vs evaluation length plot to describe its topography and roughness. Micrographs size: (A)  $5.0 \times 5.0$   $\mu\text{m}$ , (B)  $2.5 \times 2.5$   $\mu\text{m}$ , and (C)  $1.0 \times 1.0$   $\mu\text{m}$ .

## **Capítulo 4. Conclusiones**



A continuación, se sintetizan las conclusiones específicas obtenidas en cada uno de los trabajos que han derivado de la investigación desarrollada durante la presente Tesis Doctoral.

*“Characterization of a self-assembled monolayer of O-(2-Mercaptoethyl)-O'-methyl-hexa(ethylene glycol) (EG7-SAM) on gold electrodes”*

- La EG7-SAM formada sobre electrodos de oro desde EtOH alcanza una conformación helicoidal empleando un tiempo de modificación de 1h. El incremento del tiempo de adsorción parece conducir a una ligera desorganización de la película, probablemente debida a la introducción de moléculas de disolvente en el interior de la estructura. Este hecho se pone de manifiesto mediante RD, IRRAS y medidas de ángulo de contacto.
- La compacidad de EG7-SAM es menor que la encontrada en la SAM de alcanotiol E<sub>G</sub>n-terminal que presenta una huella molecular próxima a la película de alcanotiol puro, probablemente forzada por la presencia de la larga cadena de alcano que actúa como anclaje, facilitando el ordenamiento en la superficie de oro. A pesar de esto, la EG7-SAM muestra muy buenas propiedades de bloqueo tanto frente a la transferencia electrónica en presencia de la sonda redox ferrocianuro, como a la permeabilidad de iones en soluciones acuosas salinas.
- Mediante QCM, se ha determinado que la EG7-SAM formada en condiciones óptimas resiste la adsorción de la proteína BSA. El cambio de masa obtenido tras 2h de contacto con la solución de BSA corresponde a menos del 10% de una monocapa de BSA, y esta pequeña cantidad de proteína absorbida se elimina fácilmente al retirar la disolución de la proteína. Este estudio confirma la potencial aplicación que presenta la EG7-SAM en el campo biomédico.

*“Self-assembled monolayers of O-(2-Mercaptoethyl)-O'-methyl-hexa(ethylene glycol) (EG7-SAM) on gold electrodes. Effects of the nature of solution/electrolyte on formation and electron transfer blocking characteristics.”*

- Es posible obtener EG7-SAM compactas a partir de soluciones acuosas de EtOH, EtOH95, THF y soluciones acuosas de NaPi 1M sobre sustratos de oro, poniéndose esto de manifiesto mediante experimentos de RD. Cuando se emplea un electrodo de Au poliorientado, se observan sutiles diferencias en la forma y los potenciales de los distintos picos que se atribuyen a las interacciones del disolvente con las cadenas de EG7 injertadas en la superficie y a la probable retención de moléculas de agua en el interior de la película. La formación de EG7-SAM en monocristales Au(111),

Au(100) y Au(110) permite asignar los picos registrados a las diferentes facetas y especular sobre la existencia de posibles interacciones que afectan a la organización dependiendo del tamaño de los dominios dentro de la SAM.

- Las diferencias en los procesos de RD de las EG7-SAMs formadas desde diferentes medios no se traduce en un comportamiento diferencial frente al bloqueo de la transferencia electrónica el par redox  $[\text{Fe}(\text{CN})_6]^{3-/4-}$  evaluada en presencia de distintos electrolitos. Todas las películas muestran un mayor bloqueo al emplear NaPi 0.1M en comparación con  $\text{KNO}_3$ , KCl, NaCl y KPi en la misma concentración. Este hecho apunta a la presencia de interacciones específicas entre el  $\text{Na}^+$ , el fosfato, o ambos iones, que pueden cambiar la estructura de la SAM en contacto con la interfase, pudiendo establecerse interacciones específicas con los átomos de oxígeno del éter o la estructura de la película de agua que interactúa directamente con la SAM.

*“Effects of the potential and the electrolyte nature in the integrity of the O-(2-Mercaptoethyl)-O'-methyl-hexa(ethylene glycol) self-assembled monolayer by electrochemical impedance spectroscopy”*

- Se ha demostrado la efectividad de la EIS para estudiar en profundidad la permeabilidad iónica de la EG7-SAM en diferentes disoluciones acuosas electrolíticas en ausencia de sondas redox. El intervalo de estabilidad de la SAM determinado mediante CV, siendo este el rango de potenciales en los que la densidad de corriente es baja y constante situado entre los procesos de desorción oxidativa y reductiva, no aporta información sobre la permeabilidad iónica a través de la SAM. Sin embargo, la técnica EIS sí permite determinar los rangos de potencial en los que la SAM no permite la entrada de iones, y aquellos en los que sí. El intervalo de potenciales donde se produce fuga de iones más próximo a la zona de desorción reductiva se ha descrito previamente para SAMs de alcanotioles, sin embargo, hasta la fecha no se habían detallado las regiones de permeabilidad a potenciales positivos ni para EG7-SAMs. Es esperable que esta característica se encuentre en todas las SAMs, constituidas a partir de moléculas de alcanotiol o con esqueletos diferente, como el EGn estudiado en este trabajo.
- El diferente comportamiento registrado mediante EIS para la EG7-SAM en función del pH y electrolitos también indica que estas características deben ser tenidas en cuenta a la hora de utilizar estos sistemas en aplicaciones que necesitan propiedades conductoras precisas.

- La información adicional obtenida mediante el análisis de las señales por espectroscopia de capacitancia es también muy útil para comprender plenamente las propiedades de las SAMs y, en particular, de las EGn-SAMs, que están adquiriendo gran importancia en diferentes campos.
- Profundizando en los resultados experimentales obtenidos, el análisis posterior de la capacitancia pone de manifiesto la pérdida de reversibilidad, mientras que el análisis directo de los parámetros medidos muestra que los efectos de la temperatura en las SAMs se revierten. Esto indica que estas propiedades dependen claramente de la temperatura, pero merecen un estudio exhaustivo para obtener conclusiones más profundas.

*“Distinct thermoresponsive behaviour of oligo- and poly-ethylene glycol protected gold nanoparticles in concentrated salt solutions.”*

- Las EGn-AuNPs preparadas por intercambio de ligando a partir de AuNPs protegidas por iones citrato presentan gran estabilidad en suspensiones acuosas en amplios rangos de pH y temperatura. Esta estabilidad depende tanto de la densidad de empaquetamiento como de la longitud de la cadena. De hecho, aunque las cadenas EGn más largas se anclan a la superficie dando lugar a huellas moleculares superiores, estabilizan en mayor medida a las AuNP, presentando el comportamiento esperado en la estabilización estérica coloidal por cadenas poliméricas neutras.
- La evaluación de la estabilidad de la suspensión coloidal en presencia de sales depende fuertemente del tamaño de EGn que conforman el recubrimiento. Así, mientras que todas las EGn-AuNP permanecen estables prácticamente hasta 1M de NaCl, las EG7- y EG18-AuNP pierden la dispersión en presencia de concentraciones relativamente bajas de CaCl<sub>2</sub>, efecto que se atribuye al catión divalente.
- La presencia de NaCl también altera la estabilidad térmica en función del tipo de EGn-AuNP. Las EG7-AuNP presentan una transición drástica de las NP individuales a las agregadas muy dependiente de la concentración de NaCl, dando lugar a un sistema reversible únicamente en concentraciones de NaCl muy bajas (5 mM). Con el aumento de la longitud de cadena, las suspensiones resisten mayores concentraciones salinas, observándose un comportamiento diferencial en cada caso. Así, las EG18- y EG45-AuNP sufren transiciones de fase en función de la temperatura a 1 y 2 M, en el primer sistema, y 3 y 5 M, en el segundo. Sin embargo, todos ellos presentan un comportamiento irreversible, no recuperándose el estado disperso inicial, como se demuestra mediante UV-Vis y DLS.

- La suspensión coloidal EG136-AuNP es la que exhibe un comportamiento más interesante. En primer lugar, estas NPs muestran una transición reversible próxima a 85°C en 1 M de NaCl. Con el aumento de NaCl a 3 y 5 M, aparecen dos transiciones en el rango de temperatura estudiado (10-90°C). Se concluye que la primera transición a una temperatura más baja formaría pequeños agregados que pueden permanecer suspendidos en un intervalo de 15°C y luego evolucionar a un estado ensamblado donde los núcleos metálicos no están acoplados a medida que la longitud de onda LSPR disminuye desde el valor alcanzado por la primera transición. En estas condiciones se observa dispersión Rayleigh que se atribuye a los efectos de la sal, que deshidrata las cadenas de polímero haciendo que las EG136-AuNPs colapsen. En cuanto a la reversibilidad, la segunda transición es completamente reversible, mientras que la primera presenta un comportamiento histérico.

*“Characterization of self-assembled Bis[2-(2-bromoisobutyryloxy) undecyl] disulphide (DTBU) on gold surfaces suitable for use in surface-initiated atom transfer radical polymerization (SI-ATRP).”*

- Mediante XPS se confirma que la molécula DTBU, típicamente usada como iniciador en las reacciones de polimerización ATRP, forma SAMs sobre sustratos de oro a través del enlace S-Au. Además, los picos asociados a la RD de la SAM apuntan a la obtención de una película compacta con una huella molecular de 20.5 Å<sup>2</sup>, y las curvas de capacidad-potencial apoyan este hecho, dando una capacidad diferencial de 3.6 μF/cm<sup>2</sup>.
- Los estudios de integridad del DTBU sobre sustratos de Au policristalinos revelan la presencia de una película cuyas características están definidas por un sitio no polar cerca de la superficie y carácter polar en los grupos expuestos a la interfase. Así, el ángulo de fase a alta frecuencia es sensible a las propiedades dieléctricas de la doble capa del electrodo en presencia de la SAM, estableciendo una excelente correlación entre la frecuencia de transición y la capacidad diferencial.
- Los estudios IRRAS de monocapas mixtas DTBU:6MP indican que la 6MP está presente en mayor proporción en la superficie. Las bandas asignadas al *stretching* C-N de los anillos de la molécula de 6MP aparecen claramente definidos en el espectro, a 1690 cm<sup>-1</sup>, verificando la interacción de esta molécula con la superficie metálica. Así, para la proporción DTBU:6MP (90:10) en la disolución modificadora, la cantidad de 6MP en la superficie del electrodo supera la de DTBU en la SAM formada, en base a las medidas de transición de frecuencia determinadas mediante



EIS. En esta SAM mixta, la sonda  $[\text{Fe}(\text{CN})_6]^{3-/4-}$  tiene una resistencia a la transferencia de carga un orden de magnitud menor que la correspondiente a la SAM de DTBU. Esta característica proporciona unas condiciones óptimas para su adaptación y uso en SI-eATRP.

- Las medidas de ángulo de contacto de las SAMs de DTBU y DTBU:6MP sugieren la formación de estructuras aleatorias en la superficie. Las diferencias en la solvatación de las cabezas expuestas al medio acuoso provocan un efecto predominantemente hidrofóbico, dando lugar a condiciones que también favorecen la polimerización radical en la superficie del electrodo.

*“Efficient formation poly(ethylene glycol) polymer brushes on gold electrodes via surface initiated electrochemical mediated ATRP (SI-eATRP)”*

- Se ha conseguido preparar películas poliméricas p-OEGMA mediante SI-eATRP sobre superficies de Au a partir del monómero comercial OEGMA, metacrilato con EG9 en su esqueleto molecular.
- Mediante EQCM se ha investigado el proceso de síntesis de p-OEGMA, poniéndose de manifiesto el carácter vivo de la polimerización propuesta, así como el efecto del potencial aplicado en la velocidad de polimerización. Los resultados obtenidos indican que existe un amplio rango de potencial en el que se mantiene el control sobre la polimerización, obteniéndose con la aplicación de estos potenciales recubrimientos poliméricos que dan lugar a superficies relativamente uniformes.
- El análisis de las propiedades bloqueantes frente a la transferencia electrónica de la sonda  $[\text{Fe}(\text{CN})_6]^{3-/4-}$ , así como el aislamiento iónico, sugieren la presencia de canales en el interior de la película formada. Además, el análisis de los diagramas de Bode indica que la película de p-OEGMA injertada en la superficie es relativamente heterogénea si se compara con la SAM que contiene el grupo iniciador de la polimerización.
- La deposición de masa medida por EQCM permite estimar el espesor promedio de las *brush* formados en la superficie, encontrándose medidas similares microscopía AFM, en las que el análisis de la topografía y la rugosidad sugieren que los recubrimientos p-OEGMA presentan algunas imperfecciones. Las diferentes técnicas de caracterización empleadas, SEM, AFM, XPS y ángulo de contacto, apuntan a la formación de capas gruesas, pero no completamente homogéneas. Además, el análisis IRRAS sugiere la formación de brush en los que las cadenas de EG son ramificaciones de una cadena central, estando en paralelo a la superficie del sustrato.

- Es interesante señalar que no se ha detectado ninguna deposición de cobre ni por EQCM ni por XPS. Esto es esencial para validar el montaje SI-eATRP aquí propuesto. Los resultados presentados en este trabajo permiten confeccionar recubrimientos p-OEGMA de calidad que son candidatos potenciales de aplicación en una gran variedad de campos.

# **Glosario de abreviaturas**

---

## 2

### 2D

2-dimensiones / 2-dimensional · 3, 4, 7, 22, 23, 49, 52, 54, 68, 93, 146, 212, 265, 269, 325, 327, 328

---

## 3

### 3D

3-dimensiones / 3-dimensional · 3, 4, 7, 41, 42, 49, 54, 93, 212, 265, 269

---

## 6

### 6MP

6-mercaptipurina / 6-mercaptipurine · 18, 149, 177, 245, 246, 247, 255, 256, 257, 258, 259, 260, 261, 262, 266, 267, 277, 280, 282, 289, 295, 298, 311, 312, 326

---

## A

### AFM

Microscopía de fuerza atómica / Atomic Force Microscopy · 19, 68, 69, 79, 100, 146, 201, 274, 277, 280, 294, 295, 305, 312

### ARGET

ATRP basada en regeneración de activadores por transferencia de electrones / Activators ReGenerated by Electron Transfer · 59, 72, 261, 275, 295, 297

### ATRP

Polimerización por transferencia atómica radicalica / Atom Transfer Radical Polymerization · 3, 17, 18, 19, 27, 56, 57, 58, 59, 60, 61, 63, 64, 65, 71, 72, 73, 241, 243, 244, 245, 260, 261, 271, 273, 274, 275, 277, 280, 281, 286, 288, 292, 295, 296, 297, 298, 311, 312, 323, 326, 328

### AuNP

Nanopartícula(s) de oro / Gold Nanoparticle(s) · 4, 8, 16, 17, 25, 41, 42, 43, 44, 45, 49, 50, 51, 52, 53, 54, 70, 194, 195, 210, 211, 212, 213, 214, 215, 216, 217, 218, 219, 220, 221, 222, 223, 224, 225, 226, 227, 228, 229, 230, 231, 232, 233, 238, 239, 240, 310, 311

---

## C

### c-AuNPs

AuNPs recubiertas por citrato / Citrate-capped AuNPs · 213, 214, 215, 216, 231, 238

### CV

Voltametría cíclica / Cyclic Voltammetry · 1, 2, 15, 16, 38, 76, 82, 106, 107, 109, 112, 114, 115, 120, 133, 134, 141, 145, 151, 163, 171, 175, 183, 184, 186, 188, 189, 190, 191, 197, 248, 253, 254, 268, 274, 277, 278, 280, 284, 287, 309

---

## D

### DLS

Dispersión de luz dinámica / Dynamic Light Scattering · 2, 4, 8, 16, 17, 94, 95, 96, 213, 215, 216, 217, 220, 223, 224, 225, 227, 228, 230, 232, 310

### DLVO

Teoría Derjaguin, Landau, Verveij, Overbeek / Derjaguin, Landau, Verveij, Overbeek Theory · 1, 45, 48, 70

### DTBE

Bis[2-(2-bromoisobutiril)etil] disulfuro · 276, 277, 280, 282, 286, 288, 291, 292, 293, 304

## DTBU

Bis[2-(2-bromoisobutiril)undecil] disulfuro / Bis[2-(2-bromoisobutyryloxy)undecyl] disulfide · 3, 17, 18, 62, 241, 243, 245, 246, 247, 248, 249, 250, 251, 252, 253, 254, 255, 256, 257, 258, 259, 260, 261, 265, 266, 267, 268, 277, 280, 282, 288, 289, 291, 293, 295, 297, 303, 304, 311, 312, 323, 326, 328

---

## E

### eATRP

Polimerización radicalaria por transferencia atómica mediada electroquímicamente / Electrochemically Mediated Atom Transfer Radical Polymerization · 4, 8, 60, 61, 62, 72, 98, 280, 282, 286, 287, 296, 301, 302, 304, 326

### EG

Etilenglicol / Ethylene glycol · 19, 27, 35, 36, 37, 38, 50, 53, 63, 64, 68, 105, 106, 112, 116, 118, 119, 130, 140, 143, 144, 145, 160, 182, 212, 299, 312

### EG7

O-(2-Mercaptoetil)-O'-metil-hexa(etilenglicol) / O-(2-Mercaptoethyl)-O'-methyl-hexa(ethylene glycol) · 2, 4, 8, 13, 14, 15, 36, 37, 38, 53, 102, 104, 106, 107, 108, 109, 110, 111, 112, 113, 114, 115, 116, 117, 118, 119, 120, 121, 122, 127, 129, 130, 131, 132, 133, 134, 135, 136, 137, 138, 139, 140, 141, 142, 143, 144, 145, 147, 151, 153, 155, 156, 157, 160, 161, 162, 163, 164, 166, 168, 169, 170, 171, 172, 173, 174, 175, 177, 187, 195, 200, 213, 215, 216, 218, 219, 220, 221, 222, 223, 227, 232, 235, 240, 262, 290, 297, 308, 309, 310, 322, 323

### EGn

Polietilenglicol / Poly(ethylene glycol) · 3, 4, 5, 7, 8, 13, 14, 15, 16, 17, 18, 25, 27, 28, 29, 34, 35, 36, 37, 38, 39, 40, 41, 49, 50, 51, 52, 53, 54, 63, 64, 65, 105, 106, 112, 114, 116, 117, 118, 122, 130, 143, 144, 160, 161, 162, 172, 173, 175, 182, 183, 184, 186, 188, 189, 190, 193, 194, 195, 196, 197, 198, 210, 211, 212, 213, 214, 215, 216, 217, 218, 219, 220, 221, 222, 226, 230, 231, 232, 239, 276, 287, 289, 290, 308, 309, 310, 327

### EIS

Espectroscopía de impedancia electroquímica / Electrochemical Impedance Spectroscopy · 4, 14, 15, 16, 19, 36, 77, 78, 82, 83, 106, 115, 116, 131, 133, 141, 145, 160, 161, 162, 163, 167, 171, 175, 185, 197, 198, 246, 250, 253, 254, 256, 258, 259, 260, 268, 274, 277, 278, 287, 288, 289, 290, 309, 311

### EQCM

Microbalanza de cristal de cuarzo electroquímica / Electrochemical Quartz Crystal Microbalance · 4, 19, 79, 83, 84, 277, 278, 280, 283, 284, 285, 286, 294, 295, 303, 312, 326

---

## F

### FRP

Polimerización por radicales libres / Free Radical Polymerization · 54, 55, 56

---

## G

### GPC

Cromatografía de permeación en gel / Gel Permeation Chromatography · 97, 98, 99, 278, 282, 302

---

## I

### ICAR

ATRP basada en iniciadores para la regeneración continua de iniciadores / Initiators for Continuous Activator Regeneration ATRP · 59, 72, 275, 295, 296

### IRRAS

Espectroscopía de Absorción-Reflexión Infrarroja / Infrared Reflection Absorption Spectroscopy · 4, 8, 14, 18, 19, 35, 86, 87, 88, 108, 109, 117, 122, 126, 131, 245, 247, 256, 260, 265, 274, 277, 279, 292, 293, 295, 308, 311, 312

---

## **L**

### LCST

Temperatura de solución crítica más baja / Lower Critical Solution Temperature · 52, 53, 211, 222

### LSPR

Resonancia del plasmón superficial localizado / Localized Surface Plasmon Resonance · 16, 41, 49, 85, 213, 215, 218, 219, 220, 221, 222, 223, 224, 226, 228, 229, 232, 311

---

## **M**

### MW

Peso molecular promedio / Average Molecular Weight · 56, 97, 98, 184, 213, 216, 286, 287

---

## **N**

### NMs

Nanomateriales / Nanomaterials · 3, 4, 7, 16, 17, 22, 23, 24, 25, 27, 29, 41, 59, 76, 78, 84, 91, 92, 210, 274

### NP

Nanopartícula / Nanoparticle · 23, 28, 41, 44, 47, 50, 310

### NPs

Nanopartículas / Nanoparticles · 27, 29, 42, 43, 44, 45, 47, 48, 49, 50, 51, 53, 54, 61, 63, 85, 310

---

## **O**

### OEGMA

oligo(etilenglicol metil éter) metacrilato / oligo(ethylene glycol methyl ether) methacrylate · 63, 64, 276, 277, 280, 281, 282, 286, 290, 291, 292, 301, 302, 312

---

## **P**

### p-OEGMA

poli-(oligo(etilenglicol metil éter) metacrilato) / poly-(oligo(ethylene glycol methyl ether) methacrylate) · 274, 276, 277, 280, 282, 283, 284, 285, 286, 287, 288, 289, 290, 291, 292, 293, 294, 295, 302, 304, 305, 312, 313

---

## **Q**

### QCM

Microbalanza de cristal de cuarzo / Quartz Crystal Microbalance · 8, 79, 183, 308

---

## **R**

### RD

Desorción reductiva / Reductive Desorption · 13, 15, 106, 109, 110, 111, 112, 113, 116, 120, 121, 122, 130, 131, 133, 134, 135, 136, 137, 139, 140, 143, 145, 151, 153, 155, 161, 163, 164, 166, 169,

170, 171, 175, 183, 184, 185, 186, 187, 188, 189, 190, 191, 192, 193, 194, 195, 198, 205, 215, 248, 249, 250, 255, 260, 308, 309, 311

#### RDRP

Polimerización radical de desactivación reversible / Reversible Deactivation Radical Polymerization · 55, 56

---

## S

#### SAM(s)

Monocapas autoensambladas / Self-Assembled Monolayers · 3, 4, 7, 8, 13, 14, 15, 16, 17, 18, 22, 25, 26, 29, 30, 31, 33, 34, 35, 36, 37, 38, 49, 62, 68, 105, 106, 108, 109, 111, 112, 114, 115, 116, 117, 118, 119, 122, 125, 129, 130, 131, 133, 134, 135, 137, 138, 139, 140, 141, 142, 143, 144, 145, 146, 149, 151, 153, 155, 160, 161, 162, 163, 164, 165, 166, 167, 172, 173, 175, 176, 177, 182, 183, 184, 186, 187, 188, 189, 190, 191, 192, 193, 194, 195, 196, 197, 198, 205, 248, 259, 260, 261, 265, 274, 276, 280, 282, 287, 290, 291, 294, 299, 309, 310, 311, 312, 325, 326, 327, 328

#### SARA

ATRP basada en activadores suplementarios y agentes reductores / Supplemental Activator and Reducing Agent ATRP · 59, 72, 275, 296

#### SEM

Microscopía electrónica de barrido / Scanning Electron Microscopy · 19, 92, 93, 94, 274, 277, 279, 295, 305, 312

#### SI-eATRP

Polimerización radical controlada por transferencia atómica mediada electroquímicamente iniciada en superficie / Surface-Initiated electrochemically mediated Atom Transfer Radical Polymerization · 17, 18, 19, 61, 62, 63, 64, 79, 271, 273, 274, 275, 276, 277, 280, 281, 282, 283, 289, 290, 292, 294, 295, 303, 304, 311, 312

---

## T

#### TEABr

Bromuro de tetraetilamonio / Tetraethylammonium bromide · 277, 280, 281, 282, 301, 302

#### TEM

Microscopía electrónica de transmisión / Transmission Electron Microscopy · 79, 92, 93, 94, 100, 214, 215, 238

#### THF

Tetrahidrofurano / Tetrahydrofuran · 36, 37, 131, 132, 134, 136, 138, 140, 141, 142, 145, 155, 162, 308

#### TPMA

Tris(2-piridilmetil)amina / Tris(2-pyridylmethyl)amine · 57, 59, 275, 277, 280

---

## U

#### UV-vis

Espectroscopía ultravioleta - visible / Ultraviolet - visible spectroscopy · 16, 17, 85, 215

---

## X

#### XPS

Espectroscopía fotoelectrónica de rayos X / X-ray Photoelectron Spectroscopy · 8, 14, 16, 19, 89, 90, 91, 100, 106, 108, 109, 119, 120, 126, 156, 185, 186, 187, 205, 245, 247, 250, 260, 265, 269, 274, 277, 279, 292, 295, 311, 312





# **Indicios de calidad**



**Título:** Characterization of a self-assembled monolayer of O-(2-Mercaptoethyl)-O'-methyl hexa(ethylene glycol) (EG7-SAM) on gold electrodes

**Autores:** Miriam Chavez, Guadalupe Sanchez-Obrero, Rafael Madueño, José Manuel Sevilla, Manuel Blazquez, Teresa Pineda

**Tipo de producción:** Artículo

**Revista:** Journal of Electroanalytical Chemistry

**Volumen:** 880

**Número de artículo:** 114892

**Fecha de publicación:** JAN 1 2021

**Factor de impacto JCR:** 4.598 (2021)

**Categoría:** Chemistry, Analytical

**Cuartil:** Q1

---

**Título:** Distinct thermoresponsive behaviour of oligo- and poly-ethylene glycol protected gold nanoparticles in concentrated salt solutions

**Autores:** Miriam Chavez, Angela Fernandez-Merino, Guadalupe Sanchez-Obrero, Rafael Madueño, José Manuel Sevilla, Manuel Blazquez, Teresa Pineda

**Tipo de producción:** Artículo

**Revista:** Nanoscale Advances

**Volumen:** 3

**Número:** 16

**Páginas:** 4767-4779

**Fecha de publicación:** AUG 21 2021

**Factor de impacto JCR:** 5.598 (2021)

**Categoría:** Chemistry, Multidisciplinary

**Cuartil:** Q2

---

**Título:** Electrochemical evaluation of the grafting density of self-assembled monolayers of polyethylene glycol of different chain lengths formed by the grafting to approach under conditions close to the cloud point

**Autores:** Miriam Chavez, Guadalupe Sanchez-Obrero, Rafael Madueño, José Manuel Sevilla, Manuel Blazquez, Teresa Pineda

**Tipo de producción:** Artículo

**Revista:** Journal of Electroanalytical Chemistry

**Volumen:** 913

**Número de artículo:** 116294

**Fecha de publicación:** MAY 15 2022

**Factor de impacto JCR:** 4.598 (2021)

**Categoría:** Chemistry, Analytical

**Cuartil:** Q1

---

**Título:** Self-assembled monolayers of O-(2-Mercaptoethyl)-O '-methyl-hexa(ethylene glycol) (EG7-SAM) on gold electrodes. Effects of the nature of solution/electrolyte on formation and electron transfer blocking characteristics

**Autores:** Miriam Chavez, Guadalupe Sanchez-Obrero, Rafael Madueño, José Manuel Sevilla, Manuel Blazquez, Teresa Pineda

**Tipo de producción:** Artículo

**Revista:** Journal of Electroanalytical Chemistry

**Volumen:** 914

**Número de artículo:** 116303

**Fecha de publicación:** JUN 1 2022

**Factor de impacto JCR:** 4.598 (2021)

**Categoría:** Chemistry, Analytical

**Cuartil:** Q1

---

**Título:** Characterization of self-assembled Bis[2-(2-bromoisobutyryloxy) undecyl] disulphide (DTBU) on gold surfaces suitable for use in surface-initiated atom transfer radical polymerization (SI-ATRP)

**Autores:** Miriam Chavez, Fuentes-Rodriguez, L, Guadalupe Sanchez-Obrero, Rafael Madueño, José Manuel Sevilla, Manuel Blazquez, Teresa Pineda

**Tipo de producción:** Artículo

**Revista:** Journal of Electroanalytical Chemistry

**Volumen:** 918

**Número de artículo:** 116515

**Fecha de publicación:** AUG 1 2022

**Factor de impacto JCR:** 4.598 (2021)

**Categoría:** Chemistry, Analytical

**Cuartil:** Q1

# **Otras aportaciones científicas**



## Participación en publicaciones científicas que no forman parte de la memoria de la Tesis.

1. Guadalupe Sánchez-Obrero, Miriam Chávez, Rafael Madueño, Manuel Blázquez, Teresa Pineda, Juan Manuel López-Romero, Francisco Sarabia, Jesús Hierrezuelo, Rafael Contreras, Study of the self-assembly process of an oligo(ethylene glycol)-thioacetyl substituted theophylline (THEO) on gold substrates. JEAC (2018), doi:10.1016/j.jelechem.2018.07.014
2. Jie Luo, Miriam Chavez, Christian Durante, Armando Gennaro, Abdirisak Ahmed Isse, Marco Fantin, Improvement of Electrochemically Mediated Atom Transfer Radical Polymerization: Use of Aluminum as a Sacrificial Anode in Water, *Electrochimica Acta* (2022), 141183. doi: <https://doi.org/10.1016/j.electacta.2022.141183>

## Trabajos presentados en congresos.

1. *Caracterización de Monocapas de Oligoetilenglicol en Oro*  
**Póster.** Miriam Chávez, Félix del Águila, Alain Rafael Puente-Santiago, Guadalupe Sanchez Obrero, Rafael Madueño, Jose Manuel Sevilla, Manuel Blazquez, Teresa Pineda. NANOUCO VI. Encuentro sobre Nanociencia y Nanotecnología de Investigadores Andaluces. (Córdoba, 2017)
2. *Caracterización de Monocapas Autoensambladas de Etilenglicoles sobre Superficies 2D de Oro*  
**Oral.** Miriam Chavez, Teresa Pineda. II Congreso Científico de Investigadores Noveles (Córdoba, 2017)
3. *Optimization of the methodologies to obtain OEG-SAMs on Gold surfaces*  
**Póster.** Miriam Chávez, Guadalupe Sanchez Obrero, Rafael Madueño, Manuel Blazquez, Teresa Pineda. II Workshop de Electrobionet (Oviedo, 2017)
4. *Characterization of self-assembled monolayers of oligoethyleneglycol (OEG) on gold surfaces*  
**Oral.** Miriam Chávez, Guadalupe Sanchez Obrero, Rafael Madueño, Manuel Blazquez, Teresa Pineda. XXXVIII Reunión del Grupo de Electroquímica de la Real Sociedad Española de Química y XIX Encontro Ibérico de Electroquímica (Vitoria-Gasteiz, 2017)
5. *Oligoethyleneglycol (OEG) chains organization in molecular layers formed on gold substrates*  
**Oral.** Sandugash Yergeshbayeva, Miriam Chávez, Guadalupe Sanchez Obrero, Rafael Madueño, Manuel Blazquez, Teresa Pineda. XXXVIII Reunión del Grupo de Electroquímica de la Real Sociedad Española de Química y XIX Encontro Ibérico de Electroquímica (Vitoria-Gasteiz, 2017)
6. *An electrochemical quartz crystal microbalance (EQCM) study of oligoethyleneglycol self-assembled monolayers (OEG-SAMs) on gold substrates*

- Póster.** Miriam Chávez, Guadalupe Sanchez Obrero, Rafael Madueño, Manuel Blazquez, Teresa Pineda. XXXIX Reunión del Grupo de Electroquímica de la Real Sociedad Española de Química y III Simposio E3 del Mediterráneo (Madrid, 2018)
7. *Caracterización de PEG-SAMs con Aplicaciones en Bionanomedicina*  
**Oral.** Miriam Chávez, Guadalupe Sanchez Obrero, Rafael Madueño, Manuel Blazquez, Teresa Pineda. IV Reunión de Jóvenes Investigadores en Coloides e Interfases (Córdoba, 2018)
  8. *Optimización de la Metodología para la Obtención de PEG-SAMs sobre Superficies de Oro y sus Aplicaciones Bionanomédicas*  
**Oral.** Miriam Chavez, Teresa Pineda. VI Congreso Científico de Investigadores en Formación de la Universidad de Córdoba (Córdoba, 2018)
  9. *Structural and functional study of the nano-bio interface in 2- and 3-D systems*  
**Oral.** Miriam Chávez, Guadalupe Sanchez Obrero, Rafael Madueño, Manuel Blazquez, Teresa Pineda. XXXIX Reunión del Grupo de Electroquímica de la Real Sociedad Española de Química y III Simposio E3 del Mediterráneo (Madrid, 2018)
  10. *Síntesis de nanotriángulos de oro (AuNTs) y separación por tamaños*  
**Póster.** Irene Humanes, Miriam Chávez, Rafael del Caño, Guadalupe Sanchez Obrero, Rafael Madueño, Manuel Blazquez, Teresa Pineda. NANOUCO VII. Encuentro sobre Nanociencia y Nanotecnología. (Córdoba, 2019)
  11. *Caracterización de nanotriángulos de oro estabilizados con monocapas de polietilenglicol.*  
**Oral.** Miriam Chávez, Irene Humanes, Rafael del Caño, Guadalupe Sanchez Obrero, Rafael Madueño, Manuel Blazquez, Teresa Pineda. NANOUCO VII. Encuentro sobre Nanociencia y Nanotecnología. (Córdoba, 2019)
  12. *Síntesis y caracterización de DTBU-SAMs para su uso como iniciadores de reacciones ATRP en superficies de oro*  
**Oral.** Miriam Chavez, Teresa Pineda. VII Congreso Científico de Investigadores en Formación de la Universidad de Córdoba (Córdoba, 2019)
  13. *Efficient formation of polymer brushes from mixed Self-Assembly Monolayers of DTBU and 6MP using eATRP technique*  
**Oral.** Miriam Chávez, Guadalupe Sanchez Obrero, Rafael Madueño, Manuel Blazquez, Teresa Pineda. XL Reunión del Grupo de Electroquímica de la Real Sociedad Española de Química y XX Encontro Ibérico de Electroquímica (Huelva, 2019)
  14. *Synthesis and characterization of Gold Nanoplates covered with Polyethylen glycol Self Assembled Monolayers*  
**Póster.** Miriam Chávez, Guadalupe Sanchez Obrero, Rafael Madueño, Manuel Blazquez, Teresa Pineda. XL Reunión del Grupo de Electroquímica de la Real Sociedad Española de Química y XX Encontro Ibérico de Electroquímica (Huelva, 2019)



15. *Empleo de técnicas electroquímicas para la síntesis y caracterización “polímeros brush” biocompatibles en superficies 2D de oro*  
**Póster-flash.** Miriam Chavez, Teresa Pineda. VIII Congreso Científico de Investigadores en Formación de la Universidad de Córdoba (Córdoba, 2020)
16. *Nanopartículas Híbridas MetalOrgánicas: Esferas De Oro Recubiertas Con Polietilenglicol*  
**Póster.** Miriam Chavez, Teresa Pineda. IX Congreso Científico de Investigadores en Formación de la Universidad de Córdoba (Córdoba, 2021)
17. *Influencia de la fuerza iónica en la organización molecular de SAMs de polietilenglicol (PEG) sobre superficies de oro*  
**Póster.** Miriam Chavez, Teresa Pineda. Jornada Científica De Jóvenes Investigadores De La Red Sensores Y Biosensores Electroquímicos (Electrobionet) (Madrid, 2021)
18. *Influence of the medium on electron transfer of ferri/ferro-cyanide across mercaptohepta(ethylene glycol)*  
**Póster.** Miriam Chávez, Guadalupe Sanchez Obrero, Rafael Madueño, Manuel Blazquez, Teresa Pineda. XLI Reunión del Grupo de Electroquímica de la Real Sociedad Española de Química y 1st French-Spanish Atelier/Workshop on Electrochemistry (París, 2021)
19. *Effect of ionic strength on the molecular organization of polyethylene glycol (PEG) SAMs on gold surfaces*  
**Póster.** Miriam Chávez, Guadalupe Sanchez Obrero, Rafael Madueño, Jose Manuel Sevilla, Manuel Blazquez, Teresa Pineda. XLI Reunión del Grupo de Electroquímica de la Real Sociedad Española de Química y 1st French-Spanish Atelier/Workshop on Electrochemistry (París, 2021)
20. *The effect of gold metal shape in the catalytic activity of the artificial peroxidase Fe(III)-MimochromeVI\*a*  
**Póster.** Miriam Chávez, Emilia Renzi, Angela Lombardi, Flavia Nastri, Teresa Pineda. XXXVIII Reunión Bienal de la Sociedad Española de Química (Granada, 2022)
21. *Arquitectura de sams de EGn-Au. Evaluación de las condiciones de formación mediante técnicas electroquímicas*  
**Oral.** Miriam Chávez, Guadalupe Sanchez Obrero, Rafael Madueño, Jose Manuel Sevilla, Manuel Blazquez, Teresa Pineda. XLII Reunión del Grupo de Electroquímica de la Real Sociedad Española de Química (Santander, 2022)
22. *Gold nanoplates based bioconjugates that enhance redox electroactivity of the proteins*  
**Oral.** Miriam Chávez, Angela Fernandez Merino, Rafael del Caño, Guadalupe Sanchez Obrero, Rafael Madueño, Jose Manuel Sevilla, Manuel Blazquez, Teresa Pineda. 3er Workshop Electrobionet “Electrochemical Sensors and Biosensors” y “Transnanoavansens” (Madrid, 2022)

## Capítulos de libro.

1. Título del capítulo: Optimización de la Metodología para la Obtención de PEG-SAMs sobre Superficies de Oro y sus Aplicaciones Bionanomédicas  
Autores del capítulo: Miriam Chavez, Teresa Pineda  
Páginas: 233 - 236  
Título del libro: Creando redes doctorales. Vol. VI: "La generación del conocimiento"  
Año de publicación: 2018  
Editorial: UCOPress. Editorial Universidad de Córdoba  
ISBN: 978-84-9927-239-9
2. Título del capítulo: Caracterización electroquímica de Monocapas Autoensambladas (SAMs) de etilenglicoles sobre superficies 2D de oro  
Autores del capítulo: Miriam Chavez, Teresa Pineda  
Páginas: 43 - 47  
Título del libro: Investigadores de hoy para los retos del mañana  
Año de publicación: 2018  
Editorial: UCOPress. Editorial Universidad de Córdoba  
ISBN: 978-84-9927-386-0
3. Título del capítulo: Síntesis y caracterización de DTBU-SAMs para su uso como iniciadores de reacciones ATRP en superficies de oro  
Autores del capítulo: Miriam Chavez, Teresa Pineda  
Páginas: 275 - 278  
Título del libro: Creando redes doctorales. Vol. VII: "Investiga y comunica"  
Año de publicación: 2019  
Editorial: UCOPress. Editorial Universidad de Córdoba  
ISBN: 978-84-9927-341-9
4. Título del capítulo: Empleo de técnicas electroquímicas para la síntesis y caracterización "polímeros brush" biocompatibles en superficies 2D de oro  
Autores del capítulo: Miriam Chavez, Teresa Pineda  
Páginas: 313 - 316  
Título del libro: Creando redes doctorales. Vol. VIII: "La investigación del futuro"  
Año de publicación: 2020  
Editorial: UCOPress. Editorial Universidad de Córdoba  
ISBN: 978-84-9927-508-6
5. Título del capítulo: Nanopartículas híbridas metal-orgánicas: esferas de oro recubiertas con polietilenglicol  
Autores del capítulo: Miriam Chavez, Teresa Pineda  
Páginas: 363 - 366  
Título del libro: Creando redes doctorales. Vol. IX: "Nuevos desafíos, nuevas oportunidades"  
Año de publicación: 2021  
Editorial: UCOPress. Editorial Universidad de Córdoba  
ISBN: 978-84-9927-640-3

# Publicaciones





## Characterization of a self-assembled monolayer of O-(2-Mercaptoethyl)-O'-methyl-hexa(ethylene glycol) (EG7-SAM) on gold electrodes

Miriam Chávez, Guadalupe Sánchez-Obrero, Rafael Madueño, José Manuel Sevilla, Manuel Blázquez, Teresa Pineda \*

Department of Physical Chemistry and Applied Thermodynamics, Institute of Fine Chemistry and Nanotechnology, University of Córdoba, Campus Rabanales, Ed. Marie Curie 2<sup>a</sup> Plaza, Córdoba E-14014, Spain

### ARTICLE INFO

#### Article history:

Received 10 September 2020  
Received in revised form 20 November 2020  
Accepted 25 November 2020  
Available online 30 November 2020

#### Keywords:

Polyethylene glycol  
Self-assembled monolayer  
Gold  
Cyclic voltammetry  
Electrochemical impedance spectroscopy  
Infrared spectroscopy  
X ray photoelectron spectroscopy  
Contact angle measurements  
Electrochemical quartz crystal microbalance

### ABSTRACT

The modification of surfaces by polyethylene glycol (EGn) is an approach used to reduce the antifouling effects of these materials in a biological medium. It has been found that the packing density and conformational order of these molecules in the films are crucial for the inhibition of unspecific protein adsorption. In this work, we present a study of the formation and characterization of a self-assembled monolayer of O-(2-Mercaptoethyl)-O'-methyl-hexa(ethylene glycol) (EG7-SAM) on either poly-oriented or Au(111) single crystal surfaces. The final properties of the formed EG7-SAMs are studied by examining the reductive desorption process as well as the electronic and ionic blocking behaviour of these layers, under different experimental conditions, by using cyclic voltammetry and electrochemical impedance spectroscopy. Additional information of the structure, composition and organization is obtained by absorption-reflection infrared and X ray photoelectron spectroscopies and contact angle measurements. In contrast to the behaviour observed with alkanethiols, the EG7-SAM shows the best final organization at a modification time of 1 h. The antifouling properties of this EG7-SAM against the adsorption of the bovine serum albumin protein in a phosphate saline medium, has been evidenced by using the electrochemical quartz crystal microbalance technique.

### 1. Introduction

The covalent attachment of poly(ethylene glycol) chains (PEG or EGn, being n the number of EG units) to bioactive substances has been long defined as PEGylation [1] and recently, it has been applied to the modification of nanoparticle surfaces for its use in different fields to induce, on one hand, aqueous solubility, and on the other, to sterically shield nanoparticle surfaces to effectively minimize opsonisation and prolong blood circulation time *in vivo* [2,3]. Although these applications are based in the ability of avoiding protein unspecific adsorption, the factors that influence the interactions and circulation of PEGylated nanoparticles in the biological fluids are numerous and many efforts have been devoted to rationalized them. Molecular weight, surface density and conformation of the PEG chains are the most studied parameters and there is no doubt that is the precise knowledge of how they impact on the systemic administration that will lead to more efficacious products [3–5]. Complementary structural studies of these EG polymer layers on flat surfaces may help in understanding the suppressive effect for protein unspecific adsorption and in the translation to these drug delivery systems to the living systems [6,7].

Self-assembled monolayers (SAMs) of oligo(ethylene glycol) (OEG)-terminated alkanethiols on gold and silver substrates have been widely used to analyse the factors that influence the minimization of protein resistance [8–11] and within the facts responsible for this undesirable phenomenon, steric repulsion, large exclusion volume, rapid mobility of highly hydrated chains, low EG-water interfacial energy and weak interactions with the proteins have been mentioned. Earlier studies [8,12,13] comparing SAMs with short terminal EG segments to that of PEG, focussed on the steric repulsion model that attributes the protein resistance to the balance between this steric repulsion and the attractive forces. The steric repulsion has an elastic component caused by the compression and restriction of the EG segments and an osmotic component due to the loss of water by both the chains and the proteins. As the SAMs with the shorter EG terminal fragments have a more compact structure, the protein resistance was generally attributed to the osmotic component of the steric repulsion model. However, Grunze et al. [10,14] suggest that protein resistance of EG terminated SAMs is a consequence of the stability of the interfacial water layer, which prevent direct contact between the surface and the protein. Moreover, the conformation of the terminal strand contributes to the ability to bind water, being the helical

\* Corresponding author.  
E-mail address: [tpineda@uco.es](mailto:tpineda@uco.es) (T. Pineda).

## PAPER

Cite this: *Nanoscale Adv.*, 2021, 3, 4767

## Distinct thermoresponsive behaviour of oligo- and poly-ethylene glycol protected gold nanoparticles in concentrated salt solutions†

Miriam Chávez,<sup>1</sup> Ángela Fernández-Merino,<sup>1</sup> Guadalupe Sánchez-Obrero,<sup>1</sup> Rafael Madueño,<sup>1</sup> José Manuel Sevilla,<sup>1</sup> Manuel Blázquez<sup>1</sup> and Teresa Pineda<sup>1\*</sup>

In this work, the methoxy terminated oligo- and polyethylene glycol of different chain lengths (EG $n$ ,  $n = 7, 18, 45$  and  $136$ ) is grafted on AuNP surfaces under conditions where they attain maximum grafting densities. These EG $n$ -AuNPs gain stability relative to the pristine c-AuNPs in aqueous solutions and in a wide temperature interval and they form stable suspensions in solutions of high NaCl concentrations. To show the thermoresponsive properties of these EG $n$ -AuNPs, temperature titration experiments are carried out in the presence of increasing amounts of salts. The concentrations of NaCl are chosen by checking the stability of EG $n$ -AuNPs at room temperature and choosing the highest concentrations that allow them to form stable suspensions. The analysis of the temperature titration experiments monitored by UV-visible spectroscopy and dynamic light scattering allows us to establish the existence of transitions from individual to assembled nanoparticles, the reversibility of the temperature transitions and hysteretic behaviour in these systems. While EG7-AuNPs only show reversible temperature transitions in the presence of 5 mM NaCl, EG18-AuNPs do up to 1 M NaCl, becoming only partially reversible in 2 M NaCl. The titrations of EG45-AuNPs in 3 and 5 M NaCl show irreversible temperature transitions. Finally, EG136-AuNPs present a complex and interesting behaviour with two temperature transitions, the first one showing hysteresis and the second being reversible.

Received 27th May 2021

Accepted 2nd July 2021

DOI: 10.1039/d1na00392e

rsc.li/nanoscale-advances

## Introduction

Surface-grafted polymers or polymer brushes are currently used in macroscopic and nanoscopic surfaces such as gold nanoparticles (AuNPs) as they confer many interesting properties that are necessary in their applications for *in vivo* systems. One of these properties is biocompatibility and a very popular strategy followed to endow nanomaterials with it is by surrounding their surface with polyethylene glycol of different chain lengths (EG $n$ ), a process known as PEGylation.<sup>1,2</sup> It is considered that the hydrophilic and uncharged nature of EG $n$  molecules helps to avoid to a great extent the unspecific adsorption of proteins and the recognition by the immune system.<sup>3</sup> These properties of the EG $n$  protected AuNPs (EG $n$ -AuNPs) are believed to be determined by the length and grafting density of the chains in the surface, and recently, it has been reported that the specific chemical properties of the ligands are the major driving force determining the composition of the

protein corona that ultimately will be responsible for the prolongation of the blood circulation time and the immune response of the nanoparticles.<sup>4,5</sup> One of the most important parameters determining the interaction of nanoparticles with proteins is the grafting density of EG $n$  used to protect the surface and therefore its related chain conformation.<sup>6</sup> To determine the grafting density, many approximations have been reported that include nuclear magnetic resonance spectroscopy,<sup>5,7,8</sup> thermogravimetric analysis,<sup>9</sup> isothermal titration calorimetry,<sup>9</sup> analytical ultracentrifugation and total organic carbon analysis,<sup>10</sup> among others. The chain conformation of the surface-grafted polymer dictates the interfacial properties, and as described in the Alexander-de-Gennes theory,<sup>11,12</sup> good solvents make interactions with the solvent preferred over these with other polymer chains. Thus, under low grafting densities, there are no lateral constraints, and the polymer adopts a swollen conformation, behaving like a free polymer in solution, and the Flory radius describes the size of the random coil that is formed by such a polymer in the solution.<sup>13</sup> This structure is called the mushroom conformation. When the grafting density is high, the polymer chains are forced into a stretched or brush conformation.<sup>14</sup>

The grafting densities of EG $n$  in AuNPs are influenced by the EG $n$  molecular weight and the size of the nanoparticle,

Department of Physical Chemistry and Applied Thermodynamics, Institute of Fine Chemistry and Nanochemistry, University of Córdoba, Campus Rabanales, Ed. Marie Curie 2<sup>a</sup> Planta, E-14014 Córdoba, Spain. E-mail: tpineda@uco.es

† Electronic supplementary information (ESI) available. See DOI: 10.1039/d1na00392e



Contents lists available at ScienceDirect

Journal of Electroanalytical Chemistry

journal homepage: [www.elsevier.com/locate/jelechem](http://www.elsevier.com/locate/jelechem)

## Electrochemical evaluation of the grafting density of self-assembled monolayers of polyethylene glycol of different chain lengths formed by the grafting to approach under conditions close to the cloud point



Miriam Chávez, Guadalupe Sánchez-Obrero, Rafael Madueño, José Manuel Sevilla, Manuel Blázquez, Teresa Pineda\*

Department of Physical Chemistry and Applied Thermodynamics, Institute of Fine Chemistry and Nanotechnology, University of Córdoba, Campus Rabanales, Ed. Marie Curie 2ª Planta, E-14014 Córdoba, Spain

### ARTICLE INFO

**Keywords:**  
Poly-ethylene glycol  
Self-assembled monolayer  
Grafting density  
Cloud point  
Reductive desorption

### ABSTRACT

Grafting densities of polymers on gold surfaces are important parameters that inform about the chain conformation adopted by the chains, either mushroom or brush conformation. Most of the literature reports on this topic are based on ellipsometry measurements with other few results obtained from surface plasmon on resonance or quartz crystal microbalance. In this work, we report the use of cyclic voltammetry of the reductive desorption (RD) process of mercapto-polyethylene glycol self-assembled monolayers (EGn-SAMs) to get the grafting densities of these polymers with different chain lengths (c.a. EG136, EG45 and EG18). When the EGn-SAMs are formed from aqueous solutions where the polymer chains are highly hydrated, an excess of charge density is obtained that apart from the capacitive contribution found in these processes, include an extra charge due to the hydrogen evolution reaction (HER) produced by the high ratio of water contained in the film that reduces concomitantly with the SAM RD process. However, preparing the EGn-SAM in the presence of high salt concentrations that lowers the water content within the chains, that is, using the cloud point strategy, very realistic grafting density values are obtained. The RD profiles of the EGn-SAMs completely change from a broad peak with high charge density to a structured peak that allows us the determination of grafting density values. Capacitance curves and the behavior of the electrochemical process of the  $\text{Fe}(\text{CN})_6^{3-/4-}$  redox pair in the presence of the films are also in agreement with the CV results. The grafting density values obtained by this methodology are higher than those reported for these SAMs by using other techniques but agree with the footprints expected for these chains when organized in a brush conformation. Moreover, they also are close to the values obtained by thermogravimetric analysis of the same films built on gold nanoparticles that behave as planar surfaces.

### 1. Introduction

Self-assembled monolayers of alkanethiols (C-SAMs) and oligo (ethylene glycol)-terminated alkanethiols (EG-C-SAMs) formed on noble metal surfaces have been widely studied because of their organized structures and capability to be tailored with different chemical functionalities in the exposed interface [1–4]. The fact that poly(ethylene glycol) (EGn) has demonstrated to prevent protein unspecific adsorption has stimulated great efforts in research dealing with the adsorption on different solid surfaces, through a strategy known as PEGylation [5], to make these surfaces biocompatible.

Most of the studies of biocompatibility have used EG-C-SAMs as model systems since the alkanethiol arm forces the organization of the whole molecule and adopting the EGn portion a helicoidal or all-trans conformation [6–11]. Thus, the influence of the number of EG moieties, the terminal group and the nature of the metal substrate have been studied to find out the origin of the biocompatibility of these films. However, most of the PEGylated surfaces used in biological systems are built with EGn chains devoid of the alkane arm, and most frequently with larger EGn than those used in the model studies. Thus, knowledge on the organization of these layers is still necessary to get more insight into the actual structure when EGn is directly attached to metal surfaces. One of the most important parameters in

\* Corresponding author.

E-mail address: [tpineda@uco.es](mailto:tpineda@uco.es) (T. Pineda).

<https://doi.org/10.1016/j.jelechem.2022.116294>

Received 18 February 2022; Received in revised form 4 April 2022; Accepted 5 April 2022

Available online 8 April 2022

1572-6657/© 2022 The Author(s). Published by Elsevier B.V.

This is an open access article under the CC BY-NC-ND license (<http://creativecommons.org/licenses/by-nc-nd/4.0/>).



Contents lists available at ScienceDirect

Journal of Electroanalytical Chemistry

journal homepage: [www.elsevier.com/locate/jelechem](http://www.elsevier.com/locate/jelechem)

## Self-assembled monolayers of O-(2-Mercaptoethyl)-O'-methyl-hexa(ethylene glycol) (EG7-SAM) on gold electrodes. Effects of the nature of solution/electrolyte on formation and electron transfer blocking characteristics



Miriam Chávez, Guadalupe Sánchez-Obrero, Rafael Madueño, José Manuel Sevilla, Manuel Blázquez, Teresa Pineda\*

Department of Physical Chemistry and Applied Thermodynamics, Institute of Fine Chemistry and Nanodiagnostics, University of Córdoba, Campus Rabanales, Ed. Marie Curie 2<sup>a</sup> Planta, E-14014 Córdoba, Spain

### ARTICLE INFO

#### Keywords:

Polyethylene glycol  
Self-assembled monolayer  
Gold electrode  
Cyclic voltammetry  
Electrochemical impedance spectroscopy  
Contact angle measurements

### ABSTRACT

The self-assembly of O-(2-Mercaptoethyl)-O'-methyl-hexa(ethylene glycol) (EG7) on gold substrates produces monolayers whose structure should depend primarily on the solvents used for their formation. Although this should be also the case for any self-assembled monolayer (SAM) system, the presence of oxygen atoms in the EG7 chains brings about specific interactions with the solvent molecules other than just the van der Waals interactions taking place with alkanethiols. In this work we investigate the effects of the nature of the solutions for EG7-SAM formation in the reductive desorption processes using gold substrates either polycrystalline or single crystal electrodes. The patterns obtained in polycrystalline substrates are compared to the peaks observed at gold single crystal electrodes and it has been found that the main peaks correspond to the molecules desorbed from the different gold facets contained in the polycrystalline substrate. These single peaks are in fact composed of at least two contributions that can be explained as the presence of domains where the EG7 molecules are organized with different orientations, giving place to intermolecular interactions of different magnitude. The blocking properties of these films are strongly determined by the nature of the electrolyte used for the analysis and not by the solvent used in their formation. Although no experimental evidence of the specific interaction and/or retention inside the film of Na<sup>+</sup> or phosphate or both ions is obtained, a specific effect that accounts for an electron transfer rate constant of an order of magnitude lower than the obtained with other electrolytes is observed. These results can contribute to increase the understanding of the relationship between the EG7-SAMs structure and functionalities.

### 1. Introduction

The construction of multifunctional interfaces with tailored properties is an important research topic that is nowadays attracting the attention in the field of biocompatible and functional materials. Self-assembled monolayers (SAMs) constitute one of the most utilized strategies to create functional interfaces due to the easy preparation and the huge number of molecules available to assemble on different solid surfaces [1,2].

The dynamic equilibrium governing the adsorption of thiols on solid surfaces is influenced by the solvent-substrate and the solvent-adsorbate interactions, and the rates of formation depend on the magnitude of

these interactions that can be tuned by the solvent-adsorbate interaction strength [1]. In this sense, the use of polar solvents that present low solubility for alkanethiols can contribute to their assembly at the substrate surface [3,4]. Results obtained by scanning tunneling microscopy have shown that solvents of high polarity improve the quality of alkanethiol SAMs due to the strong hydrophobic interactions between the nonpolar hydrophobic tails, whereas the low polarity solvents can disturb the tight packing of the monolayer [5]. The presence of surfactants of low critical micellar concentration in water solutions has demonstrated to contribute to the formation of highly compact alkanethiol SAMs by providing hydrophobic domains that solubilize the alkane tails and facilitate their delivery to the substrate surface [6–13].

\* Corresponding author.

E-mail address: [tpineda@uco.es](mailto:tpineda@uco.es) (T. Pineda).

<https://doi.org/10.1016/j.jelechem.2022.116303>

Received 27 December 2021; Received in revised form 31 March 2022; Accepted 8 April 2022

Available online 11 April 2022

1572-6657/© 2022 The Author(s). Published by Elsevier B.V.

This is an open access article under the CC BY-NC-ND license (<http://creativecommons.org/licenses/by-nc-nd/4.0/>).





Contents lists available at ScienceDirect

Journal of Electroanalytical Chemistry

journal homepage: [www.elsevier.com/locate/jelechem](http://www.elsevier.com/locate/jelechem)

## Characterization of self-assembled Bis[2-(2-bromoisobutyryloxy) undecyl] disulphide (DTBU) on gold surfaces suitable for use in surface-initiated atom transfer radical polymerization (SI-ATRP)



Miriam Chávez, Laura Fuentes-Rodríguez, Guadalupe Sánchez-Obrero, Rafael Madueño, José Manuel Sevilla\*, Manuel Blázquez, Teresa Pineda

Departament of Physical Chemistry and Applied Thermodynamics, Institute of Fine Chemistry and Nanotechnology, University of Córdoba, Campus Rabanales, Ed. María Curie 2ª Planta, E-14014 Córdoba, Spain

### ARTICLE INFO

#### Keywords:

DTBU radical polymerization initiator  
Self-assembled monolayers  
6-Mercaptopurine (6MP)  
Mixed monolayers  
Cyclic voltammetry  
Electrochemical Impedance Spectroscopy  
Contact angle  
XPS

### ABSTRACT

Bis[2-(2-bromoisobutyryloxy) undecyl] disulphide (DTBU) is an initiator for surface-initiated atom transfer radical polymerization (SI-ATRP) able to functionalize metal surfaces through formation of self-assembled monolayers (SAM). The goal of this work is the making monolayers with the DTBU initiator on gold polycrystalline electrodes and their study by electrochemical methods as cyclic voltammetry (CV), capacity-potential curves (C-E), electrochemical impedance spectroscopy (EIS), and angle contact measurements for their characterization. Information of the integrity and permeability of the monolayers has been obtained by capacitance-potential measurements and impedance spectra. Also, the blocking effect of the physical barrier that SAM can produce to different redox probes is explored by using voltammetry and impedance. DTBU forms a compact monolayer whose main features are related with heterogeneous chain structures, having a non-polar hydrocarbon internal part and a polar head group. This is confirmed by X-ray photoelectron spectroscopy (XPS) which shows the presence of the elements of the DTBU adsorbate of SAM. Moreover, mixed monolayers of DTBU and 6-mercaptopurine (6MP) have been prepared and characterized, to check if the thiol facilitates electron exchange through monolayers. On this approach, different DTBU:6MP ratios have been employed and characterized studying IRRAS spectra, electrochemical properties, and contact angle on the modified surface. These mixed monolayers provide optimal conditions for adaptation and use in e-ATRP.

### 1. Introduction

Atom transfer radical polymerization (ATRP) is one of the polymerization techniques used to produce polymers in a controlled manner [1–5], both from the point of view of the polydispersity and the nature and structure of the final product as copolymers, linear, branched structures, etc. This radical polymerization initiated on a surface (SI-ATRP) providing a way to functionalize a wide variety of substrates with polymers [6]. Its versatility and tolerance towards a wide variety of functional groups has turned this reaction into a synthesis technique widely used to prepare brush polymers [7–11] special relevance due to their applications in the field of nanomedicine [12,13].

The self-assembled monolayers (SAM) represent a suitable approach to the design of surface chemistry in a wide range of metal substrates since the assembly of small molecules offers a convenient, simple, and highly versatile system to modify the intrinsic properties

of the surface [14–17]. Also, properties such as mechanical stability, electrical conductivity, activation potential and reactivity are essential in the initiator bound to the substrate to obtain a good yield and control in the polymerization reaction.

One of the basic objectives of the studies on the formation of a SAM with an initiator molecule for the SI-ATRP, and with electrochemical mediation (e-ATRP), is to find the experimental conditions on the surface where the electronic transfer itself of redox catalyst is facilitated, typically a copper complex with the associated pair Cu(II)/Cu(I) [10,11]. Li et al., have studied this aspect, after observing that, although short chains seem a good option because of the poorer packaging of SAM that facilitates electronic transfer [18], the polymer growth with these chains is very limited.

On the other hand, chains like those of DTBU (Bis[2-(2-bromoisobutyryloxy) undecyl] disulphide (Scheme 1) inhibit the transfer of the catalyst pair, so the alternative was to assemble a mixed mono-

\* Corresponding author.

E-mail address: [qm.sevill@um.es](mailto:qm.sevill@um.es) (J.M. Sevilla).

<https://doi.org/10.1016/j.jelechem.2022.116515>

Received 22 March 2022; Received in revised form 18 May 2022; Accepted 8 June 2022

Available online 10 June 2022

1572-6657/© 2022 Published by Elsevier B.V.

This is an open access article under the CC BY-NC-ND license (<http://creativecommons.org/licenses/by-nc-nd/4.0/>).

En todos los casos se dispone del permiso de la editorial Elsevier para incluir en la presente memoria los trabajos publicados derivados de la investigación. Por su parte, el artículo “Distinct thermoresponsive...”, publicado en *Nanoscale Advances*, es *Open Access*.



**Electrochemical evaluation of the grafting density of self-assembled monolayers of polyethylene glycol of different chain lengths formed by the grafting to approach under conditions close to the cloud point**  
Author: Miriam Chávez, Guadalupe Sánchez-Obrero, Rafael Madueño, José Manuel Sevilla, Manuel Blázquez, Teresa Pineda  
Publication: Journal of Electroanalytical Chemistry  
Publisher: Elsevier  
Date: 15 May 2022  
© 2022 The Author(s). Published by Elsevier B.V.

#### Journal Author Rights

Please note that, as the author of this Elsevier article, you retain the right to include it in a thesis or dissertation, provided it is not published commercially. Permission is not required, but please ensure that you reference the journal as the original source. For more information on this and on your other retained rights, please visit: <https://www.elsevier.com/about/our-business/policies/copyright#Author-rights>

BACK

CLOSE WINDOW



**Characterization of self-assembled Bis[2-(2-bromoisobutyryloxy) undecyl] disulphide (DTBU) on gold surfaces suitable for use in surface-initiated atom transfer radical polymerization (SI-ATRP)**  
Author: Miriam Chávez, Laura Fuentes-Rodríguez, Guadalupe Sánchez-Obrero, Rafael Madueño, José Manuel Sevilla, Manuel Blázquez, Teresa Pineda  
Publication: Journal of Electroanalytical Chemistry  
Publisher: Elsevier  
Date: 1 August 2022  
© 2022 Elsevier B.V. All rights reserved.

#### Journal Author Rights

Please note that, as the author of this Elsevier article, you retain the right to include it in a thesis or dissertation, provided it is not published commercially. Permission is not required, but please ensure that you reference the journal as the original source. For more information on this and on your other retained rights, please visit: <https://www.elsevier.com/about/our-business/policies/copyright#Author-rights>

BACK

CLOSE WINDOW




**Self-assembled monolayers of O-(2-Mercaptoethyl)-O'-methyl-hexa(ethylene glycol) (EG7-SAM) on gold electrodes. Effects of the nature of solution/electrolyte on formation and electron transfer blocking characteristics**  
Author: Miriam Chávez, Guadalupe Sánchez-Obrero, Rafael Madueño, José Manuel Sevilla, Manuel Blázquez, Teresa Pineda  
Publication: Journal of Electroanalytical Chemistry  
Publisher: Elsevier  
Date: 1 June 2022  
© 2022 The Author(s). Published by Elsevier B.V.

#### Journal Author Rights

Please note that, as the author of this Elsevier article, you retain the right to include it in a thesis or dissertation, provided it is not published commercially. Permission is not required, but please ensure that you reference the journal as the original source. For more information on this and on your other retained rights, please visit: <https://www.elsevier.com/about/our-business/policies/copyright#Author-rights>

BACK

CLOSE WINDOW



**Characterization of a self-assembled monolayer of O-(2-Mercaptoethyl)-O'-methyl-hexa(ethylene glycol) (EG7-SAM) on gold electrodes**  
Author: Miriam Chávez, Guadalupe Sánchez-Obrero, Rafael Madueño, José Manuel Sevilla, Manuel Blázquez, Teresa Pineda  
Publication: Journal of Electroanalytical Chemistry  
Publisher: Elsevier  
Date: 1 January 2021  
© 2020 Elsevier B.V. All rights reserved.

#### Journal Author Rights

Please note that, as the author of this Elsevier article, you retain the right to include it in a thesis or dissertation, provided it is not published commercially. Permission is not required, but please ensure that you reference the journal as the original source. For more information on this and on your other retained rights, please visit: <https://www.elsevier.com/about/our-business/policies/copyright#Author-rights>

BACK

CLOSE WINDOW

